**Transient numerical modeling of proton-exchange-membrane fuel cells**

by

Aslan Kosakian

A thesis submitted in partial fulfillment of the requirements for the degree of

Doctor of Philosophy

Departments of Mechanical Engineering and Mathematical and Statistical Sciences
University of Alberta

# Abstract

Hydrogen fuel cells convert the chemical energy of hydrogen directly into electricity, with the only byproducts being heat and water. The high cost of hydrogen fuel cells due to the expensive platinum catalyst is one of the limiting factors to their global commercialization. Improving fuel-cell performance while reducing the required amount of the catalyst can be achieved by optimizing the water balance in the cell that aims at striking a balance between electrolyte dry-out, which leads to high ohmic resistance, and liquid-water accumulation, which results in reactant starvation. Interpretation of the experimental measurements necessary for making design decisions is, however, often challenging due to the sub-millimeter scale of the fuel-cell components.

Mathematical models have become a valuable instrument for gaining insight into the physical processes taking place in fuel cells. Because of the coupled electrochemical reactions, heat, mass, and charge transport that occur at multiple spatial and temporal scales, fuel-cell modeling is a complex task that is best addressed with the help of numerical simulations. As the common fuel-cell characterization experiments are dynamic in nature, their analysis requires transient models.

In this thesis, an open-source transient numerical model of a hydrogen fuel cell is developed. The model is applied to interpret electrochemical impedance spectra of fuel cells, highlight the shortcomings of the analytical methods previously used for this purpose, and to better understand liquid-water dynamics in fuel cells.

First, the transient model is used to analyze water-management signatures in fuel-cell impedance spectra under dry conditions. This work shows that the low-frequency

inductive behavior observed experimentally in hydrogen fuel cells is influenced by the finite-rate water uptake by the electrolyte and water transport within the electrolyte, which impact the frequency and the size of the inductive loops in the spectra. An ohmic-resistance breakdown performed with the model shows that the high-frequency resistance extracted from the impedance spectra does not contain the protonic resistance of the carbon-supported catalyst layers (CLs) and, therefore, is not equivalent to the total ohmic resistance of the cell.

Impedance spectroscopy is commonly used to measure the charge-transport properties of catalyst layers. Some of the analytical impedance expressions in the literature disagree in the equation that relates the conductivity and resistance of the uniform CLs. The numerical model developed in this thesis is used to inspect that disagreement and to examine the impact of the catalyst-layer nonuniformity on its impedance. Practical recommendations for the experimentalists as to which analytical model, and under what conditions, should be used to reliably characterize charge transport in CLs are provided.

Finally, a novel transient two-phase fuel-cell model is developed that incorporates a pore-size-distribution sub-model to establish relationships between the microstructure of the porous fuel-cell components, their liquid- and gas-transport properties, and, ultimately, liquid-water flooding. Those relationships allow for the systematic analysis of the impact of the electrode design on the dynamic fuel-cell performance under the operating conditions that help keep the electrolyte hydrated but favor liquid-water production. For instance, the model captures how the liquid-water accumulation and drainage cycles translate into unstable fuel-cell performance.

The developed transient fuel-cell model will serve as the foundation for more advanced studies in the future, such as the simulations of membrane and catalyst degradation, carbon corrosion, and cold start-up. The open-source design of the developed software makes it an attractive option for the fuel-cell modeling community.

# Preface

Parts of Chapter 3 were reproduced with permission from D. Novitski, A. Kosakian, T. Weissbach, M. Secanell, and S. Holdcroft, "Electrochemical reduction of dissolved oxygen in alkaline, solid polymer electrolyte films," *Journal of the American Chemical Society*, vol. 138, no. 47, pp. 15 465–15 472, 2016 (Copyright 2016 American Chemical Society; available online at https://doi.org/10.1021/jacs.6b09217). I was responsible for numerical-model development, curve-fitting-code development, software implementation, data analysis (numerical model), manuscript writing (numerical model), and review. D. Novitski, T. Weissbach, and S. Holdcroft were academic collaborators. D. Novitski was responsible for conceptualization, literature review, conducting experiments, data analysis (experiments and analytical model), manuscript writing, and review. T. Weissbach was responsible for conducting experiments, data analysis (experiments), manuscript writing, and review. M. Secanell was the supervising author and assisted with software development (numerical model and curve-fitting code), manuscript review, and editing. S. Holdcroft was the supervising author and provided help with conceptualization, manuscript review, and editing.

Parts of Chapters 1, 2, and 4 have been published as A. Kosakian, L. Padilla Urbina, A. Heaman, and M. Secanell, "Understanding single-phase water-management signatures in fuel-cell impedance spectra: A numerical study," *Electrochimica Acta*, vol. 350, p. 136 204, 2020 (available online at https://doi.org/10.1016/j.electacta.2020.136204). I was responsible for conceptualization, literature review, model development, software implementation, conducting impedance-spectroscopy experiments, data analysis, and manuscript writing and review. L. Padilla Urbina was responsi-

ble for conducting experiments, technical discussions, and data analysis. A. Heaman assisted with software development. M. Secanell was the supervising author and provided help with conceptualization, software development, manuscript review, and editing.

Parts of Chapters 1 and 5 have been published as A. Kosakian and M. Secanell, "Estimating charge-transport properties of fuel-cell and electrolyzer catalyst layers via electrochemical impedance spectroscopy," *Electrochimica Acta*, vol. 367, p. 137 521, 2021 (available online at https://doi.org/10.1016/j.electacta.2020.137521). I was responsible for conceptualization, literature review, model development, software implementation, data analysis, and manuscript writing and review. M. Secanell was the supervising author and provided help with conceptualization, software development, manuscript writing and review, and editing.

Parts of Chapters 1, 2, and 6 are being prepared for an upcoming publication A. Kosakian, F. Wei, S. Jung, J. Zhou, A. Punia, J. Liu, and M. Secanell, "A transient, pore-size-distribution-based model for the analysis of the two-phase water transport in fuel cells," (in preparation). I am responsible for conceptualization, literature review, macrohomogeneous-model development, software implementation, data analysis, and manuscript writing and review. F. Wei is responsible for conducting experiments, data analysis, and manuscript writing and review. S. Jung is responsible for full-morphology- and stochastically-reconstructed-model development and software implementation, data analysis, and manuscript writing and review. J. Zhou was responsible for steady-state macrohomogeneous-model development during his time at ESDL and is responsible for manuscript review. A. Punia provided assistance with software development for fitting pore-size distributions and is responsible for manuscript review. J. Liu helped with obtaining pore-size-distribution fits and is responsible for manuscript review. M. Secanell was the supervising author and provided help with conceptualization, software development, manuscript review, and editing.

Parts of Chapter 2 have been prepared for an upcoming publication M. Secanell and A. Kosakian, "Membrane-electrode-assembly modeling using OpenFCST," in *PEMFC characterization and modelling – Current trends and challenges*, J. Stumper and J. Jankovic, Eds. de Gruyter, (in preparation). M. Secanell and I contributed equally to that publication and were responsible for conceptualization, literature review, data analysis, manuscript writing, and review. M. Secanell was the supervising author. The copyright remains with the authors and not the publisher (de Gruyter), as this thesis is published first. Nevertheless, the used materials have been significantly modified to avoid potential disputes.

I have co-authored the following publication: M. Secanell, A. Jarauta, A. Kosakian, M. Sabharwal, and J. Zhou, "PEM fuel cells, modeling," in *Encyclopedia of Sustainability Science and Technology*, R. A. Meyers, Ed. Springer New York, 2017, pp. 1–61, ISBN: 978-1-4939-2493-6 (available online at https://doi.org/10.1007/978-1-4939-2493-6_1019-1). M. Secanell, A. Jarauta, M. Sabharwal, J. Zhou, and I contributed equally to that publication and were responsible for conceptualization, literature review, manuscript writing, and review. M. Secanell was the supervising author. No material from that publication has been intentionally copied in this thesis. However, parts of Chapter 2 describe concepts, mathematical models, equations, and physical phenomena that have been previously discussed in the aforementioned publication. License 4990320645990 was obtained on January 15, 2021 from the publisher (Springer) for the entirety of the publication in case of any incidental use of any material.

<div style="text-align: right">

Aslan Kosakian

August 12, 2021

</div>

*To my family*

# Acknowledgments

First and foremost, I thank my Ph.D. supervisor, Dr. Marc Secanell (Department of Mechanical Engineering), for making this thesis possible. Moving to Canada for my doctorate was a big change, and you made me feel welcome and at home throughout these years. The amount of knowledge and savviness you have in different areas of science and engineering continues to amaze me to this day, and you have always been someone I could look up to and learn from. Your humor and endless support will not be forgotten.

I would like to express my gratitude to my second Ph.D. supervisor, Dr. Petar Minev (Department of Mathematical and Statistical Sciences), for the guidance, all the mathematical discussions we had over the years, and for the occasional cups of tea.

Besides my two supervisors, I would like to thank Dr. Bob Koch (Department of Mechanical Engineering) of my supervisory committee for all the insightful comments.

My Ph.D. years at the University of Alberta would not have been nearly as joyful without my labmates at ESDL. Special thanks to Dr. Mayank Sabharwal; we had a blast. I remember vividly our late working nights, trips to conferences, and visits to national parks. It was a pleasure working with you, and I hope our paths will cross again in the future. Many thanks to Michael Moore and Ambuj Punia for always being there for me. Thank you, Michael, for being a good roommate, and thank you, Ambuj, for satisfying my cravings for Indian food and ice cream. Thank you, Chad Balen, for brightening your labmates' days with your amazing homemade desserts and for hosting me in Seattle during my visit. Fei Wei and Luis Padilla Urbina – you

# Table of Contents

# List of Tables

# List of Figures

# List of Symbols

**Constants**

i      imaginary unit

$F$      Faraday constant, $\approx$96485 C/mol

$R$      universal gas constant, $\approx$8.314 J/(mol·K)

**Greek**

$\alpha$      charge-transfer coefficient

$\eta$      overpotential, $\eta = \phi_{e^-} - \phi_{H^+} - E_{th}$, V

$\kappa$      thermal conductivity, W/(cm $\cdot$ K), or permeability, cm$^2$

$\lambda$      water content in the electrolyte, $\text{mol}_{H_2O}/\text{mol}_{SO_3^-}$

$\mu$      dynamic viscosity, g/(cm $\cdot$ s)

$\omega$      angular frequency, rad/s

$\phi$      electrical potential, V

$\rho$      density, g/cm$^3$

$\sigma$      electrical conductivity, S/cm

$\varepsilon$      volume fraction

$\xi$      portion of water produced electrochemically at the catalyst-ionomer interface

**Latin**

$\Delta\overline{S}_{overall}$   entropy change per mole of hydrogen, J/(mol $\cdot$ K)

$\boldsymbol{N}$     molar flux, mol/(cm$^2 \cdot$ s)

$\boldsymbol{n}$     normal unit vector

$\overline{H}$     molar enthalpy, J/mol

$\overline{H}_{\mathrm{lv}}$     molar latent heat of water vaporization, J/mol

$\overline{H}_{\mathrm{sorption}}$ molar enthalpy change due to water absorption/desorption by the electrolyte, J/mol

EW     equivalent weight of the electrolyte, g/mol$_{\mathrm{SO}_3^-}$

$\boldsymbol{v}$     velocity, cm/s

$A_{\mathrm{v}}$     volumetric active area, cm$^2_{\mathrm{cat}}$/cm$^3$

$b$     Tafel slope, V

$C$     volumetric double-layer capacitance, F/cm$^3$

$c$     concentration, mol/cm$^3$

$C^*$     areal double-layer capacitance, F/cm$^2$

$C_p$     specific heat capacity, J/(g $\cdot$ K)

$D$     diffusion coefficient, cm$^2$/s

$D_{\mathrm{T}}$     thermo-osmotic diffusion coefficient for water in the electrolyte, g/(cm $\cdot$ s $\cdot$ K)

$E_{\mathrm{th}}$     theoretical half-cell potential, V

$f_{\mathrm{ORR}}$     fraction of the overall entropy change due to oxygen-reduction reaction

$i$     areal current density, A/cm$^2$

$i_0$     areal exchange current density, A/cm$^2$

$j$     volumetric current density, A/cm$^3$

$k_\lambda$     rate of absorption/desorption of water by the electrolyte, 1/s

$k_{\mathrm{c}}$     rate of water condensation, mol/ (cm$^2 \cdot$ s)

$k_\text{e}$       rate of water evaporation, $\text{mol}/(\text{cm}^2 \cdot \text{s})$

$k_\text{l, out}$    rate of liquid-water removal from the GDL-channel interface, $\text{g}/(\text{cm}^2 \cdot \text{s})$

$k_\text{H}_2$      rate constant for hydrogen dissolution into the electrolyte, m/s

$k_\text{O}_2$      rate constant for oxygen dissolution into the electrolyte, m/s

$L$        thickness, μm (unless otherwise stated)

$M$       molar mass, g/mol

$n_\text{d}$       electro-osmotic drag coefficient for water in the electrolyte, $\text{mol}_{\text{H}_2\text{O}}/\text{mol}_{\text{H}^+}$

$p$        pressure, Pa

$R$       resistance, $\text{m}\Omega \cdot \text{cm}^2$ (unless otherwise stated)

$s$        liquid saturation

$T$       temperature, K

$t$        time, s

$V$       voltage, V

$x$        molar fraction

$Z$       impedance, $\text{m}\Omega \cdot \text{cm}^2$ (unless otherwise stated)

**Subscripts and superscripts**

$\Omega$       ohmic property

$\text{e}^-$       electron

$\text{H}^+$      hydrogen proton

$\text{H}_2$      hydrogen

$\text{H}_2\text{O}$    water

$\text{N}_2$      nitrogen

$\text{O}_2$      oxygen

0       property at the given operating conditions

c       capillary

ct      charge transfer

ct+pe   charge transfer, proton and electron transport

DC      direct current

dl      double layer

eff     effective transport property

eq      equilibrium

HF      high frequency

i       ionomer (electrolyte) phase

K       Knudsen

l       liquid

lw      liquid water

ox      oxygen transport

p       liquid-free pore phase

s       solid, electronically conductive phase

tot     total

w       water

wv      water vapor

# Chapter 1

# Introduction[1]

## 1.1 Motivation

Fuel cells, like batteries, convert chemical energy directly into electricity. Polymer-electrolyte fuel cells (PEFCs) are a common type of fuel cells primarily used in the transportation sector (including passenger vehicles, trucks, buses, forklifts, and aviation [7]), as well as in portable [7] and stationary power systems, such as residential combined-heat-and-power units [7]. As a fuel, hydrogen is an attractive option for PEFCs, since it can be produced from renewable and sustainable sources, such as biomass, wind, and solar energy [8]. The only byproducts of hydrogen fuel cells are water and heat, which makes them a more ecological alternative to the conventional combustion engines. With greenhouse emissions from the transportation sector reaching 25% in Canada [9] and 28% in the United States in 2018 [10], increasing the use of zero-emission vehicles is a necessary strategy for a substantial reduction in

---

[1]Parts of this chapter are reproduced from the following publications:

1. A. Kosakian, L. Padilla Urbina, A. Heaman, and M. Secanell, "Understanding single-phase water-management signatures in fuel-cell impedance spectra: A numerical study," *Electrochimica Acta*, vol. 350, p. 136 204, 2020.

2. A. Kosakian and M. Secanell, "Estimating charge-transport properties of fuel-cell and electrolyzer catalyst layers via electrochemical impedance spectroscopy," *Electrochimica Acta*, vol. 367, p. 137 521, 2021.

3. A. Kosakian, F. Wei, S. Jung, J. Zhou, A. Punia, J. Liu, and M. Secanell, "A transient, pore-size-distribution-based model for the analysis of the two-phase water transport in fuel cells," (in preparation).

Author contributions are detailed in the Preface of this thesis.

greenhouse-gas pollution. Battery-powered electric and hybrid vehicles have already become mainstream in urban areas, and fuel-cell-powered electric vehicles are also available in limited markets with a few models, such as Toyota Mirai [11], Honda Clarity [12], and Hyundai Nexo [13]. Due to the lower weight penalty and thus better scalability compared with batteries, fuel cells have attracted attention in the area of heavy-duty transportation as well [14].

Hydrogen fuel cells have achieved the 2020 U.S. Department of Energy (DoE) targets for specific power, power density, and cold start-up time [15, 16]. Still, durability of fuel-cell systems needs to be improved [16, 17] and their manufacturing cost needs to be reduced to meet the current and future DoE targets [16, 17]. Catalyst layers account for about 40% of the cost of large-volume-production fuel-cell stacks [16]. The total amount of the expensive platinum catalyst used in automotive hydrogen fuel cells is up to about 35 g (4–6 times higher than in the catalytic converters of conventional vehicles) [18], which translates to over \$1000 USD at the time of writing this thesis. Therefore, the use of platinum in the catalyst layers needs to be decreased or eliminated to meet the DoE cost targets [19]. Indeed, platinum loading has been reduced over the past two decades from about 1 $\mathrm{mg_{Pt}/cm^2_{CL}}$ to below 0.4 $\mathrm{mg_{Pt}/cm^2_{CL}}$ in commercial applications and to 0.125 $\mathrm{mg_{Pt}/cm^2_{CL}}$ in laboratory-scale fuel cells [18, 20]. For this cost-reduction strategy to be effective, it is imperative to increase the power output of the cell per gram of catalyst. This requires improvement in the electrode design to enable higher-current operation at the same voltage. Electrode design is, however, a challenging task due to the multitude of complex physical phenomena taking place in fuel cells: electrochemical reactions, heat, mass, and charge transport are coupled and occur at multiple spatial and temporal scales. While experimentation is the ultimate way of designing and characterizing PEFCs, the small size of their components and the lack of visual access make it difficult to interpret experimental data. Mathematical models are, therefore, required to obtain valuable insight into the internal processes occurring in fuel cells. Modeling is also often more time- and

cost-effective than conducting experiments, and, therefore, it is a valuable tool for fuel-cell design.

The vast majority of fuel-cell models available in the literature have been developed under the assumption of steady state [21–44]. However, the most common fuel-cell characterization method, polarization-curve measurement accompanied with ohmic-resistance estimation [45], is dynamic in nature, as it is performed via potentiodynamic or galvanodynamic sweeps. The resulting voltage-current and resistance-current relationships often contain hysteresis [46–52], primarily due to the water-transport dynamics [46, 49–51, 53, 54], and can only be analyzed with a time-dependent model. Electrochemical impedance spectroscopy (EIS) [45, 55, 56] is another example of a transient characterization technique. It allows for the representation of the dynamic processes of different time scales in the frequency domain, thus helping to resolve the issue of the overlapping transients in the polarization curves. Operation of fuel cells in the transportation sector is also dynamic due to the acceleration and deceleration of the vehicles [57–60]. Cyclic voltammetry is yet another example of a transient fuel-cell characterization technique. It is used for estimating, for instance, the electrochemically active surface area of the electrodes, their double-layer capacitance, and reactant crossover [45]. Thus, transient models are necessary both at the laboratory level, when developing new insights by analyzing the dynamic experimental measurements, and at the industrial level, when simulating real-life operation. The overall objective of this thesis is, therefore, development of a transient fuel-cell model that captures the key physical phenomena and is capable of simulating the common characterization techniques.
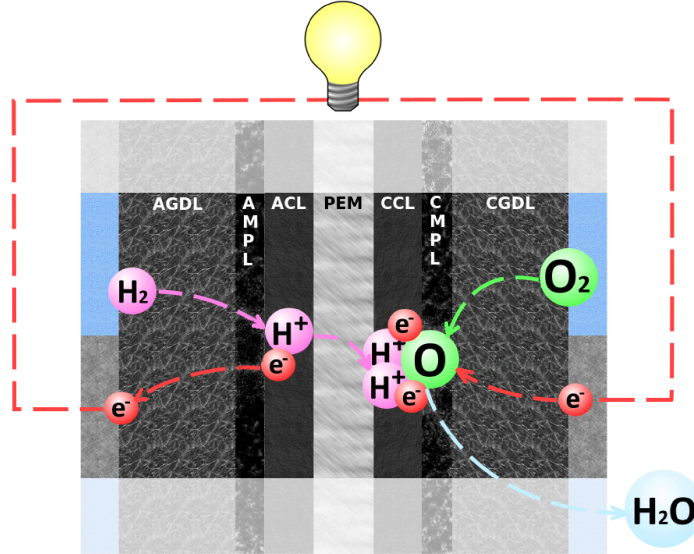
Figure 1.1: A schematic of a cross-section of a hydrogen fuel cell (not to scale). Letters "A" and "C" in the layer-name acronyms stand for "anode" and "cathode".

## 1.2 Hydrogen-Fuel-Cell Background

### 1.2.1 Principle of Operation

A schematic of a hydrogen fuel cell is shown in Figure 1.1. The outermost components of the cell are the bipolar plates (BPPs) with engraved or stamped gas channels that deliver hydrogen and oxygen (or air) to the two opposite sides of the membrane-electrode assembly (MEA). The gases are transported through the gas-diffusion layers (GDLs) and the microporous layers (MPLs) to the catalyst layers (CLs), where the electrochemical reactions occur.

In the hydrogen electrode, hydrogen oxidation reaction (HOR) takes place [61–63]:

$$H_2 \rightarrow 2H^+ + 2e^-. \tag{1.1}$$

Because electrons are produced in the oxidation reaction (1.1), the hydrogen electrode is referred to as the anode. In the oxygen electrode, oxygen reduction reaction (ORR) occurs [61–63]:

$$\frac{1}{2}O_2 + 2H^+ + 2e^- \rightarrow H_2O. \tag{1.2}$$

Electrons are consumed in this reduction reaction, and thus the oxygen electrode is

referred to as the cathode. The polymer electrolyte membrane (PEM), located at the center of the MEA, prevents the gas crossover between the electrodes and serves as an ionic filter that conducts $H^+$ and blocks the electron transport. Because the charged species exchanged between the two electrodes is a hydrogen proton, hydrogen-fueled PEFCs are commonly called proton-exchange-membrane fuel cells (PEMFCs). In this thesis, the term "fuel cell" will refer to PEMFCs.

Electrical energy is harvested by passing the electrons produced in reaction (1.1) through an external circuit before they take part in reaction (1.2). The overall reaction, obtained by combining reactions (1.1) and (1.2), is

$$H_2 + \frac{1}{2}O_2 \rightarrow H_2O. \tag{1.3}$$

The reaction above is exothermic [61, 62], and most of the heat is released in the ORR [64, 65]. The produced heat and water are removed from the cell via the ribs and channels of the bipolar plates. Depending on the operating conditions, this water can be in the form of vapor or liquid.

## 1.2.2 PEMFC Configuration

The simultaneous occurrence of mass and heat transfer, charge transport, and electrochemical reactions in a PEMFC requires intricate design of its components, each of which has different composition, structure, and functionality. Understanding those aspects is crucial for the development of a comprehensive mathematical model of a PEMFC. For that reason, the cell configuration is discussed next.

### 1.2.2.1 Bipolar Plates

Since the bipolar plates of fuel cells need to be electronically and thermally conductive, they are usually made of graphite or metals [66–71]. The flow fields, responsible for the delivery of the reactants and the removal of the product water, commonly have parallel or serpentine channels [71, 72]. The parallel-flow configuration generally leads to a lower pressure drop along the channels and a more uniform reactant distribution
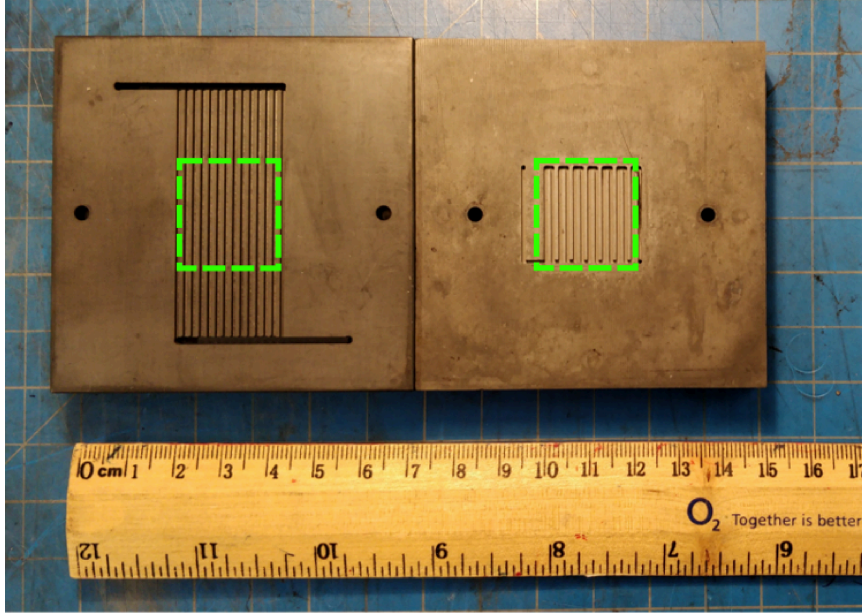
Figure 1.2: Graphite bipolar plates with parallel (left) and serpentine (right) channels used at the Energy Systems Design Laboratory, University of Alberta. The approximate size and location of the MEA are shown in the green frames.

in the MEA, but may suffer from channel blockage with liquid water that results in stagnant areas [72, 73]. The channels are typically rectangular in their cross-section, and their width and depth are 0.1–1 mm by the order of magnitude [71, 72, 74]. The bipolar-plate ribs have similar dimensions [72, 74]. The parallel- and serpentine-channel designs used at the Energy Systems Design Laboratory (ESDL), University of Alberta, are shown in Figure 1.2.

#### 1.2.2.2 Gas-Diffusion Layers

Gas-diffusion layers of PEMFCs help distribute the reactants uniformly in the catalyst layers and serve as electronic conductors [75]. They also provide the means for water and heat removal from the cell [75]. These layers are usually 100–400-μm-thick [75–77] and are made of a non-woven carbon paper or a woven carbon cloth with carbon fibers that have a diameter of 5–15 μm [75, 78–80]. Mass-, charge-, and heat-transport properties of GDLs are anisotropic due to the in-plane fiber orientation [81–85]. Gas-diffusion layers have a typical porosity of 0.7–0.9 and a mean pore

|  (a)  |  (b)  |
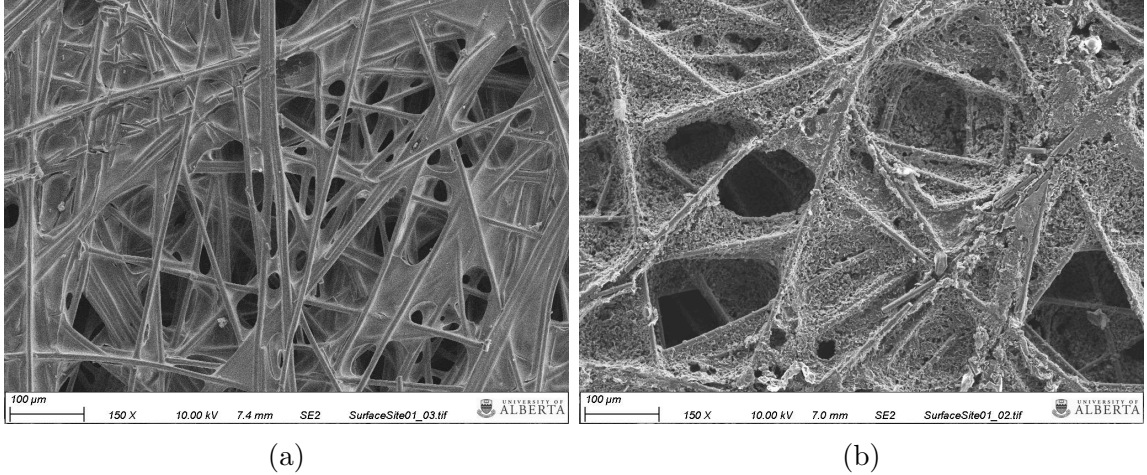
Figure 1.3: Scanning-electron-microscopy images of two GDLs: a) Toray 090 (20 wt%
PTFE); and b) SGL 28BA (5 wt% PTFE). The porous binder can be observed in the
28BA sample. The scale bars are 100 μm in both images. Image courtesy of Manas
Mandal (ESDL).

size of 10–100 μm [75–78, 86–88]. Some commercial GDLs, such as the Sigracet® se-
ries by SGL Group [87], are impregnated with a polymeric binder [75, 87, 89–91] that,
after carbonization, has the average pore radius of 0.1–2 μm [79]. Scanning-electron-
microscopy (SEM) images of two carbon-paper GDLs, one without a porous binder
(Toray 090) and one with it (SGL 28BA), are shown in Figure 1.3.

To aid liquid-water removal, GDLs are often submerged in polytetrafluoroethylene
(PTFE) during the fabrication process, which creates a hydrophobic coating of the
fibers [75, 87]. The resulting gas-diffusion layers have a mixed wettability, i.e., they
are partially hydrophobic (contact angle $\theta \in (90°, 180°]$) and partially hydrophilic
(contact angle $\theta \in [0°, 90°)$) [21, 75]. The mixed-wettability structure promotes
liquid-water transport within the GDLs while obstructing their complete flooding.

### 1.2.2.3 Microporous Layers

Microporous layers have the typical thickness of 16–100 μm [78, 92–94], porosity
of 0.3–0.8 [77, 88, 94–96], and the average pore size of 20–750 nm [86, 97–100].
The conventional MPLs are made of carbon-black particles (15–75 nm in radius [97,
101–103]) treated with PTFE [95, 97, 100, 104]. Microporous layers with carbon

7
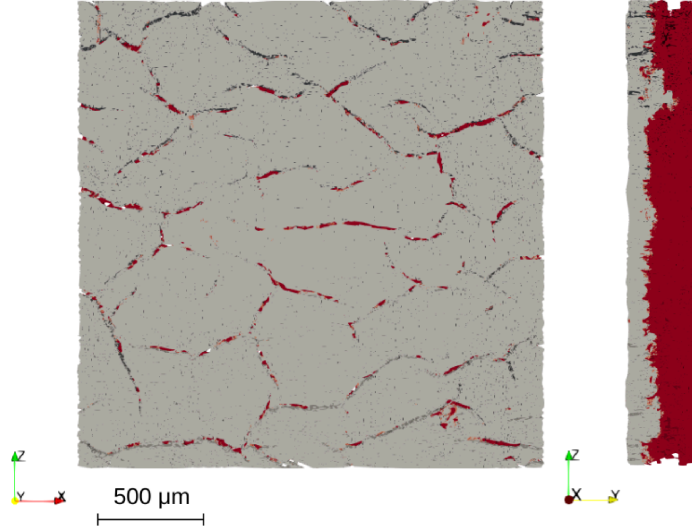
Figure 1.4: A segmented micro-computed-tomography (μCT) image of an SGL 38BC porous-transport layer. Gray: microporous layer; red: SGL 38BA gas-diffusion layer. Image courtesy of Seongyeop Jung (ESDL).

nanotubes (10–60 nm in diameter, 1–50 μm in length [105, 106]) also exist [105–107]. Microporous layers are usually deposited on top of the gas-diffusion layers to form the combined GDL-MPL porous-transport layers (PTLs), such as SGL 38BC shown in Figure 1.4.

The main function of the microporous layers is to enhance the mass, charge, and heat transfer between the gas-diffusion layers (larger pores) and the catalyst layers (smaller pores), thereby improving the cell performance [28, 35, 75, 86, 99, 100, 108–110]. In particular, MPLs reduce liquid-water saturation in GDLs [93, 111, 112] by promoting the back-diffusion of water from the cathode to the anode through the membrane [28, 35, 75, 100, 110], which also helps keep the PEM hydrated. Microporous layers also improve the reactant distribution in the catalyst layers by providing the means of gas transport around the liquid-saturated areas of the GDLs [35, 75, 100, 109, 113]. Other MPL functions include improving water vaporization to prevent flooding [35, 99] and protecting the membrane from being penetrated by the GDL fibers [21]. Microporous layers may have cracks (5–80 μm in width [78, 107, 109]) that act as liquid-water-removal pathways [40, 114, 115].

8

### 1.2.2.4 Membrane

The proton-exchange membranes used in PEMFCs, typically Nafion® membranes, are polymer electrolytes based on the perfluorosulfonic acid (PFSA) [116, 117]. Their thickness is on the order of 1–100 μm, with the modern PEMs being 5–25-μm-thick [116]. Nafion® membranes and films, often called ionomers, have an electrically neutral and hydrophobic PTFE backbone with polysulfonyl-fluoride-vinyl-ether side chains and pendant $SO_3^-$ ionic groups [116]. The latter are balanced with a hydrogen proton to form $SO_3H$ [116–118], to which water is bound via a hydrogen bond $\left(SO_3^- \cdot H_3O^+\right)$ [116]. Water uptake by the membrane (from the surrounding vapor or liquid water) enables hydrogen-proton dissociation from $SO_3H$ and proton conduction by two mechanisms: the translational motion of hydronium $\left(H_3O^+\right)$ [116] and Grotthuss hopping (exchange of $H^+$ in the hydrogen bonds of water molecules) [116–118]. As a result, the observed protonic conductivity of Nafion® membranes increases with water content [116, 117]. Therefore, it is important to keep the membrane in PEMFCs hydrated to achieve high performance.

### 1.2.2.5 Catalyst Layers

Catalyst layers are the most complex components of PEMFCs, with elaborate microstructure designed to enable the rich functionality from facilitating electrochemical reactions to the transport of gaseous reactants, liquid water, charge, and heat [119–134]. The electronically conductive skeleton of these layers is usually made of carbon-black particles that are 20–200 nm in diameter [130, 131, 134–136]. The surface of this carbon support constitutes a housing for the catalyst, typically platinum[2] [18, 137, 139], with the particle and particle-aggregate size of 2–10 nm [132–134]. The carbon-support particles are often made porous (primary-pore diameter up to 10 nm [122, 135]) to increase the surface area available for the catalyst deposition. Protonic con-

---

[2]Catalyst layers with non-precious-metal catalysts also exist and are in active stages of research and development aimed at improving their stability, durability, performance, and water management [20, 137, 138]; such layers, however, are not considered in this thesis.

ductivity and structural integrity of catalyst layers is achieved through a percolating network of a PFSA-based ionomer, such as Nafion$^{®}$ [116, 117], that is believed to at least partially cover the catalyst surface [21, 117, 140] by forming 1–10-nm-thick films [124, 132]. The ionomer, however, cannot enter the small pores of the carbon support [21, 135], and the accessibility of the platinum particles residing in those pores for the electrochemical reactions is hypothesized to be provided through water surrounding that platinum [21, 122, 135, 141, 142]. Catalyst layers have a mixed wettability that depends on the carbon-black type and the orientation of Nafion$^{®}$ side chains in space [117, 135].

An example porous structure of catalyst layers is illustrated in Figure 1.5 (note the ionomer is not visible in the presented SEM image). The diameter of the secondary pores between the carbon-platinum agglomerates of the PEMFC CLs is commonly between 10 and 100 nm [122, 131, 135, 136]. The overall porosity of the layer depends on the catalyst and ionomer loading and is typically between 0.2 and 0.7 [124, 125, 127, 134, 136, 143]. The amount of platinum and Nafion$^{®}$ in the layer also affects the CL thickness, which usually ranges from 1 to 20 μm [122, 124, 125, 127, 134]. Drying of the catalyst-layer ink during the layer fabrication may cause the formation of cracks [127, 144–146] with the effective pore diameter of over 50 μm [146]. While cracks improve gas transport under dry conditions [145, 147], they also result in a significantly lower layer conductivity [144, 145]. Liquid water can accumulate in the cracks [144, 145, 148] instead of flooding the smaller catalyst-layer pores. This, however, leads to the formation of inactive zones in the CL [144].

### 1.2.3 Cell Performance and Characterization

Polarization-curve measurement, electrochemical impedance spectroscopy, and cyclic voltammetry are common experimental techniques for fuel-cell performance analysis and characterization. Simulating cyclic voltammetry, however, requires detailed transient reaction-kinetics models and is beyond the scope of this thesis. Therefore, only
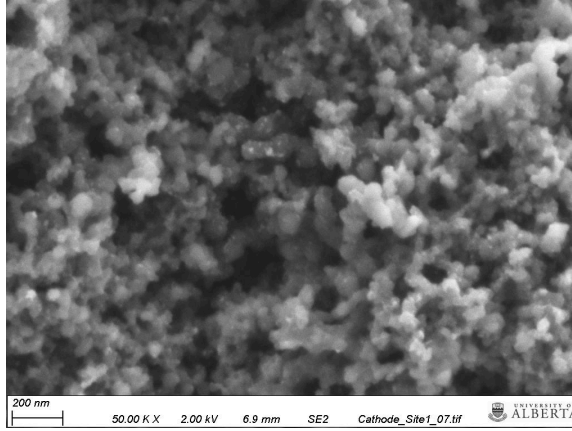
Figure 1.5: An SEM image of a PEMFC catalyst layer. The layer was fabricated in-house by Luis Padilla Urbina (ESDL) with the inkjet-printing method [124, 125, 149]. Catalyst loading was 0.15 $\mathrm{mg_{Pt}/cm^2_{layer}}$, Nafion$^{\circledR}$ loading was 30 wt%. The scale bar in the image is 200 nm. Image courtesy of Manas Mandal (ESDL).

polarization-curve and impedance measurements are discussed in this Section.

### 1.2.3.1 Polarization Curves

Fuel-cell performance is typically characterized through polarization curves that display the relationship between voltage and current. These curves are used to quantify the various voltage losses occurring in an operating cell.

The standard theoretical potential (thermodynamic potential) of a fuel cell is determined from the change in the Gibbs free energy of the reaction (1.3), $\Delta G^0$ [45, 61]:

$$E^0_{\mathrm{th}} = -\frac{\Delta G^0}{n_{\mathrm{e}} F},\tag{1.4}$$

where $n_{\mathrm{e}} = 2$ is the number of electrons transferred per mole of fuel (hydrogen). At standard conditions (25 °C, 1 atm) and assuming that water is produced in liquid form, $E^0_{\mathrm{th}} \approx 1.23$ V [45]. If water is produced in vapor form, $E^0_{\mathrm{th}}$ is approximately 1.18 V [45]. The change in the Gibbs free energy of a reagent depends on temperature and pressure through [61]

$$dG = -SdT + Vdp,$$

where $S$ is entropy. Then, the theoretical cell potential at the given operating condi-
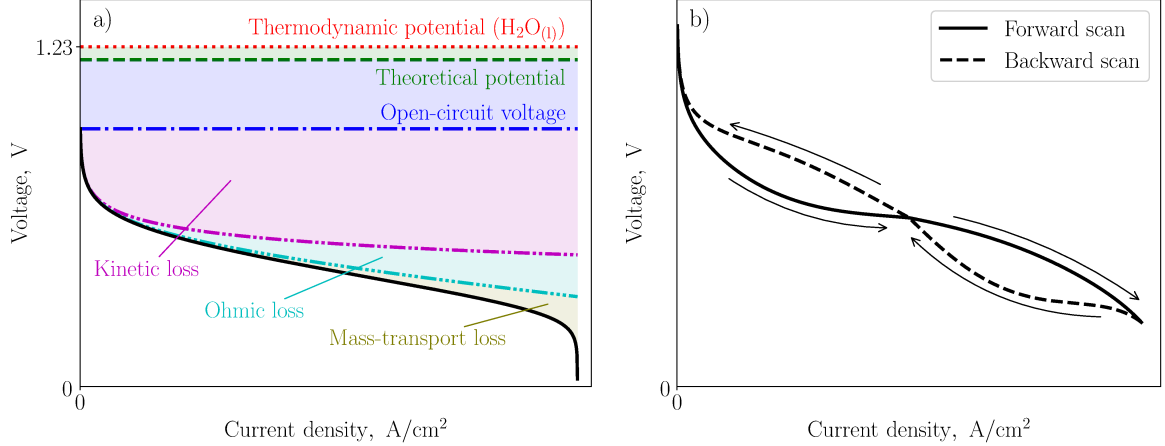
Figure 1.6: Example of a fuel-cell polarization curve: a) at steady state; b) in transient.

tions is [45, 61]

$$E_{\text{th}} = E_{\text{th}}^0 + \frac{\Delta S}{n_{\text{e}} F} \left( T - T^0 \right) + \frac{R T^0}{n_{\text{e}} F} \ln \left( \frac{p_{\text{H}_2} \sqrt{p_{\text{O}_2}}}{p_{\text{H}_2\text{O}}} \right), \quad (1.5)$$

where, for hydrogen fuel cells, $\Delta S < 0$ [61]. Operating a fuel cell at an elevated temperature is beneficial for the Arrhenius-type reaction rates [61]; however, according to equation (1.5), this leads to a voltage loss of about 1 mV/K [61]. Reactant gases are often humidified to keep the polymer electrolyte hydrated, and air is usually used instead of pure oxygen. This also results in a reduced cell potential, as evident from equation (1.5). Therefore, the theoretical cell potential at the typical fuel-cell operating conditions (80 °C, humidified reactants) is lower than 1.23 V by several millivolts. This deviation of $E_{\text{th}}$ from $E_{\text{th}}^0$ is illustrated in Figure 1.6a with a red dotted line and a green dashed line.

A potential difference (overpotential) between $E_{\text{th}}$ and the operating voltage leads to the generation of the faradaic (electrochemical) current. However, not all of that current flows through the external circuit. A few milliamperes of current [45] are used to offset the parasitic currents present in the electrodes due to reactant crossover through the membrane (which is not perfectly impermeable to gases). This compensation results in a shift of the potential at which the net current is zero from the theoretical potential to a lower value called the open-circuit voltage (OCV). The

magnitude of this deviation depends on the reactant-crossover rate. The OCV is illustrated with a blue dash-dotted line in Figure 1.6a.

When the overpotential is further increased, current starts to flow through the external circuit, forming a relationship between voltage and current called a polarization curve. Since the active area (the in-plane area) of the MEA may significantly vary between fuel cells, the generated current is often normalized per MEA area to give current density so that the performance of different cells can be compared. An example steady-state polarization curve is illustrated with a solid black line in Figure 1.6a. As current is drawn from the cell, three types of operational voltage losses occur: a) kinetic loss, predominant at low current; b) ohmic loss; and c) mass-transport loss, predominant at high current.

The amount of the faradaic current produced at a given overpotential depends on the catalyst-layer composition, such as the catalyst type and the surface area, and on the operating conditions, such as temperature, pressure, and reactant concentration [45, 150]. The overpotential associated with the generation of the faradaic current constitutes the kinetic loss, which is shown in the light-magenta area in Figure 1.6a. Strictly speaking, the difference between the theoretical potential and the OCV is a part of the activation overpotential (kinetic loss). However, it is not directly measured in the polarization-curve experiments; therefore, the crossover loss and the operational kinetic loss are shown as two distinct regions in Figure 1.6a.

The ohmic loss, demonstrated in light cyan in Figure 1.6a, occurs due to the electrical resistance of the cell components to the flow of current [45]. Protonic resistance of the electrolyte (the membrane and the ionomer phase of the catalyst layers) may account for a substantial part of the overall ohmic resistance of the cell [45], especially at high temperature and low humidity, when the protonic conductivity of Nafion® is reduced. This motivates the fuel-cell operation at a typical temperature range of 60–80 °C and with humidified reactant streams.

Cell geometry and structure of the porous cell components constraint the rate at

which the reactants are delivered to the catalyst layers. The higher the current, the larger the reactant-delivery rate should be to meet the rate of the electrochemical consumption. This explains why the mass-transport loss, depicted in light olive in Figure 1.6a, is more significant at high current. The rate of removal of the product water also affects mass transport. If the product water is not efficiently removed from the MEA, it may accumulate in the porous layers of the cell, thereby filling the pores in the media and eventually causing fuel-cell failure and shutdown due to flooding. Depending on the operating humidity, temperature, and pressure, liquid water generated in the cathode may also evaporate in the CL and then condense in the cooler regions of the cell (the so-called heat-pipe effect), thereby drastically affecting the reactant flow and reducing the performance of the cell. Thermal and water management are crucial for fuel-cell performance, since they help strike a balance between the electrolyte hydration and liquid-water flooding.

Polarization curves are usually measured by applying a linear or pseudo-linear (stair) sweep in either voltage or current. A complete sweep consists of a forward scan from high to low voltage or, equivalently, from low to high current and a subsequent backward scan in the opposite direction. Depending on the operating conditions and on the scan rate, dynamic electrolyte hydration and liquid-water accumulation may result in the appearance of hysteresis in the measured polarization curves [46, 49–52, 54]. This is illustrated in Figure 1.6b. If no significant flooding occurs, then the cell performance during the backward scan is better than during the preceding forward scan due to the better hydration of the electrolyte from the gas channels and water produced in the ORR in the cathode [46, 48, 50, 51, 53, 151]. If flooding occurs, reactant transport is obstructed by liquid water, and a self-crossing point is observed in the polarization curve, below which the backward-scan performance is worse than the forward-scan performance (Figure 1.6b). This point in the polarization curves is commonly called a threshold point, as it corresponds to a "threshold" current, below which the performance dynamics is dominated by the electrolyte hydration and

14

above - by the electrode flooding [46, 49–52, 54, 152]. The polarization-curve shape and the hysteresis magnitude may change between the subsequent voltage or current sweeps [49, 50], and more polarization-curve shapes may be observed, such as the one with partially coinciding forward and backward curves without self-crossing [50, 153] and the one during which the cell shuts down due to flooding, resulting in an incomplete polarization curve [50].

Using a high reactant flow rate or a high scan rate helps reduce flooding and improve the performance at high current density [46, 49–51], but also obstructs electrolyte hydration [46, 49–51]. Fast scans also do not represent the quasi-steady-state performance of the cell. Higher operating temperature mitigates flooding [46, 51, 152], however, it results in faster electrolyte dehydration at low current density and slower hydration at high current density [46]. Higher reactant humidification leads to significantly smaller hysteresis above the threshold point due to reduced membrane resistance as a result of better hydration, but also causes a performance decrease in the ohmic and mass-transport regions of the polarization curve due to liquid-water accumulation [51, 52]. Cell performance and hysteresis shape also depend on the cell composition. For instance, using more hydrophobic GDLs or adding hydrophobic MPLs has been shown to aid liquid-water removal, resulting in a smaller hysteresis below the threshold point [46, 152].

Thermal and water management is not the only factor affecting polarization-curve hysteresis. Platinum oxide has been reported to clear off the catalyst surface during the forward scan and to form again during the backward scan, with a lower platinum-oxide coverage during the latter half of the sweep [154, 155]. This results in a higher current density measured during the backward scan than during the forward scan [154, 156]. However, transient electrochemical kinetics are beyond the scope of this thesis.

Hysteresis also occurs in the ohmic resistance of the cell [46, 49–52, 157]. Since the rate of water production is directly proportional to the operating current, the polymer-electrolyte membrane and the ionomer phase of the catalyst layers absorb

water and become more protonically conductive by the end of the forward scan. As it takes time for water to leave the electrolyte, the ohmic resistance measured during the backward scan is typically lower, and hysteresis is observed.

### 1.2.3.2 Electrochemical Impedance Spectroscopy

Transient phenomena taking place in fuel cells occur at a number of time scales: sub-milliseconds for the HOR kinetics [158, 159] and 1 ms–1 s for the ORR kinetics [159–161], 10 ms–10 s for gas transport [160–164], 1–100 s for heat transfer [165, 166], 10–100 s for liquid-water transport [166], and 10–1000 s for membrane and catalyst-layer-ionomer hydration [159, 164, 166–168]. In addition to these processes, degradation mechanisms, such as carbon corrosion, platinum dissolution and redeposition, and cation contamination of the membrane, are observed over hundreds and thousands of operation hours [169, 170].

Dynamics of the aforementioned processes overlap during polarization-curve and ohmic-resistance measurements, which complicates their interpretation. Electrochemical impedance spectroscopy [45, 55, 56] allows for the separation of the physical processes at different time scales in the frequency domain and for the investigation of their relative importance in the overall dynamic behavior of the system. The EIS technique has been actively used in the experimental literature to investigate, for instance, charge transfer [160, 171, 172], protonic resistance of the catalyst layers [172–177], and mass transport [160, 171, 172, 178–180].

Fuel-cell impedance is typically measured by applying a sinusoidal voltage (or current) and measuring the current (voltage) output. If the amplitude of the input signal is sufficiently small, the output signal is also sinusoidal and has the same frequency as the input signal. In the time domain, voltage and current signals are given by

$$V(t,\omega) = V_{\mathrm{m}}(\omega)\sin\left(\omega t + \theta_V\right) \tag{1.6}$$

16

and

$$I(t, \omega) = I_\mathrm{m}(\omega) \sin (\omega t + \theta_I) . \tag{1.7}$$

Note that the signal magnitude is typically constant for the input signal, but may be frequency-dependent for the output signal. For a given angular frequency, $\omega$, the voltage and current phasors corresponding to the time-dependent signals (1.6) and (1.7) are given by [55]

$$V^*(\omega) = V_\mathrm{m}(\omega) e^{\mathrm{i}\theta_V}$$

and

$$I^*(\omega) = I_\mathrm{m}(\omega) e^{\mathrm{i}\theta_I} .$$

Impedance is then defined as the ratio of the voltage and current phasors [45, 55]:

$$Z(\omega) = \frac{V_\mathrm{m}(\omega)}{I_\mathrm{m}(\omega)} e^{\mathrm{i}(\theta_V - \theta_I)} . \tag{1.8}$$

The units of impedance are $\Omega$ or, if current density is used, $\Omega \cdot \mathrm{cm}^2$. Angle $\Delta\theta = \theta_V - \theta_I$ is the phase shift between the voltage and current signals. Impedance (1.8) is a complex number with a real part

$$\mathrm{Re}(Z(\omega)) = \frac{V_\mathrm{m}(\omega)}{I_\mathrm{m}(\omega)} \cos (\Delta\theta)$$

and an imaginary part

$$\mathrm{Im}(Z(\omega)) = \frac{V_\mathrm{m}(\omega)}{I_\mathrm{m}(\omega)} \sin (\Delta\theta) .$$

The real component of the fuel-cell impedance is a positive quantity, and thus $\Delta\theta$ is defined between $-\pi/2$ and $\pi/2$. When $\Delta\theta \in [-\pi/2, 0)$, voltage is said to lag current (and current is said to lead voltage) by $|\Delta\theta|$, and impedance is capacitive [55]. When $\Delta\theta \in (0, \pi/2]$, voltage is said to lead current (and current is said to lag voltage) by $\Delta\theta$, and impedance is inductive [55]. Phase shifts of $-\pi/2$, 0, and $\pi/2$ correspond to a capacitor, a resistor, and an inductor.

To analyze the dynamic performance of a fuel cell at various time scales, a range of input frequencies is tested. This results in a number of measured impedance
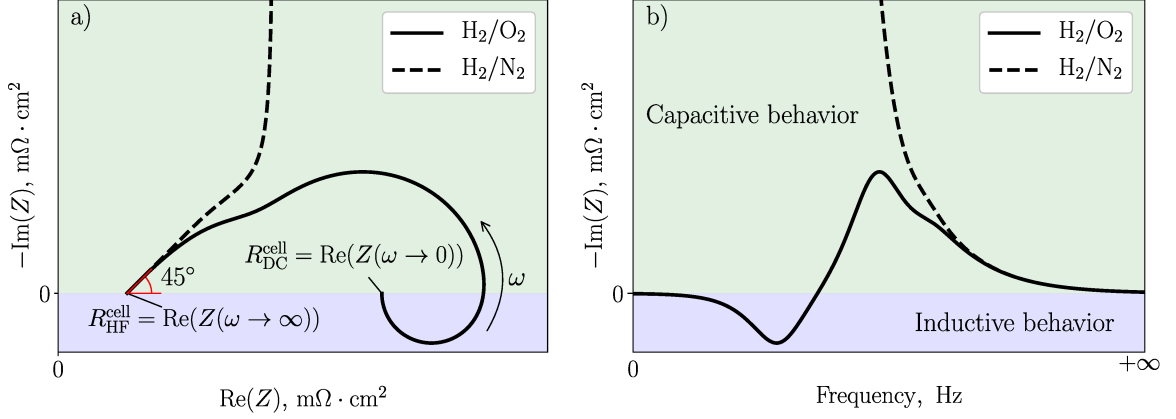
Figure 1.7: Example of a fuel-cell impedance spectrum: a) Nyquist plot; b) frequency content of the imaginary component.

values, one for each frequency, that form together an impedance spectrum. Examples of fuel-cell impedance spectra are illustrated in Figure 1.7. Two different shapes of impedance spectra are measured depending on whether or not the cathodic gas stream contains oxygen. Figure 1.7a shows the relationship between the negative-imaginary and the real components of $Z(\omega)$ and is called a Nyquist plot. Nyquist plots depict the transient phenomena taking place in the cell as capacitive arcs ($\mathrm{Im}(Z) < 0$) or inductive loops ($\mathrm{Im}(Z) > 0$) and provide characteristic resistances of the cell.

Nyquist plots do not contain frequency information and need to be accompanied with a frequency-content plot, such as the one in Figure 1.7b. Such graphs not only provide the frequency composition of the spectrum, but also help avoid ambiguity: the same Nyquist plot can be measured for different cells (or generated with multiple parameter sets in models), but the frequency-content plots will differ [181]. It must be noted that, conventionally, Bode plots of $|Z(\omega)|$ or $\Delta\theta$ as a function of $\log(\omega)$ [45, 55] are used to reflect the frequency content of the spectrum; however, providing the frequency content of the imaginary impedance component allows for a straightforward visual relation of the two graphs in Figure 1.7. In this work, plots of $-\mathrm{Im}(Z(\omega))$ against $\log(\omega)$ will be used to illustrate the frequency content of impedance spectra.

The first characteristic resistance indicated in Figure 1.7a is the so-called high-

18

frequency resistance (HFR) of the cell:

$$R_{\mathrm{HF}}^{\mathrm{cell}} = \lim_{\omega \to \infty} \mathrm{Re}(Z(\omega)).$$

For the cells with the conventional carbon-supported catalyst layers, the HFR is the sum of the electronic resistances of the cell components, the protonic resistance of the membrane, and contact resistance [174, 177]. In general, the HFR may contain a portion of the electronic and protonic resistances of the CLs if the corresponding conductivities are not too dissimilar [182].

At low current, the HFR of the cell is similar between the $H_2/O_2$ spectra (for instance, with air or pure oxygen in the cathode) and the oxygen-free spectra (commonly $H_2/N_2$) measured at the same operating conditions [177]. However, $R_{\mathrm{HF}}^{\mathrm{cell}}$ decreases with an increase in current due to the hydration of the electrolyte with the produced water. As a result, the agreement with the HFR measured under the $H_2/N_2$ conditions, when the ORR current is zero, is lost. Heat production during the ORR may cause additional deviation between the HFR measurements in the $H_2/O_2$ and $H_2/N_2$ regimes.

As frequency is decreased, fuel cells exhibit a capacitive behavior due to the dynamic charge redistribution in the electrical double layer that exists between the protonically conductive ionomer and the electronically conductive carbon-platinum phase in the catalyst layers [55, 61]. Coupled double-layer capacitance and protonic resistance of the cathode catalyst layer (CCL) result in a linear 45° impedance branch in the Nyquist plot [172, 177, 182, 183] (Figure 1.7a). This impedance feature occurs at frequencies below 100 Hz and has been reported in a number of experimental publications involving $H_2/O_2$ and $H_2/N_2$ EIS measurements [172, 173, 175, 177, 184–190].

Depending on the cell composition and the operating conditions, one or more capacitive arcs are observed in the $H_2/O_2$ spectrum as frequency is decreased further [45, 55]. The example $H_2/O_2$ spectrum in Figure 1.7 exhibits an ORR charge-transfer arc

at the higher frequencies and an oxygen-transport arc at the lower frequencies. The typical frequencies corresponding to these processes are 1 Hz–1 kHz [159–161] and 0.1–100 Hz [160, 161, 164], respectively.

The shape of the $H_2/N_2$ spectrum is different: as frequency is decreased, the spectrum tends to a straight vertical line [173, 175] as long as there is no crossover of hydrogen from the anode side and there are no contaminants in the cathode stream. This spectrum shape can be explained with a simple thought experiment. If oxygen content is reduced between $H_2/O_2$ EIS measurements, the ORR charge-transfer resistance and, hence, the size of the respective capacitive arc increase, and the impedance spectrum grows. At the limit of zero oxygen concentration, charge-transfer resistance in the ORR is infinite [55], and a vertical line is obtained at low frequencies instead of a capacitive arc.

An inductive loop may be formed in the fuel-cell impedance spectra, as illustrated in Figure 1.7. This inductance is typically observed between 0.1 mHz and 1 Hz [159, 177, 191, 192] and has been attributed to the hydration dynamics of the membrane and the ionomer phase of the catalyst layers [159, 164, 191–197], relaxation of the ORR intermediates [177, 187, 192, 196, 198–203], platinum-oxide dynamics [159, 187, 196, 200–203], and carbon-monoxide poisoning [192]. A detailed review of this topic has been written by Pivac and Barbir [192]. The effect of water management on the low-frequency inductive behavior of PEMFCs will be discussed later in this thesis.

Taking the zero-frequency limit of the real impedance gives the DC resistance of the cell (Figure 1.7a):

$$R_{DC}^{cell} = \lim_{\omega \to 0} \text{Re}(Z(\omega)).$$

When the cell is operated in the $H_2/O_2$ regime, $R_{DC}^{cell}$, having the meaning of the total resistance, accounts for all voltage losses in the steady-state polarization curve and, therefore, is equal to the negative slope of the latter [55]. The real-axis projection of the vertical low-frequency branch of the crossover-free $H_2/N_2$ spectra corresponds to the total ohmic resistance of the cell.

## 1.3 Literature Review

A transient numerical model of a PEMFC will be developed in this thesis. The model will be used to analyze the dynamic PEMFC behavior, including water management and impedance-spectroscopy characterization. An overview of the current experimental data and of the existing steady-state and transient fuel-cell models in the literature is, therefore, provided next. Focus is made on the key dynamic phenomena to be accounted for in the model developed in this thesis and on the required level of its comprehensiveness.

### 1.3.1 Overview of Transient Fuel-Cell Models

As discussed earlier in this Chapter, the main physical processes taking place in PEM-FCs include the transport of mass (gas, liquid water, and water in the electrolyte), charge (electrons and protons), and heat, as well as electrochemical kinetics. Thus, an appropriate fuel-cell model should contain an adequate description of these phenomena. The approaches taken in the literature to describing the relevant physical processes are overviewed in this Section, and the methods suitable for the model developed in this thesis are outlined.

#### 1.3.1.1 Microstructure Representation

Accurate description of the complex porous structure of fuel-cell components requires the use of three-dimensional full-morphology and pore-scale models [81–83, 91, 129–131, 204–215] that are based either on the direct imaging of the physical samples [82, 91, 129, 131, 209–215] or on their stochastic reconstruction [81, 83, 130, 131, 204–208, 212]. Sabharwal et al. [129–131, 210] and Jung et al. [212, 215] provided examples of pore-level gas-, liquid-water-, and charge-transport simulations in GDLs and CLs with the open-source fuel-cell modeling software OpenFCST. Unfortunately, these models are computationally expensive, and simulation of coupled physical phenomena in a whole MEA is not feasible, especially in transient.

Pore-scale transport can also be resolved with the less computationally demanding pore-network models (PNM) [114, 212, 216–225]. In those models, the porous medium is represented with a collection of discrete pores of varied size (or solid-material bodies if, for instance, charge transport is modeled) connected with throats that act as local transport resistances. This simplification enables transient simulations with PNM. For instance, Qin et al. [114, 221] have studied dynamic liquid-water accumulation in GDLs and MPLs. However, the computational cost of PNMs is still relatively high, even in 2D [221], and the simulation time reaches several days in some case studies [221].

This explains the predominant use of the so-called macrohomogeneous models [25, 27, 31, 33–36, 38, 41, 43, 44, 49, 52, 61, 65, 152, 157, 159, 162, 171, 183, 226–294], including those developed in OpenFCST [31, 33–36, 65, 262, 263, 265, 269–272, 276], where porous media are described as volume-averaged continuous layers. In that case, material structure is reflected in the effective transport properties that account for the tortuosity of the transport path. While volume averaging is justified in CLs and MPLs, a representative elementary volume, over which the averaging is performed, might not exist in GDLs [91, 221, 295–297] due to the larger size of the local structural features, such as the pore size and the fiber thickness, relative to the thickness of the layer. To overcome this issue, Zenyuk et al. [273] proposed iterative coupling of a continuum-based MEA model with a PNM of GDLs. A similar approach was undertaken later by Aghighi et al. [222]. However, each coupling iteration takes a significant amount of time (about 15 minutes in reference [273]), which accumulates in transient simulations. Therefore, macrohomogeneous models remain the most attractive approach to modeling PEMFCs due to their computational efficiency, despite the possibly less accurate GDL description. Thus, a transient macrohomogeneous PEMFC model will be developed in this thesis.

While direct pore-scale models and pore-network models are not typically used for MEA simulations, they have been proven invaluable when it comes to estimating

the effective transport properties of the fuel-cell materials by performing pore-scale simulations [82, 83, 91, 129–131, 204–207, 209–212, 215–219, 225]. Those properties can then be used in macrohomogeneous models so as to carry on the microstructure information to the MEA-level simulations. For instance, the macrohomogeneous fuel-cell models presented in Chapters 4 and 6 use effective transport properties obtained from microscale simulations in the literature.

### 1.3.1.2 Dimensionality of Macrohomogeneous Models

Transport processes in fuel cells are inherently three-dimensional due to the flow-field design of the bipolar plates. A number of transient 3D macrohomogeneous fuel-cell models have been developed in the past [41, 227–248]. While such models are capable of capturing the multidimensional transport effects, they are computationally expensive. A lower dimensionality of a model allows for an investment of the available computational power into a more comprehensive description of the physicochemical phenomena taking place in the MEA.

For a parallel-channel flow-field design, dimensionality of a model can be reduced to 2 by considering one of the two modeling planes indicated in Figure 1.8. Depending on which plane is chosen, 2D fuel-cell models are classified into along-the-channel [38, 159, 249–258] and through-the-channel [31, 33–36, 65, 157, 162, 259–268, 270, 271, 273–276] models. The former can predict reactant depletion and water accumulation along the channel, but are unable to account for the nonuniform distribution of the reactions [35, 157, 259, 276, 298], reactants [35, 276, 298], temperature [33, 35, 65, 157, 276], and water [21, 35, 157, 276, 298] under the channel and land areas of the bipolar plates. On the other hand, through-the-channel models are limited to the so-called "differential cells", where high flow rates are used to minimize the variation in the reactant and product distributions along the channels [19].

Pseudo-2D [27, 253, 258, 277] and pseudo-3D [43, 44, 278] models also exist, where one or more transport directions are reduced to 1D. Further reduction in the model
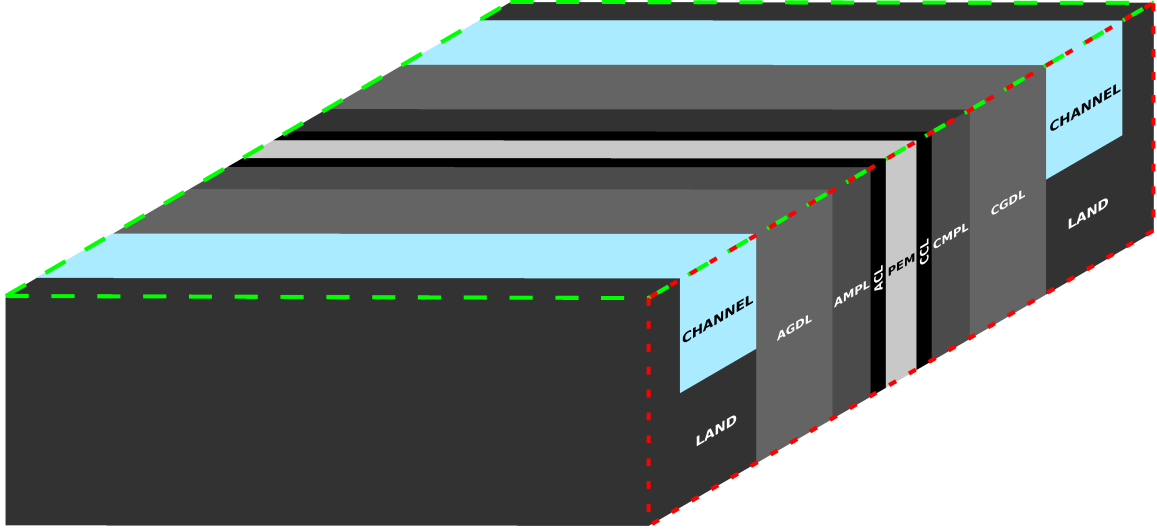
Figure 1.8: Illustration of the two-dimensional modeling planes used in along-the-channel models (long green dashes) and in through-the-channel models (short red dashes).

dimensionality gives rise to a number of one-dimensional transient models [25, 49, 52, 61, 152, 171, 183, 264, 279–294, 299], where only the through-the-MEA direction is considered.

The choice of the model dimensionality is a matter of compromise between the computational expense and the level of physical details. Inclusion of channels in the model requires coupling mass transport in the flow field and in the MEA [41, 300, 301] and necessitates three dimensions to account for the pressure and velocity variation in the channels [301], the complex dynamics of water-droplet growth and shedding at the GDL-channel interfaces [21, 302, 303], and water-film formation in the channels [21, 302, 303]. Channel description is beyond the scope of this thesis that is focused on the MEA modeling. A transient two-dimensional through-the-channel model of a PEMFC MEA will be developed, and the bipolar plates will be treated as boundary conditions, as commonly done in the literature [27, 31, 33–36, 65, 157, 162, 259–265, 270, 271, 273–276].

### 1.3.1.3 Catalyst-Layer Description

Catalyst layers are the most intricate components of fuel cells. The level of detail to which the various aspects of the catalyst-layer operation are described determines, to a large extent, the overall comprehensiveness of the model. It is, therefore, important to avoid reducing catalyst layers to interfaces as done in some models [27, 233, 250, 257, 304, 305]. Such a treatment of catalyst layers limits the understanding of their role in the cell operation and obstructs the analysis of multidimensional effects.

Since the main purpose of catalyst layers is to facilitate electrochemical reactions, the HOR in the anode and the ORR in the cathode need to be represented with suitable kinetic models. The existing transient fuel-cell models often utilize the Tafel [52, 183, 227, 228, 238–240, 243, 248, 253, 288, 290] or Butler-Volmer [42, 49, 152, 159, 162, 230, 234, 236, 238–240, 242, 243, 247, 252, 255, 257, 258, 261, 267, 273, 274, 280, 285, 288, 289, 293, 299, 306] equations to compute the faradaic current density. Those equations are valid for single-electron-transfer reactions and multistep reactions that have a single rate-determining step [63, 150]. However, the HOR [307] and the ORR [308–310] have multistep reaction mechanisms in which the rate-determining step changes with the overpotential. In this work, the more appropriate dual-path HOR model [262, 307] and the double-trap ORR model [270, 271, 308, 311, 312] will be used. These models have been implemented in OpenFCST by Secanell [262] and Moore et al. [270, 271, 311].

Electrical double layers are formed at the interfaces between the protonically conductive ionomer and the electronically conductive carbon/platinum phase of catalyst layers; those interfaces act as capacitors [55, 150]. Double-layer charging and discharging are usually assumed fast, and most of the transient fuel-cell models do not include the capacitance of the catalyst layers [42, 152, 157, 232, 234–240, 243, 246, 247, 252, 256, 267, 273, 274, 280, 288, 293, 299, 313–320]. That makes the models unfit for simulating impedance spectroscopy. Double-layer capacitance will be accounted

for in the fuel-cell model developed in this thesis to enable its EIS capabilities.

Experimental evidence suggests that the local reactant-transport resistance due to the presence of ionomer near the catalyst sites increases with a decrease in platinum loading [125, 140, 321, 322]. Such a resistance may account for a significant portion of the overall mass-transport loss and affect fuel-cell performance [36, 125, 140, 272, 321, 323–327]. This hinders the efforts to minimize fuel-cell cost by designing low-platinum-loading electrodes. A PEMFC model, therefore, needs to account for the local reactant-transport resistance in order to correctly predict cell performance.

Some transient macrohomogeneous PEMFC models include additional 0D [42, 152, 157, 159, 274] or 1D [52] sub-models for the local reactant transport in the catalyst layers. It is typically assumed in such models that a catalyst-covered support particle (or an agglomerate of such particles) is surrounded by an ionomer film and, in some models, a thin layer of liquid water. Reactant transport in the ionomer and in the liquid water, as well as through the liquid-gas and ionomer-liquid interfaces, is then modeled. Wardlaw and co-workers [272, 328] proposed a 1D model for the local reactant transport where catalyst layers are represented with a collection of spherical ionomer-covered catalyst particles (ICCPs). In that model, the reactant first dissolves into the ionomer film, then diffuses through it before reaching the reaction site. Fuel-cell simulations that incorporated the ICCP model showed that the interfacial-transport resistance was the determining factor for the predicted current density [36, 272]. That observation is in agreement with the experimental studies by Nonoyama et al. [140] and Kudo et al. [324, 325], the molecular-dynamics simulations by Jinnouchi et al. [326], and the pore-scale simulations by Sabharwal et al. [129, 131]. Muzaffar et al. [141, 142] argued that the additional local transport resistance associated with the presence of liquid water should be taken into account for the more realistic model predictions [141, 142]. Despite not accounting for that resistance, the ICCP model, implemented in OpenFCST by Wardlaw [272], has been shown in a number of publications to provide a good agreement between polarization curves that were simulated

26

with macrohomogeneous MEA models and measured experimentally [34, 35, 272, 298, 328]. For the aforementioned reasons, the ICCP model will be incorporated in the transient fuel-cell model developed in this thesis.

### 1.3.1.4 Thermal Management

Thermal management in fuel cells is of critical importance because, even though high cell temperature positively affects reaction rates and species transport, it also leads to a decrease in the protonic conductivity of the electrolyte and in the theoretical cell potential, which, in turn, reduces the power output of the cell. A large number of fuel-cell models are isothermal [27, 31, 36, 49, 162, 171, 183, 227–229, 233, 236, 244, 245, 248–250, 253–260, 262, 263, 265, 268, 270, 271, 278, 279, 281–288, 290–292, 294, 299] and do not capture the local temperature variations in the cell, such as those due to the release of the reaction heat. For instance, low thermal conductivity of the MPLs may lead to heat accumulation in the cathode catalyst layer [35, 99], which will cause electrolyte dehydration and reduced performance under dry conditions or faster water evaporation and improved performance under wet conditions. The use of non-isothermal models [33–35, 38, 41, 43, 44, 52, 65, 152, 157, 159, 230–232, 234, 235, 237–243, 246, 247, 252, 261, 264, 266, 267, 273–277, 280, 289, 293, 329–331] is, therefore, preferred. Among these models, the one by Bhaiya et al. [33, 65] and Zhou et al. [34, 35, 276], developed in OpenFCST, contain, perhaps, one of the most detailed descriptions of the non-isothermal effects. They include reversible and irreversible reaction heat, ohmic (Joule) heating, and heat consumption/release during the phase change of water [33, 65]. With that model, local temperature variations of up to 10 °C were observed within the cell operated at high current density [33, 65]. Similar temperature variations were also observed experimentally [99]. The steady-state non-isothermal model by Bhaiya et al. and Zhou et al. will be extended in this work to the transient form.

### 1.3.1.5 Water Management

Simulation of water management in PEMFCs requires consideration of water transport in porous media in both vapor and liquid forms. Formation and shedding of water droplets at the GDL-channel interfaces [21, 302, 303] is a dynamic process that cannot be modeled at steady state. Even when channels are not included in the MEA model, liquid-water transport and removal still require transient treatment for realistic predictions. Further, finding optimal strategies for automotive-fuel-cell start-up from sub-zero temperature [266–268, 332] requires transient non-isothermal modeling of not only ice melting/sublimation, but also vapor and liquid-water transport. Development of transient multi-phase PEMFC models has, therefore, been an active area of research in the past two decades [49, 52, 152, 157, 159, 231, 233, 235, 236, 238–240, 242, 243, 250–252, 260, 264, 267, 268, 273, 274, 280, 288, 289, 293, 304, 315, 320, 333, 334]. Fuel-cell operation at sub-zero temperature is, however, beyond the scope of this thesis. A subset of multi-phase PEMFC models, namely the two-phase models that consider pore-water in the form of vapor and liquid, is, therefore, of primary interest.

Liquid-water transport in the porous components of PEMFCs is driven mostly by surface tension [65, 335]. Capillary pressure and liquid-water saturation are predominantly related in fuel-cell models with an empirical relationship [21, 25, 29, 30, 37, 38, 40, 42–44, 49, 52, 65, 152, 159, 236, 242, 247, 248, 250, 251, 260, 264, 273, 274, 278, 288, 293, 304, 306, 320, 333–341], such as the Leverett $J$-function (the Udell function) and its modifications [21, 25, 29, 30, 37, 38, 40–42, 49, 52, 65, 152, 159, 236, 242, 247, 248, 250, 251, 264, 278, 288, 293, 304, 306, 320, 333–340]. However, the Leverett $J$-function was originally proposed for packed sand [21, 335, 336] and has been shown to predict incorrect water-retention curves for fuel-cell PTLs [337]. Further, empirical functions, even when fitted to experimental retention curves, are not explicitly related to the microstructure of the material and, therefore, cannot

provide design insights.

Weber et al. [26–28, 305] proposed a series of pseudo-2D isothermal fuel-cell models in which capillary pressure and liquid-water saturation in the porous media were related through experimentally measured pore-size distributions (PSDs) and contact angles. The models enabled the analysis of the effect of the pore size and wettability of the porous MEA components on liquid-water accumulation and fuel-cell performance [26–28, 305]. In the models of Weber et al., effective transport properties of the porous media were computed directly from the PSD [26–28, 305]. However, the proposed statistical approaches to modeling pore interconnectivity when computing permeability and liquid-gas interfacial area (for evaporation/condensation of water) differed from each other, as will be discussed later in this thesis. Additionally, catalyst layers were treated as interfaces in one of the models [27], and only PTLs were considered in another model [305].

Eikerling [282] presented a 1D isothermal model for the analysis of the pore-size and contact-angle effects on the CCL performance. The catalyst layer was considered in isolation from the rest of the cell and was assumed hydrophilic [282].

Mulone and Karan [39] proposed a 1D isothermal CCL model similar to that of Eikerling [282], but improved it to include a mixed-wettability PSD. Around the same time, Mateo Villanueva [342] developed 1D isothermal models of an MPL and of a CCL that were based on the mixed-wettability PSD approach of Weber et al. [26–28]. These PSD models were not integrated by Mateo Villanueva into an MEA model [342].

More recently, Zhou et al. [34, 35, 276] extended the non-isothermal PEMFC model of Bhaiya et al. [33, 65] in OpenFCST by incorporating the PSD model of Mateo Villanueva [342]. Since the models of Mateo Villanueva [342] and Zhou et al. [34, 35, 276] stem from the works of Weber et al. [26–28], they rely on a similar statistical approach that makes them self-inconsistent.

All of the PSD-based models discussed above [26–28, 34, 35, 39, 276, 282, 305, 342] share the same drawback: the assumption of steady-state operation. It turns out that

this simplification may limit the applicability of the two-phase fuel-cell models. Liu and Eikerling [343] applied the CCL model of Eikerling [282] to analyze the effects of the catalyst-layer-microsctructure properties, such as the total porosity and the fraction of the secondary pores, and the effect of oxygen diffusivity in the cathode GDL (through a boundary condition) on the predicted steady-state polarization curves. For some input parameters, the simulated voltage-current relationship was unstable, with a sudden performance drop in the middle of the polarization curve. Similar and even stronger effects, with discontinuous reduction in current density by as much as 10 times, were observed by Mateo Villanueva [342] in both steady-state MPL and CCL models. Such a peculiar shape of the polarization curve was explained by the existence of a critical operating point beyond which, at lower voltage, steady-state models predicted significant flooding of the porous media and, as a consequence, abruptly reduced current density [342, 343]. The transition between the two states at either side of the critical point can only be captured with a transient model.

Balliet and Newman [266–268] developed a transient fully 2D non-isothermal model of a PEMFC with a PSD sub-model adopted from the works of Weber et al. [26–28, 305]. The model was used to track the amounts of ice and liquid water during the cold start-ups of PEMFCs and to suggest a catalyst-layer composition that would minimize the time and energy (amount of hydrogen) required for a successful start-up. During the course of this thesis, Goshtasbi et al. [157] developed a transient 2D PEMFC model based on the steady-state two-phase model by Zhou et al. [35, 276] and the PSD formulation by Weber et al. [26–28]. They simulated the dynamic fuel-cell response to the voltage and current-density steps under various typical operating conditions and platinum loadings in the CCL. However, Goshtasbi et al. did not perform pore-size or wettability studies (catalyst loading was varied by modifying the CCL thickness, and the PSD remained unchanged).

The steady-state two-phase 2D PEMFC model implemented in OpenFCST by Zhou et al. [34, 35, 276] will be extended in this thesis to the transient form. The

PSD model of Zhou et al. will be adopted and improved for the consistency between the approaches taken for computing permeability and liquid-gas interfacial area from pore-size distributions.

Liquid-water transport is not the only motivation for the transient modeling of water management. The experimentally observed hysteresis in ohmic resistance of PEMFCs during potential or current sweeps [46, 49–52] implies that water transport in the electrolyte, conductivity of which depends on water content, is a dynamic process and must be addressed accordingly. In particular, experimental evidence suggests that water uptake and release by the polymer electrolyte is a finite-rate process [116, 344]. Yet, it is assumed instantaneous in a number of models in the literature [49, 159, 227, 228, 238–240, 243, 253, 255, 257, 258, 261, 280, 289, 345]. Further, transient fuel-cell models often describe water uptake by the ionomer in catalyst layers with the equilibrium water content measured for electrolyte membranes [42, 52, 152, 157, 159, 227, 228, 232, 243, 247, 255, 257, 273–275, 280, 299]. This is also the case for the steady-state models in OpenFCST [33–36, 65, 263, 265, 269, 270, 272, 276, 346]. However, ex-situ measurements performed with catalyst layers [121, 168, 347] and ultrathin Nafion® films [344, 348–352] show a different uptake and a stronger temperature dependence than observed with membranes [22, 121, 168, 353–355].

In this thesis, water uptake and release by the polymer electrolyte will be modeled as a finite-rate process, as done before by some authors [41, 157, 288, 320, 334, 341]. The uptake data for catalyst layers and ionomer films from the literature [121, 168, 344, 347–352] will be analyzed, and a novel relationship for modeling this process will be suggested in Chapter 2.

### 1.3.1.6 Degradation

The choice of materials and conditions at which PEM fuel cells operate limits their durability, as various degradation processes occur during the operation. A number of mathematical models have been developed to address, for instance, platinum-particle

dissolution and coarsening [283, 356, 357], carbon corrosion [284, 358], and carbon-monoxide poisoning [285, 286, 359] in catalyst layers; mechanical degradation of MEA components [275, 360]; and chemical degradation of the membrane [287, 361]. Since degradation of PEMFCs is observed over hundreds and thousands of hours [169, 170] and because the focus of this thesis is on the regular fuel-cell operation at significantly shorter time scales, degradation mechanisms will not be considered. Nevertheless, the model developed in this thesis is a necessary step toward a more general transient framework capable of simulating fuel-cell degradation.

### 1.3.1.7 Model Validation

As Richard Feynman said in one of his 1964 Messenger Lectures at Cornell University, "if it disagrees with experiment it is wrong. In that simple statement is the key to science." [362] He was talking about physical laws, but the same rule applies to mathematical models. Comparison of model predictions with experimental observations is just as important as model development. Yet, on many occasions, experimental validation of fuel-cell models in the literature has not been convincing.

For instance, some authors reported no experimental validation [162, 227–230, 235, 236, 261, 299] or did not provide a quantitative comparison of the simulated and the measured data, limiting themselves to a discussion of the qualitative similarities [152, 288]. Others developed a transient model but only reported steady-state results [247, 273]. Among the works with at least some sort of validation, it is not uncommon to come across a publication where a transient fuel-cell model was validated with a single, steady-state experimental polarization curve (or at least a curve with no observable hysteresis) [233, 242, 250, 251, 260, 264, 320], only two seemingly steady-state curves [334], or a single curve with and without ohmic correction [248, 252]. Validation limited to a single operating condition or to a change of only one variable, such as the flow rate, also appears in publications that compared model predictions with the measured cell response to voltage or current steps [277, 278, 289]. Transient fuel-cell

models were validated with experimental impedance spectra in references [159, 253], but polarization curves were only verified at steady state.

There are, however, some notable exceptions. For example, Ziegler et al. [49] compared the simulated and measured dynamic polarization and cell-resistance curves at different scan and flow rates, thus varying both the operating conditions and the type of experimental data in the validation. The agreement between the simulations and the measurements was, however, poor. Zenyuk et al. [274] validated their transient fuel-cell model with polarization curves measured at two temperature values and with voltage and temperature transients during a cell start-up in two different thermal-management scenarios [274]. However, polarization curves were simulated at steady state while experimental data exhibited hysteresis. Gerteisen et al. [52] performed validation of their 1D model with dynamic measurements of current density, resistance, and anode-plate temperature during linear voltage sweeps and step changes, all at three different relative-humidity (RH) values. The used experimental data were obtained for a cell with a single serpentine channel that, despite the small MEA area, may have required a 3D model. This casts doubt on the reasonably good agreement between the simulations and experiments reported by the authors [52]. Ko and Ju [238] and Huo et al. [293] validated their models using cell-voltage transients measured during a fuel-cell start-up under various operation scenarios. A similar validation was performed by Balliet and Newman [266, 268], who also verified the predicted amount of product water. Shamardina and Kulikovsky [254] tested their model using several impedance spectra and current-density transients after steps in voltage measured for different MEAs under various operating conditions. Polarization-curve validation was performed at steady state. Goshtasbi et al. [157] used the same experimental data as Gerteisen et al. [52] that might not have been suitable for their 2D PEMFC model. Moreover, the 2D model was reduced to 1D for the comparison with measurements [157]. Only qualitative agreement was achieved in some cases [157].

One of the reasons for the lack of a convincing experimental validation in a number

of fuel-cell-modeling publications is the scarcity of suitable experimental data. For example, through-the-channel models, such as the one developed in this thesis, can only be validated with the data from the cells with a parallel-channel or single-channel configuration (symmetry requirement) that were operated at a sufficiently high flow rate (along-the-channel transport is not modeled). Since the experimental facilities at ESDL are equipped for such measurements, in-house dynamic polarization curves, resistance curves, and impedance spectra at various operating conditions are used to validate the fuel-cell models developed in this thesis (see Chapters 4 and 6). To the best of the author's knowledge, such a validation of a transient 2D PEMFC model is done for the first time in the literature.

### 1.3.1.8  Software Implementation

The most reasonable approach to developing a mathematical model of a complex technical system, such as a fuel cell, it is to build upon an existing model that is comprehensive enough for the purpose at hand or that can be improved to the desired level with acceptable effort. To a large degree, the choice of such a base model is dictated by software implementation. This choice has an immediate consequence not only for the developer of the new model, but also for everyone who would want to use it in the future.

With rare exceptions, transient fuel-cell models available in the literature have been implemented in commercial software, such as COMSOL Multiphysics® [43, 44, 49, 52, 152, 157, 162, 232, 244, 245, 257, 261, 264, 267, 273–275, 287, 314, 319, 320, 363–365], Ansys Fluent® [41, 229, 230, 234, 236, 238, 240, 241, 243, 246–248, 252, 255, 256, 318, 366, 367], MATLAB® [253, 285, 293, 320, 363], MATLAB®/SIMULINK® [277, 283, 284, 286, 287, 356, 368, 369], and Star-CD® [227, 228]. The convenience of having ready-to-use fuel-cell modules and an interface for user-defined functions make commercial software an attractive option for developing PEMFC models. There are, however, limitations to this approach. In particular, the closed-source architecture of

the commercial products makes it difficult for the users to adopt the rapidly evolving fuel-cell models from the literature. The lack of source-code access also hides away the information on how the models are implemented and solved. The complex logical kernel necessitated by the universality of commercial software negatively affects the simulation time. For instance, an in-house code for a 2D PEMFC model was shown by Secanell [262] to simulate steady-state polarization curves three to four times faster than a similar model implemented in COMSOL Multiphysics® by Songprakorp [264]. Finally, license fees for non-academic use are usually expensive.

The need for fuel-cell modeling software that is available to everyone has led to the development of several open-source solutions, such as Fast-FC [370], openFuel-Cell [371], OpenPNM [372, 373], and OpenFCST (Open-source Fuel-Cell Simulation Toolbox) [374, 375]. There has been no development activity on the GitHub pages of Fast-FC [376] and openFuelCell [371] since 2016. There do not seem to be any publications based on Fast-FC that would shed light on the state of the software. The most recent journal paper on openFuelCell was published in 2016 [377], and, to the best of the author's knowledge, the project is still in development despite no public releases. However, openFuelCell is primarily designed for solid-oxide fuel cells that use different materials than PEMFCs and operate at the temperature of up to 1000 °C. The code of OpenPNM is in active development [378], but the software is designed primarily for the pore-network analysis of fuel-cell materials rather than for MEA simulations. On the other hand, OpenFCST offers steady-state fuel-cell simulation modules [379] that include all core physics at the level of detail that can compete with other models in the literature (as was discussed earlier). It is based on the open-source finite-element library deal.II [380–382] and is developed in-house at ESDL. As of today, OpenFCST contains 150,000 lines of C++ code and over 30,000 lines of Python code (excluding supporting libraries and comments). This is significantly more compared with about 7,000 lines in Fast-FC [376], 10,000 lines in openFuelCell (as of 2016) [377], and 18,000 lines in OpenPNM [378]. Even more compact open-source fuel-cell soft-

ware exists, such as the MATLAB® code developed by Vetter and Schumacher [341] that has less than 400 lines. The level of physical detail and parametrization offered by OpenFCST, evident in part from its size, explains the large number of advanced models developed in that software [31, 33–36, 65, 129–131, 210, 212, 215, 262, 263, 265, 269–272, 276, 298, 346] that were mentioned earlier in this literature review. Therefore, OpenFCST is a solid ground for the development of a transient PEMFC model in this thesis.

As any other large software, OpenFCST is a result of a collaboration of many individuals. It was originally developed by Marc Secanell (University of Alberta) for his Ph.D. thesis [262] at the University of Victoria, Canada, with assistance from Guido Kanschat (Texas A&M University, USA, at the time; now at Heidelberg University, Germany). Since 2009, a number of graduate, undergraduate, and visiting students and postdoctoral fellows at ESDL have contributed to the development of OpenFCST. The full list of the present and past developers can be found on the official Open-FCST website, http://www.openfcst.org. The author specifically acknowledges the work of M. Secanell [262], P. Dobson [269], M. Moore [270], P. Mateo Villanueva [342], M. Bhaiya [65], K. Domican [346], P. Wardlaw [272], A. Jarauta and V. Zingan [301], J. Zhou [276], and M. Sabharwal [131]. Details of their contributions to the model developed in this work are provided in this Chapter and later in this thesis.

## 1.3.2 Transient Phenomena Under Study

Mathematical models are needed to achieve better understanding of the transient processes taking place in PEMFCs. The model developed in this thesis will be used to perform several physical studies.

First, the effect of the electrolyte-hydration dynamics on the inductive behavior in the fuel-cell impedance spectra will be analyzed. This study will improve the current understanding of how the particular water-transport mechanisms (such as electroosmotic drag, back-diffusion, and dynamic uptake/release of water by the electrolyte)

affect fuel-cell impedance. The developed insight could be used by experimentalists to design fuel cells with more effective water management that would minimize ohmic resistance and flooding (for instance, by transporting the product water through the membrane to the anode side), thereby improving fuel-cell performance at intermediate to high current density. This will, in turn, reduce the requirements for the amount of platinum used in the catalyst layers and, therefore, the fuel-cell cost.

Second, charge-transport characterization of catalyst layers with EIS will be investigated. By having means of accurately measuring the effective electronic and protonic conductivities of CLs, experimentalists will be able to design catalyst layers with improved charge transport and thus better catalyst utilization. This work will aid that goal by analyzing the relationships between the effective conductivity, ohmic resistance, and impedance of catalyst layers.

Third, the influence of liquid-water accumulation on the dynamic performance of PEMFCs will be studied. As it will be discussed later, such an analysis has been performed in the literature mostly at steady state, and limited insight is available regarding the more realistic transient cell operation. The knowledge of how the electrode composition translates into liquid-water accumulation will help experimentalists design fuel cells that are less prone to flooding and that can, therefore, achieve a better high-current performance. Such an analysis will be enabled in the model developed in this thesis by incorporating a mixed-wettability PSD sub-model.

Before a transient PEMFC model could be implemented in OpenFCST, a numerical framework for solving time-dependent problems had to be developed in the software. As a first step in the framework development, a single transient diffusion equation was implemented in OpenFCST. The equation was then incorporated into a mathematical model for analyzing oxygen diffusion in polymer-electrolyte membranes. Literature review for that study is provided first.

### 1.3.2.1 Estimation of Oxygen-Transport Properties of Polymer-Electrolyte Materials

Motivation for the characterization of reactant transport in polymer-electrolyte materials is twofold. In the operation of fuel cells, reactant crossover through the polymer membrane is not desired, as it leads to performance loss [169, 383]. At the same time, reactants need to be transported through the ionomer film that may cover the reaction sites in the catalyst layers [21, 117, 140]. In particular, local oxygen-transport resistance in cathode catalyst layers may have a strong implication on the overall fuel-cell performance [36, 125, 140, 272, 321, 323–327]. Reliable measurement of oxygen-transport properties of polymer-electrolyte materials is, therefore, essential for fuel-cell design via development of low-crossover membranes and highly permeable ionomers for catalyst layers.

Mass transport of oxygen in polymer electrolytes is often studied by placing a microdisk electrode onto the surface of a membrane, applying a potential step, and performing a parametric fitting of the transient current response with one of the known analytical equations [309, 325, 384–392]. A detailed description of the experimental technique, known as chronoamperometry, can be found, for instance, in [392]. The transport properties measured for membranes are believed to also apply to thin ionomer films in catalyst layers. Kudo et al. [325] showed experimentally that non-interfacial oxygen-transport resistances of thin ionomer films and thicker membranes are similar. Although interfacial resistance is believed to dominate in thin films [140, 324–326], Liu et al. [393] reported no significant transport resistance at the ionomer-gas interface for films as thin as 50 nm. This is sufficiently lower than the thickness of the membranes typically used in chronoamperometric experiments (of order 10–100 μm) [309, 385, 387–392].

A number of analytical expressions for chronoamperometric current at a microdisk electrode exist [394–400] and are commonly referred to as "Cottrell-like" equations after the original work of Cottrell (1903) [394]. Mitsushima et al. [387] developed

a numerical 2D model of transient oxygen diffusion in a polymer electrolyte and illustrated dynamic oxygen-concentration distributions around a microdisk electrode. They showed that the assumption of semi-infinite diffusion in a Cottrell-like analytical model by Shoup and Szabo [397] creates an applicability limitation of the latter due to the finite thickness of the membrane. However, it appears that, even though the numerically simulated current density was in a better agreement with experiments than the analytical approximation, the numerical model was not fitted to chronoamperometric data to obtain more reliable mass-transport properties [387]. It is, therefore, important to know whether the transport properties obtained from fitting chronoamperometric current with a numerical model differ significantly from those found analytically.

### 1.3.2.2  Water-Management Signatures in Fuel-Cell Impedance Spectra

A number of studies have named dynamic electrolyte hydration one of the main causes of the low-frequency inductive behavior observed in impedance spectra of PEMFCs [159, 164, 191–197]. Since water management plays an important role in achieving high performance of hydrogen fuel cells, future cell diagnosis and design could be improved if one develops physical insight that can translate the measured impedance spectra into useful information regarding water transport in the cell. The corresponding literature review is provided next, starting with experimental studies.

**Experimental Studies**  Schneider et al. [193] analyzed the impact of water accumulation along the parallel flow channels on the impedance spectrum of a segmented PEMFC. They experimentally showed that, when the cell was operated under conditions that favored liquid-water formation in the downstream segments, the low-frequency inductive behavior was only observed in the spectra measured in the upstream segments. When the current was reduced to eliminate liquid water, the inductive loop was present in the spectra obtained from all segments, and the overall

spectrum exhibited a stronger inductive behavior compared with the previous case. Schneider et al. concluded that the low-frequency inductive loop in the PEMFC spectra is indicative of water formation and accumulation along the flow channels.

In their later study, Schneider et al. [194] experimentally investigated the effect of the operating humidity on the appearance and the size of the inductive loop. They demonstrated that, under the fully humidified conditions, the inductive behavior is virtually absent in the impedance response of a PEMFC. At a lower humidity, however, a large inductive loop was observed. It was deduced that the low-frequency inductive behavior is due to the slow water uptake and release by the membrane. Subtraction of the membrane impedance from the overall spectrum revealed a significant residual inductive loop occurring at the same frequencies as before. This means that the hydration dynamics of the ionomer in the catalyst layers may contribute to the low-frequency inductive behavior of the cell.

Holmström et al. [191] conducted a detailed experimental study on the effect of water transport on the low-frequency inductive loop in the impedance spectrum of a hydrogen fuel cell. In agreement with the studies by Schneider et al. [193, 194], a decrease in the size of that loop was observed as relative humidity was increased. This effect was also recently reported by Moçotéguy et al. [197] for an impedance spectrum of a commercial PEMFC stack. Holmström et al. repeated the experiment using a lower RH in either the cathode or the anode of the cell and reported an increase in the strength of the inductive behavior. The sensitivity to the change in the anode humidity was higher, suggesting that water transport across the membrane (electroosmotic drag, back-diffusion) plays a role in the low-frequency inductance. This also aligned well with the membrane-thickness study by the authors, in which the cells with thicker membranes exhibited a larger inductive loop that occurred at lower frequencies. The size of the inductive loop increased with current in the case of a thinner membrane (51 μm) but decreased with a thicker membrane (127 μm). This was attributed to the interplay between the electroosmotic drag and back-diffusion of

water in the membrane: at high current density, the anode side of a thicker membrane dries out, leading to an increase in the membrane resistance [191].

Recently, Schiefer et al. [187, 203] performed an experimental investigation of the PEMFC inductance. They attempted to magnify the effect of electrolyte hydration on the inductive loop by using a higher relative humidity in the cathode than in the anode but observed a reduction of the loop. The authors concluded that water transport was not the main cause of the low-frequency inductive behavior, as the latter was stronger when RH was low and equal in both compartments. However, their data also showed the inductive loop increase in size when RH was reduced in the anode, in agreement with a similar study by Holmström et al. [191]. It appears, therefore, that water imbalance in the cell does have a direct effect on the inductive behavior.

**Modeling Studies**   The most common technique for analyzing fuel-cell impedance is the use of equivalent circuits to fit the experimental spectra [160, 171, 173–177, 181, 192, 401, 402]. However, the fitted parameters are only valid in the neighborhood of the tested operating conditions and cell composition. Oversimplification of the underlying physics may also result in a questionable meaning of the circuit elements and misunderstanding of the physicochemical phenomena behind the local features of the impedance spectra.

In contrast to equivalent circuits, physical models can be used to generate the impedance spectra through a direct numerical simulation of the cell. Such models have a predictive capability, which is impossible to achieve with a fitted circuit. Due to their complexity, however, physical models have not received widespread interest from the experimental community. Among the one-dimensional [172, 182, 183, 195, 199–201, 290–292, 294, 403–405] and multi-dimensional [159, 196, 253, 254, 257, 258, 406, 407] models that were used to investigate fuel-cell impedance, only a few [159, 195, 196, 257] analyzed the effect of electrolyte hydration on the inductive behavior

of the cell.

Wiezell et al. [195] simulated impedance spectra of the anode, the cathode, the membrane, and the whole MEA using a transient 1D single-phase isothermal model. Their results indicated that the membrane impedance (frequency-dependent through the water content) was the main contributor to the low-frequency inductive loop in the overall spectrum. The electrodes also exhibited a significant inductive behavior, in agreement with the experimental study by Schneider et al. [194]. Wiezell et al. [195] simulated the experimental studies by Holmström et al. [191] and reported the same trends in the size of the inductive loop with changes in the membrane thickness, relative humidity, and current density. However, electronic potential, gas concentration, and ionomer water content were assumed uniform in the catalyst layers, which may have affected the simulation results.

Setzler and Fuller [196] developed a transient pseudo-2D single-phase model of a PEMFC and used it to analyze the cell impedance. They attributed the low-frequency inductance at frequencies below 1 Hz to platinum-oxide formation in the catalyst layers and water accumulation in the membrane. Their isothermal model was able to predict the inductive loop observed experimentally at a wide range of current densities; however, inclusion of heat generation partially or completely offset the inductive behavior. No parametric studies were performed to investigate the effect of water transport on the inductive behavior of the cell.

Bao and Bessler [164, 257] presented a transient 2D single-phase isothermal PEMFC model capable of predicting cell impedance. They showed that the low-frequency inductive loop in the PEMFC spectra decreases under the counter-flow operation of the cell (that is, when the cathode and anode flows are oriented in the opposite directions) and when the membrane thickness is reduced (in agreement with the experimental study by Holmström et al. [191]). Bao and Bessler correlated both effects with water transport and the changes in the internal humidification of the cell. However, catalyst layers were considered to be infinitely thin in the model, and thus the effect

of mass and charge transport in CLs on the impedance spectrum could not be analyzed. Additionally, water in the electrolyte was assumed to be in equilibrium with the surrounding vapor, and no finite-rate exchange was modeled.

Futter et al. [159] analyzed PEMFC impedance with their transient 2D non-isothermal two-phase model. They showed that platinum-oxide formation had a negligible effect on the inductive phenomenon at about 0.1 mHz–1 Hz, while a significant reduction in the size of the respective loop took place when the protonic conductivity of the membrane or the catalyst layers was made constant. This is in line with the experimental study by Schneider et al. [194]. However, the effect of the water-transport mechanisms on the inductive behavior of the cell was not analyzed. Additionally, the finite-rate water uptake by the polymer electrolyte was neglected. When the model was made 1D by removing the along-the-channel direction, the inductive loop was split into two smaller loops, at about 1–10 mHz and 0.1–1 Hz (in agreement with the modeling results of Wiezell et al. [195]). The nature of these two distinct inductive processes was not investigated in [159].

### 1.3.2.3 Estimation of Catalyst-Layer Charge-Transport Properties via Electrochemical Impedance Spectroscopy

One of the main roles of the catalyst layers (CLs) in the hydrogen-fueled PEM fuel cells and water electrolyzers[3] (PEMWEs) is the transport of protons and electrons to and from the reaction sites. Catalyst layers used in both PEMFC electrodes and in PEMWE cathodes are typically made of a carbon-supported catalyst (platinum or a platinum-based alloy) [137, 139, 149, 408–411] and a perfluorosulfonic-acid-based ionomer, such as Nafion® [116, 117]. The effective protonic conductivity of such layers has been shown to be up to four orders of magnitude lower than the electronic conductivity [120, 412, 413] and to affect the reaction distribution (and hence catalyst utilization) [31] and the overall performance [31, 119, 281] of PEMFC CLs. Therefore,

---

[3]Electrolyzers consume electrical energy to split water into hydrogen and oxygen. Although this thesis is focused on PEMFCs, the charge-transport characterization approaches discussed here and in Chapter 5 are also applicable to other systems, such as water electrolyzers.

measuring the protonic conductivity of those layers is an important part of the design and development of fuel cells and electrolyzers. In contrast, the anode catalyst layers (ACLs) of PEMWEs are usually made of iridium dioxide (unsupported [149, 410], supported on titanium dioxide [408, 409, 414] or on titanium [411]) and Nafion®. These layers do not exhibit the high electronic conductivity [408, 411, 415] observed in carbon-based CLs, and, therefore, estimation of both protonic and electronic conductivities of PEMWE anodes is essential.

Electrochemical impedance spectroscopy (EIS) is the primary method used to measure the proton-transport properties of fuel-cell catalyst layers [45, 120, 122, 124–127, 173–177, 184, 185, 188–190, 196, 413, 416–428] and was also recently used to estimate the protonic resistance of PEMWE ACLs under $H_2/N_2$ conditions [414, 429]. A vital part of these measurements is fitting the experimental spectra with analytical impedance expressions, such as those derived by Eikerling and Kornyshev [183] and by Makharia et al. [177] These expressions, however, are only valid for small operating current and when the electronic resistance of the catalyst layer is negligible [177, 183]. Therefore, the use of these relations in the analysis of PEMWE ACLs must be carefully assessed. More recently, Kulikovsky [182] derived a generalized analytical low-current impedance expression that takes the finite electronic conductivity of the CL into account. The relationship between the electronic/protonic resistance of a catalyst layer and its effective electronic/protonic conductivity predicted by that model [182],

$$R_\Omega = \frac{L}{3\sigma^{\text{eff}}},$$

is thrice lower than in the earlier models [177, 183],

$$R_\Omega = \frac{L}{\sigma^{\text{eff}}}. \tag{1.9}$$

Relationship (1.9) is the commonly known definition of resistance of a material to the flow of current through it [56]. It is valid, for instance, for the measurement of the protonic resistance and effective conductivity of pseudo catalyst layers (PCLs) via

the hydrogen-pump technique [121, 415, 430–434], where the catalyst layer of interest is placed between two protonically conductive membranes. However, the protonically conductive phase of the catalyst layers in the regular PEMFC and PEMWE cells terminates at the porous-transport-layer side. As it will be discussed later in this work, this has implications on the macroscopic resistance-conductivity relationship in CLs. Thus, consistency of the models from references [177, 183] and [182] and accuracy of the proposed conductivity-resistance relationships for charge-transport characterization of catalyst layers via EIS must be examined.

To date, a study that compares the available impedance expressions and conclusively assesses the validity of the resistance-conductivity relationships proposed in references [177, 182, 183] in the context of the PEMFC and PEMWE EIS measurements with an independent (non-EIS-based) technique does not exist. The analytical expressions [177, 182, 183] are also based on a simplified Tafel kinetic model, and the impact of the changing Tafel slope on the impedance spectrum in a more appropriate multistep kinetic model, such as that for oxygen reduction in PEMFCs [270, 308, 311], has not been investigated.

Another critical assumption used in the models from references [177, 182, 183] is catalyst-layer uniformity. Recent imaging data suggest that the catalyst, support, and ionomer content may vary within a catalyst layer [133, 143, 322]. Additionally, CLs can be functionally graded with nonuniform spatial composition to achieve a higher PEMFC performance [435]. Such nonuniformity has been hypothesized [173–175, 178, 186, 405, 422, 436] to cause distortion in the high-frequency 45° impedance branch in the Nyquist representation [2, 159, 173, 178, 185, 186, 197, 407, 414, 422, 429, 436–438] that is used to estimate the charge-transport properties of catalyst layers. Correlations between conductivity, ohmic resistance, and impedance of nonuniform catalyst layers have been reported by Kulikovsky [61, 405]; however, they need to be re-derived for every particular distribution of the CL properties. Numerical models are more suitable for the analysis of nonuniform CLs.

Analytical models [177, 182, 183] were derived for a single catalyst layer and ignore the effect of other cell components. Charge-transport analysis of fuel-cell impedance spectra may be obstructed by the appearance of an additional capacitive arc at high frequencies [2, 158, 195, 439, 440] (typically above 1 kHz [2, 158, 195, 439]). This arc has been hypothesized to represent faradaic processes in the anode [158, 195, 440]. On the other hand, it has been claimed to disappear in $H_2/H_2$ measurements [441], which suggests its cathodic nature. Therefore, better understanding of the physical phenomena behind the additional arc at frequencies above 1 kHz needs to be developed.

### 1.3.2.4  Effect of Electrode Design on Dynamic Water Management in Fuel Cells

Accumulation of liquid water in the porous components of PEMFCs is not desired, as it impedes reactant delivery to the catalyst sites. A systematic analysis of the electrode design is required to achieve a better understanding of how the structural characteristics of MEA components translate into their transport properties and, ultimately, into the fuel-cell performance under the conditions that favor rapid production of liquid water. As the following review will show, a number of experimental studies have been performed in the literature with a variety of electrode designs for improving fuel-cell performance. However, it is difficult to compare the experimental observations due to the diversity of the chosen cell components and operating conditions. On the other hand, detailed parametric studies can be performed with mathematical models so as to develop the required knowledge in an orderly fashion. A model suitable for such an analysis needs to be transient to capture dynamic liquid-water accumulation and drainage. Additionally, the electrode structure must be reflected in the model to provide the means for making design decisions. Dynamic fuel-cell performance under the two-phase conditions is yet to be analyzed with a model that satisfies the aforementioned requirements.

**Catalyst Layers** Porosity and pore size of catalyst layers strongly depend on the catalyst and ionomer loading [79, 125, 126, 442, 443], as well as the support type [79, 135, 136, 442, 443] and aggregate packing [444]. These characteristics translate into different CL transport properties, such as permeability [79] and gas diffusivity [79, 136, 444]. The fabrication method, including the choice of a solvent for the catalyst ink [127] and of a catalyst-deposition method [445], also affects the catalyst-layer structure and porosity [127, 445].

As transport properties of catalyst layers change with their composition, so does the fuel-cell performance [18, 122, 124, 125, 127, 134, 446]. Therefore, catalyst-layer design can be tailored toward achieving efficient liquid-water removal. For example, Ahn et al. [148] fabricated prism-patterned catalyst layers in which guided cracks acted as liquid-water reservoirs and passages. Other strategies, such as designing graded catalyst layers [417, 435, 446–448] and using pore formers [449, 450], have also been shown to improve the fuel-cell performance under a wide range of operating conditions [448, 450]. Nanostructured-thin-film (NSTF) catalyst layers with low platinum loading have been proposed as well [451–454]. They contain no carbon or ionomer, relying on liquid water for proton conduction. However, structural properties of catalyst layers, such as PSD, are seldom quantified [417] in such publications. Mathematical modeling can help bridge the gaps between the design of the electrode, its transport properties, and cell performance.

Transient simulations performed by Kongkanand and Sinha [289] and by Zenyuk et al. [274] showed that electrodes with thin low-platinum-loading catalyst layers (both Pt/C and NSTF) are prone to flooding. In fact, liquid water may accumulate so rapidly [274, 289] that the cell will shut down in a fraction of a second after a step-up in current [289]. Cell shutdown due to flooding during polarization-curve measurements has also been reported [50]. Complete flooding can be avoided by increasing catalyst-layer thickness to accommodate more water or by reducing membrane thickness to promote anode water removal [274, 289]. More recent simulations by Goshtasbi et

al. [157] demonstrated an opposite CL-thickness effect due to the increased volumetric heat production in thinner CCLs and a shorter path to the anode for the water in the ionomer [157]. Parametric pore-size and wettability studies could have shed some light on the reasons for the observed discrepancy with the earlier publications; however, such studies were not performed by Goshtasbi et al. [157].

Based on a PSD model of a CCL, Eikerling [282] argued that the optimal wetting state of a catalyst layer is when the primary pores with radii below 10 nm are flooded for water permeation and the larger secondary pores are open for gas transport. A larger fraction of primary pores and increased hydrophobicity of the layer benefited the simulated current production [282]. With help of a mixed-wettability CCL model, Mulone and Karan [39] found that small hydrophobic pores form gas-transport pathways when the layer is partially saturated with water. On the other hand, Mateo Villanueva [342] and Zhou et al. [298] showed that it is important to retain some hydrophilicity of the catalyst layers, as it helps maintain sufficient water evaporation. The benefit of a predominantly hydrophobic catalyst layer was also demonstrated with fuel-cell simulations by Zenyuk et al. [274] and Dunsmore and Litster [455]. Zhou et al. [298] deduced that fuel-cell performance can be improved by making the hydrophobic pores of catalyst layers more hydrophobic (thus requiring a higher capillary pressure to be filled) and making the overall pore size larger (for increased liquid permeability). The latter conclusion was in line with the results of the pore-scale catalyst-layer study by Sabharwal et al. [130, 131]. However, the models in references [39, 130, 131, 282, 298, 342, 455] are steady-state, and the transient model in reference [274] does not contain a dedicated sub-model for PSD analysis.

**Gas-Diffusion Layers**   The PTFE treatment of GDLs has been shown by Lin and Nguyen [110], Yu and Ziegler [46], and Tseng and Lo [456] to improve cell performance by reducing flooding. It was reported that there exists an optimal PTFE content in GDLs: hydrophobic domains aid gas transport while hydrophilic domains

form pathways for liquid-water removal [110]. On the other hand, Park et al. [457] and Hou [51] reported negative effect of the hydrophobic treatment of GDLs. The discrepancy between the studies [46, 51, 110, 456, 457] was likely due to the differences in the microstructure of the commercial GDLs (pore size, fiber thickness, PTFE content), as well as the variability in other cell components and in the operating conditions. Two-phase fuel-cell simulations performed by Weber et al. [26, 27] with a PSD-based model also indicated the existence of an optimum PTFE content and porosity of GDLs. Pore size and distribution spread did not seem to have an effect on the power output [26, 28]; this was also reported more recently by Zhou et al. [298] using a similar PSD model. However, the models developed by Weber et al. and Zhou et al. were steady-state, and transient simulations of Shah et al. [152] showed more severe flooding during polarization sweeps when the average GDL pore size was increased. The same effect was reported for a GDL with reduced hydrophobicity [152], in alignment with the experiments by Yu and Ziegler [46].

The model of Weber et al. [305] also predicted a decrease in cell performance when large (100 μm) pores were added to the GDL, while Gerteisen et al. [458] reported enhanced performance of a physical cell with GDL perforation. The disagreement between the model and the experiment was hypothesized to be due to the assumption of a constant capillary pressure at the GDL-channel boundary [305]. Indeed, Gerteisen et al. [458] measured polarization sweeps with a relatively fast scan rate (10 mV/s) and low reactant flow rates (at most 0.1 ml/min), which induced strong cell transients with large polarization and resistance hystereses due to dynamic electrolyte hydration and liquid-water accumulation. Moreover, ex-situ experiments conducted by Hartnig et al. [459], Gostick et al. [460], Lu et al. [112], and Ziegler [461] demonstrated dynamic imbibition and drainage cycles of liquid water in GDLs. This so-called eruptive regime of water removal at the GDL-channel interface was also predicted by Qin et al. [221] with a pore-network model. Weng et al. [462] provided experimental evidence that cycles in liquid-water accumulation and electrolyte hydration result in fluctuations

in the produced current density. Similar experimental observations were made by Garcia-Salaberri et al. [41], although oscillations in current density and HFR were caused in their case by water condensation from the feed stream near the anode inlet rather than by the product water. A dynamic switch in the GDL-channel boundary condition was incorporated by Zenyuk et al. [273, 274] and Goshtasbi et al. [157] in their transient macrohomogeneous fuel-cell models to capture such a cyclic fuel-cell behavior; however, the latter did not appear in the simulations.

Another unexplored aspect of the GDL design is the role of the porous resin binder used in Sigracet$^{\circledR}$ gas-diffusion layers [75, 87, 89–91]. Although adding more binder has been shown by Xu [79] to reduce GDL porosity and diffusivity, the effect of the resin pores on liquid-water transport properties of Sigracet$^{\circledR}$ layers and on fuel-cell performance has not been investigated in the literature. There is, however, experimental evidence that the porous binder in Sigracet$^{\circledR}$ samples may act as an "MPL within the GDL": performance gain after coating a Sigracet$^{\circledR}$ GDL with an MPL is lower than for other GDLs under both dry and wet conditions [35, 276]. Nevertheless, a quantitative analysis of the role of the porous GDL binder is yet to be performed.

**Microporous Layers**  Structure and wettability of MPLs are known to affect fuel-cell performance. Nagai et al. [463] improved fuel-cell performance by creating liquid-water pathways in MPLs using pore formers so that the smaller pores remained available for gas transport. Cracks that may naturally form in MPLs during fabrication [78, 107, 109, 115] have also been shown numerically by Zenyuk et al. [40], Qin et al. [114] and experimentally by Islam et al. [115] to act as reservoirs and passages for liquid water. However, optimal MPL thickness, porosity, and PTFE content exist due to a trade-off between liquid-water and gas transport, as demonstrated in PSD-based modeling studies by Weber and Newman [26, 28] and Zhou et al. [35] and in the experimental work by Tseng and Lo [456]. That balance also depends on thermal conductivity of MPLs and GDLs that should be sufficiently low to facilitate water

evaporation in the cathode, but not too low to not cause electrolyte dehydration [35].

Graded MPLs have also been proposed [435, 462, 464, 465]. While Tang et al. [464] and Chun et al. [465] suggested placing larger pores near the cathode GDL (CGDL) and smaller pores near the CCL, the opposite was found to improve fuel-cell performance by Weng et al. [462] This was possibly because the MPL porosity distribution was a result of PTFE content variation (more near the GDL) in reference [462] rather than the use of pore-forming agents as in references [464, 465]. Kitahara et al. [466–468] suggested using a dual cathode MPL (CMPL) with a hydrophilic sub-layer doped with polyvinyl alcohol near the CCL and a uniform [466, 467] or graded [468] hydrophobic sub-layer doped with PTFE near the CGDL. Under dry-cathode conditions, the hydrophilic domain helped retain water in the membrane while the hydrophobic domain prevented water removal by dry gas [466–468]. Existence of an optimal PTFE content was found under wet conditions, in agreement with the PSD modeling studies by Weber and Newman [26, 28] and Zhou et al. [35]. Using a triple MPL with a graded hydrophobic treatment and less PTFE near the GDL further improved the performance [468]. In more recent studies, Kitahara et al. [469, 470] suggested a different MPL design with 4 wt% loading of hydrophilic carbon nanotubes for an optimal fuel-cell performance under both dry and wet conditions. Such layers with carbon nanotubes have been shown to have a different PSD compared with the conventional MPLs [107].

Even though a variety of MPL designs have been suggested in the literature, their influence on the fuel-cell performance is seldom analyzed in transient. Weng et al. [462] were able to reduce the flooding- and hydration-related oscillations in current density by using graded-PTFE MPLs instead of the commercial samples with no grading. However, it is difficult to draw conclusions from their data, as the cell was operated at a constant voltage, and current density (and thus the water-production rate) varied between the cases. Impedance spectroscopy was utilized by Weng et al. [462], Lin et al. [105], Fan et al. [106], and Lee et al. [107] to verify mass-transport

and ohmic-resistance trends observed with polarization curves. Nagai et al. [463] operated their cells at constant current to show that it took significantly longer time to achieve the same saturation levels in the CGDL when pore formers were used to create large pores in the CMPL. Microporous layers also reduce flooding hysteresis in polarization curves, as evident from the experiments by Yu and Ziegler [46] and the simulations by Shah et al. [152].

## 1.4  Thesis Objectives

The main objective of this thesis is to develop an open-source transient two-phase 2D PEMFC model suitable for simulating a variety of common experimental fuel-cell characterization techniques, including the dynamic polarization sweeps and impedance spectroscopy.

In the initial phase of the implementation of the transient framework in OpenFCST, a time-dependent model for oxygen transport in polymer-electrolyte membranes will be developed. The model will be used to fulfill the following first objective of this thesis:

1. Analyze the effect of the finite membrane thickness on the oxygen-transport properties obtained in chronoamperometric measurements [1].

Next, a transient PEMFC model will be developed in OpenFCST. The model will be used to address the following thesis objectives based on the literature review:

2. Investigate the electrolyte-hydration nature of the low-frequency inductive loop in fuel-cell impedance spectra [2].

3. Study the relationship between the effective conductivity, ohmic resistance, and impedance of uniform and nonuniform catalyst layers of PEMFCs and PEMWEs [3].

4. Analyze the effect of liquid-water accumulation on the dynamic performance of PEMFCs [4].

## 1.5   Thesis Outline

There are seven chapters in this thesis. The current chapter introduced the motivation for this thesis, provided a literature review of the considered topics, and listed the objectives. A detailed description of the developed transient two-phase 2D PEMFC model and the numerical framework used to simulate it is given in Chapter 2. Individual modules of the developed model are used in Chapters 3–6 to address the objectives formulated above. Diffusivity and solubility of oxygen in a polymer-electrolyte membrane are estimated in Chapter 3. The single-phase component of the model developed in Chapter 2 is used to analyze the electrolyte-hydration nature of the low-frequency inductance in PEMFC impedance spectra in Chapter 4. The performed parametric studies shed light on the fuel-cell inductance and, for the first time in the literature, unveil its relation to the water absorption/desorption kinetics in the ionomer. Suitability of the analytical methods [177, 182, 183] for estimating catalyst-layer charge-transport properties from $H_2/O_2$ and $H_2/N_2$ impedance spectra is examined in Chapter 5 using a numerical catalyst-layer model. Practical recommendations are provided for experimentalists so as to assist them in the EIS measurement and in the selection of suitable analytical models for the catalyst-layer charge-transport analysis of fuel-cell and water-electrolyzer impedance spectra. The impact of the liquid-water accumulation on the dynamic performance of PEMFCs is investigated in Chapter 6 with the developed transient two-phase model. The main findings of this thesis are summarized in Chapter 7, and outlook for the future work is given therein.

# Chapter 2

# Mathematical Model[1]

Chapters 3–6 are arranged in chronological order in which the mathematical models discussed therein have been developed by the author. Description of those models is unified in this Chapter in the form of the general two-phase fuel-cell model from Chapter 6 that incorporates the individual sub-models from Chapters 3–5. Relationships for computing the effective transport properties in the governing equations and some

---

[1]Parts of this chapter are reproduced from the following publications:

1. A. Kosakian, L. Padilla Urbina, A. Heaman, and M. Secanell, "Understanding single-phase water-management signatures in fuel-cell impedance spectra: A numerical study," *Electrochimica Acta*, vol. 350, p. 136 204, 2020.

2. A. Kosakian and M. Secanell, "Estimating charge-transport properties of fuel-cell and electrolyzer catalyst layers via electrochemical impedance spectroscopy," *Electrochimica Acta*, vol. 367, p. 137 521, 2021.

3. A. Kosakian, F. Wei, S. Jung, J. Zhou, A. Punia, J. Liu, and M. Secanell, "A transient, pore-size-distribution-based model for the analysis of the two-phase water transport in fuel cells," (in preparation).

Portions of this chapter were used in the following upcoming publication:

3. M. Secanell and A. Kosakian, "Membrane-electrode-assembly modeling using OpenFCST," in *PEMFC characterization and modelling – Current trends and challenges*, J. Stumper and J. Jankovic, Eds. de Gruyter, (in preparation).

The copyright remains with the author and not the publisher of the item immediately above (de Gruyter), as this thesis is published first. However, the used materials were significantly modified to avoid potential disputes.

License 4990320645990 was obtained from Springer in case of incidental use of any material from the following publication:

4. M. Secanell, A. Jarauta, A. Kosakian, M. Sabharwal, and J. Zhou, "PEM fuel cells, modeling," in *Encyclopedia of Sustainability Science and Technology*, R. A. Meyers, Ed. New York, NY: Springer New York, 2017, pp. 1–61, ISBN: 978-1-4939-2493-6. DOI: 10.1007/978-1-4939-2493-6_1019-1.

Author contributions are detailed in the Preface of this thesis.

of the model inputs are also provided in this Chapter. Additional relationships and material properties specific to Chapters 3–6 are given therein. The numerical framework developed by the author for solving the aforementioned models is discussed in detail in this Chapter.

# 2.1 Membrane-Electrode-Assembly Model

## 2.1.1 Assumptions

The transient mathematical model presented in this Chapter is based on the steady-state two-phase PEMFC model by Zhou et al. [34, 276]. The main simplifying assumptions of the steady-state component of the model are listed below.

1. Gas mixtures were assumed to be dilute, isobaric, and ideal. Gas flow was assumed purely diffusive at the considered operating conditions based on the recent study by Zhou et al. [35, 276].

2. Liquid-water transport was driven by capillary forces, based on the dimensional analysis by Bhaiya [65].

3. Liquid water was assumed incompressible and Newtonian, and its flow was assumed creeping and governed by Darcy's law [34, 65]. To describe liquid-water flow, each porous medium in the MEA was represented by a network of cylindrical capillaries of mixed wettability [34, 342].

4. The proton-exchange membrane was assumed impermeable to gases and liquid water [34].

5. Water was assumed to be transported in the polymer electrolyte in the absorbed form via osmosis and back-diffusion [22, 33–35, 65, 262, 263].

6. A single-energy-conservation-equation approach was used to describe heat transport under the assumption of local thermal equilibrium between the gas and

solid phases due to sufficiently large interfacial area of the porous layers in the MEA [33, 65].

7. In order to account for the local reactant transport resistance in the catalyst layers, a uniform distribution of spherical ionomer-covered catalyst particles [272, 328] was assumed in the CLs. Reactant gases (oxygen in the cathode and hydrogen in the anode) dissolved into and diffused through a thin layer of ionomer before reaching the reaction sites.

The main assumptions specific to the transient processes were as follows.

1. Double-layer capacitance of the interface between the carbon/platinum and ionomer phases of catalyst layers was considered. It was assumed constant and uniformly distributed (unless stated otherwise).

2. Kinetic models for the ORR and the HOR were assumed quasi-stationary. Transient terms describing dynamics of the reaction-intermediate species were omitted.

3. The ICCP model was assumed quasi-stationary due to the small thickness of the ionomer film (1–10 nm [124, 132]).

Other assumptions were the same as in references [33, 34, 65, 262, 263, 276].

## 2.1.2   Governing Equations

### 2.1.2.1   Gas Transport

Gas transport in the porous MEA components is governed by [6, 21, 65, 276]

$$\frac{\partial}{\partial t}\left(\varepsilon_{\mathrm{v}} c_i\right) + \nabla \cdot \boldsymbol{N}_i^{\mathrm{eff}} = S_i. \tag{2.1}$$

Coefficient $\varepsilon_{\mathrm{v}} \in (0,\,1)$ in the equation above is the volume fraction of the void phase. It is related to the porosity $\varepsilon_{\mathrm{p}} \in (0,\,1)$ of the dry layer through $\varepsilon_{\mathrm{v}} = \varepsilon_{\mathrm{p}}(1-s)$, where $s \in [0,\,1]$ is liquid-water saturation (fraction of the void space occupied by

liquid water). Variable $c_i$ represents concentration of gas species $i$ (mol/cm³). The second term in equation (2.1) describes volume-averaged gas transport. Under the assumption of an ideal and dilute gas mixture, the effective molar flux, $\boldsymbol{N}_i^{\mathrm{eff}}$, is given by [21, 276]

$$\boldsymbol{N}_i^{\mathrm{eff}} = -D_i^{\mathrm{eff}}\nabla c_i + c_i\boldsymbol{v}_{\mathrm{g}}, \tag{2.2}$$

where the first term is the diffusive flux as given by Fick's first law [472] and the second term is the convective flux [472]. Coefficient $D_i^{\mathrm{eff}}$ is the effective diffusivity of species $i$ (cm²/s), and $\boldsymbol{v}_{\mathrm{g}}$ is the molar-averaged velocity of the mixture (cm/s). The source/sink term $S_i$ describes consumption and production of species $i$.

Zhou et al. [35, 276] have demonstrated that diffusion is the main mode of gas transport in PEMFCs with parallel-channel flow fields. Therefore, convective gas transport is not considered in this thesis. Equation (2.1) is then simplified to

$$\frac{\partial}{\partial t}\left(\varepsilon_{\mathrm{v}}c_i\right) - \nabla \cdot \left(D_i^{\mathrm{eff}}\nabla c_i\right) = S_i. \tag{2.3}$$

Even though gas pressure is assumed constant in this thesis, concentration changes with temperature according to the ideal-gas law:

$$c_i = \frac{p_i}{RT}, \tag{2.4}$$

where $p_i$ is the partial pressure of species $i$ (Pa), $R \approx 8.314$ J/(mol·K) is the universal gas constant, and $T$ is temperature (K). However, for the typical temperature variation inside an MEA of at most 10 °C [33, 65, 99, 157, 320], equation (2.4) suggests that gas concentration varies by less than about 3%. Additionally, thermodiffusion is negligible in fuel cells [336, 473]. Therefore, equation (2.3) can be formulated with respect to the molar fraction

$$x_i = \frac{p_i}{p_{\mathrm{tot}}} = \frac{c_i}{c_{\mathrm{tot}}},$$

where $c_{\mathrm{tot}}$ is the total mixture concentration computed from the total gas pressure, $p_{\mathrm{tot}}$, using the ideal-gas law (2.4). The resulting governing equation for gas transport

is

$$c_{\mathrm{tot}}\frac{\partial}{\partial t}\left(\varepsilon_{\mathrm{v}}x_i\right) - \nabla \cdot \left(c_{\mathrm{tot}}D_i^{\mathrm{eff}}\nabla x_i\right) = S_i. \qquad (2.5)$$

The equation above represents Fick's second law of diffusion [472] and is commonly used to describe gas transport in fuel-cell models [31, 33, 34, 36, 65, 129–131, 162, 253, 254, 261–263, 265, 269, 270, 272, 276, 289, 290, 346, 369, 474, 475]. It has been implemented in OpenFCST in the steady-state form by Secanell [262], Bhaiya [65], Zhou [276], and Sabharwal [131] and was extended to the transient form in this work. Equation (2.5) was solved for the molar fractions of oxygen in the cathode, $x_{\mathrm{O}_2}$, and of water vapor in both electrodes, $x_{\mathrm{wv}}$. Nitrogen in the cathode and hydrogen in the anode were assumed to be solvents, and their molar fractions were obtained as $x_{\mathrm{N}_2} = 1 - x_{\mathrm{O}_2} - x_{\mathrm{wv}}$ and $x_{\mathrm{H}_2} = 1 - x_{\mathrm{wv}}$.

Consumption of oxygen in the ORR was described with a sink term

$$S_{\mathrm{O}_2} = \begin{cases} -\dfrac{j}{n_{\mathrm{e}}F} & \text{in CCL;} \\ 0 & \text{everywhere else,} \end{cases} \qquad (2.6)$$

where $j$ is the volumetric faradaic current density (A/cm$^3$), $n_{\mathrm{e}} = 4$ is the number of electrons consumed in the ORR per mole of oxygen (see equation (1.2)), and $F = 96,485$ C/mol is Faraday's constant. This term was only applied in the CCL, as that is where the ORR takes place. Models for computing faradaic current are discussed later in this Chapter.

For the electrochemical production of water, $n_{\mathrm{e}} = 2$. It was assumed that water could be produced in either liquid or vapor form. This was controlled with parameter $\chi$ that was equal to unity for vapor production and to zero for liquid production. Additionally, since the catalyst surface is at least partially covered with the ionomer in the catalyst layers [21, 117, 140], it is reasonable to assume that some water may be produced at the catalyst surface under the ionomer film, into which it is then directly absorbed. The amount of water that may directly enter the ionomer has not been measured experimentally and was approximated in this thesis with parameter

$\xi \in [0, 1]$. Thus, the source term for the generation of water vapor in the ORR is

$$S_{\mathrm{wv}}^{\mathrm{ORR}} = \begin{cases} \chi(1-\xi)\dfrac{j}{2F} & \text{in CCL;} \\ 0 & \text{everywhere else.} \end{cases} \tag{2.7}$$

One may expect that there exists some resistance to the uptake of water that is produced electrochemically at the catalyst-ionomer interface. Such resistance can be approximated by introducing a rate constant to the water-production source term. That rate constant is not known experimentally, and the associated resistance was not considered in this work to avoid introducing additional fitting parameters to the model.

**Local Gas-Transport Resistance**   Local reactant-transport resistance in the catalyst layers was accounted for by incorporating an additional sub-model describing transport of reactants through the thin ionomer films covering spherical catalyst particles (the ICCP model [272, 328]). A schematic of the ICCP idealization of the catalyst-layer structure is shown in Figure 2.1. This model, implemented in Open-FCST by Wardlaw [272], is based on a mass balance between the reactant transport through the gas-ionomer interface, its diffusion through the ionomer film, and consumption at the catalyst surface.

The rate of oxygen entering the ICCP through the gas-ionomer interface (in mol/s) is given by [272, 328]

$$R_{\mathrm{O_2}}^{\mathrm{int}} = -4\pi(r_{\mathrm{core}} + \delta)^2 k_{\mathrm{O_2}} \left( c_{\mathrm{O_2,g|f}} - c_{\mathrm{O_2,g|f}}^{\mathrm{eq}} \right), \tag{2.8}$$

where $r_{\mathrm{core}}$ is the radius of the ICCP carbon-platinum core, $\delta$ is the thickness of the ionomer film in the ICCP computed from the known platinum and ionomer loading of the catalyst layer [272, 328], $k_{\mathrm{O_2}}$ is a rate constant (m/s), $c_{\mathrm{O_2,g|f}}$ is the oxygen concentration in the ionomer at the gas-ionomer film interface, and $c_{\mathrm{O_2,g|f}}^{\mathrm{eq}}$ is its equilibrium value obtained from Henry's law at the given partial pressure of oxygen. The rate of
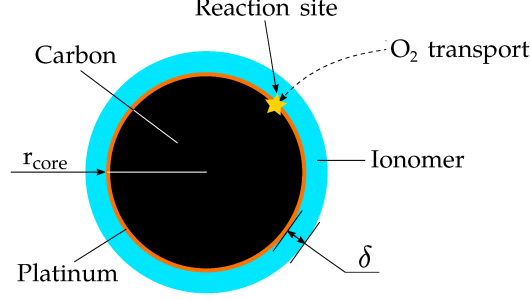
Figure 2.1: Schematic of the ICCP idealization of the catalyst-layer structure (not to scale).

oxygen diffusion through a spherical surface of area $4\pi r^2$ is given by [272, 328]

$$R_{O_2}^{\text{diff}} = 4\pi r^2 D_{O_2,i}\frac{dc_{O_2}}{dr},$$

where $D_{O_2,i}$ is the diffusion coefficient of oxygen in the ionomer. Consumption of oxygen in the ORR at the catalyst surface is described by [272, 328]

$$R_{O_2}^{\text{ORR}} = \frac{i(c_{O_2,c|f}, \eta)A_s}{4F},$$

where $i(c_{O_2,c|f}, \eta)$ is the current density ($\text{A/cm}_{\text{Pt}}^2$) computed based on the concentration of oxygen in the ionomer at the catalyst surface, $c_{O_2,c|f}$. Here, $A_s$ is the active surface area of the catalyst in one ICCP ($\text{cm}_{\text{Pt}}^2$) [328]:

$$A_s = \frac{A_v}{1 - \varepsilon_p}\frac{4}{3}\pi(r_{\text{core}} + \delta)^3, \tag{2.9}$$

where $A_v$ is the experimentally measured active area per volume of the catalyst layer ($\text{mg}_{\text{Pt}}/\text{cm}_{\text{CL}}^2$).

At steady state, $R_{O_2}^{\text{ORR}} = R_{O_2}^{\text{int}}$ and $R_{O_2}^{\text{ORR}} = R_{O_2}^{\text{diff}}$ form a system of equations for the unknown $c_{O_2,g|f}$ and $c_{O_2,c|f}$. Integrating the ODE $R_{O_2}^{\text{ORR}} = R_{O_2}^{\text{diff}}$ from $r_{\text{core}}$ to $r_{\text{core}} + \delta$ and eliminating $c_{O_2,g|f}$, the following equation is obtained [272, 328]:

$$c_{O_2,c|f} = c_{O_2,g|f}^{\text{eq}} - \frac{i(c_{O_2,c|f}, \eta)A_s}{16F\pi}\left(\frac{1}{(r_{\text{core}} + \delta)^2 k_{O_2}} + \frac{\delta}{r_{\text{core}}(r_{\text{core}} + \delta)D_{O_2,i}}\right). \tag{2.10}$$

Equation (2.10) is implicit in $c_{O_2,c|f}$ and nonlinear. It was solved using Newton's method; the solution was accepted once the residual of equation (2.10) reached $10^{-12}$.

The ICCP model enables the correction of the local current density for the local oxygen transport resistance in the cathode catalyst layer. Volumetric faradaic current density (per unit volume of the catalyst layer) was computed as $j = i(c_{O_2,c|f}, \eta)A_v$.

Similar equations apply for the anode side. The ICCP model is quasi-stationary and depends on time through gas concentration and overpotential. The original implementation of the ICCP model in OpenFCST was corrected in this thesis for the missing film thickness $\delta$ in equation (2.9).

### 2.1.2.2   Water Transport in the Electrolyte

Water in the polymer electrolyte was assumed in this thesis to be in the absorbed form, as suggested by Springer et al. [22] and commonly done in the literature [33, 34, 36, 52, 65, 152, 157, 227, 234, 247, 262–265, 269, 270, 272, 276, 289, 293, 299, 319, 320, 333, 334, 345, 346]. The amount of water in the electrolyte was described with a variable $\lambda$ that represents the ratio of the number of moles of water to the number of moles of the ionic groups ($mol_{H_2O}/mol_{SO_3^-}$). Three modes of transport were considered for the absorbed water, namely electroosmotic drag, back-diffusion, and thermoosmosis [33, 65, 157, 320].

Electroosmotic flux $(mol/(cm^2 \cdot s))$ is given by [6, 22, 33, 65]

$$\boldsymbol{N}^{\text{eff}}_{\lambda,\text{electroosmosis}} = -n_{\text{d}}\frac{\sigma^{\text{eff}}_{\text{H}^+}}{F}\nabla\phi_{\text{H}^+} \tag{2.11}$$

and describes how water molecules, owing to their dipolar nature, are dragged by hydrogen protons from the anode to the cathode. The electroosmotic drag coefficient, $n_{\text{d}}$, represents the water-to-proton flux ratio when concentration gradients are negligible. Electroosmotic drag is driven by the gradient in the protonic potential, $\phi_{\text{H}^+}$, and depends on the effective protonic conductivity of the electrolyte, $\sigma^{\text{eff}}_{\text{H}^+}$.

Concentration gradients of water give rise to back-diffusion [6, 22, 33, 65]:

$$\boldsymbol{N}^{\text{eff}}_{\lambda,\text{diffusion}} = -\frac{\rho_{\text{i, dry}}}{\text{EW}}D^{\text{eff}}_{\lambda}\nabla\lambda, \tag{2.12}$$

where $\rho_{\text{i, dry}}$ is the density of the dry electrolyte (g/cm$^3$) and EW is its so-called equivalent weight (mass of the dry electrolyte per mole of the ionic groups, g/mol$_{\text{SO}_3^-}$). Ratio $\rho_{\text{i, dry}}\lambda/\text{EW}$ is the equivalent water concentration in the electrolyte (mol$_{\text{H}_2\text{O}}$/cm$^3$). Coefficient $D_\lambda^{\text{eff}}$ is the effective absorbed-water diffusivity.

Flux of water associated with the temperature gradient (mol/(cm$^2 \cdot$ s)) is defined as [6, 33, 65]

$$\boldsymbol{N}_{\lambda,\text{thermoosmosis}}^{\text{eff}} = -\frac{D_T^{\text{eff}}}{M_{\text{H}_2\text{O}}}\nabla T, \tag{2.13}$$

where $M_{\text{H}_2\text{O}}$ is the molar mass of water (g/mol). The coefficient of thermoosmotic diffusion, $D_T^{\text{eff}}$ (g/(cm $\cdot$ s $\cdot$ K)), is negative, and water is transported from cold to hot regions of the electrolyte [476].

The overall flux of the absorbed water is a combination of fluxes (2.11)–(2.13):

$$\begin{aligned}\boldsymbol{N}_\lambda^{\text{eff}} &= \boldsymbol{N}_{\lambda,\text{electroosmosis}}^{\text{eff}} + \boldsymbol{N}_{\lambda,\text{diffusion}}^{\text{eff}} + \boldsymbol{N}_{\lambda,\text{thermoosmosis}}^{\text{eff}} \\ &= -n_{\text{d}}\frac{\sigma_{\text{H}^+}^{\text{eff}}}{F}\nabla\phi_{\text{H}^+} - \frac{\rho_{\text{i, dry}}}{\text{EW}}D_\lambda^{\text{eff}}\nabla\lambda - \frac{D_T^{\text{eff}}}{M_{\text{H}_2\text{O}}}\nabla T. \end{aligned} \tag{2.14}$$

Equation (2.1) written for the water transport in the electrolyte is, therefore,

$$\varepsilon_{\text{i}}\frac{\rho_{\text{i, dry}}}{\text{EW}}\frac{\partial\lambda}{\partial t} - \nabla\cdot\left(n_{\text{d}}\frac{\sigma_{\text{H}^+}^{\text{eff}}}{F}\nabla\phi_{\text{H}^+} + \frac{\rho_{\text{i, dry}}}{\text{EW}}D_\lambda^{\text{eff}}\nabla\lambda + \frac{D_T^{\text{eff}}}{M_{\text{H}_2\text{O}}}\nabla T\right) = S_\lambda,$$

where $\varepsilon_{\text{i}}$ is the polymer-electrolyte volume fraction that belongs to (0, 1) in catalyst layers and takes the value of unity in the membrane. This equation has been implemented in OpenFCST in its steady-state form by Secanell [262] and Bhaiya [65].

The source/sink term $S_\lambda$ (g/(cm$^3 \cdot$ s)) is

$$S_\lambda = S_\lambda^{\text{sorption}} + S_\lambda^{\text{ORR}} = \begin{cases} \varepsilon_{\text{i}}k_\lambda\dfrac{\rho_{\text{i, dry}}}{\text{EW}}\left(\lambda_{\text{eq}} - \lambda\right) + \xi\dfrac{j}{2F} & \text{in CCL;} \\ \varepsilon_{\text{i}}k_\lambda\dfrac{\rho_{\text{i, dry}}}{\text{EW}}\left(\lambda_{\text{eq}} - \lambda\right) & \text{in ACL;} \\ 0 & \text{everywhere else,} \end{cases} \tag{2.15}$$

where

$$S_\lambda^{\text{sorption}} = \begin{cases} \varepsilon_{\text{i}}k_\lambda\dfrac{\rho_{\text{i, dry}}}{\text{EW}}\left(\lambda_{\text{eq}} - \lambda\right) & \text{in CLs;} \\ 0 & \text{everywhere else} \end{cases} \tag{2.16}$$

and

$$S_\lambda^{\text{ORR}} = \begin{cases} \xi\dfrac{j}{2F} & \text{in CCL;} \\ 0 & \text{everywhere else.} \end{cases}$$

Term $S_\lambda^{\text{sorption}}$ describes the exchange of water between the ionomer and the pore phase of the catalyst layers. This exchange takes place at a finite rate $k_\lambda$ (1/s), and $\lambda_{\text{eq}}$ is the equilibrium water content in the ionomer under the given operating conditions. Term $S_\lambda^{\text{ORR}}$ accounts for water generated directly in the ionomer phase of the CCL.

Desorption and absorption of water by the ionomer were reflected in the following source/sink term of the vapor-transport equation (2.5):

$$S_{\text{wv}}^{\text{sorption}} = \begin{cases} -\varepsilon_i k_\lambda \dfrac{\rho_{\text{i, dry}}}{\text{EW}} \left(\lambda_{\text{eq}} - \lambda\right) & \text{in CLs;} \\ 0 & \text{everywhere else.} \end{cases} \tag{2.17}$$

### 2.1.2.3  Liquid-Water Transport

The flow of liquid water through the porous MEA components is commonly modeled as a creeping flow of an incompressible Newtonian fluid. It is described with a continuity equation [336],

$$\frac{\partial \left(\varepsilon_{\text{p}} s \rho_{\text{lw}}\right)}{\partial t} + \nabla \cdot \left(\rho_{\text{lw}} \boldsymbol{v}_{\text{lw}}\right) = S_{\text{lw}}, \tag{2.18}$$

in which the superficial liquid-water velocity, $\boldsymbol{v}_{\text{lw}}$, is obtained from the Darcy equation [336, 472]

$$\boldsymbol{v}_{\text{lw}} = -\frac{\kappa_{\text{lw}}}{\mu_{\text{lw}}} \nabla p_{\text{lw}}. \tag{2.19}$$

Variables $\rho_{\text{lw}}$, $\kappa_{\text{lw}}$, and $p_{\text{lw}}$ are, respectively, the density of liquid water (g/cm$^3$), its permeability (cm$^2$), and intrinsic pressure (Pa). Superficial and intrinsic averaging is discussed later in this Chapter and is defined in Appendix A. The product $\varepsilon_{\text{p}} s$ is the volume fraction of liquid water in the pores. Substituting velocity (2.19) into equation (2.18), one obtains the governing equation often used to model liquid-water transport in fuel cells [6, 25, 34, 35, 40, 43, 44, 52, 65, 152, 157, 273, 274, 276, 335, 336]:

$$\varepsilon_{\text{p}} \rho_{\text{lw}} \frac{\partial s}{\partial t} - \nabla \cdot \left(\frac{\rho_{\text{lw}} \kappa_{\text{lw}}}{\mu_{\text{lw}}} \nabla p_{\text{lw}}\right) = S_{\text{lw}}. \tag{2.20}$$

Dynamic viscosity $\mu_{lw}$ (g/(cm · s)) was computed as [65]

$$\mu_{lw} = 2.414 \cdot 10^{247.8/(T-140.0)-4}. \tag{2.21}$$

The source/sink term $S_{lw}$ describes production and phase change of water.

Capillary pressure is defined as the difference between the pressure of the non-wetting (injected) phase and the pressure of the wetting (displaced) phase [477]:

$$p_c = p_{\text{non-wetting}} - p_{\text{wetting}}.$$

Since the porous MEA components are mostly hydrophobic, liquid water is the non-wetting phase and gas is the wetting phase [34, 35, 40, 43, 44, 65, 157, 273, 274, 276]:

$$p_c = p_{lw} - p_g.$$

When the gas pressure, $p_g$, is assumed constant (as in this thesis), $\nabla p_c = \nabla p_{lw}$, and equation (2.20) can be formulated in terms of the capillary pressure:

$$\varepsilon_p \rho_{lw} \frac{\partial s}{\partial t} - \nabla \cdot \left( \frac{\rho_{lw} \kappa_{lw}}{\mu_{lw}} \nabla p_c \right) = S_{lw}. \tag{2.22}$$

Phase change of water was modeled with a source/sink term (mol/(cm$^3$ · s))

$$S_{H_2O} = \begin{cases} k_e a_{l\text{-g}} \left( \dfrac{p_{wv} - p_K^{\text{sat}}}{p_K^{\text{sat}}} \right), & p_{wv} \leq p_K^{\text{sat}}, \\ k_c a_{l\text{-g}} \left( \dfrac{p_{wv} - p_K^{\text{sat}}}{p_K^{\text{sat}}} \right), & p_{wv} > p_K^{\text{sat}}, \end{cases} \tag{2.23}$$

where $k_e$ and $k_c$ are rate constants for evaporation and condensation (mol/ (cm$^2$ · s)), $a_{l\text{-g}}$ is the volumetric interfacial area between the liquid and gas phases (cm$^2_{l\text{-g}}$/cm$^3_{\text{layer}}$), and $p_{wv} = p_g x_{wv}$ is the vapor pressure (Pa). Pressure $p_K^{\text{sat}}$ is given by [34]

$$p_K^{\text{sat}} = p^{\text{sat}} \exp \left( \frac{p_c M_{H_2O}}{\rho_{lw} RT} \right),$$

which is the Kelvin equation describing the relationship between the saturated-vapor pressure at the curved liquid-gas interface in a capillary and the saturated-vapor

pressure at a flat interface, $p^{\text{sat}}$. The latter was computed, in atmospheres, with [22]

$$\log_{10}(p^{\text{sat}}) = -\,2.1794 + 0.02953(T - 273.15)$$
$$-\,9.1837 \cdot 10^{-5}(T - 273.15)^2 + 1.4454 \cdot 10^{-7}(T - 273.15)^3. \quad (2.24)$$

The right-hand side of equations (2.20) and (2.22) includes the term $S_{\text{H}_2\text{O}}$ and also accounts for the electrochemical generation of liquid water:

$$S_{\text{lw}} = \begin{cases} (1 - \xi)(1 - \chi)\dfrac{j}{2F}M_{\text{H}_2\text{O}} + M_{\text{H}_2\text{O}}S_{\text{H}_2\text{O}} & \text{in CCL;} \\ M_{\text{H}_2\text{O}}S_{\text{H}_2\text{O}} & \text{in ACL, MPLs, GDLs;} \\ 0 & \text{in PEM,} \end{cases} \quad (2.25)$$

Electrolyte water uptake from liquid [116] should also be modeled. This can be done by incorporating an exchange term similar to the one in equation (2.15). However, the corresponding rate constant is not known. In this thesis, the effect of the liquid-water uptake by the ionomer in the catalyst layers was approximated by modifying the coefficient $\xi$ (water in the pore space was assumed in two-phase applications to be produced in liquid form, i.e., $\chi = 0$).

The change in vapor concentration due to evaporation and condensation of water was modeled with the following term added to the right-hand side of the vapor-transport equation (2.5):

$$S_{\text{wv}}^{\text{e/c}} = \begin{cases} -S_{\text{H}_2\text{O}} & \text{in CLs, MPLs, GDLs;} \\ 0 & \text{in PEM.} \end{cases} \quad (2.26)$$

The overall source/sink term of that equation is a combination of terms (2.7), (2.17), and (2.26):

$$S_{\text{wv}} = S_{\text{wv}}^{\text{ORR}} + S_{\text{wv}}^{\text{sorption}} + S_{\text{wv}}^{\text{e/c}}$$
$$= \begin{cases} (1 - \xi)\chi\dfrac{j}{2F} - S_{\text{H}_2\text{O}} - \varepsilon_{\text{i}}k_\lambda\dfrac{\rho_{\text{i, dry}}}{\text{EW}}(\lambda_{\text{eq}} - \lambda) & \text{in CCL;} \\ -S_{\text{H}_2\text{O}} - \varepsilon_{\text{i}}k_\lambda\dfrac{\rho_{\text{i, dry}}}{\text{EW}}(\lambda_{\text{eq}} - \lambda) & \text{in ACL;} \\ -S_{\text{H}_2\text{O}} & \text{in GDLs, MPLs;} \\ 0 & \text{in PEM.} \end{cases} \quad (2.27)$$

### 2.1.2.4 Charge Transport

**Electron Transport**   Electrons are transported through the carbon phase of GDLs and MPLs and through the carbon/platinum phase of CLs. In this thesis, those phases are collectively referred to as the solid phase in the context of charge transport (not to be confused with the structural solid phase that includes ionomer in CLs and PTFE in GDLs and MPLs). The electron-conservation equation is given by [262]

$$\varepsilon_\text{s}\frac{\partial c_\text{e}^-}{\partial t} + \nabla \cdot \boldsymbol{N}_\text{e}^{-\text{eff}} = R_\text{e}^-, \tag{2.28}$$

where $\varepsilon_\text{s}$ is the volume fraction of the electronically conductive solid phase, $c_\text{e}^-$ is the electron concentration (mol/cm$^3$) and $R_\text{e}^-$ (mol/(cm$^3 \cdot$ s)) describes production of electrons in the HOR (1.1) and their consumption in the ORR (1.2):

$$R_\text{e}^- = \begin{cases} -\dfrac{j}{F} & \text{in CCL;} \\ \dfrac{j}{F} & \text{in ACL;} \\ 0 & \text{everywhere else.} \end{cases}$$

Introducing electron charge density $\hat{\rho}_\text{e}^- = F z_\text{e}^- c_\text{e}^-$ (C/cm$^3$) [21], using the definition of current density $\boldsymbol{i}_\text{e}^- = F z_\text{e}^- \boldsymbol{N}_\text{e}^{-\text{eff}}$ (A/cm$^2$) [21, 262], and noting that the charge number (valence) of an electron, $z_\text{e}^-$, is equal to -1, one can transform equation (2.28) into

$$\varepsilon_\text{s}\frac{\partial \hat{\rho}_\text{e}^-}{\partial t} + \nabla \cdot \boldsymbol{i}_\text{e}^- = S_\text{e}^-, \tag{2.29}$$

where

$$S_\text{e}^- = -F R_\text{e}^- = \begin{cases} j & \text{in CCL;} \\ -j & \text{in ACL;} \\ 0 & \text{everywhere else.} \end{cases} \tag{2.30}$$

Current density $\boldsymbol{i}_\text{e}^-$ in equation (2.29) is given by Ohm's law [262]:

$$\boldsymbol{i}_\text{e}^- = -\sigma_\text{e}^{-\text{eff}}\nabla\phi_\text{e}^-, \tag{2.31}$$

where $\sigma_\text{e}^{-\text{eff}}$ is the effective electronic conductivity of the medium (S/cm) and $\phi_\text{e}^-$ is the electronic potential (V).

The first term of equation (2.29) describes accumulation of charge. The charging/discharging current represented by that term only exists in catalyst layers, where an electrical double layer is formed between the solid and ionomer phases that acts as a capacitor [55, 56, 61, 150, 478, 479]. Using the definition of the volume-averaged double-layer capacitance (F/cm$^3$) [478, 479],

$$C_{dl} = \varepsilon_s \frac{\partial \hat{\rho}_{e^-}}{\partial \left(\phi_{e^-} - \phi_{H^+}\right)}, \tag{2.32}$$

where $\phi_{H^+}$ is the protonic potential (V), one can write the capacitive current as

$$j_{c,e^-} = \varepsilon_s \frac{\partial \hat{\rho}_{e^-}}{\partial t} = \varepsilon_s \frac{\partial \hat{\rho}_{e^-}}{\partial \left(\phi_{e^-} - \phi_{H^+}\right)} \frac{\partial \left(\phi_{e^-} - \phi_{H^+}\right)}{\partial t} = C_{dl} \frac{\partial \left(\phi_{e^-} - \phi_{H^+}\right)}{\partial t}. \tag{2.33}$$

Substituting equations (2.31) and (2.33) into equation (2.29), the governing equation for electron transport is obtained:

$$C_{dl} \frac{\partial \left(\phi_{e^-} - \phi_{H^+}\right)}{\partial t} - \nabla \cdot \left(\sigma_{e^-}^{\text{eff}} \nabla \phi_{e^-}\right) = S_{e^-}.$$

The steady-state component of this equation has been implemented in OpenFCST by Secanell [262] and Bhaiya [65].

**Proton Transport**  The conservation equation for protons is similar to that for electrons, equation (2.28):

$$\varepsilon_i \frac{\partial c_{H^+}}{\partial t} + \nabla \cdot \boldsymbol{N}_{H^+}^{\text{eff}} = R_{H^+}. \tag{2.34}$$

Like electrons, protons are produced in the HOR (1.1) and consumed in the ORR (1.2). Thus,

$$R_{H^+} = \begin{cases} -\dfrac{j}{F} & \text{in CCL;} \\ \dfrac{j}{F} & \text{in ACL;} \\ 0 & \text{everywhere else.} \end{cases}$$

Assuming that the ionic groups in the polymer electrolyte are immobile and that the only transported species are sufficiently diluted hydrogen protons, one can follow

the same approach as before and substitute $\hat{\rho}_{H^+} = F z_{H^+} c_{H^+}$ (C/cm$^3$) [21], $\boldsymbol{i}_{H^+} = F z_{H^+} \boldsymbol{N}_{H^+}^{\text{eff}}$ (A/cm$^2$) [21, 262], and $z_{H^+} = 1$ into equation (2.34) to obtain

$$\varepsilon_{\text{i}} \frac{\partial \hat{\rho}_{H^+}}{\partial t} + \nabla \cdot \boldsymbol{i}_{H^+} = S_{H^+}, \tag{2.35}$$

where

$$S_{H^+} = F R_{H^+} = \begin{cases} -j & \text{in CCL;} \\ j & \text{in ACL;} \\ 0 & \text{everywhere else.} \end{cases} \tag{2.36}$$

Ohm's law was used to compute the protonic current density [6, 21]:

$$\boldsymbol{i}_{H^+} = -\sigma_{H^+}^{\text{eff}} \nabla \phi_{H^+}, \tag{2.37}$$

where $\sigma_{H^+}^{\text{eff}}$ is the effective protonic conductivity (S/cm). Double-layer capacitance (2.32) was introduced in the temporal derivative of equation (2.35) as follows:

$$\varepsilon_{\text{i}} \frac{\partial \hat{\rho}_{H^+}}{\partial t} = \varepsilon_{\text{i}} \frac{\partial \hat{\rho}_{H^+}}{\partial (\phi_{H^+} - \phi_{e^-})} \frac{\partial (\phi_{H^+} - \phi_{e^-})}{\partial t} = -C_{\text{dl}} \frac{\partial (\phi_{e^-} - \phi_{H^+})}{\partial t}. \tag{2.38}$$

Combining equations (2.35), (2.37), and (2.38), one obtains the governing equation for proton transport used in this thesis:

$$-C_{\text{dl}} \frac{\partial (\phi_{e^-} - \phi_{H^+})}{\partial t} - \nabla \cdot \left( \sigma_{H^+}^{\text{eff}} \nabla \phi_{H^+} \right) = S_{H^+}.$$

The steady-state version of this equation has been implemented in OpenFCST by Secanell [262] and Bhaiya [65].

### 2.1.2.5   Heat Transport

The governing equation for heat transport used in this thesis was obtained by extending the steady-state equation implemented in OpenFCST by Bhaiya [65] and Zhou [276] to the transient form:

$$\sum_{i=\text{phase}} \rho_i C_{p,i} \frac{\partial (\varepsilon_i T)}{\partial t} - \nabla \cdot \left( \kappa^{\text{eff}} \nabla T \right) + \sum_{j=\text{gas}, \lambda} \boldsymbol{N}_j \cdot \nabla \overline{H}_j = S_T. \tag{2.39}$$

In the equation above, $C_p$ is specific heat capacity (J/(g · K)) that was assumed constant in this work, $\kappa^{\text{eff}}$ is effective thermal conductivity (W/(cm · K)), $\overline{H}$ is molar enthalpy (J/mol), and $S_T$ contains source and sink terms (W/cm$^3$) that will be

discussed shortly. A single equation was used to predict temperature changes in all phases of the MEA assuming local thermal equilibrium due to the large surface area of porous media, as commonly done in the literature [21, 33–35, 43, 44, 52, 65, 152, 157, 159, 230–232, 234, 235, 237, 238, 241–243, 246, 247, 252, 261, 264, 266, 267, 273–277, 280, 289, 293]. Quantity

$$\sum_{i=\text{phase}} \varepsilon_i \rho_i C_{p,i} \tag{2.40}$$

in the first term of equation (2.39) represents the effective volumetric heat capacity $(\text{J}/(\text{cm}^3 \cdot \text{K}))$. Due to the small density of gases, their contribution to the overall heat capacity is negligible and was not considered. Thus, the summation is performed over the rest of the phases, for example, carbon, PTFE, and liquid water in GDLs and MPLs. The second and third terms in equation (2.39) represent heat transport due to the effective Fourier conduction and inter-diffusion of gases and water in the electrolyte.

The first of the source terms contained in $S_T$ describes heat release in the overall PEMFC reaction (1.3), which is exothermic [61, 62]. The corresponding entropy change per mole of hydrogen is [65]

$$\Delta \bar{S}_{\text{overall}} = 4.184(8(1 + \ln(T)) - 92.84) \ \text{J}/(\text{mol} \cdot \text{K}).$$

This quantity is negative for the fuel-cell temperature range. It is believed that most of the reversible reaction heat is released in the ORR [64, 65]. The exact contribution of the half-cell reactions to the total heat release is unknown and was controlled in the model with parameter $f_{\text{ORR}} \in [0, 1]$ [33, 65]: $\Delta \bar{S}_{\text{ORR}} = f_{\text{ORR}} \Delta \bar{S}_{\text{overall}}$ and $\Delta \bar{S}_{\text{HOR}} = (1 - f_{\text{ORR}}) \Delta \bar{S}_{\text{overall}}$. In this thesis, it was assumed that $f_{\text{ORR}} = 1$ [33, 65]. The source term for the reversible heat release in the ORR is, therefore [33, 65],

$$S_T^{\text{rev,ORR}} = \begin{cases} \dfrac{j}{2F} \left(-T \Delta \bar{S}_{\text{overall}}\right) & \text{in CLs;} \\ 0 & \text{everywhere else.} \end{cases} \tag{2.41}$$

The factor of 2 is the number of moles of electrons per mole of hydrogen (reactions (1.1) and (1.2)).

The irreversible electrochemical heat generation due to activation polarization was reflected in the following source terms that were applied in both catalyst layers [33, 65]:

$$S_T^{\text{irrev,ORR}} = \begin{cases} -j\eta = -j\left(\phi_{\text{e}^-} - \phi_{\text{H}^+} - E_{\text{ORR}}\right) & \text{in CCL;} \\ 0 & \text{everywhere else;} \end{cases} \tag{2.42}$$

$$S_T^{\text{irrev,HOR}} = \begin{cases} j\eta = j\left(\phi_{\text{e}^-} - \phi_{\text{H}^+} - E_{\text{HOR}}\right) & \text{in ACL;} \\ 0 & \text{everywhere else.} \end{cases} \tag{2.43}$$

The theoretical anodic potential was taken as a zero-point reference, $E_{\text{HOR}} = 0$, since the ACL is a standard hydrogen electrode [62]. The cathodic potential $E_{\text{ORR}}$ was then computed with respect to $E_{\text{HOR}}$. The difference in the signs of the source terms (2.42) and (2.43) is due to the cathodic overpotential being negative and anodic overpotential being positive [33, 65].

As current flows through the electrically conductive materials of the MEA, irreversible ohmic (Joule) heating takes place. The amount of this heat generated due to the conduction of protons and electrons is given by $\boldsymbol{i}_{\text{H}^+} \cdot \boldsymbol{i}_{\text{H}^+} / \sigma_{\text{H}^+}^{\text{eff}}$ and $\boldsymbol{i}_{\text{e}^-} \cdot \boldsymbol{i}_{\text{e}^-} / \sigma_{\text{e}^-}^{\text{eff}}$, respectively, where current density is defined with equations (2.31) and (2.37). The corresponding source term is [33, 65]

$$S_T^{\text{ohmic}} = \begin{cases} \sigma_{\text{H}^+}^{\text{eff}} \left(\nabla\phi_{\text{H}^+} \cdot \nabla\phi_{\text{H}^+}\right) & \text{in PEM;} \\ \sigma_{\text{H}^+}^{\text{eff}} \left(\nabla\phi_{\text{H}^+} \cdot \nabla\phi_{\text{H}^+}\right) + \sigma_{\text{e}^-}^{\text{eff}} \left(\nabla\phi_{\text{e}^-} \cdot \nabla\phi_{\text{e}^-}\right) & \text{in CLs;} \\ \sigma_{\text{e}^-}^{\text{eff}} \left(\nabla\phi_{\text{e}^-} \cdot \nabla\phi_{\text{e}^-}\right) & \text{in MPLs and GDL.} \end{cases} \tag{2.44}$$

Phase change of water is also accompanied with heat generation or consumption. Molar enthalpies of water absorbed into the electrolyte, $\bar{H}_{\text{H}_2\text{O, abs}}$, and water vapor, $\bar{H}_{\text{H}_2\text{O, vap}}$, differ from each other by $\bar{H}_{\text{sorption}}$, the molar enthalpy change during water absorption/desorption, which was assumed in this work to be 45 kJ/mol [33, 65]:

$$\bar{H}_{\text{H}_2\text{O, abs}} = \bar{H}_{\text{H}_2\text{O, vap}} - \bar{H}_{\text{sorption}}. \tag{2.45}$$

Heat is produced when water is absorbed by the electrolyte and consumed when water is desorbed. This was accounted for with a source/sink term [33, 65]

$$S_T^{\text{sorption}} = \begin{cases} S_\lambda^{\text{sorption}} \bar{H}_{\text{sorption}} & \text{in CLs;} \\ 0 & \text{everywhere else,} \end{cases} \tag{2.46}$$

where $S_\lambda^{\text{sorption}}$ is given by equation (2.16).

The final thermal source/sink term of the model describes heat absorption during evaporation of liquid water and heat release during water condensation [34, 65]:

$$S_T^{\text{evap/cond}} = \begin{cases} S_{\text{H}_2\text{O}} \overline{H}_{\text{lv}} & \text{in CLs, MPLs, GDLs;} \\ 0 & \text{in PEM,} \end{cases} \qquad (2.47)$$

where [33, 65]

$$\overline{H}_{\text{lv}} = M_{\text{H}_2\text{O}} \big( 2500.304 - 2.252(T - 273.15) - 0.0215(T - 273.15)^{1.5}$$
$$+ 3.175 \cdot 10^{-4}(T - 273.15)^{2.5} - 2.861 \cdot 10^{-5}(T - 273.15)^3 \big) \quad (2.48)$$

is the molar latent heat of water vaporization (J/mol). In the single-phase component of the PEMFC model, where liquid-water transport is not considered (Chapter 4), complete vaporization of the product water was assumed. Instead of equation (2.47), a different sink term was used in that case [33, 65]:

$$S_T^{\text{evap/cond}} = \begin{cases} -(1 - \xi) \dfrac{j}{2F} \overline{H}_{\text{lv}} & \text{in CLs, MPLs, GDLs;} \\ 0 & \text{in PEM.} \end{cases} \qquad (2.49)$$

Combination of equations (2.41)–(2.46) and (2.47) (or (2.49)) gives the overall source/sink term of the heat-transport equation (2.39):

$$S_T = S_T^{\text{ohmic}} + S_T^{\text{sorption}} + S_T^{\text{evap/cond}} + S_T^{\text{rev,ORR}} + S_T^{\text{irrev,ORR}} + S_T^{\text{irrev,HOR}}. \quad (2.50)$$

### 2.1.2.6   Electrochemical Reactions

Volumetric faradaic current density of the ORR (1.2) was computed in this thesis with the double-trap kinetic model proposed by Wang et al. [308] and implemented in OpenFCST by Moore [270], Bhaiya [65], and Wardlaw [272]:

$$j_{\text{ORR}} = 2i^* A_{\text{v}} \left[ \theta_{\text{OH}} \exp\left( -\frac{\Delta G_{\text{RD}}^*}{kT} \right) - \theta_{\text{Pt}} \exp\left( -\frac{\Delta G_{\text{-RD}}^*}{kT} \right) \right], \qquad (2.51)$$

where $i^*$ is a reference prefactor (A/cm$_{\text{Pt}}^2$), $\theta_i$ is the coverage of the platinum surface with species $i$, $\Delta G_{\text{RD}}^*$ and $\Delta G_{\text{-RD}}^*$ denote the potential-dependent free energy of activation (eV) for the forward and backward reductive-desorption steps in the ORR,

respectively, and $k \approx 8.617 \cdot 10^{-5}$ eV/K is the Boltzmann constant. In one of the parametric studies in Chapter 5, ORR current was also computed using the Tafel kinetics [63, 150, 312] implemented by Secanell [262], Moore [270], and Bhaiya [65]:

$$j_{\text{ORR}} = i_0 A_{\text{v}} \left( \frac{c_{\text{O}_2}^{\text{cat|i}}}{c_{\text{O}_2}^{\text{ref}}} \right)^{\gamma} \exp \left( -\frac{\alpha F \eta}{RT} \right), \tag{2.52}$$

where $c_{\text{O}_2}^{\text{ref}}$ is the reference oxygen concentration (mol/cm$^3$), $c_{\text{O}_2}^{\text{cat|i}}$ is the oxygen concentration at the catalyst-ionomer interface (mol/cm$^3$) computed using Henry's law, $\gamma = 1$ [36, 310] is the reaction order with respect to oxygen concentration, and $\alpha = 0.5$ [36] is the charge-transfer coefficient.

The HOR current density for reaction (1.1) was computed with the dual-path kinetic model proposed by Wang et al. [307] and implemented in OpenFCST by Secanell [262], Moore [270], and Bhaiya [65]:

$$j_{\text{HOR}} = A_{\text{v}} \frac{c_{\text{H}_2}^{\text{cat|i}}}{c_{\text{H}_2}^{\text{ref}}} \left( i_{0\text{T}} \left[ 1 - \exp \left( \frac{-2F\eta}{\beta RT} \right) \right] \right.$$
$$\left. + i_{0\text{H}} \left[ \exp \left( \frac{F\eta}{2RT} \right) - \exp \left( \frac{-F\eta}{\beta RT} \right) \exp \left( \frac{-F\eta}{2RT} \right) \right] \right), \tag{2.53}$$

where $i_{0\text{T}} = 0.47$ A/cm$^2$, $i_{0\text{H}} = 0.01$ A/cm$^2$ are the exchange-current densities of the Tafel and Heyrovsky steps of the HOR, respectively, and $\beta = 1.2$.

### 2.1.2.7 Summary of the Governing Equations

The governing equations of the transient two-phase PEMFC model developed in this thesis are summarized as follows:

$$\varepsilon_{\text{p}} c_{\text{tot}} \frac{\partial}{\partial t} \left( (1 - s) x_{\text{O}_2} \right) - \nabla \cdot \left( c_{\text{tot}} D_{\text{O}_2}^{\text{eff}} \nabla x_{\text{O}_2} \right) = S_{\text{O}_2}, \tag{2.54}$$

$$\varepsilon_{\text{p}} c_{\text{tot}} \frac{\partial}{\partial t} \left( (1 - s) x_{\text{wv}} \right) - \nabla \cdot \left( c_{\text{tot}} D_{\text{wv}}^{\text{eff}} \nabla x_{\text{wv}} \right) = S_{\text{wv}}, \tag{2.55}$$

$$-C_{\text{dl}} \frac{\partial \left( \phi_{\text{e}^-} - \phi_{\text{H}^+} \right)}{\partial t} - \nabla \cdot \left( \sigma_{\text{H}^+}^{\text{eff}} \nabla \phi_{\text{H}^+} \right) = S_{\text{H}^+}, \tag{2.56}$$

$$C_{\text{dl}} \frac{\partial \left( \phi_{\text{e}^-} - \phi_{\text{H}^+} \right)}{\partial t} - \nabla \cdot \left( \sigma_{\text{e}^-}^{\text{eff}} \nabla \phi_{\text{e}^-} \right) = S_{\text{e}^-}, \tag{2.57}$$

$$\varepsilon_{\text{i}} \frac{\rho_{\text{i, dry}}}{\text{EW}} \frac{\partial \lambda}{\partial t} - \nabla \cdot \left( n_{\text{d}} \frac{\sigma_{\text{H}^+}^{\text{eff}}}{F} \nabla \phi_{\text{H}^+} + \frac{\rho_{\text{i, dry}}}{\text{EW}} D_{\lambda}^{\text{eff}} \nabla \lambda + \frac{D_{\text{T}}^{\text{eff}}}{M_{\text{H}_2\text{O}}} \nabla T \right) = S_{\lambda}, \tag{2.58}$$

$$\sum_{i=\text{phase}} \rho_i C_{p,i} \frac{\partial(\varepsilon_i T)}{\partial t} - \nabla \cdot \left(\kappa^{\text{eff}} \nabla T\right) + \sum_{j=\text{gas},\lambda} \left(\boldsymbol{N}_j \cdot \nabla \overline{H}_j\right) = S_{\text{T}}, \qquad (2.59)$$

$$\varepsilon_{\text{p}} \rho_{\text{lw}} \frac{\partial s}{\partial t} - \nabla \cdot \left(\frac{\rho_{\text{lw}} \kappa_{\text{lw}}}{\mu_{\text{lw}}} \nabla p_{\text{c}}\right) = S_{\text{lw}}. \qquad (2.60)$$

The source/sink terms of the model are defined in equations (2.6), (2.15), (2.25), (2.27), (2.30), (2.36), and (2.50). Parts of the MEA where these equations were solved are indicated in Table 2.1.

Equations (2.54)–(2.60) represent the most general of the models developed in this thesis that is used in Chapter 6 to analyze two-phase flow in fuel cells. Mathematical models used in Chapters 3–5 only utilize subsets of equations (2.54)–(2.60). Computational domains and initial and boundary conditions vary depending on the model at hand. Those details are provided in Chapters 3–6.

Calculation of the main material properties and effective transport properties that appear in governing equations (2.54)–(2.60) is discussed next. The rest of the model inputs and relationships can be found in Chapters 3–6 and references [65, 262, 270, 312].

Table 2.1: Solution-variable domains in the model.

| Solution variable | AGDL, AMPL | ACL | PEM | CCL | CMPL, CGDL |
|---|---|---|---|---|---|
| $x_{\text{O}_2}$ | | | | ✓ | ✓ |
| $x_{\text{wv}}$ | ✓ | ✓ | | ✓ | ✓ |
| $\phi_{\text{H}^+}$ | | ✓ | ✓ | ✓ | |
| $\phi_{\text{e}^-}$ | ✓ | ✓ | | ✓ | ✓ |
| $\lambda$ | | ✓ | ✓ | ✓ | |
| $T$ | ✓ | ✓ | ✓ | ✓ | ✓ |
| $p_{\text{lw}}$ | ✓ | ✓ | | ✓ | ✓ |

### 2.1.3 Constitutive Relationships

#### 2.1.3.1 Layer Composition and Structure

**Catalyst Layers**  Instead of the volume fractions of the pores, the solid phase, and the ionomer, a typical catalyst-layer fabrication recipe would specify the desired catalyst and ionomer contents. Those experimental design characteristics need to be converted to the volume fractions used in mathematical models. The solid-phase volume fraction was estimated from the mass fraction of platinum in the carbon/-platinum powder, $M_{C+Pt}^{Pt}$, and the aerial platinum loading, $m_{Pt}$ (mass of platinum per in-plane CL area, in g/cm$^2$) [281]:

$$\varepsilon_s^{CL} = \left( \frac{1}{\rho_{Pt}} + \frac{1}{\rho_C} \left[ \frac{1 - M_{C+Pt}^{Pt}}{M_{C+Pt}^{Pt}} \right] \right) \frac{m_{Pt}}{L_{CL}}, \tag{2.61}$$

where $\rho$ is density (g/cm$^3$). Catalyst-layer thickness, $L_{CL}$, can be controlled during fabrication [124–126, 434] and is often determined from microscopy imaging [121, 122, 124–127, 443].

Knowing the mass fraction of the ionomer in the carbon/platinum/ionomer mixture, $M_{C+Pt+i}^{i}$, one can find the electrolyte volume fraction [281]:

$$\varepsilon_i^{CL} = \frac{1}{\rho_{i, dry}} \frac{M_{C+Pt+i}^{i}}{1 - M_{C+Pt+i}^{i}} \frac{1}{M_{C+Pt}^{Pt}} \frac{m_{Pt}}{L_{CL}}, \tag{2.62}$$

where $\rho_{i, dry}$ is the density of the ionomer prior to hydration. Another composition characteristic used by experimentalists, the ionomer-to-carbon weight ratio, $M_C^i$, is related to the ionomer loading, $M_{C+Pt+i}^{i}$, through

$$M_C^i = \frac{M_{C+Pt+i}^{i}}{1 - M_{C+Pt+i}^{i}} \frac{1}{1 - M_{C+Pt}^{Pt}}.$$

Finally, porosity of the catalyst layer was obtained as

$$\varepsilon_p^{CL} = 1 - \varepsilon_s^{CL} - \varepsilon_i^{CL}. \tag{2.63}$$

Volume fractions estimated with equations (2.61)–(2.63) appear in the governing equations discussed earlier in this Chapter and were used to compute the effective transport properties in the catalyst layers.
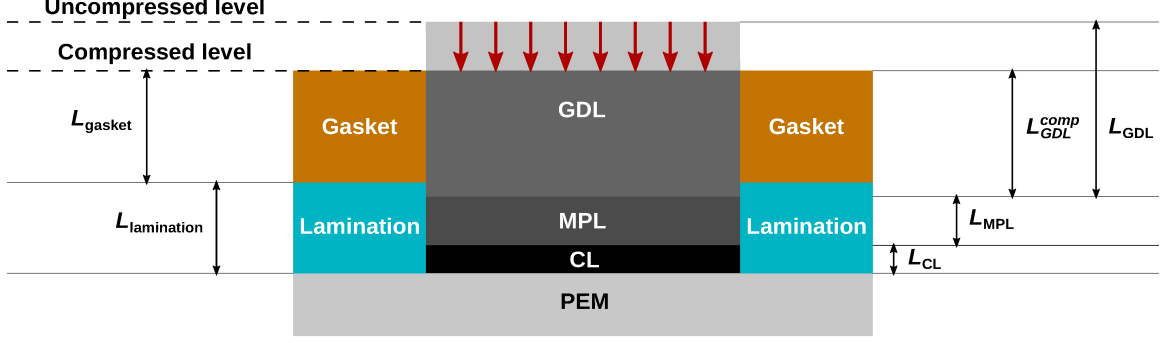
Figure 2.2: Cross-sectional schematic of a cell assembly prior to and after compression.

Volume fractions of carbon support and platinum catalyst were estimated using

$$\varepsilon_{s,\,C}^{CL} = \varepsilon_s \frac{\rho_{Pt} \left(1 - M_{C+Pt}^{Pt}\right)}{\rho_{Pt} + (\rho_C - \rho_{Pt}) M_{C+Pt}^{Pt}} \tag{2.64}$$

and

$$\varepsilon_{s,\,Pt}^{CL} = \varepsilon_s \frac{\rho_C M_{C+Pt}^{Pt}}{\rho_{Pt} + (\rho_C - \rho_{Pt}) M_{C+Pt}^{Pt}}, \tag{2.65}$$

respectively. Quantities (2.62), (2.64), and (2.65) were used in the computation of the effective heat capacity (2.40) in the heat-transport equation (2.59).

**Gas-Diffusion and Microporous Layers**   Some properties of the porous transport layers, such as porosity and thickness of GDLs and MPLs, are usually known from the manufacturer or are measured experimentally. However, when a fuel cell is assembled, PTLs are compressed to ensure sufficient electrical contact between the cell components. It was assumed in this work that GDLs were compressible while MPLs and CLs, being more compact, were not. The compressed GDL thickness was found from the known geometric properties of the cell assembly illustrated in Figure 2.2, namely the thickness of the rigid gaskets, $L_{gasket}$, lamination thickness, $L_{lamination}$, and the thickness of other MEA components. Compression was assumed uniform, even though it is higher under the bipolar-plate ribs and lower under the channels in physical cells.

The compressed thickness of the GDL-MPL combination, denoted here with the

"comp" subscript, was found from

$$L_{\text{GDL+MPL}}^{\text{comp}} = L_{\text{lamination}} + L_{\text{gasket}} - \frac{L_{\text{ACL}} + L_{\text{CCL}}}{2}.$$

The difference between the ACL and CCL thicknesses (at most a few microns) is small compared to the GDL thickness (over 100 µm), and so their average thickness was considered in the equation above so that the resulting compressed thicknesses of anode and cathode GDLs would be the same. The latter were computed as follows:

$$L_{\text{GDL}}^{\text{comp}} = L_{\text{GDL+MPL}}^{\text{comp}} - L_{\text{MPL}}.$$

Porosity of the compressed GDL was obtained using [480]

$$\varepsilon_{\text{p}}^{\text{GDL, comp}} = 1 - \frac{(1 - \varepsilon_{\text{p}}^{\text{GDL}})L_{\text{GDL}}}{L_{\text{GDL}}^{\text{comp}}}.$$

Subscript "comp" will be omitted in the rest of this thesis for brevity.

Once compression is taken into account, volume fractions of carbon and PTFE in GDLs and MPLs can be estimated. Since the exact amount of the porous binder and its physical properties are unknown, GDLs were assumed in this work to consist only of carbon, PTFE, and void phase. Given a known PTFE mass fraction in the layer, $M_{\text{C+PTFE}}^{\text{PTFE}}$, one can define a system of equations that can be solved with respect to the volumes of carbon, $V_{\text{C}}$, and PTFE, $V_{\text{PTFE}}$:

$$\begin{cases} M_{\text{C+PTFE}}^{\text{PTFE}} = \dfrac{\rho_{\text{PTFE}}V_{\text{PTFE}}}{\rho_{\text{C}}V_{\text{C}} + \rho_{\text{PTFE}}V_{\text{PTFE}}}, \\ V_{\text{C}} + V_{\text{PTFE}} = (1 - \varepsilon_{\text{p}}^{\text{GDL/MPL}})V_{\text{layer}}, \end{cases} \tag{2.66}$$

where $V_{\text{layer}}$ is the total volume of the layer. The first of these equations is the definition of $M_{\text{C+PTFE}}^{\text{PTFE}}$, and the second one is a simple rearrangement of

$$\varepsilon_{\text{p}}^{\text{GDL/MPL}} + \varepsilon_{\text{C}}^{\text{GDL/MPL}} + \varepsilon_{\text{PTFE}}^{\text{GDL/MPL}} = 1$$

with $\varepsilon_{\text{C}} = V_{\text{C}}/V_{\text{layer}}$ and $\varepsilon_{\text{PTFE}} = V_{\text{PTFE}}/V_{\text{layer}}$. Solving system (2.66) with respect to the volume fractions of carbon and PTFE, one finds

$$\varepsilon_{\text{C}} = \frac{(1 - \varepsilon_{\text{p}}^{\text{GDL/MPL}})\rho_{\text{PTFE}}(1 - M_{\text{C+PTFE}}^{\text{PTFE}})}{\rho_{\text{PTFE}} + (\rho_{\text{C}} - \rho_{\text{PTFE}})M_{\text{C+PTFE}}^{\text{PTFE}}},$$

$$\varepsilon_{\text{PTFE}} = \frac{(1 - \varepsilon_{\text{p}}^{\text{GDL/MPL}})\rho_{\text{C}}M_{\text{C+PTFE}}^{\text{PTFE}}}{\rho_{\text{PTFE}} + (\rho_{\text{C}} - \rho_{\text{PTFE}})M_{\text{C+PTFE}}^{\text{PTFE}}}.$$

These volume fractions were used in the computation of the effective heat capacity (2.40).

### 2.1.3.2  Gas Diffusivity

Diffusion coefficient of gas $i$, $D_i$ ($cm^2/s$), was calculated based on its molecular diffusivity, $D_i^m$, and its Knudsen diffusivity, $D_i^K$, using the Bosanquet approximation [21, 276, 481, 482]

$$\frac{1}{D_i} = \frac{1}{D_i^m} + \frac{1}{D_i^K}.$$

(2.67)

Molecular diffusivity was computed from the Chapman-Enskog theory [472]. Knudsen diffusivity was found using [21, 336, 472, 477, 483]

$$D_i^K = \frac{2r_K}{3} \sqrt{\frac{8RT}{\pi M_i}},$$

where $r_K$ is the average Knudsen pore radius of the medium (cm). In the single-phase component of the PEMFC model, where liquid saturation is zero, $r_K$ was either taken from experimental porosimetry data or, in case of catalyst layers, computed with the relationship proposed by Sabharwal et al. [130, 131] based on the stochastic analysis of inkjet-printed CLs:

$$r_K = r_p \left(1.66\varepsilon_p^{1.65} + 0.289\right),$$

where $r_p$ is the radius of the primary particles known from the manufacturer of the carbon support. In the two-phase model, the Knudsen pore radius was computed from the pore-size distribution of each porous layer as discussed later in this Chapter.

Under dry operating conditions, the effective diffusion coefficient, $D_i^{eff}$, was calculated from the percolation theory [279, 484]:

$$D_i^{eff} = D_i \left(\frac{\varepsilon_p - \varepsilon_{p,th}}{1 - \varepsilon_{p,th}}\right)^{\mu} \Theta(\varepsilon_p - \varepsilon_{p,th}),$$

(2.68)

where $D_i$ is found from equation (2.67) and $\mu$ is a material-dependent constant. No transport was assumed to take place when porosity was lower than the percolation

threshold of the given medium $\varepsilon_{\mathrm{p,th}}$. This was enforced with the Heaviside step-function

$$\Theta(\varepsilon_{\mathrm{p}} - \varepsilon_{\mathrm{p,th}}) = \begin{cases} 0, & \epsilon < \varepsilon_{\mathrm{p,th}}; \\ 1, & \epsilon \geq \varepsilon_{\mathrm{p,th}}. \end{cases} \tag{2.69}$$

The values of $\mu$ and $\varepsilon_{\mathrm{p,th}}$ for the materials considered in this thesis are provided in Chapter 4.

A modification of equation (2.68) was used under wet conditions. In catalyst layers, the following relationship proposed by Sabharwal et al. [130, 131] was utilized:

$$D_i^{\mathrm{eff}} = D_i \left( \frac{\varepsilon_{\mathrm{p}}(1 - s) - \varepsilon_{\mathrm{p,th}}}{1 - \varepsilon_{\mathrm{p,th}}} \right)^{\mu} \Theta(\varepsilon_{\mathrm{p}}(1 - s) - \varepsilon_{\mathrm{p,th}}) \tag{2.70}$$

with the porosity threshold $\varepsilon_{\mathrm{p,th}} = 0.05$ and $\mu = 1.9$. This equation is valid for catalyst layers with the average particle radius of about 40 nm and porosity between 0.3 and 0.6 [130, 131], which is the case for the CLs considered in this thesis. Equation (2.70) is equivalent to equation (2.68) under dry conditions ($s = 0$). Changes in porosity and ionomer volume fraction of catalyst layers due to electrolyte swelling were not considered in this work. Since microporous layers, like CLs, commonly contain carbon black and binder, the same diffusivity (2.70) was used in MPLs. Catalyst layers and microporous layers were assumed in this thesis to be isotropic to gas transport.

Effective diffusivity in gas-diffusion layers was computed as [34, 276, 296]

$$D_i^{\mathrm{eff}} = D_i \varepsilon_{\mathrm{p}} \left( \frac{\varepsilon_{\mathrm{p}} - \varepsilon_{\mathrm{p,th}}}{1 - \varepsilon_{\mathrm{p,th}}} \right)^{\mu} (1 - s)^{\gamma} \Theta(\varepsilon_{\mathrm{p}} - \varepsilon_{\mathrm{p,th}}), \tag{2.71}$$

where $\varepsilon_{\mathrm{p,th}} = 0.12$. Parameters $\mu$ and $\gamma$ vary between GDLs and are different for the in-plane and through-plane transport, as gas-diffusion layers are anisotropic due to the orientation of carbon fibers. Values of these parameters used in this thesis are reported in Chapter 6. Due to the porosity multiplier in equation (2.71), the value of $\mu$ in it is different from that in equation (2.68). Those equations, however, are equivalent as long as $\mu$ is adjusted for the two equations to result in the same diffusivity under dry conditions (the percolation threshold can be kept the same).

### 2.1.3.3 Water Uptake by the Electrolyte

**Water Content in the Catalyst-Layer Ionomer**   Equilibrium water content, $\lambda_{\text{eq}}$, that appears in the source/sink term (2.16) was computed with a so-called sorption isotherm that related water content to water activity (equilibrium RH), $a_{\text{w}}$, and temperature. Mathematical models of PEMFCs available in the literature primarily use sorption isotherms measured for the electrolyte membranes (see, for instance, [42, 52, 152, 157, 159, 227, 228, 232, 243, 247, 255, 257, 273–275, 280, 299]). Those isotherms often do not contain temperature correction [42, 52, 152, 232, 247, 255, 275, 299], which may limit their applicability at different operating temperature and in non-isothermal applications. Moreover, a number of studies [168, 347–352] suggested that water uptake in the catalyst layers and ultrathin Nafion® films is suppressed compared to bulky membranes at the same temperature and RH conditions. Water uptake similar to that in the membranes was also observed [121, 344, 350, 351, 485].

In this thesis, a novel water-uptake relation was obtained for fuel-cell CLs by fitting experimentally measured sorption isotherms for catalyst layers [168, 347] and pseudo catalyst layers (PCLs) [121]. The original data and the resulting fits are shown in Figure 2.3 along with the water-uptake curves for ultrathin Nafion® films [344, 348–352]. The latter are shown for comparison only to highlight the discrepancy between the catalyst-layer and thin-film uptake. Their consideration resulted in a significantly worse fit quality and the PEMFC model failing to accurately predict the hydration and resistance dynamics of the cell.

Lines in Figure 2.3 are the best fits resulting in the following equation with the coefficient of determination, $R^2$, of at least 0.990 (0.993 on average):

$$\lambda_{\text{eq}} = \left[ 6.932 a_{\text{w}} - 14.53 a_{\text{w}}^2 + 11.82 a_{\text{w}}^3 \right] \exp\left( -2509 \left( \frac{1}{T} - \frac{1}{303.15} \right) \right). \qquad (2.72)$$

The fitting was performed with the Sequential Least SQuares Programming (SLSQP) algorithm available in SciPy [486]. This was done by minimizing the overall residual computed as the $L_2$ norm of the sum of the squared residuals normalized by the
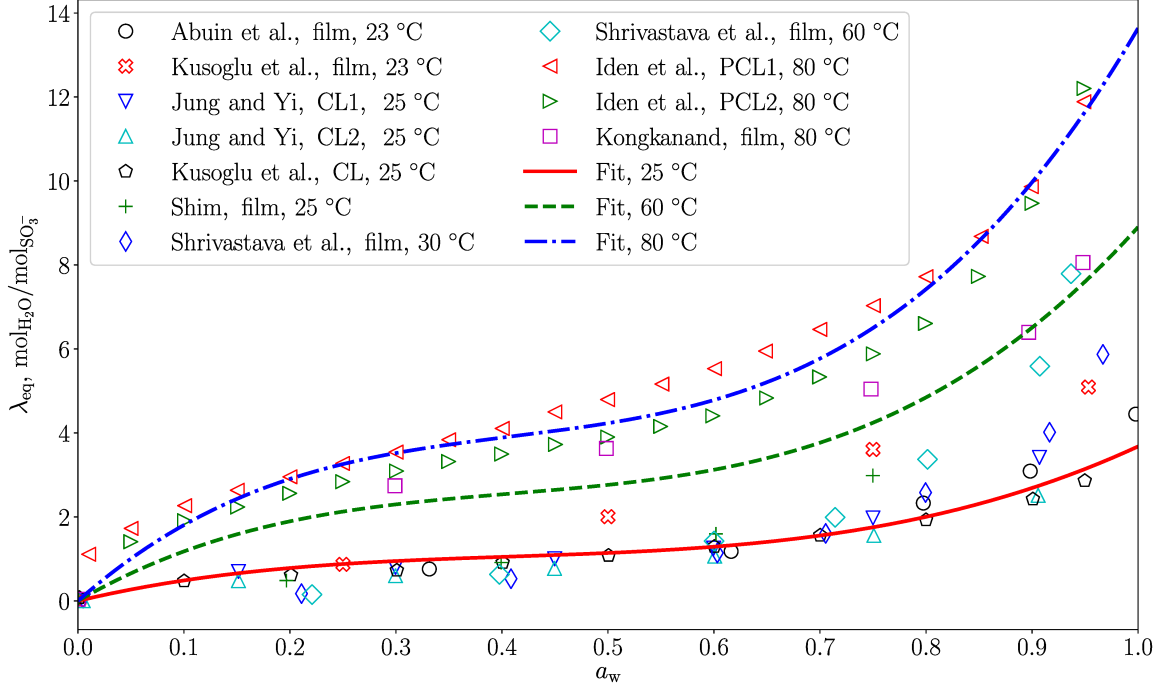
Figure 2.3: Comparison of the experimentally measured sorption isotherms for catalyst layers, pseudo catalyst layers, ultrathin Nafion® membranes, and their fits at the indicated temperature values. Markers represent the data from Abuin et al. [348] (17-nm film on Au), Kusoglu et al. [349] (11-nm film on Au), Jung and Yi [347] (CL1: $0.2\,\mathrm{mg_{Pt}/cm_{CL}^2}$; CL2: $0.1\,\mathrm{mg_{Pt}/cm_{CL}^2}$; both on Teflon®), Kusoglu et al. [168] (CL with $0.11\,\mathrm{mg_{Pt}/cm_{CL}^2}$ and I/C ratio of 0.8 on PTFE), Shim and coworkers [350, 351] (25-nm film on Au), Shrivastava et al. [352] (15-nm film on Pt), Iden et al. [121] (averaged data for GKB and KB PCLs, I/C ratio 0.7-1.3 in all), and Kongkanand [344] (33-nm film on Au). Measurements at the ambient temperature [348, 349] were assumed to had been performed at 23 °C. Lines represent the sorption isotherms computed with equation (2.72).

number of the points in each data set so that the data with more points would not contribute more to the fitting:

$$\mathrm{Residual} = \left\| \frac{\sum_{i=1}^{N_j} \left( \lambda_{\mathrm{eq},i}^{j} - \lambda_{\mathrm{eq},i}^{\exp,j} \right)^2}{N_j} \right\|_2,$$

where the $L_2$ norm is taken with respect to the data-set index $j$. Equation (2.72) can be used to model vapor-equilibrated water uptake in the catalyst layers of fuel cells at 25–80 °C and produces reasonable sorption isotherms (in terms of the shape of the curve) at the temperature values up to 120 °C. The value of $\lambda_{\mathrm{eq}}$ is capped in this thesis

at 22 $\text{mol}_{\text{H}_2\text{O}}/\text{mol}_{\text{SO}_3^-}$, which corresponds to the water content in liquid-equilibrated Nafion® [22, 116].

**Water Content in the Membrane**  Even though electrolyte hydration was described in this thesis with $\lambda_{\text{eq}}$-dependent source terms (2.15) in catalyst layers, sorption isotherms for membranes were of interest in terms of their appearance in the computation of the back-diffusivity of absorbed water. Therefore, a sorption isotherm was obtained in this work that described water uptake by a variety of Nafion® membranes.

Figure 2.4 illustrates the experimentally measured water-uptake curves for various Nafion® membranes at different temperature values [121, 168, 353–355, 487]. While there is some variation in the water uptake with temperature, the exact dependence of the equilibrium water content on temperature cannot be established from the figure. This goes against the common understanding that the elevated temperature leads to the lower water uptake in PFSA-based ionomers [116]. At the same time, higher temperature reduces the stiffness of the polymer backbone, allowing for more uptake and swelling [116]. Comparing Figure 2.3 with Figure 2.4, one should note that the temperature dependence is more pronounced in the water-uptake curves for catalyst layers and thin ionomer films. This suggests that the chemico-mechanical balance between sorption kinetics and swelling may be different in Nafion® confined to ultrathin films and coatings.

The experimental data in Figure 2.4 were fitted with the SLSQP algorithm. The fitting resulted in the following equation for the water uptake in Nafion® membranes with $R^2$ of at least 0.992 (average 0.996):

$$\lambda_{\text{eq}} = \left[18.37 a_{\text{w}} - 37.46 a_{\text{w}}^2 + 31.70 a_{\text{w}}^3\right] \exp\left(-66.28\left(\frac{1}{T} - \frac{1}{303.15}\right)\right). \qquad (2.73)$$

The resulting sorption isotherms at 25–80 °C are almost identical to the water-uptake curve measured by Zawodzinski et al. [353] for Nafion® 117 at 30 °C with the maximum deviation of about 7% at the unit water activity.
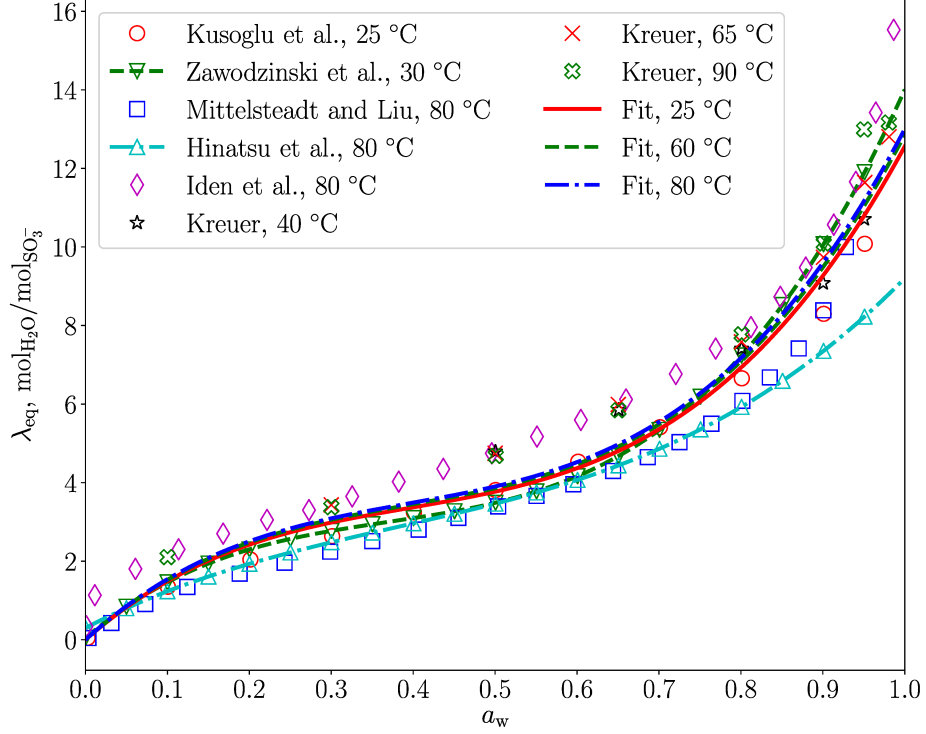
Figure 2.4: Comparison of the experimentally measured sorption isotherms for Nafion® membranes and their fits at the indicated temperature values. Markers represent the data from Kusoglu et al. [168] (Nafion® 212 at 25 °C), Zawodzinski et al. [353] (Nafion® 117 at 30 °C, fit by Springer et al. [22]), Mittelsteadt and Liu [355] (Nafion® 112 at 80 °C), Hinatsu et al. [354] (Nafion® 117 and 125 at 80 °C, their own fit), Iden et al. [121] (Nafion® D2020 at 80 °C), and Kreuer [487] (Nafion® 117 at varied temperature). Lines represent the sorption isotherms computed with equation (2.73) fitted to all shown experimental data.

**Kinetics of Water Absorption and Desorption by the Electrolyte**    The absorption/desorption rates for the ionomer water in the source/sink term (2.16) was calculated using [2, 41, 157, 234, 319, 320, 340, 488]

$$k_\lambda = \frac{\alpha_{\mathrm{abs/des}}}{L_{\mathrm{CL}}} f_{\mathrm{V}} \exp\left[\frac{20000}{R}\left(\frac{1}{303} - \frac{1}{T}\right)\right],$$

where $\alpha_{\mathrm{abs/des}}$ (cm/s) is the rate constant for absorption ($\lambda < \lambda_{\mathrm{eq}}$) or desorption ($\lambda > \lambda_{\mathrm{eq}}$),

$$f_{\mathrm{V}} = \frac{\lambda V_{\mathrm{w}}}{V_{\mathrm{e}} + \lambda V_{\mathrm{w}}} \tag{2.74}$$

is the volume fraction of water in the ionomer, $V_{\mathrm{w}}$ is the molar volume of water, and $V_{\mathrm{e}}$ is the molar volume of the dry ionomer (both in cm³/mol). These molar volumes

are given by [489]

$$V_{\text{w}} = \frac{M_{\text{H}_2\text{O}}}{\rho_{\text{lw}}}$$

and

$$V_{\text{e}} = \frac{\text{EW}}{\rho_{\text{i, dry}}}.$$

The interfacial ionomer-water transport rate, $\alpha_{\text{abs/des}}$, has been reported to vary between $10^{-5}$ and $10^{-1}$ cm/s depending on relative humidity, temperature, and thickness of the ionomer [116, 344]. These values may not all be valid for the water absorption/desorption kinetics in the catalyst layers since they were obtained for relatively thick, unconstrained electrolyte membranes [116, 344] or for thin films deposited on metals and quartz crystals [344, 485] instead of carbon. The absorption/desorption rates of water by the polymer electrolyte in a fuel-cell MEA were experimentally estimated by Ge et al. [490] to be $1.14 \cdot 10^{-3}$ cm/s and $4.59 \cdot 10^{-3}$ cm/s, respectively, with an Arrhenius-type temperature correction. However, they assumed infinitely thin catalyst layers in their analysis. Therefore, absorption/desorption coefficients were treated as fitting parameters in Chapters 4 and 6. The influence of $\alpha_{\text{abs/des}}$ on the dynamic behavior of PEMFCs is demonstrated in Chapter 4.

### 2.1.3.4   Absorbed-Water Diffusivity

**Catalyst Layers**   Diffusion coefficient for water absorbed into the ionomer of catalyst layers was computed through [353, 489–491]

$$D_\lambda = \mathcal{D} D_\mu,$$

where

$$\mathcal{D} = \frac{\partial \ln a_{\text{w}}}{\partial \ln \lambda_{\text{eq}}} \tag{2.75}$$

is the Darken factor,

$$D_\mu = \alpha_\lambda f_{\text{V}} \exp\left[\frac{20000}{R}\left(\frac{1}{303} - \frac{1}{T}\right)\right] \tag{2.76}$$

is the diffusion coefficient of water related to the chemical-potential gradient, and $\alpha_\lambda$ $(cm^2/s)$ is a constant prefactor.

Ge et al. [490] measured the water flux across the catalyst-coated membrane in an in-operando cell and estimated the absorbed-water diffusivity prefactor, $\alpha_\lambda$, to be $2.72 \cdot 10^{-5}$ $cm^2/s$. However, the given value may not be accurate due to the assumption of zero catalyst-layer thickness by Ge et al. [490]. In this thesis, the value of $\alpha_\lambda$ was adjusted in Chapters 4 and 6 for the model to correctly predict the experimentally measured ohmic-resistance dynamics. A parametric study showing the effect of $\alpha_\lambda$ on the dynamic PEMFC behavior is performed in Chapter 4.

Direct substitution of the isotherm (2.72) into the Darken factor (2.75) results in a large relation with many terms that is inconvenient to use and analyze. For that reason, a different approach was taken, in which equation (2.72) was used to generate the equilibrium water content for 1000 values of water activity between $10^{-12}$ and 1, and natural logarithms of both data arrays were taken. The smallest value of water activity was chosen so as to limit the natural logarithm $\ln a_w$. Then, derivatives $\mathcal{D} = \partial \ln a_w / \partial \ln \lambda_{eq}$ were approximated with the first-order backward differences and plotted against the temperature-corrected water-content values

$$\tilde{\lambda}_{eq} = \lambda_{eq} \exp\left(2509\left(\frac{1}{T} - \frac{1}{303.15}\right)\right) = 6.932a_w - 14.53a_w^2 + 11.82a_w^3 \qquad (2.77)$$

to remove the temperature dependence from the water-content axis. The exponent in the equation above comes from the isotherm (2.72). The Darken factors $\mathcal{D} = \partial \ln a_w / \partial \ln \lambda_{eq}$ were plotted against $\tilde{\lambda}_{eq}$, and the best fits were found using the SLSQP algorithm as

$$\mathcal{D} = \begin{cases} \exp\left(0.7647\tilde{\lambda}_{eq}^{2.305}\right), & \tilde{\lambda}_{eq} < 1.209; \\ 3.266 + 2.930\left[\exp\left(-6.735(\tilde{\lambda}_{eq} - 1.209)\tilde{\lambda}_{eq}^{-0.8994}\right) - 1\right], & \tilde{\lambda}_{eq} \geq 1.209. \end{cases} \qquad (2.78)$$

The $R^2$ of the fit is 0.999. The fitted Darken factor (2.78) depends on temperature through $\tilde{\lambda}_{eq}$ computed using equation (2.77). Fits of the temperature-corrected and uncorrected data are shown in Figure 2.5. The distinct peak in the Darken factor is
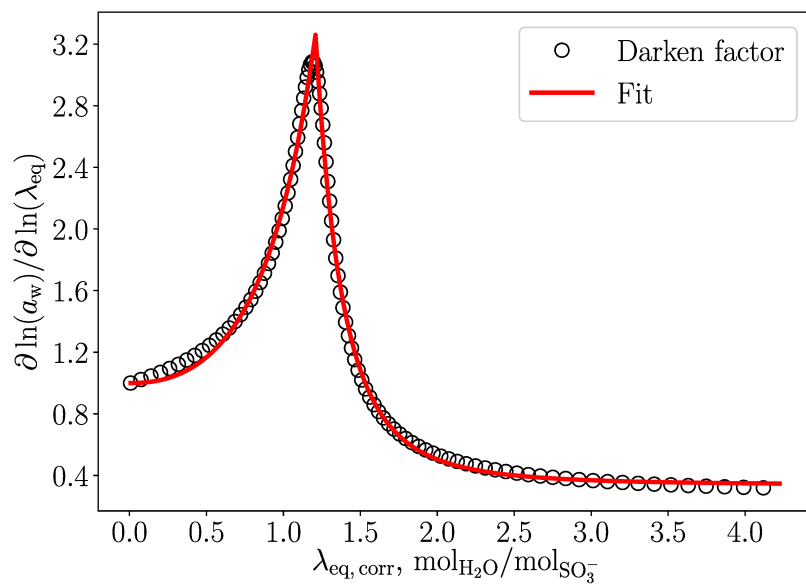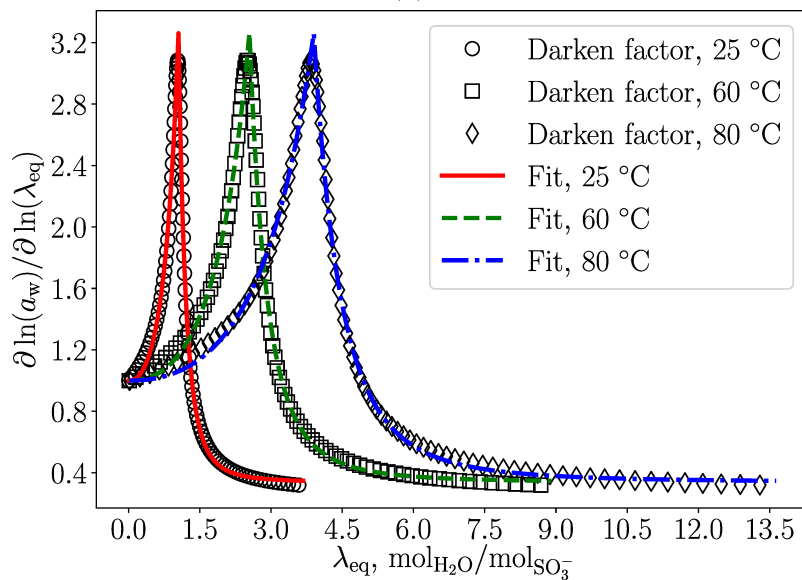
Figure 2.5: The Darken factor $\partial \ln a_{\mathrm{w}} / \partial \ln \lambda_{\mathrm{eq}}$ computed from the sorption isotherm (2.72) for catalyst layers (markers) and the corresponding fits with equation (2.78) (lines). The temperature-corrected data are shown in graph (a). The dependency of the Darken factor on temperature is illustrated in graph (b).

due to the slower water uptake at the intermediate water activities seen in Figure 2.3.

Since transport of absorbed water and transport of protons occur in the same medium (the ionomer phase of catalyst layers), the effective absorbed-water diffusivity $D_\lambda^{\text{eff}}$ was computed the same way as the effective protonic conductivity $\sigma_{\text{H}^+}^{\text{eff}}$. This calculation is discussed in Section 2.1.3.8.

**Membrane** Substitution of equation (2.73) into the Darken factor (2.75) results in a diffusion coefficient that is similar, up to a constant scaling factor, to that from Motupally et al. [491],

$$
D_\lambda = \begin{cases} 3.10 \cdot 10^{-3} \lambda \left( \exp(0.28\lambda) - 1 \right) \exp \left[ -\dfrac{2436}{T} \right], & 0 < \lambda \leq 3; \\ 4.17 \cdot 10^{-4} \lambda \left( 161 \exp(-\lambda) + 1 \right) \exp \left[ -\dfrac{2436}{T} \right], & \lambda > 3, \end{cases}
$$

who used Zawodzinski et al.'s [353] sorption isotherm to compute the Darken factor. Ge et al. [490] estimated a higher diffusivity when the finite-rate exchange between the water in the ionomer and in the pores was accounted for (it was not considered by Motupally et al.). However, as discussed earlier, the simplifying assumptions made by Ge et al. might have affected their estimated hydration properties. Thus, a scaled version of the diffusivity from Motupally et al. was used for the simulated ohmic resistance to match the experimental data (Chapters 4 and 6).

### 2.1.3.5 Electroosmotic Drag Coefficient

The available data for the coefficient of the electroosmotic drag of water in the electrolyte, $n_{\text{d}}$, in equation (2.58) suggest that it is either about 1 $\text{mol}_{\text{H}_2\text{O}}/\text{mol}_{\text{H}^+}$ [353, 492] or depends quasi-linearly on the water content, $\lambda$ [116, 493–495]. The following relationship proposed by Springer et al. [22] for Nafion® 117 membranes captures this dependency fairly well:

$$
n_{\text{d}} = \frac{2.5\lambda}{22}. \tag{2.79}
$$

Equation (2.79) was used in this thesis to compute the electroosmotic drag coefficient.

### 2.1.3.6 Thermoosmotic Diffusivity

Thermoosmotic diffusivity of water in the electrolyte was calculated with the relationship reported by Kim and Mench [476] for Nafion® 112 membranes (in g/(cm·s·K)):

$$D_T = -1.04 \cdot 10^{-4} \exp\left(-\frac{2362}{T}\right). \tag{2.80}$$

Correction for the tortuosity of the water pathways in the ionomer phase of catalyst layers was performed the same way as that for the protonic pathways that is discussed in Section 2.1.3.8.

### 2.1.3.7 Electronic Conductivity

The effective electronic conductivity of catalyst layers was computed using the percolation theory [279, 484]:

$$\sigma_{e^-}^{\text{eff}} = \sigma_{e^-} \left(\frac{\varepsilon_s - \varepsilon_{s,\text{th}}}{1 - \varepsilon_{s,\text{th}}}\right)^{\mu} \Theta(\varepsilon_s - \varepsilon_{s,\text{th}}), \tag{2.81}$$

where $\sigma_{e^-} = 88.84$ S/cm, $\varepsilon_{s,\text{th}} = 0.12$, and $\mu = 2$ as fitted by Secanell [262] for Vulcan XC-72 carbon black. This relationship was assumed in this thesis to be universal for all catalyst layers.

Effective in-plane and through-plane electronic conductivities of GDLs were assumed constant, and the values reported by the GDL manufacturer [87] were used. Effective electronic conductivity of microporous layers was estimated from the known effective conductivity of the separate GDL and GDL-MPL combination [87] (both compressed at 1 MPa) by representing the layers with a set of resistors connected either in series (for the through-plane transport) or in parallel (for the in-plane transport) [480]. Each resistance was defined as

$$R = \frac{L^*}{\sigma^{\text{eff}} A},$$

where $L^*$ is the thickness of the layer in the direction of the electron transport (cm) and $A$ is the cross-sectional area (cm$^2$) orthogonal to that direction. The resulting

equations for the through-plane and in-plane electrical conductivity of the MPL are as follows:

$$\sigma_{\mathrm{e^-,MPL}}^{\mathrm{eff,TP}} = \frac{L_{\mathrm{MPL}}}{\dfrac{L_{\mathrm{GDL+MPL}}^{\mathrm{comp}}}{\sigma_{\mathrm{e^-,GDL+MPL}}^{\mathrm{eff,TP}}} - \dfrac{L_{\mathrm{GDL}}^{\mathrm{comp}}}{\sigma_{\mathrm{e^-,GDL}}^{\mathrm{eff,TP}}}}, \tag{2.82}$$

$$\sigma_{\mathrm{e^-,MPL}}^{\mathrm{eff,IP}} = \frac{\sigma_{\mathrm{e^-,GDL+MPL}}^{\mathrm{eff,IP}} L_{\mathrm{GDL+MPL}}^{\mathrm{comp}} - \sigma_{\mathrm{e^-,GDL}}^{\mathrm{eff,IP}} L_{\mathrm{GDL}}^{\mathrm{comp}}}{L_{\mathrm{MPL}}}. \tag{2.83}$$

Relations (2.82) and (2.83) result in a highly anisotropic conductivity of the MPL while it is believed to have an isotropic structure. However, this may be attributed to the composite sub-layer at the GDL-MPL interface [92, 496], the transport properties of which depend on the alignment of the GDL fibers in that region.

### 2.1.3.8 Protonic Conductivity

Protonic conductivity of the membrane was computed with the following expression fitted by Dobson et al. [269, 497] for Nafion® NR-211 membranes (in S/cm):

$$\sigma_{\mathrm{H^+}} = \left(0.020634 + 0.01052\lambda - 1.0125 \cdot 10^{-4}\lambda^2\right) \exp\left[\frac{6248}{R}\left(\frac{1}{303} - \frac{1}{T}\right)\right]. \tag{2.84}$$

The effective property in catalyst layers was estimated as

$$\sigma_{\mathrm{H^+}}^{\mathrm{eff}} = \varepsilon_{\mathrm{i}}^{1.6}\sigma_{\mathrm{H^+}}, \tag{2.85}$$

where

$$\begin{aligned} \sigma_{\mathrm{H^+}} = \big(&-8 \cdot 10^{-3} + 7.5 \cdot 10^{-4}\omega - 6.375 \cdot 10^{-6}\omega^2 \\ &+ 1.93 \cdot 10^{-7}\omega^3\big) \exp\left[\frac{6248}{R}\left(\frac{1}{353} - \frac{1}{T}\right)\right] \end{aligned} \tag{2.86}$$

and

$$\omega = \begin{cases} 100\left(-0.1254 + 0.1832\lambda - 0.00865\lambda^2 + 0.000094\lambda^3\right), & 0 < \lambda < 13; \\ 100, & \lambda \geq 13. \end{cases}$$

Equation (2.85) was fitted by Domican [346] to the experimental data reported by Iden et al. [121].

### 2.1.3.9 Thermal Conductivity

Thermal conductivity of the membrane and the catalyst layers was assumed in this thesis to be constant and independent of water content. A value of 1.5 mW/(cm · K) was used for the membrane, which is within the range reported for the dry Nafion® by Khandelwal and Mench [498] and for the hydrated Nafion® by Burheim et al. [499]. An effective thermal conductivity of 2.7 mW/(cm · K) was used for catalyst layers as measured by Khandelwal and Mench [498] and within the range reported by Burheim et al. [123] Effective thermal conductivity of microporous layers was taken as 0.8 mW/(cm · K) based on the measurements by Burheim et al. [92, 500].

Effective in-plane and through-plane thermal conductivities of gas-diffusion layers fitted by Bhaiya et al. [33, 65] to the experimental data for Toray® TGP-H-120 GDLs [84, 85] were used (W/(m · K)):

$$\kappa_{\text{GDL}}^{\text{eff,IP}} = -7.166 \cdot 10^{-6} T_{\text{C}}^3 + 2.24 \cdot 10^{-3} T_{\text{C}}^2 - 0.237 T_{\text{C}} + 20.1,$$

$$\kappa_{\text{GDL}}^{\text{eff,TP}} = M(T_{\text{C}}) \kappa_{\text{GDL}}^{\text{eff,IP}},$$

where

$$M(T_{\text{C}}) = -1.495 \cdot 10^{-11} T_{\text{C}}^5 + 2.601 \cdot 10^{-9} T_{\text{C}}^4 - 6.116 \cdot 10^{-8} T_{\text{C}}^3$$
$$- 9.829 \cdot 10^{-6} T_{\text{C}}^2 + 8.754 \cdot 10^{-4} T_{\text{C}} + 0.0664$$

and $T_{\text{C}}$ is temperature in degrees Celsius.

### 2.1.3.10 Pore-Size-Distribution Model

Each porous medium was assumed uniform and represented with a bundle of cylindrical capillaries whose pore-size distribution satisfied the one measured experimentally for the given material. At any location of the medium, pores of all radii present in the PSD were assumed to statistically coexist. Conceptually, each infinitesimal portion of the medium could then be "extracted" and "unfolded" into porous slices, such as those schematically illustrated in Figure 2.6. Cylindrical capillaries in each

slice obeyed the same pore-size distribution and had the same saturation, but were randomly distributed. Two-phase transport through the medium was then described taking the interconnectivity between the capillaries in each of the two neighboring slices into account. The general approach and the mathematical equations used in this work are similar to those developed previously by Weber et al. [26, 27, 305] and Mateo Villanueva [342] and used by Zhou et al. [34, 35, 276, 298] and Goshtasbi et al. [157]. However, some improvements have been made in this thesis, and the derivation of the updated pore-size-distribution-based microstructural model is presented next. A comparison with the earlier PSD models is provided after the derivation.
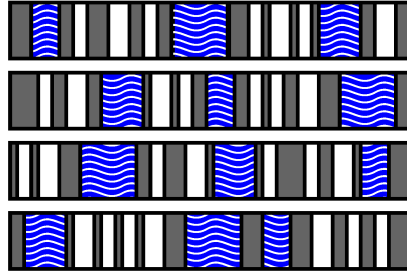


Figure 2.6: Illustration of stacked porous-medium slices with equivalent pore-size distributions. In each slice, solid phase is shown in gray, liquid-invaded pores are shown in blue with white waves, and empty pores are shown in white.

**Pore-Size Distribution and Saturation**     The bundle of capillaries was described by two pore-size distributions: one for the hydrophilic pore network (contact angle $\theta_{\text{HI}} \in [0, 90°)$) and one for the hydrophobic pore network ($\theta_{\text{HO}} \in (90°, 180°]$)). The critical pore radii of those domains were related to capillary pressure through [26, 27, 34, 305, 342]

$$r_{\text{c}} = -\frac{2\gamma \cos\theta}{p_{\text{c}}}, \tag{2.87}$$

where $\gamma$ is surface tension of the intruding liquid (N/m) and $\theta$ is contact angle. At any given capillary pressure, the critical radius, $r_{\text{c}}$, found from (2.87) is the largest radius of the liquid-invaded hydrophilic pores or the smallest radius of the liquid-invaded hydrophobic pores. All pores are empty (liquid-free) when $p_{\text{c}} \to -\infty$ and filled when

90

$p_c \rightarrow \infty$; at $p_c = 0$, all hydrophilic pores are filled and all hydrophobic pores are empty.

The pore-size distribution considered in this work is given by [34, 276, 342]

$$\frac{dX(r)}{dr} = \frac{dX_{\text{HI}}(r)}{dr} + \frac{dX_{\text{HO}}(r)}{dr},$$

where $X(r) = V_{\text{lw}}(r)/V_{\text{p}}$ is the ratio of the total liquid-invaded pore volume to the total pore volume. Distribution $dX(r)/dr$ is log-normal and is defined as [34, 276, 342]

$$\frac{dX(r)}{dr} = \sum_{i=\text{HI, HO}} F_i \sum_k \frac{f_{i,k}}{r s_{i,k} \sqrt{2\pi}} E_{i,k}^{(s)}(r), \tag{2.88}$$

where

$$E_{i,k}^{(s)}(r) = \exp\left(-\left[\frac{\ln r - \ln r_{i,k}}{s_{i,k}\sqrt{2}}\right]^2\right),$$

$F_i$ is the volume fraction of hydrophilic ($i = \text{HI}$) or hydrophobic ($i = \text{HO}$) pores, $f_{i,k}$ is the fraction of the $k$th distribution mode in $F_i$, $s_{i,k}$ is the standard deviation, and $r_{i,k}$ is the characteristic pore radius of the respective mode. These properties were determined in this thesis by fitting experimental data and by analyzing numerical-reconstruction data for MEA components as discussed in Chapter 6.

Integration of $dX/dr$ over pore radii results in the relative volume of the liquid-invaded pores, i.e., saturation. For the hydrophilic pores, integration is performed between 0 and the critical radius $r_{\text{c,HI}}$, while the integration limits are from $r_{\text{c,HO}}$ to $\infty$ for the hydrophobic pores:

$$s = \int_0^{r_{\text{c,HI}}} \frac{dX_{\text{HI}}}{dr} dr + \int_{r_{\text{c,HO}}}^{\infty} \frac{dX_{\text{HO}}}{dr} dr. \tag{2.89}$$

Using result (A.5) from Appendix A, equation (2.89) can be expanded into

$$s = \sum_{i=\text{HI, HO}} F_i \sum_k \frac{f_{i,k}}{2}\left[1 + \zeta_i \text{erf}\left(\frac{\ln(r_{\text{c},i}) - \ln(r_{i,k})}{s_{i,k}\sqrt{2}}\right)\right], \tag{2.90}$$

where $\zeta_{\text{HI}} = 1$ and $\zeta_{\text{HO}} = -1$. Saturation (2.90) depends on capillary pressure via critical radii and equation (2.87).

91

**Statistical Representation of Pore Interconnectivity**  Let $P_{\text{l-l}}$ be the probability of a single point between two neighboring slices lying at a liquid-liquid interface (between two blue wavy domains in different slices in Figure 2.6). To obtain the expression for $P_{\text{l-l}}$, a single liquid-invaded capillary with radius $r$ is considered first. The cross-sectional area per volume of that pore is given by

$$\frac{\pi r^2}{\pi r^2 L} = \frac{1}{L},$$

where $L$ is the length of the pore and a linear relationship $L = M_{\text{PSD}} r$ is assumed with a fitting parameter $M_{\text{PSD}}$ [34, 276, 342] (its determination is discussed in Chapter 6). Taking the superficial average, $\langle \cdot \rangle$ (defined in equation (A.1) of Appendix A), of this result, the average volumetric cross-sectional area of liquid-invaded pores is obtained:

$$a_{\text{c}} = \left\langle \frac{1}{L} \right\rangle = \frac{1}{M_{\text{PSD}}} \left\langle \frac{1}{r} \right\rangle = \frac{\varepsilon_{\text{p}}}{M_{\text{PSD}}} \left( \int_0^{r_{\text{c,HI}}} \frac{1}{r} \frac{dX}{dr} dr + \int_{r_{\text{c,HO}}}^{\infty} \frac{1}{r} \frac{dX}{dr} dr \right). \tag{2.91}$$

Application of equation (A.5) results in

$$a_{\text{c}} = \frac{\varepsilon_{\text{p}}}{M_{\text{PSD}}} \sum_{i=\text{HI, HO}} F_i \sum_k \frac{f_{i,k}}{2 r_{i,k}} \exp\left( \frac{s_{i,k}^2}{2} \right) \left[ 1 + \zeta_i E_{i,k}^{(a_{\text{c}})}(r) \right], \tag{2.92}$$

where

$$E_{i,k}^{(a_{\text{c}})} = \text{erf}\left( \frac{\ln(r_{\text{c},i}) - \ln(r_{i,k})}{s_{i,k}\sqrt{2}} + \frac{s_{i,k}}{\sqrt{2}} \right).$$

The maximum volumetric cross-sectional pore area is obtained by changing integration limits in equation (2.91) to all radii from $0$ to $\infty$ (or, equivalently, by taking limits $r_{\text{c,HI}} \to \infty$ and $r_{\text{c,HO}} \to 0$ in (2.92)). This operation yields

$$a_{\text{max}} = \frac{\varepsilon_{\text{p}}}{M_{\text{PSD}}} \sum_{i=\text{HI, HO}} F_i \sum_k \frac{f_{i,k}}{r_{i,k}} \exp\left( \frac{s_{i,k}^2}{2} \right). \tag{2.93}$$

Then, $P_{\text{l-l}}$ can be defined as

$$P_{\text{l-l}} = \lambda_{\text{PSD}} \left( \frac{a_{\text{c}}}{a_{\text{max}}} \right)^2, \tag{2.94}$$

where $\lambda_{\text{PSD}} \in [0, 1]$ is a pore-interconnectivity factor that is treated as a fitting parameter for calibrating liquid permeability (see Chapter 6). Values $\lambda_{\text{PSD}} = 0$ and

$\lambda_{\mathrm{PSD}} = 1$ correspond to no pore interconnectivity and ideal pore interconnectivity between the neighboring slices in Figure 2.6, respectively. Probability (2.94) is proportional to the squared relative area of the liquid-invaded pores, in contrast to having a quadratic dependency on saturation as in references [26, 27, 34, 157, 276, 305, 342].

Similarly, the probabilities of a single point between two slices lying on a gas-gas interface (between two white domains in different slices in Figure 2.6) and on a liquid-gas interface (between a wavy blue domain in once slice and a white domain in another slice in Figure 2.6) are defined as

$$P_{\mathrm{g\text{-}g}} = \lambda_{\mathrm{PSD}} \left( 1 - \frac{a_{\mathrm{c}}}{a_{\mathrm{max}}} \right)^2$$

and

$$P_{\mathrm{l\text{-}g}} = 2\lambda_{\mathrm{PSD}} \frac{a_{\mathrm{c}}}{a_{\mathrm{max}}} \left( 1 - \frac{a_{\mathrm{c}}}{a_{\mathrm{max}}} \right), \tag{2.95}$$

respectively. The factor of 2 in $P_{\mathrm{l\text{-}g}}$ comes from the binomial distribution of the interface probabilities:

$$\left. (P_{\mathrm{l\text{-}l}} + P_{\mathrm{g\text{-}g}} + P_{\mathrm{l\text{-}g}}) \right|_{\lambda_{\mathrm{PSD}}=1} = 1. \tag{2.96}$$

Probability (2.95) accounts for pore interconnectivity, which was not considered in references [34, 276, 342] when defining $P_{\mathrm{l\text{-}g}}$. For the ideal pore interconnectivity, $P_{\mathrm{l\text{-}g}}$ used in this work is twice higher than that in references [34, 276, 342].

**Liquid and Gas Permeability** The fraction of an area $\pi r^2$ located between the liquid-invaded pores of two neighboring slices in Figure 2.6 is given by $P_{\mathrm{l\text{-}l}} \pi r^2$. A one-dimensional Hagen-Poiseuille flow [501] was considered to take place through a single cylindrical pore of effective radius $r''$ that satisfies $\pi (r'')^2 = P_{\mathrm{l\text{-}l}} \pi r^2$. The Hagen-Poiseuille equation in the $y$-direction (along the capillary length) is given by [501]

$$Q = -\frac{\pi (r'')^4}{8\mu_{\mathrm{lw}}} \frac{dp_{\mathrm{lw}}}{dy},$$

where $Q$ is the total discharge (cm$^3$/s). Velocity (cm/s) of the flow through the considered capillary is

$$v_{\mathrm{lw}} = \frac{Q}{\pi (r'')^2} = -\frac{(r'')^2}{8\mu_{\mathrm{lw}}} \frac{dp_{\mathrm{lw}}}{dy}$$

Applying superficial averaging to this velocity and using the averaging property (A.6) and the Leibniz integral rule, one obtains

$$\langle v_{\mathrm{lw}} \rangle = -\frac{P_{\mathrm{l\text{-}l}}}{8\mu_{\mathrm{lw}}} \langle r^2 \rangle \frac{d}{dy} \langle p_{\mathrm{lw}} \rangle^{\mathrm{lw}}, \tag{2.97}$$

where the intrinsic average (A.2) is used for pressure.

The volume-averaged Darcy's law is given by [502]

$$\langle v_{\mathrm{lw}} \rangle = -\frac{\kappa_{\mathrm{lw}}}{\mu_{\mathrm{lw}}} \frac{d}{dy} \langle p_{\mathrm{lw}} \rangle^{\mathrm{lw}}, \tag{2.98}$$

where the superficial average is taken for the velocity and the intrinsic average is taken for the pressure [472, 502]. Comparing equations (2.97) and (2.98), one finds the average liquid permeability:

$$\kappa_{\mathrm{lw}} = \frac{P_{\mathrm{l\text{-}l}}}{8} \langle r^2 \rangle = \frac{P_{\mathrm{l\text{-}l}}}{8} \varepsilon_{\mathrm{p}} \left( \int_0^{r_{\mathrm{c,HI}}} r^2 \frac{dX}{dr} dr + \int_{r_{\mathrm{c,HO}}}^{\infty} r^2 \frac{dX}{dr} dr \right). \tag{2.99}$$

This result is equivalent to that of Bear [501] and Mateo Villanueva [342], except for the saturation-based definition of $P_{\mathrm{l\text{-}l}}$ in references [342, 501] and the missing porosity multiplier in reference [342]. Applying the integration result (A.5) to equation (2.99), the expanded form of the liquid permeability is obtained:

$$\kappa_{\mathrm{lw}} = \frac{P_{\mathrm{l\text{-}l}}\varepsilon_{\mathrm{p}}}{16} \sum_{i=\mathrm{HI,\,HO}} F_i \sum_k f_{i,k} r_{i,k}^2 \exp\left(2s_{i,k}^2\right) \left[1 + \zeta_i E_{i,k}^{(\kappa)}(r)\right], \tag{2.100}$$

where

$$E_{i,k}^{(\kappa)} = \mathrm{erf}\left(\frac{\ln(r_{\mathrm{c},i}) - \ln(r_{i,k})}{s_{i,k}\sqrt{2}} - s_{i,k}\sqrt{2}\right).$$

Gas permeability is computed by changing the integration limits in (2.100) to liquid-free pores (compare equations (A.1) and (A.3)):

$$\kappa_{\mathrm{g}} = \frac{P_{\mathrm{g\text{-}g}}}{8} \langle r^2 \rangle = \frac{P_{\mathrm{g\text{-}g}}}{8} \varepsilon_{\mathrm{p}} \left( \int_{r_{\mathrm{c,HI}}}^{\infty} r^2 \frac{dX}{dr} dr + \int_0^{r_{\mathrm{c,HO}}} r^2 \frac{dX}{dr} dr \right) \tag{2.101}$$

with the expanded form

$$\kappa_{\mathrm{g}} = \frac{P_{\mathrm{g\text{-}g}}\varepsilon_{\mathrm{p}}}{16} \sum_{i=\mathrm{HI,\,HO}} F_i \sum_k f_{i,k} r_{i,k}^2 \exp\left(2s_{i,k}^2\right) \left[1 - \zeta_i E_{i,k}^{(\kappa)}(r)\right]. \tag{2.102}$$

94

There is no mathematical necessity for porosity in (2.100) and (2.102) due to the treatment of the pore-interconnectivity factor $\lambda_{\text{PSD}}$ as a fitting parameter. However, keeping $\varepsilon_{\text{p}}$ and $\lambda_{\text{PSD}}$ separate makes the latter porosity-independent.

Global saturated permeability is defined as liquid permeability of a liquid-filled medium or gas permeability of a dry medium. As such, it was computed by setting either $a_{\text{c}} = a_{\text{max}}$ in (2.99) or $a_{\text{c}} = 0$ in (2.101) and combining the two integrals in those equations into one, over all radii. This gives

$$\kappa_{\text{sat}} = \frac{\lambda_{\text{PSD}}}{8}\varepsilon_{\text{p}} \int_0^\infty r^2 \frac{dX}{dr} dr \tag{2.103}$$

with the expanded form

$$\kappa_{\text{sat}} = \frac{\lambda_{\text{PSD}}\varepsilon_{\text{p}}}{8} \sum_{i=\text{HI, HO}} F_i \sum_k f_{i,k} r_{i,k}^2 \exp\left(2s_{i,k}^2\right). \tag{2.104}$$

Relative liquid and gas permeabilities are defined as

$$\kappa_{\text{r,lw}} = \kappa_{\text{lw}}/\kappa_{\text{sat}} \tag{2.105}$$

and

$$\kappa_{\text{r,g}} = \kappa_{\text{g}}/\kappa_{\text{sat}}, \tag{2.106}$$

respectively.

**Liquid-Gas Interfacial Area**  Liquid-liquid, gas-gas, and liquid-gas volumetric interfacial areas are

$$a_{\text{l-l}} = P_{\text{l-l}}a_{\text{max}}, \quad a_{\text{g-g}} = P_{\text{g-g}}a_{\text{max}}, \quad a_{\text{l-g}} = P_{\text{l-g}}a_{\text{max}}. \tag{2.107}$$

When the pores are ideally interconnected ($\lambda_{\text{PSD}} = 1$), these interfacial areas sum up to $a_{\text{max}}$ due to probability relation (2.96).

Areas $a_{\text{l-l}}$ and $a_{\text{g-g}}$ are not used in the governing equations (2.54)–(2.60), but $a_{\text{l-g}}$ appears in the phase-change source term (2.23). The expression for $a_{\text{l-g}}$ used in this thesis is proportional to porosity (through equation (2.93)), which ensures that the liquid-gas interfacial area is calculated, as desired, per volume of the layer, not per pore volume. This also makes the fitting parameter $M_{\text{PSD}}$ porosity-independent.

**Average Pore Radius**   The average Knudsen pore radius is obtained directly from the pore-size distribution as an integral average of all liquid-free pore radii:

$$r_{\mathrm{K}} = \left( \int\limits_{r_{\mathrm{c,HI}}}^{\infty} r \frac{dX}{dr} dr + \int\limits_{0}^{r_{\mathrm{c,HO}}} r \frac{dX}{dr} dr \right). \tag{2.108}$$

Note that the volume-averaging theory is not used to define the Knudsen radius because porosity of the medium is taken into account at a later stage when the effective diffusivity is computed (as discussed in Section (2.1.3.2)). The expanded form of equation (2.108) is

$$r_{\mathrm{K}} = \sum_{i=\mathrm{HI,\,HO}} F_i \sum_{k} \frac{f_{i,k} r_{i,k}}{2} \exp \left( \frac{s_{i,k}^2}{2} \right) \left[ 1 - \zeta_i E_{i,k}^{(r_{\mathrm{K}})}(r) \right], \tag{2.109}$$

where

$$E_{i,k}^{(r_{\mathrm{K}})} = \mathrm{erf} \left( \frac{\ln(r_{\mathrm{c},i}) - \ln(r_{i,k})}{s_{i,k}\sqrt{2}} - \frac{s_{i,k}}{\sqrt{2}} \right).$$

**Comparison with Earlier Models**   The earlier implementation of the PSD model in OpenFCST by Zhou et al. [34, 276] has been modified in this thesis in accordance with the derivation provided in this Chapter. The changes made in this work are summarized in Table 2.2.

For the permeability calculation in the earlier models, the liquid-liquid and gas-gas interface probabilities were defined through liquid saturation, $s$ [26, 27, 34, 157, 276, 305, 342]. However, the liquid-gas interfacial area was computed differently. It was either assumed constant and independent of the pore-size distribution [27, 305] or was calculated based on the volumetric cross-sectional area of the liquid-invaded pores, $a_{\mathrm{c}}$ [26, 34, 157, 276, 342]. In this thesis, probabilities of liquid-liquid, gas-gas, and liquid-gas interfaces were all defined through $a_{\mathrm{c}}$ for the self-consistency of the proposed model.

The expressions for the liquid-gas interface probability in Table 2.2 are similar, but the one used in this thesis accounts for the pore interconnectivity through $\lambda_{\mathrm{PSD}}$ and has a multiplier of 2 so that all probabilities sum up to one when $\lambda_{\mathrm{PSD}} = 1$ (i.e., so

Table 2.2: Comparison of the key relationships of the PSD model developed in this thesis with those from previous publications [34, 276, 342].

| Quantity | Integration limits | Approach | |
|---|---|---|---|
| | | This work | Previous publications [34, 276, 342] |
| Volumetric cross-sectional area of liquid-invaded pores, $a_{\mathrm{c}}$ | 0 to $r_{\mathrm{c,HI}}$, $r_{\mathrm{c,HO}}$ to $\infty$ | $\dfrac{\varepsilon_{\mathrm{p}}}{M_{\mathrm{PSD}}}\displaystyle\int_{r}\dfrac{1}{r}\dfrac{dX}{dr}dr$ | $\dfrac{1}{M_{\mathrm{PSD}}}\displaystyle\int_{r}\dfrac{1}{r}\dfrac{dX}{dr}dr$ |
| Maximum volumetric cross-sectional pore area, $a_{\mathrm{max}}$ | 0 to $\infty$ | $\dfrac{\varepsilon_{\mathrm{p}}}{M_{\mathrm{PSD}}}\displaystyle\int_{r}\dfrac{1}{r}\dfrac{dX}{dr}dr$ | $\dfrac{1}{M_{\mathrm{PSD}}}\displaystyle\int_{r}\dfrac{1}{r}\dfrac{dX}{dr}dr$ |
| Liquid-liquid interface probability, $P_{\mathrm{l\text{-}l}}$ | N/A | $\lambda_{\mathrm{PSD}}\left(\dfrac{a_{\mathrm{c}}}{a_{\mathrm{max}}}\right)^2$ | $\lambda_{\mathrm{PSD}}(\varepsilon_{\mathrm{p}}s)^2$ |
| Gas-gas interface probability, $P_{\mathrm{g\text{-}g}}$ | N/A | $\lambda_{\mathrm{PSD}}\left(1-\dfrac{a_{\mathrm{c}}}{a_{\mathrm{max}}}\right)^2$ | $\lambda_{\mathrm{PSD}}(\varepsilon_{\mathrm{p}}(1-s))^2$ |
| Liquid-gas interface probability, $P_{\mathrm{l\text{-}g}}$ | N/A | $2\lambda_{\mathrm{PSD}}\dfrac{a_{\mathrm{c}}}{a_{\mathrm{max}}}\left(1-\dfrac{a_{\mathrm{c}}}{a_{\mathrm{max}}}\right)$ | $\dfrac{a_{\mathrm{c}}}{a_{\mathrm{max}}}\left(1-\dfrac{a_{\mathrm{c}}}{a_{\mathrm{max}}}\right)$ |
| Liquid-water permeability, $\kappa_{\mathrm{lw}}$ | 0 to $r_{\mathrm{c,HI}}$, $r_{\mathrm{c,HO}}$ to $\infty$ | $\dfrac{P_{\mathrm{l\text{-}l}}\varepsilon_{\mathrm{p}}}{8}\displaystyle\int_{r}r^2\dfrac{dX}{dr}dr$ | $\dfrac{P_{\mathrm{l\text{-}l}}}{8}\displaystyle\int_{r}r^2\dfrac{dX}{dr}dr$ |
| Gas permeability, $k_{\mathrm{g}}$ | 0 to $r_{\mathrm{c,HO}}$, $r_{\mathrm{c,HI}}$ to $\infty$ | $\dfrac{P_{\mathrm{g\text{-}g}}\varepsilon_{\mathrm{p}}}{8}\displaystyle\int_{r}r^2\dfrac{dX}{dr}dr$ | $\dfrac{P_{\mathrm{g\text{-}g}}}{8}\displaystyle\int_{r}r^2\dfrac{dX}{dr}dr$ |
| Global saturated permeability, $k_{\mathrm{sat}}$ | 0 to $\infty$ | $\dfrac{\lambda_{\mathrm{PSD}}\varepsilon_{\mathrm{p}}}{8}\displaystyle\int_{r}r^2\dfrac{dX}{dr}dr$ | $\dfrac{\lambda_{\mathrm{PSD}}\varepsilon_{\mathrm{p}}^2}{8}\displaystyle\int_{r}r^2\dfrac{dX}{dr}dr$ |
| Knudsen pore radius, $r_{\mathrm{K}}$ | 0 to $r_{\mathrm{c,HO}}$, $r_{\mathrm{c,HI}}$ to $\infty$ | $\displaystyle\int_{r}r\dfrac{dX}{dr}dr$ | Twice the ratio of pore volume to its wall area [34, 276, 342] |

that equation (2.96) holds). Additionally, the new relationships contain a porosity multiplier in the volumetric cross-sectional pore area and permeabilities that arises from volume averaging.

Sabharwal et al. [130, 131] have recently shown that computing the average Knudsen pore radius as an integral average of all radii in the PSD results in the effective gas diffusivity in catalyst layers that is in a good agreement with the experimental and numerical literature. That approach was adopted in this work instead of the more cumbersome and computationally expensive definition of the Knudsen pore radius as twice the ratio between the volume of the cylindrical pores and their lateral surface area [34, 276, 342].

The differences between the transport properties predicted by the previous and the new implementations of the PSD model are illustrated in Chapter 6.

## 2.2 Solution Approach

### 2.2.1 Temporal Discretization

Since temporal and spatial discretization can be performed independently, it is convenient to discuss the former alone by representing the governing equations of the developed fuel-cell model (2.54)–(2.60) as a system of ODEs

$$\frac{d\boldsymbol{u}}{dt} = \boldsymbol{f}(t, \boldsymbol{u}(t)), \quad \boldsymbol{u}(t_0) = \boldsymbol{u}_0, \tag{2.110}$$

where $\boldsymbol{f}(t, \boldsymbol{u}(t))$ contains the source/sink terms and the spatial operators of the original problem. Due to the nature of the coupled physical and electrochemical processes simulated in OpenFCST, the resulting system (2.110) may exhibit stiffness. The commonly accepted informal definition of stiffness is that it is a property of the problem to be solved that makes implicit numerical methods perform significantly better than explicit ones[2] [503–505]. Therefore, it was important to develop a transient framework

---

[2]More formally, a large ratio of the largest to the smallest eigenvalues of the Jacobian $\partial \boldsymbol{f}/\partial \boldsymbol{u}$ is an indicator of a stiff problem [503]. Other factors, such as the dimension of system (2.110), integration

in OpenFCST that would contain implicit methods for the temporal discretization of (2.110).

### 2.2.1.1 First Stage of Development: $\theta$-Scheme

As a first step in developing a framework for solving transient problems with Open-FCST, the $\theta$-scheme was implemented. In this method, the transient term of equation (2.110) is replaced with a first-order finite difference, and $\boldsymbol{f}(t, \boldsymbol{u}(t))$ is treated in a combined explicit/implicit fashion by introducing a variable $\theta \in [0, 1]$ [505]:

$$\frac{\boldsymbol{u}^{(n+1)} - \boldsymbol{u}^{(n)}}{\tau} = \theta \boldsymbol{f}^{(n+1)} + (1 - \theta)\boldsymbol{f}^{(n)}, \tag{2.111}$$

where $\tau = t_{n+1} - t_n$ is the time-step size and $\boldsymbol{f}^{(n)} = \boldsymbol{f}\left(t_n, \boldsymbol{u}^{(n)}\right)$. The $\theta$-scheme has three well-known and commonly used particular cases:

- $\theta = 0$: the explicit Euler method (order 1, conditionally stable [503, 505]);

- $\theta = 1/2$: the Crank-Nicolson (trapezoidal) method (implicit, order 2, absolutely stable [503, 505]);

- $\theta = 1$: the implicit Euler method (order 1, absolutely stable [503, 505]).

This scheme with $\theta = 1/2$ (the Crank-Nicolson method) is used in Chapter 3, where the developed transient framework in OpenFCST is applied to analyze oxygen transport in polymer-electrolyte membranes.

The $\theta$-scheme has two major limitations. First, it is at most second-order accurate. To increase the accuracy and to control the time-step size, Richardson extrapolation was implemented (see Section 2.2.1.3). However, this approach requires solving the problem thrice on each time layer, which may be inefficient, especially for stiff problems [505]. These drawbacks led to the necessity of implementing a different, more robust transient solver.

---

interval, and smoothness of the solution also play a role [504, 505]. In some cases, stiffness can be observed for the models with rapid changes in the transient solution [504, 505]; that, however, is neither necessary nor sufficient for the problem to be stiff [504].

### 2.2.1.2 Method Selection for Stiff Problems

Two most common families of methods for solving stiff ODEs are implicit Runge-Kutta methods (IRK) and backward-differentiation formulae (BDF) [503–506]. Even though both IRK and BDF methods are available in a variety of software libraries [504, 507–517], their use would have required a significant modification of the existing OpenFCST framework. Therefore, a direct implementation in OpenFCST was favored. A literature review was performed and the IRK and BDF families were compared in terms of their stability, efficiency, and implementation convenience in order to choose one that would be most suitable for OpenFCST.

Runge-Kutta methods arise from the application of some quadrature formula to the integral of the original ODE system (2.110) [503, 505, 506]:

$$\boldsymbol{u}(t) = \boldsymbol{u}_0 + \int_{t_0}^{t} \boldsymbol{f}(t, \boldsymbol{u})dt. \tag{2.112}$$

The order and stability of Runge-Kutta methods depend on the choice of the quadrature rule for equation (2.112) [503–506]. For example, application of the $s$-point Gauss-Legendre quadrature results in an implicit Runge-Kutta method of order $2s$ that is absolutely stable [503–505]. The single-stage IRK method obtained from the right-rectangle rule is equivalent to the implicit Euler method [503, 505, 506].

In contrast to Runge-Kutta methods, BDF methods rely on numerical approximations of $d\boldsymbol{u}/dt$ in the original ODE (2.110). A general $k$-step BDF method (BDF$k$) for solving problem (2.110) is given by [503, 505, 506]

$$\alpha_{n+1}\boldsymbol{u}^{(n+1)} + \alpha_n\boldsymbol{u}^{(n)} + \cdots + \alpha_{n-k+1}\boldsymbol{u}^{(n-k+1)} = \tau\boldsymbol{f}^{(n+1)}, \tag{2.113}$$

where $\alpha_i$, $i \in \{n-k+1,\, n+1\}$, are some real coefficients. Formulas for $1 \leq k \leq 6$ can be found in references [503, 505, 506]. Their order matches $k$, and they are absolutely stable for $k = 1$ and $k = 2$, conditionally stable for $3 \leq k \leq 6$, and unstable for $k > 6$ [503, 505, 506]. The implicit Euler method is recovered when $k$ is set to 1 (then $\alpha_{n+1} = 1$ and $\alpha_n = -1$) [503, 505, 506].

Based on the discussion above, the clear advantage of the IRK methods is their absolute stability [503–505]. Higher-order BDF methods ($3 \leq k \leq 6$) are not only conditionally stable [503, 505, 506], but also have relatively strict bounds for the time-step change in the variable-step formulation [505, 506, 518–522]. On the other hand, some IRK methods may suffer from a phenomenon called order reduction, when the expected order of accuracy is not achieved in practical applications to stiff problems [503, 505]. Order reduction does not occur for BDF methods [503]. Additionally, Runge-Kutta methods rely on $\boldsymbol{f}(t, \boldsymbol{u})$ evaluations at custom points $(t, \boldsymbol{u})$ that depend on the chosen method and the time-step size, which can be expensive for large problems.

Stability and accuracy are important, but what ultimately matters in practical software applications is the overall computational time for the given error tolerance. Depending on the problem at hand, its dimension, error tolerance, and, of course, particular implementation, performance of the BDF methods is either similar to IRK methods [504], superior [523, 524], or poorer [525].

Given the comparable performance of IRK and BDF methods, the choice of the family of methods to be developed was based on the implementation convenience. Runge-Kutta methods would have required a significant modification of the existing OpenFCST framework, including the transient framework that was developed earlier for the $\theta$-scheme (Section 2.2.1.1), and thus the preference was given to the BDF methods.

For the fuel-cell and catalyst-layer models considered in Chapters 4–6, the BDF1 method (implicit Euler) with Richardson extrapolation (Section 2.2.1.3) had a reasonable performance, and the higher-order methods were not used. The $\theta$-scheme also offers the implicit Euler method, but the development of the separate BDF framework in the general form (2.113) was motivated by the outlook on the higher-order [503, 505, 506], variable-step [505, 506, 518–522], and variable-order [510, 526] BDF formulations that may benefit other OpenFCST developers and their applications that will

stretch beyond fuel-cell research. These formulations, however, require sophisticated error-control algorithms that are beyond the scope of this thesis.

### 2.2.1.3  Time-Step Control

The developed $\theta$-scheme and BDF1 transient solvers support adaptive time-stepping with solution-error control via Richardson extrapolation. The algorithm implemented in this work is as follows. Suppose a single-step method of order $k$ is used to obtain a numerical solution $\boldsymbol{u}_1$ to the initial-value problem (2.110) at $t = t^*$ with a time-step size $\tau$. Denoting the exact solution $\boldsymbol{u}^* = \boldsymbol{u}(t^*)$, the local error of this step is given by [505, 506, 527, 528]

$$\boldsymbol{u}^* - \boldsymbol{u}_1 = \boldsymbol{c}\tau^{k+1} + \mathcal{O}\left(\tau^{k+2}\right). \tag{2.114}$$

Then, a different approximation $\boldsymbol{u}_2$ is obtained for $t = t^*$ utilizing time steps of size $\tau/2$. The local error of these two steps viewed as a single step is [505, 506, 527, 528]:

$$\boldsymbol{u}^* - \boldsymbol{u}_2 = 2\boldsymbol{c}\left(\frac{\tau}{2}\right)^{k+1} + \mathcal{O}\left(\tau^{k+2}\right). \tag{2.115}$$

From (2.114) and (2.115), the unknown vector $\boldsymbol{c}$ can be found:

$$\boldsymbol{c} \approx \frac{\boldsymbol{u}_2 - \boldsymbol{u}_1}{\tau^{k+1}} \frac{2^k}{2^k - 1}. \tag{2.116}$$

Therefore, the exact solution is given by

$$\boldsymbol{u}^* \approx \boldsymbol{u}_2 + \frac{\boldsymbol{u}_2 - \boldsymbol{u}_1}{2^k - 1} + \mathcal{O}\left(\tau^{k+2}\right). \tag{2.117}$$

Thus, one can construct a new approximation $\boldsymbol{u}_3$ of order $k+1$ using $\boldsymbol{u}_1$ and $\boldsymbol{u}_2$ [506, 527–529]:

$$\boldsymbol{u}_3 = \boldsymbol{u}_2 + \frac{\boldsymbol{u}_2 - \boldsymbol{u}_1}{2^k - 1}. \tag{2.118}$$

The absolute-error estimate is obtained from equation (2.115) [528, 529]:

$$\Delta_\tau = \|\boldsymbol{u}^* - \boldsymbol{u}_2\|_{l^2} \approx \|\boldsymbol{c}\|_{l^2} \frac{\tau^{k+1}}{2^k} \approx \frac{\|\boldsymbol{u}_2 - \boldsymbol{u}_1\|_{l^2}}{2^k - 1}. \tag{2.119}$$

The relative-error estimate is defined as

$$\delta_\tau = \left\|\frac{\boldsymbol{u}^* - \boldsymbol{u}_2}{\boldsymbol{u}_3}\right\|_{l^2} \approx \left\|\frac{\boldsymbol{u}_2 - \boldsymbol{u}_1}{(2^k - 1)\boldsymbol{u}_3}\right\|_{l^2}, \tag{2.120}$$

where the division of solution vectors is performed element-wise. Estimates (2.119) and (2.120) are calculated in the discrete $l^2$ norm defined as

$$\|\boldsymbol{u}\|_{l^2} = \sqrt{\frac{\sum_{i=1}^{N} u_i^2}{N-1}} = \frac{\|\boldsymbol{u}\|_2}{\sqrt{N-1}}, \tag{2.121}$$

where $N$ is the length of the solution vector.

Automatic selection of the time-step size is performed based on the error estimates (2.119) and (2.120). Suppose an optimal time-step size $\hat{\tau}_{\text{abs}}$ needs to be found that makes the absolute solution-error match the desired tolerance:

$$\Delta_{\hat{\tau}} \approx \|\boldsymbol{c}\|_{l^2} \frac{\hat{\tau}_{\text{abs}}^{k+1}}{2^k} \approx \epsilon_{\text{abs}}.$$

From this, using equation (2.116), one obtains

$$\hat{\tau}_{\text{abs}} \approx \sqrt[k+1]{\frac{\epsilon_{\text{abs}} \tau^{k+1} (2^k - 1)}{\|\boldsymbol{u}_2 - \boldsymbol{u}_1\|_{l^2}}} = \tau \sqrt[k+1]{\frac{\epsilon_{\text{abs}}}{\Delta_{\tau}}}.$$

In practice, a precaution factor $\omega$ is introduced [529]:

$$\hat{\tau}_{\text{abs}} \approx \omega \tau \sqrt[k+1]{\frac{\epsilon_{\text{abs}}}{\Delta_{\tau}}}. \tag{2.122}$$

In this work, $\omega = 0.9$ is used, which is a common choice in the literature [529].

To satisfy the relative-error tolerance $\epsilon_{\text{rel}}$, it is required that

$$\delta_{\hat{\tau}} \approx \left\| \frac{\boldsymbol{u}^* - \boldsymbol{u}_2}{\boldsymbol{u}_3} \right\|_{l^2} \approx \left\| \frac{\boldsymbol{c}\hat{\tau}_{\text{rel}}^{k+1}}{2^k \boldsymbol{u}_3} \right\|_{l^2} \approx \epsilon_{\text{rel}}.$$

Substituting equation (2.116) into the equation above, one finds

$$\hat{\tau}_{\text{rel}} \approx \sqrt[k+1]{\epsilon_{\text{rel}} \tau^{k+1} \left\| \frac{(2^k - 1)\boldsymbol{u}_3}{\boldsymbol{u}_2 - \boldsymbol{u}_1} \right\|_{l^2}} \approx \tau \sqrt[k+1]{\frac{\epsilon_{\text{rel}}}{\delta_{\tau}}}.$$

With the precaution factor, this result becomes

$$\hat{\tau}_{\text{rel}} \approx \omega \tau \sqrt[k+1]{\frac{\epsilon_{\text{rel}}}{\delta_{\tau}}}. \tag{2.123}$$

The optimal time-step size must satisfy both absolute and relative tolerances. Therefore, it is chosen as

$$\hat{\tau} = \min(\hat{\tau}_{\text{abs}}, \hat{\tau}_{\text{rel}}). \tag{2.124}$$

103

The discussed extrapolation algorithm is an iterative process. Every time layer is first resolved with the old value of the time-step size (or with its initial value if the first time layer is being computed), and solutions $\boldsymbol{u}_1$ and $\boldsymbol{u}_2$ are obtained. Then, a new value of the time-step size is computed using relation (2.124) and error estimates (2.119) and (2.120). If $\Delta_\tau < \epsilon_{\text{abs}}$ and $\delta_\tau < \epsilon_{\text{rel}}$, solution $\boldsymbol{u}_3$, defined in equation (2.118), is accepted as the numerical solution of the given problem on the given time layer. Otherwise, new $\boldsymbol{u}_1$ and $\boldsymbol{u}_2$ are obtained with $\hat{\tau}$, and the process repeats.

Additional time-step control is performed in cases when the nonlinear solver (Section 2.2.2) experienced divergence or slow convergence. In such cases, the time-step size is halved, and the solution on the given time layer is recomputed. This process is repeated until the nonlinear-solver iterations successfully converged, and then the time-step size is gradually increased by doubling. This algorithm is always invoked before the time-step size is modified by Richardson extrapolation so as to ensure the solution satisfies the given error tolerances.

## 2.2.2   Linearization

The governing equations of the PEMFC model (2.54)–(2.60) are highly nonlinear in both the source/sink terms and in the effective transport properties. Before they can be solved, these equations need to be linearized. Two nonlinear solvers were used in this thesis: Picard's method [530–532], implemented by Sabharwal [131], and Newton's method [530–534], implemented by Secanell [262] and Boisvert and co-workers [36]. Picard's method was used in Chapter 3, and Newton's method was used in Chapters 4–6. These solvers were integrated in the transient framework developed in this thesis and, therefore, are discussed next.

### 2.2.2.1 Picard's Method

Consider the following equation representative of the governing equations (2.54)–(2.60) of the PEMFC model:

$$C\frac{\partial u_\alpha}{\partial t} - \nabla \cdot (\boldsymbol{A}_\alpha(\boldsymbol{u})\nabla u_\alpha) = f_\alpha(\boldsymbol{u}), \tag{2.125}$$

where $u_\alpha$ represents one of the original solution variables in $\boldsymbol{u}$, $C$ is some constant, $\boldsymbol{A}_\alpha(\boldsymbol{u})$ is a tensor of an effective transport property, and $f_\alpha(\boldsymbol{u})$ is a source/sink term. The Greek index $\alpha$ is the index of the given equation in the original system of PDEs (or, equivalently, the index of the respective solution variable in $\boldsymbol{u}$) and not the spatial-component index; no summation is performed over it. Some of the terms in equations (2.54)–(2.60) depend on more than one solution variable. Their treatment follows the same general idea of Picard's method that will be illustrated for the example equation (2.125).

To demonstrate how Picard's method (fixed-point iteration) [530–532] is applied to equation (2.125), the $\theta$-scheme temporal discretization (2.111) will be assumed. Combination of this linearization method with the BDF discretization (2.113) is done in a similar fashion.

Application of the $\theta$-scheme to equation (2.125) results in

$$C\frac{u_\alpha^{(n+1)} - u_\alpha^{(n)}}{\tau} - \theta\nabla \cdot \left(\boldsymbol{A}_\alpha\left(\boldsymbol{u}^{(n+1)}\right)\nabla u_\alpha^{(n+1)}\right) - (1-\theta)\nabla \cdot \left(\boldsymbol{A}_\alpha(\boldsymbol{u}^{(n)})\nabla u_\alpha^{(n)}\right)$$
$$= \theta f_\alpha\left(\boldsymbol{u}^{(n+1)}\right) + (1-\theta)f_\alpha(\boldsymbol{u}^{(n)}). \tag{2.126}$$

As before, superscript $(n)$ denotes the time layer. Note that the terms with coefficient $\theta$ depend on the unknown solution vector $\boldsymbol{u}^{(n+1)}$. In Picard's method, the sought solution on time layer $n+1$ is $u_\alpha^{(n+1,m+1)}$, where $m+1$ denotes the current iteration of the nonlinear solver. Nonlinearities are treated explicitly using the solution from the same time layer but the previous Picard iteration, $u_\alpha^{(n+1,m)}$ [531]:

$$C\frac{u_\alpha^{(n+1,m+1)} - u_\alpha^{(n)}}{\tau} - \theta\nabla \cdot \left(\boldsymbol{A}_\alpha\left(\boldsymbol{u}^{(n+1,m)}\right)\nabla u_\alpha^{(n+1,m+1)}\right) - (1-\theta)\nabla \cdot \left(\boldsymbol{A}_\alpha(\boldsymbol{u}^{(n)})\nabla u_\alpha^{(n)}\right)$$
$$= \theta f_\alpha\left(\boldsymbol{u}^{(n+1,m)}\right) + (1-\theta)f_\alpha(\boldsymbol{u}^{(n)}),$$

or, after rearranging,

$$
\frac{C}{\tau} u_\alpha^{(n+1,m+1)} - \theta \nabla \cdot \left( \boldsymbol{A}_\alpha \left( \boldsymbol{u}^{(n+1,m)} \right) \nabla u_\alpha^{(n+1,m+1)} \right)
$$
$$
= \frac{C}{\tau} u_\alpha^{(n)} + (1-\theta) \nabla \cdot \left( \boldsymbol{A}_\alpha (\boldsymbol{u}^{(n)}) \nabla u_\alpha^{(n)} \right)
$$
$$
+ \theta f_\alpha \left( \boldsymbol{u}^{(n+1,m)} \right) + (1-\theta) f_\alpha (\boldsymbol{u}^{(n)}). \quad (2.127)
$$

The initial guess for the first Picard iteration is the previous transient solution: $\boldsymbol{u}^{(n+1,0)} = \boldsymbol{u}^{(n)}$. Equation (2.127) is linear in the new solution iterate $u_\alpha^{(n+1,m+1)}$.

Adaptive underrelaxation is used in this work to aid convergence of the Picard iterations. In this method, quantities $\boldsymbol{A}_\alpha \left( \boldsymbol{u}^{(n+1,m)} \right)$ and $f_\alpha \left( \boldsymbol{u}^{(n+1,m)} \right)$ are updated with the modified Picard solution given by [131, 535]

$$
\tilde{\boldsymbol{u}}^{(n+1,m+1)} = \boldsymbol{u}^{(n+1,m)} + \gamma \left( \boldsymbol{u}^{(n+1,m+1)} - \boldsymbol{u}^{(n+1,m)} \right), \quad (2.128)
$$

where $\boldsymbol{u}^{(n+1,m+1)}$ is the solution of the regular Picard method (2.127). Parameter $\gamma \in (0, 1]$ is varied based on the solution error according to equation [131, 535]

$$
\gamma = \begin{cases} \gamma_{\min} + (1 - \gamma_{\min}) e^{-\alpha(\Delta - \epsilon_{\text{abs}})}, & \Delta > \epsilon_{\text{abs}}; \\ 1, & \Delta \leq \epsilon_{\text{abs}}, \end{cases}
$$

where $\Delta$ is the absolute solution-error estimate defined as

$$
\Delta = \left\| \tilde{\boldsymbol{u}}_\alpha^{(n+1,m+1)} - \boldsymbol{u}_\alpha^{(n+1,m)} \right\|_{l^2} \quad (2.129)
$$

and $\epsilon_{\text{abs}}$ is the respective tolerance. Parameters $\gamma_{\min}$ and $\alpha$ are such that $\gamma_{\min} \in (0, 1)$ and $\alpha > 0$. In this work, $\gamma_{\min} = 0.3$ and $\alpha = 6$ are used.

The iterations are assumed to have converged when the absolute solution-error estimate (2.129) and the relative solution-error estimate[3]

$$
\delta = \left\| \frac{\tilde{\boldsymbol{u}}^{(n+1,m+1)} - \boldsymbol{u}^{(n+1,m)}}{\tilde{\boldsymbol{u}}^{(n+1,m+1)}} \right\|_{l^2} \quad (2.130)
$$

satisfy the given tolerances $\epsilon_{\text{abs}}$ and $\epsilon_{\text{rel}}$, respectively. As $\Delta \to \epsilon_{\text{abs}}$ and $\delta \to \epsilon_{\text{rel}}$, $\tilde{\boldsymbol{u}}^{(n+1,m+1)} \to \boldsymbol{u}^{(n+1,m)}$ and $\gamma \to 1$, which corresponds to the regular Picard's method. Further details of this algorithm can be found in [131, 535].

---

[3] As before, notation $\boldsymbol{a}/\boldsymbol{b}$ means element-wise division.

### 2.2.2.2 Newton's Method

In Newton's method (also called Newton-Raphson method) [530–534], the solution iterate is represented as $\boldsymbol{u}^{(n+1,m+1)} = \boldsymbol{u}^{(n+1,m)} + \delta\boldsymbol{u}$, $\boldsymbol{u}^{(n+1,0)} = \boldsymbol{u}^{(n)}$, and the linearized equations are solved with respect to the solution update $\delta\boldsymbol{u}$. Newton's method for linearizing a system of transient PDEs that are discretized in time and are written as $\boldsymbol{R}(\boldsymbol{u}) = \boldsymbol{0}$ is given by [536]

$$\delta\boldsymbol{u} = -\boldsymbol{J}^{-1}\left(\boldsymbol{u}^{(n+1,m)}\right)\boldsymbol{R}\left(\boldsymbol{u}^{(n+1,m)}\right),\tag{2.131}$$

where

$$\boldsymbol{J}\left(\boldsymbol{u}^{(n+1,m)}\right) = \left[\frac{\partial R_\alpha}{\partial u_\beta}\right]\bigg|_{\boldsymbol{u}^{(n+1,m)}}\tag{2.132}$$

is the Jacobian matrix with components $J_{\alpha\beta}$ equal to the partial Fréchet derivatives of the residuals of each equation with index $\alpha$ with respect to the $\beta$th variable in the solution vector $\boldsymbol{u}$. This Jacobian matrix is computed through the Gateaux differential[4] [536]

$$\delta\boldsymbol{R}(\boldsymbol{u};\boldsymbol{h}) = \lim_{\zeta\to 0}\frac{\boldsymbol{R}(\boldsymbol{u}+\zeta\boldsymbol{h}) - \boldsymbol{R}(\boldsymbol{u})}{\zeta}\tag{2.133}$$

using [536]

$$\delta\boldsymbol{R}(\boldsymbol{u};\boldsymbol{h}) = \boldsymbol{J}(\boldsymbol{u})\boldsymbol{h}.\tag{2.134}$$

The Gateaux derivative is a generalization of the directional derivative from differential calculus [536, 537]. In Newton's method, one needs to know how the residual changes in the direction of the solution update $\delta\boldsymbol{u}$, and so $\boldsymbol{h} = \delta\boldsymbol{u}$ is taken. Then, from equations (2.131) and (2.134), Newton's method can be expressed as

$$\delta\boldsymbol{R}(\boldsymbol{u}^{(n+1,m)};\delta\boldsymbol{u}) = -\boldsymbol{R}\left(\boldsymbol{u}^{(n+1,m)}\right).\tag{2.135}$$

---

[4]The Fréchet derivative is directly related to the Fréchet differential $\delta\boldsymbol{R}(\boldsymbol{u};\boldsymbol{h})$ that, when it exists, satisfies [536]
$$\lim_{\boldsymbol{h}\to\boldsymbol{0}}\frac{\|\boldsymbol{R}(\boldsymbol{u}+\boldsymbol{h}) - \boldsymbol{R}(\boldsymbol{u}) - \delta\boldsymbol{R}(\boldsymbol{u};\boldsymbol{h})\|}{\|\boldsymbol{h}\|} = 0.$$
Existence of the Gateaux differential follows from the existence of the Fréchet differential, and the two differentials are equal [536]. This enables the convenient calculation of the Fréchet derivative through the Gateaux differential.

Newton's method is demonstrated next for equation (2.126) discretized with the $\theta$-scheme. An example of coupling Newton's method with the BDF temporal discretization is shown in Appendix B. Residual $R_\alpha(\boldsymbol{u})$ of equation (2.126) at $\boldsymbol{u}^{(n+1,m)} + \zeta\delta\boldsymbol{u}$ is given by

$$
\begin{aligned}
R_\alpha\left(\boldsymbol{u}^{(n+1,m)} + \zeta\delta\boldsymbol{u}\right) = {} & C\frac{u_\alpha^{(n+1,m)} + \zeta\delta u_\alpha - u_\alpha^{(n)}}{\tau} \\
& - \theta\nabla \cdot \left(\boldsymbol{A}_\alpha\left(\boldsymbol{u}^{(n+1,m)} + \zeta\delta\boldsymbol{u}\right)\nabla\left(u_\alpha^{(n+1,m)} + \zeta\delta u_\alpha\right)\right) \\
& - (1-\theta)\nabla \cdot \left(\boldsymbol{A}_\alpha(\boldsymbol{u}^{(n)})\nabla u_\alpha^{(n)}\right) \\
& - \theta f_\alpha\left(\boldsymbol{u}^{(n+1,m)} + \zeta\delta\boldsymbol{u}\right) - (1-\theta)f_\alpha(\boldsymbol{u}^{(n)})
\end{aligned}
\tag{2.136}
$$

Substituting linear expansions [536, 537]

$$
\boldsymbol{A}_\alpha\left(\boldsymbol{u}^{(n+1,m)} + \zeta\delta\boldsymbol{u}\right) \approx \boldsymbol{A}_\alpha\left(\boldsymbol{u}^{(n+1,m)}\right) + \sum_\beta \left.\frac{\partial\boldsymbol{A}_\alpha(\boldsymbol{u})}{\partial u_\beta}\right|_{\boldsymbol{u}^{(n+1,m)}}\zeta\delta u_\beta,
\tag{2.137}
$$

$$
f_\alpha\left(\boldsymbol{u}^{(n+1,m)} + \zeta\delta\boldsymbol{u}\right) \approx f_\alpha\left(\boldsymbol{u}^{(n+1,m)}\right) + \sum_\beta \left.\frac{\partial f_\alpha(\boldsymbol{u})}{\partial u_\beta}\right|_{\boldsymbol{u}^{(n+1,m)}}\zeta\delta u_\beta
\tag{2.138}
$$

into equation (2.136) and neglecting their truncation errors, one can write

$$
\begin{aligned}
R_\alpha\left(\boldsymbol{u}^{(n+1,m)} + \zeta\delta\boldsymbol{u}\right) = {} & C\frac{u_\alpha^{(n+1,m)} + \zeta\delta u_\alpha - u_\alpha^{(n)}}{\tau} \\
& - \theta\nabla \cdot \left(\boldsymbol{A}_\alpha\left(\boldsymbol{u}^{(n+1,m)}\right)\nabla u_\alpha^{(n+1,m)}\right) \\
& - \zeta\theta\nabla \cdot \left(\boldsymbol{A}_\alpha\left(\boldsymbol{u}^{(n+1,m)}\right)\nabla\left(\delta u_\alpha\right)\right) \\
& - \zeta\theta\nabla \cdot \left(\sum_\beta \left.\frac{\partial\boldsymbol{A}_\alpha(\boldsymbol{u})}{\partial u_\beta}\right|_{\boldsymbol{u}^{(n+1,m)}}\delta u_\beta\nabla u_\alpha^{(n+1,m)}\right) \\
& - \zeta^2\theta\nabla \cdot \left(\sum_\beta \left.\frac{\partial\boldsymbol{A}_\alpha(\boldsymbol{u})}{\partial u_\beta}\right|_{\boldsymbol{u}^{(n+1,m)}}\delta u_\beta\nabla\delta u_\alpha\right) \\
& - (1-\theta)\nabla \cdot \left(\boldsymbol{A}_\alpha(\boldsymbol{u}^{(n)})\nabla u_\alpha^{(n)}\right) \\
& - \theta f_\alpha\left(\boldsymbol{u}^{(n+1,m)}\right) - \zeta\theta\sum_\beta \left.\frac{\partial f_\alpha(\boldsymbol{u})}{\partial u_\beta}\right|_{\boldsymbol{u}^{(n+1,m)}}\delta u_\beta \\
& - (1-\theta)f_\alpha(\boldsymbol{u}^{(n)}).
\end{aligned}
\tag{2.139}
$$

Following the definition (2.133) and subtracting $R_\alpha\left(\boldsymbol{u}^{(n+1,m)}\right)$ from equation (2.139),

dividing the difference by $\zeta$, and taking the limit of the result at $\zeta \to 0$, one finds

$$\delta R_\alpha \left( \boldsymbol{u}^{(n+1,m)}; \delta \boldsymbol{u} \right) = \frac{C}{\tau} \delta u_\alpha - \theta \nabla \cdot \left( \boldsymbol{A}_\alpha \left( \boldsymbol{u}^{(n+1,m)} \right) \nabla \left( \delta u_\alpha \right) \right)$$

$$- \theta \nabla \cdot \left( \sum_\beta \left. \frac{\partial \boldsymbol{A}_\alpha(\boldsymbol{u})}{\partial u_\beta} \right|_{\boldsymbol{u}^{(n+1,m)}} \delta u_\beta \nabla u_\alpha^{(n+1,m)} \right)$$

$$- \theta \sum_\beta \left. \frac{\partial f_\alpha(\boldsymbol{u})}{\partial u_\beta} \right|_{\boldsymbol{u}^{(n+1,m)}} \delta u_\beta. \qquad (2.140)$$

In order to arrive at Newton's method (2.135), the right-hand of equation (2.140) needs to be equated to $-R_\alpha \left( \boldsymbol{u}^{(n+1,m)} \right)$:

$$\delta R_\alpha(\boldsymbol{u}^{(n+1,m)}; \delta \boldsymbol{u}) = -R_\alpha \left( \boldsymbol{u}^{(n+1,m)} \right).$$

This gives

$$\frac{C}{\tau} \delta u_\alpha - \theta \nabla \cdot \left( \boldsymbol{A}_\alpha \left( \boldsymbol{u}^{(n+1,m)} \right) \nabla \left( \delta u_\alpha \right) \right)$$

$$- \theta \nabla \cdot \left( \sum_\beta \left. \frac{\partial \boldsymbol{A}_\alpha(\boldsymbol{u})}{\partial u_\beta} \right|_{\boldsymbol{u}^{(n+1,m)}} \delta u_\beta \nabla u_\alpha^{(n+1,m)} \right) - \theta \sum_\beta \left. \frac{\partial f_\alpha(\boldsymbol{u})}{\partial u_\beta} \right|_{\boldsymbol{u}^{(n+1,m)}} \delta u_\beta$$

$$= \frac{C}{\tau} u_\alpha^{(n)} - \frac{C}{\tau} u_\alpha^{(n+1,m)} + \theta \nabla \cdot \left( \boldsymbol{A}_\alpha \left( \boldsymbol{u}^{(n+1,m)} \right) \nabla u_\alpha^{(n+1,m)} \right)$$

$$+ (1 - \theta) \nabla \cdot \left( \boldsymbol{A}_\alpha(\boldsymbol{u}^{(n)}) \nabla u_\alpha^{(n)} \right) + \theta f_\alpha \left( \boldsymbol{u}^{(n+1,m)} \right)$$

$$+ (1 - \theta) f_\alpha(\boldsymbol{u}^{(n)}). \quad (2.141)$$

The equation above is linear with respect to the solution update.

The convergence of Newton's method is verified based on the solution-error estimates (2.129) and (2.130). Additionally, the Euclidean norm of the overall residual, defined as

$$\left\| \boldsymbol{R} \left( \boldsymbol{u}^{(n+1,m+1)} \right) \right\|_2 = \sqrt{\sum_\alpha \| R_\alpha(\boldsymbol{u}^{(n+1,m+1)}) \|_2^2} = \sqrt{\sum_\alpha \sum_i R_{\alpha i}^2(\boldsymbol{u}^{(n+1,m+1)})},$$

is also controlled and ensured to satisfy a given tolerance.

A modified Newton's method with a three-point parabolic line search [538, 539] is used in this thesis. The idea behind that algorithm is to scale the solution update with such a step size $h$ that minimizes the scalar function

$$g(h) = \left\| \boldsymbol{R} \left( \boldsymbol{u}^{(n+1,m)} + h \delta \boldsymbol{u} \right) \right\|_2^2$$

at every Newton iteration $m$. The first line-search iteration is performed with a full step $\delta\boldsymbol{u}$ ($h^{(1)} = 1$). If this step size does not satisfy the so-called Armijo rule

$$\left\|\boldsymbol{R}\left(\boldsymbol{u}^{(n+1,m)} + h^{(k)}\delta\boldsymbol{u}\right)\right\|_2 \leq \left(1 - \gamma h^{(k)}\right)\left\|\boldsymbol{R}\left(\boldsymbol{u}^{(n+1,m)}\right)\right\|_2, \qquad (2.142)$$

where $\gamma = 10^{-3}$, it is rejected. The second and the subsequent step sizes are subjected to the safeguard constraint $h^{(k)} \in [h_{\min}, h_{\max}] \subset (0, 1)$, for which $h_{\min} = 0.5$ and $h_{\max} = 0.9$ are used. Three most recently rejected values of $g(h)$ are fitted with a quadratic polynomial, and the new step size is assigned the location of the minimum of $g(h)$. The line search is performed iteratively over the predicted step sizes $h^{(k)}$ until condition (2.142) is satisfied. Further details of the algorithm can be found in [538, 539].

### 2.2.2.3 Discussion

The advantage of Newton's method is that, when it converges, it converges quadratically as opposed to the linear convergence of Picard's method [530–533]. On the other hand, Picard's method does not require calculation of the Jacobian matrix, i.e., the terms corresponding to the derivatives of $\boldsymbol{A}_\alpha(\boldsymbol{u})$ and $f_\alpha(\boldsymbol{u})$ with respect to the solution variables, and retains symmetry of the linear-system matrix. The ultimate factor in the choice of the linearization method is, however, the computational time.

Picard's method showed reasonable performance when applied to a single diffusion equation of type (2.54) with a zero right-hand side in Chapter 3. However, for more complex models, such as the transient cathode model, governed by equations (2.54), (2.56), and (2.57), Newton's method had a significant advantage, sometimes by 2 orders of magnitude, in both the number of iterations required for convergence and the overall simulation time. Even though each Picard iteration took less time to assemble and solve the system, that was not enough to counterbalance the increased number of iterations. Therefore, Newton's method was used to linearize the single-electrode and fuel-cell models in Chapters 4–6.

## 2.2.3  Weak Formulation and Spatial Discretization

Spatial discretization of the linearized equations ((2.127) or (2.141)) was performed with the Galerkin (Bubnov-Galerkin) finite-element method [532, 540]. For conciseness, equation (2.141) will be considered and $\theta = 1$ will be assumed, i.e., the discussion will be based on implicit-Euler temporal discretization and Newton's linearization:

$$
\frac{C}{\tau}\delta u_\alpha - \nabla \cdot \left( \boldsymbol{A}_\alpha \left( \boldsymbol{u}^{(n+1,m)} \right) \nabla \left( \delta u_\alpha \right) \right)
$$
$$
- \nabla \cdot \left( \sum_\beta \left. \frac{\partial \boldsymbol{A}_\alpha(\boldsymbol{u})}{\partial u_\beta} \right|_{\boldsymbol{u}^{(n+1,m)}} \delta u_\beta \nabla u_\alpha^{(n+1,m)} \right) - \sum_\beta \left. \frac{\partial f_\alpha(\boldsymbol{u})}{\partial u_\beta} \right|_{\boldsymbol{u}^{(n+1,m)}} \delta u_\beta
$$
$$
= \frac{C}{\tau} u_\alpha^{(n)} - \frac{C}{\tau} u_\alpha^{(n+1,m)} + \nabla \cdot \left( \boldsymbol{A}_\alpha \left( \boldsymbol{u}^{(n+1,m)} \right) \nabla u_\alpha^{(n+1,m)} \right)
$$
$$
+ f_\alpha \left( \boldsymbol{u}^{(n+1,m)} \right). \tag{2.143}
$$

To obtain the weak formulation, equation (2.143) is multiplied by a test function $v_\alpha$ and then integrated over the computational domain $\Omega$:

$$
\frac{C}{\tau} \int_\Omega v_\alpha \delta u_\alpha \, d\Omega - \int_\Omega v_\alpha \nabla \cdot \left( \boldsymbol{A}_\alpha \left( \boldsymbol{u}^{(n+1,m)} \right) \nabla \left( \delta u_\alpha \right) \right) \, d\Omega
$$
$$
- \int_\Omega v_\alpha \nabla \cdot \left( \sum_\beta \left. \frac{\partial \boldsymbol{A}_\alpha(\boldsymbol{u})}{\partial u_\beta} \right|_{\boldsymbol{u}^{(n+1,m)}} \delta u_\beta \nabla u_\alpha^{(n+1,m)} \right) \, d\Omega
$$
$$
- \int_\Omega v_\alpha \sum_\beta \left. \frac{\partial f_\alpha(\boldsymbol{u})}{\partial u_\beta} \right|_{\boldsymbol{u}^{(n+1,m)}} \delta u_\beta \, d\Omega
$$
$$
= \int_\Omega v_\alpha \frac{C}{\tau} u_\alpha^{(n)} \, d\Omega - \int_\Omega v_\alpha \frac{C}{\tau} u_\alpha^{(n+1,m)} \, d\Omega
$$
$$
+ \int_\Omega v_\alpha \nabla \cdot \left( \boldsymbol{A}_\alpha \left( \boldsymbol{u}^{(n+1,m)} \right) \nabla u_\alpha^{(n+1,m)} \right) \, d\Omega
$$
$$
+ \int_\Omega v_\alpha f_\alpha \left( \boldsymbol{u}^{(n+1,m)} \right) \, d\Omega.
$$

Using integration by parts (Gauss's theorem) [537]

$$
\int_\Omega a \nabla \cdot \boldsymbol{b} \, d\Omega = \int_{\Gamma = \partial \Omega} a \boldsymbol{b} \cdot \boldsymbol{n} \, d\Gamma - \int_\Omega \nabla a \cdot \boldsymbol{b} \, d\Omega
$$

and adopting a compact representation of integrals

$$(a,\, b)_\Omega = \int_\Omega ab\, d\Omega,$$

$$(\boldsymbol{a},\, \boldsymbol{b})_\Omega = \int_\Omega \boldsymbol{a} \cdot \boldsymbol{b}\, d\Omega,$$

one obtains

$$\frac{C}{\tau}\left(v_\alpha,\, \delta u_\alpha\right)_\Omega - \left(v_\alpha \boldsymbol{A}_\alpha\left(\boldsymbol{u}^{(n+1,m)}\right)\nabla\left(\delta u_\alpha\right),\, \boldsymbol{n}\right)_\Gamma$$

$$+ \left(\nabla v_\alpha,\, \boldsymbol{A}_\alpha\left(\boldsymbol{u}^{(n+1,m)}\right)\nabla\left(\delta u_\alpha\right)\right)_\Omega$$

$$- \left(v_\alpha \sum_\beta \left.\frac{\partial \boldsymbol{A}_\alpha(\boldsymbol{u})}{\partial u_\beta}\right|_{\boldsymbol{u}^{(n+1,m)}} \delta u_\beta \nabla u_\alpha^{(n+1,m)},\, \boldsymbol{n}\right)_\Gamma$$

$$+ \left(\nabla v_\alpha,\, \sum_\beta \left.\frac{\partial \boldsymbol{A}_\alpha(\boldsymbol{u})}{\partial u_\beta}\right|_{\boldsymbol{u}^{(n+1,m)}} \delta u_\beta \nabla u_\alpha^{(n+1,m)}\right)_\Omega$$

$$- \left(v_\alpha,\, \sum_\beta \left.\frac{\partial f_\alpha(\boldsymbol{u})}{\partial u_\beta}\right|_{\boldsymbol{u}^{(n+1,m)}} \delta u_\beta\right)_\Omega$$

$$= \frac{C}{\tau}\left(v_\alpha,\, u_\alpha^{(n)}\right)_\Omega - \frac{C}{\tau}\left(v_\alpha,\, u_\alpha^{(n+1,m)}\right)_\Omega$$

$$+ \left(v_\alpha \boldsymbol{A}_\alpha\left(\boldsymbol{u}^{(n+1,m)}\right)\nabla u_\alpha^{(n+1,m)},\, \boldsymbol{n}\right)_\Gamma$$

$$- \left(\nabla v_\alpha,\, \boldsymbol{A}_\alpha\left(\boldsymbol{u}^{(n+1,m)}\right)\nabla u_\alpha^{(n+1,m)}\right)_\Omega$$

$$+ \left(v_\alpha,\, f_\alpha\left(\boldsymbol{u}^{(n+1,m)}\right)\right)_\Omega. \tag{2.144}$$

Equation (2.144) represents the weak formulation of equation (2.143).

Boundary integrals in equation (2.144) can be replaced with the given Neumann (second-type) or Robin (third-type) boundary conditions. Those conditions can be written in the general form

$$-\left(\boldsymbol{A}_\alpha(\boldsymbol{u}^{(n+1,m+1)})\nabla u_\alpha^{(n+1,m+1)}\right)\cdot \boldsymbol{n} = d_1 u_\alpha^{(n+1,m+1)} + d_2, \tag{2.145}$$

where $d_1$ and $d_2$ are some real coefficients. Application of the same linearization procedure as before to equation (2.145), multiplication of the result by the test function,

and integration over the boundary results in

$$- \left( v_\alpha \boldsymbol{A}_\alpha(\boldsymbol{u}^{(n+1,m)}) \nabla u_\alpha^{(n+1,m)}, \, \boldsymbol{n} \right)_\Gamma$$

$$- \left( v_\alpha \sum_\beta \left. \frac{\partial \boldsymbol{A}_\alpha(\boldsymbol{u})}{\partial u_\beta} \right|_{\boldsymbol{u}^{(n+1,m)}} \delta u_\beta \nabla u_\alpha^{(n+1,m)}, \, \boldsymbol{n} \right)_\Gamma$$

$$- \left( v_\alpha \boldsymbol{A}_\alpha(\boldsymbol{u}^{(n+1,m)}) \nabla \left( \delta u_\alpha \right), \, \boldsymbol{n} \right)_\Gamma$$

$$= \left( v_\alpha, \, d_1 u_\alpha^{(n+1,m)} \right)_\Gamma + \left( v_\alpha, \, d_1 \delta u_\alpha \right)_\Gamma + \left( v_\alpha, \, d_2 \right)_\Gamma. \quad (2.146)$$

Integrals in the left-hand side of equation (2.146) appear naturally in equation (2.144). Their substitution gives

$$\frac{C}{\tau} \left( v_\alpha, \, \delta u_\alpha \right)_\Omega + \left( v_\alpha, \, d_1 \delta u_\alpha \right)_\Gamma$$

$$+ \left( \nabla v_\alpha, \, \boldsymbol{A}_\alpha \left( \boldsymbol{u}^{(n+1,m)} \right) \nabla \left( \delta u_\alpha \right) \right)_\Omega$$

$$+ \left( \nabla v_\alpha, \, \sum_\beta \left. \frac{\partial \boldsymbol{A}_\alpha(\boldsymbol{u})}{\partial u_\beta} \right|_{\boldsymbol{u}^{(n+1,m)}} \delta u_\beta \nabla u_\alpha^{(n+1,m)} \right)_\Omega$$

$$- \left( v_\alpha, \, \sum_\beta \left. \frac{\partial f_\alpha(\boldsymbol{u})}{\partial u_\beta} \right|_{\boldsymbol{u}^{(n+1,m)}} \delta u_\beta \right)_\Omega$$

$$= \frac{C}{\tau} \left( v_\alpha, \, u_\alpha^{(n)} \right)_\Omega - \frac{C}{\tau} \left( v_\alpha, \, u_\alpha^{(n+1,m)} \right)_\Omega$$

$$- \left( v_\alpha, \, d_1 u_\alpha^{(n+1,m)} \right)_\Gamma - \left( v_\alpha, \, d_2 \right)_\Gamma$$

$$- \left( \nabla v_\alpha, \, \boldsymbol{A}_\alpha \left( \boldsymbol{u}^{(n+1,m)} \right) \nabla u_\alpha^{(n+1,m)} \right)_\Omega$$

$$+ \left( v_\alpha, \, f_\alpha \left( \boldsymbol{u}^{(n+1,m)} \right) \right)_\Omega. \quad (2.147)$$

Dirichlet (first-type) boundary conditions are applied directly to the linear system of equations resulting from the spatial discretization of the weak form (2.147).

Spatial discretization is performed by dividing the computational domain $\Omega$ into elements $\Omega_e$. In this thesis, only two-dimensional problems are solved, and the elements are quadrilateral. Since all equations are implemented in a dimension-independent form, they also support the use of hexahedral elements in 3D. Purely one-dimensional simulations are currently not supported in OpenFCST; they are performed in two dimensions by making one of the dimensions significantly smaller than the other one,

as done for the pseudo-1D catalyst-layer model in Chapter 5. Other common choices of element shapes in two and three dimensions are triangles and tetrahedrons; however, those shapes are currently not supported by the finite-element library used in OpenFCST, deal.II.

Inside of each element, the solution, its Newton update, and the test function are replaced with their finite-element approximations [532, 540]

$$w_\alpha(\boldsymbol{x}) \approx \sum_{i=1}^{N_e} w_{\alpha i} \varphi_{\alpha i}(\boldsymbol{x}), \qquad (2.148)$$

where $w_\alpha(\boldsymbol{x})$ is $u_\alpha(\boldsymbol{x})$, $\delta u_\alpha(\boldsymbol{x})$, or $v_\alpha(\boldsymbol{x})$ and $w_{\alpha i}$ is $u_{\alpha i}$, $\delta u_{\alpha i}$, or $v_{\alpha i}$, respectively, $N_e$ is the number of nodes in the element, and $\varphi_{\alpha i}(\boldsymbol{x})$ is the shape function corresponding to the element node $i$. Quadrilateral elements with second-order Lagrange shape functions [540] are used in this thesis. Approximation (2.148) depends on time through coefficients $u_{\alpha i}$ that change between the time layers.

Mesh refinement is used to achieve a grid-independent solution. Both global and adaptive refinement are utilized in this thesis. In the global algorithm, all mesh cells are split into four at each refinement cycle. The a posteriori Kelly error estimator [541], available through the deal.II library [380–382], is used in the adaptive algorithm. The error estimate is computed for each cell as [262, 541]

$$\eta_K^2 = \frac{h}{24} \int_\Gamma [[(\nabla \boldsymbol{u})\boldsymbol{n}]]^2 \ d\Gamma, \qquad (2.149)$$

where $h$ is a measure of the cell size and the double square brackets denote the jump of the function at the cell boundary $\Gamma$. In each cycle, a given percentage of the cells with the largest error is refined and a given percentage with the smallest error is coarsened. The number of the refinement cycles and the frequency of the refinement in time are determined based on the desired level of solution accuracy and computational cost.

Substituting approximations (2.148) into equation (2.147), one arrives at

$$
\sum_{i=1}^{N}\sum_{j=1}^{N} v_{\alpha i}\left[\frac{C}{\tau}\left(\varphi_{\alpha i},\, \delta u_{\alpha j}\varphi_{\alpha j}\right)_{\Omega} + \left(\varphi_{\alpha i},\, d_1 \delta u_{\alpha j}\varphi_{\alpha j}\right)_{\Gamma}\right.
$$

$$
+ \left(\nabla\varphi_{\alpha i},\, \boldsymbol{A}_\alpha\left(\boldsymbol{u}^{(n+1,m)}\right)\nabla\left(\delta u_{\alpha j}\varphi_{\alpha j}\right)\right)_{\Omega}
$$

$$
+ \left(\nabla\varphi_{\alpha i},\, \sum_\beta \left.\frac{\partial \boldsymbol{A}_\alpha(\boldsymbol{u})}{\partial u_\beta}\right|_{\boldsymbol{u}^{(n+1,m)}} \delta u_{\beta j}\varphi_{\beta j}\nabla u_\alpha^{(n+1,m)}\right)_{\Omega}
$$

$$
- \left(\varphi_{\alpha i},\, \sum_\beta \left.\frac{\partial f_\alpha(\boldsymbol{u})}{\partial u_\beta}\right|_{\boldsymbol{u}^{(n+1,m)}} \delta u_{\beta j}\varphi_{\beta j}\right)_{\Omega}\right]
$$

$$
= \sum_{i=1}^{N} v_{\alpha i}\left[\frac{C}{\tau}\left(\varphi_{\alpha i},\, u_\alpha^{(n)}\right)_{\Omega} - \frac{C}{\tau}\left(\varphi_{\alpha i},\, u_\alpha^{(n+1,m)}\right)_{\Omega}\right.
$$

$$
- \left(\varphi_{\alpha i},\, d_1 u_\alpha^{(n+1,m)}\right)_{\Gamma} - \left(\varphi_{\alpha i},\, d_2\right)_{\Gamma}
$$

$$
- \left(\nabla\varphi_{\alpha i},\, \boldsymbol{A}_\alpha\left(\boldsymbol{u}^{(n+1,m)}\right)\nabla u_\alpha^{(n+1,m)}\right)_{\Omega}
$$

$$
+ \left(\varphi_{\alpha i},\, f_\alpha\left(\boldsymbol{u}^{(n+1,m)}\right)\right)_{\Omega}\right]. \tag{2.150}
$$

Note that solutions $\boldsymbol{u}^{(n+1,m)}$ and $\boldsymbol{u}^{(n)}$ are known from the previous Newton iteration and the previous time layer, respectively, and thus do not need to be approximated with (2.148).

Integrals in equation (2.150) were computed using the Gauss-Legendre rule [532, 534, 540] with 3 quadrature points in each direction. Numerical integration was performed with the deal.II library [380–382].

Since $v_{\alpha i}$ are arbitrary, they can be removed from equation (2.150), leaving only summation over $j$. This results in a system of linear equations

$$
\boldsymbol{A}\delta\boldsymbol{u} = \boldsymbol{b}, \tag{2.151}
$$

where the Newton update $\delta\boldsymbol{u}$ is a block-vector with index $\alpha$ corresponding to the solution variables and index $j$ corresponding to the components of those variables in approximation (2.148). If the problem is linearized with Picard's method, one obtains a linear system of the form

$$
\boldsymbol{A}\boldsymbol{u} = \boldsymbol{b}. \tag{2.152}
$$

Systems (2.151) and (2.152) are solved with the methods discussed in Section 2.2.4.

## 2.2.4 Linear Solvers

For linear diffusion-type models and nonlinear diffusion-type models linearized with Picard's method in Chapter 3, governed with equation of type (2.54) with a zero right-hand side, the linear system obtained from temporal and spatial discretization was solved with the conjugate-gradient (CG) method [530–532, 538]. The latter is designed for systems with positive-definite and symmetric matrices [530–532, 538], which is the case for diffusion equations [531]. The linear-solver iterations were assumed to have converged when the Euclidean norm of the residual of the linear system was below the given threshold, typically $10^{-10}$. The CG solver was provided by the deal.II library [380–382].

The system matrices corresponding to the linearized fuel-cell models (equations (2.54)–(2.60), see Chapters 4–6) were not symmetric, and the linear systems were solved with either the unsymmetric-pattern multifrontal method (UMFPACK) [542–544] in serial mode or with the multifrontal massively parallel solver (MUMPS) [545] in parallel mode. Both UMFPACK and MUMPS are direct solvers based on sparse $LU$ and $LDL^{\mathrm{T}}$ decomposition [542, 543, 545]. They were provided by the deal.II library through SuiteSparse [546] and PETSc [547, 548] packages. Direct solvers applied to large problems, especially in 3D, are computationally demanding. For the 2D problems considered in this thesis, the performance of the UMFPACK and MUMPS solvers was acceptable.

## 2.2.5 Summary of the Transient Framework

The structure of the transient framework developed in this thesis and implemented in OpenFCST is schematically illustrated in the block diagram in Figure 2.7. The new transient solution, $\boldsymbol{u}^{(n+1)}$, is obtained from the old solution, $\boldsymbol{u}^{(n)}$, in several steps. First, if the given time layer has been marked for adaptive mesh refinement or coarsening (which takes place only on every certain time layer), the mesh is modified in accordance with the error estimator (2.149), and $\boldsymbol{u}^{(n)}$ is interpolated onto the new
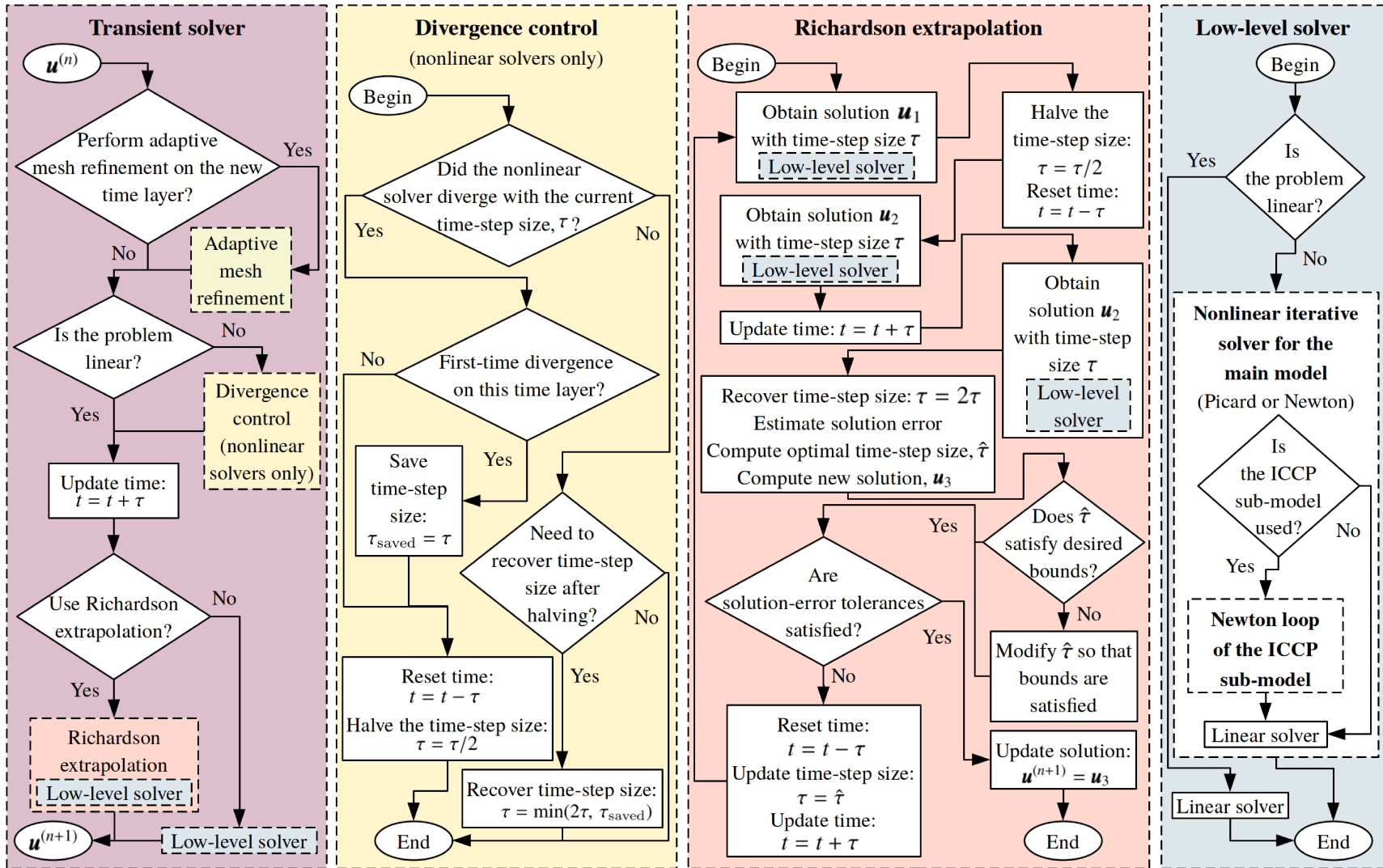
Figure 2.7: Block diagram of the transient framework in OpenFCST implemented in this thesis.

mesh.

If the problem is linear, the simulated time is then updated with the current time-step size: $t = t + \tau$. For nonlinear problems, it is possible that Picard's or Newton's method would diverge when attempting to find $\boldsymbol{u}^{(n+1)}$ with the given time-step size. The divergence control by time-step halving and recovery that was discussed earlier in this Chapter is performed in that case prior to updating the simulated time.

Next, if enabled, the Richardson-extrapolation algorithm is executed as discussed in Section 2.2.1.3. During that process, a low-level solver is called multiple times as shown in Figure 2.7. When Richardson extrapolation is not used, the low-level solver is called directly to compute $\boldsymbol{u}^{(n+1)}$. The low-level solver is a linear solver (CG, UMFPACK, or MUMPS) in the case of linear applications or a nonlinear solver (Picard's or Newton's method, both wrapping a linear solver) when linearization is required. In this context, the transient solver ($\theta$-scheme or BDF) is regarded as a high-level solver, as it embeds lower-level algorithms. If the ICCP sub-model is used, equation (2.10) is solved in an additional Newton loop that is entered on every iteration of the overall model's nonlinear solver.

The solution process in Figure 2.7 is repeated for every time layer until the simulation is over.

## 2.3   Post-Processing

Solving governing equations (2.54)–(2.60) with a set of appropriate initial and boundary conditions results in a temporal series of spatial distributions of the solution variables. Additional post-processing routines are used in OpenFCST to compute and output a number of quantities of interest for each simulated time instant.

First of these quantities is the faradaic current density (A/cm$^2$):

$$i_{\mathrm{f}} = \frac{1}{A} \int_V j \, dV, \tag{2.153}$$

where $A$ is the in-plane MEA area (cm$^2$), $V$ is the catalyst-layer volume (cm$^3$), and

$j$ is the volumetric faradaic current density (A/cm$^3$) computed as discussed in Section 2.1.2.6. In transient simulations, the total current density does not match $i_\mathrm{f}$ due to the capacitive double-layer effect in the catalyst layers. A post-processing routine was implemented to compute the total current density (A/cm$^2$) as

$$i = -\frac{1}{A} \int\limits_V \nabla \cdot \left( \sigma_{\mathrm{e}^-}^{\mathrm{eff}} \nabla \phi_{\mathrm{e}^-} \right) \, dV,$$

or, applying the divergence theorem [537] to avoid computation and storage of the second-order derivatives of the electronic potential,

$$i = -\frac{1}{A} \int\limits_S \sigma_{\mathrm{e}^-}^{\mathrm{eff}} \nabla \phi_{\mathrm{e}^-} \cdot \boldsymbol{n} dS, \tag{2.154}$$

where $S = \partial V$ is the boundary surface of the MEA. Capacitive current density (A/cm$^2$) is obtained using equations (2.57), (2.153), and (2.154):

$$i_\mathrm{c} = \frac{1}{A} \int\limits_V C_{\mathrm{dl}} \frac{\partial \eta}{\partial t} \, dV = i_\mathrm{f} - i. \tag{2.155}$$

Computation of the total current density that accounts for both faradaic and double-layer processes in the MEA enables impedance-spectroscopy analysis with OpenFCST (Section 2.3.1 and Chapters 4 and 5).

Another useful quantity computed in OpenFCST is the ohmic resistance (in $\Omega \cdot$cm$^2$) of the MEA layers. The calculation is based on the ohmic (Joule) heating:

$$R_{\mathrm{H}^+}^{\mathrm{eff}} = \frac{1}{i^2 A} \int\limits_V \frac{\boldsymbol{i}_{\mathrm{H}^+} \cdot \boldsymbol{i}_{\mathrm{H}^+}}{\sigma_{\mathrm{H}^+}^{\mathrm{eff}}} \, dV = \frac{1}{i^2 A} \int\limits_V \sigma_{\mathrm{H}^+}^{\mathrm{eff}} \nabla \phi_{\mathrm{H}^+} \cdot \nabla \phi_{\mathrm{H}^+} \, dV, \tag{2.156}$$

$$R_{\mathrm{e}^-}^{\mathrm{eff}} = \frac{1}{i^2 A} \int\limits_V \frac{\boldsymbol{i}_{\mathrm{e}^-} \cdot \boldsymbol{i}_{\mathrm{e}^-}}{\sigma_{\mathrm{e}^-}^{\mathrm{eff}}} \, dV = \frac{1}{i^2 A} \int\limits_V \sigma_{\mathrm{e}^-}^{\mathrm{eff}} \nabla \phi_{\mathrm{e}^-} \cdot \nabla \phi_{\mathrm{e}^-} \, dV. \tag{2.157}$$

This approach was proposed by Secanell et al. [328] and Zhou et al. [35, 276] and is validated in Chapter 4 using impedance spectroscopy. Computation of the effective electronic and protonic resistances of the MEA layers with equations (2.156) and (2.157) allows for model validation with experimentally measured ohmic resistance and is a valuable tool for the analysis of impedance spectra (see Chapters 4, 5).

When analyzing dynamic behavior of PEMFCs, it is sometimes convenient to look at the evolution of average quantities in each MEA layer rather than of their spatial distributions. A post-processing routine was implemented for outputting some useful average quantities, such as the average liquid-water saturation and the average capillary pressure used in Chapter 6. This is done by integrating the quantity of interest, $q$, over the given MEA layer and dividing the result by the volume of the layer:

$$\langle q \rangle = \frac{1}{V} \int\limits_V q \, dV.$$

Once a transient simulation is over, its results can be processed with the Python-based data-analysis package within OpenFCST called pyFCST. In this thesis, a new framework has been developed in pyFCST for analyzing impedance-spectroscopy simulations. That framework is discussed next.

## 2.3.1 Impedance-Spectroscopy Framework

The transient framework for fuel-cell modeling developed in this thesis enables simulations of common experimental characterization techniques, such as polarization-curve measurement and electrochemical impedance spectroscopy. The latter requires additional post-processing to analyze the simulated current-density response to a change in voltage.

In the conventional EIS approach, simulations mirror experiments: a sinusoidal input signal is applied (for example, voltage) and the transient response is measured (current). This process needs to be repeated for every frequency of interest, which means the transient numerical problem needs to be solved as many times as frequencies needed to resolve the impedance spectrum.

In the more computationally efficient approach proposed by Wiese and Weil [549], the whole impedance spectrum is obtained from a single simulation of the current relaxation after a step-excitation in voltage. This approach was adopted by Bessler [249] to simulate impedance spectra of solid-oxide fuel cells and, more recently, applied by

Bao and Bessler [164] and Futter et al. [159] to PEMFCs. The impedance spectra simulated with the rapid-EIS approach have been shown to match those obtained with the sine-wave approach (see [249] and Chapter 4). The rapid-EIS approach can also be used in physical experiments as long as the common laboratory-grade potentiostats are equipped with additional modules that enable high sampling rate (on the order of GHz) to resolve the initial transients.

Another method recently proposed as an alternative to the conventional sine-wave approach is the use of a sine signal with a time-dependent frequency (a chirp signal) [550]. Similarly to the rapid-EIS approach, this method also allows for the extraction of a range of frequencies from a single simulation or experiment. The chirp-signal EIS approach has been validated with numerical simulations and physical experiments involving electrical circuits [550, 551], but, to the best of the author's knowledge, not with an electrochemical cell or its physical model. Additionally, in order to avoid spectral leakage, a more complicated technique involving two chirp signals with shifted phases and additional filtering of the results is required [551]. For those reasons, chirp-signal simulations are not considered in this thesis.

In all cases, a steady-state solution is obtained at the voltage of interest $V_0$ by solving equations (2.54)-(2.60) with setting all transient terms to zero. That solution is then used as an initial solution for the transient simulation, in which a small-amplitude voltage perturbation (1–5 mV) is applied and the current-density response is computed using equation (2.154). Impedance is then obtained by processing the simulation data with the routines developed in pyFCST. The framework for the EIS simulations with the sine-wave and rapid-EIS approaches and their post-processing is discussed next.

### 2.3.1.1 Conventional Approach

The typical process in the conventional approach involves simulating several periods of a sine wave with high resolution (for instance, 256–1024 temporal nodes per period).

Both the number of periods and the temporal resolution are determined by analyzing the impedance convergence at different frequencies. In order to maintain the linearity of the system response, a sufficiently small perturbation amplitude should be used. The upper limit of the PEMFC voltage perturbation in linear EIS is approximately 30 mV at 80 °C [163]. In this thesis, a peak-to-peak amplitude of 1 mV is used in sine-wave simulations.

Once the simulation is over, the output signal is scaled with a Welch window [534]

$$w(t) = 1 - (2t)^2, \quad t \in [-1/2,\ 1/2]$$

to minimize aliasing and then processed with the Fast Fourier Transform (FFT) from SciPy [486], which is an efficient implementation of the Discrete Fourier Transform (DFT) defined as [552, 553]

$$H_n = H(n\Delta f) = \sum_{k=0}^{N-1} h(k\Delta t)e^{-ink2\pi/N} = \sum_{k=0}^{N-1} h(k\Delta t)e^{-i(2\pi n\Delta f)k\Delta t}, \quad n \in \{0,\ N-1\},$$

where $N = T/\Delta t$ is the number of points sampled from the original signal $h(t)$ with a step $\Delta t$ over the time interval $[0,\ T]$, and $\Delta f = 1/T$, $1/N = \Delta t/T = \Delta t\Delta f$. Spectral leakage due to numerical error is filtered out by taking the current-density frequency to be the frequency at which the FFT magnitude reaches maximum. Impedance is then computed as the ratio of the known voltage phasor to the reconstructed current-density phasor.

### 2.3.1.2 Rapid-EIS Approach

In this approach, a rapid voltage ramp is applied to the cell at $t = 0$:

$$V(t) = \begin{cases} V_0 + V_\mathrm{m}\dfrac{t}{t_\mathrm{r}}, & t \in [0,\ t_\mathrm{r}], \\ V_0 + V_\mathrm{m}, & t \in (t_\mathrm{r},\ T], \end{cases} \tag{2.158}$$

where $V_\mathrm{m}$ is the size of the voltage ramp with the duration $t_\mathrm{r}$. The latter should be sufficiently shorter than the time scale of the fastest response of the system and is typically below $10^{-6}$ s [249]. In this thesis, a 1–5 mV ramp is applied over $10^{-9}$ s so

as to not affect the frequencies relevant to fuel-cell impedance spectra (typically up to $10^5$ Hz). The simulation is then continued at the constant voltage $V_0 + V_{\mathrm{m}}$ until reaching time $T = 10^{10}$ s [249] in order for the total simulation time to be sufficiently longer than the time scale of the slowest system response.

The time-step size is controlled in the rapid-EIS simulations using Richardson extrapolation (Section 2.2.1.3) with an initial time-step size of $10^{-10}$ s. To avoid sudden changes in the simulated output signal, the increase of the time-step size between time layers is capped with $\tau_{n+1}/\tau_n \leq \Theta$, where $\Theta = 1.001$ is often a good balance between the accuracy of the spectrum and the computational time. The effect of $\Theta$ on the computed impedance spectrum is shown in Chapter 4.

Rapid EIS simulations need to resolve a wide range of time scales and thus are typically performed on nonuniform grids [249, 549], which makes the common Fourier-transform algorithms inapplicable. Instead, the Fourier transform proposed by Wiese and Weil [549] is used. For a time-dependent signal $h(t)$, the Fourier transform is defined as [549, 553]

$$H(\omega) = \int_{-\infty}^{\infty} h(t)e^{-i\omega t}dt, \tag{2.159}$$

where $\omega = 2\pi f$ is the angular frequency corresponding to the harmonic frequency $f$. If the signal is sampled at nodes $t_n$ ($n \in \{0,\ N\}$) and satisfies the conditions

$$h(t \leq t_0) = 0 \text{ and } h(t \geq t_N) = 0, \tag{2.160}$$

the Fourier transform (2.159) can be written as

$$H(\omega) = \sum_{n=0}^{N-1} \int_{t_n}^{t_{n+1}} h(t)e^{-i\omega t}dt. \tag{2.161}$$

Integral (2.161) can be computed analytically when $h(t)$ is interpolated between the sampling points [549]. Linear interpolation

$$h(t) = h_n + \frac{h_{n+1} - h_n}{t_{n+1} - t_n}(t - t_n), \quad t \in [t_n,\ t_{n+1}],$$

corresponds to the trapezoidal quadrature rule and results in the following discrete Fourier transform [249, 549]:

$$H^*(\omega) = \frac{1}{\omega^2} \sum_{n=0}^{N-1} \left[ (a_n + i\omega h_{n+1}) e^{-i\omega t_{n+1}} - (a_n + i\omega h_n) e^{-i\omega t_n} \right], \quad (2.162)$$

where $a_n = (h_{n+1} - h_n)/(t_{n+1} - t_n)$. Because of the condition (2.160) used to obtain this transform, the integrand $h(t)$ must vanish at the end nodes. This is achieved by subtracting the initial values of voltage and current density from the respective data and adding artificial zero points at $t_{N+1} = 2t_N$ as proposed in [249]. Since the last temporal node is placed at $t_N = 10^{10}$ s, the time scale of the artificial ramp at the interval $[t_N, t_{N+1}]$ is sufficiently long and does not affect the lowest frequencies in the fuel-cell response [249] (usually as low as $10^{-4}$ Hz). Impedance spectrum is then computed as the ratio of Fourier transforms (2.162) of voltage $V^*(\omega)$ and current density $i^*(\omega)$ [249, 549]: $Z(\omega) = V^*(\omega)/i^*(\omega)$ (units of $m\Omega \cdot cm^2$ are used in this thesis).

# Chapter 3

# Numerical Estimation of Oxygen-Transport Properties of Polymer-Electrolyte Materials[1]

Oxygen transport in polymer-electrolyte membranes and films is commonly analyzed by encasing the sample in a solid-state cell, placing a platinum disk electrode in contact with the surface of the sample, and drawing ORR current [309, 325, 384–387, 389–392]. At the cell potentials where the ORR is limited by the rate of oxygen transport toward the disk electrode (oxygen concentration at the electrode is assumed zero in that case), the chronoamperometric current can be fitted with one of the analytical equations available in the literature [394–400] to obtain oxygen diffusivity and solubility. However, the analytical models used in chronoamperometry at disk electrodes are only valid under the assumption of semi-infinite diffusion [394–400], i.e., when the polymeric sample is infinitely thick. While this technique is appropriate for thick membranes and short measurement times, the sample-thickness limitation of the analytical models may be problematic for thin electrolyte films. This obstructs the use of chronoamperometry in measuring gas-transport properties of modern thin

---

[1]Parts of this chapter were reproduced with permission from:

1. D. Novitski, A. Kosakian, T. Weissbach, M. Secanell, and S. Holdcroft, "Electrochemical reduction of dissolved oxygen in alkaline, solid polymer electrolyte films," *Journal of the American Chemical Society*, vol. 138, no. 47, pp. 15 465–15 472, 2016. Copyright 2016 American Chemical Society.

Author contributions are detailed in the Preface of this thesis.

membranes (5–25 μm [116]) and ionomer films in catalyst layers (1–10 nm [124, 132]).

A numerical model for oxygen diffusion at a microdisk electrode is developed in this Chapter and used to estimate oxygen-transport properties of polymer-electrolyte membranes by analyzing chronoamperometric measurements. The numerically obtained diffusivity and solubility of oxygen are compared with those estimated with the analytical Shoup-Szabo equation [397]. Large deviation between the numerical and analytical transport properties (up to about 29%) is obtained when the diffusion front reaches the open boundary of the membrane. These results indicate that numerical models are more suitable for the analysis of chronoamperometric data than their analytical counterparts, especially in the case of nanometer-scale thin films that attracted a considerable amount of attention in the literature in the past decade [117, 131, 324–326].

## 3.1   Experiment

Experimental data were provided by the Holdcroft Group (Simon Fraser University), and details on the sample preparation, the equipment used, and the testing protocols can be found in [1, 392]. A brief description of the physical experiment is provided next.

The ionomer samples were prepared by drop-casting HMT-PMBI (hexamethyl-$p$-terphenyl poly(methylbenzimidazolium)) onto a platinum microdisk electrode (radius 5 μm) embedded in glass. The resulting 53-μm-thick films were initially equilibrated under controlled temperature and relative-humidity conditions and contained dissolved oxygen molecules. A platinum mesh was pressed against the free surface of each ionomer film and used as a reference/counter electrode. The two electrodes were held together in a solid-state cell shown in Figure 3.1a.

If an electrochemical reaction is fast, its rate is limited by the rate of reactant mass transport. Such mode of electrode operation is called mass-transport-limited (or diffusion-limited, diffusion-controlled). In the chronoamperometric experiment, a
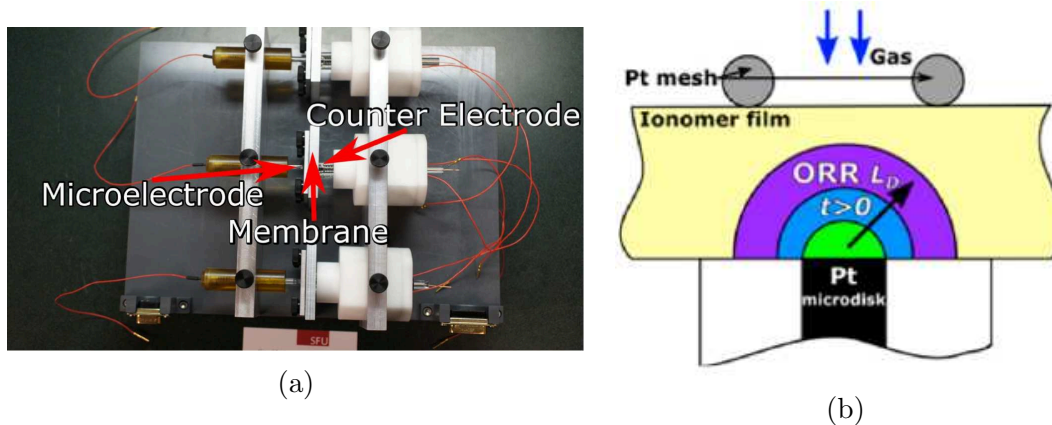
Figure 3.1: Experimental setup (a) and a schematic of oxygen diffusion toward the microdisk electrode (b). Diffusion length, $L_D$, is illustrated. Reprinted with permission from [1]. Copyright 2016 American Chemical Society.

potential difference was applied between the electrodes from the value at which no faradaic reaction occurred (+0.2 V vs. Pt) to the value at which the ORR at the working electrode was diffusion-limited (-0.5 to -0.4 V vs. Pt). The operating conditions were 60 °C, 1 atm, and varying RH of 70%, 80%, 90%, and 98%. When current was drawn, the dissolved oxygen was transported toward the platinum disk electrode, as illustrated in Figure 3.1b. Current transients were then measured every 2.5 ms for approximately 5 seconds (Figure 3.2), and the obtained data were fitted with analytical and numerical models to extract oxygen-transport properties, namely solubility (equilibrium concentration), $c_{b,O_2}$, and diffusivity, $D_{b,O_2}$. Double-layer effects at the interface between the disk electrode and the membrane were significant in the initial 0.2 s, where the measured current was potential-dependent. Oxygen transport was characterized in this work by analyzing the diffusion-limited current at $t \gtrapprox 0.2$ s.

## 3.2 Numerical Model

Since HMT-PMBI membranes are alkaline (in contrast to acidic Nafion®), ORR differs from reaction (1.2) and is given by [1, 392]

$$\frac{1}{2}O_2 + H_2O + 2e^- \rightarrow 2OH^-. \tag{3.1}$$
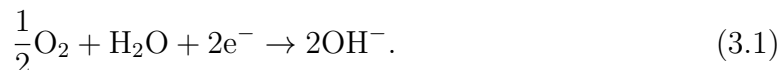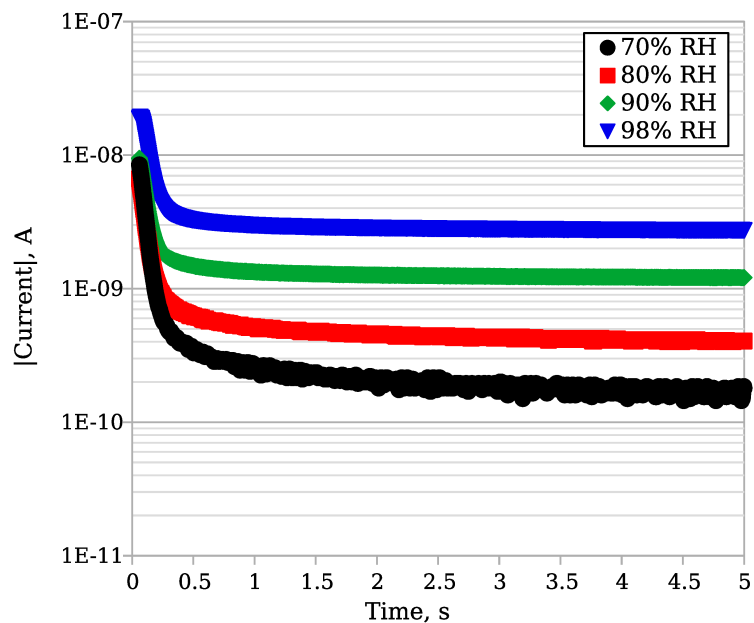
Figure 3.2: Current measured with the experimental setup shown in Figure 3.1 under diffusion-limited conditions.

The charged species transported through the membrane are, in this case, $OH^-$ anions. Although water is a reactant in the alkaline ORR (3.1), oxygen transport was assumed independent of water transport and was modeled with Fick's second law of diffusion, in consistency with the analytical models [394–397, 399, 400]. Changes in ionomer structure with RH were not considered.

Two models were developed, a diffusion-limited model and a kinetics-controlled model. The former model was used to fit oxygen solubility and diffusivity to the experimental chronoamperometric data. The kinetics-controlled model was used to find out whether the developed model was able to predict the experimentally measured potential range in which the current was diffusion-limited.

### 3.2.1 Diffusion-Limited Model

Due to the fact that the in-plane area of the ionomer sample was much larger than the surface of the working electrode, the diffusion problem was axisymmetric and could be reduced to a two-dimensional case in cylindrical coordinates. The corresponding
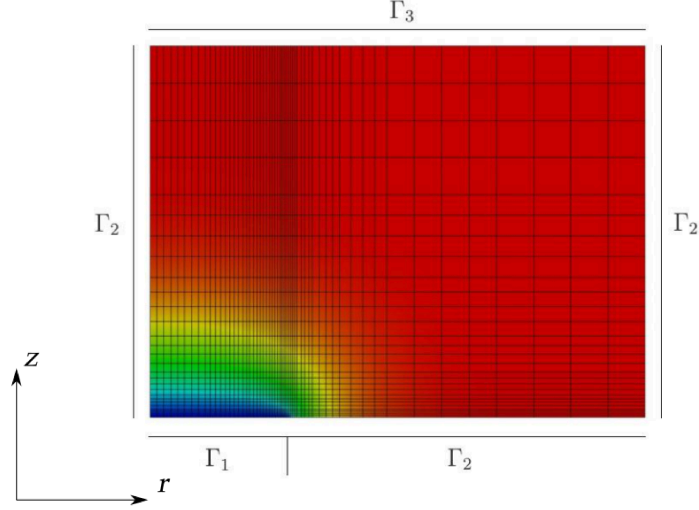
Figure 3.3: A typical computational grid with example oxygen-concentration distribution and boundary labels: $\Gamma_1$ - the ionomer-electrode interface; $\Gamma_2$ - the interface between the ionomer and the insulating support of the electrode, as well as symmetric boundaries; $\Gamma_3$ - the ionomer-surroundings interface. Image not to scale. Area near the electrode is shown.

mathematical model is given by

$$\frac{\partial c}{\partial t} - \nabla \cdot \left(D_{\mathrm{b,O_2}} \nabla c\right) = 0, \qquad \boldsymbol{x} \in \Omega, \quad t > 0, \tag{3.2}$$

$$c = c_{\mathrm{b,O_2}}, \quad \boldsymbol{x} \in \Omega, \quad t = 0, \tag{3.3}$$

$$c = 0, \qquad \boldsymbol{x} \in \Gamma_1, \quad t > 0, \tag{3.4}$$

$$-\left(D_{\mathrm{b,O_2}} \nabla c\right) \cdot \boldsymbol{n} = 0, \qquad \boldsymbol{x} \in \Gamma_2, \quad t > 0, \tag{3.5}$$

$$c = c_{\mathrm{b,O_2}}, \quad \boldsymbol{x} \in \Gamma_3, \quad t > 0, \tag{3.6}$$

where $\Omega$ is the domain of interest shown in Figure 3.3 with coordinates $\boldsymbol{x} = (r, z)$ and $\boldsymbol{n}$ is the normal vector. Boundaries $\Gamma_1$, $\Gamma_2$, and $\Gamma_3$ represent the interfaces between the ionomer and the working electrode, the glass insulation of the working electrode (and symmetric boundaries), and the surroundings, respectively. A zero-concentration boundary condition at the working electrode (interface $\Gamma_1$) was used to describe complete consumption of oxygen during the diffusion-limited operation of the solid-state cell.

The developed model does not account for the finite-rate oxygen dissolution into

129

the film from its surroundings. In the considered case, the thickness of the ionomer was approximately 53 μm, and no significant oxygen-transport resistance at the gas interface for films thicker than 50 nm has been observed in the literature [393]. Moreover, for such materials, the exact value of the dissolution rate constant is yet to be determined. The Dirichlet boundary condition $c = c_{b,O_2}$ at the medium-surroundings interface ($\Gamma_3$) was, therefore, used. The reference electrode used in the experiments at the interface $\Gamma_3$ was a platinum mesh with 150-μm openings and 75-μm-thick wires (see Figure 3.1b). In analytical models, it is assumed that the interface $\Gamma_3$ directly opposite to the working electrode is infinitely far from it and is at equilibrium [397, 399, 400]. The same equilibrium assumption was used in the finite-domain numerical approach for the axisymmetric simplification.

Because the surface of the working electrode was rough, its effective area, $\pi r_{\text{eff}}^2$, differed from the geometric area, $\pi r_{\text{geo}}^2$. The effective electrode radius, $r_{\text{eff}}$, was estimated from the electrochemically active surface area (ECSA) of the electrode measured with cyclic voltammetry: $\pi r_{\text{eff}}^2 = \text{ECSA}$. An increase in $r_{\text{eff}}$ was observed from 4.7 μm at 70% RH to about 7.0 μm at 98% RH. This was attributed to the expansion of the ionically conductive domains in the ionomer, similar to what has been reported for PFSA-based electrolytes, such as Nafion® [116]. Four different computational meshes were generated for the selected experimental operating conditions to account for the changes in the effective electrode radius with RH.

Current was computed in the model by integrating the oxygen flux over the ionomer-electrode interface:

$$I = n_e F \int_{\Omega_1} D_{b,O_2} \nabla c \cdot \boldsymbol{n} \; d\Omega, \tag{3.7}$$

where $n_e = 4$ is the number of electrons transferred in the electrochemical reaction, $F$ is Faraday's constant, and $\Omega_1$ is the electrode area. Negative current was assumed for a reduction reaction.

## 3.2.2 Kinetics-Controlled Model

When the cell is operated in the diffusion-limited regime, the current response is independent of the applied potential. However, this is not generally the case, and, to capture the effect of the operating voltage, the mathematical model given by equations (3.2)–(3.6) was modified to include electrochemical kinetics. This was done by replacing the boundary condition (3.4) with

$$
\boldsymbol{N}_{O_2} \cdot \boldsymbol{n} = -\frac{i(c^{i|e}, \eta)}{4F}, \quad \boldsymbol{x} \in \Gamma_1, \quad t > 0, \tag{3.8}
$$

where $\boldsymbol{N}_{O_2} \cdot \boldsymbol{n} = -D_{b,O_2} \nabla c \cdot \boldsymbol{n}$ is oxygen flux, $i$ is current density (current $I$ normalized by the effective electrode area) that depends on the species concentration $c^{i|e} = c|_{\Gamma_1}$ at the ionomer-electrode interface, $\Gamma_1$, and the applied potential difference, $\eta$. Since a kinetic model for the alkaline ORR (3.1) is not available in OpenFCST, the double-trap kinetic model [270, 311] for ORR on platinum covered with PFSA-based electrolytes was used as an approximation for computing the faradaic current.

## 3.2.3 Solution Approach and Model Inputs

The numerical model (3.2)–(3.6) was brought to a dimensionless form by introducing variables $\widetilde{c} = c/c_{b,O_2}$, $\widetilde{t} = t/T$, $\widetilde{\nabla} = \nabla L$, $\widetilde{D}_{b,O_2} = D_{b,O_2} T/L^2$, $\widetilde{\boldsymbol{x}} = \boldsymbol{x}/L$ ($T$ is the total simulation time and $L$ is the membrane thickness):

$$
\frac{\partial \widetilde{c}}{\partial \widetilde{t}} - \widetilde{\nabla} \cdot \left( \widetilde{D}_{b,O_2} \widetilde{\nabla} \widetilde{c} \right) = 0, \quad \widetilde{\boldsymbol{x}} \in \widetilde{\Omega}, \quad \widetilde{t} > 0, \tag{3.9}
$$

$$
\widetilde{c} = 1, \quad \widetilde{\boldsymbol{x}} \in \widetilde{\Omega}, \quad \widetilde{t} = 0, \tag{3.10}
$$

$$
\widetilde{c} = 0, \quad \widetilde{\boldsymbol{x}} \in \widetilde{\Gamma}_1, \quad \widetilde{t} > 0, \tag{3.11}
$$

$$
-\left( \widetilde{D}_{b,O_2} \widetilde{\nabla} \widetilde{c} \right) \cdot \boldsymbol{n} = 0, \quad \widetilde{\boldsymbol{x}} \in \widetilde{\Gamma}_2, \quad \widetilde{t} > 0, \tag{3.12}
$$

$$
\widetilde{c} = 1, \quad \widetilde{\boldsymbol{x}} \in \widetilde{\Gamma}_3, \quad \widetilde{t} > 0. \tag{3.13}
$$

The kinetics-controlled boundary condition (3.8) was transformed into

$$
\widetilde{D}_{b,O_2} \widetilde{\nabla} \widetilde{c} \cdot \boldsymbol{n} = \frac{i(c^{i|e}, \eta)}{n_e F} \frac{T}{L c_{b,O_2}}, \quad \widetilde{\boldsymbol{x}} \in \widetilde{\Gamma}_1, \quad \widetilde{t} > 0. \tag{3.14}
$$

The dimensionless model was discretized in space using the finite-element method with second-order Lagrange shape functions. Computational meshes, similar to the one shown in Figure 3.3, were generated with the open-source pre- and post-processing platform for numerical simulations SALOME [554, 555]. The meshes were made sufficiently long in the radial (horizontal) direction so that the right-hand symmetric boundary would not affect the solution for the simulated time duration of 5 s. An automated adaptive mesh-refinement algorithm based on the Kelly error estimator (equation (2.149)) was incorporated in the model through the deal.II library [380–382] to adaptively refine the mesh as the transient simulation proceeded. Adaptive local refinement of 10% of the cells with the largest error and coarsening of 1% of the cells with the smallest error was performed a given number of times, $n_{\mathrm{ref}}$, at each tenth time layer.

The optimal initial mesh density and the number of the refinement cycles, found by comparing the simulated current between the refinement levels, are shown in Table 3.1, where $\alpha$ represents the maximum point-wise relative difference between the simulated current at the given and the next global-refinement levels. Solubility and diffusivity used for these tests were estimated based on their analytical fits. Depending on the model inputs and the refinement level, each simulation took 3–10 minutes on an Intel® Xeon® E5-2690 v2 CPU at 3.00 GHz. Due to the large number of simulations performed for fitting solubility and diffusivity in each of the RH cases (400, as discussed later) and because of 10–600 times longer computational time at the higher refinement levels (global or adaptive), the achieved numerical precision was deemed reasonable.

The diffusion-limited model (3.9)–(3.13) was linear, and no problem linearization was required. The kinetics-controlled model was nonlinear due to the dependency of the current density in the boundary condition (3.14) on oxygen concentration. This nonlinear problem was linearized with the Picard's method (Section 2.2.2.1) using the absolute and relative solution-error tolerances of $10^{-9}$ and $10^{-7}$ (in Euclidean norm),

Table 3.1: Details of the mesh-refinement study: size and refinement level of the computational domain, tested solubility and diffusivity.

| RH, % | $r_{\text{eff}}$, μm | Domain size μm×μm | DoFs (coarse mesh) | $n_{\text{ref}}$ | $(c_{\text{b,O}_2}, D_{\text{b,O}_2})$, (mol/cm$^3$, cm$^2$/s) | $\alpha$, % |
|---|---|---|---|---|---|---|
| 70 | 4.688 | $4r_{\text{eff}} \times 5r_{\text{eff}}$ | 779 | 1 | $(10^{-5}, 10^{-8})$ | 4.94 |
| 80 | 4.766 | $53.0 \times 132.5$ | 1407 | 0 | $(3.5 \cdot 10^{-6}, 1.2 \cdot 10^{-7})$ | 2.61 |
| 90 | 5.625 | $53.0 \times 132.5$ | 1235 | 0 | $(1.7 \cdot 10^{-6}, 7.0 \cdot 10^{-7})$ | 2.76 |
| 98 | 6.952 | $53.0 \times 132.5$ | 1159 | 0 | $(10^{-6}, 2.0 \cdot 10^{-6})$ | 2.84 |

respectively, and the underrelaxation parameters $\alpha = 6$, $\gamma_{\text{min}} = 0.3$.

Temporal discretization was performed with the $\theta$-scheme method (Section 2.2.1.1), and the particular case of the Crank-Nicolson scheme was used. In order to capture the fast change in the solution at the beginning of the transient response, adaptive time-stepping based on Richardson extrapolation was used (Section 2.2.1.3). A value of $10^{-8}$ was used as the tolerance for the absolute solution error in the Euclidean norm while $10^{-5}$ was the tolerance for the relative solution error. The initial time-step size was chosen to be $10^{-12}$ s. A time-step study was performed to ensure that the chosen parameters of the temporal discretization did not introduce any significant numerical errors.

## 3.3 Analytical Models

A number of analytical models for diffusion toward disk electrodes have been derived in the literature. Several commonly known relationships for the diffusion-controlled current were analyzed in order to select one, both accurate and convenient to use, to fit chronoamperometric data.

In 1981, Aoki and Osteryoung [396] derived exact analytical short- and long-time expansions of the solution of the semi-infinite diffusion problem in cylindrical coordinates. In the original paper, a mistake was made in the long-term expansion, which was corrected by Shoup and Shabo in 1982 [397]. The corrected relations are as

follows [396–398]:

$$I(\tau) = -\frac{4n_{\mathrm{e}}FADc}{\pi r_0} \cdot$$
$$\begin{cases} 0.88623\tau^{-1/2} + 0.78540 + 0.0940\tau^{1/2} + \dots, & \tau = \frac{4Dt}{r_0^2} < 1, \\ 1 + 0.71835\tau^{-1/2} + 0.05626\tau^{-3/2} + \dots, & \tau > 1, \end{cases} \quad (3.15)$$

where $A = \pi r_0^2$ is the surface area of the electrode.

In practice, other known analytical relations are used that are approximations to Aoki and Osteryoung's expansions. They have also been derived under the assumption of semi-infinite diffusion. The following equation was obtained by Soos and Lingane in 1964 [395]:

$$I(t) = -\frac{n_{\mathrm{e}}F\pi r_0^2 c\sqrt{D}}{\sqrt{\pi t}} - 4nFcDr_0. \quad (3.16)$$

It is a modification of the original Cottrell equation from 1903 [394], given by the first term, with addition of the steady-state current. Equation (3.16) consists of the leading terms of both Aoki and Osteryoung's expansions (3.15). The steady-state component of equation (3.16) is the same as in the long-term expansion (3.15). Because the electrode-edge effect is only described by the second and subsequent terms in each expansion (3.15) [396], equation (3.16) cannot be expected to produce very accurate results.

A modification of the Soos-Lingane equation (3.16), given by

$$I(t) = -\frac{n_{\mathrm{e}}F\pi r_0^2 c\sqrt{D}}{\sqrt{\pi t}} - \pi nFcDr_0, \quad (3.17)$$

represents the first two terms in the short-time expansion (3.15). This modified version of the Soos-Lingane equation is commonly used in the literature [309, 385, 386, 388–391]. The reason for the popularity of equation (3.17) among the electrochemical community is its higher accuracy compared to equation (3.16) at small time scales of chronoamperometric experiments (normally several seconds) due to the inclusion of the edge effect. However, equation (3.17) is less accurate than equation (3.16) at longer time intervals, as it converges to a different steady-state current. For example,

134

equation (3.17) was used by Gunasekara et al. [389] to analyze chronoamperometric data measured for 20 s with a 50-μm disk electrode. In that case, the applicability limitation of the short-term expansion (3.15), $4Dt/r_0^2 < 1$, gives $D < 3.125 \cdot 10^{-7}$ cm$^2$/s. However, some of the diffusivity values fitted by Gunasekara et al. significantly exceeded this limitation, and thus the reported oxygen-transport properties might not have been accurate. This highlights the importance of using analytical models only within their applicability range.

In 1982, Shoup and Szabo derived their model as an all-time approximation to the first two terms in each expansion (3.15) [397]:

$$
\begin{aligned}
I(\tau) &= -4n_{\mathrm{e}}FDcr_0 f(\tau), \\
f(\tau) &= \left(0.7854 + 0.8862\tau^{-1/2} + 0.2146e^{-0.7823\tau^{-1/2}}\right),
\end{aligned}
\tag{3.18}
$$

where $\tau$ is the same as in equation (3.15). Equation (3.18) has been used to fit oxygen-transport properties of polymer electrolytes in a number of publications [325, 387, 391, 392, 556].

Yet another expression was derived by Rajendran and Sangaranarayanan in 1999 using the Laplace transform and the [5/4] Padé approximation [399]:

$$
\begin{aligned}
I(\tau) &= -4n_{\mathrm{e}}FDcr_0 f(\chi), \\
f(\chi) &= \frac{1 + 2.5929\chi + 3.9686\chi^2 + 4.51506\chi^3 + 3.47861\chi^4 + 1.34989\chi^5}{1 + 1.87459\chi + 2.62197\chi^2 + 2.57529\chi^3 + 1.52319\chi^4},
\end{aligned}
\tag{3.19}
$$

where $\chi = (4t)^{-1/2}$.

A more recent equation for the chronoamperometric current is that of Mahon and Oldham from 2004 [400]:

$$
\begin{aligned}
I(\vartheta) &= -n_{\mathrm{e}}\pi FcDr_0 f(\vartheta), \\
f(\vartheta) &= \begin{cases}
\frac{1}{\sqrt{\pi\vartheta}} + 1 + \sqrt{\frac{\vartheta}{4\pi}} - 0.12003\vartheta + 0.013273\vartheta^{3/2}, & \vartheta \leq 1.281, \\
\frac{4}{\pi} + \frac{8}{\sqrt{\pi^5\vartheta}} + 0.0089542\vartheta^{-3/2} - 0.00025664\vartheta^{-5/2} \\
\quad - 0.00022312\vartheta^{-7/2} + 0.000027628\vartheta^{-9/2}, & \vartheta \geq 1.281,
\end{cases}
\end{aligned}
\tag{3.20}
$$

where $\vartheta = \tau/4$.

## 3.4  Fitting Approach

Analytical fitting of oxygen diffusivity and solubility to the experimental chronoamperometric data was performed with nonlinear least-squares method. The effective electrode radii from Table 3.1 were used in the calculations. The normalized root-mean-square deviation (NRMSD) between the predicted and experimental current was used as the fitting residual:

$$
\text{NRMSD} = \frac{\sqrt{\sum_{i=1}^{m} \frac{(I_{\text{exp},i} - I_{\text{pred},i})^2}{m}}}{\max\left(I_{\text{exp}}\right) - \min\left(I_{\text{exp}}\right)}, \tag{3.21}
$$

where $m$ is the number of data points. The initial current transients were allowed to be truncated and shifted in time between $t = 0.10$ s and $t = 0.25$ s to eliminate the double-layer charging effects seen in Figure 3.2. The optimal oxygen-transport properties were, therefore, found through a combined fitting of four unknowns: oxygen solubility, diffusion coefficient, and truncation and shifting times ($t_{\text{trunc}}$ and $t_{\text{shift}}$).

The analytically fitted solubility and diffusivity were then used to construct search bounds for the numerical simulations. Twenty points were used in each direction, totaling in 400 simulations for each of the four experimental RH conditions. The same approach to time truncation and shifting was used as in the analytical case. For each pair ($c_{\text{b},O_2}$, $D_{\text{b},O_2}$), NRMSD from the experimental data was computed. The resulting contour plots of NRMSD were linearly interpolated onto a $77 \times 77$-point grid, and the point that corresponded to the smallest NRMSD was taken as the optimal fit. If necessary, simulations were repeated with narrowed search bounds to achieve a higher fitting resolution in the areas where the NRMSD was the smallest.

## 3.5  Results and Discussion

### 3.5.1  Comparison of the Analytical Models

The chronoamperometric current predicted with analytical relationships (3.16)–(3.19) was compared for a wide range of oxygen solubility and diffusivity, $\boldsymbol{c}_{\text{b},O_2} \times \boldsymbol{D}_{\text{b},O_2} =$

$[10^{-7}, 10^{-5}]$ mol/cm$^3 \times [10^{-9}, 10^{-5}]$ cm$^2$/s, with one hundred and one thousand points in the respective directions. The ranges were chosen to cover the typical $\boldsymbol{c}_{b,O_2}$ and $\boldsymbol{D}_{b,O_2}$ values reported in the literature for both acidic and alkaline membranes (see, for example, [309, 325, 388–392]). The radius of the electrode was assumed to be the same as the geometric radius of the electrode in the experimental setup used in this work, $5~\mu$m. The Mahon-Oldham equation (3.20), containing a relatively large number of terms in the short-term and long-term expansions, was chosen as a reference for the comparison of equations (3.16)–(3.18) and (3.19). The relative difference between the computed current transients was evaluated with the NRMSD (3.21), where the Mahon-Oldham current was used instead of the experimental data. Since analytical models (3.16)–(3.19) predict infinitely large current at $t = 0$, the time interval of the comparison was limited to $[0.01, 5]$ s, where one thousand time instants were evaluated. The upper limit of the time interval matched the duration of the physical experiment considered in this work.

The resulting contour plots of the computed NRMSD are shown in Figure 3.4. It is clear that the difference between the analytical models is contributed to by diffusivity and not solubility, as the isolines in the contour plots are horizontal. The relative error of each model increased with diffusivity. The largest error of up to about 35% was observed with the modified Soos-Lingane equation (3.17), as it is limited by the condition $\tau < 1$ of the short-term expansion in equation (3.15). Practical application of that equation is, therefore, limited to diffusivity of less than $10^{-7}$ cm$^2$/s. The second-largest error of up to about 2.5% was obtained with the original Soos-Lingane equation (3.16), likely because it does not account for the electrode-edge effect. The Shoup-Szabo (3.18) and Rajendran-Sangaranarayanan (3.19) equations had the smallest deviation of about 0.16% and 0.013%, respectively.

The above results indicate that the Shoup-Szabo equation (3.18) is optimal for analyzing chronoamperometric data. It is nearly as accurate as the Mahon-Oldham (3.20) and Rajendran-Sangaranarayanan equations (3.19) while being more compact. There-
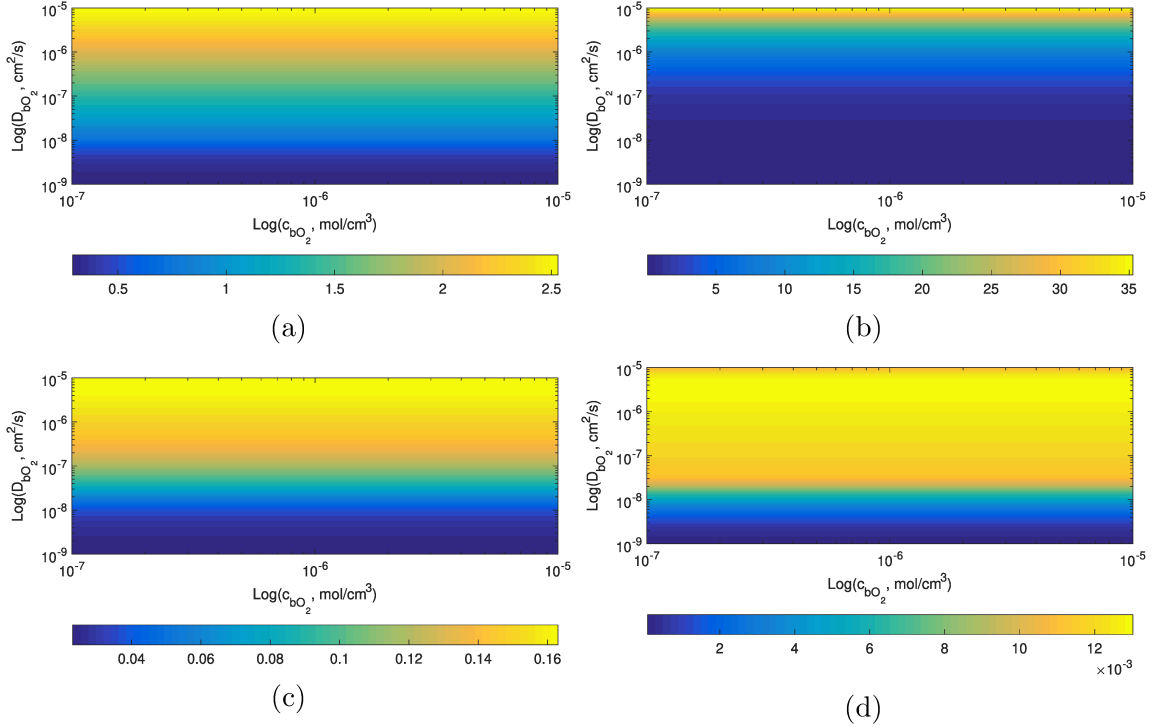
Figure 3.4: Contour plots of the % NRMSD (3.21) in the predicted current response with respect to the Mahon-Oldham model (3.20) for the following equations: a) Soos-Lingane (3.16); b) modified Soos-Lingane (3.17); c) Shoup-Szabo (3.18); d) Rajendran-Sangaranarayanan (3.19).

fore, numerical simulations were compared in this work with the predictions of the Shoup-Szabo equation (3.18).

## 3.5.2 Validation of the Numerical Model

In order to validate the transient framework developed in Chapter 2 and, in particular, the solid-state-cell model (3.9)–(3.13), a test case of one-dimensional diffusion in cylindrical coordinates was considered. Since OpenFCST does not currently support 1D models, a unit-square domain was used in the numerical model. The test model was similar to that given in equations (3.9)–(3.13) and in Figure 3.3, except the electrode-surface boundary, $\Gamma_1$, was assumed to stretch the whole bottom side of the domain ($z = 0$).

Because the initial and boundary conditions (3.10) and (3.11) are inconsistent, the

138

solution of the test problem (and of the original problem) is discontinuous around $t = 0$. It is, however, possible to obtain an analytical solution for the 1D diffusion problem at hand as the following infinite series [557]:

$$\widetilde{c}(\widetilde{z}, \widetilde{t}) = \widetilde{z} + 2 \sum_{n=1}^{\infty} \sin(n\pi\widetilde{z}) \exp\left(-\widetilde{D}_{b,O_2}(n\pi)^2\widetilde{t}\right) \frac{1 + (-1)^n - \cos(n\pi)}{n\pi}. \qquad (3.22)$$

Since the diffusion-limited current (3.7) at the electrode surface ($z = 0$) was of primary interest in this Chapter, numerical predictions were also compared with the analytical oxygen flux through the electrode surface:

$$\int_0^{2\pi} \int_0^1 \widetilde{\boldsymbol{N}}_{O_2} \cdot \boldsymbol{n}\widetilde{r} \, d\widetilde{r} \, d\theta = \pi\widetilde{D}_{b,O_2} \left.\frac{\partial \widetilde{c}(\widetilde{z}, \widetilde{t})}{\partial \widetilde{z}}\right|_{\widetilde{z}=0}, \qquad (3.23)$$

where the concentration derivative was obtained by differentiating equation (3.22):

$$\left.\frac{\partial \widetilde{c}(\widetilde{z}, \widetilde{t})}{\partial \widetilde{z}}\right|_{\widetilde{z}=0} = 1 + 2 \sum_{n=1}^{\infty} \exp\left(-\widetilde{D}_{b,O_2}(n\pi)^2\widetilde{t}\right) \left(1 + (-1)^n - \cos(n\pi)\right). \qquad (3.24)$$

It took 15 and 953 terms for the series (3.22) and (3.24) to converge with the relative error of $10^{-10}\%$ for the tested diffusivity $D_{b,O_2} = 3.6 \cdot 10^{-6}$ cm$^2$/s and solubility $c_{b,O_2} = 1.4 \cdot 10^{-7}$ mol/cm$^3$.

The unit square was meshed with 25 equally sized cells, 5 in each direction. Second-order Lagrange shape functions were used for the discretization, which resulted in 121 computational nodes. The Crank-Nicolson method was used for the temporal discretization.

Dimensionless analytical and numerical concentration distributions in the $\widetilde{z}$ direction are compared in Figure 3.5. In this case, the original mesh was not refined and a time-step size of 1 ms was used. A good agreement was achieved. It took about 248 s for both analytical and numerical solutions to converge to the steady state where the flux (3.23) stopped changing in the fifth significant digit.

Numerical simulations were conducted with the constant time-step sizes of 1 s, 0.1 s, 10 ms, and 1 ms, and the predicted oxygen-concentration distributions in the $\widetilde{z}$ direction were compared with the analytical solution (3.22). The absolute and relative
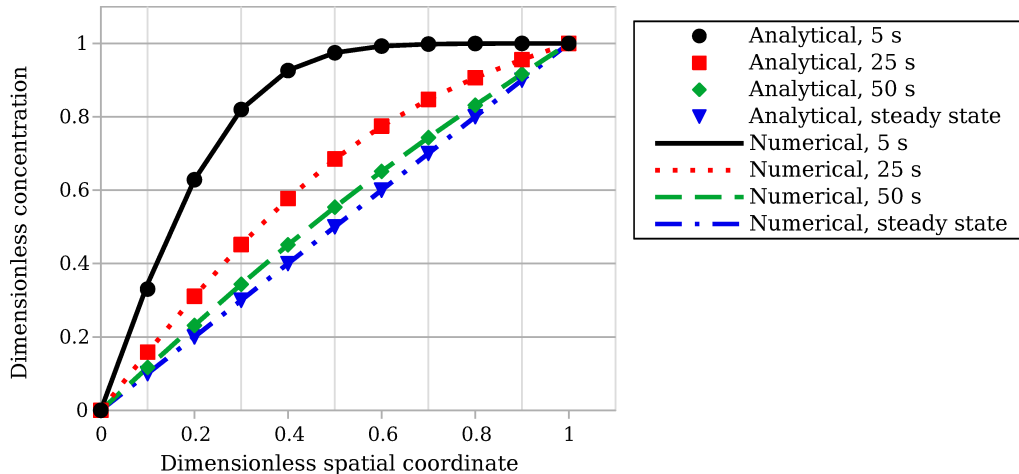
Figure 3.5: Comparison of the analytical and numerical concentration distributions in the 1D test case. The time-step size was 1 ms in the numerical model. No mesh refinement was performed.

errors of the numerical model, computed with respect to the analytical concentration distributions, are plotted in Figure 3.6 for $t = 5$ s, $t = 25$ s, and $t = 50$ s. As evident from the figure, the numerically computed distribution at $t = 5$ s was not accurate for any of the time-step sizes used. This was because of the solution discontinuity at $t = 0$ caused by the inconsistent initial and boundary conditions. For such problems, the Crank-Nicolson method, usually absolutely stable [503, 505], is known to produce solution oscillations that are damped with time as the solution moves away from the initial discontinuity [558] and to suffer from order reduction [559]. Indeed, error damping is observed in Figure 3.6, where the absolute and relative differences from the analytical solution decrease between $t = 5$ s and $t = 25$ s and between $t = 25$ s and $t = 50$ s for all time-step sizes. As the time-step size decreased from 1 s to 0.1 s, the error at $t = 25$ s and $t = 50$ s reduced by a factor of about 10, indicating linear convergence (Figures 3.6a, 3.6b and 3.6c, 3.6d). The convergence became sublinear between the time-step sizes of 0.1 s and 10 ms (the error decreased by less than 10 times, as seen in Figures 3.6c, 3.6d and 3.6e, 3.6f) and was lost when the time-step size was further reduced (the errors are similar in Figures 3.6e, 3.6f and 3.6g, 3.6h). When the mesh was globally refined once or twice, the linear convergence was also observed
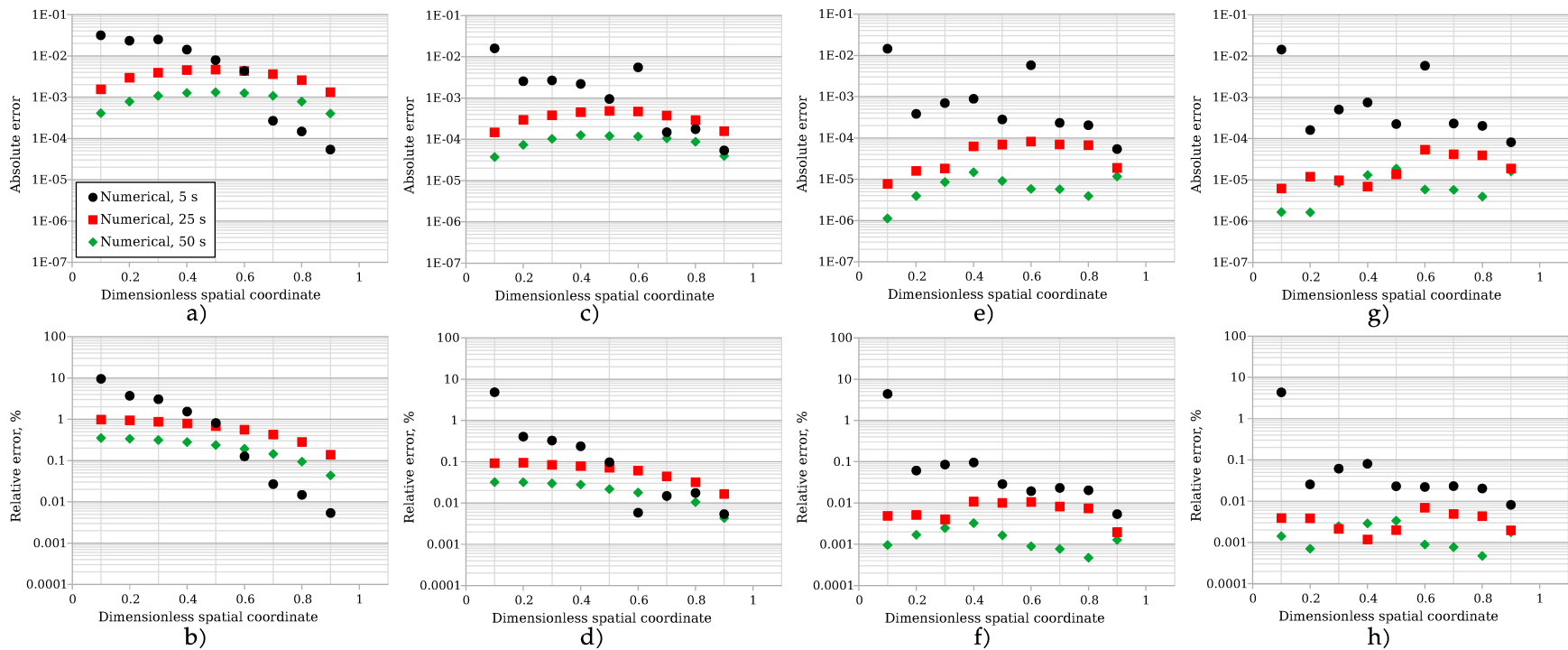
Figure 3.6: Absolute and relative errors of the numerical solution evaluated at $t = 5$ s, $t = 25$ s, and $t = 50$ s with the time-step sizes of: a), b) 1 s; c), d) 0.1 s; e), f) 10 ms; g), h) 1 ms. No mesh refinement was used

between the time-step sizes of 0.1 s and 10 ms, and a further sublinear error reduction was observed with the step size of 1 ms (not shown). Several modifications of the Crank-Nicolson method for reducing solution oscillations and recovering quadratic convergence have been proposed in the literature [558, 559]. However, they were not in the scope of this thesis and, thus, were not considered.

Since order reduction was observed for the Crank-Nicolson method, the test in Figure 3.6 was repeated with the implicit and explicit Euler methods (coefficients $\theta = 1$ and $\theta = 0$ in the $\theta$-scheme, respectively). As expected [503, 505], linear convergence was observed with both methods, although the explicit method diverged when the time-step size of 1 s was used (convergence was restored with $\tau = 0.1$ s; not shown).

So far, the numerical error in concentration distributions was quantified. Because the accuracy of the chronoamperometric simulations is determined by how well the model can predict the oxygen flux at the electrode surface, the numerical error with respect to the flux (3.23) was quantified next. Two additional time-stepping strategies with Richardson extrapolation were considered for the Crank-Nicolson method in this test. In the first Richardson strategy, labeled "Richardson 1", absolute and relative solution-error tolerances were the same as those used for the original problem (3.9)–(3.13): $10^{-8}$ and $10^{-5}$, respectively. Ten times stricter tolerances were used in the second strategy ("Richardson 2"). The initial time-step size was $10^{-12}$ s in both cases.

The numerically and analytically computed fluxes are compared in Figure 3.7. At the lowest refinement level (Figure 3.7a), a significant error was observed at the start of all numerical simulations (up to about 100% at 5 ms). The error reduced to below 0.5% by $t = 50$ s for all time-stepping strategies (constant or adaptive). As the mesh was refined once (Figure 3.7b) and twice (Figure 3.7c), the relative error in the predicted flux decreased to below 0.15% and 0.07% at $t = 50$ s, respectively. Initial flux oscillations were observed at the highest refinement level when the time-step size of 0.1 s was used (Figure 3.7c). As expected [558], the oscillations were damped in
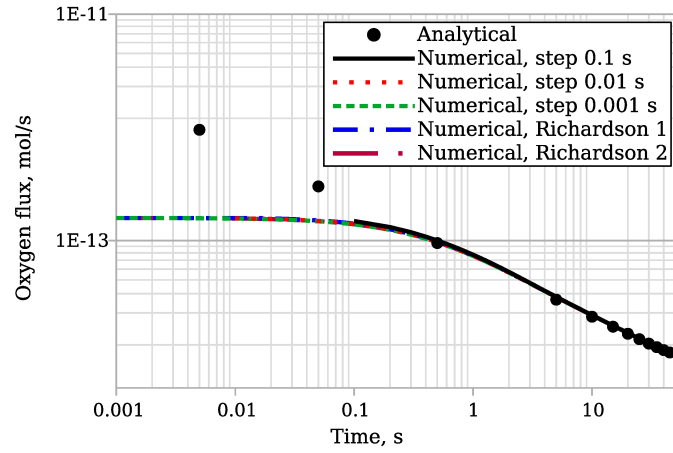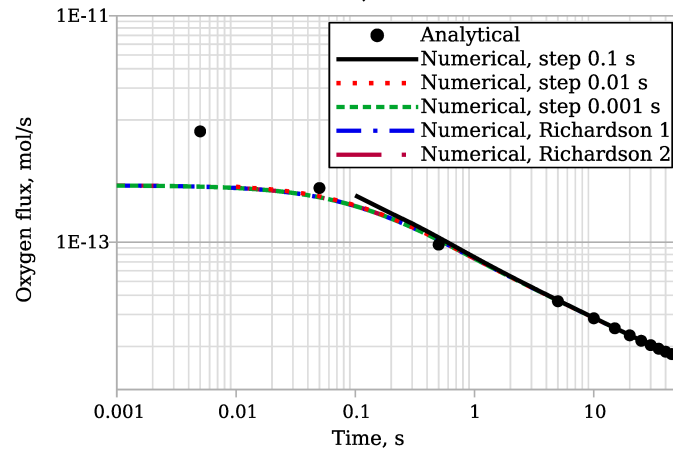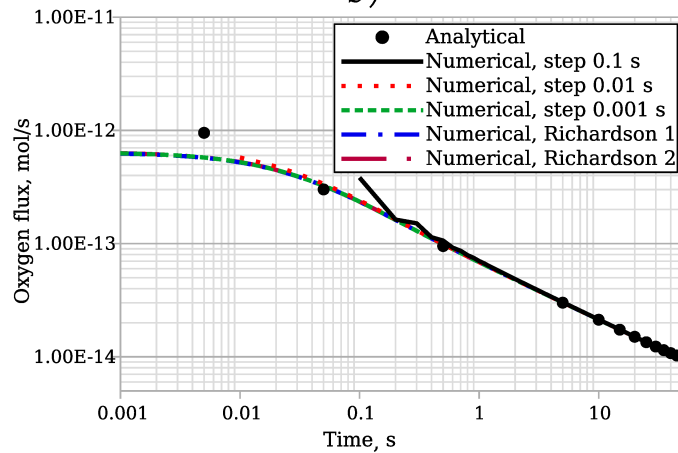
Figure 3.7: Comparison of the analytical and numerical fluxes at $z = 0$ in the 1D test case for various time-step sizes (labeled) and mesh-refinement levels: a), b) no refinement; c), d) one global refinement; e), f) two global refinements.

time and disappeared when the time-step size was reduced.

It can be seen from Figure 3.7 that the error in the simulated flux was significant during the initial transients. However, as discussed earlier in this Chapter, the experimental current was not analyzed for the time instants below 0.1–0.25 s. With the time-step size of 0.001 s or with the adaptive time-stepping, the relative flux error at the time interval 0.1–0.5 s was within 2–10% when the mesh was refined once or twice. By $t = 5$ s, the error reduced to under 1.6% and 0.4% for one and two mesh refinements, respectively.

### 3.5.3 Comparison of the Analytically and Numerically Fitted Oxygen-Transport Properties

The analytical fits of the experimentally measured chronoamperometric current with the Shoup-Szabo equation (3.18) are shown in Figure 3.8 (the time in the plots is shifted left by the fitted $t_{\text{shift}}$). Similar graphs were obtained with the numerical model. The resulting fitted solubility, diffusivity, and truncation and shifting times are listed in Table 3.2. The analytically fitted solubility and diffusivity reported in Table 3.2 correspond to the minimum fitting residual (3.21) of 0.53–0.73%, and the ranges given in parentheses represent the points with the residual of less than the experimental NRMSD (about 1%). The residual of the numerical fits was about 1% in all cases, and a unique optimum point was found at each RH. Contour plots of the NRMSD between the numerically computed and experimental current are shown in Figure 3.9 for the considered ranges of solubility and diffusivity at different RH values, where the best fits $(c_{\text{b,O}_2}, D_{\text{b,O}_2})$ with the smallest NRMSD are marked with red stars. The fitted solubility and diffusivity values were within the ranges $\boldsymbol{c}_{\text{b,O}_2} \times \boldsymbol{D}_{\text{b,O}_2} = [10^{-7}, 10^{-5}]$ mol/cm$^3 \times [10^{-9}, 10^{-5}]$ cm$^2$/s reported in the literature for alkaline and acidic membranes [309, 325, 388–392]; however, they cannot be compared directly due to the differences in the tested materials. With an increase in RH, oxygen diffusivity increased and solubility decreased, in agreement with the literature [116, 388, 391,
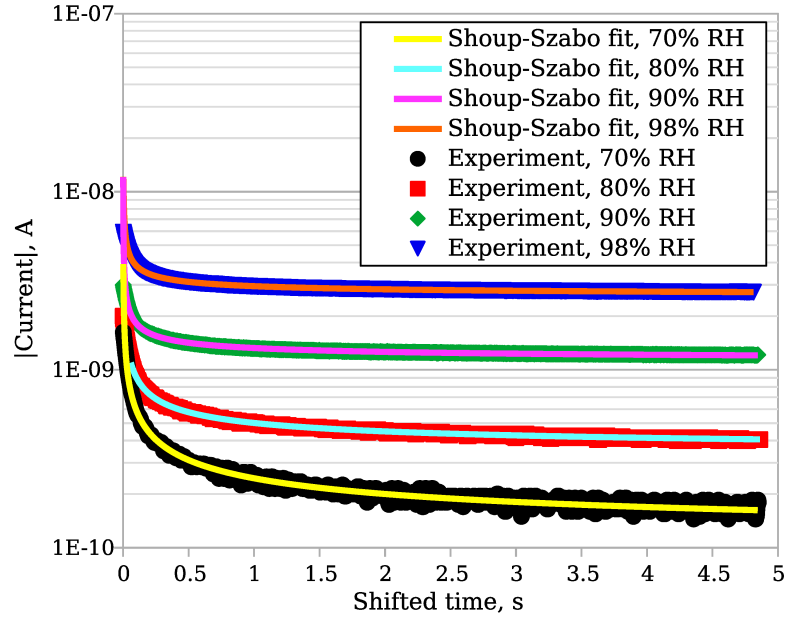
Figure 3.8: Experimental chronoamperometric current fitted with the Shoup-Szabo equation (3.18).

392]. These trends are commonly attributed to the changes in the water content and in the structure of the membrane with RH [116, 388, 391, 392].

The relative difference between the analytically and numerically fitted solubility and diffusivity is provided in Table 3.2. The smallest difference of 3.9–14.9% was observed at 70% and 80% RH. With a further increase in relative humidity, the discrepancy between the two models increased, reaching 26.4–28.5%. This was because the increase in diffusivity with RH led to the propagation of the diffusion front further into the membrane. The numerically computed dimensionless distributions of oxygen concentration along the axis of symmetry, $\widetilde{r} = 0$, at the time $t \approx 5$ s of the end of the physical experiment are shown in Figure 3.10. In order to estimate how significant the intake flux at the open boundary $\widetilde{z} = 1$ was compared to the oxygen consumption at the electrode ($\widetilde{z} = 0$), derivative $\partial \widetilde{c}(\widetilde{z}, \widetilde{t})/\partial \widetilde{z}$ was evaluated at $(\widetilde{r}, \widetilde{z}) = (0, 0)$ and $(\widetilde{r}, \widetilde{z}) = (0, 1)$. At 70% and 80% RH, the intake derivative at $\widetilde{z} = 1$ was only 0.01% and $3 \cdot 10^{-4}$% of the consumption derivative at $\widetilde{z} = 0$. Therefore, the rate of oxygen intake from the open boundary was negligible at those conditions compared

145

Table 3.2: Analytically and numerically fitted solubility, diffusivity, and truncation and shifting times. For the analytical fits, solubility and diffusivity ranges for which the fitting NRMSD was lower than the experimental error are indicated in parentheses. Relative difference between the analytical and numerical fits (computed with respect to the latter) is given below the numerically obtained values.

| Variable | Method | 70% RH | 80% RH | 90% RH | 98% RH |
|---|---|---|---|---|---|
| $c_{\mathrm{b,O_2}}$, $10^{-6}$ mol/cm$^3$ | Analytical | 8.63 (8.02–11.4) | 3.74 (3.15–4.58) | 1.16 (1.02–1.32) | 0.887 (0.809–0.975) |
| | Numerical | 7.95 (8.6%) | 3.60 (3.9%) | 1.59 (27.0%) | 1.24 (28.5%) |
| $D_{\mathrm{b,O_2}}$, $10^{-7}$ cm$^2$/s | Analytical | 0.158 (0.146–0.199) | 1.20 (0.993–1.41) | 11.0 (9.83–12.1) | 26.8 (24.7–28.4) |
| | Numerical | 0.185 (14.6%) | 1.41 (14.9%) | 8.70 (26.4%) | 21.1 (27.0%) |
| $t_{\mathrm{trunc}}$ s | Analytical | 0.165 (min. point) | 0.167 (min. point) | 0.187 (min. point) | 0.211 (min. point) |
| | Numerical | 0.165 (0%) | 0.162 (3.1%) | 0.165 (13.3%) | 0.179 (17.9%) |
| $t_{\mathrm{shift}}$ s | Analytical | 0.151 (min. point) | 0.140 (min. point) | 0.154 (min. point) | 0.182 (min. point) |
| | Numerical | 0.150 (0.67%) | 0.138 (1.4%) | 0.140 (10%) | 0.162 (12.3%) |
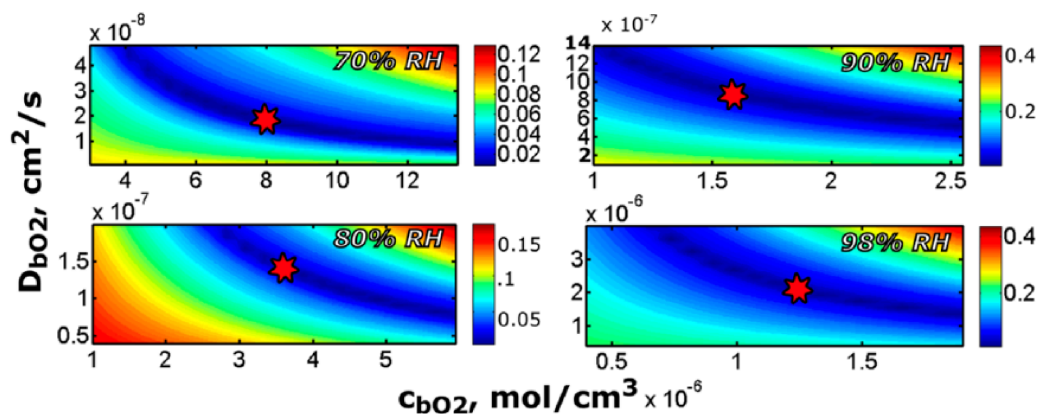


Figure 3.9: Contour plots of NRMSD between the simulated and experimental current. Solubility and diffusivity values that led to the smallest NRMSD are marked with red stars. Reprinted with permission from [1]. Copyright 2016 American Chemical Society.

146
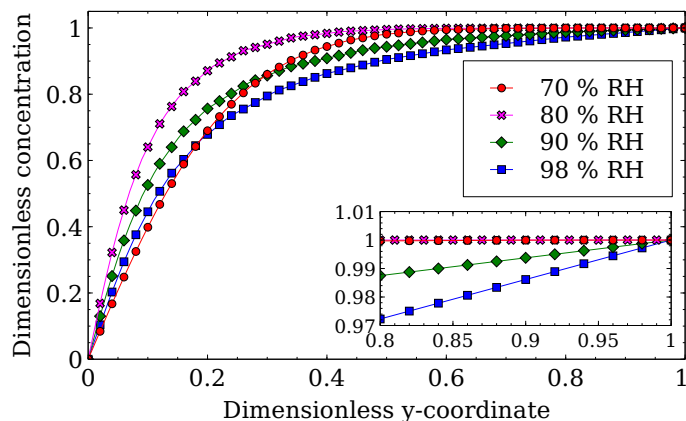
Figure 3.10: Dimensionless distribution of oxygen concentration along the axis of symmetry of the electrode, $\tilde{r} = 0$, at $t \approx 5$ s ($y = \tilde{z}$ in the figure). Reprinted with permission from [1]. Copyright 2016 American Chemical Society.

to the rate of oxygen consumption at the electrode. However, as RH increased to 90% and 98%, the contribution of the open boundary increased to about 1% and 3%, respectively. Because intake of oxygen from the surroundings is not accounted for in the analytical models due to the assumption of the semi-infinite sample size, the discrepancy between the numerically and analytically fitted oxygen-transport properties increased significantly when the diffusion front reached the open boundary at 90% and 98% RH.

It is important to note that the Shoup-Szabo equation (3.18) is claimed to be accurate to 0.6% [397] when the assumption of semi-infinite diffusion is not violated, i.e., when the diffusion length is sufficiently small compared to the thickness of the sample. Yet, the discrepancy between the analytical and numerical fits obtained in this work was 3.9–14.9% at 70% and 80% RH, when the open-boundary effect was negligible. Using a higher mesh-refinement level could have improved these results. However, as mentioned earlier in this Chapter, denser meshes led to the computational times that were not practical from the experimental perspective (several days or more for each operating condition), while the improvement in the simulated current between the mesh-refinement levels was minor (2–3%). It has been recognized in the literature that simulating diffusion-controlled current at a disk electrode is numerically

147

challenging [560]. Some of the mathematical approaches to solving the problem at hand that are required for improving both the accuracy and the computational time of the simulations can be found, for instance, in the works of Britz et al. [560, 561], although only semi-infinite diffusion was considered in those publications. Those approaches include conformal mapping of the computational domain, modification of the spatial-discretization method, and other techniques [560, 561]. As the diffusion model discussed in this Chapter was only a first step toward developing a PEMFC model in this thesis, specialized techniques for chronoamperometric simulations were not considered.

The significant increase in the discrepancy between the numerical and analytical fits with RH in Figure 3.2 is a good illustration for the applicability limitation of the analytical models. It is clear that estimation of gas-transport properties of thin polymer-electrolyte membranes, and especially of nanometer-scale films, should only be performed with numerical models, albeit attempts should be made to improve the accuracy and efficiency of the latter.

### 3.5.4 Effect of Reaction Kinetics

Numerical simulations were conducted with the modified boundary condition (3.8) that accounted for the oxygen-reduction kinetics in order to find out whether the developed model could predict the cell voltage at which diffusion-limited current was measured in experiments. The case of 80% RH was considered for these simulations. The computed current at several values of the applied potential difference, $\eta$, and the measured current are shown in Figure 3.11. The diffusion-limited case, where the boundary condition (3.4) was used, is also shown. Sensitivity of the simulated current output to the cell voltage decreased as $\eta$ was changed between -0.38 V and -0.55 V (with no significant difference obtained at -0.50 V and -0.55 V), indicating that the cell reached the potential-independent, diffusion-limited regime. The experimental data were an average between multiple data sets measured in the potential-difference
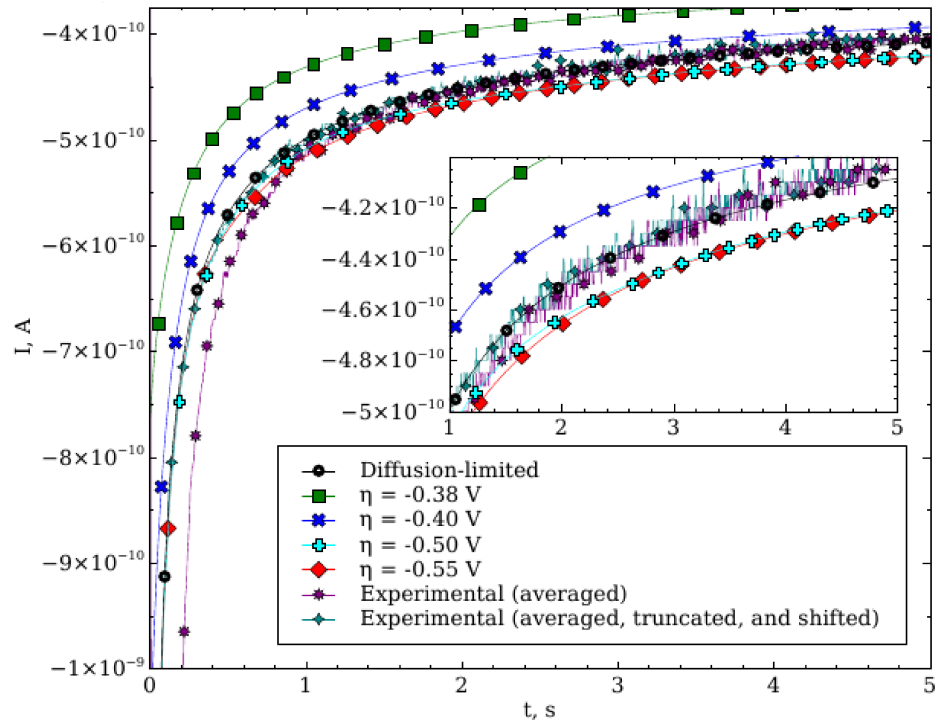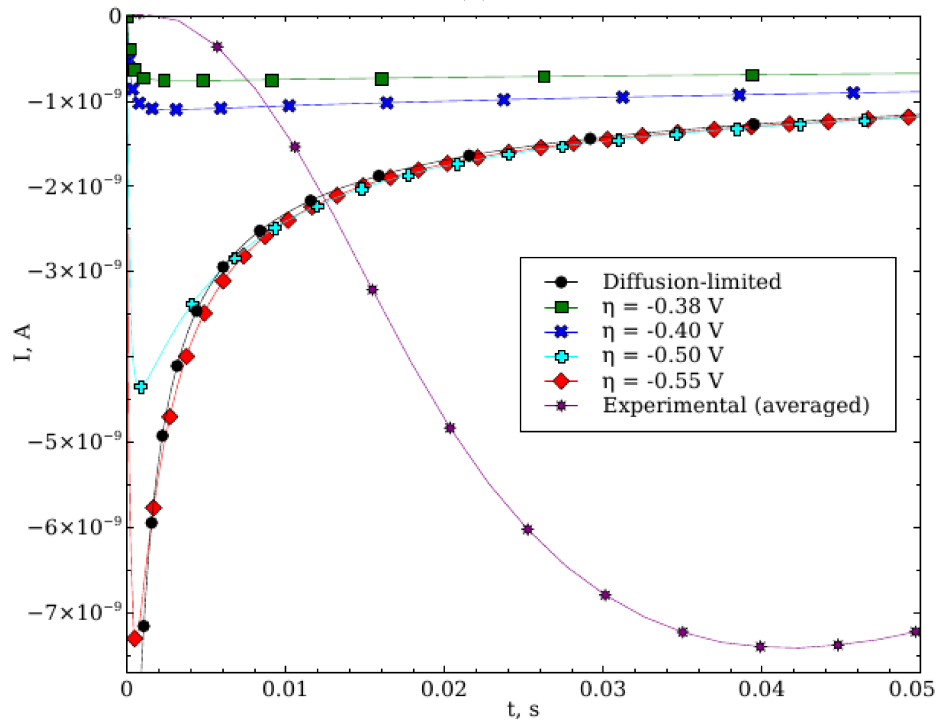
Figure 3.11: Simulated and experimental current for the 80% RH case from [1]: (a) the whole experiment duration of 5 s; (b) first 0.05 s (enlarged).

range between $\eta = -0.5$ V and $\eta = -0.4$ V and are matched well with the simulated current for those values of $\eta$, as seen in Figure 3.11a. These results demonstrate that the developed model is capable of predicting the potential range in which the chronoamperometric current is diffusion-limited.

The peak in the initial current transients was delayed in the experimental data due to the presence of the capacitive current (Figure 3.11b). Since the double-layer capacitance was not taken into account in the model considered in this Chapter, the simulated current peaks took place significantly earlier compared to the experimental data. Double-layer effects are taken into account in the PEMFC model developed in this thesis (see Chapter 2).

## 3.6    Conclusion

An open-source model for simulating chronoamperometry at disk electrodes was developed. The limitations of the analytical models commonly used in the electrochemical studies for estimating gas-transport properties in the polymer-electrolyte membranes were underlined and assessed by the means of numerical modeling. It was shown that, when the diffusion length exceeds the sample thickness, the analytical models discussed in this Chapter cannot provide reliable fits of the transport properties.

The developed model was extended to include an electrochemical reaction at the surface of the working electrode. The potential range predicted by the model as diffusion-limiting was in a good agreement with the experimental observations.

Computational cost of the developed model, however, needs to be reduced to make the time required to process the chronoamperometric data with numerical simulations acceptable for the quick and reliable estimation of gas-transport properties of polymer-electrolyte materials. Additionally, the finite-rate dissolution of oxygen into the membrane at the open surface opposite to the disk electrode should be taken into account in the numerical model for the higher reliability of the estimated transport properties.

# Chapter 4

# Analysis of Single-Phase Water-Management Signatures in Fuel-Cell Impedance Spectra[1]

Electrochemical impedance spectroscopy is a powerful technique used in fuel-cell diagnosis and characterization. A low-frequency inductive behavior may appear in the fuel-cell-impedance spectrum and is believed to be related to the electrolyte-hydration dynamics [159, 164, 191–197]. Since water management is crucial for achieving high performance, understanding the electrolyte-hydration-related signatures of the impedance spectrum may help better interpret experimental data and design future fuel cells. However, as discussed in Chapter 1, the effect of water transport in the electrolyte on the inductive behavior of PEMFCs has not been studied in detail in the literature [159, 164, 195, 196, 257].

In this Chapter, a single-phase version of the PEMFC model presented in Chapter 2 is used to analyze impedance spectra of proton-exchange-membrane fuel cells. Special care is taken to compare the model predictions to the transient polarization, ohmic-resistance, and impedance data measured in-house. The model reveals

---

[1]Parts of this chapter are reproduced from the following publication:

1. A. Kosakian, L. Padilla Urbina, A. Heaman, and M. Secanell, "Understanding single-phase water-management signatures in fuel-cell impedance spectra: A numerical study," *Electrochimica Acta*, vol. 350, p. 136 204, 2020.

Author contributions are detailed in the Preface of this thesis.

that the finite-rate exchange of water between the ionomer and the pores, commonly assumed instantaneous in the modeling literature [49, 159, 227, 228, 238–240, 243, 253, 255, 257, 258, 261, 280, 289, 345], plays an important role in the formation of the low-frequency inductive loops in the impedance spectra of PEMFCs. The influence of water transport in the membrane and in the ionomer phase of the catalyst layers on fuel-cell inductance is also investigated. The ohmic-resistance-breakdown study performed with the model demonstrates that the high-frequency resistance of a PEMFC comprises the ohmic resistance of the membrane and of the electronically conductive components of the cell, but does not include protonic resistance of the carbon-supported catalyst layers.

## 4.1 Mathematical Model

### 4.1.1 Governing Equations

The single-phase version of the PEMFC model described in Chapter 2 is used in this Chapter to elucidate and isolate the electrolyte-hydration effects in the impedance spectra. The model represents a two-dimensional, through-the-channel cross-section of a membrane-electrode assembly between parallel channels illustrated in Figure 4.1.

Governing equations used in the model describe: a) transport of gases in the porous media of the MEA; b) electron transport in the gas-diffusion layers (GDLs), microporous layers (MPLs), and catalyst layers; c) proton transport in the proton-exchange membrane (PEM) and the ionomer phase of the catalyst layers; d) transport of water absorbed in the PEM and the ionomer phase of the CLs; and e) thermal transport in all MEA components. The simplifying assumptions of the model can be found in Section 2.1. Governing equations (2.54)–(2.59) of the two-phase model are
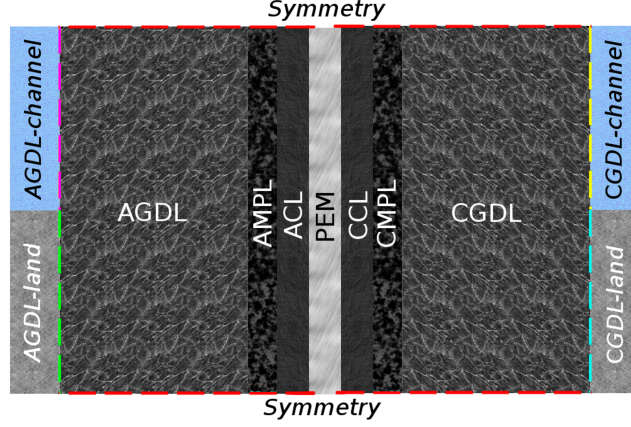
Figure 4.1: Computational domain of the model. Image not to scale.

adapted here for the single-phase case (zero liquid saturation):

$$\varepsilon_{\mathrm{p}} c_{\mathrm{tot}} \frac{\partial x_{\mathrm{O_2}}}{\partial t} - \nabla \cdot \left( c_{\mathrm{tot}} D_{\mathrm{O_2}}^{\mathrm{eff}} \nabla x_{\mathrm{O_2}} \right) = S_{\mathrm{O_2}}, \qquad (4.1)$$

$$\varepsilon_{\mathrm{p}} c_{\mathrm{tot}} \frac{\partial x_{\mathrm{wv}}}{\partial t} - \nabla \cdot \left( c_{\mathrm{tot}} D_{\mathrm{wv}}^{\mathrm{eff}} \nabla x_{\mathrm{wv}} \right) = S_{\mathrm{wv}}, \qquad (4.2)$$

$$-C_{\mathrm{dl}} \frac{\partial \left( \phi_{\mathrm{e^-}} - \phi_{\mathrm{H^+}} \right)}{\partial t} - \nabla \cdot \left( \sigma_{\mathrm{H^+}}^{\mathrm{eff}} \nabla \phi_{\mathrm{H^+}} \right) = S_{\mathrm{H^+}}, \qquad (4.3)$$

$$C_{\mathrm{dl}} \frac{\partial \left( \phi_{\mathrm{e^-}} - \phi_{\mathrm{H^+}} \right)}{\partial t} - \nabla \cdot \left( \sigma_{\mathrm{e^-}}^{\mathrm{eff}} \nabla \phi_{\mathrm{e^-}} \right) = S_{\mathrm{e^-}}, \qquad (4.4)$$

$$\varepsilon_{\mathrm{i}} \frac{\rho_{\mathrm{i,dry}}}{\mathrm{EW}} \frac{\partial \lambda}{\partial t} - \nabla \cdot \left( n_{\mathrm{d}} \frac{\sigma_{\mathrm{H^+}}^{\mathrm{eff}}}{F} \nabla \phi_{\mathrm{H^+}} + \frac{\rho_{\mathrm{i,dry}}}{\mathrm{EW}} D_{\lambda}^{\mathrm{eff}} \nabla \lambda + \frac{D_{\mathrm{T}}^{\mathrm{eff}}}{M_{\mathrm{H_2O}}} \nabla T \right) = S_{\lambda}, \qquad (4.5)$$

$$\sum_{i=\mathrm{phase}} \rho_i C_{p,i} \frac{\partial (\varepsilon_i T)}{\partial t} - \nabla \cdot \left( \kappa^{\mathrm{eff}} \nabla T \right) + \sum_{j=\mathrm{gas},\lambda} \left( \boldsymbol{N}_j \cdot \nabla \overline{H}_j \right) = S_{\mathrm{T}}. \qquad (4.6)$$

Source terms of equations (4.1)-(4.6) are listed in Table 4.1. They have been discussed in detail in Chapter 2.

## 4.1.2  Initial and Boundary Conditions

The initial solution was pre-computed by solving equations (4.1)-(4.6) at steady state, i.e., with all transient terms set to zero. This solution was then imported into the transient model as an initial solution at the start of the voltage-sweep and impedance-spectroscopy simulations.

Boundary conditions are listed in Table 4.2, where $V_{\mathrm{cell}}(t)$ is the time-dependent operating voltage and the values with the zero superscript are computed based on

Table 4.1: Source terms in the single-phase PEMFC model.

| Term | GDL & MPL | CCL | ACL | PEM |
|---|---|---|---|---|
| $S_{O_2}$ | $0$ | $-\dfrac{j}{4F}$ | $0$ | $0$ |
| $S_{wv}$ | $0$ | $(1-\xi)\dfrac{j}{2F} - \varepsilon_i k_\lambda \dfrac{\rho_{i,\,dry}}{EW}\left(\lambda_{eq}-\lambda\right)$ | $-\varepsilon_i k_\lambda \dfrac{\rho_{i,\,dry}}{EW}\left(\lambda_{eq}-\lambda\right)$ | $0$ |
| $S_{H^+}$ | $0$ | $-j$ | $j$ | $0$ |
| $S_{e^-}$ | $0$ | $j$ | $-j$ | $0$ |
| $S_\lambda$ | $0$ | $\varepsilon_i k_\lambda \dfrac{\rho_{i,\,dry}}{EW}\left(\lambda_{eq}-\lambda\right) + \xi\dfrac{j}{2F}$ | $\varepsilon_i k_\lambda \dfrac{\rho_{i,\,dry}}{EW}\left(\lambda_{eq}-\lambda\right)$ | $0$ |
| $S_T$ | $\sigma_{e^-}^{eff}\left(\nabla\phi_{e^-}\cdot\nabla\phi_{e^-}\right)$ | $\begin{aligned}&-j\eta + \dfrac{j}{2F}\left(-Tf_{ORR}\Delta\overline{S}_{overall} - (1-\xi)\overline{H}_{lv}\right)\\ &+\sigma_{e^-}^{eff}\left(\nabla\phi_{e^-}\cdot\nabla\phi_{e^-}\right)\\ &+\sigma_{H^+}^{eff}\left(\nabla\phi_{H^+}\cdot\nabla\phi_{H^+}\right)\\ &+\varepsilon_i k_\lambda \dfrac{\rho_{i,\,dry}}{EW}\left(\lambda_{eq}-\lambda\right)\overline{H}_{sorption}\end{aligned}$ | $\begin{aligned}&j\eta + \dfrac{j}{2F}\left(-T\left(1-f_{ORR}\right)\Delta\overline{S}_{overall}\right)\\ &+\sigma_{e^-}^{eff}\left(\nabla\phi_{e^-}\cdot\nabla\phi_{e^-}\right)\\ &+\sigma_{H^+}^{eff}\left(\nabla\phi_{H^+}\cdot\nabla\phi_{H^+}\right)\\ &+\varepsilon_i k_\lambda \dfrac{\rho_{i,\,dry}}{EW}\left(\lambda_{eq}-\lambda\right)\overline{H}_{sorption}\end{aligned}$ | $\sigma_{H^+}^{eff}\left(\nabla\phi_{H^+}\cdot\nabla\phi_{H^+}\right)$ |

Table 4.2: Boundary conditions in the single-phase PEMFC model.

| Solution variable | AGDL-channel | AGDL-land | CGDL-channel | CGDL-land | Symmetry |
|---|---|---|---|---|---|
| $x_{O_2}$ | no flux | no flux | $x_{O_2} = x_{O_2}^0$ | no flux | no flux |
| $x_{wv}$ | $x_{wv} = x_{wv,a}^0$ | no flux | $x_{wv} = x_{wv,c}^0$ | no flux | no flux |
| $\phi_{H^+}$ | no flux | no flux | no flux | no flux | no flux |
| $\phi_{e^-}$ | no flux | $\phi_{e^-} = 0$ | no flux | $\phi_{e^-} = V_{cell}(t)$ | no flux |
| $\lambda$ | no flux | no flux | no flux | no flux | no flux |
| $T$ | $\kappa^{eff}\nabla T \cdot \boldsymbol{n} = 0$ | $T = T^0$ | $\kappa^{eff}\nabla T \cdot \boldsymbol{n} = 0$ | $T = T^0$ | no flux |

the operating conditions as discussed in reference [262]. Gaseous species were not allowed to leave the domain through the GDL-land interfaces; similarly, no charge was allowed to leave the MEA through the GDL-channel boundaries. This, along with the symmetry conditions, was described by the no-flux boundary conditions.

## 4.1.3 Model Inputs

Some of the model inputs and relations used to compute various material and transport properties have been provided in Chapter 2. Model inputs specific to this Chapter are listed in Tables 4.3–4.7. The majority of the material properties came from the literature, independent in-house measurements, and the manufacturer data. The unknown properties were modified in this work to calibrate the model so that the predicted data were in agreement with the experiments. Those properties are discussed in this section with a special attention to the hydration-related characteristics that play a central role in the ability of the model to accurately predict the electrolyte-hydration dynamics and ohmic resistance of the cell.

All of the necessary property estimation was performed in the polarization-curve simulations. When estimating the hydration-related properties, the simulated ohmic resistance, corresponding to the membrane and the electronically conductive components, was compared with the HFR values from the EIS experiments at multiple oxygen-content values in the cathode and two humidity conditions as discussed later

in the validation section. In order to ensure the correct hydration time scale, the simulated resistance hysteresis was compared to that in the HFR and in the current-interrupt-based resistance. The known relations and values from the literature were used as baselines and modified as little as possible in the property estimation to avoid bias toward any particular property while maintaining good agreement with the experimental resistance dynamics.

Table 4.3: Operating conditions and geometrical properties.

| Property | Value | Details |
|---|---|---|
| **Operating conditions** | | |
| Temperature, K | 353.15 | |
| Pressure, atm | 1.5 | 50 kPa backpressure |
| RH | 0.3, 0.5, or 0.7 | |
| **Cell geometry** | | |
| Land width, μm | 827 | Measured (optical microscope) |
| Channel width, μm | 819 | Measured (optical microscope) |
| MEA area, cm$^2$ | 5 | Controlled (inkjet printing) |

#### 4.1.3.1 Absorbed-Water Diffusivity in the Electrolyte

**Catalyst Layers** The constant prefactor $\alpha_\lambda$ of the absorbed-water diffusivity $D_\lambda$ in catalyst layers (see Table 4.4 and Chapter 2) was treated as a fitting parameter using the value of $2.72 \cdot 10^{-5}$ cm$^2$/s [490] as the baseline. It was found that $\alpha_\lambda = 5.44 \cdot 10^{-5}$ cm$^2$/s provided a sufficient agreement between the simulated and experimental resistance data. The effect of the absorbed-water back-diffusion coefficient on the dynamic behavior of fuel cells is analyzed later in this Chapter.

**Membrane** As discussed in Chapter 2, an upscaled version of the electrolyte-water diffusion coefficient proposed by Motupally et al. [491] was used in the membrane (shown in Table 4.5). A constant scaling factor of 3.2 was introduced in order for the model predictions to match the experimental resistance data. Figure 4.2 shows

Table 4.4: Model inputs for the catalyst layers.

| Property | Value/expression | Details |
|---|---|---|
| **Geometry and structure** | | |
| Thickness, μm | 2.8 (anode), 4.5 (cathode) | Measured (SEM) |
| Platinum loading on support, wt% | 40 | Manufacturer |
| Platinum loading per unit area, mg/cm$^2$ | 0.1008 (anode), 0.1455 (cathode) | Controlled (inkjet printing) |
| Electrolyte loading, wt% | 30 | Controlled (ink preparation) |
| Porosity | $\varepsilon_{\mathrm{p}} = 0.47$ (anode), $\varepsilon_{\mathrm{p}} = 0.53$ (cathode) | Computed[a] |
| Solid-phase volume fraction | $\varepsilon_{\mathrm{s}} = 0.34$ (anode), $\varepsilon_{\mathrm{s}} = 0.30$ (cathode) | Computed[a] |
| Ionomer-phase volume fraction | $\varepsilon_{\mathrm{i}} = 0.19$ (anode), $\varepsilon_{\mathrm{i}} = 0.17$ (cathode) | Computed[a] |
| Active area, cm$^2_{\mathrm{Pt}}$/cm$^3_{\mathrm{CL}}$ | 212,000 | Measured (cyclic voltammetry) |
| Primary-particle radius, nm | $r_{\mathrm{p}} = 39.5$ | Manufacturer [563] |
| Support density (carbon black), g/cm$^3$ | 1.69 | [125] |
| Platinum density, g/cm$^3$ | 21.5 | [281] |
| Electrolyte density, g/cm$^3$ | 2 | [281] |
| Equivalent weight of the electrolyte, g/mol$_{\mathrm{SO}_3^-}$ | 1100 | [65, 262, 263] |
| **Gas transport** | | |
| Knudsen pore radius | $r_{\mathrm{K}} = r_{\mathrm{p}} \left(1.66\varepsilon_{\mathrm{p}}^{1.65} + 0.289\right)$ | Refs. [130, 131] |
| Effective gas diffusivity | $D^{\mathrm{eff}} = \begin{cases} D \left(\frac{\varepsilon_{\mathrm{p}}-0.05}{0.95}\right)^{1.9}, & \varepsilon_{\mathrm{p}} \geq 0.05 \\ 0, & 0 < \varepsilon_{\mathrm{p}} < 0.05 \end{cases}$ | Refs. [130, 131] |
| **Electrolyte hydration and absorbed-water transport** | | |
| Back-diffusion coefficient for absorbed water, cm$^2$/s | $D_\lambda = 5.44 \cdot 10^{-5} f_{\mathrm{V}} \frac{\partial \ln a_{\mathrm{w}}}{\partial \ln \lambda_{\mathrm{eq}}} \exp\left[\frac{20000}{R}\left(\frac{1}{303} - \frac{1}{T}\right)\right]$ | Refs. [489, 490], this work[b] |

Table 4.4: (Continued) Model inputs for the catalyst layers.

| Property | Value/expression | Details |
|---|---|---|
| Rate of water absorption/desorption by the electrolyte, 1/s | $k_\lambda = \frac{\alpha_{\text{abs/des}}}{L_{\text{CL}}} f_V \exp\left[\frac{20000}{R}\left(\frac{1}{303} - \frac{1}{T}\right)\right]$ where $\alpha_{\text{abs/des}} = \begin{cases} 4.59 \cdot 10^{-5} \text{ cm/s}, & \lambda < \lambda_{\text{eq}}, \\ 41.31 \cdot 10^{-5} \text{ cm/s}, & \lambda > \lambda_{\text{eq}} \end{cases}$ | Refs. [157, 490], this work[b] |
| Portion of ORR water produced in the electrolyte phase | $\xi = 0.03$ | This work[c] |
| **Charge transport** | | |
| Volumetric double-layer capacitance, F/cm$^3$ | 54 | Measured (cyclic voltammetry) |
| **Thermal transfer** | | |
| Effective volumetric heat capacity, J/(cm$^3 \cdot$ K) | $\sum_{i=\text{C, Pt, i}} \varepsilon_i \rho_i C_{p,i}$ | Computed[a] |
| Specific heat capacity of the carbon support, J/(g$\cdot$K) | $C_{p,\text{C}} = 0.875$ | Ref. [564] |
| Specific heat capacity of platinum, J/(g$\cdot$K) | $C_{p,\text{Pt}} = 0.13$ | Ref. [565] |
| Volumetric heat capacity of the electrolyte, kJ/(m$^3 \cdot$ K) | $\rho_i C_{p,i} = 1800$[d] | Refs. [152, 157, 238] |
| **ICCP sub-model inputs** | | |
| ICCP film thickness, nm | 6.4 | Computed[a] |
| ICCP oxygen-dissolution rate constant, m/s | $k_{\text{O}_2} = 7.4 \cdot 10^{-4}$ | This work[e] |
| ICCP hydrogen-dissolution rate constant, m/s | $k_{\text{H}_2} = 0.158$ | Ref. [328], this work[f] |

[a] Computed from catalyst and ionomer loading as discussed in Section 2.1.3.1.

[b] Adopted from the cited literature and modified for the simulated dynamic HFR response to match the in-house experimental data. See the details in the text.

[c] Estimated based on the simulated and experimental HFR dynamics. See the details in the text.

[d] Assumed constant value withing the range used in the modeling studies [152, 157, 238].

[e] Estimated based on the simulated and experimental limiting current density with 1% oxygen. See the details in the text.

[f] Originally reported as $k_{\text{H}_2} = 0.1$ m/s [328] and corrected in this work for the ionomer-film thickness in equation (2.9).

Table 4.5: Model inputs for the Nafion® NR-211 membrane.

| Property | Value/expression | Details |
|---|---|---|
| Thickness, μm | 25 | Manufacturer |
| Density, g/cm$^3$ | 2 | Refs. [65, 262, 263] |
| Equivalent weight, g/mol$_{SO_3^-}$ | 1100 | Refs. [65, 262, 263] |
| Back-diffusion coefficient for absorbed water, cm$^2$/s | $D_\lambda = 3.2 \cdot \begin{cases} 3.10 \cdot 10^{-3}\lambda\left(\exp(0.28\lambda) - 1\right)\exp\left[-\dfrac{2436}{T}\right], & 0 < \lambda \leq 3 \\ 4.17 \cdot 10^{-4}\lambda\left(161\exp(-\lambda) + 1\right)\exp\left[-\dfrac{2436}{T}\right], & \lambda > 3 \end{cases}$ | Ref. [491], this work[a] |
| Volumetric heat capacity, kJ/(m$^3 \cdot$ K) | 1800[b] | Refs. [152, 157, 238] |

[a] Adopted from the cited literature and modified for the simulated dynamic HFR response to match the in-house experimental data. See the details in the text.

[b] Assumed constant value withing the range used in other modeling studies [152, 157, 238].

Table 4.6: Model inputs for the gas-diffusion layers (SGL 29BC).

| Property | Value/expression | Details |
|---|---|---|
| Thickness, μm | 192 (uncompressed), 109 (compressed)[a] | Manufacturer [87], ref. [443], this work |
| PTFE loading, wt% | 5 | Manufacturer [87] |
| Porosity | 0.89 (uncompressed), 0.81 (compressed)[a] | Manufacturer [87], ref. [443], this work |
| Effective gas diffusivity (in-plane)[b] | $D^{\text{eff}} = \begin{cases} D\left(\dfrac{\varepsilon_{\text{p}} - 0.12}{0.88}\right)^2, & \varepsilon_{\text{p}} \geq 0.12 \\ 0, & 0 < \varepsilon_{\text{p}} < 0.12 \end{cases}$ | Refs. [79, 131] |

Table 4.6: (Continued) Model inputs for the gas-diffusion layers (SGL 29BC).

| Property | Value/expression | Details |
|---|---|---|
| Effective gas diffusivity (through-plane)[b] | $D^{\text{eff}} = \begin{cases} D \left( \frac{\varepsilon_{\text{p}} - 0.12}{0.88} \right)^{4.9}, & \varepsilon_{\text{p}} \geq 0.12 \\ 0, & 0 < \varepsilon_{\text{p}} < 0.12 \end{cases}$ | Refs. [79, 131] |
| Effective electron conductivity (in-plane), S/cm | 180[c] | Manufacturer [87] |
| Effective electron conductivity (through-plane), S/cm | 3.75[c] | Manufacturer [87] |
| Effective volumetric heat capacity, J/(cm$^3 \cdot$K) | $\sum\limits_{i=\text{C, PTFE}} \varepsilon_i \rho_i C_{p,i}$ | Computed[d] |
| Specific heat capacity of carbon, J/(g$\cdot$K) | $C_{p,\text{C}} = 0.875$ | Ref. [564] |
| Specific heat capacity of PTFE, J/(g$\cdot$K) | $C_{p,\text{PTFE}} = 1.3$ | Ref. [566] |

[a] Computed compressed values based on the SGL 29AA GDL data from the manufacturer [87] using the approach discussed in Section 2.1.3.1.
[b] Taken to match the in-plane diffusibility $D^{\text{eff}}/D$ of SGL 29BA GDL measured by Xu [79] and to account for the fact that the through-plane diffusibility of GDLs is typically half of that in the in-plane direction [131, 567].
[c] At 1 MPa of compression [87].
[d] Computed from the PTFE content as discussed in Section 2.1.3.1.

Table 4.7: Model inputs for the microporous layers (SGL 29BC).

| Property | Value/expression | Details |
|---|---|---|
| Thickness, μm | 37 | Ref. [443] |
| PTFE loading, wt% | 23 | Manufacturer [87] |
| Porosity | 0.58 | Measured (MIP)[a] |
| Knudsen pore radius, nm | 56 | Measured (MIP)[a] |

Table 4.7: (Continued) Model inputs for the microporous layers (SGL 29BC).

| Property | Value/expression | Details |
|---|---|---|
| Effective gas diffusivity | $D^{\text{eff}} = \begin{cases} D\left(\frac{\varepsilon_{\text{p}}-0.05}{0.95}\right)^{1.9}, & \varepsilon_{\text{p}} \geq 0.05 \\ 0, & 0 < \varepsilon_{\text{p}} < 0.05 \end{cases}$ | Refs. [130, 131][b] |
| Effective electron conductivity (in-plane), S/cm | 121[c] | Manufacturer [87], this work |
| Effective electron conductivity (through-plane), S/cm | 0.95[c] | Manufacturer [87], this work |
| Effective volumetric heat capacity, J/(cm$^3 \cdot$ K) | $\sum\limits_{i=\text{C, PTFE}} \varepsilon_i \rho_i C_{p,i}$ | Computed[d] |
| Specific heat capacity of carbon, J/(g$\cdot$ K) | $C_{p,\text{C}} = 0.875$ | Ref. [564] |
| Specific heat capacity of PTFE, J/(g$\cdot$ K) | $C_{p,\text{PTFE}} = 1.3$ | Ref. [566] |

[a] Based on the raw mercury-intrusion porosimetry (MIP) data from another publication from our laboratory [443]. Pore-size distribution (PSD) of the MPL was found by subtracting the PSD of SGL 29BA GDL samples from SGL 29BC GDL-MPL samples.

[b] Assumed same expression as in the stochastically reconstructed catalyst layers [130, 131] due to similar microstructure.

[c] Computed compressed values based on the SGL 29AA GDL and SGL 29BC GDL-MPL data from the manufacturer [87]. See the approach in Section 2.1.3.7. The artificial anisotropy of the MPL may be attributed to the composite sub-layer that exists at the GDL-MPL interface [92, 496], which is affected by the alignment of the GDL fibers in that region.

[d] Computed from the PTFE content as discussed in Section 2.1.3.1.

a comparison of the back-diffusion coefficients used in the membrane and the CL ionomer in this Chapter and those in the literature [490, 491, 562].

### 4.1.3.2 Kinetics of Water Absorption and Desorption by the Electrolyte

The absorption/desorption rates for the electrolyte water were calculated using equation (2.1.3.3). The baseline values of the absorption and desorption prefactors, $\alpha_{abs}$ and $\alpha_{des}$, were taken as $1.14 \cdot 10^{-5}$ cm/s and $4.59 \cdot 10^{-5}$ cm/s as reported by Goshtasbi et al. [157] with a reference to the experimental work of Ge et al. [490]. The values of $\alpha_{abs}$ and $\alpha_{des}$ estimated in this Chapter from the experimental resistance data were $4.59 \cdot 10^{-5}$ cm/s (about 4 times higher than in reference [157]) and $41.31 \cdot 10^{-5}$ cm/s (9 times higher), respectively.

The units of the absorption and desorption prefactors were not explicitly stated by Ge et al. [490]. A more thorough look at the equations used by Ge et al. [490] revealed later during the course of this thesis that the units of $\alpha_{abs}$ and $\alpha_{des}$ worked out to be meters per second, i.e., their values were 100 times higher than reported by Goshtasbi et al. [157]. As a result, the absorption and desorption rates used in this Chapter were about 25 and 11 times lower than measured by Ge et al. [490]. However, Ge et al. [490] assumed infinitely thin catalyst layers in their analysis, and thus the values they reported may not have been accurate. A parametric study on the ionomer-water-exchange rates is shown later in this Chapter.

### 4.1.3.3 Amount of Water Produced Electrochemically Directly in the Ionomer Phase

Since the catalyst surface is at least partially covered by the ionomer in the catalyst layers [21, 117, 140], it is reasonable to assume that some water may be produced at the catalyst surface under the ionomer film, into which it is then directly absorbed. The amount of water that may directly enter the ionomer has not been measured experimentally. The simulations exhibited high sensitivity, especially in the predicted ohmic resistance, to the amount of water set to be produced in the ionomer phase.
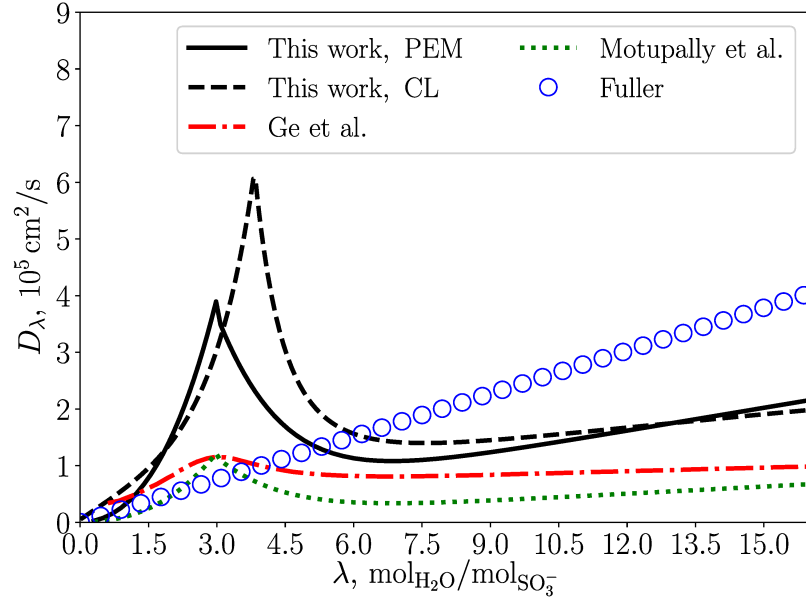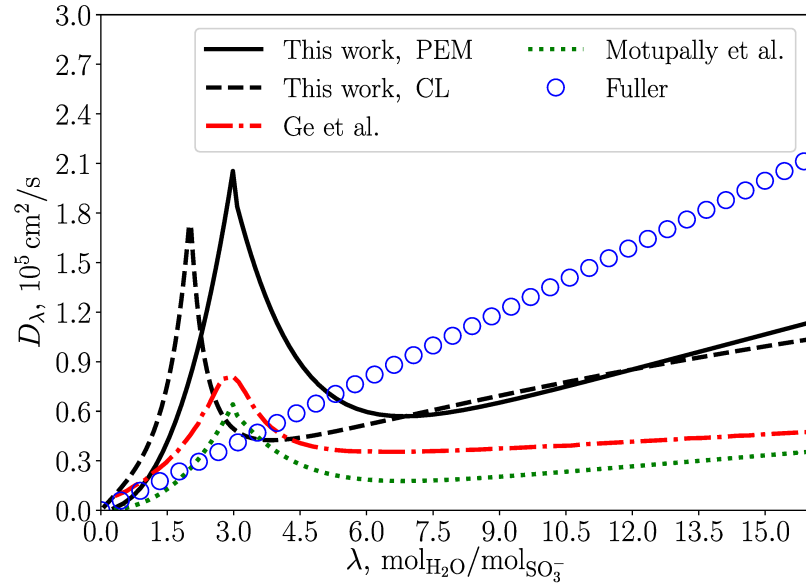
Figure 4.2: Comparison of the back-diffusion coefficients for water in the electrolyte used in this work to those by Ge et al. [490], Motupally et al. [491], and Fuller [562] at (a) 80 °C and (b) 50 °C. Bulk diffusivity is shown, and the effective back-diffusion coefficient was computed as $D_\lambda^{\text{eff}} = \varepsilon_{\text{i}}^{1.6} D_\lambda$ in the catalyst layers.

In this work, a good agreement with the experimental resistance data was achieved when 3% of water was assumed to be produced in the ionomer phase.

#### 4.1.3.4 Local Oxygen-Transport Resistance in Catalyst Layers

The experimental value for the oxygen-dissolution rate constant $k_{O_2}$ used in the ICCP model (Chapter 2) can be estimated by fitting the oxygen-transport resistance and limiting current density [125, 328]. Previously, Secanell et al. [328] found $k_{O_2}$ to be $10^{-3}$ m/s using a steady-state PEMFC model similar to what is described in this Chapter. In this work, the value of this rate coefficient was estimated by comparing the experimental and numerical limiting current density with 1% oxygen supply. The resulting value of $k_{O_2}$ was $7.4 \cdot 10^{-4}$ m/s.

### 4.1.4 Solution Approach

The model presented in this work was implemented in the in-house, open-source software for fuel cell modeling, OpenFCST [374, 375]. For the temporal discretization, implicit Euler method (BDF1) was used with a constant time step of 0.25 or 1 s in the polarization-curve simulations and with an automatic time-stepping based on Richardson extrapolation (Section 2.2.1.3) with a relative solution-error tolerance of $10^{-3}$ in the EIS simulations. Spatial discretization was performed using the finite-element method with second-order Lagrange shape functions and 16,350 degrees of freedom (2,725 computational nodes). The computational grid is shown in Figure 4.3. The nonlinear problem was linearized with Newton's method and a relative solution-error tolerance of $10^{-4}$ was used. Time-step-size and mesh-independence studies were performed to ensure the numerical accuracy of the solution.

Polarization-curve simulations were performed by applying 2 to 3 voltage sweeps at 0.44 mV/s (equivalent to the experimental voltage steps of 20 mV each 45 s). A computationally efficient EIS approach discussed in Section 2.3.1.2 was used to simulate impedance spectroscopy using a 1-mV voltage ramp over $10^{-9}$ s followed
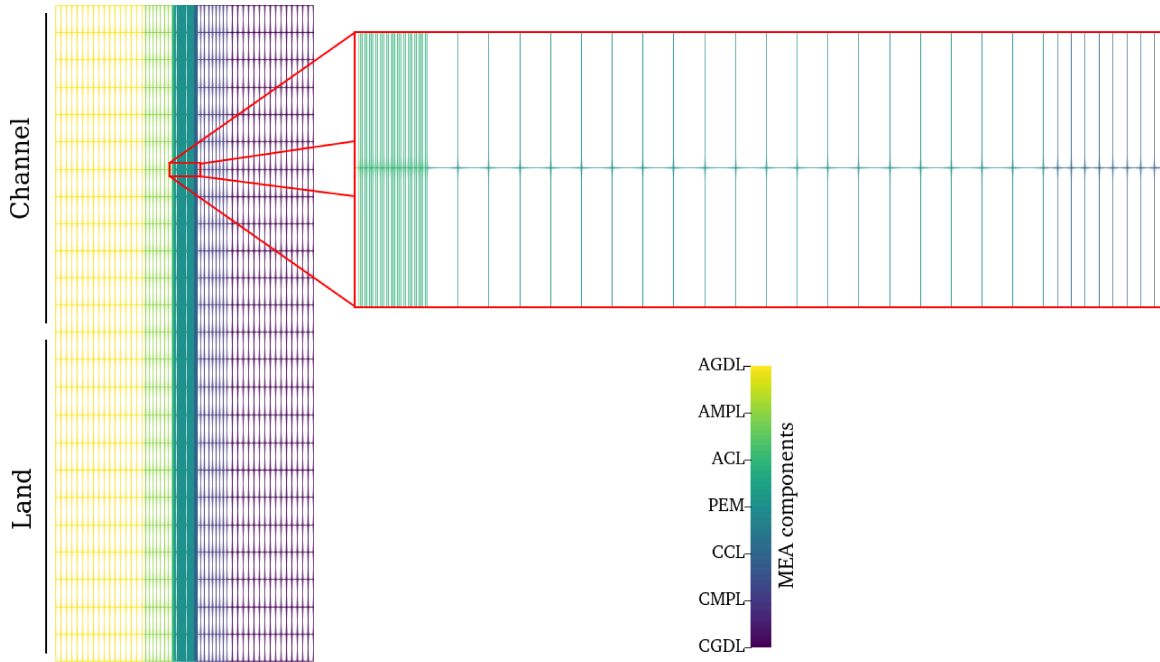
Figure 4.3: The computational grid used for the PEMFC model in this Chapter.

by $10^{10}$-s long voltage hold. Time-step size was gradually increased by 0.1% from $10^{-10}$ to $10^9$ s during the simulation. A non-equispaced Fourier transform suggested by Wiese and Weil [549] was performed on both voltage and current-density data, and the ratio of their Fourier transforms was computed to give impedance. Each spectrum, consisting of 2,000 logarithmically spaced frequencies between $10^{-6}$ and $10^6$ Hz, was extracted from a single simulation. This rapid-EIS approach is shown later in this Chapter to produce the same impedance spectrum as the conventional sine-wave approach, in which each spectrum is obtained frequency-by-frequency.

The simulation time varied between 8 and 27 hours for the polarization-curve simulations depending on the voltage range, time-step size, and the number of the performed sweeps. Each EIS simulation took 2 to 4 days. All simulations were performed in parallel using 4 threads of Intel® Xeon® E5-2690 v2 CPU at 3.00 GHz.

## 4.2 Experiment

### 4.2.1 Fuel-Cell Fabrication

The membrane-electrode assemblies were manufactured by inkjet-printing following the protocol described in references [124, 125, 149]. A mixture of 37.5 mg of 40 wt% Pt/C catalyst (HySa-K40 on Ketjenblack® EC300J, HyPlat), 37.3 ml of Nafion® ionomer solution (Liquion 5 wt% LQ-1105, Ion Power), 1.9 ml of 2-propanol (99.5%, Fisher Scientific), and 1.6 ml of propylene glycol (99.5%, Sigma-Aldrich) was prepared to obtain a catalyst ink with a 30 wt% Nafion® loading. The 5-cm$^2$ catalyst layers were directly deposited on a 25.4-$\mu$m thick Nafion® membrane (NR-211, Ion-Power) with a commercial piezoelectric inkjet printer (Fujifilm Dimatix DPM-2800). Catalyst loading was controlled by means of the number of the printed layers on the membrane. For the cathode side, a loading of 0.15 mg$_{Pt}$/cm$^2_{CL}$ was used. Once the CCL was printed, it was left to dry overnight before printing the ACL. The anode side had a catalyst loading of 0.10 mg$_{Pt}$/cm$^2_{CL}$. Each printed layer was inspected in an optical microscope to ensure there were no major cracks. Scanning-electron microscopy was also used to verify the uniformity of the catalyst-layer structure.

Catalyst-layer thickness was measured from the cross-sectional SEM images. The average thickness was 4.50 $\pm$ 0.19 $\mu$m for the cathode side and 2.81 $\pm$ 0.11 $\mu$m for the anode side. The catalyst-coated membrane (CCM) was sandwiched between two 5-cm$^2$ Sigracet® SGL 29BC carbon-paper layers (GDL and MPL) and two graphite bipolar plates with a parallel-channel configuration. Rigid, 150 $\mu$m-thick PTFE gaskets were used to control the diffusion-media thickness and to seal the cell to avoid gas leakage.

### 4.2.2 Electrochemical Characterization

A Scribner 850e test station and a Bio-Logic SP-300 potentiostat were used to carry out the electrochemical characterization of the cell. First, the cells were conditioned

at 80 °C with hydrogen and air at 80% RH for 16 one-hour-long steps from 0.1 to 5 A with 30-second OCV intervals between each step. Before each test, a preconditioning was performed at the given operating conditions by holding the cell voltage at 0.6 V for 30 min.

Electrochemical surface area (ECSA) was calculated by the means of cyclic voltammetry (CV) at 30 and 80 °C using fully humidified hydrogen and nitrogen as the anode and cathode gas supply, respectively. The hydrogen-adsorption and desorption peaks (between 0.05 and 0.4 V) resulted in an ECSA of $58.1 \pm 9.5$ $m^2_{Pt}/g_{Pt}$ based on the measurements of three cells. The double-layer capacitance baselines were computed from the non-faradaic process region of the CV (between 0.3 and 0.6 V) following the methodology in reference [568]. The measured double-layer capacitance value was $24.1 \pm 1.2$ $mF/cm^2$.

Polarization curves were obtained at 80 °C using hydrogen in the anode and 1, 10, 21, and 100% oxygen-in-nitrogen mixture in the cathode, with both streams humidified to 50 and 70% RH. The gas-flow rates were fixed at 0.2 and 1.0 slpm for hydrogen and oxygen, respectively, resulting in stoichiometry of 4.5–4.8 ($H_2$) and 0.4–48 ($O_2$) at 1 $A/cm^2$. In all tests, a backpressure of 50 kPa was applied and controlled by an automatic backpressure regulator (Scribner 850BP). The scans were performed with the Scribner test station in the potentiodynamic mode from OCV to 0.05–0.2 V in 20-mV steps every 45 s and verified with 0.44 mV/s scans with the Bio-Logic potentiostat. Current-interrupt-based resistance was measured during the experiments performed with the Scribner station.

The EIS tests were performed in the galvanodynamic mode by applying a sinusoidal perturbation with an amplitude of 3–4% of the current for a frequency range of 100 kHz–0.1 Hz with two measurements per frequency and the resolution of 10 points per decade. Each spectrum was measured thrice to ensure the data were self-consistent. The spectra were measured at 0.1, 0.4, 0.7, 1.0, and 1.4 $A/cm^2$ holding the desired current for 3–5 min before each test to let the cell stabilize and to

minimize voltage drift. After the data were gathered with increasing current between the tests, the experiments were repeated in the reversed order to ensure no significant polarization-hysteresis effect on the impedance spectra. The resulting six spectra per current density were averaged, and uncertainty analysis was performed. The impedance-spectrum and polarization-curve data were verified for consistency by comparing the measured voltage-current relationships.

Even though the lower-frequency limit of 0.1 Hz was not sufficient to observe the full inductive loop in the measured spectra, it was found to be reasonable in light of the increase in the measurement uncertainty with a decrease in the applied frequency. Extension to 10 and 1 mHz would increase the time required to obtain each averaged spectrum from about 9 minutes to about 1 and 11 hours, respectively, magnifying the voltage-drift effect over such long periods of time. This, in turn, would decrease the quality of the EIS measurements.

Linearity of the measured spectra was checked with the Kramers-Kronig test, which is also used as a test for stability and causality of the analyzed system [56, 569]. The Kramers-Kronig relations can reconstruct the real part of impedance from its imaginary part and vice versa [56, 569]:

$$\text{Re}(\hat{Z}(\omega)) = \lim_{\hat{\omega} \to \infty} \text{Re}(Z(\hat{\omega})) + \frac{2}{\pi} \int_0^\infty \frac{\hat{\omega} \, \text{Im}(Z(\hat{\omega}))}{\omega^2 - \hat{\omega}^2} d\hat{\omega}, \tag{4.7}$$

$$\text{Im}(\hat{Z}(\omega)) = -\frac{2}{\pi} \int_0^\infty \frac{\omega \, \text{Re}(Z(\hat{\omega}))}{\omega^2 - \hat{\omega}^2} d\hat{\omega}. \tag{4.8}$$

Residuals between the original and the reconstructed impedance were defined as [569]

$$\delta_{\text{Re}}(\omega) = \frac{|\text{Re}(\hat{Z}(\omega)) - \text{Re}(Z(\omega))|}{|\hat{Z}(\omega)|}, \tag{4.9}$$

$$\delta_{\text{Im}}(\omega) = \frac{|\text{Im}(\hat{Z}(\omega)) - \text{Im}(Z(\omega))|}{|\hat{Z}(\omega)|}. \tag{4.10}$$

Note that the Kramers-Kronig relations (4.7) and (4.8) require integration over frequencies ranging from 0 to $\infty$. The maximum relative difference between the original

and the reconstructed spectra was under 9%, which was considered sufficient given the constrained frequency range used in the experiments.

All measured spectra exhibited a high-frequency inductive behavior due to cables and were inductance-corrected. The high-frequency portion of each spectrum with positive imaginary impedance values was first fitted with an impedance of an inductor-resistor circuit using the Bio-Logic EC-Lab$^{\circledR}$ software. Then, impedance of an inductor with the fitted inductance of $11.6 \pm 0.3$ nH was computed for the whole frequency range and subtracted from the original data.

### 4.2.3 Effect of Oxygen Concentration and Stoichiometry on Fuel-Cell Impedance Spectra

Bipolar plates with a parallel-channel configuration were chosen so as to limit the number of the modeled dimensions to two by considering a cross-section of the cell instead of its full three-dimensional geometry [6]. Depending on the goals of the study, either along-the-channel or through-the-channel models can be used [6]. Along-the-channel models [159, 253–258] account for the reactant depletion and water accumulation along the parallel channels of the flow field, but are unable to predict the channel-land interaction, which may be significant in fuel cells [259]. A number of through-the-channel models [33–35, 268, 274, 275], including the model in this work, have been developed in the past relying on the concept of a "differential cell" [19]. It is believed that under the "differential" conditions, i.e., high flow rates with stoichiometry above 10, the variation in the reactant concentration and water accumulation along the parallel channels of the cell are eliminated [19]. These conditions make it possible to analyze the performance of the MEA independently of the flow field and thus are ideal for through-the-channel models as those do not take the along-the-channel dimension of the cell into account.

In this work, the experimental cell was initially operated with a humidified hydrogen flow in the anode channel at 0.2 slpm (stoichiometry of 4.8 at 1 A/cm$^2$) and a

humidified air flow in the cathode channel at 0.4 slpm (oxygen stoichiometry of 4.1 at 1 A/cm$^2$). Under such conditions, a spectrum with two arcs, at 10–20 Hz and at 50-100 Hz, was observed in the impedance measurements, which the model failed to predict with any given set of input parameters: no variation in the mass, heat, or charge-transfer parameters induced that shape of the spectrum. The appearance of an additional capacitive arc at lower frequencies in the fuel-cell impedance spectra has been attributed to along-the-channel mass transport in the modeling literature [159, 253, 257], and so the experiments were repeated with higher cathodic flow rates. The lower-frequency arc of the measured spectra shown in Figure 4.4 decreased with an increase in the cathode flow rate, confirming the relation of the arc to the along-the-channel transport. The arc, however, did not disappear even when oxygen-in-air stoichiometry was increased to 41 at 1 A/cm$^2$. The inability to eliminate the channel effects is in agreement with the results of a numerical study by Balen [300] that showed oxygen depletion and water vapor accumulation along the fuel-cell channel in a parallel-channel configuration even at stoichiometry as high as 10.

An appropriate choice of the operating conditions had to be made in order to obtain experimental data with which the model could be validated, and thus all impedance spectra in the validation section of this work have been measured with a pure oxygen supply in the cathode. Passing pure oxygen through the cathode channel at 1 slpm resulted in a stoichiometry of about 48 at 1 A/cm$^2$. The along-the-channel arc was minimized in the obtained spectra, as illustrated in Figure 4.4 at 1 A/cm$^2$, where the simulated spectrum is also shown for comparison.

The observations made above indicate that achieving operation close to the "differential" mode might require a stoichiometry significantly exceeding the recommended minimum value of 10 (see reference [19]). Since the "differential" mode was not possible to achieve in our laboratory with the air flow, pure oxygen was used to ensure the experimental EIS data were gathered under the conditions suitable for validating the model in use.
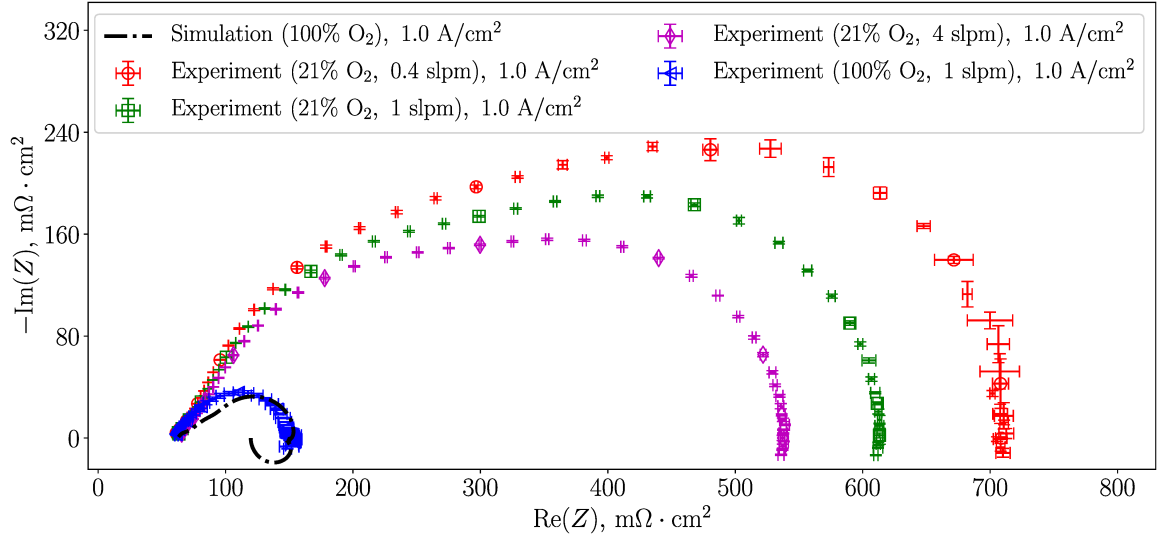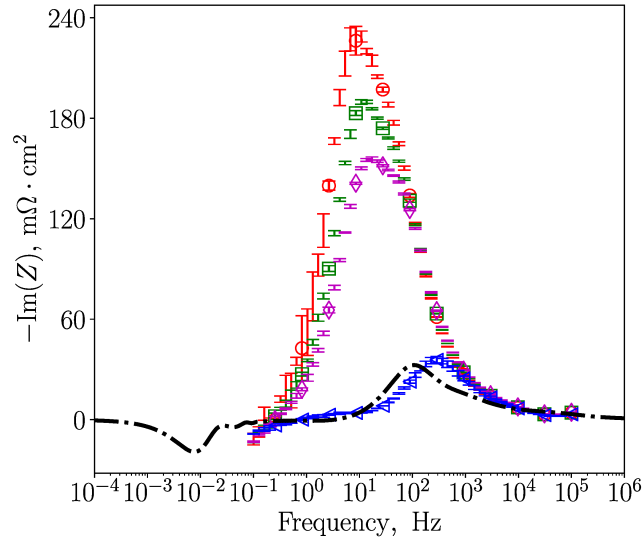
Figure 4.4: Effect of the cathodic flow composition and rate on the impedance spectrum at 1 A/cm²: (a) Nyquist plots and (b) frequency-content plots of the imaginary part. Oxygen stoichiometry was about 4.1, 10, and 41 in air and 48 in the pure-oxygen case. The cell was operated at 80 °C, 50% RH, and 1.5 atm.

## 4.3 Results and Discussion

### 4.3.1 Model Validation

#### 4.3.1.1 Validation of the Rapid-EIS Approach

The implemented rapid-EIS approach [249] and the non-equidistant Fourier transform [549] were validated by comparing the resulting impedance spectra to those found with the conventional sine-wave approach. Figure 4.5 shows a comparison between the two approaches. Three different time-scale resolutions were considered in the rapid-EIS simulations by limiting the maximum ratio of the current to the previous time-step size $\tau_{n+1}/\tau_n$ to 1.01, 1.001, and 1.0001 (1, 0.1, and 0.01% increase between the time layers, respectively). All spectra exhibited excellent agreement in the capacitive domain, but deviated from each other in the low-frequency inductive loop.

The rapid-EIS spectrum with the highest time-scale resolution was the most accurate; however, it required about 27 days of computation. The significant computational time may be a shortcoming of the first-order-accurate implicit Euler (BDF1) method used in this work and the Richardson extrapolation algorithm that increases the temporal accuracy at the cost of solving the problem thrice to compute each time layer. The lowest-resolution case required 7 hours of computation, but had the highest uncertainty in approximating the characteristic frequency and the size of the inductive loop. Since the primary interest of this work was in the effect of the different physical phenomena on the relative change in the inductive loop rather than on accurately predicting its size, the case with the medium time-scale resolution ($\tau_{n+1}/\tau_n \leq 1.001$), which took about 65 hours of the computational time, was considered optimal and was used in all EIS studies shown in this work. The frequency range of the main inductive behavior, 0.1–200 mHz, was resolved correctly in this case, as seen in Figure 4.5b. The minor inductive loop at 0.2–5 Hz was time-step-size-independent among the considered cases, and thus was computed accurately.

(a)



(b)



(c)
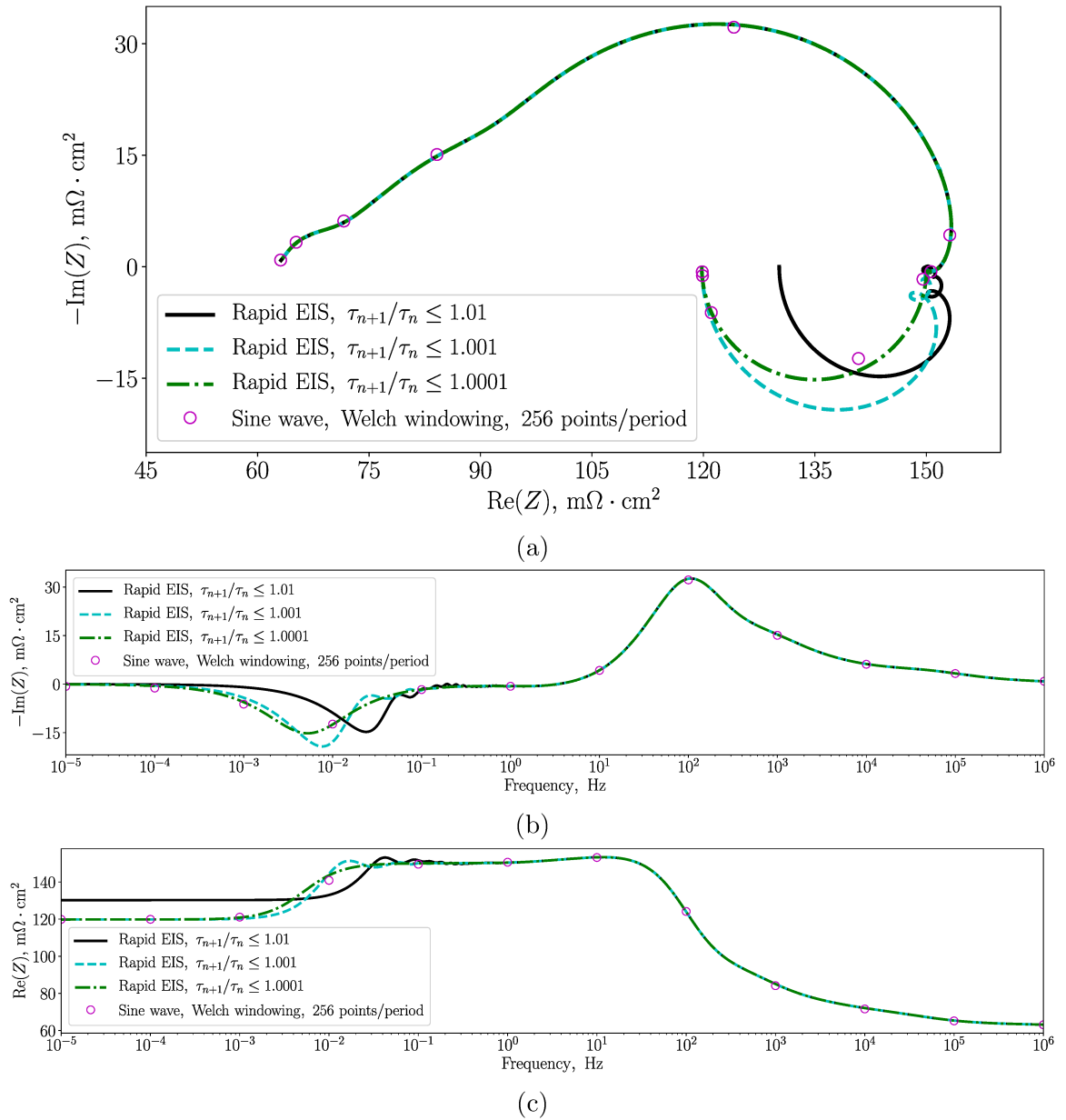
Figure 4.5: Comparison of the impedance spectra obtained with the rapid-EIS approach using three different time-scale resolutions to the spectrum computed using the sine-wave approach: (a) Nyquist plot; (b) frequency-content plot of the negative imaginary part; (c) frequency-content plot of the real part.

The local impedance oscillations at 0.02–1 Hz observed in the two coarser time-discretization cases in Figure 4.5 were not present in the finer case, which indicates that they were a numerical artifact.

Sine-wave simulations were performed by generating 13 periods of a sinusoidal wave in voltage at the given single frequency. Impedance was then computed as discussed in Section 2.3.1.1. Convergence studies were performed on the resulting phase angle and frequency of the current-density signal, as well as the imaginary and real parts of the impedance. It was found that using 256 equidistant nodal points per period of the wave was optimal in terms of the achieved accuracy of the results and the computational time. Since each sine-wave simulation took between 1.5 and 2.5 hours per frequency, the overall computational time may reach and exceed that for the rapid-EIS approach depending on the desired frequency resolution of the spectrum. This is because the frequencies are analyzed after a rapid-EIS simulation is complete, and thus any number of frequencies can be extracted from a single simulation (to a certain extent where aliasing may start to occur).

### 4.3.1.2 Experimental Validation

Experimental and simulated polarization and ohmic-resistance curves at varying oxygen concentration are shown in Figure 4.6. The ohmic resistance was measured using the current-interrupt and EIS techniques, and thus only contained the high-frequency portion of the resistance. Ohmic resistance was computed in the model through ohmic heating as discussed in Section 2.3. Only the membrane, gas-diffusion layers, and microporous layers were included in the resistance calculation, as the resistance of only those layers is believed to comprise the HFR [174, 177, 570]. The electronic resistance of the catalyst layers was also included in the resistance calculation, but was negligible compared to the ohmic resistance of other components. Contact resistances were not directly considered in the model as the overall agreement with the experimental resistance (shown later) negated the necessity of modifying the conductivity values

of the cell components. The experimentally measured contact resistance between the MEA components was about 1.3 m$\Omega \cdot$cm$^2$ with the additional resistance of the bipolar plates and the current collectors of approximately 8.7 m$\Omega \cdot$cm$^2$.

The experimental current-interrupt-based resistance is known to overestimate the EIS-based HFR [570]. Therefore, the model's ability to predict the ohmic resistance of the cell was validated with the experimental HFR values. Agreement within about 3% was achieved between the experimental EIS-based HFR and the simulated ohmic-heating-based equivalent. The latter will also be referred to as HFR in this work.

Oxygen content in the cathode channel prior to humidification was varied between 1% and 100%. As mentioned earlier, the 1% oxygen case was used to estimate the local oxygen transport resistance in the catalyst layers (i.e., the $k_{O_2}$ rate constant in equation (2.10)), and the 100% oxygen case was used to estimate the hydration-related properties (absorption/desorption rates, absorbed-water-diffusivity prefactor, and the amount of water produced in the ionomer phase). The current density was limited to about 1.8 A/cm$^2$ in the latter case to avoid flooding of the cell with product water.

Good agreement was achieved in both limiting current density at 1% oxygen and the HFR at 100% oxygen. The drop in the resistance due to electrolyte hydration was similar between the model and the experiments. It can be seen as well in Figure 4.6b that the predicted HFR remained the same at the same current density when the oxygen content in the cathode channel was varied unless mass-transport limitations were observed. This is as expected since the rate of water production, and thus the rate of the electrolyte hydration, should be approximately the same at the same current density. The observed agreement with the experimental data validates the model's capability to predict single-phase mass transport losses and hydration of the electrolyte.

Even though only the first full sweep is shown in both the simulated and the experimental data, two to three subsequent sweeps have been performed in all cases,

both simulated and measured, to ensure no drift in the performance or the resistance between the sweeps. This was important in the experiments to make sure the cell was correctly conditioned prior to the experiment and no transient history, such as hydration, affected the measurements. In the simulations, no drift between the sweeps meant that the time scales of the major cell responses were correct and the stable performance was achieved within one sweep, as seen in the experiments.

The predicted polarization-curve hysteresis was significantly lower than that observed in the experimental data; its largest magnitude was 10–40 mA/cm$^2$ at 0.7 V in the simulations, but varied between 130 and 200 mA/cm$^2$ in the experimental data. The simulated resistance hysteresis, however, was similar to the experiments, e.g., depending on the oxygen concentration, hysteresis magnitude was 1–4 m$\Omega \cdot$ cm$^2$ at 0.75 A/cm$^2$ in the model and 1–3 m$\Omega \cdot$ cm$^2$ in the experimental data. Therefore, the larger polarization hysteresis in the experimental data in Figure 4.6a was not associated with the HFR hysteresis and was possibly due to platinum-oxide dynamics at the catalyst surface [154, 155], which was not considered in the model. The model also overpredicted the cell performance at the intermediate oxygen contents (10% and 21%). The discrepancies in the predicted performance and polarization hysteresis at these oxygen contents may be because it was not possible to achieve a high enough flow rate in the experiments to avoid the additional mass transport losses due to the oxygen depletion and liquid water accumulation along the parallel channels. Liquid-water formation in the MEA may have also been the reason for the observed performance discrepancy [298]. Furthermore, the double-trap ORR model [311] used in this Chapter predicts the reaction order (with respect to oxygen) of about 0.3–0.5, which is significantly lower than the experimentally measured order of about 0.8–1 [125, 310, 571] and affects the dependency of the simulated current on oxygen concentration [311][b].

---

[b]The double-trap ORR model was recently refitted by Moore et al. [312] to the experimental data by Parthasarathy et al. [310]. The updated model with the reaction order of about 0.85 is used in Chapter 6 of this thesis.
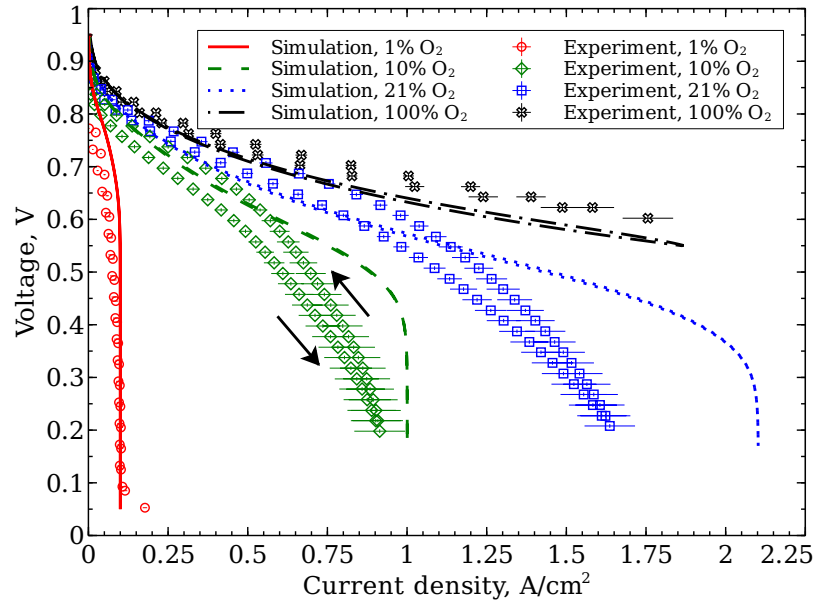
(a)
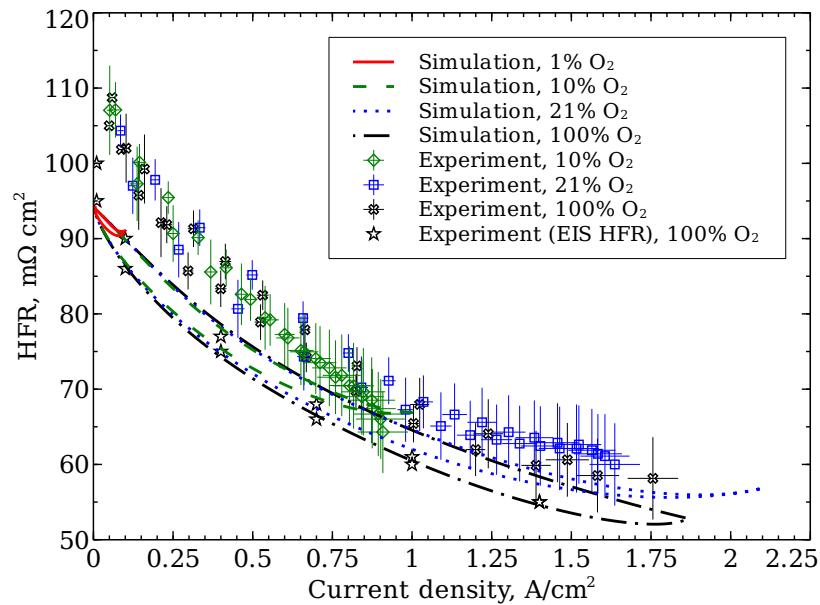


(b)

Figure 4.6: Comparison of the simulated and experimental polarization (a) and HFR (b) curves with varied oxygen content in the cathode channel (prior to humidification). Only the first sweep is shown. Error bars in the experimental data represent standard deviation estimated from three tested cells. The cell was operated at 80 °C, 50% RH, and 1.5 atm.

Next, the model's ability to predict the changes in the ohmic resistance with RH was verified by comparing the simulated polarization and HFR curves to the experimental data obtained at 50% and 70% RH with 21% oxygen. The comparison with the experimental data is shown in Figure 4.7. The resistance drop with increased RH in Figure 4.7b was similar to that in the experiments. The predicted resistance hysteresis also remained similar to that in the experimental data. Apart from the along-the-channel and liquid-water effects that the model could not capture at the current density approximately above 0.75 A/cm$^2$, it can be seen from Figure 4.7a that the performance predictions are in reasonable agreement with the experimental data. Mass-transport losses were larger in the 70%-RH simulation compared to the 50% RH case due to the lower oxygen content in the cathode after the humidification. Interestingly, this trend was opposite in the experiment. The limiting current density at both conditions is dominated by the local transport resistance at the catalyst-ionomer interface. It is hypothesized that the reason for the discrepancy is the value of the oxygen-dissolution rate constant used. In the proposed model, the oxygen-dissolution rate constant, $k_{O_2}$, was calibrated using data at 50% RH and maintained constant; however, experimental data suggest that the interfacial oxygen-transport resistance decreases with increase in relative humidity [125, 325]. The latter would result in an increasing limiting current with increasing RH. The oxygen-dissolution rate constant is varied with operating conditions in Chapter 6.

Finally, predicted and measured impedance spectra were compared in the pure-oxygen case at varying current density. This validation was conducted with the same, single set of model inputs that was used in the simulations shown in Figures 4.6 and 4.7, making it the second independent validation of the model with a different type of transient analysis.

The rapid EIS approach discussed earlier was used to compute the impedance spectra. Since the model was operated in the potentiodynamic mode, the cell voltages producing the current densities from the EIS experiments were found in the model,
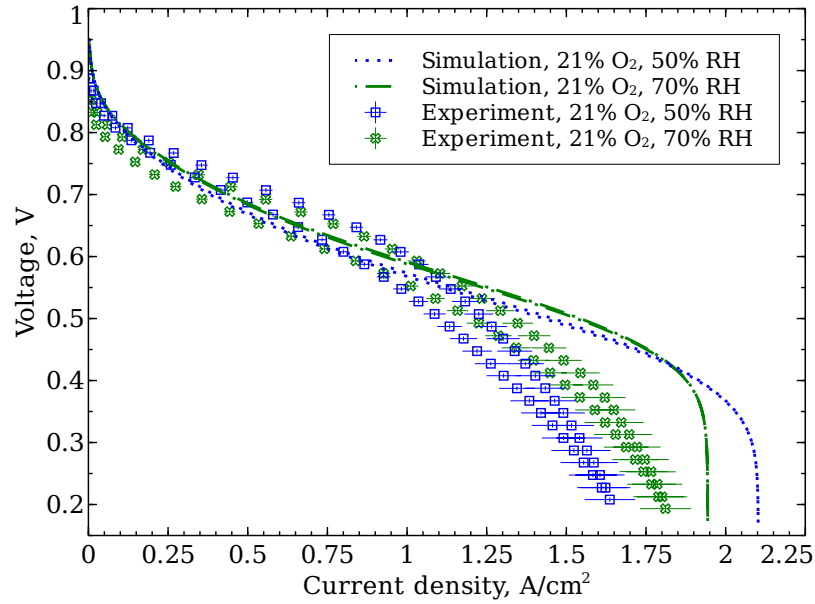
(a)
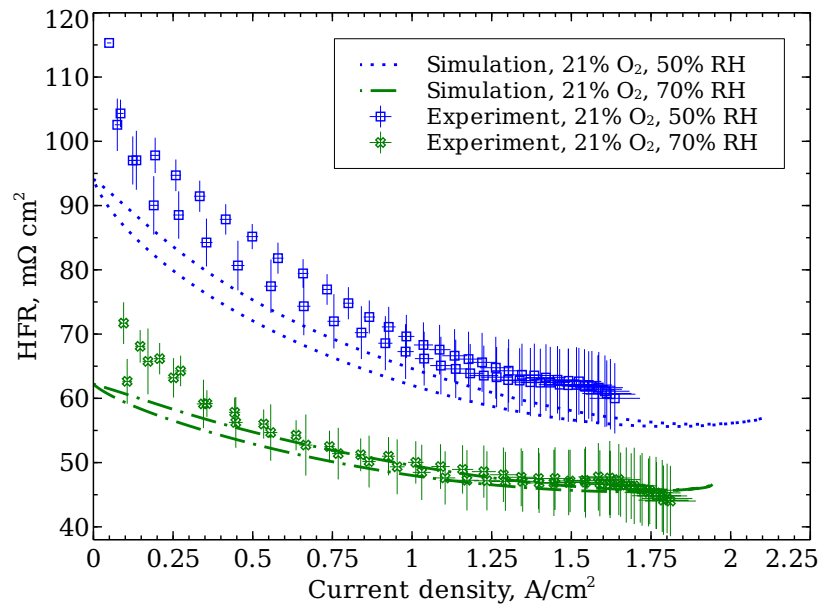


(b)

Figure 4.7: Comparison of the simulated and experimental polarization (a) and HFR (b) curves with varied RH. Only the first sweep is shown. Error bars in the experimental data represent standard deviation estimated from three tested cells. The cell was operated at 80 °C, 50% RH, 1.5 atm, and 21% oxygen in the cathode flow (prior to humidification).

and the spectroscopy was simulated at those potentials. The magnitude of the perturbation was chosen sufficiently small in both the experiments and the model so as not to deviate significantly from the operating point and to ensure the linearity of the dynamic response, and, at the same time, not too small to avoid large noise-to-signal ratio. Thus, the approaches taken in the measurements and the simulations were assumed equivalent, even though obtained through different modes (galvano- and potentiodynamic). Linearity of the simulated spectra was verified with the Kramers-Kronig relations (4.7) and (4.8). Relative residuals defined in equations (4.9) and (4.10) were below 1% for the simulated and the reconstructed spectra.

The simulated and the experimental spectra are shown in Figures 4.8 and 4.9 along with the respective polarization and HFR curves in Figure 4.6. A good overall agreement was achieved in the impedance spectra in the current-density range between 0.1 and 1.4 A/cm$^2$. A significant deviation was, however, observed between the simulated and the measured spectra in the high-frequency portion, where the spectrum is known to be associated with the double-layer and electrolyte-conductivity dynamics [164, 176, 177, 181, 183, 253]. Parametric studies on the hydration-related properties discussed later in this work show that water management has a significant effect on the impedance spectrum at high frequencies. At the same time, varying the double-layer capacitance in the model resulted in no change in the Nyquist plot (Figures 4.8a and 4.9a), but the halved capacitance shifted the capacitive peak in the frequency-content plot (Figure 4.8b and 4.9b) closer to the experimental frequencies. This may indicate that the double-layer capacitance measured in a cyclic-voltammetry experiment at 100% RH may be an overestimation due to the RH-dependent catalyst-ionomer interfacial area [1, 391].

The simulated spectra shown in Figures 4.8 and 4.9 deviated from the experimental data at high frequencies (of order 100 Hz and higher), and the magnitude of the deviation increased with current density. As it will be shown later in this work, the high-frequency portion of the fuel-cell impedance spectrum is highly dependent on
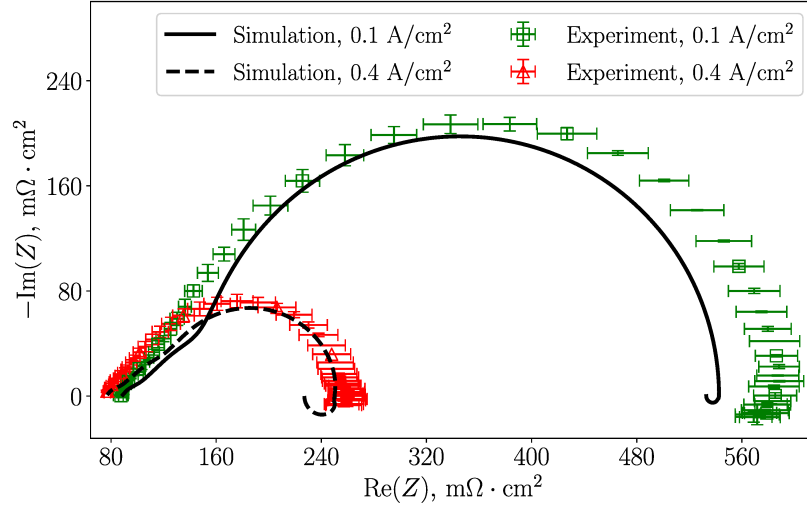
(a)
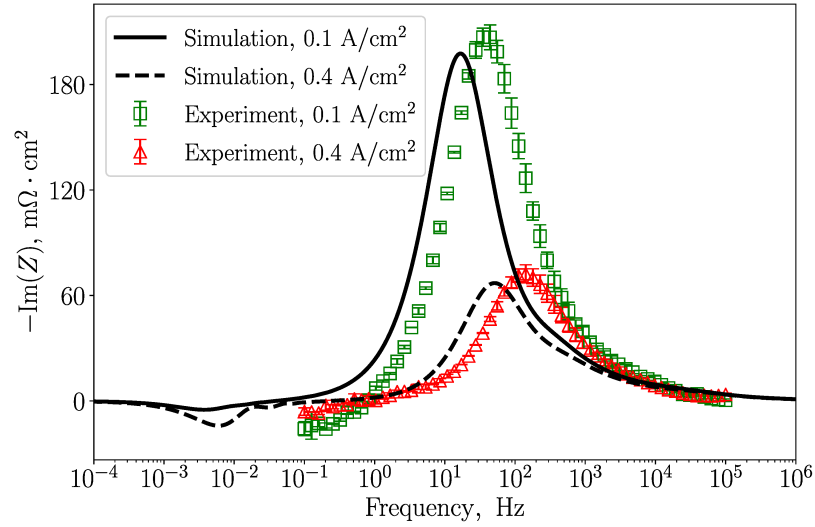


(b)

Figure 4.8: Comparison of the simulated and experimental impedance spectra: (a) Nyquist and (b) frequency-content plots for the current density of 0.1 A/cm$^2$ and 0.4 A/cm$^2$. The corresponding polarization and HFR curves are shown in Figure 4.6. Error bars in the measured spectra represent the standard deviation from two experiments. The cell was operated at 80 °C, 50% RH, 1.5 atm, and 100% oxygen in the cathode flow (prior to humidification).
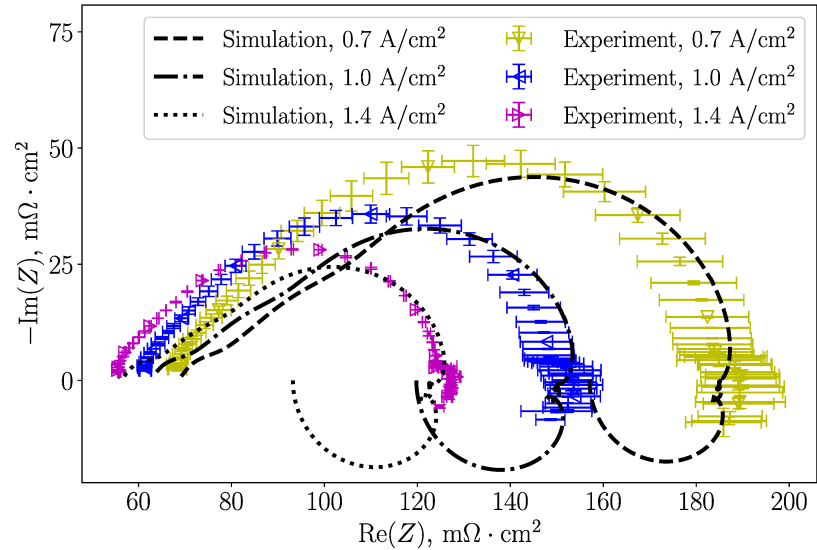
(a)
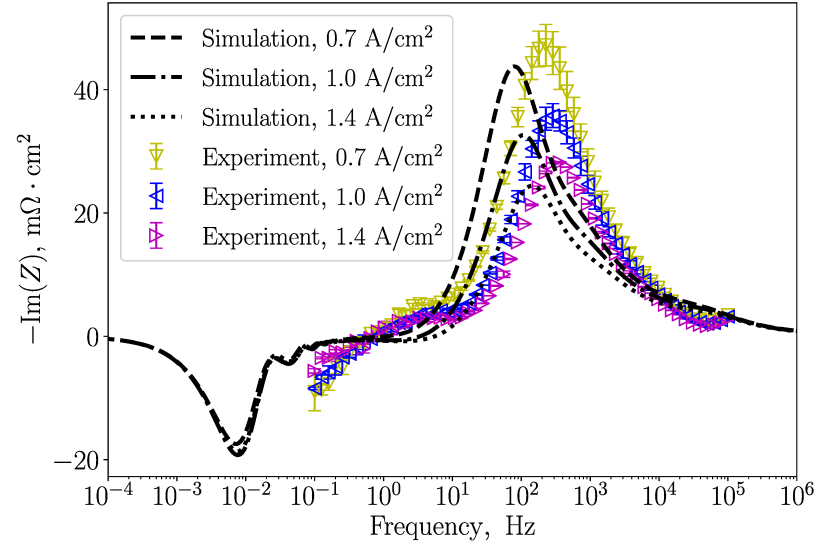


(b)

Figure 4.9: Comparison of the simulated and experimental impedance spectra: (a) Nyquist and (b) frequency-content plots for the current density of 0.7 A/cm², 1.0 A/cm², and 1.4 A/cm². The corresponding polarization and HFR curves are shown in Figure 4.6. Error bars in the measured spectra represent the standard deviation from two experiments. The cell was operated at 80 °C, 50% RH, 1.5 atm, and 100% oxygen in the cathode flow (prior to humidification).
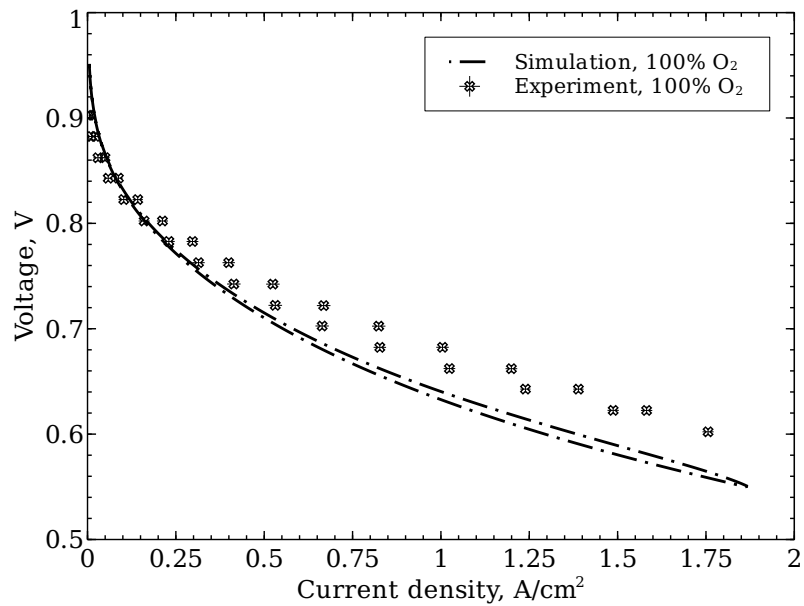
(a)
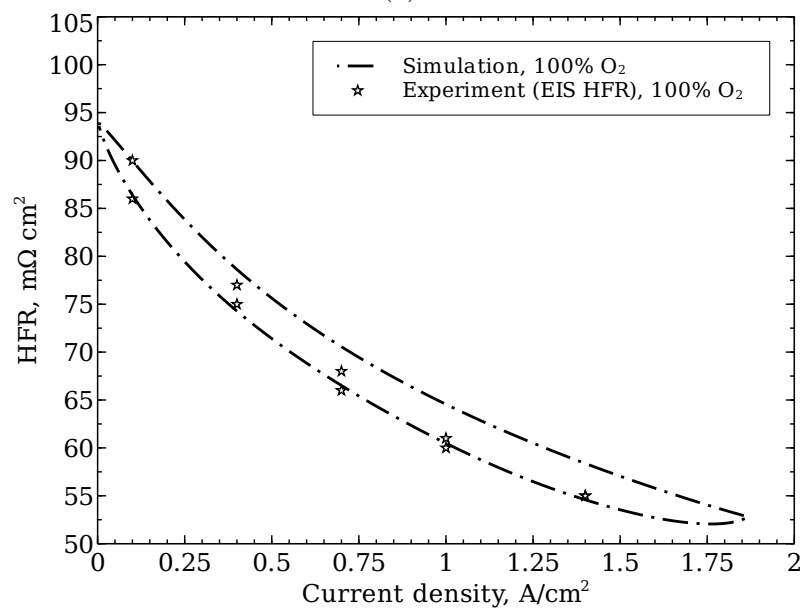


(b)

Figure 4.10: Comparison of the simulated and experimental polarization (a) and HFR (b) curves that correspond to the spectra shown in Figures 4.8 and 4.9. Only the first sweep is shown. Error bars in the experimental polarization curve represent the standard deviation estimated from three tested cells. The cell was operated at 80 °C, 50% RH, 1.5 atm, and 100% oxygen in the cathode flow (prior to humidification).

the catalyst-layer ionomer hydration and conductivity.

The capacitive behavior of the cell was accompanied by an inductive loop at about 0.1 mHz–6 Hz at moderate to high current densities. The nature of this low-frequency inductive behavior in the fuel-cell impedance spectra is discussed further in this work.

A distinctive feature of the spectra simulated at moderate to high current densities was the presence of impedance spirals between 0.02 and 1 Hz. These local impedance oscillations were equidistant in the frequency-content plot with about 50 mHz between the local extrema, indicating a resonance between the simulated hydration and conductivity dynamics of the membrane and the ionomer phase of the catalyst layers (the effect of these phenomena on the impedance spectrum is discussed in this work). Even though the regions of the simulated spectra with local oscillations have all passed the Kramers-Kronig test and similar oscillations have been reported in both experimental [179] and modeling [406, 572, 573] studies (although at higher frequencies of 1-100 Hz [179, 573] and attributed to the resonance between the oxygen transport along the channel and in the MEA [573]), the time-step-size analysis shown earlier revealed that the observed resonance was, at least in this thesis, a numerical artifact (the inductive behavior was, however, resolved with a sufficient degree of accuracy). This highlights the importance of verifying the unexpected impedance behavior by using a smaller time-step size in the simulations or a higher sampling frequency in the EIS experiments.

Another point of validation was the HFR extracted from the impedance spectra as

$$\mathrm{HFR} = \lim_{\omega \to \infty} \mathrm{Re}(Z(\omega)).$$

As seen in Figures 4.8a and 4.9a, a good HFR agreement was achieved in all cases with both the EIS experiments (within about 3%) and the ohmic-heating-based values in Figure 4.6b (within about 1%). This validates the model's ability to predict the high-frequency resistance in the EIS and serves as another validation of the earlier computed ohmic resistance.

The DC resistance was found in the EIS simulations as

$$R_{\mathrm{DC}} = \lim_{\omega \to 0} \mathrm{Re}(Z(\omega)).$$

However, the lowest frequency used in the experiments (0.1 Hz) was not sufficient to observe the DC resistance. Instead, it was computed as the local negative slope of the polarization curve:

$$R_{\mathrm{DC}} = \frac{\partial \eta}{\partial i} = -\frac{\partial V}{\partial i}.$$

A steady-state-polarization-curve simulation was considered as a true stationary reference for computing the DC resistance with the formula above. The deviation of the EIS-based DC resistance from that computed from the polarization curve was between 0.8% and 3% depending on the current density. Therefore, the EIS simulations were consistent with the polarization curves.

## 4.3.2 Ohmic-Resistance Breakdown

Before discussing the hydration-related parametric studies, an ohmic resistance breakdown is carried out for the pure-oxygen case from Figures 4.10a and 4.10b in order to verify that the HFR does not include the ionic resistance of the platinum-on-carbon catalyst layers [174, 177, 570]. The ohmic-resistance breakdown is shown in Figure 4.11a. It is clear that the HFR does not include the protonic resistance of the catalyst layers: the experimental HFR is in close agreement (within 3%) with the sum of the protonic resistance of the membrane and the electronic resistance of the other MEA components. The highly electronically conductive carbon-support phase of the catalyst layers forms a path of the least resistance for the current, and thus the significantly less conductive ionic phase does not appear in the HFR. The HFR composition is further confirmed by even closer, within 1%, agreement between the simulated HFR and the ohmic-heating-based resistance of the aforementioned layers. This study also validates the ohmic-heating approach for computing the individual ohmic resistances of the MEA components.

A comparison between the ohmic and DC resistance is illustrated in Figure 4.11b. As current density increases, the DC resistance approaches the total ohmic resistance from Figure 4.11a in this case, where mass-transport losses are not dominant. The region of the graph with the blue stroke corresponds to the difference between the DC and the total ohmic resistance and corresponds to other losses, such as mass-transfer and charge-transfer resistance.

### 4.3.3 Water-Management Analysis

The transient terms in the reaction-kinetics sub-models were neglected in the model, and thus the dynamics of the ORR intermediates and platinum oxide could not be the cause of the inductive behavior in the simulated spectra. Carbon monoxide poisoning was also not modeled. The presence and the strength of the inductive behavior in the simulated spectra highly depended on the hydration-related properties of the model. A number of parametric studies were performed in order to understand the effect of water management on the appearance of the low-frequency inductive loops in the impedance spectra. Current density of 1 A/cm$^2$ was chosen for these studies as the inductive behavior was sufficiently strong, as seen in Figure 4.9.

#### 4.3.3.1 Effect of Relative Humidity

A study similar to the experimental RH imbalance analysis by Schiefer et al. [203] was carried out first to find if the model can correctly predict the trends in the inductive-loop-size dependency on RH. The spectra simulated at 1 A/cm$^2$ (as in reference [203]) with varied relative humidity in anode and cathode are shown in Figure 4.12b, where the 50%/50% case is the reference taken from Figure 4.9. Similarly to reference [203], the lower RH of 30% in both compartments resulted in the largest inductive loop followed by the case with a higher cathode RH of 70% and the case with 50% RH in both sides (Figure 4.12b). The inductive loop was the smallest in the case of the highest RH of 70% in both anode and cathode. These observations validate the
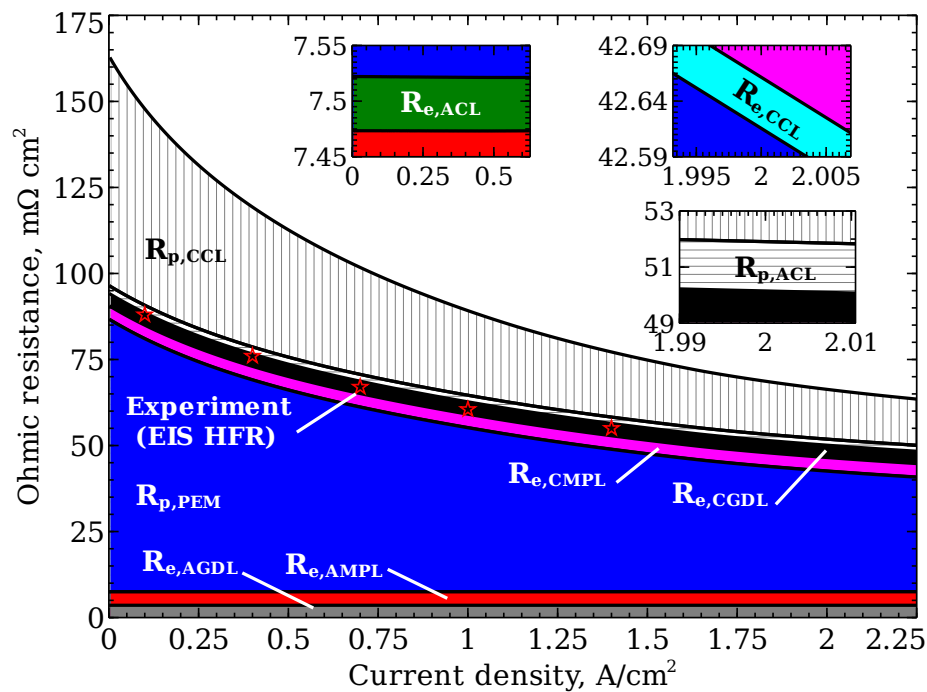
(a)
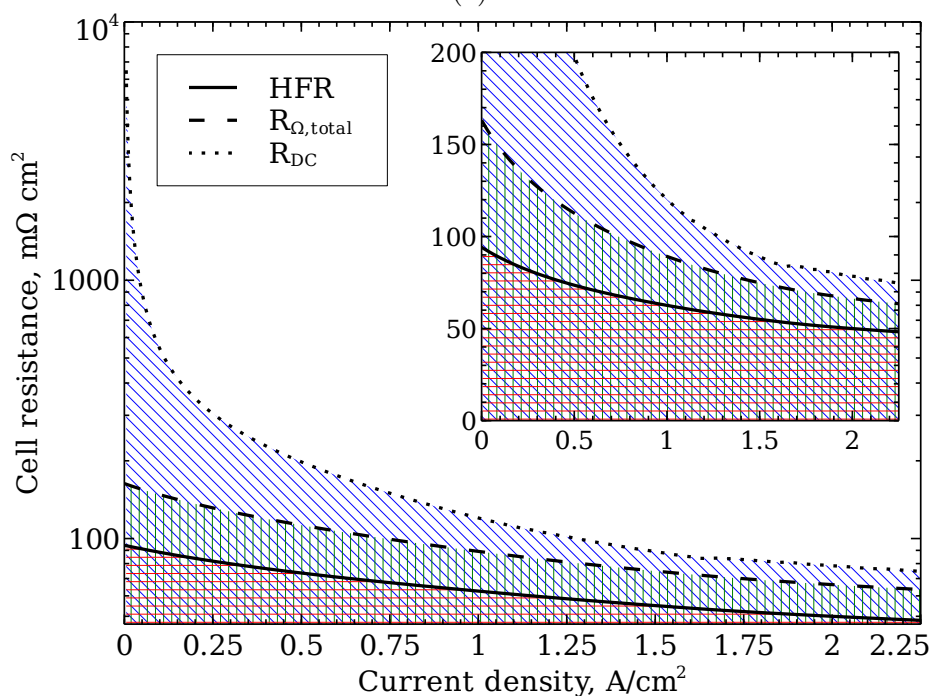


(b)

Figure 4.11: Breakdown of the simulated ohmic resistance (a) and cell resistance (b). Electronic and protonic resistances were marked $R_e$ and $R_p$, respectively. The experimental EIS HFR data were taken from Figure 4.6b and averaged (the error bars represent the standard deviation). The cell was operated at 80 °C, 50% RH, 1.5 atm, and 100% oxygen in the cathode flow (prior to humidification).

model predictions of the RH effect on the inductive loop and hint that the inductive behavior may be affected by the rate and direction of the water transport across the CCM. The additional case with 70% anode RH, 30% cathode RH, not considered in the reference study [203], resulted in the second-smallest inductive loop.

Steady-state water-content distribution in the CCM at 1 A/cm$^2$ is illustrated in Figure 4.13. Interestingly, water content was higher in the 30%/70% anode/cathode RH case than in the 70%/30% RH case due to the insufficient back-diffusion of product water compared to electroosmosis in the latter case. Water content in the CCM had a direct effect on the imaginary impedance at frequencies above 100 Hz, which increased by up to 54% between the symmetrical 70% RH and symmetrical 30% RH cases. At the same time, it had no direct correlation with the size of the inductive loop as evident from the imbalanced-RH cases. Thus, the low-frequency inductive behavior of fuel cells has a more complex nature rather than water distribution in the membrane and catalyst layers.

### 4.3.3.2 Effect of Water Absorption/Desorption Kinetics

A parametric study was performed on the rates of water absorption and desorption by the ionomer in the catalyst layers to further investigate the nature of the low-frequency inductive loop of the fuel-cell-impedance spectra. The inductive loop was not present in the spectrum at 1 A/cm$^2$ with absorption/desorption rates reduced by a factor of 10$^4$ (compared to the reference case from Figure 4.9) as seen in Figure 4.14. The inductive loop became evident at about 0.1–20 mHz with the absorption/desorption kinetics from Goshtasbi et al. [157] (4 times slower absorption and 9 times slower desorption than in Figure 4.9) and reached its maximum in the reference case. As the water-exchange rates were further increased, the inductive loop gradually decreased in size and shifted to higher frequencies until reaching 10 mHz–6 Hz as seen in Figure 4.14 for the rates scaled up by 10$^4$ times. When vapor diffusivity in the porous layers was also increased by four orders of magnitude to quickly remove the product water, the
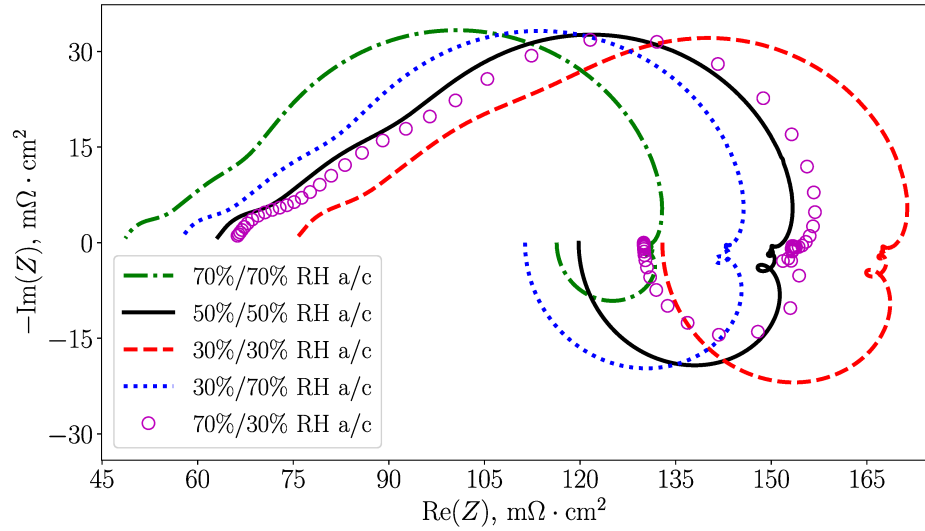
(a)
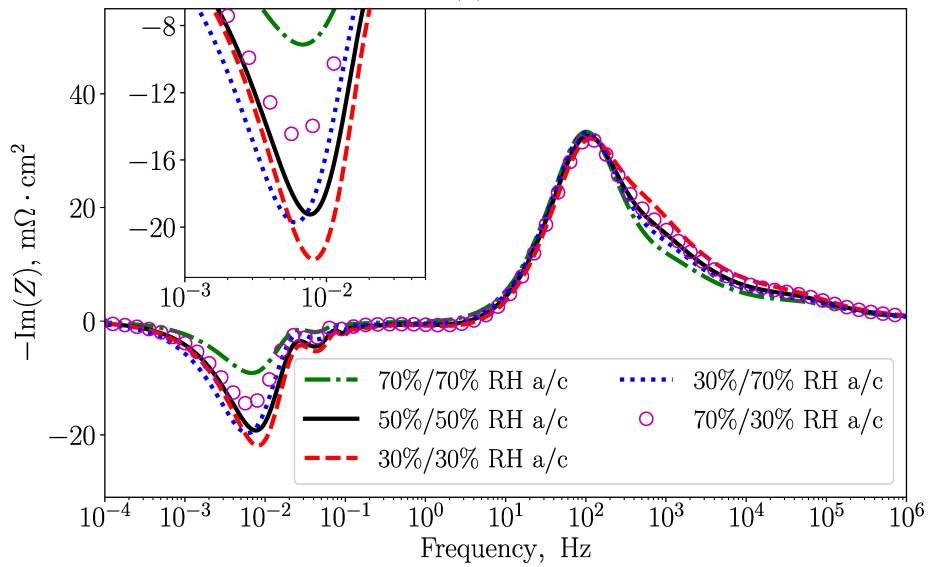


(b)

Figure 4.12: Effect of relative humidity on the predicted impedance spectrum at 1 A/cm²: (a) Nyquist plots, (b) frequency-content plots of the imaginary part. The cell was operated at 80 °C, 1.5 atm, and 100% oxygen in the cathode flow (prior to humidification).
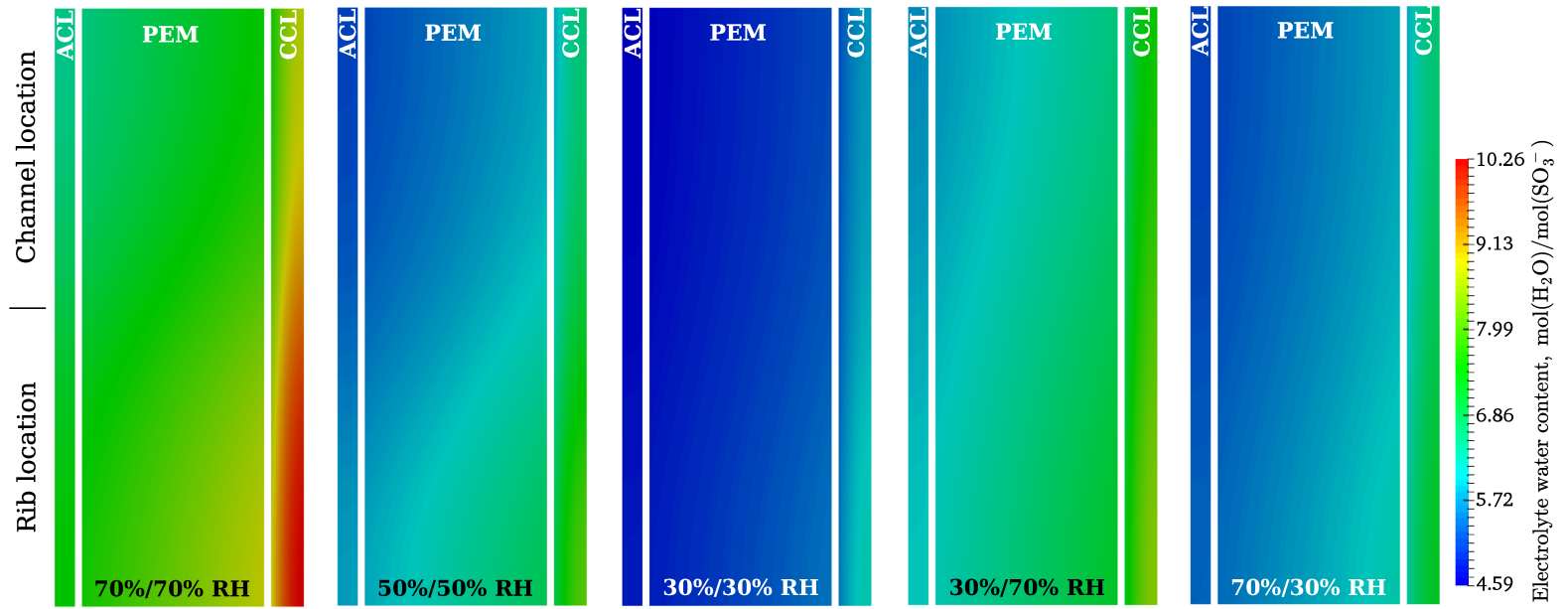
Figure 4.13: Comparison of the steady-state electrolyte-water-content distribution within the CCM at 1 A/cm² with varied RH in the anode and cathode compartments (the domains were upscaled along the horizontal axis by a factor of 10 and gaps between the layers were added for clarity). The cell was operated at 80 °C, 1.5 atm, and 100% oxygen in the cathode flow (prior to humidification).

inductive loop disappeared. This study indicates that the hydration-related inductive behavior of fuel cells depends on the dynamics of water absorption and desorption by the ionomer.

Absorption/desorption kinetics of water also had a distinctive effect on the spectrum at frequencies between 100 Hz and 1 MHz. A direct relationship can be established between the strength of the capacitive behavior of fuel cells in that frequency range and the ionomer-water exchange rates based on Figure 4.14b. In alignment with the RH-imbalance study, a lower water content in the CCM observed with higher absorption/desorption rates (Figure 4.16) led to a stronger capacitive behavior of the cell as seen in Figure 4.14b.

Figures 4.15a and 4.15b show that the water-exchange rates affected the polarization and HFR hystereses and magnitude. The larger the absorption/desorption rates and vapor diffusivity, the larger HFR and the lower performance were predicted as water produced directly in the ionomer phase of the catalyst layers was allowed to desorb from the ionomer and leave the MEA faster. The largest hysteresis, up to about 40 m$\Omega \cdot$cm$^2$, was observed with the rates from Goshtasbi et al. [157], in which case the quasi-stationary state was not achieved in one sweep, and, unlike the reference case and the experimental data in Figure 4.6, the cell exhibited an incomplete loop.

### 4.3.3.3 Effect of Back-Diffusion of Water in the Electrolyte

The nature of the two separate inductive loops in the fuel-cell impedance spectra was investigated further by modifying the water back-diffusion coefficient in the electrolyte. In this study, $D_\lambda$ was scaled down by a factor of 3.2 first in the membrane, then in the catalyst layers, and finally in the whole CCM. Note that 3.2 was the scaling factor for the back-diffusion coefficient from Motupally et al. [491] as discussed Section 4.1.3.1.

The results of this parametric study at 1 A/cm$^2$ are shown in Figures 4.17 and 4.18.
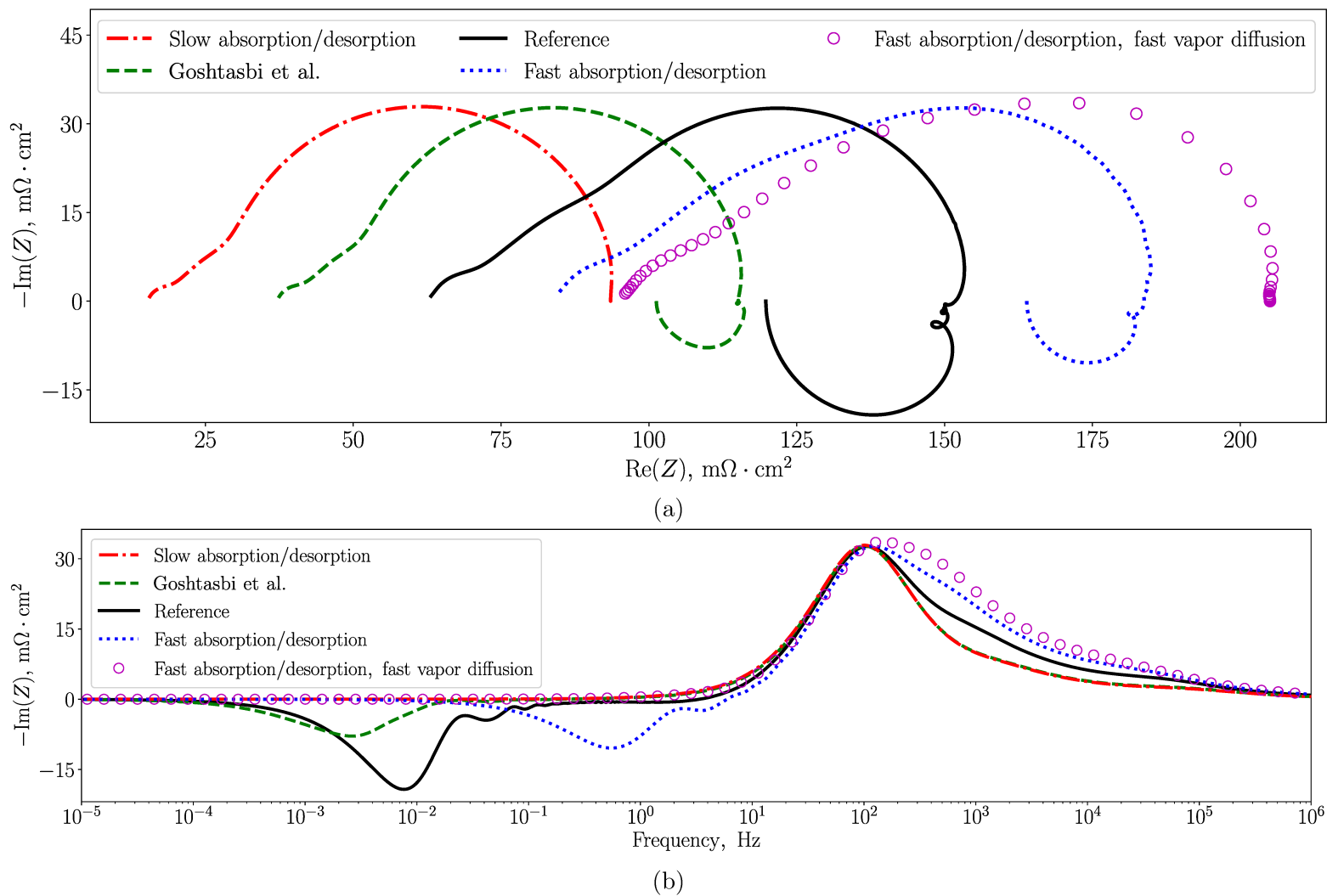
Figure 4.14: Effect of the rate of water absorption/desorption by the ionomer on the predicted impedance spectra at 1 A/cm$^2$: (a) Nyquist plot; (b) frequency-content plot of the negative imaginary part. The corresponding polarization and HFR curves are shown in Figure 4.15. The cell was operated at 80 °C, 1.5 atm, and 100% oxygen in the cathode flow (prior to humidification).
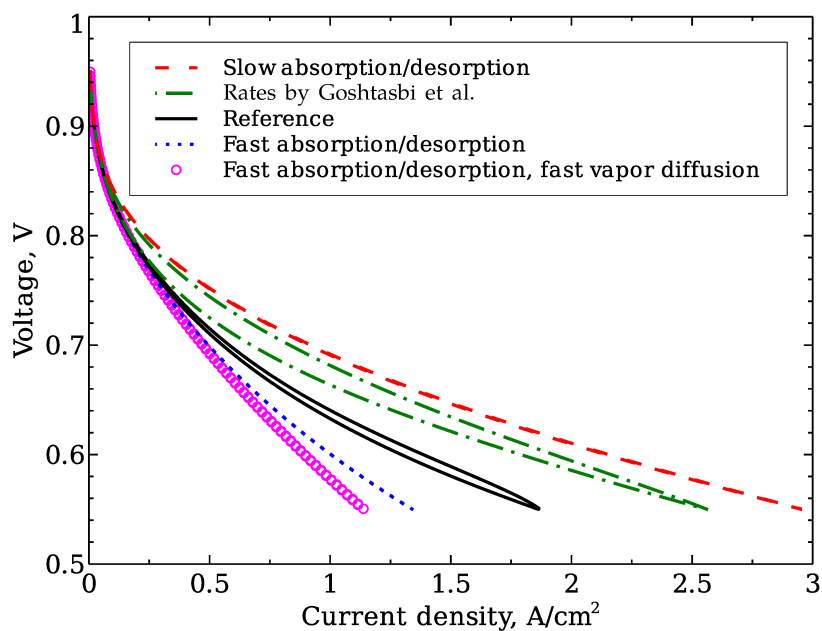
(a)
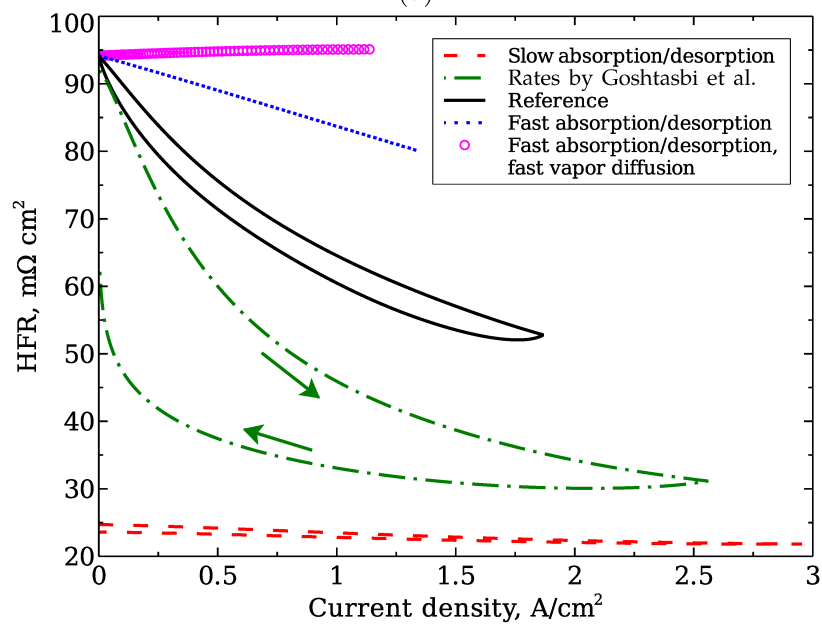


(b)

Figure 4.15: Effect of the rate of water absorption/desorption by the ionomer on the predicted polarization curve (a) and HFR (b). The cell was operated at 80 °C, 1.5 atm, and 100% oxygen in the cathode flow (prior to humidification).
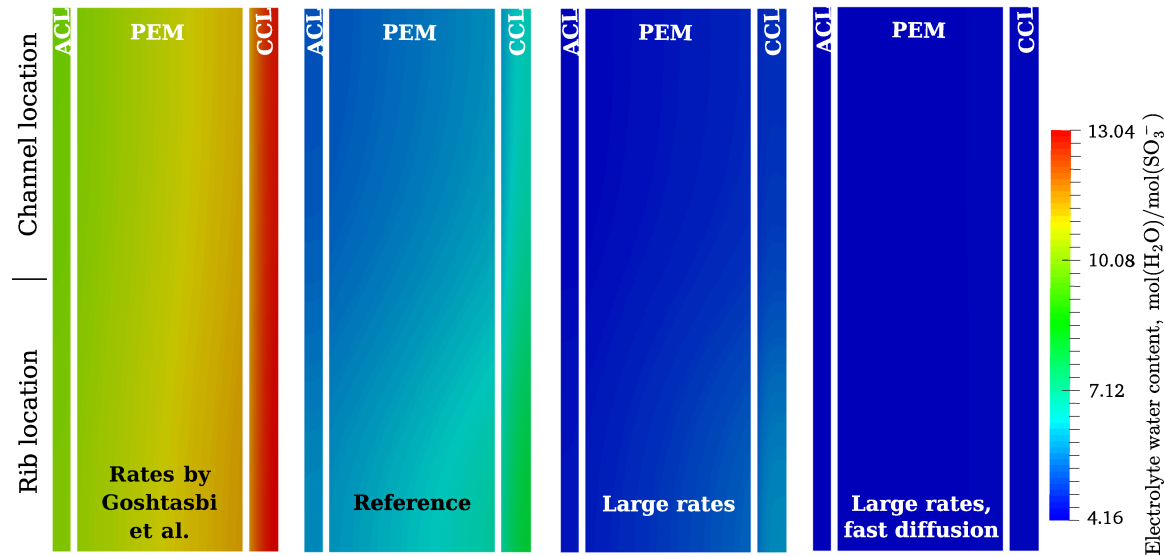
Figure 4.16: Comparison of the steady-state electrolyte-water-content distribution within the CCM at 1 A/cm² with varied water absorption/desorption rates (the domains were upscaled along the horizontal axis by a factor of 10 and gaps between the layers were added for clarity). Left to right: rates by Goshtasbi et al. [157] ($\alpha_{\text{abs}} = 1.14 \cdot 10^{-5}$ cm/s, $\alpha_{\text{des}} = 4.59 \cdot 10^{-5}$ cm/s), reference case ($\alpha_{\text{abs}} = 4.59 \cdot 10^{-5}$ cm/s, $\alpha_{\text{des}} = 41.31 \cdot 10^{-5}$ cm/s), large rates ($\alpha_{\text{abs}} = 4.59 \cdot 10^{-1}$ cm/s, $\alpha_{\text{des}} = 41.31 \cdot 10^{-1}$ cm/s), and large rates with $D_{\text{wv}}^{\text{eff}}$ scaled up by a factor of $10^4$. The cell was operated at 80 °C, 1.5 atm, 50% RH, and 100% oxygen in the cathode flow (prior to humidification).

A lower back-diffusion coefficient led to a weaker inductive behavior at 0.1–200 mHz, especially in the catalyst layers. This aligns well with the earlier observation that this inductive loop is sensitive to anode and cathode RH (see Figure 4.12b). When the rate of back-diffusion was reduced in the whole CCM, the inductive process at 0.1–200 mHz was transformed into a capacitive process due to the increased role of electroosmosis (a parametric study on the thermal osmosis of water in the PEM was also performed, but no significant change in the impedance spectrum was found at the considered operating conditions). In this case, the direction of the water-transport across the CCM was reversed to anode-to-cathode, and a significant anode dry-out took place (Figure 4.19), which resulted in the increase of the HFR at current densities approximately above 0.5–0.6 A/cm$^2$ with a reversed direction of the resistance hysteresis at higher current densities (Figure 4.18b) and a lowered performance (Figure 4.18a). These observations indicate that the inductive process at 0.1–200 mHz is affected by the individual mechanisms of water transport in the electrolyte. The reduced flux of the product water from cathode to anode leads to a decrease of the phase-lead of voltage, which weakens the inductive behavior. If the direction of water transport across the CCM is reversed, for example, due to stronger electroosmosis, then the electrolyte cannot be sufficiently hydrated by the product water, as seen in Figure 4.19, to support the voltage-phase-lead, and the dynamic behavior becomes capacitive.

In addition to the main inductive loop at 0.1–200 mHz, a second inductive loop at 0.2–5 Hz became apparent with the lower back-diffusion of water in CLs or the whole CCM as seen in Figures 4.17a and 4.17b. Due to the lower rate of back-diffusion, more water was accumulated in the CCL while the ACL dried further (Figure 4.19), thus inducing more absorption and desorption of water. Note that this inductive process took place at frequencies similar to the "fast absorption/desorption" case in Figure 4.14b. Therefore, this second process at 0.2–5 Hz is likely associated with the ionomer-hydration dynamics in the catalyst layers rather than membrane hydration,
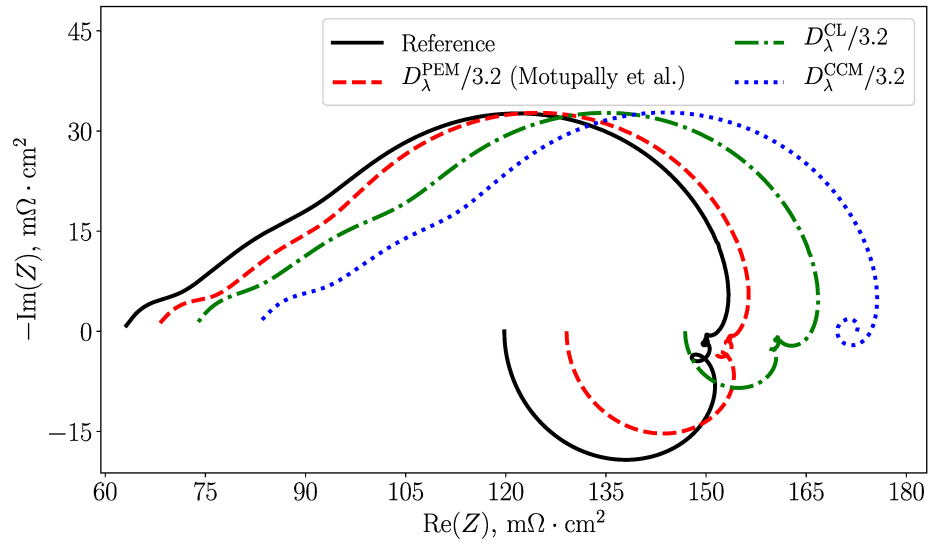
(a)
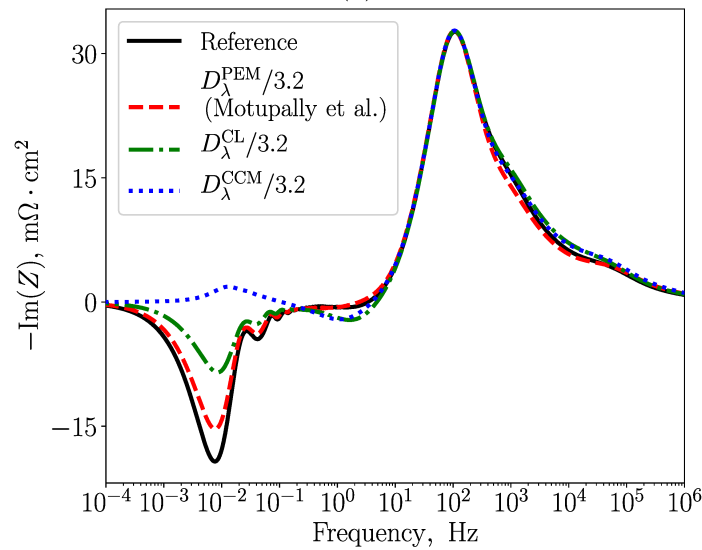


(b)

Figure 4.17: Effect of the back-diffusion coefficient of water in the electrolyte on the predicted impedance spectra: (a) Nyquist plot; (b) frequency-content plot of the negative imaginary part. The corresponding polarization and HFR curves are shown in Figure 4.18. The cell was operated at 80 °C, 1.5 atm, and 100% oxygen in the cathode flow (prior to humidification).
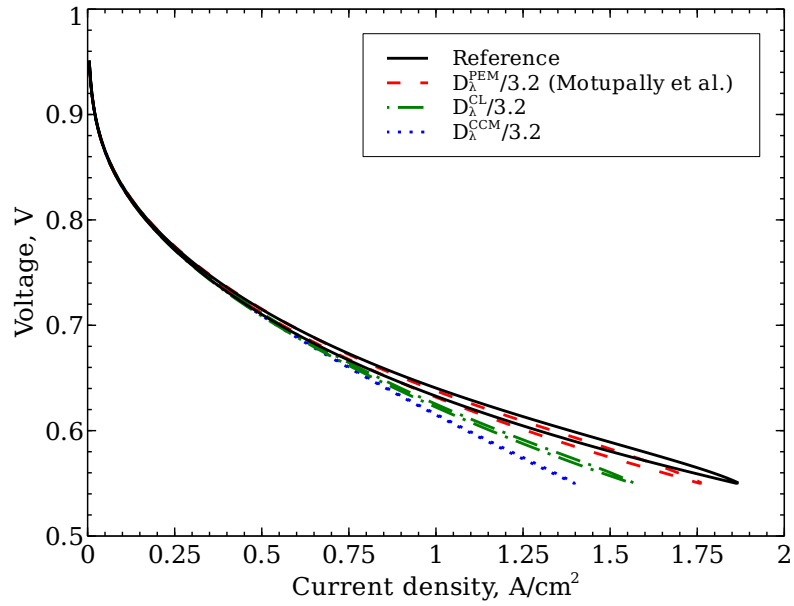
(a)
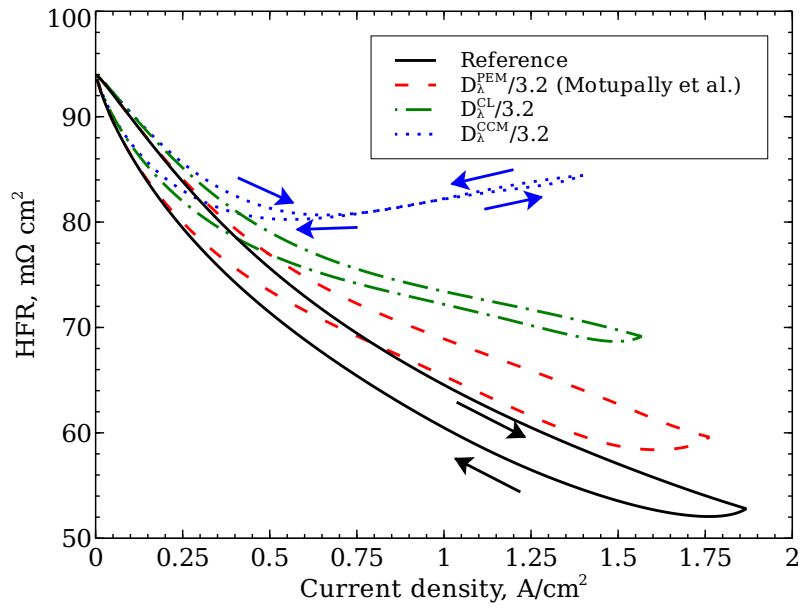


(b)

Figure 4.18: Effect of the back-diffusion coefficient of water in the electrolyte on the predicted polarization curve (a) and HFR (b). The cell was operated at 80 °C, 1.5 atm, and 100% oxygen in the cathode flow (prior to humidification).
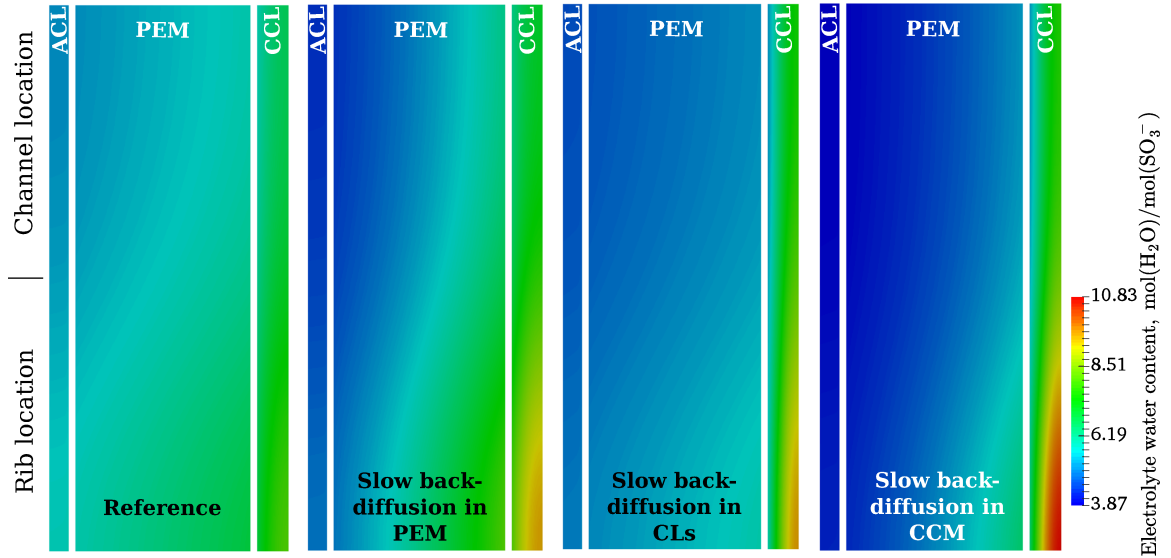
Figure 4.19: Comparison of the steady-state electrolyte-water-content distribution within the CCM at 1 A/cm$^2$ with varied back-diffusion coefficient of the absorbed water (the domains were upscaled along the horizontal axis by a factor of 10 and gaps between the layers were added for clarity). Left to right: reference case, $D_\lambda$ reduced by a factor of 3.2 in the membrane, $D_\lambda$ reduced by a factor of 3.2 in the catalyst layers, and $D_\lambda$ reduced by a factor of 3.2 in the whole CCM. The cell was operated at 80 °C, 1.5 atm, 50% RH, and 100% oxygen in the cathode flow (prior to humidification).

with a stronger effect of the better-hydrated CCL since the dominating behavior at the given frequencies is inductive.

## 4.4   Conclusion

The single-phase version of the open-source, transient 2D PEMFC model developed in Chapter 2 was used in this Chapter to analyze dynamic water management in fuel cells and its effect on their inductive behavior. A distinct feature of the model is its ability to reproduce the experimentally measured dynamic polarization, resistance, and impedance data with a single parameter set.

The developed model was used to perform a comprehensive analysis of the inductive phenomena observed in fuel cells, which has not been addressed in the literature with a detailed physical model. The study shows that there are two distinct inductive

processes in the fuel-cell-impedance spectra that are related to the electrolyte hydration, one at 0.1–200 mHz and another at 0.2–5 Hz. Parametric studies performed in this work help deduce the nature of these inductive processes.

The first process occurring at 0.1–200 mHz strongly depends on the electrolyte-conductivity dynamics in the CCM. This inductive behavior only appears when non-zero rates of exchange of water between the ionomer and the pores are used in the model. The size of the respective inductive loop directly depends on the magnitude of these rates and the ratio of the diffusive to osmotic fluxes of the absorbed water. If back-diffusion of water is weak, this inductive process is transformed into a capacitive process. An inductive loop in this frequency range had been previously reported in experimental [196, 203] and numerical [159, 196] studies, and it can also be seen, in part, in the experimental data reported in this work.

The second process at 0.2–5 Hz induces a minor inductive loop of negligible size, which becomes larger when a weaker back-diffusion of water (stronger osmotic drag) is used in CLs. The water-diffusion analysis shows that this loop is associated with the hydration and ionomer-conductivity dynamics in the catalyst layers.

Water management was also shown to affect the high-frequency portion of the spectrum. Impedance at 100 Hz–1 MHz appeared to be highly sensitive to the interfacial water-exchange kinetics in the ionomer of the catalyst layers, with a stronger capacitive behavior indicating faster interfacial transport of water and a lower water content in the ionomer.

The ohmic-heating-based approach proposed by Secanell et al. [328] and Zhou et al. [35, 276] for calculating ohmic resistance of the individual fuel-cell components was validated in this work. The ohmic-resistance breakdown performed with the model showed that the high-frequency resistance contains membrane resistance and electronic resistance of other components, but does not include protonic resistance of the platinum-on-carbon catalyst layers and thus is not equivalent to the total ohmic resistance of the cell.

# Chapter 5

# Estimating Charge-Transport Properties of Fuel-Cell and Electrolyzer Catalyst Layers via Electrochemical Impedance Spectroscopy[1]

Electrochemical impedance spectroscopy is the most common experimental technique for measuring the charge-transport properties of catalyst layers [45, 120, 122, 124–127, 173–177, 184, 185, 188–190, 196, 413, 416–428]. Such a measurement relies on fitting the impedance spectrum with analytical impedance expressions. To date, a study that examines the suitability of the analytical models from references [177, 182, 183] for such an analysis does not exist. In this Chapter, a numerical one-dimensional catalyst-layer model is used to assess the appropriateness of the analytical models for estimating catalyst-layer charge-transport properties. An ohmic-heating-based approach to computing ohmic resistance is used to examine the relationship between conductivity, resistance, and impedance of various uniform and nonuniform catalyst layers representative of those used in proton-exchange-membrane fuel cells and water

---

[1]Parts of this chapter are reproduced from the following publication:

1. A. Kosakian and M. Secanell, "Estimating charge-transport properties of fuel-cell and electrolyzer catalyst layers via electrochemical impedance spectroscopy," *Electrochimica Acta*, vol. 367, p. 137 521, 2021.

electrolyzers. The two-dimensional fuel-cell model from Chapter 4 is used to show that the anode catalyst layer may cause a distortion of the impedance spectrum at frequencies above 5 Hz that obstructs the charge-transport characterization of the cathode catalyst layer with analytical models.

## 5.1 Numerical Model

### 5.1.1 Catalyst-Layer Model

#### 5.1.1.1 Assumptions

The transient two-dimensional PEMFC model from Chapter 4 was reduced to a one-dimensional model of a catalyst layer. The simplifying assumptions, additional to those listed in Chapter 4, are given below:

1. the ionomer phase of the catalyst layer was assumed to have a constant and uniform conductivity;

2. transport of water in the layer was not considered;

3. the model is isothermal; temperature was assumed constant and uniform;

4. a macrohomogeneous catalyst-layer model was assumed [262] (the ICCP model from Chapter 2 was not used).

Assumptions 1–3 were used in order to analyze the catalyst-layer impedance in isolation from other cell components and dynamic processes, such as polymer-electrolyte hydration and heat generation. The assumptions listed above allow for a direct comparison of the numerical model to the analytical expressions, which rely on similar simplifications.

### 5.1.1.2 Governing Equations

The model describes transport of oxygen, protons, and electrons in a cathode catalyst layer (CCL) of a PEMFC via the following set of governing equations:

$$\varepsilon_p c_{tot} \frac{\partial x_{O_2}}{\partial t} - \nabla \cdot \left( c_{tot} D_{O_2}^{eff} \nabla x_{O_2} \right) = -\frac{j}{4F}, \tag{5.1}$$

$$-C_{dl} \frac{\partial \left( \phi_{e^-} - \phi_{H^+} \right)}{\partial t} - \nabla \cdot \left( \sigma_{H^+}^{eff} \nabla \phi_{H^+} \right) = -j, \tag{5.2}$$

$$C_{dl} \frac{\partial \left( \phi_{e^-} - \phi_{H^+} \right)}{\partial t} - \nabla \cdot \left( \sigma_{e^-}^{eff} \nabla \phi_{e^-} \right) = j. \tag{5.3}$$

The equations above are given in a multidimensional form since the model considered in this Chapter is a derivative of the earlier developed 2D PEMFC model from Chapter 4 and is inherently multi-dimensional. The single spatial dimensionality was achieved by reducing the in-plane domain size to 0.1 μm. When reduced to equations (5.2) and (5.3), the model also represents a PEMWE anode catalyst layer operating under $H_2/N_2$ conditions (i.e., fed with nitrogen).

To retain consistency with analytical models [177, 182, 183], the volumetric faradaic current density in equations (5.1)–(5.3) was computed using Tafel kinetics (equation (2.52)). The developed numerical model also supports computation of the faradaic current density from the double-trap kinetic model for oxygen-reduction-reaction (ORR) on platinum (equation (2.51)). The two kinetic models are shown in this Chapter to produce the same catalyst-layer impedance at high frequencies, confirming that it is independent of the charge-transfer resistance.

### 5.1.1.3 Initial and Boundary Conditions

The initial solution for the transient problem given in equations (5.1)–(5.3) was obtained by first solving the governing equations at steady state and then importing the resulting solution into the transient simulation at $t = 0$. Boundary conditions listed in Table 5.1 reflect the fact that the anode, the proton-exchange membrane, the porous transport layer, and contact resistance are not considered in the CL model. The bulk oxygen molar fraction $x_{O_2}^0$ was computed with the ideal gas law for the

Table 5.1: Boundary conditions in the CL model ($\Gamma$ denotes a domain boundary).

| Solution variable | CL-PEM | CL-PTL | Symmetry |
|---|---|---|---|
| $x_{O_2}$ | no flux | $x_{O_2}(t, \Gamma) = x_{O_2}^0$ | no flux |
| $\phi_{H^+}$ | $\phi_{H^+}(t, \Gamma) = 0$ | no flux | no flux |
| $\phi_{e^-}$ | no flux | $\phi_{e^-}(t, \Gamma) = V(t)$ | no flux |

given operating conditions as discussed in reference [262]. The EIS simulations were performed by applying a time-dependent voltage $V(t)$ at the CL-PTL interface.

### 5.1.1.4 Model Inputs

Model inputs and operating conditions are listed in Table 5.2. The majority of the material properties and other inputs were taken from Chapter 4, except for the kinetic parameters for the Tafel equation (2.52). The selected kinetic parameters for the Tafel model were obtained by fitting the high operating current density in a Tafel plot, where a doubled Tafel slope was observed [309, 310]. When the double-trap model (2.51) was used, the kinetic parameters were taken to be the same as in Chapter 4. The layer properties given in Table 5.2 correspond to an inkjet-printed catalyst layer with platinum loading of about 0.15 mg/cm² and Nafion® loading of 30 wt% and were either measured experimentally or computed for the given operating conditions as discussed in Chapters 2 and 4.

Protonic- and electronic-conductivity values were varied in order to investigate the effect of charge transport in both conductive phases of uniform fuel-cell and electrolyzer CLs on the impedance spectrum. Case I in Table 5.3 corresponds to the effective charge-transport properties computed for a Pt/C PEMFC CL in Chapter 4. The reference protonic conductivity in case I corresponds to the average absorbed-water content of 4 $\text{mol}_{H_2O}/\text{mol}_{SO_3^-}$ in a vapor-equilibrated CL at 50% RH. Since ionomer-hydration effects were neglected, the same protonic conductivity was used at all current densities considered in this work, thus allowing for an unambiguous attribution of the impedance-spectrum changes to the varied current distribution in the

layer rather than to the complex hydration effects. Twice lower protonic conductivity (corresponding to 3 $mol_{H_2O}/mol_{SO_3^-}$, 30% RH) was used in case II to highlight its effect on the length of the linear high-frequency feature in the catalyst-layer impedance spectrum. Cases III and IV were designed to illustrate the shape of the spectrum when the conductivity of both conductive phases is either high or low, respectively. The protonic conductivity used in case III was made higher than the conductivity of a liquid-equilibrated Nafion® membrane [116] to eliminate protonic-resistance contribution to impedance. The electronic conductivity in case IV reflects the lower $\sigma_{e^-}^{eff}$ reported for iridium-based catalyst layers for PEMWE anodes [408]. Protonic- and electronic-conductivity values were swapped in case V, mirroring case I. As it will be shown in this Chapter, swapping conductivities does not affect the catalyst-layer impedance spectrum (in line with the analytical models from references [182, 574]). Therefore, analysis of the spectra simulated with the model inputs from Table 5.3 reflects the conductivity relationships of not only PEMFC CLs and PEMWE CCLs ($\sigma_{e^-}^{eff} > \sigma_{H^+}^{eff}$), but also PEMWE ACLs ($\sigma_{e^-}^{eff} \lessapprox \sigma_{H^+}^{eff}$, swapped cases I–IV).

The effect of macroscopic catalyst-layer nonuniformity on the impedance spectrum was analyzed by varying the ionomer distribution along the CL thickness. Continuous conductivity distributions have been commonly considered in the impedance-modeling literature, such as exponential [404, 405, 438, 576] and linear [173] distributions and a distribution with an inflection point [577]. At the same time, multilayered (graded) CLs have been a focus in a number of experimental investigations [417, 435, 446–448]. Analytical modeling of such layers (with sharp changes in the composition) is difficult, and simulation of their impedance is best performed numerically.

A graded catalyst layer was considered in this work with five through-plane zones, each 0.9-μm-thick and containing a different amount of ionomer (the average ionomer content was the same in all cases). Local nonuniformities that may appear between the sublayers during the fabrication of a graded CL were not considered in this work. The ionomer-loading distributions and the corresponding effective protonic conductivities

Table 5.2: Model inputs for the CL model.

| Property/parameter | Value/expression | Details |
|---|---|---|
| Operating temperature, $T$, K | 353.15 | Chapter 4 |
| Operating pressure, atm | 1.5 | Chapter 4 |
| Relative humidity | 0.5 | Chapter 4 |
| Bulk molar fraction of oxygen prior to humidification | 0.21 ($H_2/O_2$EIS), $10^{-10}$ ($H_2/N_2$ EIS) | Assumed |
| Catalyst-layer thickness, μm | 4.5 | Chapter 4 |
| Catalyst-layer porosity, $\varepsilon_{p}$ | 0.53 | Chapter 4 |
| Effective oxygen diffusivity, $D_{O_2}^{\mathrm{eff}}$, $cm^2/s$ | 0.0185[a] | Chapter 4 |
| Effective proton conductivity, $\sigma_{H^+}^{\mathrm{eff}}$, S/cm | Table 5.3 | Varied |
| Effective electron conductivity, $\sigma_{e^-}^{\mathrm{eff}}$, S/cm | Table 5.3 | Varied |
| Volumetric double-layer capacitance, $C_{\mathrm{dl}}$, $F/cm^3$ | 54 | Chapter 4 |
| Henry's law constant for oxygen in Nafion®, $H_{O_2,N}$, $Pa\,cm^3/mol$ | $3.1664 \cdot 10^{10}$ | Ref. [575] |
| Reference oxygen concentration, $c_{O_2}^{\mathrm{ref}}$, $mol/cm^3$ | $5 \cdot 101325/H_{O_2,N}$ | Ref. [309] |
| Exchange current density, $i_0$, $A/cm_{\mathrm{cat}}^2$ | $3.08 \cdot 10^{-6} \exp\left(-\frac{28920.95}{R}\left(\frac{1}{T} - \frac{1}{323.15}\right)\right)$ | Ref. [36][b] |
| Active area, $A_{\mathrm{v}}$, $cm_{\mathrm{cat}}^2/cm^3$ | 212,000 | Chapter 4 |
| Oxygen reaction order, $\gamma$ | 1 | Ref. [36, 310] |
| Charge-transfer coefficient, $\alpha$ | 0.5 | Ref. [36] |

[a] Includes Knudsen effects as discussed in Chapter 4.

[b] The exchange-current-density equation was fitted by Moore et al. [36] to the experimental data from Parthasarathy et al. [309] with different values of the reference temperature and the pre-exponential factor. Those experimental data, however, do not match those in another publication by Parthasarathy et al. [310]. The equation for $i_0$ shown here produces the exchange current density between the experimental values found in references [309, 310].

Table 5.3: The uniform-CCL properties varied between the considered cases.

| Case | $\sigma_{\mathrm{H^+}}^{\mathbf{eff}}$, mS/cm | $\sigma_{\mathrm{e^-}}^{\mathbf{eff}}$, mS/cm |
|------|------|------|
| I | 2.00 | 3788 |
| II | 1.00 | 3788 |
| III | 2000 | 3788 |
| IV | 2.00 | 37.9 |
| V | 3788 | 2.00 |

are given in Figure 5.1, where the uniform distribution corresponds to case I. The transport properties of the layer were computed with the relations from Chapters 2 and 4 to automatically account for structural variations. The electronic conductivity remained the same as in case I (the volume fraction of the electronically conductive phase was about 0.30 in all cases). Porosity varied between 0.37 and 0.63, which translated into an effective diffusivity that was about 2 times lower and 1.4 times higher than in the reference case.

The effect of catalyst distribution was analyzed in isolation from ionomer content by considering a graded catalyst layer with nonuniform active area. In each of the five CL zones, $A_{\mathrm{v}}$ was scaled by the same factors as ionomer loading in Figure 5.1a. Because double-layer capacitance is related to active area, it was also scaled by the same factors. The active-area and capacitance distributions used in the simulations are shown in Figure 5.2. All other catalyst-layer properties were taken from the uniform case I.

### 5.1.1.5 Solution Approach and Post-Processing

The transient catalyst-layer model was implemented in the open-source, in-house fuel-cell modeling software OpenFCST [374, 375] based on the finite-element library deal.II [380–382]. The implicit Euler (BDF1) method was used for the temporal discretization, and the time-step size was automatically adjusted by Richardson extrapolation (Section 2.2.1.3) with the relative solution-error tolerance of $10^{-3}$. The
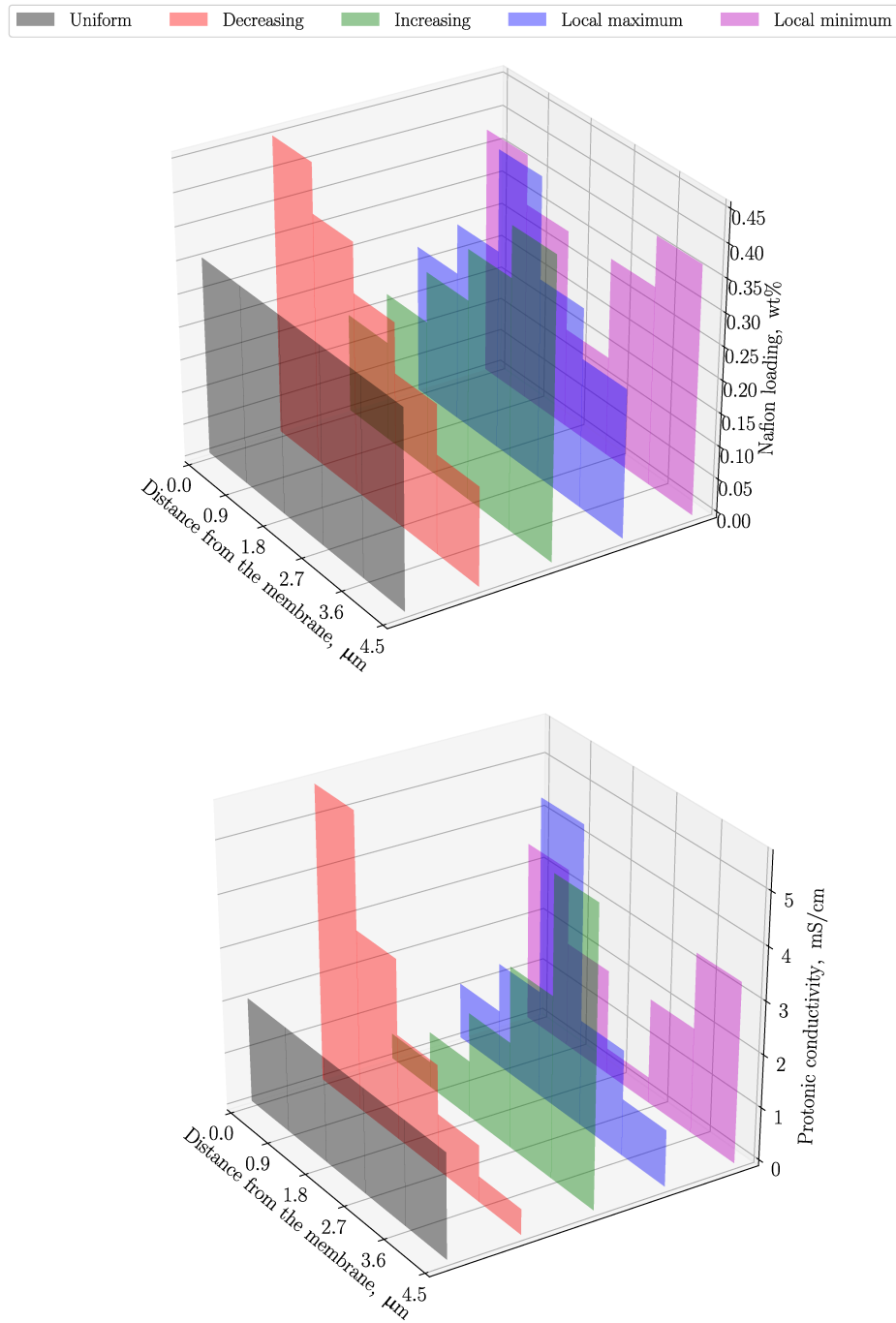
Figure 5.1: Illustration of the nonuniform-catalyst-layer property distributions used in this work: a) ionomer loading; and b) effective protonic conductivity. The resulting ionomer-to-carbon weight ratio and ionomer volume fraction varied from 0.29 to 1.4 and from 0.07 to 0.33, respectively.
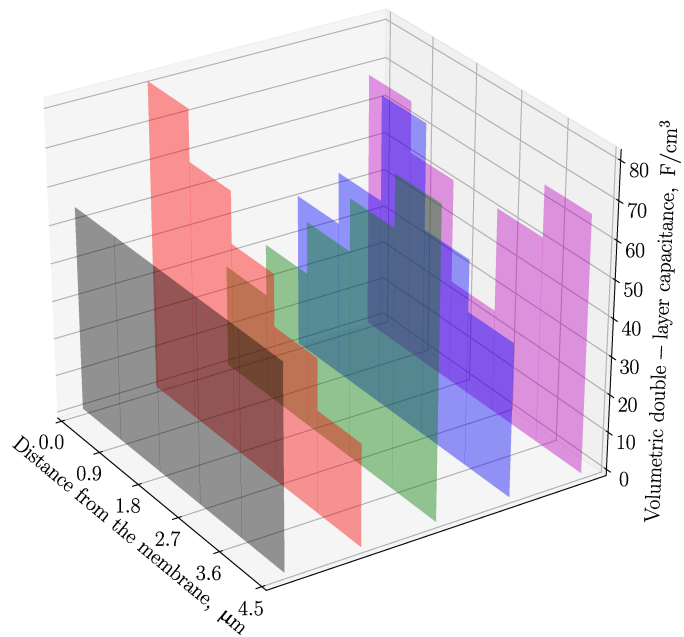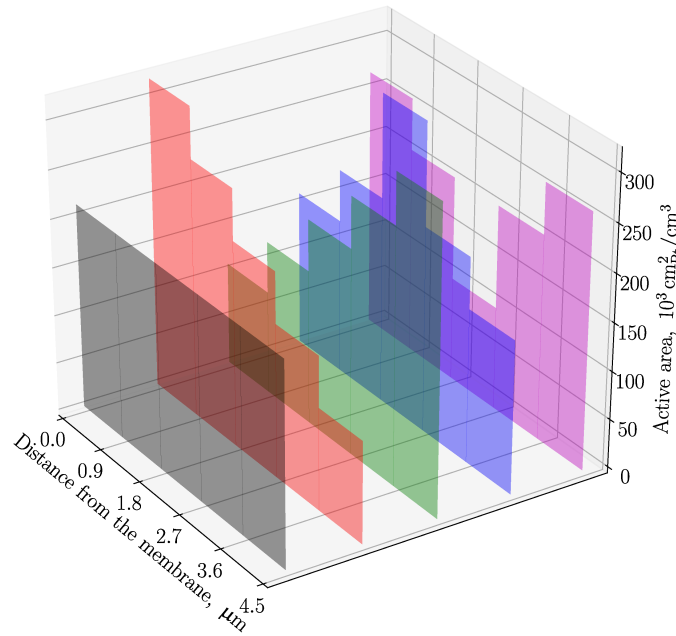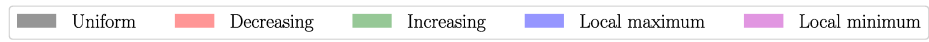
Figure 5.2: Illustration of the nonuniform-catalyst-layer property distributions used in this work: a) active area; and b) volumetric double-layer capacitance.
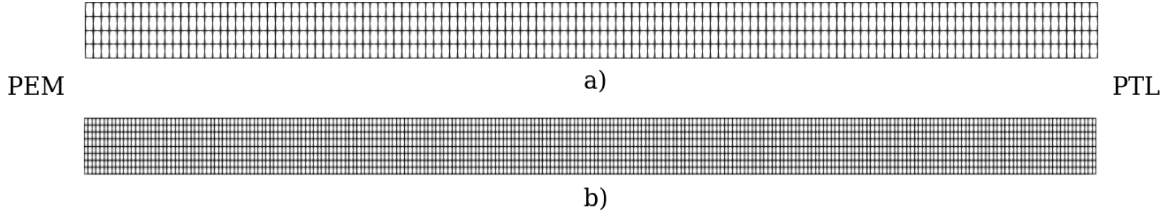
Figure 5.3: The computational grids used for the numerical catalyst-layer model: a) cases I–IV; b) case V. The domains were upscaled vertically by a factor of 5 for clarity.

finite-element method with second-order Lagrange shape functions was used for the spatial discretization that resulted in a problem with 1,935 and 6,939 degrees of freedom depending on the model inputs. The respective computational grids are shown in Figure 5.3. The coarse mesh contained a single cell in the vertical direction; more cells appear in that direction in Figure 5.3 due to the spatial discretization and mesh refinement. Newton's method with the relative solution-error tolerance of $10^{-4}$ was used to linearize the problem. Mesh-refinement studies were performed, and the produced DC current density and the computed electronic and protonic resistances were the same between the refinement levels (up to 6 significant digits), indicating accurate numerical solution.

The $H_2/O_2$ impedance spectra were computed by simulating a current-density response to a fast, 1-ns-long linear ramp of 1 mV in voltage followed by a $10^4$–$10^6$-s long voltage hold (typically several orders of magnitude longer than required to achieve a new steady state). The initial and final voltages were chosen such that the respective current densities were within 1% of the target operating value. Details about this method can be found in Section 2.3.1.2. This rapid-EIS approach was shown in Chapter 4 and in reference [249] to be equivalent to the conventional sine-wave approach to EIS. The time-step size was gradually increased from the initial value of $10^{-10}$ s by 1% between the time layers, which was found sufficient in terms of the numerical accuracy of the resulting spectra (see Figure 4.5 and note that only capacitive behavior is of interest in this Chapter). Each impedance spectrum was

computed as the ratio of non-equispaced Fourier transforms [549] of the voltage and current-density signals for 2,000 logarithmically spaced frequencies between $10^{-6}$ and $10^7$ Hz. The numerical error in the simulated impedance spectra was the highest at the highest frequencies (10 kHz to 10 MHz) but was found insignificant compared to the size of the spectra and their linear high-frequency portions in particular.

To simulate the $H_2/N_2$ spectra, the oxygen molar fraction at the boundary with the gas-diffusion layer was reduced to $10^{-10}$ and the steady-state voltage was set to 0.9 V. The resulting faradaic current density was of the order of $10^{-12}$ A/cm$^2$ in both steady-state and transient simulations and was considered sufficiently small to approximate the oxygen-free operation. Numerical simulations with zero faradaic current density were not possible due to the coupling of the governing equations (5.1)–(5.3) via electrochemical kinetics. The capacitive current density was of the order of $10^{-5}$–1 A/cm$^2$ during the entire sinusoidal transients, depending on the applied voltage frequency. Therefore, the overall current was capacitive, as expected for $H_2/N_2$ conditions. The rapid-EIS approach was found inefficient in the $H_2/N_2$ simulations, as the time-step size was severely restricted by the Richardson-extrapolation algorithm. Instead, the $H_2/N_2$ spectra were computed by simulating sinusoidal voltage waves at 134 frequencies between 1 and $10^7$ Hz with the peak-to-peak amplitude of 1 mV. At each frequency, 5 wave periods were generated and resolved with 1024 points per period for numerical accuracy. The current-density response, scaled with the Welch window function [534] to minimize aliasing, was processed with the Fast Fourier Transform (FFT) from SciPy [486]. The frequency content of current density had a clear peak at the frequency of the voltage input. Spectral leakage due to numerical error was filtered out by taking the current-density frequency to be the frequency at which the FFT magnitude reached maximum. Impedance was then computed as the ratio of the known voltage phasor to the reconstructed current-density phasor. Depending on the input frequency, the chosen model parameters resulted in a frequency match between the current output and the voltage input within 0.01–0.1% in the whole range of the

considered frequencies (1 Hz to 10 MHz). As in the $H_2/O_2$ case, the numerical error in the simulated $H_2/N_2$ impedance spectra was found to be insignificant.

Ohmic resistance was computed in the numerical model through ohmic heating as discussed in Section 2.3. Note that equations (2.156) and (2.157) are prone to numerical error at close-to-zero current. At current density of the order of $10^{-12}$ A/cm$^2$ that was used to approximate $H_2/N_2$ operation, the potential gradients were also small, and, due to the limited-precision arithmetic, this resulted in numerically inaccurate ohmic-heating-based resistances. Nevertheless, the computed $H_2/N_2$ impedance agreed with the analytical predictions as will be shown later.

All simulations were performed using a single thread of an Intel® Xeon® E5-2690 v2 CPU at 3.00 GHz. The simulation time varied between 1 and 21 h depending on the chosen EIS approach and the model inputs. Each steady-state polarization curve took approximately 20–25 s of computational time.

### 5.1.2   Fuel-Cell Model

The two-dimensional PEMFC model from Chapter 4 was used with no changes except for the following two simplifications:

1. microporous layers were not included in the model;

2. catalyst layers were assumed to be macrohomogeneous [262].

The listed assumptions were made to reduce the computational time and had no effect on the generality of the impedance analysis presented in this work. All model inputs were taken the same as in Chapter 4 (353.15 K, 1.5 atm, 50% RH, pure-oxygen supply in the cathode). Spatial discretization with the finite-element method and the second-order Lagrange shape functions resulted in a problem with 54,390 degrees of freedom. Since high accuracy of the impedance spectrum was required, a higher mesh-refinement level was used as compared to that in Chapter 4. The computational grid is shown in Figure 5.4. Impedance spectra were simulated using
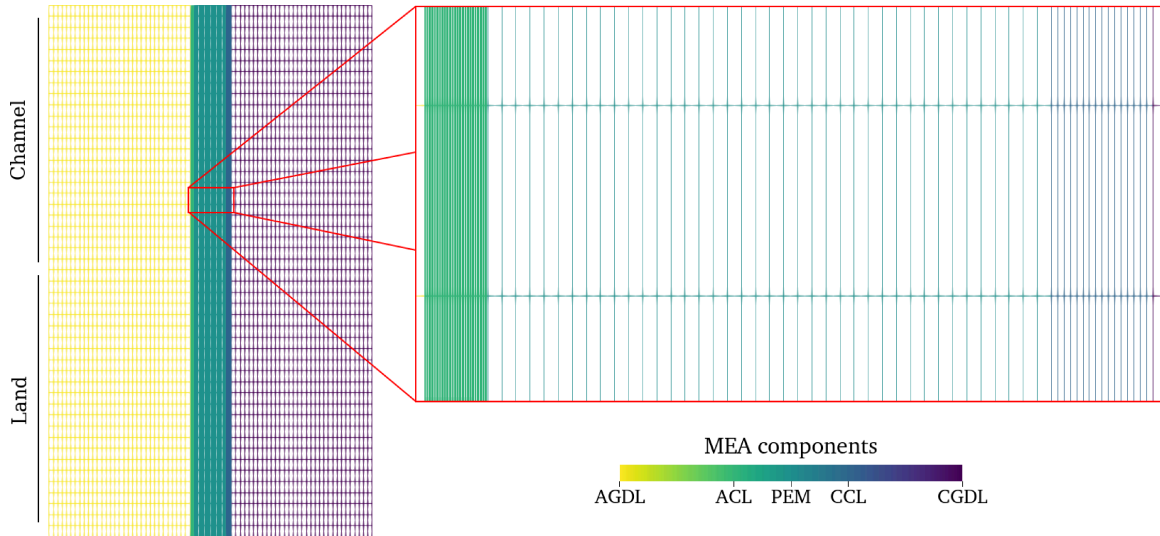
Figure 5.4: The computational grid used for the PEMFC model in this Chapter.

the rapid-EIS approach with the time-stepping algorithm discussed earlier in this Chapter. Computational time varied in the presented parametric studies between 11 and 36 hours using five threads of an Intel® Xeon® E5-2690 v2 CPU at 3.00 GHz.

## 5.2 Analytical Models for Uniform Catalyst Layers

The analytical expressions for the $H_2/O_2$ and $H_2/N_2$ impedance considered in this Section were derived in references [177, 182, 183] from 1D catalyst-layer models, similar to the one given by equations (5.1)–(5.3), under the assumption of the catalyst-layer uniformity. The main differences between the models by Eikerling and Kornyshev [183] (and Makharia et al. [177]) and by Kulikovsky [182] is the transmission-line representation of the catalyst layer and the assumption of high electronic conductivity in the former work, where carbon-supported PEMFC CLs were considered. The analytical impedance relations from references [177, 182, 183], as well as their assumptions and limiting cases, are discussed in detail in this Section.

Since the models considered here are for catalyst layers only, they cannot be applied directly to analyze experimental impedance spectra. In the PEMFC and PEMWE

EIS experiments, resistance of the membrane, the porous transport layers, the bipolar plates, and contact resistance are a part of the measured real impedance at all frequencies. If those resistances are known, they should be subtracted from the real impedance to obtain a spectrum that is representative of a catalyst layer. Such a correction is only valid under $H_2/N_2$ and low-current $H_2/O_2$ conditions (when the effects of other cell components, such as membrane hydration and gas transport in PTLs, are minimized) and when the reference-electrode effects are negligible (PEMFC anode and PEMWE cathode usually serve as a reference/counter electrode). Ohmic resistance of cell components can be measured independently (see references [578–582]), though contact resistance is difficult to estimate, as it may vary between cell assemblies. The analysis performed in this Section is for the catalyst-layer impedance in isolation from the effects of other cell components. Later in this Chapter, a numerical study analyzing the effect of the reference/counter electrode is performed with a PEMFC model.

## 5.2.1   $H_2/O_2$ Spectroscopy

### 5.2.1.1   Estimation of Proton-Transport Properties

The first equation describing impedance of an electrode pore is attributed to de Levie [583]. It was obtained from a transmission-line representation of a pore and is given (in $\Omega$) by [583]

$$Z_{\text{pore}} = \sqrt{Z_{\text{int}} R_{\text{pore}}} \coth \left( L_{\text{pore}} \sqrt{\frac{R_{\text{pore}}}{Z_{\text{int}}}} \right), \tag{5.4}$$

where $Z_{\text{int}}$ is the interfacial impedance in $\Omega \cdot \text{cm}$, $R$ is the ohmic resistance of the pore in $\Omega/\text{cm}$, and $L$ is the pore length in cm.

Eikerling and Kornyshev [183] considered a transmission-line representation of a cathode catalyst layer shown in Figure 5.5 and derived expressions of the form similar to equation (5.4) for various operating regimes of a fuel cell. For the $H_2/O_2$ operation at small current and under the assumptions of the catalyst-layer uniformity and the negligible electronic resistance (the latter is a fair simplification for the carbon-
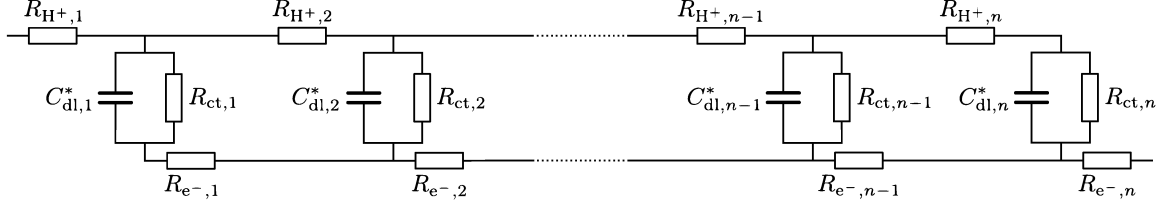
Figure 5.5: Transmission-line representation of a catalyst layer. The circuit is connected to the membrane at the left end and to the microporous/gas-diffusion layer at the right end. Oxygen-transport limitations are neglected.

supported catalyst layers), they found [183]

$$Z = \sqrt{R_{\mathrm{H}^+,i} Z_{\mathrm{int},i}} \coth\left(\sqrt{\frac{R_{\mathrm{H}^+,i}}{Z_{\mathrm{int},i}}} \frac{L}{L_{\mathrm{e}}}\right), \tag{5.5}$$

where

$$Z_{\mathrm{int},i} = \frac{R_{\mathrm{ct},i}}{1 + i\omega R_{\mathrm{ct},i} C^*_{\mathrm{dl},i}}, \tag{5.6}$$

$L$ and $L_{\mathrm{e}}$ are the thickness of the catalyst layer and the length of each link in the transmission line, respectively, $R_{\mathrm{H}^+,i}$ and $R_{\mathrm{ct},i}$ are in $\Omega \cdot \mathrm{cm}^2$, and $C^*_{\mathrm{dl},i}$ is in $\mathrm{F/cm}^2$.

Equation (5.5) is given in terms of the elementary resistances and capacitances of the circuit (the common index $i$ is used to emphasize the assumption of uniformity). Makharia et al. [177] rearranged equation (5.5) to obtain the impedance relation involving the macroscopic properties of the catalyst layer:

$$Z^{\mathrm{EKM}} = \sqrt{R^{\mathrm{EKM}}_{\mathrm{H}^+} Z^{\mathrm{EKM}}_{\mathrm{int}}} \coth\left(\sqrt{\frac{R^{\mathrm{EKM}}_{\mathrm{H}^+}}{Z^{\mathrm{EKM}}_{\mathrm{int}}}}\right), \tag{5.7}$$

where

$$Z^{\mathrm{EKM}}_{\mathrm{int}} = \frac{R^{\mathrm{EKM}}_{\mathrm{ct}}}{1 + i\omega R^{\mathrm{EKM}}_{\mathrm{ct}} C^{*\,\mathrm{EKM}}_{\mathrm{dl}}}, \tag{5.8}$$

$$R^{\mathrm{EKM}}_{\mathrm{H}^+} = R_{\mathrm{H}^+,i} \frac{L}{L_{\mathrm{e}}}, \quad R^{\mathrm{EKM}}_{\mathrm{ct}} = R_{\mathrm{ct},i} \frac{L_{\mathrm{e}}}{L}, \quad C^{*\,\mathrm{EKM}}_{\mathrm{dl}} = C^*_{\mathrm{dl},i} \frac{L}{L_{\mathrm{e}}}. \tag{5.9}$$

The "EKM" superscript (Eikerling-Kornyshev-Makharia) is used here to distinguish this result from the rest of the results discussed in this Chapter. Impedance (5.7) can be derived directly from the governing equations (5.1)–(5.3); an example derivation for the simple 1D case with fast oxygen and electron transport is given in Appendix C.

214

This analytical model has been used in the literature to estimate the catalyst-layer protonic resistance of low-temperature PEMFCs [174, 177] and high-temperature PEMFCs [424].

Ratio $L/L_e$ gives the number of the links considered in the transmission-line representation of the catalyst layer. Because it was assumed in reference [183] that the elementary protonic resistance is related to the macroscopic protonic conductivity through $R_{H^+,i} = L_e/\sigma_{H^+}^{eff}$, equation (5.9) suggests that the macroscopic protonic resistance is [177]

$$R_{H^+}^{EKM} = \frac{L}{\sigma_{H^+}^{eff}}.$$  (5.10)

At high frequencies, equation (5.7) is transformed into [183]

$$Z^{EKM} = \omega^{-1/2}\sqrt{\frac{R_{H^+}^{EKM}}{C_{dl}^{*\,EKM}}}\frac{\sqrt{2}}{2}(1-i).$$  (5.11)

Unlike equation (5.7), equation (5.11) is not restricted to small current [183]. Because the real and the negative imaginary parts of equation (5.11) are equal, it predicts a linear 45° branch in the spectrum. It is convenient to rewrite equation (5.11) as

$$\left|Z^{EKM}\right| = \omega^{-1/2}\sqrt{\frac{R_{H^+}^{EKM}}{C_{dl}^{*\,EKM}}}.$$  (5.12)

When the double-layer capacitance is known (for instance, from an independent measurement, such as cyclic voltammetry), equation (5.12) provides a simple way to extract $R_{H^+}^{EKM}$ from the slope of the experimental impedance magnitude plotted against $\omega^{-1/2}$. Equation (5.12) has been used to measure the catalyst-layer proton-transport properties of PEMFCs [122, 176] and direct-methanol fuel cells (DMFCs) [425, 426].

Eikerling and Kornyshev [183] provided some alternative forms of equation (5.7) that account for oxygen transport but are limited to either fast proton transport or negligible spatial gradients in the potential and oxygen distributions in the catalyst layer. Cruz-Manzo and Chen [403] generalized the impedance equation (5.7) by using constant-phase elements ($Z_{CPE} = \left(Q(i\omega)^\beta\right)^{-1}$, $\beta \in [0, 1]$) instead of capacitors ($Z_C = (i\omega C)^{-1}$) to account for nonuniform charge distribution in the catalyst layer due to

an electrochemical reaction. They also considered oxygen transport in their model; however, it does not directly affect the high-frequency spectrum (an indirect effect could occur through the ionomer hydration, which was not modeled).

### 5.2.1.2 Simultaneous Estimation of Proton- and Electron-Transport Properties

Kulikovsky [182] derived a more general expression (compared to equation (5.7)) for a 1D catalyst-layer impedance that accounts for the transport of protons, electrons, and oxygen (in $\Omega \cdot \text{cm}^2$):

$$Z^{\text{K}} = Z^{\text{K}}_{\text{ct+pe}} + Z^{\text{K}}_{\text{ox}}, \tag{5.13}$$

where

$$Z^{\text{K}}_{\text{ct+pe}} = \frac{L}{\sigma^{\text{eff}}_{\text{H}^+}} \frac{iq\sin(p) + (1+i)\left(2k_\sigma + (1+k_\sigma^2)\cos(p)\right)}{k_\sigma\left(iq - (1+i)p\right)\sin(p)}, \tag{5.14}$$

$$Z^{\text{K}}_{\text{ox}} = \frac{b(1-W)}{i\left(W - \frac{\omega^2}{\omega_{\text{ct}}\omega_0} + i\omega\left(\frac{1}{\omega_{\text{ct}}} + \frac{1}{\omega_0}\right)\right)\left(1 + \frac{i\omega}{\omega_{\text{ct}}}\right)},$$

$$p = \sqrt{-\left(\hat{i} + i\hat{\Omega}\right)\left(1 + \frac{1}{k_\sigma}\right)},$$

$$q = \sqrt{2k_\sigma\left(1 + k_\sigma\right)\left(i\hat{i} - \hat{\Omega}\right)},$$

$$k_\sigma = \frac{\sigma^{\text{eff}}_{\text{e}^-}}{\sigma^{\text{eff}}_{\text{H}^+}}, \quad \hat{i} = \frac{iL}{\sigma^{\text{eff}}_{\text{H}^+}b}, \quad \hat{\Omega} = \frac{\omega C_{\text{dl}}L^2}{\sigma^{\text{eff}}_{\text{H}^+}},$$

$$W = \frac{\tanh\left(\sqrt{\left(i + i4Fc^0L\omega\right)/i_{\text{ox}}}\right)}{\sqrt{\left(i + i4Fc^0L\omega\right)/i_{\text{ox}}}},$$

$$\omega_0 = \frac{i}{4Fc^0L}, \quad \omega_{\text{ct}} = \frac{i}{C_{\text{dl}}bL}, \quad i_{\text{ox}} = \frac{4FD^{\text{eff}}_{\text{O}_2}c^0}{L},$$

$i$ is the operating current density ($\text{A/cm}^2$), $b = RT/(\alpha F)$ is the Tafel slope (V), and $c^0$ is the oxygen concentration at the CL-PTL interface ($\text{mol/cm}^3$; corresponds to $x^0_{\text{O}_2}$ in Table 5.1). Here, $Z^{\text{K}}_{\text{ct+pe}}$ (denoted with the "K" superscript for Kulikovsky [182]) is the impedance due to charge-transfer and charge-transport processes taking place in the catalyst layer and $Z^{\text{K}}_{\text{ox}}$ is the impedance due to oxygen transport. Equation (5.13) can

be used to simultaneously fit electronic and protonic conductivity of the catalyst layer (after the measured impedance is corrected for other cell components, as discussed before). However, it has not been applied in the literature to analyze experimental impedance spectra.

When oxygen transport is fast or the applied frequency is sufficiently high, $Z_{ox}$ vanishes from equation (5.13) and the total impedance of the catalyst layer is given by equation (5.14). The latter, in contrast to equation (5.7), contains the high-frequency resistance of the catalyst layer, $R_{HF}^{CL}$, that can be found by taking the limit of $Z_{ct+pe}^{K}$ at $\omega \to \infty$ [182]:

$$R_{HF}^{K} = \frac{L}{\sigma_{H^+}^{eff} + \sigma_{e^-}^{eff}}. \tag{5.15}$$

Note that $R_{HF}^{CL}$ depends on both protonic and electronic conductivity. The reason for this is best illustrated with the transmission-line representation of the catalyst layer. When $\omega$ is large, capacitors in the transmission line shown in Figure 5.5 act as shorts. If electronic resistance is negligible, current flows through the electronically conductive network (the bottom line) and the observed $R_{HF}^{CL}$ is zero, as predicted by equation (5.11). In contrast, if the resistance of neither of the two conductive phases can be neglected, current flows through portions of each ohmic-resistance network. In this case, the observed $R_{HF}^{CL}$ is non-zero and is composed of a portion of the electronic resistance and a portion of the protonic resistance of the CL, as seen in equation (5.15). If one of the conductivities is known, the other one can be estimated from $R_{HF}^{CL}$ using equation (5.15).

The low-frequency limit of equation (5.13) gives the DC resistance of the catalyst layer [182]:

$$R_{DC}^{K} = \mathrm{Re}(Z^{K}(\omega \to 0)) = \frac{b}{i} + \frac{L}{3\sigma_{H^+}^{eff}} + \frac{L}{3\sigma_{e^-}^{eff}} + \frac{bL}{12FD_{O_2}^{eff}c^0}. \tag{5.16}$$

The four terms in the equation above describe the charge-transfer resistance, effective ohmic resistance due to proton and electron transport, and oxygen-transport

resistance. Note that the ohmic-resistance terms

$$R_{\mathrm{H}^+}^{\mathrm{K}} = \frac{L}{3\sigma_{\mathrm{H}^+}^{\mathrm{eff}}}, \quad R_{\mathrm{e}^-}^{\mathrm{K}} = \frac{L}{3\sigma_{\mathrm{e}^-}^{\mathrm{eff}}} \tag{5.17}$$

were derived directly from the governing equations and differ from equation (5.10) by a factor of 3.

The applicability of equation (5.13) is limited to small current densities that satisfy [182]

$$i \ll \min \left\{ i_{\mathrm{H}^+}^* = \frac{\sigma_{\mathrm{H}^+}^{\mathrm{eff}} b}{L}, \; i_{\mathrm{e}^-}^* = \frac{\sigma_{\mathrm{e}^-}^{\mathrm{eff}} b}{L}, \; i_{\mathrm{ox}} \right\}. \tag{5.18}$$

The characteristic current density for electron transport, $i_{\mathrm{e}^-}^*$, was not included in condition (5.18) in the original work [182], but must naturally appear in it in the general case when electronic resistance cannot be neglected. For the model inputs listed in Tables 5.2 and 5.3, condition (5.18) becomes $i \ll 0.1$ A/cm$^2$.

## 5.2.2 H$_2$/N$_2$ Spectroscopy

### 5.2.2.1 Estimation of Proton-Transport Properties

During the H$_2$/N$_2$ EIS measurements, no faradaic reaction occurs in the nitrogen-fed catalyst layer. In this case, impedance is obtained by assuming infinitely large charge-transfer resistance in equation (5.7) [177, 183]:

$$Z^{\mathrm{EKM}} = \sqrt{\frac{R_{\mathrm{H}^+}^{\mathrm{EKM}}}{\mathrm{i}\omega C_{\mathrm{dl}}^{*\,\mathrm{EKM}}}} \coth \sqrt{\mathrm{i}\omega R_{\mathrm{H}^+}^{\mathrm{EKM}} C_{\mathrm{dl}}^{*\,\mathrm{EKM}}}. \tag{5.19}$$

This analytical model has been actively used in the literature to extract the catalyst-layer protonic-transport properties from the impedance spectra of PEMFCs [120, 173–175, 177, 189, 190, 196, 416–418], DMFCs [427], and PEMWEs [429]$^2$.

At high frequencies, equation (5.19) is equivalent to equation (5.7), and thus equation (5.12) holds for H$_2$/N$_2$ EIS as well. As the frequency approaches infinity, impedance given by equation (5.19) approaches zero due to the assumption of

---

$^2$A generalized form of equation (5.19) with constant-phase elements was used in references [189, 196, 416, 417, 427].

high electronic conductivity of the catalyst layer. The Taylor-series expansion of equation (5.19) around zero frequency yields [177]

$$Z^{\text{EKM}} = \frac{R_{\text{H}^+}^{\text{EKM}}}{3} + \frac{1}{i\omega C_{\text{dl}}^{*\,\text{EKM}}}. \qquad (5.20)$$

As frequency tends to zero, impedance computed from equation (5.20) tends to the negative imaginary infinity. This results in a vertical line in the Nyquist plot located at $R_{\text{H}^+}^{\text{EKM}}/3$, which suggests that the protonic resistance of the CL is obtained by multiplying the length of the projection of the linear high-frequency impedance branch onto the real axis by 3 (this result can also be found in earlier works by Lefebvre et al. [438, 584]). Equation (5.20) has been used to estimate protonic resistance and conductivity of fuel-cell [122, 124–127, 184, 185, 188, 413, 419–422] and electrolyzer [414, 429] catalyst layers.

### 5.2.2.2 Simultaneous Estimation of proton- and Electron-Transport Properties

Because $H_2/N_2$ spectroscopy is a particular case of $H_2/O_2$ spectroscopy performed at zero oxygen concentration and at zero current, taking the limit of equation (5.13) at $i \to 0$ and $c^0 \to 0$ results in the following impedance for $H_2/N_2$ EIS [182]:

$$Z^{\text{K}} = \frac{L}{\sigma_{\text{H}^+}^{\text{eff}}} \frac{iq_0 \sin(p_0) + (1+i)\left(2k_\sigma + (1+k_\sigma^2)\cos(p_0)\right)}{k_\sigma\left(iq_0 - (1+i)p_0\right)\sin(p_0)}, \qquad (5.21)$$

where

$$p_0 = \sqrt{-i\hat{\Omega}\left(1 + \frac{1}{k_\sigma}\right)},$$

$$q_0 = \sqrt{-2k_\sigma(1+k_\sigma)\hat{\Omega}}.$$

This model was recently used to estimate electronic and protonic conductivity of Fe-N-C catalyst layers for PEMFCs [585].

Impedance computed with equation (5.21) is equivalent to that found from equation (5.13) at high frequencies and results in the same $R_{\text{HF}}^{\text{CL}}$ given in equation (5.15).

Expansion of equation (5.21) around $\hat{\Omega} = 0$ ($\omega = 0$) was not given in reference [182], but it is provided here (taking only the leading terms proportional to $\hat{\Omega}^{-1}$ and $\hat{\Omega}^{0}$):

$$Z^{\mathrm{K}} = \frac{L}{3\sigma_{\mathrm{H^+}}^{\mathrm{eff}}} + \frac{L}{3\sigma_{\mathrm{e^-}}^{\mathrm{eff}}} + \frac{1}{\mathrm{i}\omega C_{\mathrm{dl}}L}, \tag{5.22}$$

where the first two terms are the DC resistance of the catalyst layer:

$$R_{\mathrm{DC}}^{\mathrm{K}} = \mathrm{Re}(Z^{\mathrm{K}}(\omega \to 0)) = \frac{L}{3\sigma_{\mathrm{H^+}}^{\mathrm{eff}}} + \frac{L}{3\sigma_{\mathrm{e^-}}^{\mathrm{eff}}}. \tag{5.23}$$

When the catalyst layer is highly electronically conductive, equation (5.22) is equivalent to equation (5.20) (with $C_{\mathrm{dl}}^{*\,\mathrm{EKM}} = C_{\mathrm{dl}}L$). However, there is an important difference between these two impedance relations; it is illustrated in Figure 5.6. When electronic conductivity is not significantly higher than protonic conductivity (or the other way around), the catalyst layer will exhibit a perceptible high-frequency resistance (denoted as $R_{\mathrm{HF}}^{\mathrm{CL}}$). Equation (5.15) suggests that, for $R_{\mathrm{HF}}^{\mathrm{CL}}$ of a catalyst layer with a typical thickness of 1, 10, and 100 µm to be more than 1 mΩ·cm², protonic and electronic conductivities of the layer must be below 0.1, 1, and 10 S/cm. Correction of the spectrum with the measured high-frequency resistance of the cell, $R_{\mathrm{HF}}^{\mathrm{cell}}$, will result in a loss of information regarding $R_{\mathrm{HF}}^{\mathrm{CL}}$ and $R_{\mathrm{DC}}^{\mathrm{CL}}$. That is why it is important to obtain independent measurements of the ohmic resistance of other cell components (which will be equal to $R_{\mathrm{HF}}^{\mathrm{cell}} - R_{\mathrm{HF}}^{\mathrm{CL}}$) for the extraction of the catalyst-layer impedance from the overall spectrum. The appropriate correction of the spectrum will result in its shift to the left along the real axis by $R_{\mathrm{HF}}^{\mathrm{cell}} - R_{\mathrm{HF}}^{\mathrm{CL}}$, revealing the true $R_{\mathrm{HF}}^{\mathrm{CL}}$ and $R_{\mathrm{DC}}^{\mathrm{CL}}$. Analysis of the corrected spectrum with equations (5.19) and (5.20) will provide ohmic resistance equal to $R_{\mathrm{DC}}^{\mathrm{CL}} - R_{\mathrm{HF}}^{\mathrm{CL}}$ and will interpret it as a third of the effective protonic resistance of the catalyst layer (Figure 5.6a). If equations (5.21) and (5.23) are used, both $R_{\mathrm{HF}}^{\mathrm{CL}}$ and $R_{\mathrm{DC}}^{\mathrm{CL}}$ will be correctly identified and the latter will be composed of the effective protonic and electronic resistances (Figure 5.6b).

Equations (5.15) and (5.22) provide a more accurate (compared to equation (5.20)) graphical approach to estimating the proton-transport properties of the catalyst layers
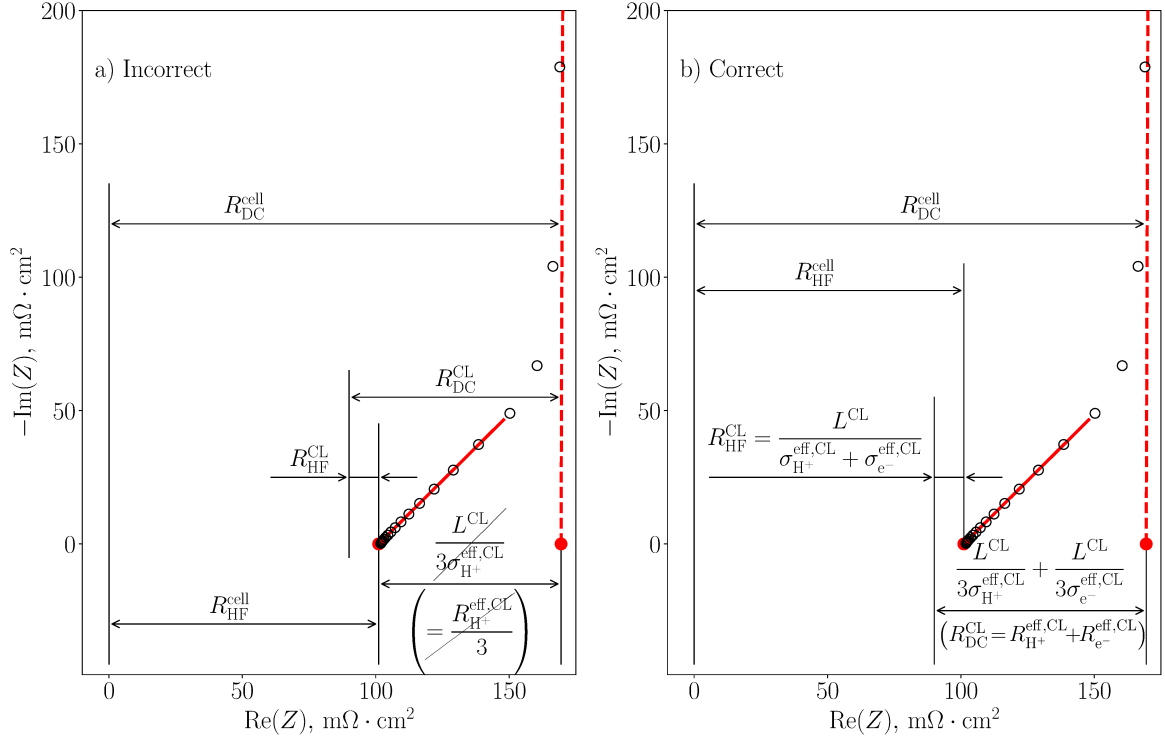
Figure 5.6: Illustration of the fitting procedure for an $H_2/N_2$ spectrum of a cell with uniform catalyst layers using the graphical approach when $\sigma_{e^-}^{\text{eff,CL}} \gg \sigma_{H^+}^{\text{eff,CL}}$ does not hold: a) incorrect interpretation with equation (5.20); b) correct interpretation with equations (5.15) and (5.22). Hollow markers represent the numerical catalyst-layer spectrum simulated for case IV (every fifth point is shown). A resistance of $90 \text{ m}\Omega \cdot \text{cm}^2$ (an estimate based on Chapter 4) was added to the real impedance component to illustrate the ohmic contribution of other cell components. Reference-electrode effects were assumed negligible. Solid and dashed red lines represent the linear high-frequency and low-frequency fits, respectively. The low-frequency fit was obtained with the data at 1–1.6 Hz ($\text{Im}(Z) > 4 \ \Omega \cdot \text{cm}^2$).

that is shown in Figure 5.6b. The protonic and electronic conductivities of the CL can be found by solving the system of algebraic equations (5.15) and (5.23). There are two pairs ($\sigma_{H^+}^{\text{eff}}$, $\sigma_{e^-}^{\text{eff}}$) that satisfy that system:

$$\sigma_{H^+}^{\text{eff}} = \frac{L}{2R_{\text{HF}}^{\text{K}}} \left( 1 \pm \sqrt{1 - \frac{4R_{\text{HF}}^{\text{K}}}{3R_{\text{DC}}^{\text{K}}}} \right), \quad (5.24)$$

$$\sigma_{e^-}^{\text{eff}} = \frac{L}{2R_{\text{HF}}^{\text{K}}} \left( 1 \mp \sqrt{1 - \frac{4R_{\text{HF}}^{\text{K}}}{3R_{\text{DC}}^{\text{K}}}} \right). \quad (5.25)$$

The fact that two pairs of distinct solutions to equations (5.15) and (5.23) exist means that two catalyst layers with the same but swapped protonic and electronic conductiv-

221

ities exhibit the same high-frequency spectrum. The numerical and analytical results of this work show that this is true, in fact, for the whole spectrum and holds in the frequency domain and at high current density as well. This is expected from equations (5.2) and (5.3), which are the same in $\phi_{H^+}$ for the protonic current and $\phi_{e^-}$ for the electronic current as long as $E_{th}$ is constant and uniform in the layer (i.e., under the isobaric, isothermal condition). Note that the expression under the square root in equations (5.24) and (5.25) is non-negative (due to non-negative conductivities) and becomes zero when $\sigma_{H^+}^{eff} = \sigma_{e^-}^{eff}$.

### 5.2.3 Fitting Approach

The impedance spectra computed through a direct numerical simulation of equations (5.1)–(5.3) were analyzed with the analytical relations given in equations (5.12), (5.14), (5.19), (5.20), (5.21), (5.24) and (5.25) in order to assess the ability of the latter to provide the correct charge-transport properties of the catalyst layers. Since only the ohmic properties were of interest, the analytical-model fitting was limited to the linear high-frequency portion of each impedance spectrum with the apparent 45° slope. This portion was identified as a part of the high-frequency spectrum where the $R_{HF}^{CL}$-corrected real part and the imaginary part were within 2% from each other. This helped reduce the effect of the error in the numerical high-frequency spectra on the quality of the analytical fits. Note that the small difference between the real and imaginary parts of the computed impedance in the high-frequency region was in line with the analytical predictions of the 45° branch that were discussed earlier. In experiments, fitting only high-frequency spectra might also be preferable due to the current or voltage drift, the effect of which on the measured spectrum becomes more severe as frequency is decreased. In order to ensure the intermediate region between the linear branch and the charge-transport arc was not included in the fitting, the latter was limited to data points with the real part below a certain threshold. That threshold, found through visual inspection of the spectra, was 120 m$\Omega\cdot$cm$^2$ in case IV

and 60 mΩ·cm$^2$ in other cases (except case III that was not fitted as discussed later). Only ohmic-resistance and conductivity values were treated as fitting parameters, and the rest of the model inputs were taken form Table 5.2.

Equation (5.12) was fitted to both H$_2$/O$_2$ and H$_2$/N$_2$ spectra using the linear least-squares regression algorithm available in SciPy [486]. The sequential least-squares programming method from SciPy [486] was used to fit the H$_2$/N$_2$ spectra with equation (5.19). The residual of the fitting was defined as

$$\text{Residual} = \sqrt{\frac{\sum_{n=1}^{N} \delta_{\text{Re}}^2(\omega_n) + \delta_{\text{Im}}^2(\omega_n)}{N}}, \tag{5.26}$$

where

$$\delta_{\text{Re}}(\omega) = \frac{|\text{Re}(Z_{\text{num}}(\omega)) - \text{Re}(Z_{\text{an}}(\omega))|}{|Z_{\text{an}}(\omega)|}, \tag{5.27}$$

$$\delta_{\text{Im}}(\omega) = \frac{|\text{Im}(Z_{\text{num}}(\omega)) - \text{Im}(Z_{\text{an}}(\omega))|}{|Z_{\text{an}}(\omega)|}, \tag{5.28}$$

and $N$ is the number of points in the portion of the spectrum to be fitted. Equations (5.14) and (5.21) were fitted to the H$_2$/O$_2$ and H$_2$/N$_2$ spectra, respectively, by minimizing the residual defined in equation (5.26). In this case, residuals were computed on a two-dimensional grid of 38–69 protonic and electronic conductivities spanning around the expected values. Then, the minimum point was found and refined by subsequently applying the Nelder-Mead (downhill simplex) minimization from SciPy [486]. The graphical approaches shown in Figure 5.6 were used to extract the protonic-transport properties from the H$_2$/N$_2$ spectra without any fitting as suggested by equations (5.20), (5.24), and (5.25). The position of the vertical low-frequency branch was determined from a linear fit of the 5 data points at the lowest frequencies of about 1–1.6 Hz.

Protonic-resistance estimates obtained with equations (5.12), (5.19), and (5.20) were converted into conductivity values using equation (5.10) in accordance with reference [183]. Protonic and electronic conductivities estimated with equations (5.14)

and (5.21) were converted into resistances using equation (5.23) as discussed in reference [182] and in this Chapter. The quality of the conductivity estimates was assessed by comparing the fitted values to the exact effective conductivities listed in Table 5.3. The fitted ohmic resistances were compared to the numerical predictions obtained through ohmic heating as shown in equations (2.156) and (2.157). The duality in the fitted conductivity and resistance values (that follows from equations (5.24) and (5.25)) was resolved by the appropriate choice of the initial guess or the search region in the fitting algorithms. In experiments, information on which phase of the catalyst layer is more conductive may not be available, and the aforementioned duality can only be resolved through additional independent measurements (for instance, by estimating the protonic conductivity with the hydrogen-pump technique [121, 415, 430–434] or the electronic conductivity with the four-probe method [120, 412, 415]).

The developed Python script for estimating catalyst-layer charge-transport properties with equations (5.14) and (5.21) and with the graphical method from Figure 5.6b has been made available at https://github.com/OpenFCST/EIS/archive/main.zip. Because catalyst-layer impedance is frequency-dependent, it is required that experimental data contain frequency of each impedance point. Thus, the fitting cannot be performed for those spectra in the literature that are reported only as Nyquist plots.

## 5.3   Results and Discussion

### 5.3.1   Validation of the Numerical Model

The numerical catalyst-layer model was first validated using the experimental impedance data measured by Makharia et al. [177] Two catalyst layers were considered, one with an ionomer-to-carbon weight ratio of 0.8 and another with a ratio of 0.4, both 13-$\mu$m-thick [177]. The respective effective protonic conductivities were obtained from the reported protonic resistance values using equation (5.10) (assumed by Makharia et al. in their resistance estimation) and were approximately 13.0 mS/cm and 5.53 mS/cm.

The volumetric double-layer capacitance was 16.2 F/cm$^3$ [177]. The operating conditions were 80 °C, 270 kPa, and 100% RH [177]. The rest of the model inputs were unchanged. All experimental spectra were corrected by Makharia et al. [177] for the external inductance and $R_{HF}^{cell}$. Since the catalyst layers were carbon-based, their electronic conductivity was relatively high, and the correction performed with the whole measured $R_{HF}^{cell}$ did not significantly affect the catalyst-layer impedance.

The simulated and the experimental spectra are compared in Figure 5.7. Only high-frequency data from reference [177] were considered, as impedance at low frequencies may have been affected by physical phenomena taking place in the cell components that are not accounted for in the model (for example, mass transport in gas-diffusion layers). A reasonable agreement was achieved under both $H_2/O_2$ and $H_2/N_2$ conditions. Frequency of only a handful of data points was reported in reference [177]; those points are shown in Figure 5.7 as filled markers (circles, squares, and diamonds) and are labeled. The points in the simulated spectra that correspond to the reported frequencies are marked with triangles and stars and are labeled. The simulated impedance points at 0.1, 1, and 10 kHz were in close proximity of their experimental counterparts. The discrepancy between the simulated and the experimental $H_2/N_2$ spectra at frequencies around and below 100 Hz may be due to hydrogen cross-over in the tested cell [173, 174, 586]. As expected, the simulated $H_2/N_2$ spectrum coincided with the $H_2/O_2$ spectrum at 5 mA/cm$^2$ in the shown frequency range.

An additional validation of the numerical model was performed by comparing the impedance spectra simulated for uniform catalyst layers to the spectra predicted by equations (5.13) and (5.21) with varied conductivities from Table 5.3. The $H_2/O_2$ spectra computed at 0.01 and 0.1 A/cm$^2$ are shown in Figures 5.8 and 5.9. In this Chapter, most spectra are reported in four plots for completeness and clarity. The Nyquist plots are provided in Figures 5.8a and 5.9a; they show the characteristic resistances, such as $R_{HF}^{CL}$ and $R_{DC}^{CL}$. The frequency-content plots in Figures 5.8b
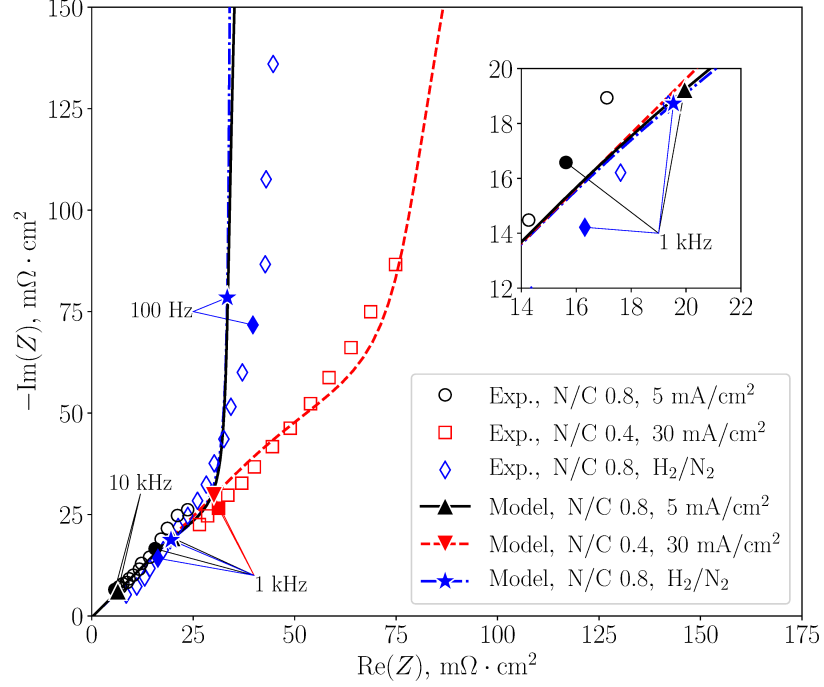
Figure 5.7: Comparison of the $H_2/O_2$ and $H_2/N_2$ spectra simulated numerically (lines) to those measured by Makharia et al. [177] Solid circles, squares, and diamonds represent experimental points for which frequency was reported. The corresponding simulated points are marked with triangles and stars.

and 5.9b display the frequency composition of the spectra, including the frequency of their main capacitive arcs. Inclusion of the frequency-content plot is required to eliminate the ambiguity of the Nyquist plot: multiple sets of cell properties can lead to the same Nyquist plot, but the frequency composition will differ [181]. The enlarged Nyquist plots in Figures 5.8c and 5.9c allow for a clear visualization of the high-frequency linear branches of the spectra and their $R_{HF}^{CL}$. The frequency composition of those branches is given in the enlarged plots (Figures 5.8d and 5.9d). The difference between the numerical and the analytical spectra was quantified with the relative residual

$$\delta_Z(\omega) = \sqrt{\delta_{Re}^2(\omega) + \delta_{Im}^2(\omega)}, \tag{5.29}$$

where $\delta_{Re}(\omega)$ and $\delta_{Im}(\omega)$ are defined in equations (5.27) and (5.28). Graphs of $\delta_Z(\omega)$ are provided in Figures 5.8e and 5.9e.

The agreement with the analytical model (5.13) was good at 0.01 A/cm$^2$ with

226

some minor deviations at frequencies below 10 Hz at 0.1 A/cm$^2$, in alignment with the limiting condition (5.18). Values of $\delta_Z(\omega)$ were below about 2% for frequencies up to 8 kHz in case V and up to at least 350 kHz in other cases. Discrepancy between the models increased as frequency approached 10 MHz. This was because of the diminishing impedance magnitude in cases I–III and V and the larger numerical error at high frequencies. In case IV, $R_{HF}^{CL}$ was about 11–12 m$\Omega \cdot$ cm$^2$, and $\delta_Z(\omega)$ did not exceed 4%. The relative residual $\delta_Z(\omega)$ was lower for case I than for case V that had swapped electronic and protonic conductivities (Figures 5.8e, 5.9e, and 5.10d). This was likely due to the different boundary conditions used for the protonic and electronic potentials (Table 5.1), which affected the numerical error differently in those two cases.

The agreement between the numerically simulated $H_2/N_2$ spectra and those computed with equation (5.21) was good (Figure 5.10). As expected, the high-frequency $H_2/N_2$ spectra in Figure 5.10b resembled those in the $H_2/O_2$ spectra at 0.01 A/cm$^2$ in Figure 5.8c. As in the $H_2/O_2$ spectra, the relative residual $\delta_Z(\omega)$ in the $H_2/N_2$ spectra generally increased as the frequency approached 10 MHz due to the decreasing impedance magnitude. The value of $\delta_Z(\omega)$ was below about 3% at all frequencies in cases III and IV. It did not exceed 3% for frequencies up to 1 MHz in case I, 550 kHz in case II, and 5 kHz in case V.

In all of the considered cases, the numerical model was also able to correctly predict the shape of the high-frequency portion of the spectrum. In agreement with equation (5.17) and Figure 5.6b, the length of the linear 45° branch increased as the protonic conductivity decreased between cases I and II. When both conductivities were high (case III), the real-axis projection of the linear branch became negligible at less than 0.04 m$\Omega \cdot$ cm$^2$. For the catalyst layer with poor electron conductivity (case IV), $R_{HF}^{CL}$ was about 11.9 m$\Omega \cdot$ cm$^2$ and was significant compared to the overall length of the linear branch. This value was reasonably close to the theoretical result of 11.3 m$\Omega \cdot$ cm$^2$ found from equation (5.15). Due to the sensitivity of $R_{HF}^{CL}$ to the nu-
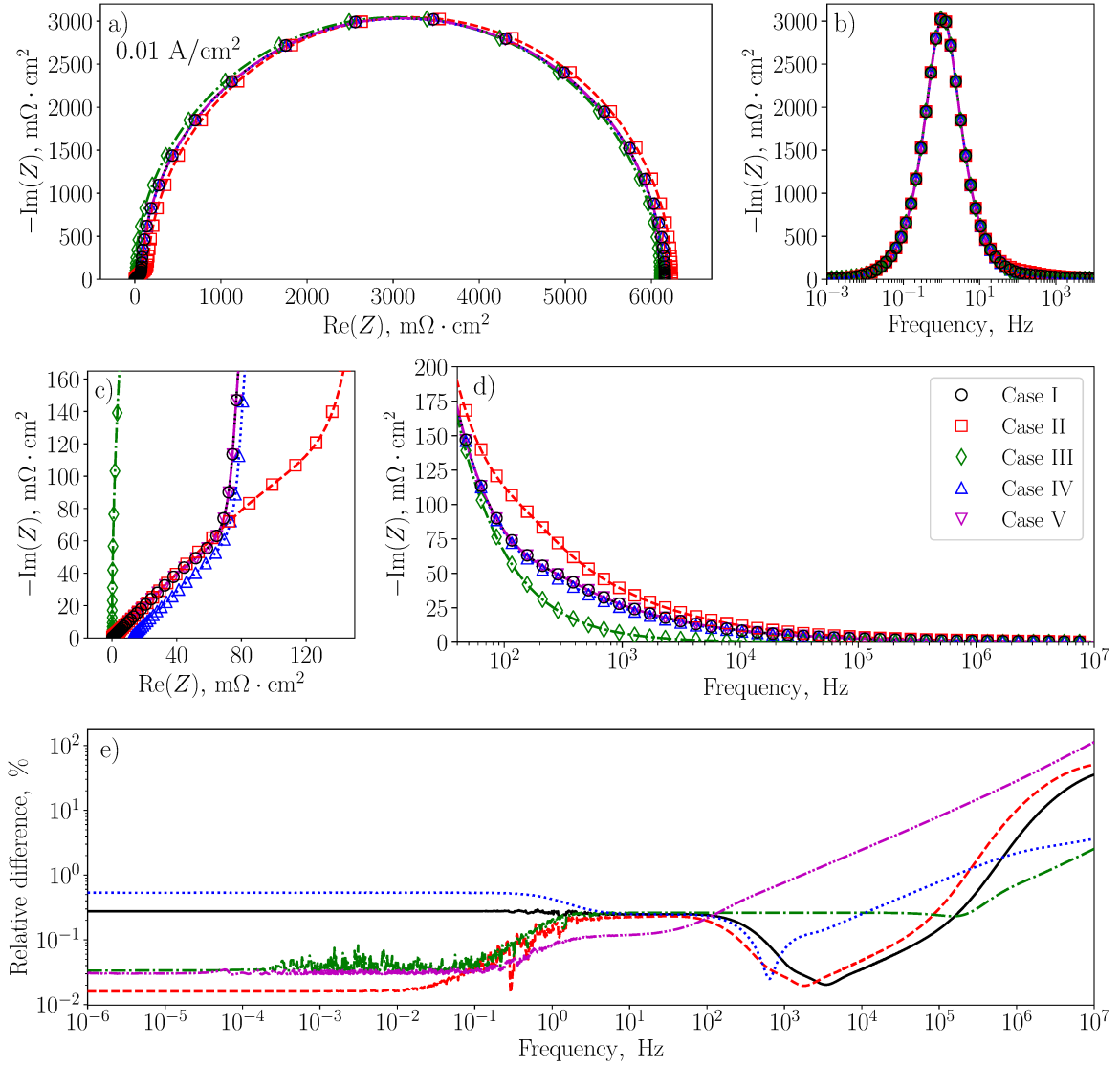
Figure 5.8: Comparison of the $H_2/O_2$ spectra simulated numerically (markers) to those computed analytically with equation (5.13) (lines) at 0.01 A/cm$^2$: a), c) Nyquist plot and its high-frequency portion; b), d) frequency-content plot of the imaginary impedance component and its high-frequency portion; e) relative residual (5.29). Every twentieth point is shown for clarity.
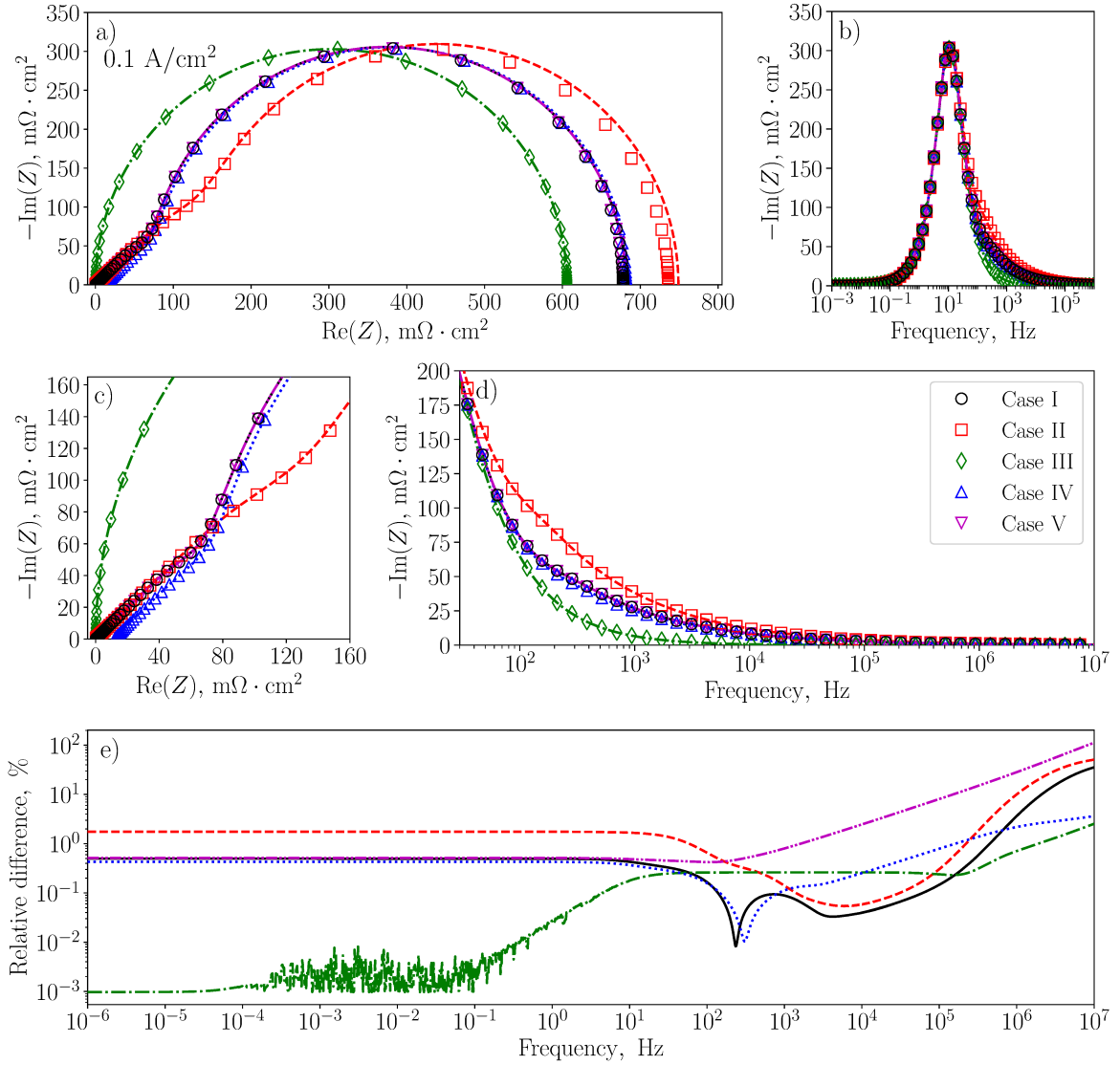
Figure 5.9: Comparison of the $H_2/O_2$ spectra simulated numerically (markers) to those computed analytically with equation (5.13) (lines) at 0.1 A/cm$^2$: a), c) Nyquist plot and its high-frequency portion; b), d) frequency-content plot of the imaginary impedance component and its high-frequency portion; e) relative residual (5.29). Every twentieth point is shown for clarity.
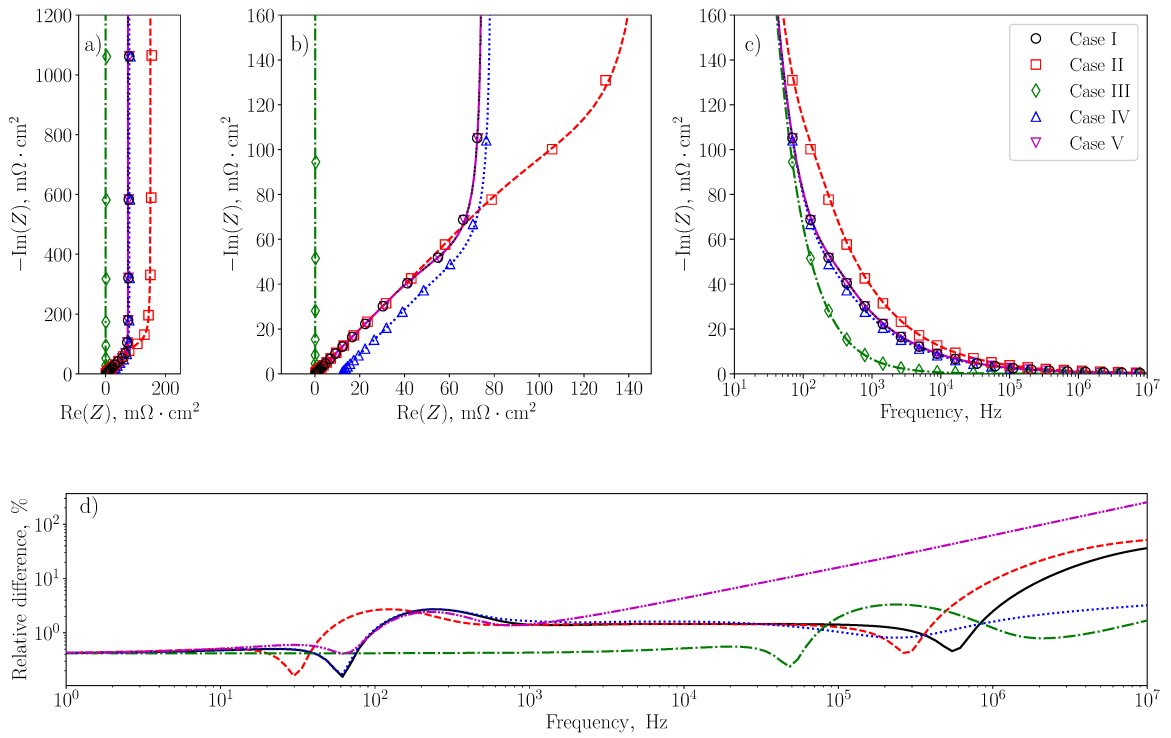
Figure 5.10: Comparison of the $H_2/N_2$ spectra simulated numerically (markers) to those computed analytically with equation (5.21) (lines): a), b) Nyquist plot and its high-frequency portion; c) frequency-content plot of the imaginary impedance component (high-frequency portion); d) relative residual (5.29). Every fifth point is shown for clarity.

merical error, it is not reported for other parametric cases, where this resistance was about $0.1 \ \text{m}\Omega \cdot \text{cm}^2$ or less. The impedance spectra for cases I and V were visually indistinguishable, as these cases reflected two catalyst layers with swapped protonic and electronic conductivities. This was expected from the discussion of equations (5.24) and (5.25).

### 5.3.1.1 Effect of High Current Density

Applicability of the analytical model (5.13) is limited by condition (5.18). As expected from that condition, discrepancy between the numerical and the analytical predictions increased as the current density exceeded the validity range of equation (5.13), as demonstrated in Figures 5.11 and 5.12.

## 5.3.2 Effect of Multi-Step Kinetics

Depending on the catalyst-layer properties and on the operating conditions, faradaic processes may take place at frequencies similar to those at which the linear 45° branch is observed, making it difficult to separate faradaic and charge-transport phenomena [436]. The frequency and the current density at which the linear impedance branch becomes independent of the faradaic processes (and thus of the reaction mechanism) was estimated analytically and numerically for PEMFCs operating under $H_2/O_2$ conditions.

The analytical estimation given next was inspired by the discussion in reference [436]. The characteristic angular frequency of a charge-transport process can be approximated as a reciprocal of the characteristic time constant $\tau = RC$ [55, 56] of a parallel $RC$ circuit consisting of a double-layer capacitor and an ohmic resistor with resistance equal to the sum of the protonic and electronic resistances in equation (5.17):

$$\omega_\Omega = \frac{3\sigma_{\text{H}^+}^{\text{eff}} \sigma_{\text{e}^-}^{\text{eff}}}{\left(\sigma_{\text{H}^+}^{\text{eff}} + \sigma_{\text{e}^-}^{\text{eff}}\right) C_{\text{dl}} L^2}. \tag{5.30}$$

Note that this frequency represents the lower bound of the charge-transport-frequency estimate (that is of interest in this analysis), as it is lower than the characteristic
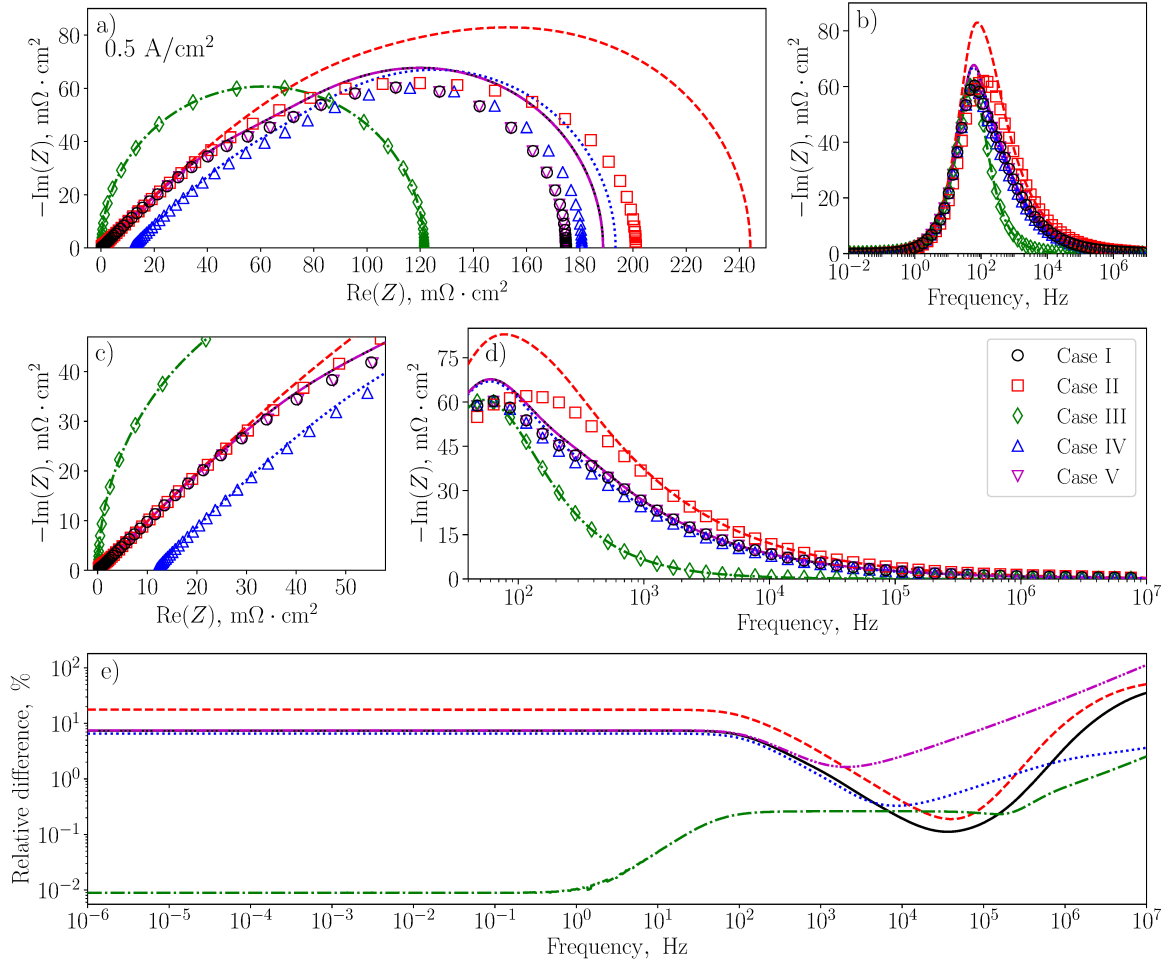
Figure 5.11: Comparison of the $H_2/O_2$ spectra simulated numerically (markers) to those computed analytically with equation (5.13) (lines) at 0.5 A/cm$^2$: a), c) Nyquist plot and its high-frequency portion; b), d) frequency-content plot of the imaginary impedance component and its high-frequency portion; e) relative residual (5.29). Every twentieth point is shown for clarity.
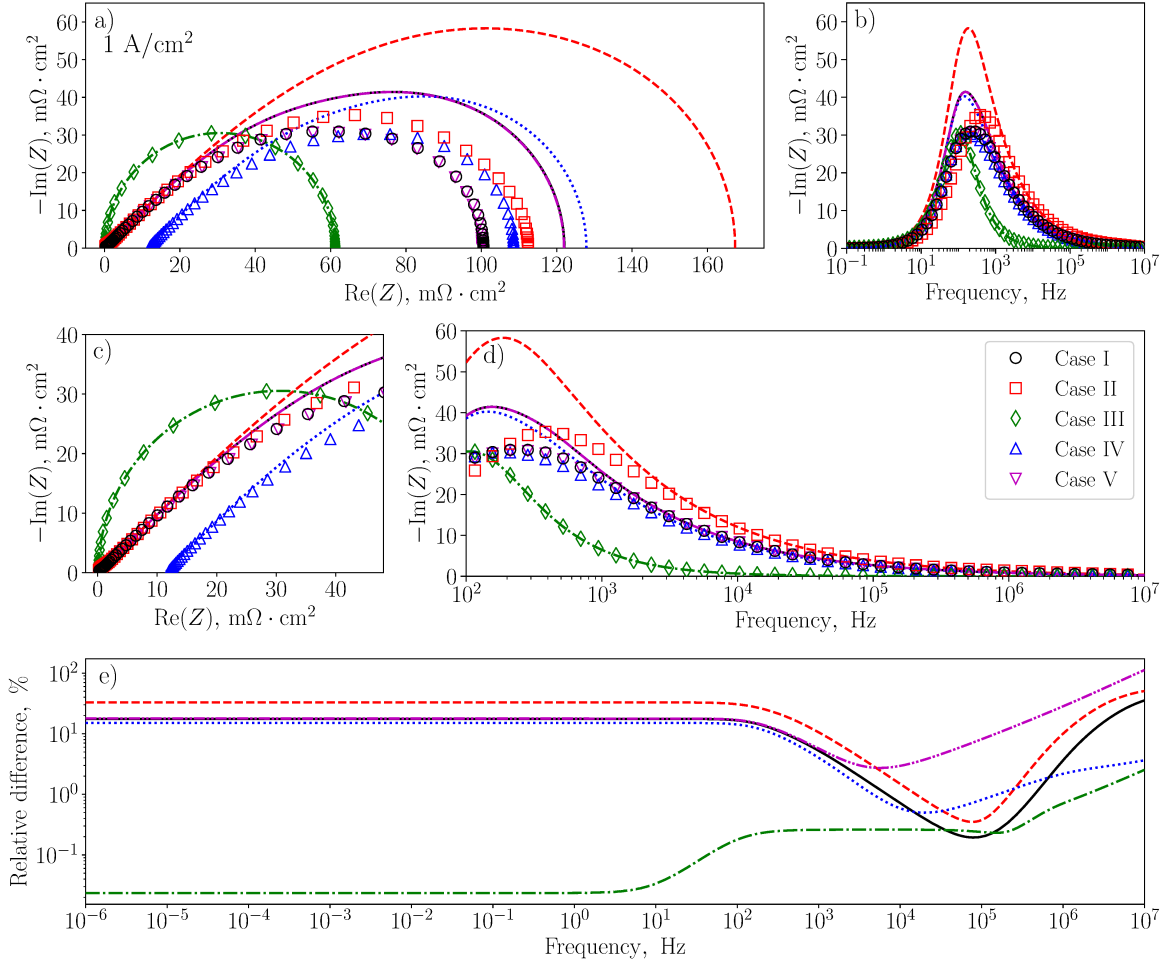
Figure 5.12: Comparison of the $H_2/O_2$ spectra simulated numerically (markers) to those computed analytically with equation (5.13) (lines) at 1 A/cm²: a), c) Nyquist plot and its high-frequency portion; b), d) frequency-content plot of the imaginary impedance component and its high-frequency portion; e) relative residual (5.29). Every twentieth point is shown for clarity.

frequency of parallel $RC$ circuits with purely protonic resistance of a CL, purely electronic resistance of a CL, or resistance equal to $R_{\text{DC}}^{\text{CL}} - R_{\text{HF}}^{\text{CL}}$. Similarly, the characteristic frequency of a faradaic process can be estimated using charge-transfer resistance. As shown in Appendix C, the latter is given by $R_{\text{ct}} = b/\left(i_0 A_{\text{v}} L\right)$ when $\eta \approx 0$ and by $R_{\text{ct}} = b/i$ in the Tafel regime (the latter appears in equation (5.16)). The two respective estimates are

$$\omega_{\text{ct}} = \frac{i_0 A_{\text{v}}}{b C_{\text{dl}}} \tag{5.31}$$

and

$$\omega_{\text{ct}} = \frac{i}{b C_{\text{dl}} L}. \tag{5.32}$$

For the 45° branch to be free of the faradaic effects, $\omega_\Omega$ must be sufficiently larger than $\omega_{\text{ct}}$ and impedance must be measured at a frequencies that satisfy the following:

$$\omega > \omega_\Omega \gg \omega_{\text{ct}}. \tag{5.33}$$

This results in an upper limit of the recommended operating current density:

$$i \ll i_{\text{HF}} = \omega_\Omega b C_{\text{dl}} L. \tag{5.34}$$

For the catalyst-layer properties given in Table 5.2 and electrical and protonic conductivities of 3.79 S/cm and 2 mS/cm, respectively (case I from Table 5.3), $f_\Omega = \omega_\Omega/(2\pi)$ is 87.3 Hz and $i_{\text{HF}}$ is 0.811 A/cm$^2$. Similar or less strict estimates were obtained for other cases considered in this Chapter except for case III, where protonic conductivity was significantly higher than that in Nafion®-based CLs; in that case, $f_\Omega$ was 57.2 kHz and $i_{\text{HF}}$ was 531 A/cm$^2$. Therefore, in general, charge-transport characterization of Nafion®-based PEMFC and PEMWE catalyst layers via EIS should be performed either under H$_2$/O$_2$ conditions at or below 10 mA/cm$^2$ or under H$_2$/N$_2$ conditions; the applied frequency range should exceed 1 kHz.

Spectra simulated for case I from Table 5.3 using Tafel kinetics (equation (2.52)) and double-trap kinetics (equation (2.51)) were compared (Figure 5.13). The frequency at which impedance became independent of the faradaic effects was estimated as the frequency at which the spectra computed with the two kinetic models
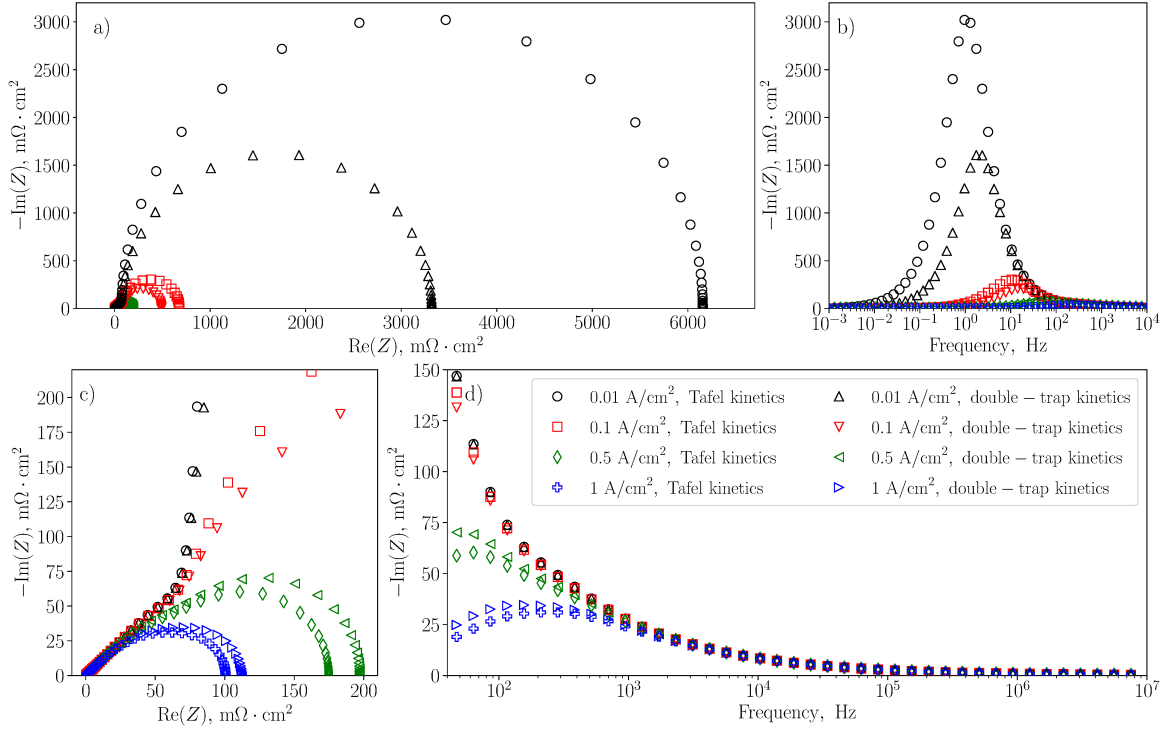
Figure 5.13: Comparison of the $H_2/O_2$ spectra simulated numerically for case I using the Tafel and the double-trap ORR kinetics: a), c) Nyquist plots; b), d) frequency-content plots of the imaginary impedance component. Every twentieth point is shown for clarity.

started to deviate by more than 2% at high frequencies[3]. The threshold frequency increased with current density and was 61.8, 129, 550, and 1,216 Hz at 0.01, 0.1, 0.5, and 1 A/cm², respectively. This was in agreement with equations (5.30)–(5.34) that limited the catalyst-layer charge-transport characterization to $f > 87.3$ Hz and $i \ll 0.811$ A/cm² for the given CL properties. Therefore, catalyst-layer impedance spectra are independent of faradaic processes under conditions (5.33) and (5.34), and the analytical models from Section 5.2 can be applied to estimate CL charge-transport properties.

---

[3]The differences between the spectra simulated at the same current density were solely due to the faradaic process since the oxygen-transport effects were negligible. The latter was confirmed by performing additional simulations with a 10 times higher oxygen diffusivity and observing no change in the spectra.

### 5.3.3 Assessment of the Analytical Models for Uniform Catalyst Layers

Analytical models for estimating catalyst-layer charge-transport properties were discussed in detail in Section 5.2. The corresponding impedance expressions are mathematically valid under the simplifying assumptions used in their derivation: low current for all models [177, 182, 183] and high effective electronic conductivity for the models by Eikerling and Kornyshev [183] and Makharia et al. [177]. In this Section, the discrepancy in the relationships between the ohmic resistance and effective conductivity of a catalyst layer (equations (5.10) and (5.17)) is addressed with the help of the ohmic-heating-based CL resistance computed in the numerical model. Additionally, the impact of using the analytical models beyond their applicability limitations on the fitted charge-transport properties is illustrated.

#### 5.3.3.1 $H_2/O_2$ Spectroscopy

The numerical $H_2/O_2$ spectra simulated at 0.01, 0.1, 0.5, and 1 A/cm$^2$ (Figures 5.8, 5.9, 5.11, and 5.12) were analyzed with equations (5.12) and (5.14) using the methodology discussed earlier (equation (5.13) was reduced to equation (5.14) due to no oxygen-transport limitations). In case of equation (5.14), conductivities were fitted and then converted into resistances using equation (5.17). The fitted protonic and electronic resistances are given in Table 5.4 along with those resistances computed in the numerical model via ohmic heating (equations (2.156) and (2.157)). The $R^2$ of the fitting was at least 0.999. No resistance is reported in case III as it was not possible to achieve a reliable fit due to the significant effect of the numerical error (up to 1 m$\Omega \cdot$cm$^2$ by the order of magnitude) on the small high-frequency branch (less than 0.04 m$\Omega \cdot$cm$^2$ in the real component). Plots of the fitted spectra can be found in Figures 5.14 and 5.15.

Table 5.4 shows that the protonic resistance fitted with equation (5.14) closely matched the numerical estimate (which has the meaning of the resistance necessary

Table 5.4: Catalyst-layer protonic and electronic resistances fitted to the $H_2/O_2$ spectra using equations (5.12) and (5.14) along with those resistances estimated via ohmic heating with equations (2.156) and (2.157). In case of equation (5.14), conductivities were fitted and then converted into resistances using equation (5.17). Two resistance pairs given in case V for equation (5.14) resulted in similar, within $10^{-12}$, residuals (resistance corresponding to the smaller residual is given first).

| Case | $R_{H+}^{EKM}$, m$\Omega \cdot$cm$^2$ (Fit, Eq. (5.12)) | $R_{H+}^{K}$, m$\Omega \cdot$cm$^2$ (Fit, Eq. (5.14)) | $R_{e-}^{K}$, m$\Omega \cdot$cm$^2$ (Fit, Eq. (5.14)) | $R_{H+}^{eff}$, m$\Omega \cdot$cm$^2$ (Est., Eq. (2.156)) | $R_{e-}^{eff}$, m$\Omega \cdot$cm$^2$ (Est., Eq. (2.157)) |
|---|---|---|---|---|---|
| | | **0.01 A/cm$^2$** | | | |
| I | 226 | 75.0 | 0.0414 | **74.6** | **0.0398** |
| II | 452 | 150 | 0.0437 | **149** | **0.0399** |
| IV | 182 | 75.0 | 3.96 | **74.6** | **3.98** |
| V | 231 | 75.3, 0.139 | 0.139, 75.3 | **0.0398** | **74.6** |
| | | **0.1 A/cm$^2$** | | | |
| I | 225 | 75.0 | 0.0423 | **71.4** | **0.0413** |
| II | 449 | 150 | 0.0440 | **136** | **0.0430** |
| IV | 187 | 74.9 | 3.99 | **71.6** | **4.12** |
| V | 228 | 0.148, 75.2 | 75.2, 0.148 | **0.0413** | **71.4** |
| | | **0.5 A/cm$^2$** | | | |
| I | 224 | 74.8 | 0.0483 | **59.4** | **0.0476** |
| II | 448 | 150 | 0.0474 | **97.2** | **0.0542** |
| IV | 192 | 74.1 | 4.05 | **60.2** | **4.70** |
| V | 222 | 0.194, 74.4 | 74.4, 0.194 | **0.0476** | **59.4** |
| | | **1 A/cm$^2$** | | | |
| I | 224 | 74.5 | 0.0551 | **48.6** | **0.0542** |
| II | 447 | 149 | 0.0515 | **70.6** | **0.0640** |
| IV | 189 | 73.1 | 4.10 | **49.9** | **5.30** |
| V | 220 | 0.226, 73.4 | 73.4, 0.226 | **0.0543** | **48.5** |
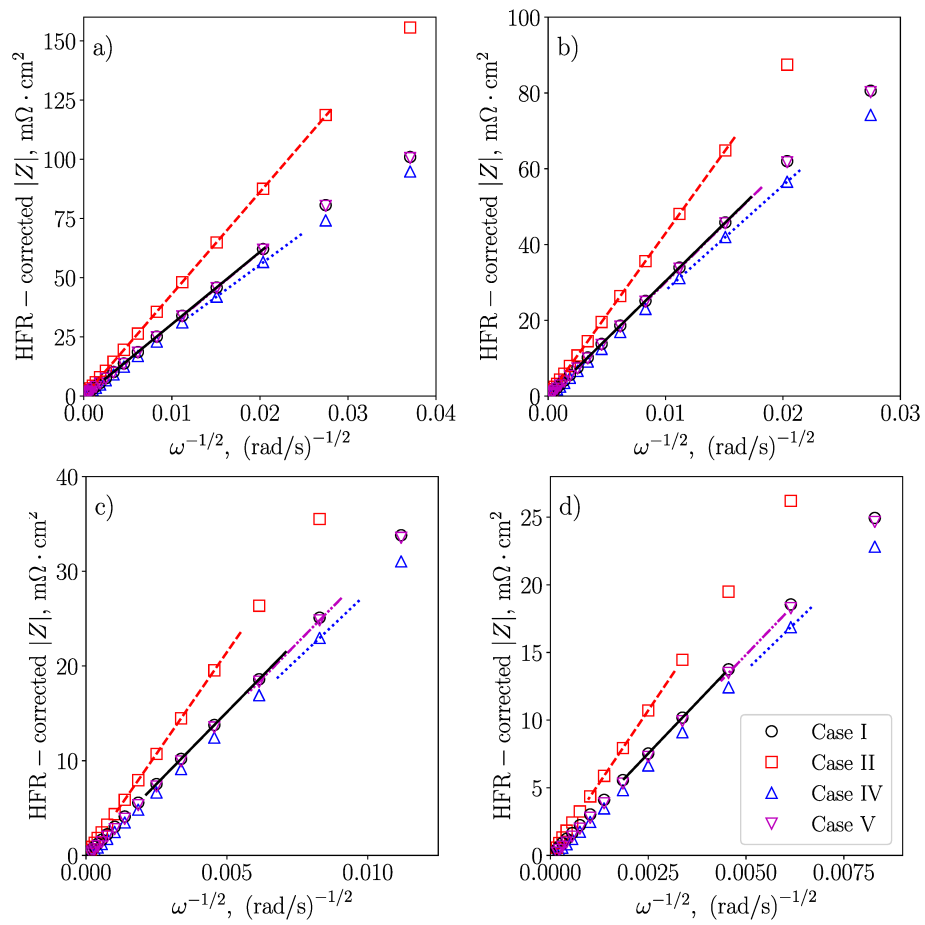
Figure 5.14: High-frequency portions of the $R_{\mathrm{HF}}^{\mathrm{CL}}$-corrected $H_2/O_2$ impedance magnitude against $\omega^{-1/2}$ (markers) and their fits obtained with equation (5.12) (lines): a) 0.01 A/cm²; b) 0.1 A/cm²; c) 0.5 A/cm²; and d) 1 A/cm². Every fortieth data point is shown for clarity.
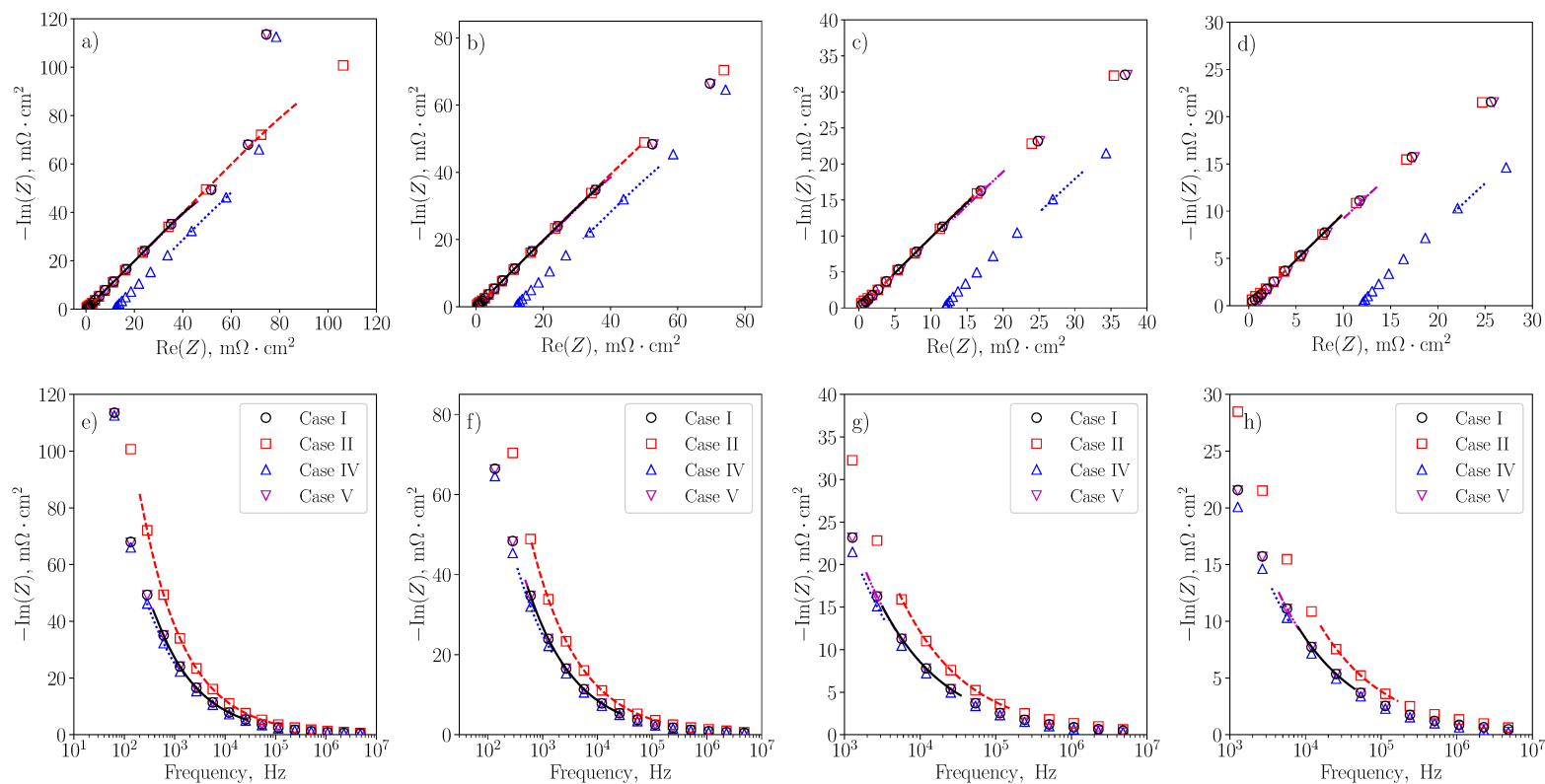
Figure 5.15: High-frequency portions of the simulated $H_2/O_2$ spectra (markers) and their fits obtained with equation (5.14) (lines): a), e) 0.01 A/cm$^2$; b), f) 0.1 A/cm$^2$; c), g) 0.5 A/cm$^2$; and d), h) 1 A/cm$^2$. Graphs a)–d) are Nyquist plots; graphs e)–h) are frequency-content plots of the imaginary impedance component. Every fiftieth data point is shown for clarity.

poor electronic-resistance fits will be discussed shortly.

The two resistance values obtained in case V correspond to the two search regions used in the fitting: the first region corresponded to the exact conductivities used in the simulations and the second region covered the swapped conductivities (i.e., those from case I). The fitting residuals at the two optimum points were nearly the same (within $10^{-12}$), as expected from the discussion of equations (5.24) and (5.25). This means that the assignment of the fitted charge-transport properties to one of the two conductive phases of a CL is not possible without knowing which of the phases is more conductive.

Deviation between the analytical fits and the numerical resistance increased with current density. The numerical model showed a gradual decrease in the protonic resistance and a gradual increase in the electronic resistance (in cases I, II, and IV; vice versa in case V) as more and more current was produced at the catalyst-layer/membrane interface (or at the CL-PTL interface in case V; Figure 5.16), affecting the travel distance of protons and electrons. This was not captured with the analytical equations (5.12) and (5.14), which are limited to low current (see Section 5.2).

The conductivity values corresponding to the resistances from Table 5.4 are listed in Table 5.5. In case of equation (5.12), the fitted resistance was converted into conductivity using equation (5.10). Both analytical models (5.12) and (5.14) produced reasonably good conductivity estimates for the less conductive phase at all current densities. Therefore, these models can be used to estimate effective CL conductivity even beyond their low-current applicability limitations (note this is not the case for ohmic resistance). However, the analytical models discussed here should only be applied to experimental data measured at relatively low current due to the nonuniformities that develop in the CL operating at high current, such as nonuniform current density and ionomer hydration (and thus nonuniform protonic conductivity). Analysis of the impedance spectra of nonuniform CLs is performed later in this Chapter

240
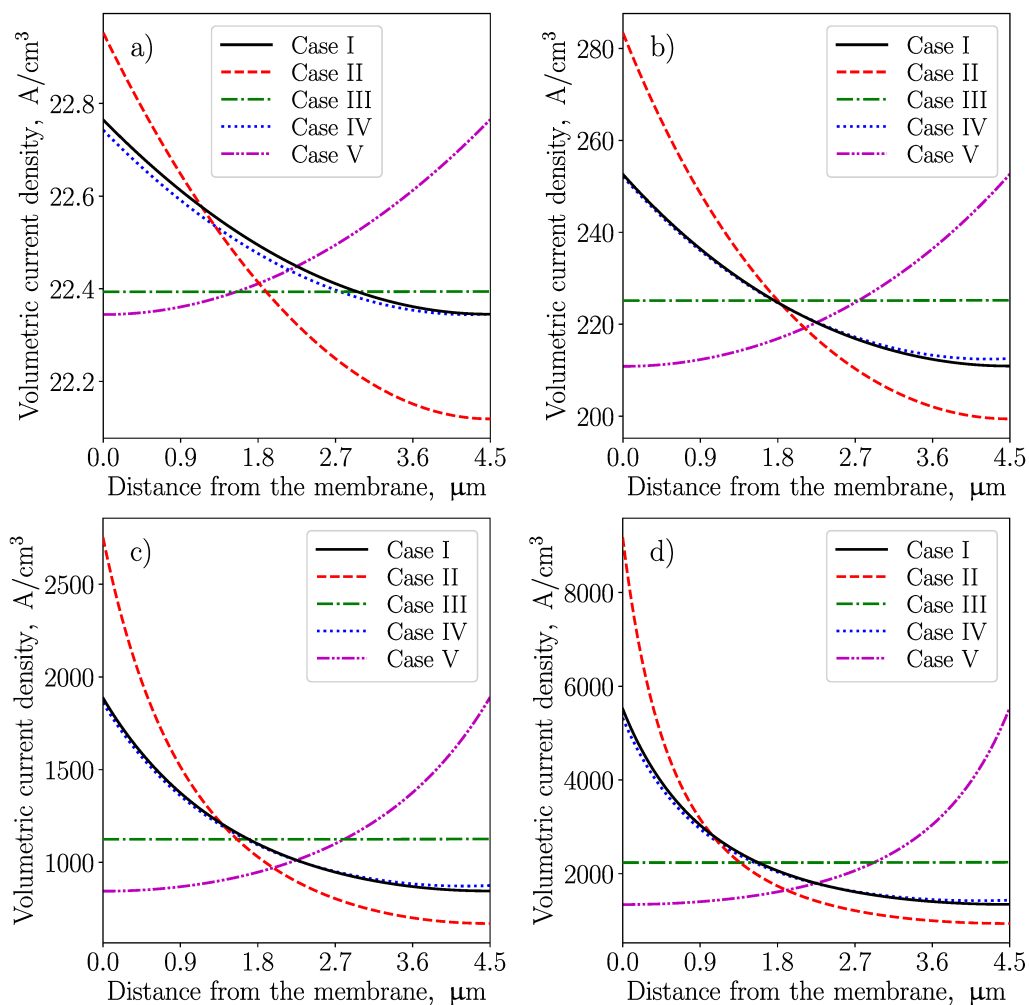
Figure 5.16: Comparison of the simulated steady-state volumetric-current-density distributions in the catalyst layer at: a) 0.01 A/cm²; b) 0.1 A/cm²; c) 0.5 A/cm²; and d) 1 A/cm². The membrane is located at the left end and the microporous/gas-diffusion layer is located at the right end of each graph.

and can also be found in references [173, 404, 405, 438, 576, 577].

The conductivity results in Table 5.5 indicate that equation (5.12) can be used to extract the lower of the two conductivities from the impedance spectrum, despite the resistance overestimation, as long as equation (5.10) is used for the conversion. It is worth noting that conductivity estimated using EIS is reported less often in the literature than resistance (some examples are references [120, 122, 174, 184, 185, 190, 196, 421, 423, 426]).

Contour plots of the fitting residuals obtained with equation (5.14) are shown in Figure 5.17. The fitted and the exact conductivities are marked with the solid red and the hollow black markers, respectively, and their labels indicate the corresponding residuals. The residual computed with the exact conductivities was higher due to the numerical error in the simulations. In cases I and II, the simulated catalyst layer was highly electronically conductive, and the residual plots contain a range of electronic conductivities with relatively low residual values. Both protonic and electronic conductivities were low in case IV, and each residual graph has a unique optimum point. Two search regions are shown for case V, with region 1 neighboring the conductivities used in the EIS simulation and region 2 neighboring the mirrored conductivities. As expected, the residual plots of the mirrored case V were qualitatively similar to those in case I. These results indicate the low sensitivity of catalyst-layer impedance to the highest-conductivity phase. As a result, the quality of the fits obtained with equation (5.14) for the more conductive phase was relatively poor in Tables 5.4 and 5.5.

### 5.3.3.2   $H_2/N_2$ Spectroscopy

The catalyst-layer charge-transport properties were extracted from the simulated $H_2/N_2$ spectra shown in Figure 5.10 using the two graphical approaches illustrated in Figure 5.6 and by fitting equations (5.12), (5.19), and (5.21). The $R^2$ of the fits was at least 0.999. Plots of the fitted spectra are provided in Figures 5.18 and 5.19.

In this case, the ohmic-heating-based approach to estimating the ohmic resistance

Table 5.5: Catalyst-layer protonic and electronic conductivities fitted to the $H_2/O_2$ spectra using equations (5.12) and (5.14) along with the exact conductivities from Table 5.3. In case of equation (5.12), resistance was fitted and then converted into conductivity using equation (5.10). Two conductivity pairs given in case V for equation (5.14) resulted in similar, within $10^{-12}$, residuals (conductivity corresponding to the smaller residual is given first).

| Case | $\sigma_{H^+}^{\mathbf{EKM}}$, mS/cm (Fit, Eq. (5.12)) | $\sigma_{H^+}^{\mathbf{K}}$, mS/cm (Fit, Eq. (5.14)) | $\sigma_{e^-}^{\mathbf{K}}$, mS/cm (Fit, Eq. (5.14)) | $\sigma_{H^+}^{\mathbf{eff}}$, mS/cm (Model input, Table 5.3) | $\sigma_{e^-}^{\mathbf{eff}}$, mS/cm Model input, (Table 5.3) |
|---|---|---|---|---|---|
| **0.01 A/cm²** | | | | | |
| I | 1.99 | 2.00 | 3622 | **2.00** | **3788** |
| II | 0.996 | 1.00 | 3431 | **1.00** | **3788** |
| IV | 2.47 | 2.00 | 37.9 | **2.00** | **37.9** |
| V | 1.95 | 1.99, 1076 | 1076, 1.99 | **3788** | **2.00** |
| **0.1 A/cm²** | | | | | |
| I | 2.00 | 2.00 | 3544 | **2.00** | **3788** |
| II | 1.00 | 1.00 | 3411 | **1.00** | **3788** |
| IV | 2.41 | 2.00 | 37.6 | **2.00** | **37.9** |
| V | 1.98 | 1011, 1.99 | 1.99, 1011 | **3788** | **2.00** |
| **0.5 A/cm²** | | | | | |
| I | 2.01 | 2.01 | 3109 | **2.00** | **3788** |
| II | 1.00 | 1.00 | 3167 | **1.00** | **3788** |
| IV | 2.34 | 2.02 | 37.0 | **2.00** | **37.9** |
| V | 2.02 | 771, 2.01 | 2.01, 771 | **3788** | **2.00** |
| **1 A/cm²** | | | | | |
| I | 2.01 | 2.01 | 2720 | **2.00** | **3788** |
| II | 1.01 | 1.00 | 2913 | **1.00** | **3788** |
| IV | 2.38 | 2.05 | 36.6 | **2.00** | **37.9** |
| V | 2.04 | 664, 2.04 | 2.04, 664 | **3788** | **2.00** |
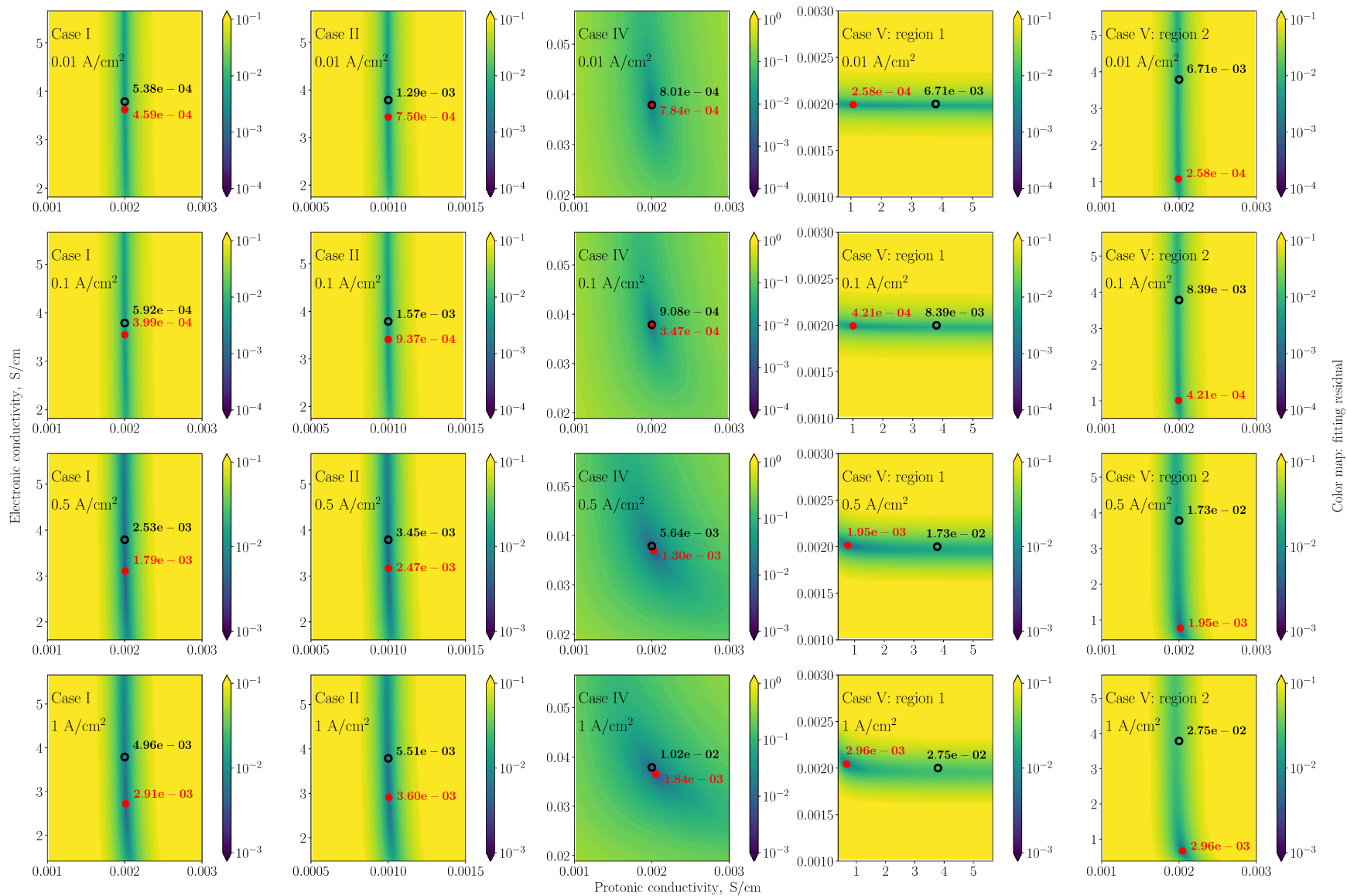
Figure 5.17: Residual distributions of the fits given in Tables 5.4 and 5.5 for equation (5.14). The solid red and the hollow black markers in each graph indicate the fitted and the exact conductivity values, respectively. The corresponding labels provide the residual values between the numerical and the analytical spectra.
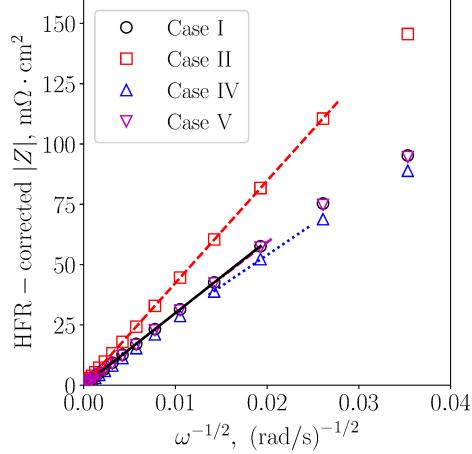
Figure 5.18: High-frequency portions of the $R_{\mathrm{HF}}^{\mathrm{CL}}$-corrected $H_2/N_2$ impedance magnitude against $\omega^{-1/2}$ (markers) and their fits obtained with equation (5.12) (lines). Every fifth data point is shown for clarity.

of the catalyst layer (equations (2.156) and (2.157)) could not be used due to the current density being nearly zero, as discussed earlier. Instead, equation (5.17) was used to obtain the reference protonic and electronic resistances since its accuracy increases as current approaches zero.

The ohmic resistances extracted from the $H_2/N_2$ spectra are shown in Table 5.6. Similarly to the $H_2/O_2$-spectra fits, the resistances of the less conductive phase obtained from equations (5.12) and (5.19), as well as from the graphical method from Figure 5.6a (equation (5.20)), were about 3 times larger than the reference values with the worst fit in case IV. Interestingly, the modified graphical approach from Figure 5.6b resulted in more accurate resistances than those fitted with equation (5.21). This validates the graphical method in Figure 5.6b, based on equations (5.24) and (5.25), as a novel and more convenient graphical method for estimating the catalyst-layer charge-transport properties.

The effective conductivities were extracted as before. Because substitution of equation (5.10) into equation (5.20) results in the same real impedance component at low frequencies as in equation (5.17), all of the considered methods provided good conductivity estimates for the less conductive phase (Table 5.6). The resistance and

245
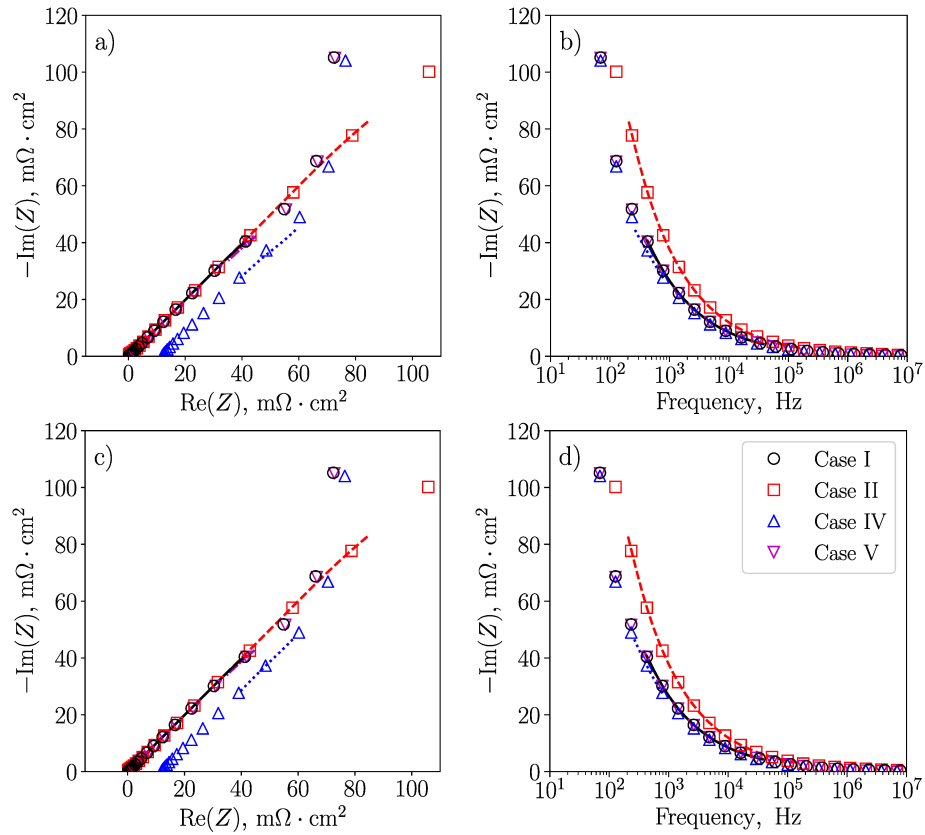
Figure 5.19: High-frequency portions of the simulated $H_2/N_2$ spectra and their fits obtained with: a), b) equation (5.19) and c), d) equation (5.21). Graphs a) and c) are Nyquist plots; graphs b) and d) are frequency-content plots of the imaginary impedance component. Every fifth data point is shown for clarity.

Table 5.6: Catalyst-layer protonic and electronic resistances and conductivities fitted to the $H_2/N_2$ spectra using the two graphical approaches illustrated in Figure 5.6 and equations (5.12), (5.19), and (5.21), along with the reference resistances computed with equation (5.17) and the exact conductivities (model input). In case of equations (5.12) and (5.19), resistance was fitted and then converted into conductivity using equation (5.10). In case of equation (5.21), conductivities were fitted and then converted into resistances using equation (5.17). The modified graphical approach from Figure 5.6b resulted in two equally valid pairs of protonic and electronic resistances/conductivities. Two resistance/conductivities pairs given in case V for equation (5.21) resulted in similar, within $10^{-12}$, residuals (resistance/conductivity corresponding to the smaller residual is given first).

| Case | $R_{H^+}^{EKM}$, mΩ·cm² (Fit, Fig. 5.6a) | $R_{H^+}^{K}$, mΩ·cm² (Fit, Fig. 5.6b) | $R_{e^-}^{K}$, mΩ·cm² (Fit, Fig. 5.6b) | $R_{H^+}^{EKM}$, mΩ·cm² (Fit, Eq. (5.12)) | $R_{H^+}^{EKM}$, mΩ·cm² (Fit, Eq. (5.19)) | $R_{H^+}^{K}$, mΩ·cm² (Fit, Eq. (5.21)) | $R_{e^-}^{K}$, mΩ·cm² (Fit, Eq. (5.21)) | $R_{H^+}^{K}$, mΩ·cm² (Est, Eq. (5.17)) | $R_{e^-}^{K}$, mΩ·cm² (Est, Eq. (5.17)) |
|---|---|---|---|---|---|---|---|---|---|
| I | 226 | 75.5, 0.0271 | 0.0271, 75.5 | 218 | 216 | 72.6 | 0.0533 | **75** | **0.0396** |
| II | 453 | 151, 0.0224 | 0.0224, 151 | 437 | 434 | 145 | 0.0497 | **150** | **0.0396** |
| IV | 227 | 75.6, 3.89 | 3.89, 75.6 | 162 | 180 | 71.8 | 3.97 | **75** | **3.96** |
| V | 231 | 75.3, 0.490 | 0.490, 75.3 | 207 | 212 | 72.5, 0.319 | 0.319, 72.5 | **0.0396** | **75** |

| Case | $\sigma_{H^+}^{EKM}$, mS/cm (Fit, Fig. 5.6a) | $\sigma_{H^+}^{K}$, mS/cm (Fit, Fig. 5.6b) | $\sigma_{e^-}^{K}$, mS/cm (Fit, Fig. 5.6b) | $\sigma_{H^+}^{EKM}$, mS/cm (Fit, Eq. (5.12)) | $\sigma_{H^+}^{EKM}$, mS/cm (Fit, Eq. (5.19)) | $\sigma_{H^+}^{K}$, mS/cm (Fit, Eq. (5.21)) | $\sigma_{e^-}^{K}$, mS/cm (Fit, Eq. (5.21)) | $\sigma_{H^+}^{eff}$, mS/cm (Model input, Table 5.3) | $\sigma_{e^-}^{eff}$, mS/cm (Model input, Table 5.3) |
|---|---|---|---|---|---|---|---|---|---|
| I | 1.99 | 1.99, 5526 | 5526, 1.99 | 2.06 | 2.08 | 2.07 | 2812 | **2.00** | **3788** |
| II | 0.993 | 0.993, 6707 | 6707, 0.993 | 1.03 | 1.04 | 1.03 | 3020 | **1.00** | **3788** |
| IV | 1.98 | 1.98, 38.6 | 38.6, 1.98 | 2.77 | 2.50 | 2.09 | 37.8 | **2.00** | **37.9** |
| V | 1.95 | 1.99, 306 | 306, 1.99 | 2.18 | 2.13 | 2.07, 470 | 470, 2.07 | **3788** | **2.00** |

conductivity estimates obtained with equation (5.21) and the corresponding graphical method were not as accurate for the more conductive phase (to which catalyst-layer impedance is less sensitive). Contour plots of the fitting residuals obtained with equation (5.21) are shown in Figure 5.21. As it was the case for $H_2/O_2$ spectra, sensitivity of $H_2/N_2$ spectra to the highest-conductivity phase was low.

### 5.3.4 Effect of Nonuniform Ionomer Loading

#### 5.3.4.1 Polarization and Ohmic-Resistance Curves

Before the impedance spectra of nonuniform catalyst layers were analyzed, some insight on the resistance-conductivity relationship was gathered by performing DC polarization-curve simulations. The voltage-current relationships of the catalyst layers described in Figure 5.1 are shown in Figure 5.20a. The catalyst-layer performance simulated in this work was relatively low and close to the performance of a whole cell (cf. references [298, 328]) due to the chosen kinetic parameters. This, however, had no effect on the generality of the results and conclusions of this Chapter that was focused on charge transport. The performance of a graded catalyst layer was higher when the zone located closer to the membrane was more conductive than all or most of the other zones (the "Decreasing" and the "Local minimum" cases). Gerteisen [404] reported a similar effect of the conductivity distribution in a CL.

Additional information can be obtained from the ohmic-heating analysis. The computed effective ohmic resistances are plotted in Figures 5.20b and 5.20c. In all cases, similar protonic resistances were observed at current densities above 10 A/cm$^2$, while the electronic resistances converged as current densities decreased below 0.1 A/cm$^2$. This was due to the changing current-density distribution within the catalyst layer (Figures 5.22a–d) that affected the travel distances of protons and electrons.

Interestingly, the protonic resistance converged to different values in each case as current density tended to zero (Figure 5.20b). Those limiting values are provided in Table 5.7 and are accompanied with the analytical estimates obtained from equa-
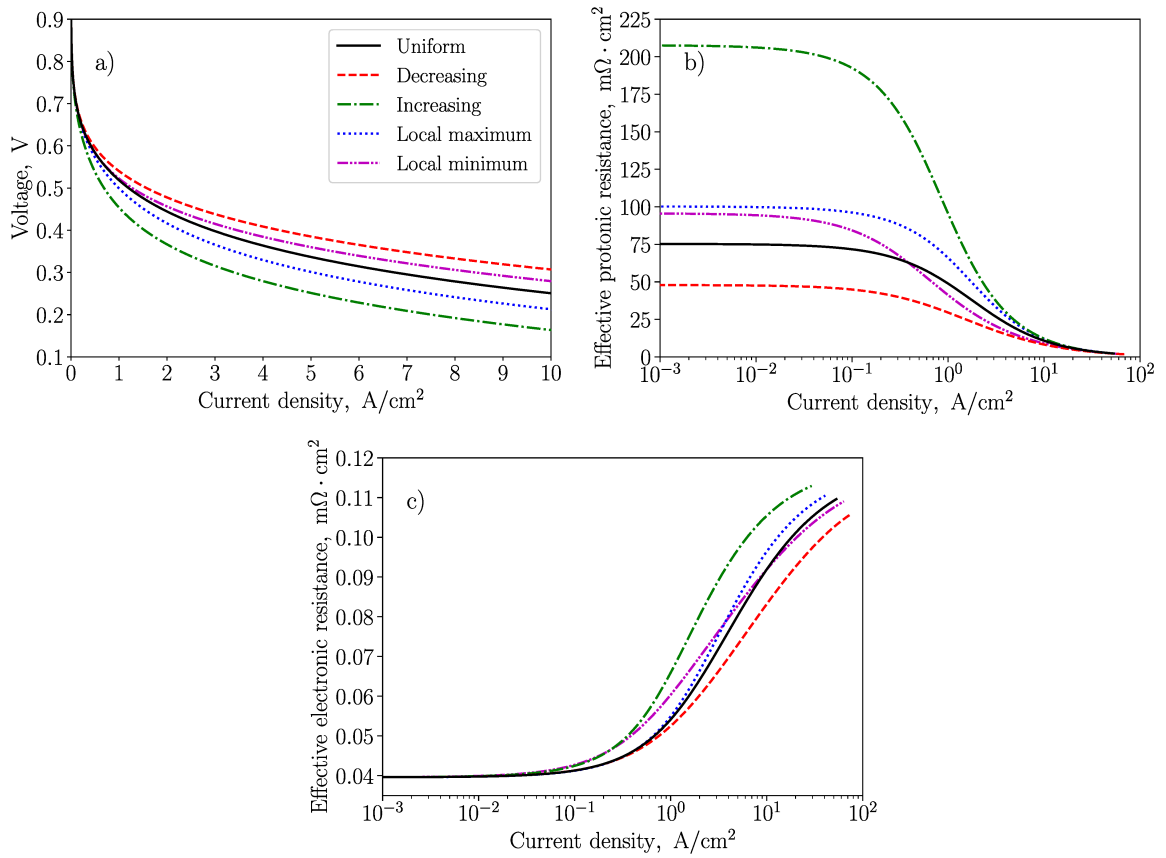
Figure 5.20: Comparison of the polarization curves (a) and ohmic resistances (b, c) of the catalyst layer simulated numerically for the ionomer-loading distributions from Figure 5.1. The ohmic resistance was computed through ohmic heating (equations (2.156) and (2.157)).
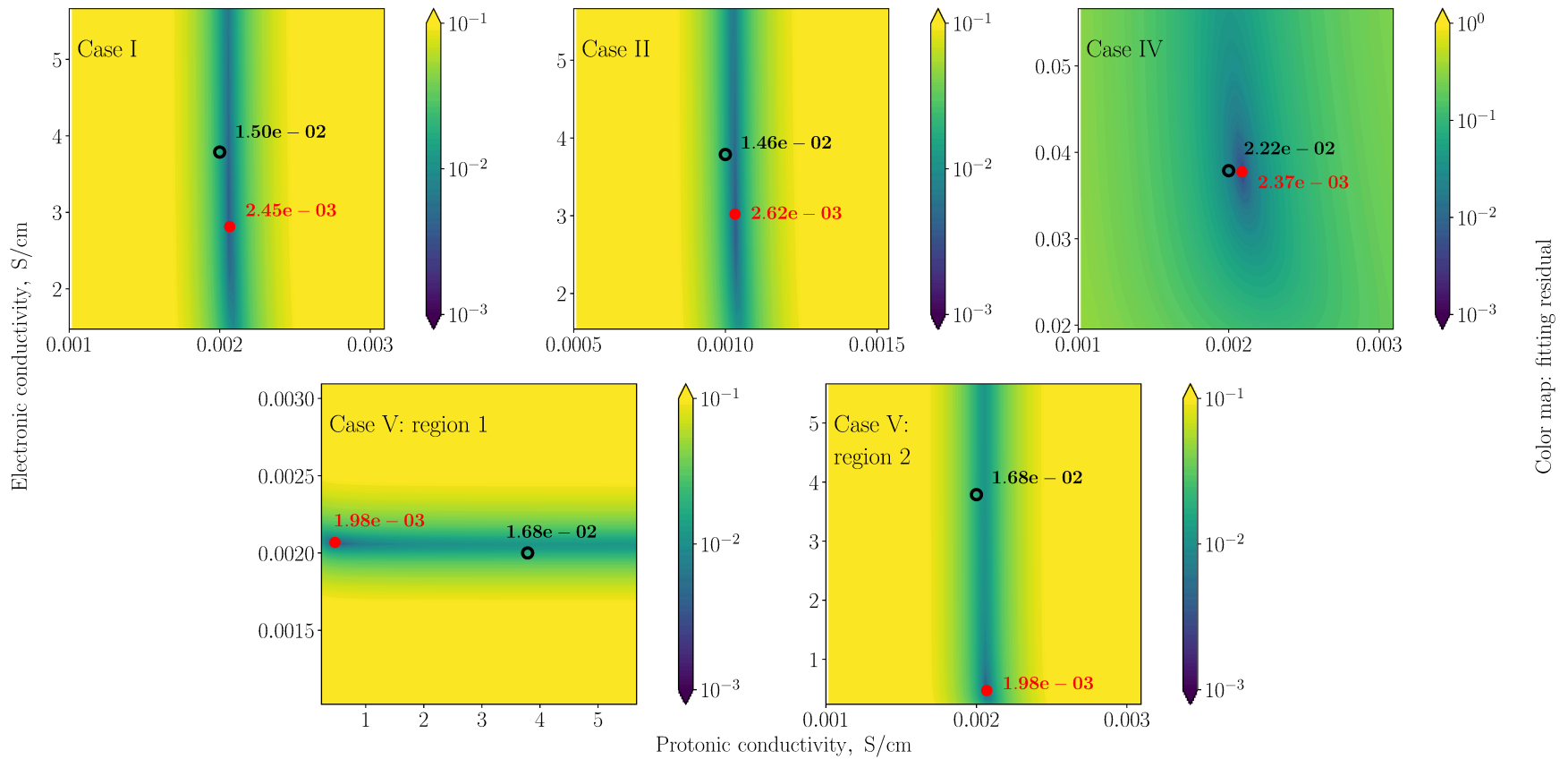
Figure 5.21: Residual distributions of fits given in Table 5.6 for equation (5.21). The solid red and the hollow white markers in each graph indicate the fitted and the exact conductivity values, respectively. The corresponding labels provide the residual values between the numerical and the analytical spectra.
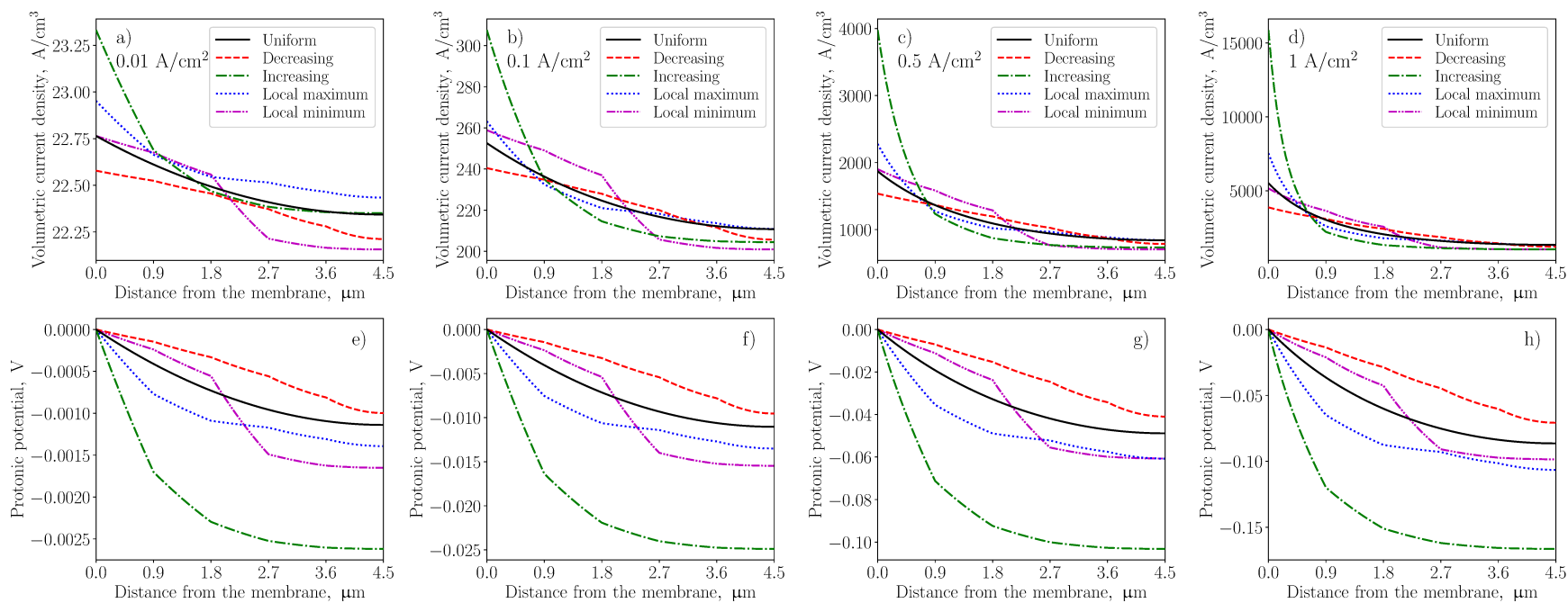
Figure 5.22: Comparison of the volumetric-current-density and protonic-potential distributions simulated for the ionomer-loading distributions from Figure 5.1 at: a), e) 0.01 A/cm²; b), f) 0.1 A/cm²; c), g) 0.5 A/cm²; and d), h) 1 A/cm².

Table 5.7: Comparison of the ohmic-heating based protonic resistance computed at 0.1 mA/cm$^2$ using equation (2.156) to the analytical estimates obtained from equation (5.17) via the three methods explained in the text.

| Distribution | $R_{H^+}^{eff}$, m$\Omega \cdot$ cm$^2$ (Eq. (2.156)) | $R_{H^+}^{K}$, m$\Omega \cdot$ cm$^2$ (Eq. (5.17)) | | |
|---|---|---|---|---|
| | | Method a) | Method b) | Method c) |
| Uniform | 75.3 | 75.0 | 75.0 | 75.0 |
| Decreasing | 47.9 | 59.7 | 120 | 598 |
| Increasing | 208 | 59.7 | 120 | 598 |
| Local maximum | 100 | 64.0 | 91.6 | 458 |
| Local minimum | 95.7 | 66.4 | 110 | 550 |

tion (5.17) with the following three methods: a) averaging the protonic conductivity in the catalyst layer and then applying equation (5.17); b) averaging the resistances calculated for each zone; and c) summing the resistances of all zones due to the series connection. The ohmic-heating-based resistance was in agreement with the analytical estimate found from equation (5.17) only in the case of the uniform ionomer distribution. When the protonic conductivity varied in the catalyst layer, the effective protonic resistance significantly differed from the analytical estimates. This means that equation (5.17) cannot be used for nonuniform CLs, even if the layer consists of multiple uniform sublayers.

To explain why the resistance-conductivity relationship (5.17) does not hold, the protonic-potential distributions were analyzed (Figures 5.22e–h). If the catalyst layer had only one conductive phase, its potential distribution would have been linear. Because it has two conductive phases, each of which terminates at one of the boundaries, the potential distribution is nonlinear even in the uniform case. It turns out that the shape of this distribution is such that equation (2.156) gives $L/\left(3\sigma_{H^+}^{eff}\right)$ only for uniform catalyst layers and at low current. As current density increased, the shape of the potential distribution started to change (Figure 5.23). Since equations (2.156) and (2.157) do not capture this effect, their estimates deviated from the
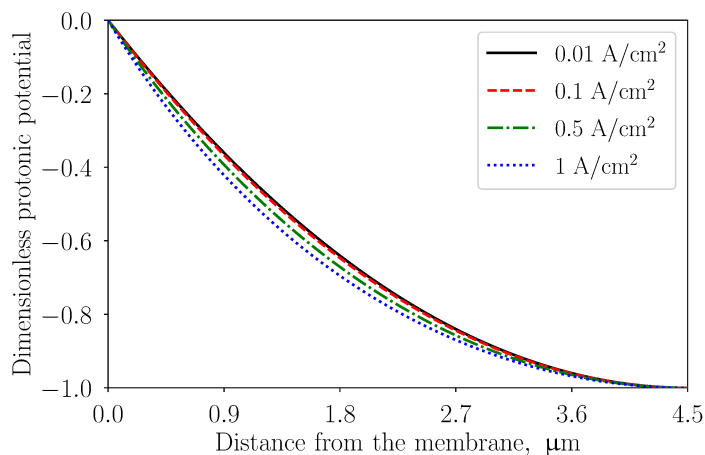
Figure 5.23: Comparison of the dimensionless protonic-potential distributions in a uniform CL (case I). The potential distribution was normalized by the magnitude of the potential drop across the layer.

ohmic-heating-based resistance (see Table 5.4).

### 5.3.4.2 $H_2/O_2$ Spectroscopy

The $H_2/O_2$ EIS simulations were repeated with the model inputs from Figure 5.1. Uniform ionomer loading in the graded catalyst layer was used as a control case to ensure the results obtained with a single uniform catalyst layer were reproduced. The computed spectra are shown in Figures 5.24–5.27. In those figures, graphs of the phase angle (computed from the point $(R_{HF}^{CL}, 0)$) against frequency are provided to visualize the convergence of the slope of the high-frequency linear impedance branch to 45° (for example, Figure 5.24d). The shape of the spectrum varied significantly depending on the ionomer distribution. The decrease in the oxygen diffusivity due to the reduced porosity did not have an effect on the simulated spectra. This was confirmed by observing no change in the impedance spectrum computed in the increasing-ionomer-loading case at 1 A/cm² with a 10 times higher oxygen diffusivity.

As seen in Figures 5.24d–5.27c, the phase angle converged to -45° at about 10 kHz in all spectra and remained approximately constant until the frequency reached 100 kHz. At higher frequencies, the phase angle was very sensitive to the numerical error due to the small impedance magnitude. The spectra corresponding to the "decreasing" and
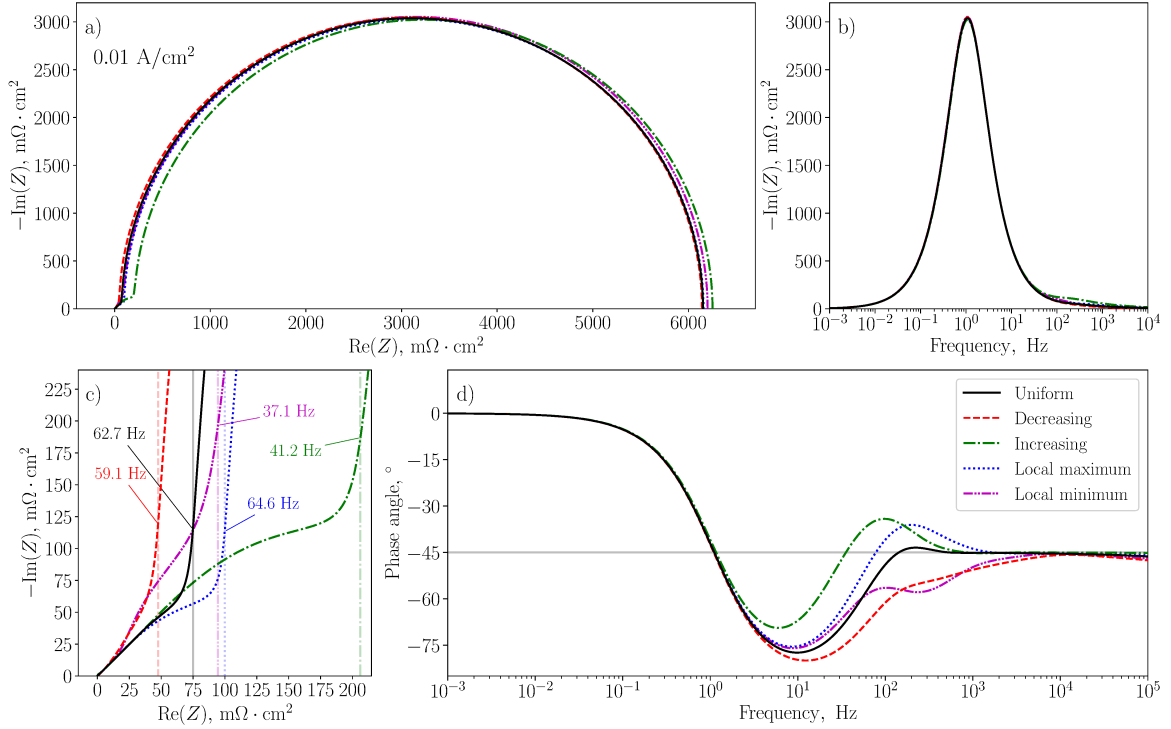
Figure 5.24: Comparison of the $H_2/O_2$ spectra simulated numerically for the ionomer-loading distributions from Figure 5.1 at 0.01 A/cm$^2$: a), c) Nyquist plot and its high-frequency portion; b) frequency-content plot of the imaginary impedance component; and d) Bode plot of the phase angle. Vertical lines represent the total ohmic resistance computed through ohmic heating (equations (2.156) and (2.157)).

the "local minimum" cases converged to -45° from a higher impedance slope (except for the latter case at 1 A/cm$^2$). In the "increasing" and "local maximum" cases, the intermediate region between the linear high-frequency branch and the charge-transfer arc transformed into a distinct capacitive arc at about 0.01-1 kHz (Figures 5.24c, 5.25c, 5.26a, and 5.27a). The observed shape of the high-frequency spectra was in agreement with other modeling studies [173, 404, 405, 576].

The ohmic-heating analysis performed in this work provides additional insight on whether the apparent linear impedance branch represents the total ohmic resistance of a nonuniform catalyst layer. The total ohmic resistance computed with equations (2.156) and (2.157) is marked with vertical lines in Figures 5.24c, 5.25c, 5.26a, and 5.27a, and the frequency at which it intersects with each spectrum is labeled. The real-axis projection of the apparent linear branch of the high-frequency spectrum

254
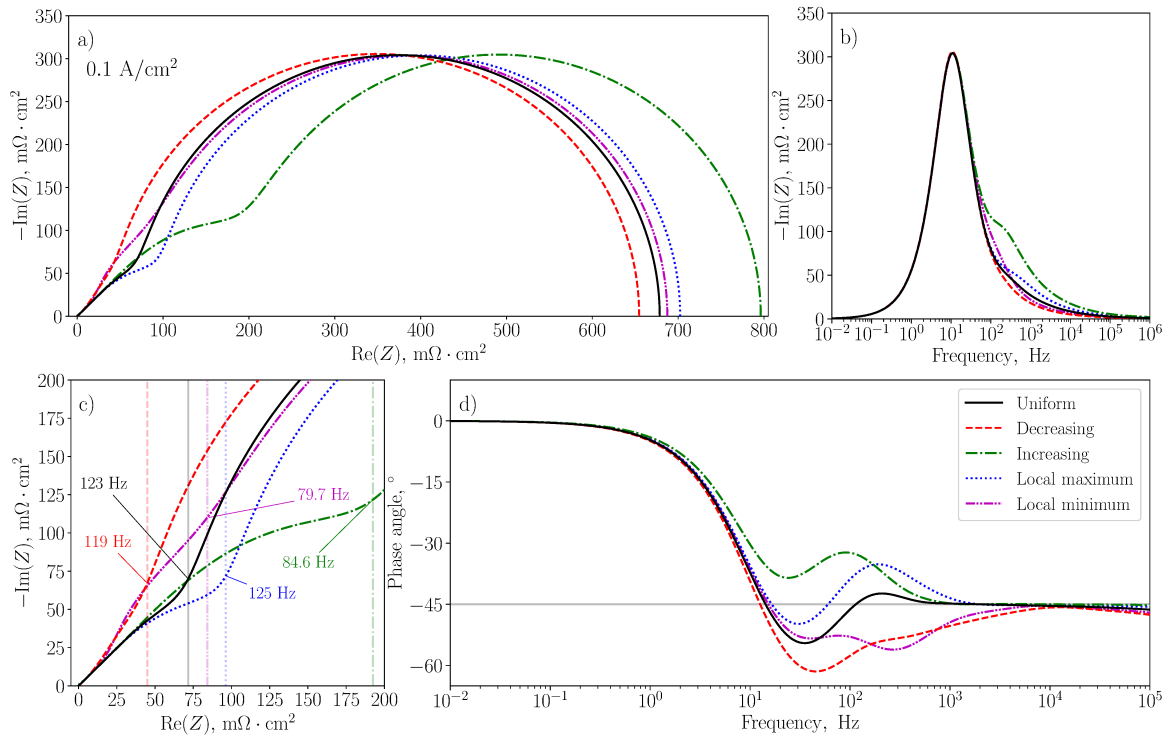
Figure 5.25: Comparison of the $H_2/O_2$ spectra simulated numerically for the ionomer-loading distributions from Figure 5.1 at 0.1 A/cm$^2$: a), c) Nyquist plot and its high-frequency portion; b) frequency-content plot of the imaginary impedance component; and d) Bode plot of the phase angle. Vertical lines represent the total ohmic resistance computed through ohmic heating (equations (6) and (7)).
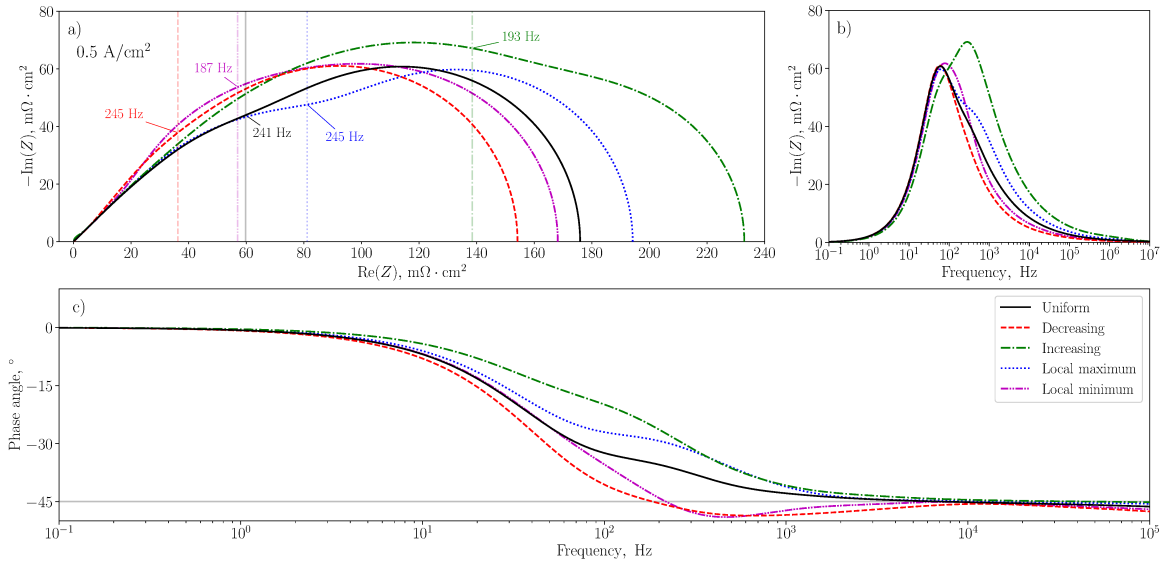
Figure 5.26: Comparison of the $H_2/O_2$ spectra simulated numerically for the ionomer-loading distributions from Figure 5.1 at 0.5 A/cm²: a) Nyquist plot; b) frequency-content plot of the imaginary impedance component; and c) Bode plot of the phase angle. Vertical lines represent the total ohmic resistance computed through ohmic heating (equations (6) and (7)).
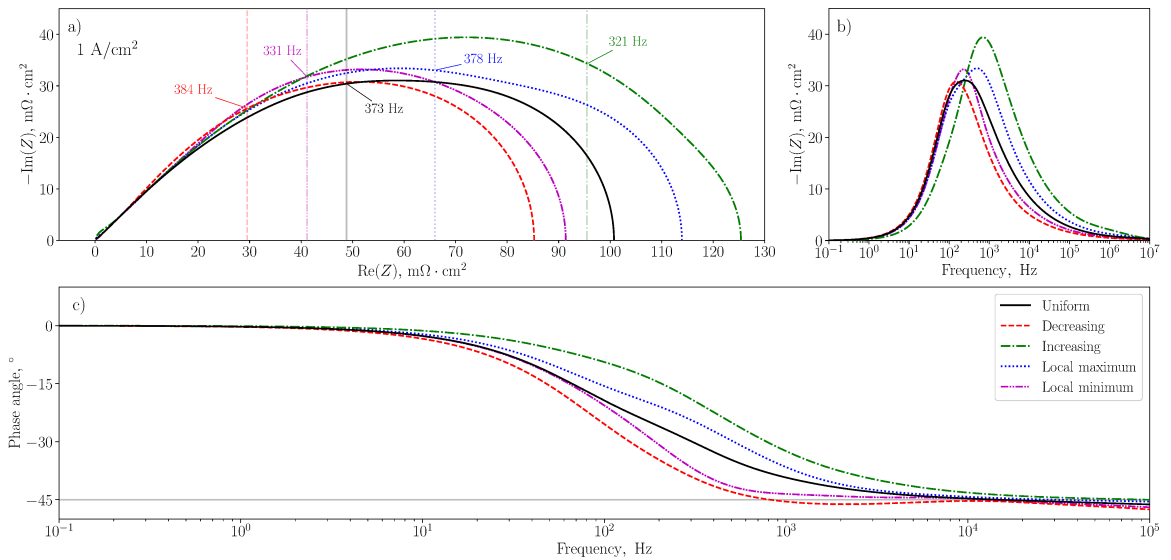


Figure 5.27: Comparison of the $H_2/O_2$ spectra simulated numerically for the ionomer-loading distributions from Figure 5.1 at 1 A/cm²: a) Nyquist plot; b) frequency-content plot of the imaginary impedance component; and c) Bode plot of the phase angle. Vertical lines represent the total ohmic resistance computed through ohmic heating (equations (2.156) and (2.157)).

was always shorter than the total ohmic resistance. Moreover, the junction point that indicates the total ohmic resistance may be located on a capacitive arc, as observed in the "increasing" and the "local-maximum" ionomer-distribution cases in Figures 5.26a and 5.27a. At 1 A/cm$^2$, all catalyst layers exhibit seemingly similar high-frequency impedance, while their ohmic resistances vary significantly (Figure 5.20b). Therefore, no conclusions on the catalyst-layer charge-transport properties should be made from the qualitative comparison of the high-frequency spectra alone.

### 5.3.4.3   H$_2$/N$_2$ Spectroscopy

The H$_2$/N$_2$ spectra that correspond to the catalyst layers considered in the previous Section are shown in Figure 5.28. Unlike the H$_2$/O$_2$ spectroscopy, H$_2$/N$_2$ EIS allows to unambiguously determine the total ohmic resistance of the catalyst layer from the position of the linear low-frequency impedance branch (at frequencies below 1–10 Hz), as seen in Figures 5.28a and 5.28b. However, the protonic and electronic conductivities of a nonuniform catalyst layer cannot be determined from the impedance spectrum, as equation (5.17) does not hold even at the zero-current limit (Figure 5.20 and Table 5.7). The impedance spectra simulated for a catalyst layer with nonuniform ionomer loading and low electronic conductivity (for case IV from Table 5.3; shown in Figure 5.29) were qualitatively similar to those obtained with higher electronic conductivity. It must be noted that, when $R_{\mathrm{HF}}^{\mathrm{CL}}$ is significant (as in this case), the reported phase angle, computed based on the $R_{\mathrm{HF}}^{\mathrm{CL}}$-corrected spectra and having the meaning of the slope of the linear branch at high frequencies, is different from the phase angle of the impedance (i.e., the voltage-current phase shift).

## 5.3.5   Effect of Nonuniform Active Area and Double-Layer Capacitance

The effect of catalyst distribution was analyzed by considering a graded catalyst layer with nonuniform active area and double-layer capacitance illustrated in Figure 5.2. All other catalyst-layer properties were taken from the uniform case I. The simu-
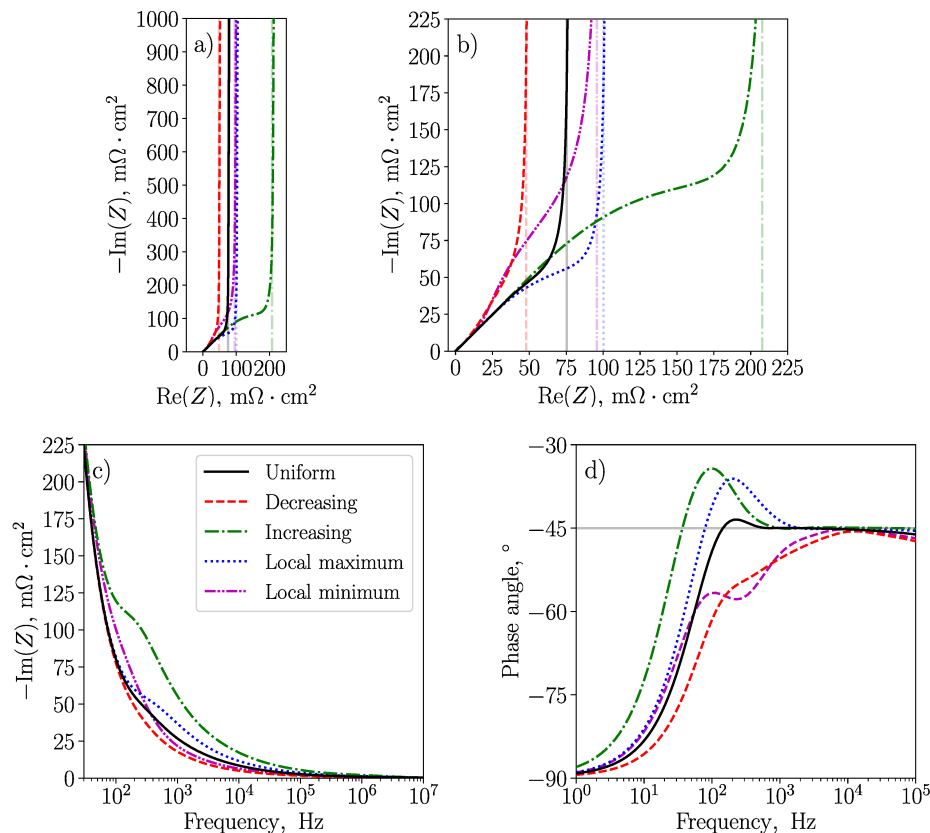
Figure 5.28: Comparison of the $H_2/N_2$ spectra simulated numerically for the ionomer-loading distributions from Figure 5.1: a), b) Nyquist plot and its high-frequency portion; c) frequency-content plot of the imaginary impedance component (high-frequency portion); and d) Bode plot of the phase angle. Vertical lines represent the total ohmic resistance computed through ohmic heating (equations (2.156) and (2.157); estimates at 0.1 mA/cm$^2$ are shown).

lated ohmic resistance and impedance spectra exhibited trends similar to those in the ionomer-loading study (Figures 5.30–5.32). Even though impedance was significantly less sensitive to the changes in active area and double-layer capacitance, it is clear that the spectrum distortion seen in Figures 5.24–5.29 is not indicative of the ionomer-loading distribution alone. Such an impedance distortion may also be caused by strong nonuniformity in active area (and double-layer capacitance). Therefore, no conclusions on catalyst-layer structure should be made from the shape of the impedance spectrum, unless the EIS analysis is complemented with additional information, such as CL spatial composition obtained through microscopy imaging [132, 133, 143, 447]. Moreover, even small differences in the spectrum shape may indicate

258
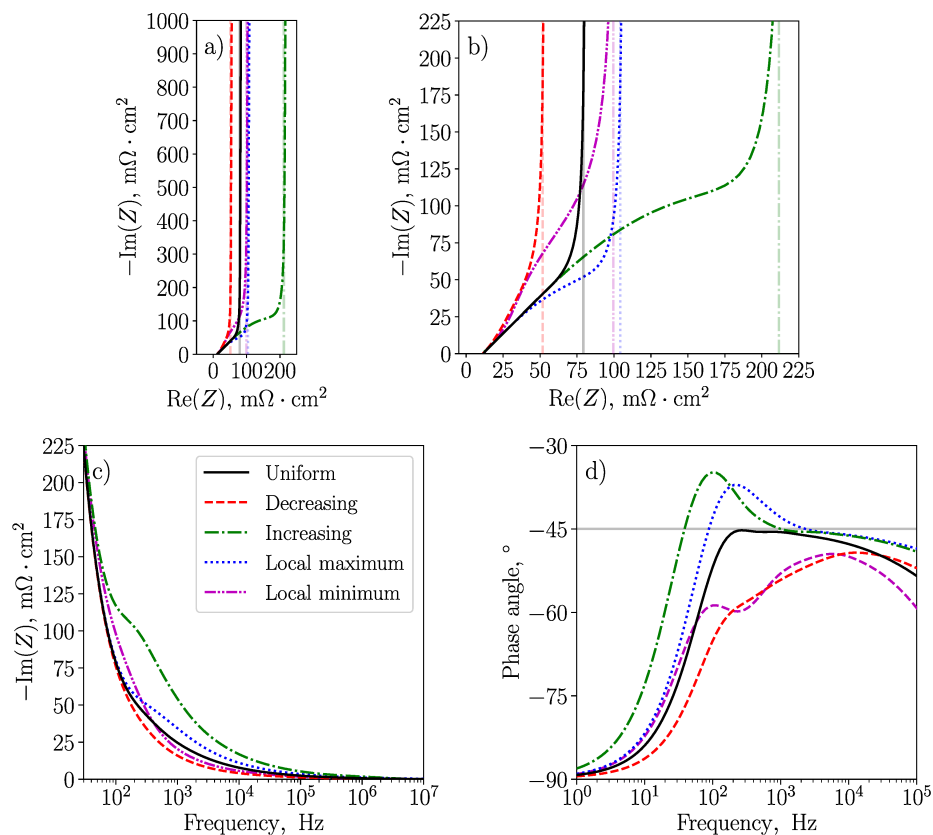
Figure 5.29: Comparison of the H$_2$/N$_2$ spectra simulated numerically for the ionomer-loading distributions from Figure 5.1 and the low electronic conductivity for case IV from Table 5.3: a), b) Nyquist plot and its high-frequency portion; c) frequency-content plot of the imaginary impedance component (high-frequency portion); and d) Bode plot of the phase angle (computed from the point $(R_{\mathrm{HF}}^{\mathrm{CL}}, 0)$). Vertical lines represent the total ohmic resistance computed through ohmic heating (equations (6) and (7); estimates at 0.1 mA/cm$^2$ are shown).

a noticeable change in the effective protonic and electronic resistances of the layer, as shown in Figures 5.30b and 5.30c. Thus, the impedance relations for uniform catalyst layers from references [177, 182, 183] should not be used to analyze distorted spectra. Impedance-spectrum distortions should be interpreted with numerical models, as analytical expressions for nonuniform CLs are often limited to a particular catalyst-layer-property distribution (see, for instance, references [404, 405, 576]).
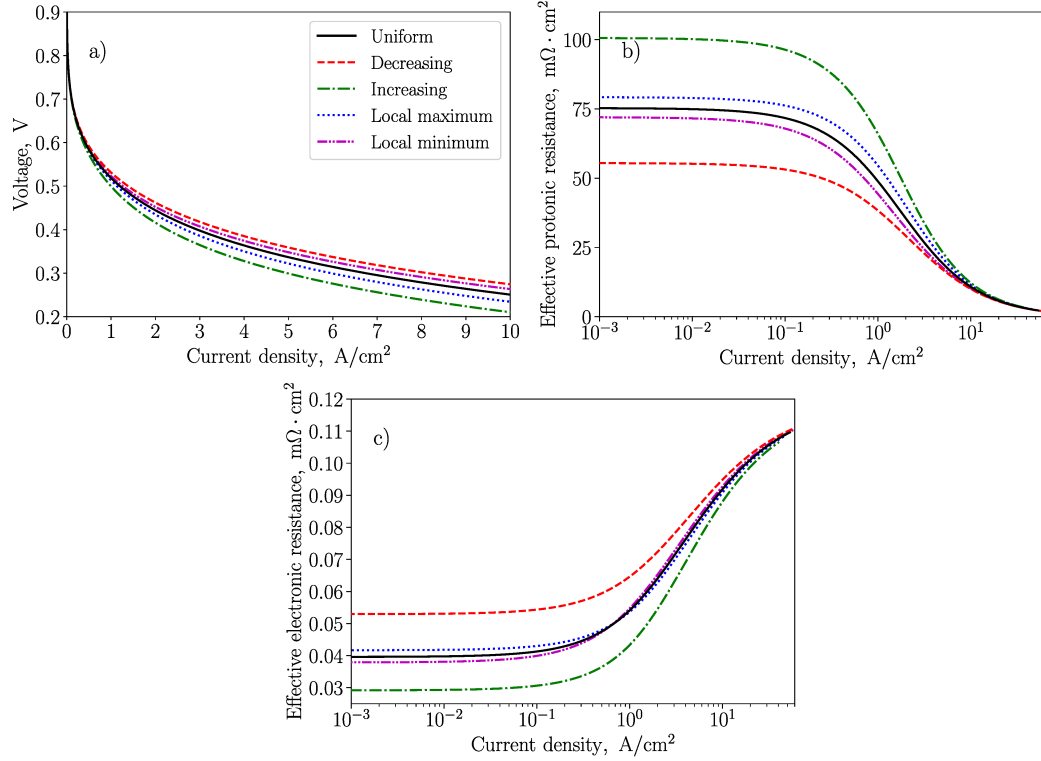
Figure 5.30: Comparison of the polarization curves (a) and ohmic resistances (b, c) of the catalyst layer simulated numerically for the active-area and double-layer capacitance distributions from Figure 5.2. The ohmic resistance was computed through ohmic heating (equations (6) and (7)).

### 5.3.6 Effect of Anode Catalyst Layer on $H_2/O_2$ PEMFC Impedance

Transient responses from anode and cathode catalyst layers may interfere with each other in physical experiments, where impedance spectra are measured for a whole electrochemical cell in contrast to a single catalyst layer. In order to analyze the effect of the anode catalyst layer on the fuel-cell $H_2/O_2$ EIS measurements, a parametric study was performed at 0.01 A/cm$^2$ using the 2D PEMFC model from Chapter 4 (Figure 5.33). The $H_2/O_2$ conditions were chosen over the $H_2/N_2$ conditions as the former allow for the rapid-EIS approach discussed in this Chapter, Chapter 4, and in reference [249]. As shown earlier, the two methods result in similar impedance spectra at high frequencies when $H_2/O_2$ EIS is performed at 0.01 A/cm$^2$.

In the reference case, two distinct arcs were observed, one between 100 Hz and
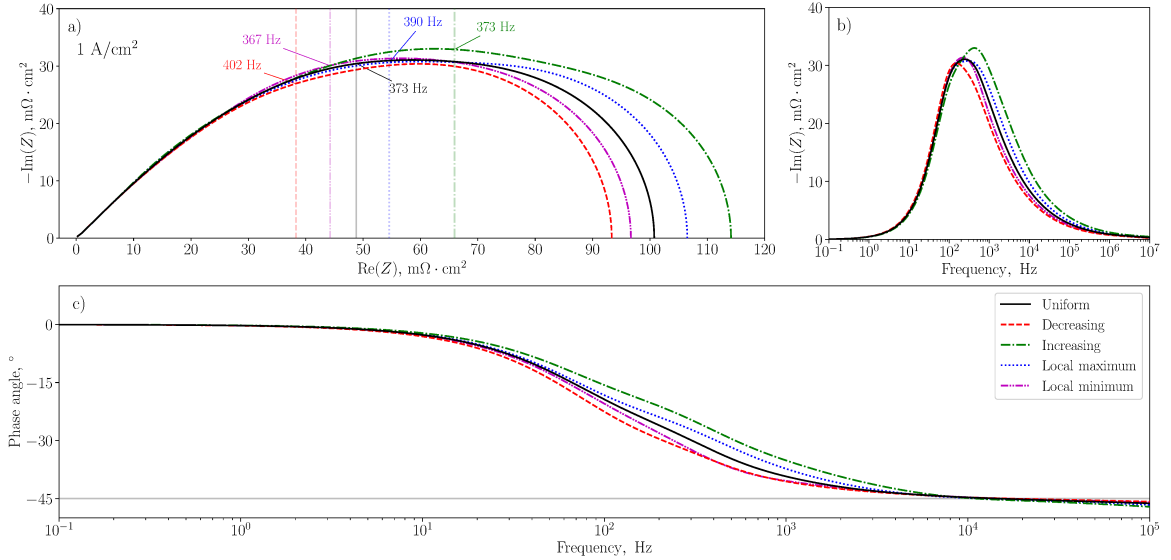
Figure 5.31: Comparison of the $H_2/O_2$ spectra simulated numerically for the active-area and double-layer capacitance distributions from Figure 5.2 at 1 A/cm²: a) Nyquist plot; b) frequency-content plot of the imaginary impedance component; and c) Bode plot of the phase angle. Vertical lines represent the total ohmic resistance computed through ohmic heating (equations (6) and (7)).

1 kHz and another at frequencies above 1 kHz (Figures 5.33c and 5.33d). In order to identify the nature of these arcs, protonic conductivities of the catalyst layers and the membrane were first made constant and uniform (independently in each layer). This had no effect on the impedance spectrum, as polymer-electrolyte hydration was relatively uniform at the given current density. Further modifications were made by increasing the protonic conductivity of first the ACL, then the CCL by a factor of $10^4$. When the ACL was highly protonically conductive, the arc at frequencies above 1 kHz disappeared, revealing the linear 45° branch as seen in Figures 5.33c and 5.33d. On the other hand, a high protonic conductivity of the CCL resulted in a spectrum with a capacitive arc at frequencies above 1 kHz but without the arc at frequencies between 100 Hz and 1 kHz. With high protonic conductivity of both catalyst layers, both arcs were negligible in size. Therefore, the arc at frequencies between 100 Hz and 1 kHz represents the CCL, and the arc at higher frequencies is related to the ACL, where a faster (compared to the ORR) hydrogen oxidation reaction occurs.
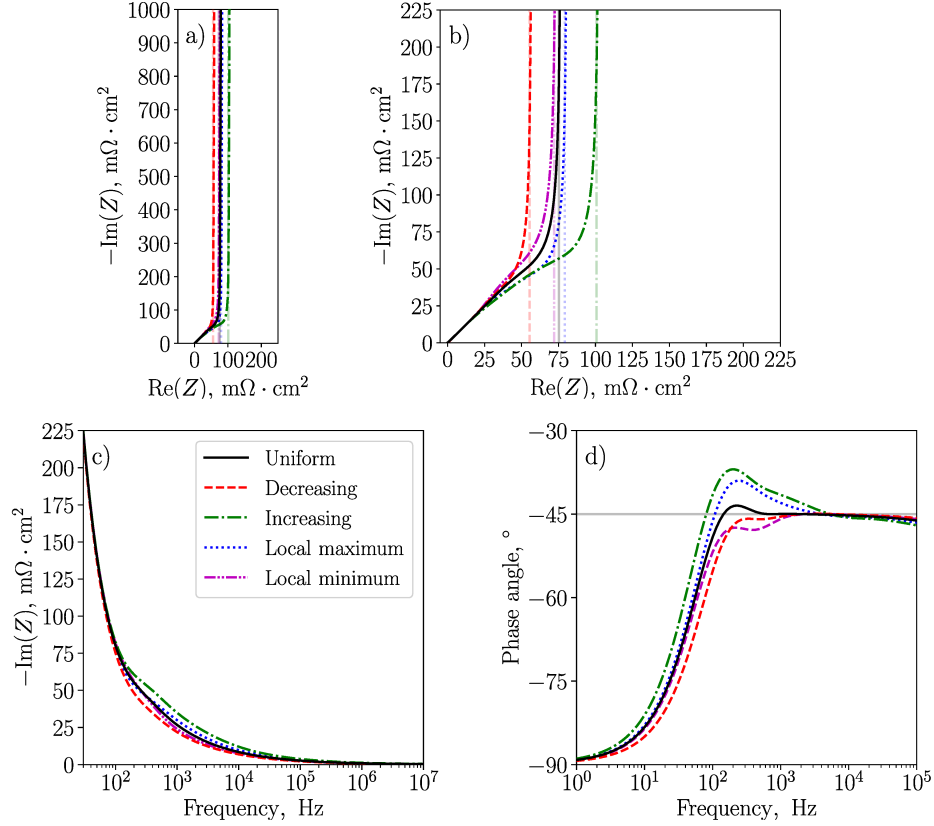
Figure 5.32: Comparison of the $H_2/N_2$ spectra simulated numerically for the active-area and double-layer capacitance distributions from Figure 5.2: a), b) Nyquist plot; c) frequency-content plot of the imaginary impedance component; and d) Bode plot of the phase angle. Vertical lines represent the total ohmic resistance computed through ohmic heating (equations (6) and (7)).

The ACL effect on the PEMFC impedance spectrum was investigated further by modifying active area. Increasing the active area of the ACL by a factor of $10^2$ revealed the 45° branch (Figures 5.33c and 5.33d; that spectrum overlaps with the $\sigma_{H^+}^{\mathrm{eff,ACL}} \times 10^4$ case). On the other hand, active-area reduction in the ACL by two orders of magnitude resulted in a significant spectrum distortion at frequencies above 5 Hz (Figures 5.33c and 5.33d) due to the increase in the protonic resistance of the ACL from 2.28 to 21.2 $m\Omega \cdot cm^2$. Such a distortion was not a multidimensional effect, as the protonic potential was nearly uniform in the in-plane direction in the two catalyst layers and the membrane. Total ohmic resistance of the ACL and the CCL, computed through ohmic heating with equations (2.156) and (2.157), was smaller than
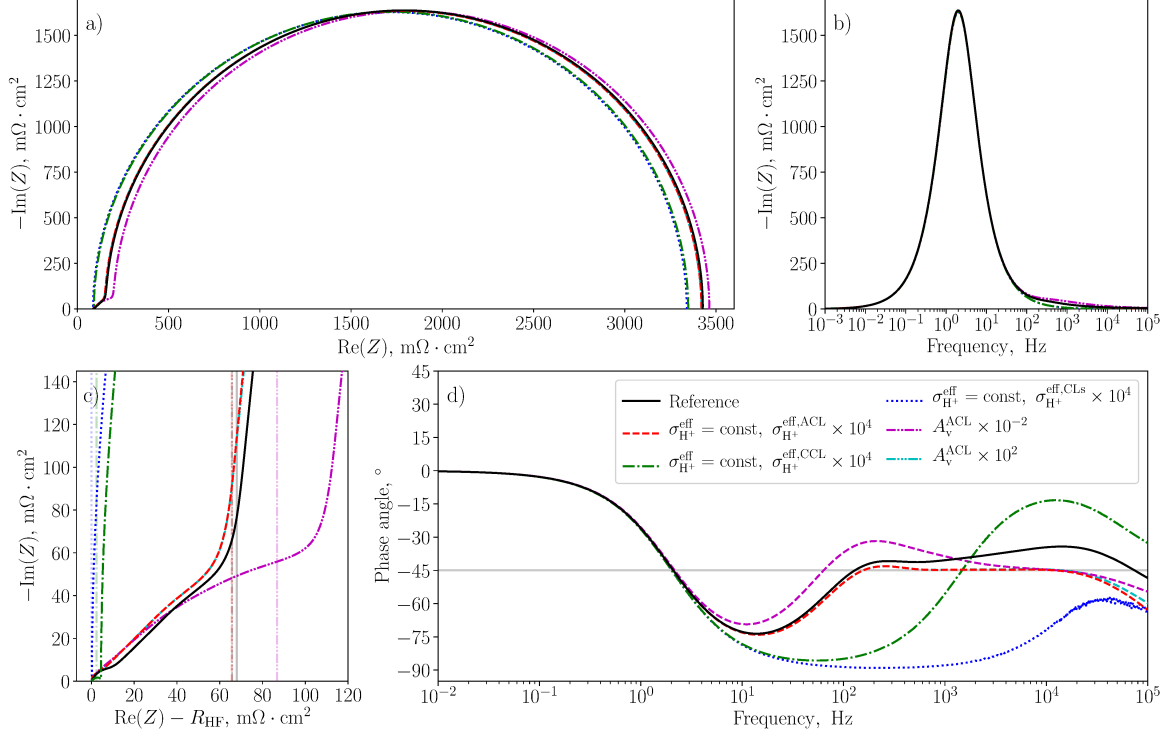
Figure 5.33: Comparison of the H$_2$/O$_2$ spectra simulated numerically at 0.01 A/cm$^2$ with the 2D PEMFC model from Chapter 4: a), c) Nyquist plot and its high-frequency portion; c) frequency-content plot of the imaginary impedance component; and d) Bode plot of the phase angle. Vertical lines represent the total ohmic resistance of the ACL and the CCL computed through ohmic heating (equations (2.156) and (2.157)). Curves corresponding to the highly conductive ACL and the ACL with large active area coincide in the shown plots. Phase angle is reported for the $R_{\mathrm{HF}}^{\mathrm{cell}}$-corrected spectra.

the projection of the apparent high-frequency arc onto the real axis (Figure 5.33c), indicating a significant contribution of the faradaic ACL impedance. The same was observed when a highly protonically conductive CCL was used, but not in other cases. Therefore, in order for the PEMFC spectrum to contain the 45° branch that enables catalyst-layer charge-transport analysis with analytical models, both faradaic and ohmic effects of the ACL must be minimized.

Equation (5.14) was fitted to the two spectra from Figure 5.33 that exhibited the 45° branch. Since these cases (high ACL protonic conductivity and active area) did not contain the anode effects, a single catalyst-layer impedance was used, as opposed to a sum of two impedance relations (5.14) representing a series connection

263

of the ACL and the CCL. The spectra were corrected for the ohmic resistance of the membrane and the gas-diffusion layers (computed through ohmic heating) prior to the fitting. Residual of both fits (equation (5.26)) was below 0.01, and $R^2$ was at least 0.9999. The fitted protonic conductivity was 2.23 mS/cm for the case with high ACL protonic conductivity and 2.22 mS/cm for the case with high ACL active area. Both fitted conductivities were close to the exact average effective protonic conductivity of the CCL, 2.27 mS/cm. Effective electronic conductivity was fitted to be 1.54 S/cm in the case with a highly conductive ACL and 0.91 S/cm in the case with a high-active-area ACL. These values were significantly different from the exact one, about 3.79 S/cm, due to the low sensitivity of the CL impedance to the relatively high effective electronic conductivity. This illustrates the applicability of equation (5.14) to estimating CCL proton-transport properties when a PEMFC spectrum is free of anodic effects. Electron-transport properties can also be extracted, as shown earlier, if electronic conductivity is not significantly higher than protonic conductivity.

## 5.4   Conclusions

A one-dimensional transient numerical model was used to generate impedance spectra of PEMFC catalyst layers (under $H_2/O_2$ and $H_2/N_2$ conditions) and PEMWE catalyst layers (under $H_2/N_2$ conditions) with known electronic and protonic conductivity. The simulated spectra and the estimated ohmic-heating-based resistance were used to assess the validity of the analytical expressions proposed in the literature for estimating effective catalyst-layer charge-transport properties under a variety of conditions, such as multi-step kinetics, nonuniform ionomer and active-area distributions, and strong anodic effects (a two-dimensional PEMFC model was used in the latter study).

Based on this Chapter, the following recommendations can be given for the estimation of the catalyst-layer charge-transport properties via EIS. Under the $H_2/O_2$ operating conditions, equation (5.14) should be chosen over equation (5.12) for fitting as

the former allows to simultaneously estimate the proton- and electron-transport properties and does not overestimate the ohmic resistance. Ohmic resistance and effective conductivity are related with equation (5.17). While the conductivity estimation is reasonably accurate at any current density (Table 5.5), a reliable ohmic-resistance measurement is only possible at low current densities confined by equation (5.18). If one of the catalyst-layer conductivities is known (for example, from a four-probe measurement [120, 412, 415]), the other one can be found from $R_{HF}^{CL}$ using equation (5.15) (after a correction of $R_{HF}^{cell}$ for other cell components). Additionally, the ORR kinetic study performed in this work indicates that the catalyst-layer charge-transport characterization should only be performed at low current density and at sufficiently high frequencies to avoid the propagation of the faradaic effects to the frequencies of interest. If the order of magnitude of the catalyst-layer conductivities can be estimated, the required minimum frequency and the maximum applicable current density can be found from equations (5.33) and equation (5.34), respectively.

The $H_2/N_2$ spectroscopy is more commonly used in the literature for the charge-transport characterization as it allows for better control of the local relative humidity and temperature due to the absence of faradaic reactions in the working electrode. Equations (5.12) and (5.19) can be used to analyze the $H_2/N_2$ spectra, but equation (5.21) should be preferred as it has the same advantages as equation (5.14) in the $H_2/O_2$ case, e.g., the ability to estimate both electronic- and protonic-transport properties, which is important in case of PEMWE ACLs that may exhibit low electronic conductivity. If the vertical low-frequency branch is present in the measured $H_2/N_2$ spectrum, a simple graphical approach can be used to extract the protonic and electronic conductivities (Figure 5.6b and equations (5.24) and (5.25)). The respective ohmic resistances can then be accurately calculated with equation (5.17).

As discussed in Section 5.3.3, catalyst-layer impedance is less sensitive to the more conductive phase. If one of the conductivities is significantly higher than the other, the obtained charge-transport properties may not be as accurate as those for the less

conductive phase (Tables 5.4 and 5.5). Moreover, two pairs of conductivities (and thus two pairs of ohmic resistances) satisfy the same impedance spectrum (equations (5.24) and (5.25)). Assignment of the extracted property to a given phase is not possible without knowing which phase is more conductive.

If the spectrum deviates from the ideal 45° line at high frequencies after the inductance correction (performed via either equivalent-circuit fitting [2, 177] or short-circuit measurements [587]), the observed impedance may signify catalyst-layer nonuniformity [173, 175, 178, 404, 405, 414, 422, 438, 576, 577]. This nonuniformity may be caused either by the structural properties of the layer, such as the ionomer and active-area distributions, or by the nonuniform hydration and degradation. Other hypothesized reasons include complex pore structure [178, 186, 414, 422, 574], nonuniform pore- and particle-size distribution [574], nonuniform CL thickness [175, 178], and additional double-layer capacitance of the ionomer-carbon and ionomer-water interfaces [436]. Even though analytical [405, 436, 576] and equivalent-circuit [175] models exist that account for some of the aforementioned factors, they either were designed for a specific type of nonuniformity [175, 405, 576] and are not general, or represent a catalyst layer as a single pore [436], which is not accurate. Therefore, catalyst-layer conductivity cannot be reliably extracted from the spectrum with a distortion at frequencies between 10 Hz–10 kHz. However, total ohmic resistance can be estimated from $H_2/N_2$ measurements as long as the vertical impedance branch is observed at frequencies below 1–10 Hz (Figures 5.28 and 5.29).

Catalyst-layer nonuniformity has been hypothesized [174, 184, 188, 414, 420, 438, 577, 586] to also induce a deviation from the low-frequency 90° slope in the $H_2/N_2$ spectra [120, 124, 126, 174, 175, 184, 185, 188, 189, 196, 413, 414, 417–422, 429, 438, 586, 588]. However, it has been shown in this work and in references [173, 175] that the 90° branch is observed even in catalyst layers with nonuniform distributions of conductivity, active area, and double-layer capacitance. Therefore, the commonly observed distortion of the $H_2/N_2$ impedance spectra at frequencies below 1–10 Hz

is likely due to other phenomena, such as hydrogen crossover [173, 174, 586, 588], oxygen traces in the cathode stream [422, 586], and specific adsorption of sulfonate groups (from the ionomer) on platinum [586]. The resulting faradaic processes cannot be described with equations (5.19) and (5.21) or with the respective graphical methods, and equations (5.12) and (5.14) should be used instead.

It has been shown in this work that uniformity of the catalyst layer in the working electrode is necessary but not sufficient for the spectrum to contain the 45° branch. Significant faradaic and ohmic effects of the reference electrode (e.g., ACL in PEM-FCs) may also distort the spectrum and obstruct its analysis with analytical models.

Nonuniformity in ionomer loading, nonuniformity in active area, and strong effects of the reference electrode all lead to similar changes in the shape of the spectrum at frequencies above 5 Hz, and no conclusions on the working-electrode structure can be made. This highlights the importance of advanced mathematical modeling in the interpretation of experimental PEMFC and PEMWE impedance spectra.

# Chapter 6

# A Transient, Pore-Size-Distribution-Based Model for the Analysis of the Two-Phase Water Transport in Fuel Cells[1]

Water management is crucial for achieving high performance of PEMFCs. On the one hand, the electrolyte (Nafion®) needs to be kept well hydrated to support its protonic conductivity [116, 117]. On the other hand, liquid water that is either produced in the ORR or condensed in the cell needs to be removed in order to avoid reactant starvation and performance loss. A number of pore-size-distribution-based fuel-cell models have been proposed in the literature to account for the microstructure of the porous MEA components when computing their liquid-transport properties [26–28, 34, 35, 39, 276, 282, 305, 342]. However, stationary operation was assumed in those models while, as discussed in Chapter 1, accumulation and removal of liquid water is, most likely, a dynamic process [50, 112, 157, 221, 274, 289, 459–462]. Transient PSD-based models were developed by Balliet and Newman [266–268] and Goshtasbi

---

[1]Parts of this chapter are based on the following upcoming publication:

1. A. Kosakian, F. Wei, S. Jung, J. Zhou, A. Punia, J. Liu, and M. Secanell, "A transient, pore-size-distribution-based model for the analysis of the two-phase water transport in fuel cells," (in preparation).

Author contributions are detailed in the Preface of this thesis and in the text of this Chapter.

et al. [157], but the effect of the pore-size distributions on the cell performance was not analyzed.

A transient two-phase PSD-based PEMFC model was developed in Chapter 2 to study how the microstructure of the MEA components translates into their transport properties and into the cell performance in the presence of liquid water. In this Chapter, the model predictions are compared with experimental data, and parametric studies are performed to understand the impact of the liquid-water breakthrough at the GDL-channel interface, the evaporation rate, the wettability of the MEA components, and the CCL catalyst loading on the dynamic two-phase fuel-cell performance.

## 6.1 Mathematical Model

The transient two-phase PEMFC model used in this Chapter is the one described in Chapter 2. The governing equations of the model were summarized in Section 2.1.2.7 and are not repeated here. The computational domain represented a through-the-channel cross-section of a fuel cell and was similar to the one used in Chapter 4 (Figure 4.1).

### 6.1.1 Initial and Boundary Conditions

Before each transient simulation, equations (2.54)–(2.60) were solved at steady state at the voltage that corresponded to the starting point of the experimental measurements, 0.8–0.9 V. The obtained solution was then used as an initial condition in the transient model with which the polarization-curve simulations were performed.

The boundary conditions are provided in Table 6.1, where the quantities with a zero superscript were computed based on the operating conditions as discussed in reference [262]. At the GDL-channel interface of each electrode, a boundary condition was imposed that described the experimentally observed [112, 459–461] dynamic liquid-water accumulation and drainage from the cell. At the beginning of each transient simulation, a no-flux condition was used at the whole interface. When the capillary

Table 6.1: Boundary conditions in the two-phase PEMFC model.

| Solution variable | AGDL-channel | AGDL-land | CGDL-channel | CGDL-land | Symmetry |
|---|---|---|---|---|---|
| $x_{O_2}$ | no flux | no flux | $x_{O_2} = x_{O_2}^0$ | no flux | no flux |
| $x_{wv}$ | $x_{wv} = x_{wv,a}^0$ | no flux | $x_{wv} = x_{wv,c}^0$ | no flux | no flux |
| $\phi_{H^+}$ | no flux | no flux | no flux | no flux | no flux |
| $\phi_{e^-}$ | no flux | $\phi_{e^-} = 0$ | no flux | $\phi_{e^-} = V_{cell}(t)$ | no flux |
| $\lambda$ | no flux | no flux | no flux | no flux | no flux |
| $T$ | $\kappa^{eff}\nabla T \cdot \boldsymbol{n} = 0$ | $T = T^0$ | $\kappa^{eff}\nabla T \cdot \boldsymbol{n} = 0$ | $T = T^0$ | no flux |
| $p_c$ | no-flux or (6.1) | no flux | no-flux or (6.1) | no flux | no flux |

pressure reached the breakthrough value, $p_{c,bt}$, at some interface locations, liquid water was allowed to leave the cell by imposing the following boundary condition at those locations:

$$\boldsymbol{v}_{lw} \cdot \boldsymbol{n} = -\frac{\rho_{lw}\kappa_{lw}}{\mu_{lw}}\nabla p_c \cdot \boldsymbol{n} = k_{l,out}\frac{p_c - p_{c,eq}}{p_0}, \tag{6.1}$$

where $k_{l,out}$ is a rate constant in $g/(cm^2 \cdot s)$, $p_0 = 1$ Pa [34, 276] is an arbitrary constant, and $p_{c,eq}$ is the equilibrium capillary pressure at the GDL-channel interface when $k_{l,out} \to \infty$. At the boundary locations where the capillary pressure decreased to the given minimum value, $p_{c,min}$, a no-flux condition was imposed again, and water was allowed to accumulate until the next breakthrough took place.

Condition (6.1) was applied in both electrodes only in the transient simulations. It was only applied in the cathode in the steady-state simulations, and a Dirichlet condition was used on the anode side to numerically pin the solution so that the capillary-pressure distribution that satisfies the given boundary conditions was unique. A steady-state solution could not be reached with the boundary condition (6.1) imposed in both anode and cathode. Since the steady-state simulations were only performed at low current density, a constant capillary pressure of $-50$ MPa, corresponding to zero saturation, was set at the AGDL-channel interface.

## 6.1.2 Model Inputs

### 6.1.2.1 Cell Properties

The physical cell simulated in this Chapter was similar to the one described in Chapter 4, and most of the model inputs were identical to those provided in Section 4.1.3. However, some of the model inputs were modified to reflect the changes in the cell design. Bipolar plates with a single straight channel were used to minimize the channel blockage with liquid-water droplets, and a smaller MEA was designed for the new flow-field geometry. The dimensions of the new cell[2] and the operating conditions are provided in Table 6.2. The operating temperature and RH were set to 60 °C, 90% RH so as to elucidate the effects of liquid-water accumulation. Additionally, some model inputs were changed to account for liquid water and to achieve a better agreement with the experimental polarization curves and HFR measurements. Those parameters are given in Table 6.3 and are explained next. As it will be discussed later, a number of parameters governing liquid-water transport in fuel cells are unknown; their calibration with the in-house fuel-cell measurements is currently in progress.

The effective diffusion coefficient for the CLs and the MPLs was computed with equation (2.70). To compute the effective diffusivity in the GDLs, equation (2.71) was used, where parameters $\mu = 2.76$ and $\mu = 1.22$ were chosen that result, respectively, in the through-plane and in-plane dry diffusibility (the ratio of the effective diffusivity to its bulk value when $s = 0$) of 39BA GDLs (similar in structure to 29BA GDLs) that was recently measured in-house [215]: $0.414 \pm 0.040$ and $0.602 \pm 0.005$, respectively. Constants $\gamma = 2.77$ and $\gamma = 1.58$ of equation (2.71) were found by fitting, respectively, the through-plane and in-plane diffusivity ratios of the partially saturated and dry SGL 39BA GDLs reported by Jung [212] with the least-squares

---

[2]Symmetry (no-flux) conditions are imposed in the model a the center of the channel and the center of the land. Since the physical cell had only one channel, twice the land width was used in the model to impose the no-flux (symmetry) conditions at the computational-domain boundaries that corresponded to the edges of the physical MEA. The dimensions of the physical cell are discussed later in this Chapter.

Table 6.2: Operating conditions and geometrical properties.

| Property | Value | Details |
|---|---|---|
| **Operating conditions** | | |
| Temperature, K | 333.15 | Controlled |
| Pressure, kPa | 140 (anode), 145 (cathode) | Controlled |
| RH | 0.9 | Controlled |
| **Cell geometry** | | |
| Land width, μm | 2180 | Measured (optical microscope) |
| Channel width, μm | 820 | Measured (optical microscope) |
| MEA area, cm$^2$ | 0.9 | Controlled (inkjet printing) |

Table 6.3: Model inputs for the catalyst layers.

| Property | Value/expression | Details |
|---|---|---|
| Thickness, μm | 2.8 | Table 4.4 |
| Active area, cm$^2_{Pt}$/cm$^3_{CL}$ | 143,000 | Measured (cyclic voltammetry) |
| Volumetric double-layer capacitance, F/cm$^3$ | 43 | Measured (cyclic voltammetry) |
| Effective gas diffusivity[a] | $D^{\mathrm{eff}} = \begin{cases} D\left(\frac{\varepsilon_{\mathrm{p}}(1-s)-0.05}{0.95}\right)^{1.9}, & \varepsilon_{\mathrm{p}}(1-s) \geq 0.05 \\ 0, & 0 < \varepsilon_{\mathrm{p}}(1-s) < 0.05 \end{cases}$ | [130, 131] |
| Portion of the ORR water produced in the ionomer phase | $\xi = 0.4$ | This work[b] |
| ICCP oxygen-dissolution rate constant, m/s | $k_{O_2} = 1.3 \cdot 10^{-3}$ | This work[c] |

[a] Equivalent to the diffusivity used in Chapter 4 at $s = 0$.
[b] Estimated based on the simulated and experimental HFR data.
[c] Estimated based on the simulated and experimental limiting current density with 1% oxygen.

algorithm from SciPy [486] ($R^2$ of the fit was at least 0.9998, the root-mean-square

residual was less than $7.3 \cdot 10^{-3}$).

The rates of water condensation and evaporation in the source/sink term (2.23) are generally unknown. Zenyuk et al. [209] reported the rate of liquid-water evaporation in the SGL 10BA and 24BA GDLs reconstructed with the X-ray computed tomography to be $10^{-6}$–$10^{-4}$ mol/(cm$^2 \cdot$ s) by the order of magnitude. The evaporation rate was shown to increase with temperature and to decrease with an increase in RH [209]. Based on these results and on the additional parametric studies performed with their steady-state two-phase PEMFC model, Zhou et al. [34] estimated the evaporation rate, assumed the same in all the porous MEA layers, to be $2 \cdot 10^{-4}$ mol/(cm$^2 \cdot$ s) at 60 °C, 90% RH. The condensation rate was found to be $2 \cdot 10^{-2}$ mol/(cm$^2 \cdot$s) [34]. The same condensation rate was assumed in the transient two-phase PEMFC model used in this Chapter. However, the evaporation rate reported by Zhou et al. [34] resulted in negligible liquid-water accumulation, and a ten times lower rate, $2 \cdot 10^{-5}$ mol/(cm$^2 \cdot$s), was assumed in this thesis. Parametric studies on the effect of the liquid-water phase-change rates were performed and will be discussed later in this Chapter.

As it was discussed in Chapter 2, liquid-water uptake by the polymer electrolyte was approximated in this work by assuming that a portion of the ORR product water was directly absorbed by the ionomer phase of the CCL. Typically, more liquid water is produced at lower temperature and at higher relative humidity. Therefore, the fraction of the ORR produced in the ionomer, $\xi$, was set to 0.4 at the considered operating conditions of 60 °C, 90% RH. These parameters were chosen so that the simulated HFR (the ohmic resistance of the membrane and of the electronically conductive components computed with equations (2.156) and (2.157)) would be closer to the experimental data.

The dissolution-rate constant in the ICCP sub-model, $k_{O_2}$ (equation (2.8)), was also modified. It was assumed in Chapter 4 to be independent of the operating conditions. However, the experimental data by Shukla et al. [125] and Kudo et al. [325] suggest that the local oxygen-transport resistance in the catalyst layers decreases with an

increase in temperature and RH. Therefore, $k_{O_2}$ should increase with temperature and RH. As in Chapter 4, the updated value of the oxygen-dissolution rate constant was obtained by performing a parametric study on $k_{O_2}$ and comparing the model predictions with the polarization curves measured with 1% oxygen in the cathode stream. The resulting dissolution rate was $1.3 \cdot 10^{-3}$ m/s.

The effective volumetric heat capacity of all porous layers was computed as discussed in Chapters 2 and 4. An additional term, $\varepsilon_{\mathrm{p}} s \rho_{\mathrm{lw}} C_{p,\mathrm{lw}}$, was used in equation (2.40) to account for the heat capacity of liquid water. The specific heat capacity of liquid water, $C_{p,\mathrm{lw}}$, was set to 4.2 J/(g · K) [589].

The parameters of the PSD sub-model were calibrated with the experimental data and with the results of the pore-level simulations from the literature. Those parameters are discussed later in this Chapter.

### 6.1.2.2    Liquid-Water Breakthrough Properties

The equilibrium capillary pressure, $p_{\mathrm{c,eq}}$, was set to zero in equation (6.1) under the assumption that liquid water remained in the hydrophilic pores during the drainage. The breakthrough capillary pressure, $p_{\mathrm{c,bt}}$, and the minimum capillary pressure, $p_{\mathrm{c,min}}$, in equation (6.1) depend on the type of the GDL. The experimental data used in this Chapter were measured with a cell that had SGL 29BA GDLs, and thus a literature survey was conducted to find the breakthrough data for such materials. Ziegler [461] recently reported the experimentally measured saturation variations between 0.08 and 0.14 during the liquid-water accumulation and drainage cycles in SGL 39BA GDLs, the internal structure of which is similar to SGL 29BA. Similar saturation was obtained for SGL 29BA GDLs with the PSD model in this work at the capillary pressure of 0.65 kPa and 0.77 kPa, and those values were used as $p_{\mathrm{c,min}}$ and $p_{\mathrm{c,bt}}$, respectively, in the boundary condition (6.1) of the two-phase PEMFC model. However, the corresponding pressure values measured by Ziegler [461] were higher than computed with the PSD model for the indicated saturation, 1.3 kPa and

1.6 kPa. The saturation-pressure curves computed with the PSD model and a parametric study that illustrates the effect of $p_{\mathrm{c,bt}}$ and $p_{\mathrm{c,min}}$ on the transient two-phase performance of PEMFCs are shown later in this Chapter.

The liquid-water eruption rate in equation (6.1), $k_{\mathrm{l,out}}$, is not known. Zhou et al. [34] performed parametric studies on that rate constant and found that $k_{\mathrm{l,out}} = 10^{-6}$ g/$(\mathrm{cm}^2 \cdot \mathrm{s})$ worked well for their steady-state model. In the transient model developed in this thesis that utilizes an updated PSD sub-model compared with reference [34], a baseline value of $2 \cdot 10^{-7}$ g/$(\mathrm{cm}^2 \cdot \mathrm{s})$ was chosen based on the simulated and experimental polarization curves.

## 6.1.3 Solution Approach

The numerical model was implemented in the in-house open-source fuel-cell simulation software, OpenFCST [374, 375]. The computational domain was discretized with the finite-element method using second-order Lagrange shape functions and 11,319 degrees of freedom (1,617 computational nodes). The computational grid is shown in Figure 4.3. Newton's method was used to linearize the problem. The residual tolerance was set to $10^{-8}$, and the absolute and relative solution-error tolerances were 0.1 and $10^{-3}$. The implicit Euler method (BDF1) with the time-step size of either 0.5 s or 1 s was used for the temporal discretization. As discussed in Chapter 2, successive step-size halving was performed when the Newton solver reported no convergence, followed with the step-doubling recovery to the baseline time-step size. The chosen simulation parameters were found sufficient for the preliminary simulations shown in this Chapter, with no significant change in the predicted current density and HFR at a higher refinement level or with a smaller time-step size. The simulations were performed in parallel using 2 threads of Intel® Core™ i7-2600 CPU at 3.40 GHz. The simulation time varied between 4 and 28 hours depending on the model inputs.
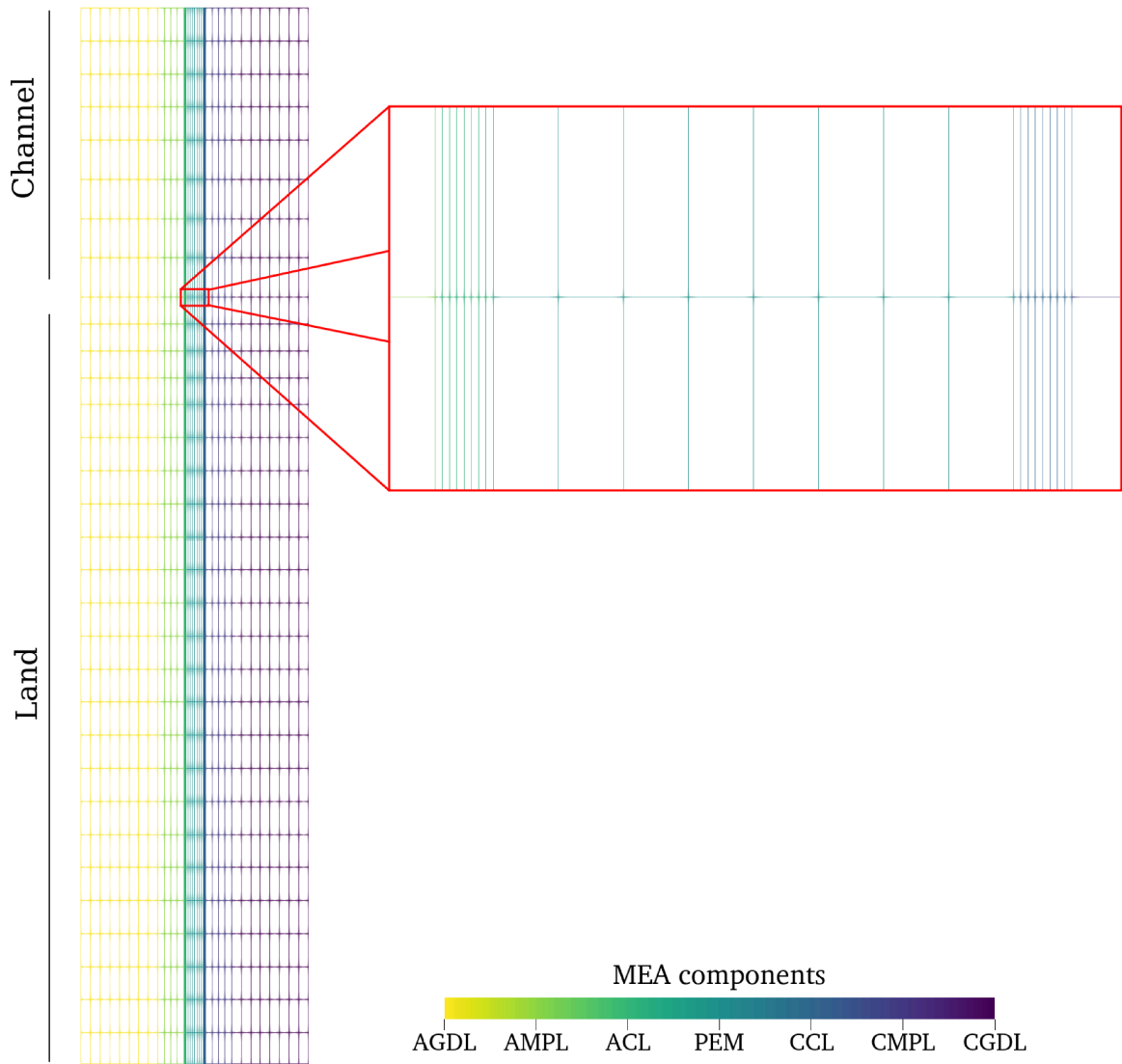
Figure 6.1: The computational grid used for the PEMFC model in this Chapter.

## 6.2 Experiment

### 6.2.1 Fuel-Cell Fabrication and Testing

The experimental measurements described in this Chapter were performed by F. Wei, a Ph.D. student at ESDL. The catalyst-ink preparation, catalyst-layer fabrication, and cell assembly were performed the same way as discussed in Chapter 4 except for the changes described next.

Compared with the previous cell, a lower platinum loading of 0.1 $mg_{Pt}/cm^2$ was used to fabricate the cathode catalyst layer of the new cell. The same loading was used in the anode catalyst layer. The membrane area printed with the catalyst layers was 3-cm long and 3-mm wide. The resulting active area of 0.9 $cm^2$ was smaller compared with 5 $cm^2$ in Chapter 4, since different bipolar plates with a single straight 0.82-mm-wide and 1-mm-deep channel were used this time. The channel was located in the middle of the active area and extended by 1.75 cm beyond the catalyst-layer edges to reduce the inlet and outlet effects.

Since the bipolar-plate geometry has changed compared with Chapter 4, new gas-flow rates had to be found that would eliminate the along-the-channel effects to make the measurements more suitable for the validation of the through-the-channel numerical model. The flow rates of hydrogen and air were chosen by comparing the polarization curves at 4.8 mV/s and the potentiodynamic impedance spectra between 100 kHz and 0.1 Hz at 80 °C, 90% RH measured with increasing gas-supply rates in the 0.1–4 slpm range. The flow rates at which the changes in the measurements were minimal compared with the two neighboring values were chosen as optimal. They were 0.5 slpm and 3 slpm for hydrogen and oxygen, respectively. When polarization curves were measured with 1% oxygen in the cathode stream, the same flow rate of 3 slpm was used.

Polarization-curve and HFR measurements were performed simultaneously using the Bio-Logic SP-300 potentiostat. The polarization sweeps were performed at

0.44 mV/s and at 4.8 mV/s between the OCV (0.8–0.9 V, depending on the operating conditions) and about 0.2 V. The HFR was determined from 50-kHz impedance probed every 50 mV of the voltage scan.

## 6.2.2 Ex-Situ Characterization

Ex-situ characterization of the MEA components was performed to obtain data for the calibration of the mass-transport properties computed with the PSD model. Through-plane permeability of the SGL 29BA GDLs (with no MPL coating), of the SGL 29BC MPLs, and of the catalyst layers were measured in-house as discussed in references [78, 79, 215, 567, 590–592]. The permeabilities were found to be $4.14 \pm 0.06 \cdot 10^{-11}$ m$^2$ for the GDLs, $6.56 \pm 0.34 \cdot 10^{-14}$ m$^2$ for the MPLs, and $3.16 \pm 0.11 \cdot 10^{-16}$ m$^2$ for the CLs. These values are used later in this Chapter to find the pore-interconnectivity factor, $\lambda_{\mathrm{PSD}}$, for the calculation of the global saturated (or dry) permeability in the model (equation (2.103)), which was assumed the same in the through-plane and in-plane directions. The CLs used in the permeability measurements had the same weight loading of platinum (40%) and Nafion$^\circledR$ (30%) as the catalyst layers considered in this Chapter, but a higher areal catalyst loading of 0.15 mg$_{\mathrm{Pt}}$/cm$^2_{\mathrm{CL}}$. In the absence of data for the CLs with 0.1 mg$_{\mathrm{Pt}}$/cm$^2_{\mathrm{CL}}$, the reported permeability was assumed representative.

Pore-size distributions of the gas-diffusion layers and microporous layers were found from the mercury-intrusion-porosimetry (MIP) data measured in-house as discussed in reference [443]. The catalyst-layer PSD obtained with this method was not repeatable and was taken from the literature instead as discussed later. A Python code for processing the raw experimental MIP data was developed by A. Punia, a Ph.D. student at ESDL, and by the author. The procedure is illustrated in Figure 6.2. The intruded-volume data were interpolated on a log-uniform pressure grid with cubic splines and then smoothed with the Savitzki-Golay filter [593] from SciPy [486] (Figure 6.2a). A quadratic polynomial was used in the filter to fit the data windows with

the size equal to 5% of the raw input data. Pressure values were then converted into the pore radii using equation (2.87) (Figure 6.2b). The mercury-air contact angle was taken to be $\theta = 140°$ [215]. The smoothed intruded volume was then differentiated with respect to the pore radius using the finite-difference formulae for uneven grids [594]. The resulting experimental PSD $\Delta X/\Delta r$ (Figure 6.2c, black line) was noisy due to the differentiation and required additional smoothing. The PSD was interpolated on a log-uniform radius grid with cubic splines, and the Savitzki-Golay filter was applied with the same parameters as before. The obtained smoothed PSD (Figure 6.2c, red line) was integrated with the trapezoidal rule and normalized by the result to ensure that the final PSD integrated to unity.

The computed PSD, $dX/dr$, was fitted to the experimental PSD, $\Delta X/\Delta r$, by minimizing the root-mean-square deviation:

$$\text{Residual} = \sqrt{\left(\sum_{i=1}^{N} \frac{\Delta X_i}{\Delta r_i} - \frac{dX(r_i)}{dr}\right)^2 / N}. \tag{6.2}$$

The minimization was performed with respect to the quantities $f_{i,k}$, $r_{i,k}$, and $s_{i,k}$ of the PSD equation (2.88). The volume fractions $f_{i,k}$ were constrained to sum up to 1.

The GDL PSD was fitted by J. Liu, a Ph.D. student at ESDL, using the COLINY pattern search from the open-source optimization package Dakota [595] using the Python interface developed by A. Punia. A Python code was developed by the author for fitting the MPL and CL PSDs using the SLSQP algorithm from SciPy [486]. The MPL PSD was obtained by subtracting the 29BA GDL PSD from the PSD of the 29BC GDL-MPL combination.

## 6.3 Results and Discussion

### 6.3.1 Fitting and Validation of the PSD Model

#### 6.3.1.1 Pore-Size Distribution

**Gas-Diffusion Layers** The PSD parameters of the SGL 29BA GDLs fitted to the experimental data are given in Table 6.4, where they are marked as "SGL 29BC-
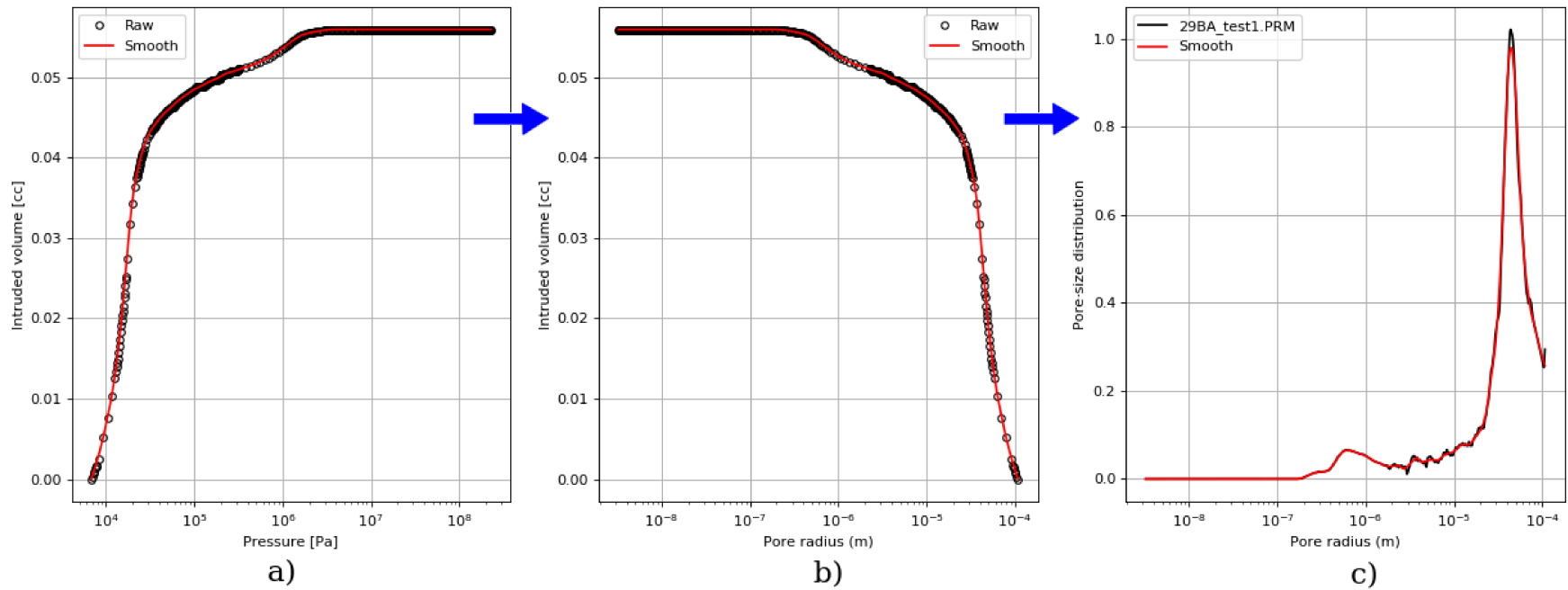
Figure 6.2: Illustration of the MIP data processing for the example PSD of a 29BA GDL: a) raw and smoothed intrusion data; b) the same, with the pressure converted to the pore radius; c) the resulting PSD with and without the final smoothing.

GDL-A." Here and later in this Chapter, the term "29BC GDL" is used to emphasize that the GDL in question is the substrate of the 29BC GDL-MPL combination. The experimental and the fitted pore-size distributions of the SGL 29BC GDL are shown in black circle markers and the solid red line in Figure 6.3a. A good fit with the residual of 0.01 was obtained with six PSD modes.

The distribution in Figure 6.3a has two clear peaks, one at 0.5–0.6 μm and another at 40–50 μm. The former falls into the binder-pore range of 0.1–2 μm reported by Xu [79], and the latter corresponds to the inter-fiber pores of the GDL. The binder-free peak at 40–50 μm was isolated into a separate case in Table 6.4 marked "SGL 29BC-GDL-B."

Wettability of the individual PSD modes is unknown, and three parametric cases were considered. In the baseline case ("SGL 29BC-GDL-A"), the binder modes with the radii of 0.673 and 3.53 μm were assumed hydrophilic. This resulted in a volume fraction of the hydrophilic pores of 0.097, which was in line with $F_{\mathrm{HI}} \in [0.04, 0.13]$ reported for various GDLs by Gostick et al. [596] The hydrophilic and hydrophobic contact angles were assumed to be the same for all modes and to match those used by Zhou et al. [35] for modeling SGL 24BA GDLs that have the same PTFE loading (5%) and similar porosity (0.74) as the 29BA GDLs: $\theta_{\mathrm{HI}} = 70°$ and $\theta_{\mathrm{HO}} = 122°$. Pore-interconnectivity factor $\lambda_{\mathrm{PSD}} = 0.121$ was used to match the experimentally measured dry gas permeability of SGL 29BA GDLs, $4.14 \cdot 10^{-11}$ m$^2$. Two more cases were considered, one with 90% hydrophobic binder pores ("29BC-GDL-C") and one with the binder being 50% hydrophilic ("29BC-GDL-D"). The respective PSD parameters are provided in Table 6.4. Because pore interconnectivity is a structural property independent of wettability, the same $\lambda_{\mathrm{PSD}} = 0.121$ was used in cases 29BC-GDL-A/C/D. It was assumed the same in case 29BC-GDL-B as well.

The experimental and fitted GDL PSDs are compared in Figure 6.3a with the pore-size distribution reported for an SGL 39BA GDL by Jung [212] based on a μCT reconstruction. Since the resolution of the reconstruction was 1.79 μm, the binder

Table 6.4: Pore-size-distribution-model parameters used in this work for SGL 29BC gas-diffusion layers.

| Parameter | Value/expression | Details |
|---|:---:|---|
| Contact angle | $\theta_{HI} = 70°$, $\theta_{HO} = 122°$ | [34] |
| Pore-interconnectivity factor | $\lambda_{PSD} = 0.121$ | This work[a] |
| Pore-shape factor | $M_{PSD} = 0.0642$ | This work[b] |
| **SGL 29BC-GDL-A** | | |
| Hydrophilic and hydrophobic volume fractions | $F_{HI} = 0.097$, $F_{HO} = 0.903$ | This work |
| Characteristic pore fractions | $(f_{HI}) = (0.6580, 0.3420)$, $(f_{HO}) = (0.0798, 0.1599, 0.6156, 0.1447)$ | This work[c] |
| Characteristic pore radii, μm | $(r_{HI}) = (0.673, 3.53)$, $(r_{HO}) = (12.8, 43.9, 47.0, 91.8)$ | This work[c] |
| Characteristic standard deviations | $(s_{HI}) = (0.431, 0.525)$, $(s_{HO}) = (0.462, 0.150, 0.400, 0.338)$ | This work[c] |
| **SGL 29BC-GDL-B** | | |
| Hydrophilic and hydrophobic volume fractions | $F_{HI} = 0$, $F_{HO} = 1$ | This work |
| Characteristic pore fractions | $(f_{HI}) = (0, 0)$, $(f_{HO}) = (0.0798, 0.1599, 0.6156, 0.1447)$ | This work |
| Characteristic pore radii, μm | $(r_{HI}) = (0.673, 3.53)$, $(r_{HO}) = (12.8, 43.9, 47.0, 91.8)$ | This work |
| Characteristic standard deviations | $(s_{HI}) = (0.431, 0.525)$, $(s_{HO}) = (0.462, 0.150, 0.400, 0.338)$ | This work |
| **SGL 29BC-GDL-C** | | |
| Hydrophilic and hydrophobic volume fractions | $F_{HI} = 0.0097$, $F_{HO} = 0.9903$ | This work |
| Characteristic pore fractions | $(f_{HI}) = (0.6580, 0.3420)$, $(f_{HO}) = (0.0579, 0.0301, 0.0728, 0.1458, 0.5614, 0.1320)$ | This work |
| Characteristic pore radii, μm | $(r_{HI}) = (0.673, 3.53)$, $(r_{HO}) = (0.673, 3.53, 12.8, 43.9, 47.0, 91.8)$ | This work |

Table 6.4: (Continued) Pore-size-distribution-model parameters used in this work for SGL 29BC gas-diffusion layers.

| Parameter | Value/expression | Details |
|---|---|---|
| Characteristic standard deviations | $(s_{\text{HI}}) = (0.431, 0.525)$, $(s_{\text{HO}}) = (0.431, 0.525, 0.462, 0.150, 0.400, 0.338)$ | This work |
| **SGL 29BC-GDL-D** | | |
| Hydrophilic and hydrophobic volume fractions | $F_{\text{HI}} = 0.048$, $F_{\text{HO}} = 0.952$ | This work |
| Characteristic pore fractions | $(f_{\text{HI}}) = (0.6580, 0.3420)$, $(f_{\text{HO}}) = (0.0335, 0.0174, 0.0757, 0.1517, 0.5843, 0.1374)$ | This work |
| Characteristic pore radii, $\mu$m | $(r_{\text{HI}}) = (0.673, 3.53)$, $(r_{\text{HO}}) = (0.673, 3.53, 12.8, 43.9, 47.0, 91.8)$ | This work |
| Characteristic standard deviations | $(s_{\text{HI}}) = (0.431, 0.525)$, $(s_{\text{HO}}) = (0.431, 0.525, 0.462, 0.150, 0.400, 0.338)$ | This work |

[a] Fitted in this work to the experimental through-plane gas permeability of Sigracet® 29BA GDLs.
[b] Fitted in this work to the liquid-gas interfacial area of Sigracet® 39BA GDLs.
[c] Fitted in this work to the experimental pore-size distribution of Sigracet® 29BA GDLs.

pores seen in the experimental PSD were not present in the reconstructed distribution. This also led to a larger PSD peak at about 40–50 μm. The $rdX/dr$ curve computed with the PSD model for the binder-free SGL 29BC-GDL-B case is shown in the dashed green line in Figure 6.3a (the PSD was normalized to integrate to unity). The size of the analytical PSD peak was smaller than that in the reconstructed PSD likely due to the noise in the latter (no smoothing was used). Overall, a reasonable agreement was achieved between the prediction of the PSD model and the reconstructed PSD.

**Microporous Layers** The fitted PSD parameters for the SGL 29BC MPLs are provided in Table 6.5 ("29BC-MPL-A"), for which the fitting residual was 0.002. The fitted PSD is shown in Figure 6.3b. Due to the wide pore-size distribution, nine modes were used to obtain a good fit of the experimental PSD data.

Three distinct regions of the MPL PSD can be seen in Figure 6.3b: the MPL pores at 40–50 nm, the cracks at 8–9 μm (see Figure 1.4), and a wide distribution of the intermediate GDL-MPL pores in between. The pores of the intermediate layer were assumed a part of the MPL in the two-phase PEMFC model. The MPL was assumed mostly hydrophobic with 1% of all pores being hydrophilic [35]. The contact angles were taken the same as those used by Zhou et al. [35] to model SGL 24BC MPLs: $\theta_{\mathrm{HI}} = 84°$ and $\theta_{\mathrm{HO}} = 110°$. To match the experimental gas permeability of $6.56 \cdot 10^{-14}$ m$^2$, $\lambda_{\mathrm{PSD}} = 0.0185$ was used.

The MPL PSD was compared with the numerically reconstructed pore-size distribution obtained by S. Jung, an M.Sc. graduate and a research assistant at ESDL. Two MPL structures were generated by randomly placing spherical particles with 60-nm radius into a $1.5 \times 1.5 \times 1.5$-μm$^3$ domain until the target porosity of 60% (Table 4.7) was reached. The details of this stochastic-reconstruction algorithm can be found in the works of Sabharwal et al. [130, 131]. The analytical MPL PSD from which the GDL-MPL pores and cracks were removed ("SGL-29BC-MPL-B") was in good agreement with the reconstruction data, as seen in Figure 6.3b.
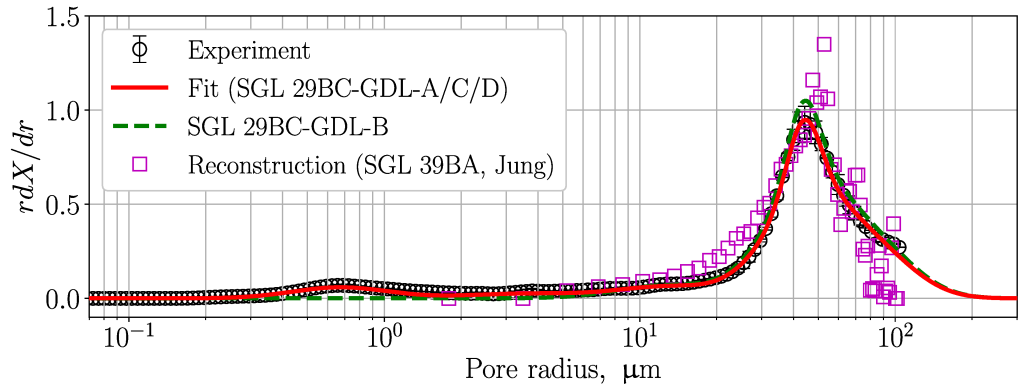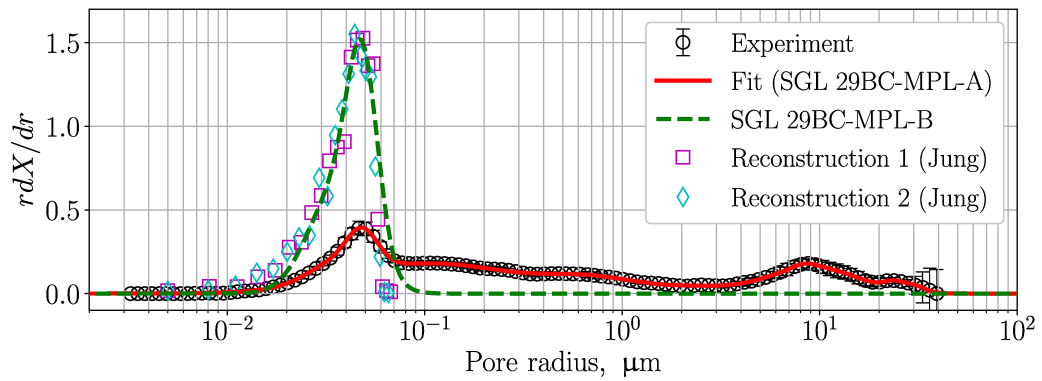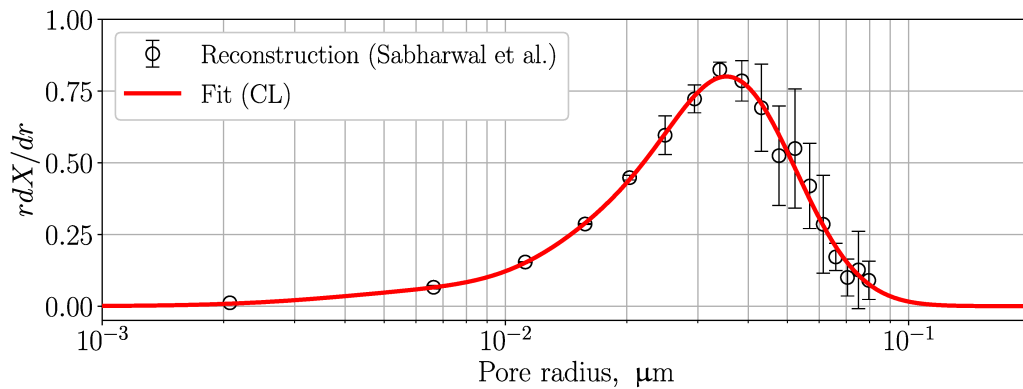
Figure 6.3: Experimental and reconstructed pore-size distributions of SGL 29BC GDL (a), SGL 29BC MPL (b), and CL (c) along with the respective log-normal fits. Reconstruction data are from references [130, 131, 212]. Error bars represent standard deviation.

Table 6.5: Pore-size-distribution-model parameters used in this work for SGL 29BC microporous layers.

| Parameter | Value/expression | Details |
|---|---|---|
| Contact angle | $\theta_{HI} = 84°$, $\theta_{HO} = 110°$ | [34] |
| Pore-interconnectivity factor | $\lambda_{PSD} = 0.0185$ | This work[a] |
| Pore-shape factor | $M_{PSD} = 0.00956$ | This work[b] |
| **SGL 29BC-MPL-A** | | |
| Hydrophilic and hydrophobic volume fractions | $F_{HI} = 0.01$, $F_{HO} = 0.99$ | [34] |
| Characteristic pore fractions | $(f_{HI}) = (f_{HO}) = (0.0941, 0.0852, 0.4329, 0.1114, 0.0381, 0.0071, 0.2074, 0.0143, 0.0095)$ | This work[c] |
| Characteristic pore radii, μm | $(r_{HI}) = (r_{HO}) = (0.0363, 0.0484, 0.110, 0.715, 2.34, 8.37, 9.22, 24.0, 30.7)$ | This work[c] |
| Characteristic standard deviations | $(s_{HI}) = (s_{HO}) = (0.338, 0.177, 0.959, 0.541, 0.448, 0.125, 0.520, 0.121, 0.111)$ | This work[c] |
| **SGL 29BC-MPL-B** | | |
| Hydrophilic and hydrophobic volume fractions | $F_{HI} = 0.01$, $F_{HO} = 0.99$ | [34] |
| Characteristic pore fractions | $(f_{HI}) = (f_{HO}) = (0.525, 0.475)$ | This work |
| Characteristic pore radii, μm | $(r_{HI}) = (r_{HO}) = (0.0363, 0.0484)$ | This work |
| Characteristic standard deviations | $(s_{HI}) = (s_{HO}) = (0.338, 0.177)$ | This work |

[a] Fitted in this work to the experimental through-plane gas permeability of Sigracet® 29BC MPLs.
[b] Fitted in this work to the reconstructed liquid-gas interfacial area of Sigracet® 29BC MPLs.
[c] Fitted in this work to the difference in the experimental pore-size distributions of Sigracet® 29BC GDL-MPL pairs and 29BA GDLs.

Table 6.6: Pore-size-distribution-model parameters used in this work for catalyst layers.

| Parameter | Value/expression | Details |
|---|---|---|
| Contact angle | $\theta_{\mathrm{HI}} = 79°$, $\theta_{\mathrm{HO}} = 91°$ | [35] |
| Pore-interconnectivity factor | $\lambda_{\mathrm{PSD}} = 4.09$ | This work[a] |
| Pore-shape factor | $M_{\mathrm{PSD}} = 2.56$ | This work[b] |
| Hydrophilic and hydrophobic volume fractions | $F_{\mathrm{HI}} = 0.0249$, $F_{\mathrm{HO}} = 0.9751$ | This work[b] |
| Characteristic pore fractions | $(f_{\mathrm{HI}}) = (1)$, $(f_{\mathrm{HO}}) = (0.0907, 0.3387, 0.5706)$ | This work[c] |
| Characteristic pore radii, nm | $(r_{\mathrm{HI}}) = (8.79)$, $(r_{\mathrm{HO}}) = (8.79, 22.2, 38.4)$ | This work[c] |
| Characteristic standard deviations | $(s_{\mathrm{HI}}) = (0.725)$, $(s_{\mathrm{HO}}) = (0.725, 0.446, 0.348)$ | This work[c] |

[a] Fitted in this work to the experimental through-plane gas permeability of inkjet-printed CLs.
[b] Fitted in this work to the liquid-gas interfacial area of the stochastically reconstructed inkjet-printed CLs from [130, 131].
[c] Fitted in this work to the pore-size distribution of the stochastically reconstructed inkjet-printed CLs from [130, 131].

**Catalyst Layers** The PSD of the inkjet-printed catalyst layers with 50% porosity (also fabricated at ESDL and similar to the CLs used in this work) reconstructed from FIB-SEM (focused-ion-beam SEM) images by Sabharwal et al. [130, 131] was fitted as discussed earlier. The residual of the fit shown in Figure 6.3c was 0.03, and the fitted PSD parameters are given in Table 6.6. The experimentally measured gas permeability of $3.16 \cdot 10^{-16}$ m$^2$ was matched with $\lambda_{\mathrm{PSD}} = 4.09$. A pore-interconnectivity factor of more than 1 was obtained likely because the reconstructed PSD did not contain cracks present in the experimental sample as observed with an optical microscope (not shown).

### 6.3.1.2 Intrusion Curves

The PSD model was validated next by comparing the predicted GDL saturation during the mercury-intrusion experiment with the literature data [215, 596]. All six modes of SGL 29BC GDL from Table 6.4 were used to compute the MIP curve. The comparison of the MIP curves is shown in Figure 6.4, where only the imbibition measurements are shown. It is known that, for the fuel-cell materials, the dependency of saturation on capillary pressure exhibits hysteresis, i.e., the injection and withdrawal curves do not match [596–598]. The saturation hysteresis is hypothesized to be due to the complex shape of the pores that affects the sequence of the liquid-gas interfacial configurations during imbibition and draining [596, 598, 599]. Variations in the internal morphology may also lead to hysteresis in the observed contact angles [305]. In the PSD model developed in this thesis, however, it is assumed that all pores are cylindrical and have a constant contact angle. Zhou et al. [34, 276] argued that it is sufficient to consider only the imbibition curve when modeling liquid-water transport in PEMFCs, as the removal of water (saturation reduction) occurs mostly through evaporation.

As shown in Figure 6.4, the mercury-intrusion curve computed with the PSD model was in good agreement with the experimental data for SGL 39BA GDL, as

expected from the structural similarity of the latter with 29BA. The agreement with the numerical-reconstruction data by Jung et al. [215], obtained with either a full-morphology model or a pore-network model, was good up to the saturation of about 0.8. Jung et al. argued that the discrepancy at higher saturation was due to the insufficient voxel resolution (1.79 μm). Indeed, according to the PSD model, the binder pores that account for 9.7% of the total pore volume (Table 6.4) are intruded when the capillary pressure exceeds about 0.1 MPa, which is close to where the discrepancy starts. The intrusion curve of another SGL sample, 10BA, can be seen to be different from that of the 29BA and 39BA GDLs. The SEM images by Wong et al. [600] show that SGL 10AA does not appear to have a resin binder that is found in 39AA GDLs (SGL AA-series GDLs are zero-PTFE versions of their BA-series counterparts). Moreover, the carbon fibers of 10AA GDLs are curved, in contrast to the straight fibers in the 39AA GDLs. The intrusion data for Toray 090 samples are shown for comparison: the absence of the porous binder in those materials and their different morphology compared with SGL GDLs result in the different intrusion curves in Figure 6.4.

Water-intrusion curves at 60 °C for the GDL, MPL, and CL PSDs from Tables 6.4–6.6 were compared next. They are presented in Figure 6.5. As expected, all pores were empty when the capillary pressure was negative and large by magnitude. At zero capillary pressure, all hydrophilic pores were filled (all curves crossed the saturation axis at $F_{HI}$), and liquid water entered the hydrophobic pores as the pressure increased further.

As the binder pores in the GDL were made more hydrophobic (29BC-GDL-A to 29BC-GDL-C to 29BC-GDL-D), the fraction of the pores filled at negative capillary pressure decreased, and the higher pressure was required to completely fill the GDL with liquid water. The binder-free SGL 29BC-GDL-B sample remained dry until about 200 Pa and followed the 29BC-GDL-A curve afterward, as the remaining pores of the two samples were the same.
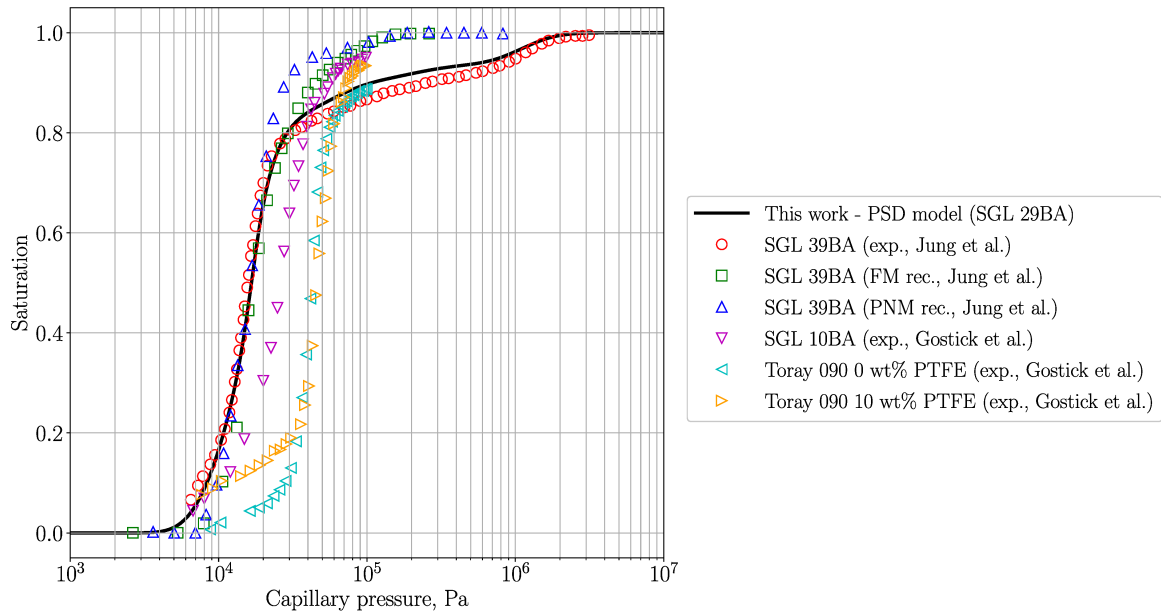
Figure 6.4: Comparison of the mercury-intrusion curves for SGL 29BC GDL computed in this work with the PSD model with the literature data for SGL 39BA GDL [215], SGL 10BA GDL [596], and Toray 090 GDL [596]. Labels "exp." and "rec." denote experimental and reconstruction data.
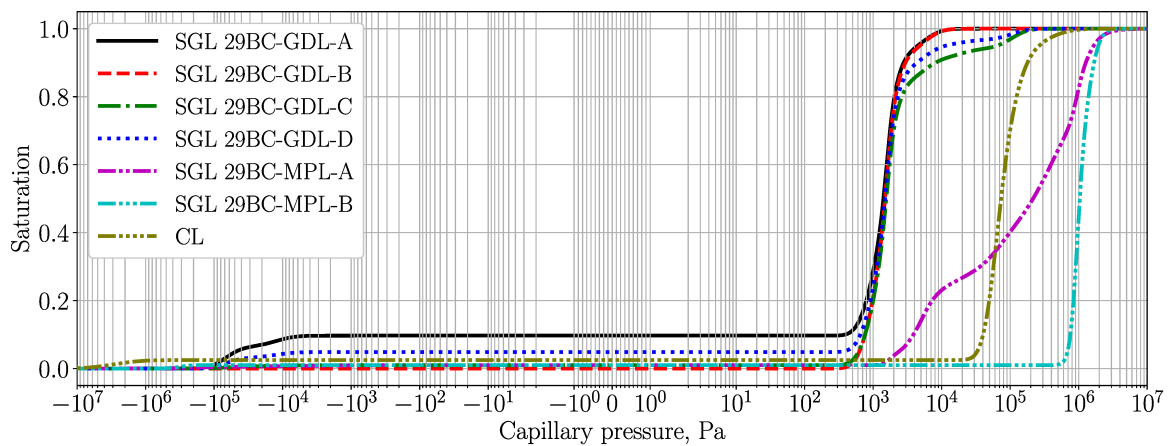


Figure 6.5: Comparison of the water-intrusion curves for SGL 29BC GDL, SGL 29BC MPL, and CL computed with the PSD model.

The intrusion curves of the two MPL samples illustrate the effect of the cracks and of the intermediate GDL-MPL region, the PSD of which are only present in the SGL 29BC-MPL-A case. When these larger pores were included in the PSD, the hydrophobic portions of the layer started to fill with liquid water significantly earlier, at about 1 kPa, compared with about 0.3 MPa for SGL 29BC-MPL-B.

### 6.3.1.3 Liquid-Gas Interfacial Area

**Gas-Diffusion Layers** The pore-shape factor, $M_{\mathrm{PSD}}$ (see Table 2.2), was found by comparing the volumetric liquid-gas interfacial area computed with the PSD model (equation (2.107)) with two sets of reconstruction data. The first set, shown in black circle markers in Figure 6.6a, was calculated by S. Jung for the partially saturated reconstructed SGL 39BA GDLs from reference [212]. The second data set (magenta squares) was taken from the work of Zenyuk et al. [209], where the reconstructed SGL 10BA and 24BA GDLs were analyzed (in this case, the volumetric liquid-gas area was computed from the reported porosity, saturation, liquid-water area and volume). Since neither of the reconstructions resolved the binder pores, the 29BC-GDL-B properties were used to compute the liquid-gas area with the PSD model and to estimate the pore-shape factor (which linearly scales the curve according to equations (2.93) and (2.107)). The asymmetry of the reconstructed liquid-gas area was captured well with the PSD model, thus validating the ability of the latter to account for the structure of the porous material. The estimated value $M_{\mathrm{PSD}} = 0.0642$ was assumed for all other considered GDL cases, although a larger area was predicted when the binder pores were included in the PSD (Figure 6.6a). The location of the maximum in the curve depended on the wettability assumptions made in each case: a hydrophilic binder (SGL 29BC-GDL-A) shifted the maximum to low saturation, and a mostly hydrophobic binder (SGL 29BC-GDL-C) resulted in a maximum liquid-gas area at high saturation values. When the binder was assumed 50% hydrophilic (SGL 29BC-GDL-D), the interfacial liquid-gas area was relatively constant for all

saturation values but close to the end points where either the liquid phase or the gas phase vanished.

**Microporous Layers**   The 29BC-MPL-B PSD was used to estimate the pore-shape factor of the MPL by comparing the liquid-gas interfacial area predicted with the PSD model with that found from the reconstruction data provided by S. Jung (Figure 6.6b). A reasonable agreement was achieved with $M_{PSD} = 0.00956$. Liquid-gas interfacial area computed with the same $M_{PSD}$ for 29BC-MPL-A was lower than that of 29BC-MPL-B due to the presence of larger pores in the PSD of the former. This trend was opposite to that observed with 29BC-GDL-A/B (Figure 6.6a), since the inclusion of small pores in the PSD increases the interfacial area.

**Catalyst Layers**   Wettability of catalyst layers depends on their composition and is generally unknown. Sabharwal et al. [130, 131] considered the smallest CL pores as hydrophilic liquid-water nucleation sites. The same assumption was made in this work. The smallest-radius PSD mode ($r = 8.79$ nm) was assumed partially hydrophilic, and its hydrophilic fraction was adjusted alongside the pore-shape factor, $M_{PSD}$, to achieve the agreement with the reconstructed liquid-gas interfacial area from references [130, 131] shown in Figure 6.6c. This resulted in the smallest-radius mode being 22% hydrophilic, which translated into $F_{HI} = 0.0249$ that was reasonably close to the volume fraction of the water-nucleation sites in reference [131], 3.9–4.6%. The obtained pore-shape factor was $M_{PSD} = 2.29$.

#### 6.3.1.4   Permeability

**Gas-Diffusion Layers**   The GDL wettability assumptions affect the relative liquid and gas permeability computed with equations (2.105) and (2.106). This is illustrated in Figure 6.7, where the predicted permeability of 29BC-GDL-A/B/C/D is compared with the experimental [601–603] and reconstruction [82, 205, 215, 217] data for various GDLs from the literature. Good agreement in both relative liquid and gas perme-
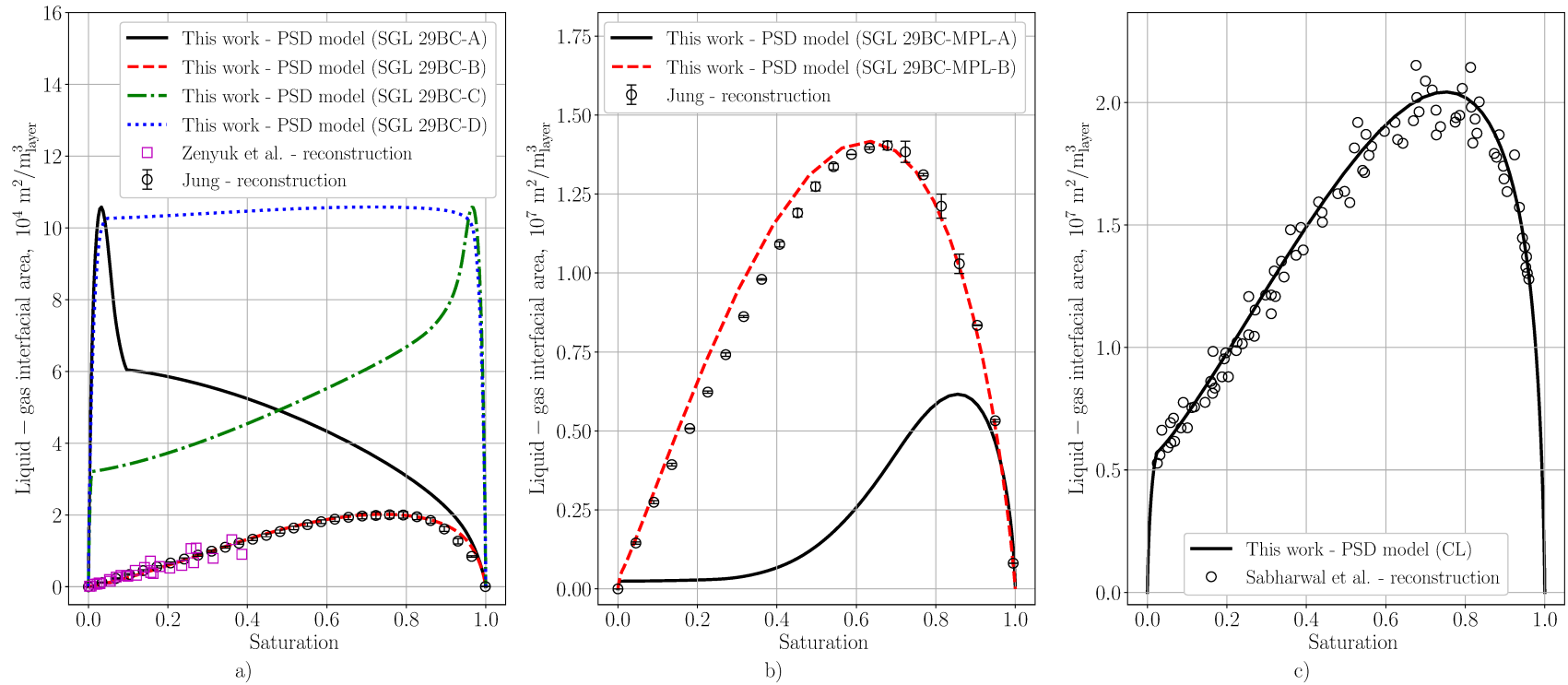
Figure 6.6: Comparison of the volumetric liquid-gas interfacial area of SGL 29BC GDL (a), SGL 29BC MPL (b), and CL (c) predicted with the PSD model with the reconstruction data obtained in this work and in the literature [130, 131, 209, 212]. Error bars represent standard deviation.

ability was achieved only for the GDL with no binder pores (SGL 29BC-GDL-B, the dashed red line). Including the small binder pores of any wettability (SGL 29BC-GDL-A/C/D) caused deviation of the predicted permeability from the shape of its dependency on saturation that is expected from the literature. However, most of the gas-diffusion layers for which the permeability-saturation dependence was reported in the literature did not contain the binder pores (such as the Toray samples). The reconstructed SGL data sets shown in Figure 6.7 were obtained from the samples with the resolution of 1.5 μm [82] and 1.79 μm [215], which was likely not sufficient to resolve the binder pores that, at least for the SGL 29BC GDL, have the equivalent pore radii of less than 2 μm (Figure 6.3a). The only experimental gas permeability of an SGL GDL in Figure 6.7 is that of a 10BA sample that, as discussed earlier, does not contain a porous binder and has curved fibers. Therefore, to the best of the author's knowledge, the effect of the binder pores on the permeability of SGL GDLs has not been studied experimentally in the literature. This served as an additional motivation for considering the SGL 29BC-GDL-A/B/C/D cases in the parametric studies in this work.

Figure 6.7 shows that the relative gas and liquid permeabilities found in the experimental and reconstruction literature do not always follow the $(1 - s)^3$ and $s^3$ curves commonly used in the fuel-cell modeling literature[3] [25, 29, 30, 38, 40, 42–44, 49, 52, 152, 235, 236, 238, 242, 247, 248, 250, 274, 288, 304, 334, 341]. The cubic dependency is observed only for the reconstructed 39BA liquid-permeability curve by Jung et al. [215] and for one of the reconstructed 34BA gas-permeability curves by Bosomoiu et al. [82] (but not for the other). Therefore, it is important to use a microscale-transport model that accounts for the structure of the porous medium, such as the PSD model proposed in this thesis. However, more experimental and reconstruction data are required for the further calibration of the PSD model.

---

[3]Effective saturation, $s_e = (s - s_r)/(1 - s_r)$, was considered in some of the cited publications [25, 44, 52, 341], where $s_r \in (0, 1)$ is the residual (immobile) saturation. The relative gas and liquid permeabilities were then given by $(1 - s_e)^3$ and $s_e^3$, respectively.
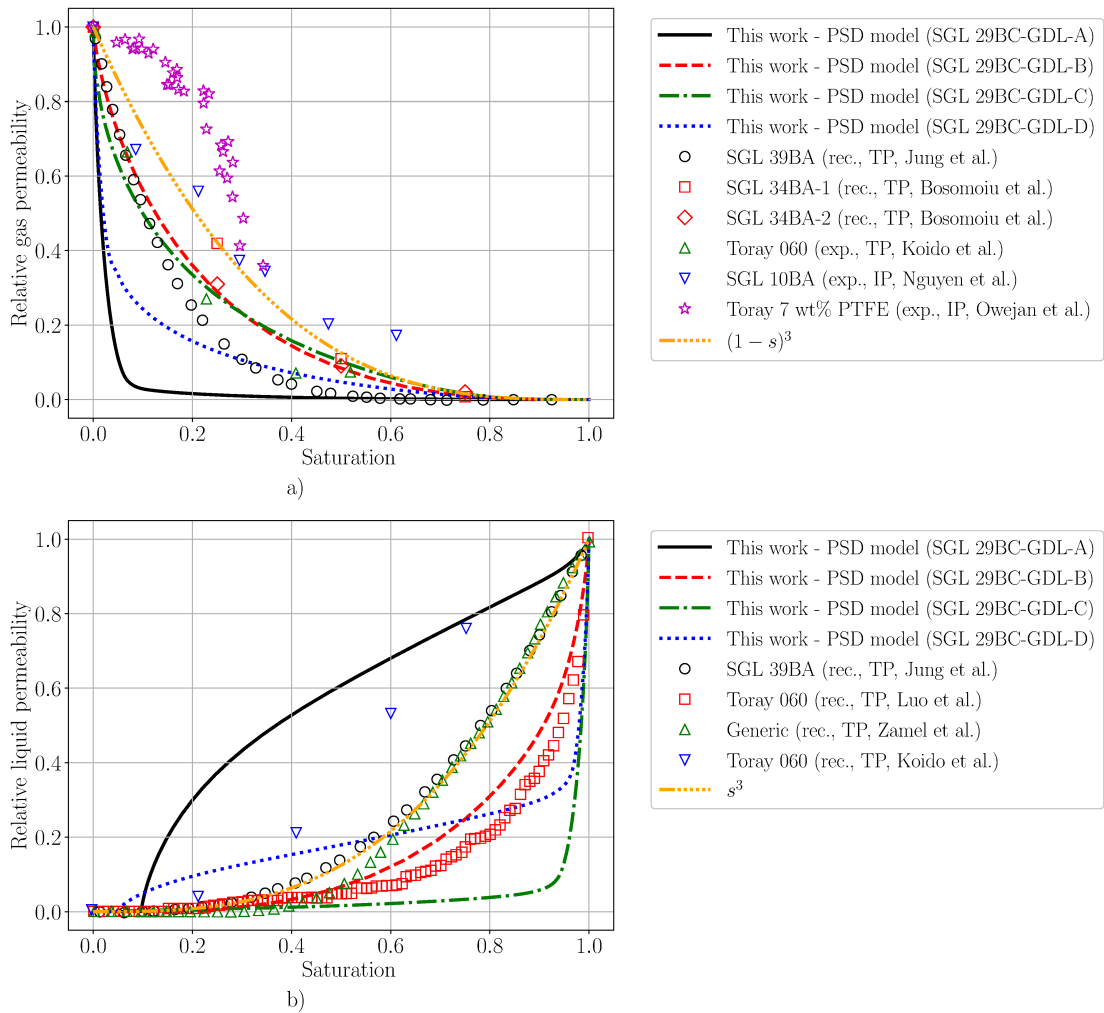
Figure 6.7: Comparison of the relative gas permeability (a) and relative liquid permeability (b) of SGL 29BC GDL predicted with the PSD model to the reconstruction data obtained in this work and with the experimental ("exp.") [601–603] and reconstruction ("rec.") [82, 205, 212, 217] data from the literature. Through-plane and in-plane directions are denoted "TP" and "IP", respectively. Error bars represent standard deviation.

**Microporous Layers**  To the best of the author's knowledge, the dependency of the MPL permeability on saturation has not been reported in the literature. The relative liquid and gas permeabilities computed with equations (2.105) and (2.106) for the two MPL cases are shown in Figure 6.8. The nearly unimodal PSD of 29BC-MPL-B produced permeability-saturation relationships that were close to cubic. Inclusion of larger, mostly hydrophobic pores in the MPL PSD (SGL 29BC-MPL-A) resulted in lower gas and liquid permeabilities.

**Catalyst Layers**  Permeability of partially saturated catalyst layers is not known. The relative gas and liquid permeabilities of the CL shown in Figure 6.8 were close to those of 29BC-GDL-B. It was found that the permeability curves computed with the PSD model did not follow a simple power law $(1 - s)^\alpha$ for the gas phase and $s^\alpha$ for the liquid phase, even when unimodal distributions were used (not shown). This, along with the experimental and reconstruction data in Figure 6.7, may indicate that the porous structure of the fuel-cell materials leads to more complex permeability-saturation curves than the power law.

### 6.3.1.5  Comparison with the Previous Implementation of the PSD Model

The differences between the PSD model developed in this thesis and its previous implementation [34, 276, 342] were highlighted in Table 2.2 of Chapter 2. Those differences are illustrated next for the catalyst-layer PSD from Table 6.6. The same values of the pore-interconnectivity factor, $\lambda_{\mathrm{PSD}}$, and of the pore-shape factor, $M_{\mathrm{PSD}}$, were used in both versions of the PSD model.

The probabilities of the liquid-liquid, liquid-gas, and gas-gas interfaces are compared in Figure 6.9. Because the same statistical considerations were made in the derivation of all probabilities in this work, their sum, $P_{\mathrm{tot}}$, was independent of saturation and was equal to $\lambda_{\mathrm{PSD}}$, as expected from Table 2.2 ($P_{\mathrm{tot}} = 1$ when the pores are ideally interconnected, i.e., when $\lambda_{\mathrm{PSD}} = 1$). On the other hand, the total prob-
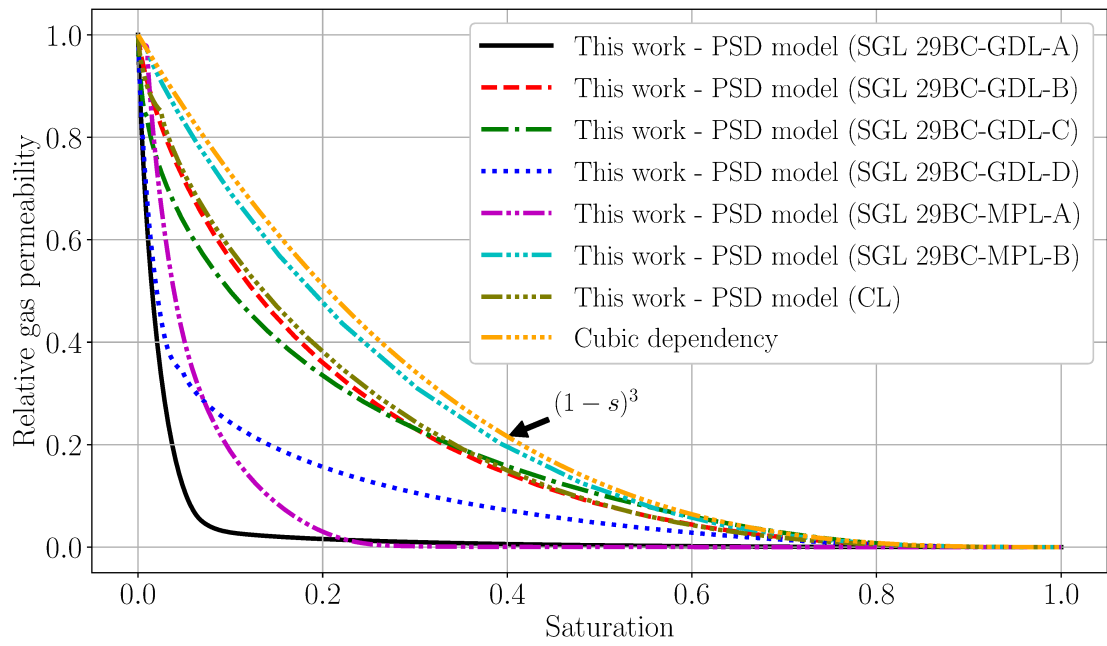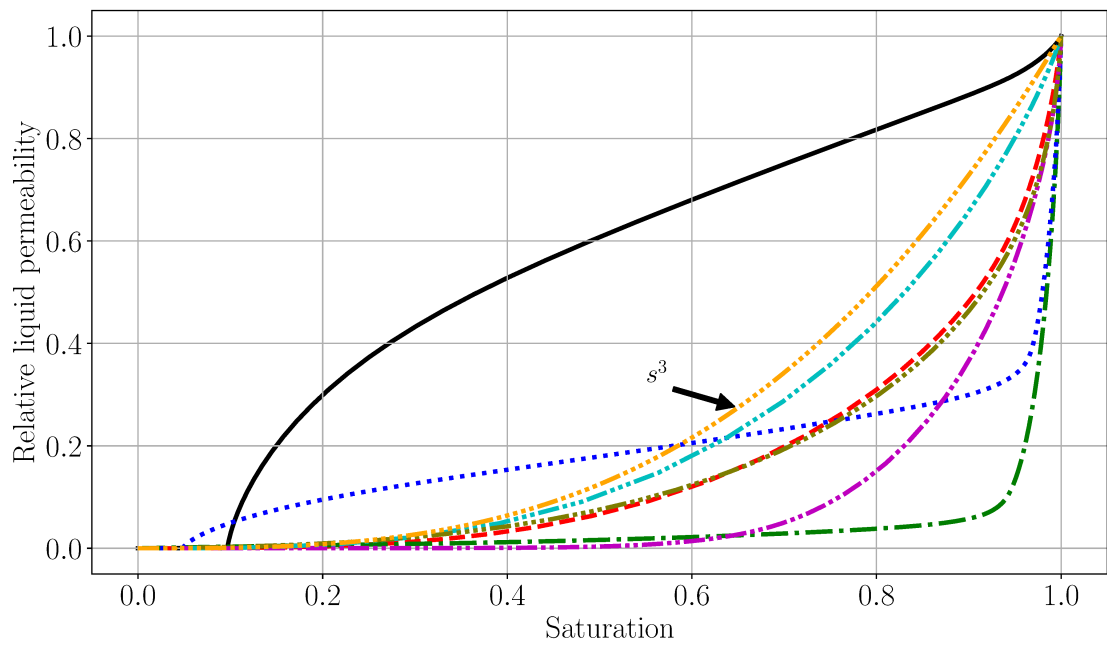
Figure 6.8: Relative gas permeability (a) and relative liquid permeability (b) of SGL 29BC GDL, SGL 29BC MPL, and CL predicted with the PSD model.
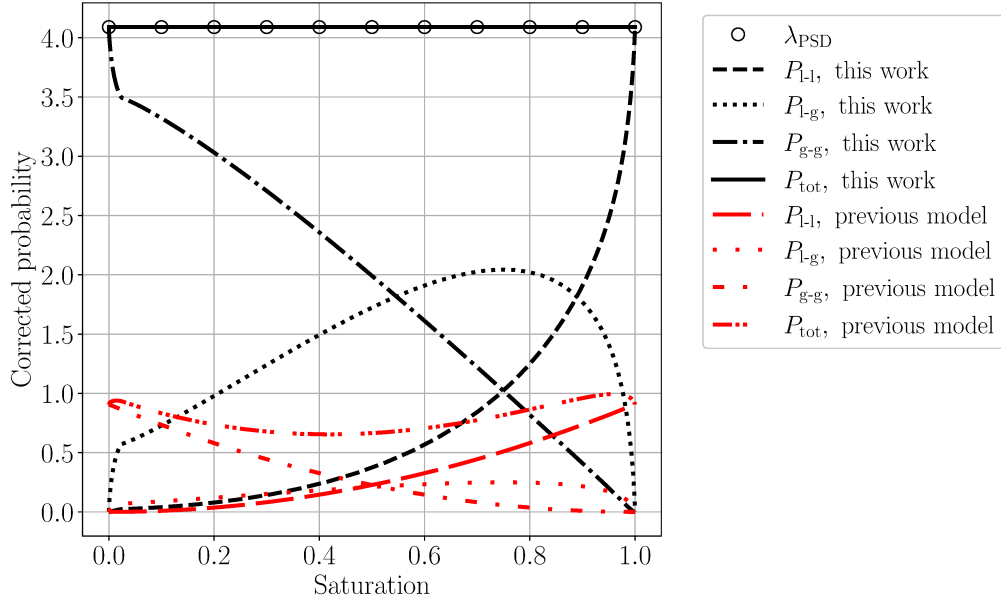
Figure 6.9: Comparison of the interfacial probabilities of the CL computed with the updated PSD model developed in this work and with the previous version of the model [34, 276, 342]. All probabilities were corrected for the pore interconnectivity as shown in Table 2.2.

ability computed with the previous PSD model [34, 276, 342] was not constant due to the saturation-based approach taken to compute $P_{l-l}$ and $P_{g-g}$ that results in their quadratic dependency on saturation (see Table 2.2). Since probability $P_{tot}$ cannot be saturation-dependent, the updated PSD model appears to be more realistic than the earlier formulation.

As illustrated in Figure 6.10, the saturation dependency of the volumetric liquid-gas interfacial area, $a_{l-g}$, predicted by the two models was the same up to a constant scaling factor (that factor was $2\varepsilon_p\lambda_{PSD}$, as expected from Table 2.2). The computed relative permeabilities of the gas and liquid phases, however, differed from each other significantly, as shown in Figure 6.11. The difference in the relative liquid permeability was particularly prominent, with the new formulation predicting a slower-than-cubic increase in permeability with saturation, while that increase was nearly quadratic in the old formulation.

It is worth noting that, if the liquid-liquid and gas-gas interface probabilities are
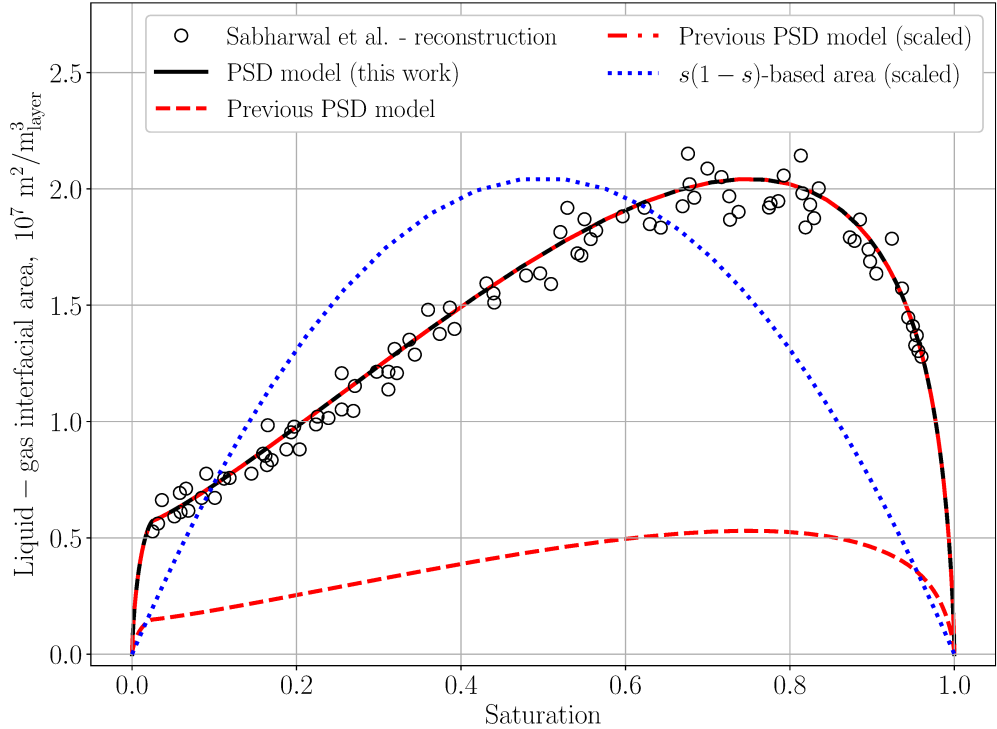
Figure 6.10: Comparison of the volumetric liquid-gas interfacial area of the CL computed with the updated PSD model developed in this work and with the previous implementation of the model [34, 276, 342].

assumed to be proportional to $s^2$ and $(1-s)^2$, as done in the earlier PSD models [26, 27, 34, 157, 276, 305, 342], then, using the argument of the binomial distribution of the pore interfaces, the corresponding liquid-gas interface must be proportional to $2s(1-s)$. As shown in Figure 6.10, this results in a parabolic dependency of $a_{\text{l-g}}$ on saturation. However, the reconstructed liquid-gas interfacial area is asymmetric. Evidently, the pore-interconnectivity approach that relies on the liquid-invaded cross-sectional area (equation (2.91)) instead of saturation better preserves the microstructural information in the computed mass-transport properties.

A similar comparison was made in Figure 6.12 for the SGL 29BC-GDL-A/B cases from Table 6.4. Compared with the new implementation, the effect of the binder pores (that are not present in the 29BC-GDL-B PSD) on the relative gas permeability was not as significant when the previous PSD model was used (Figure 6.12a). The earlier
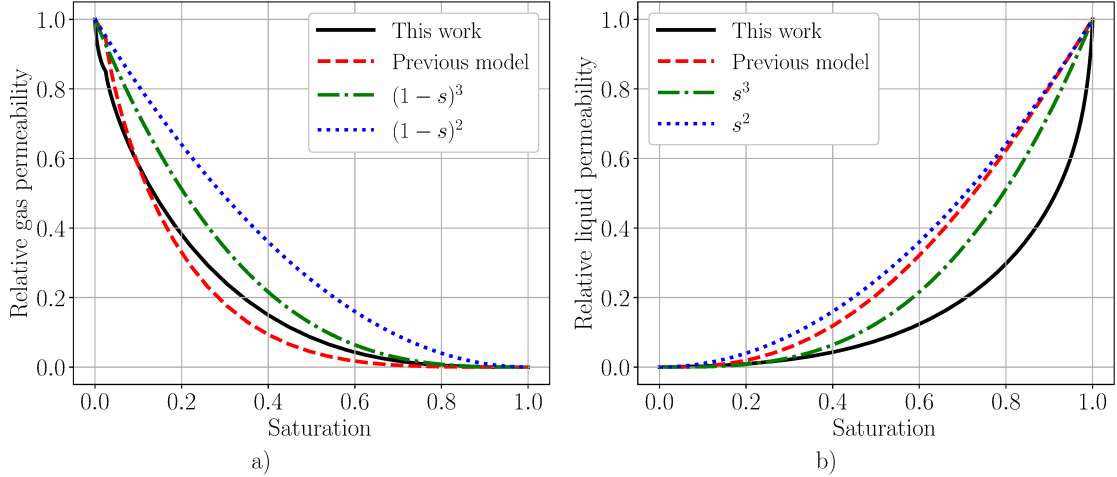
Figure 6.11: Comparison of the relative gas (a) and liquid (b) permeabilities of the CL computed with the updated PSD model developed in this work and with the previous version of the model [34, 276, 342].

model also predicted a slower decrease in the gas permeability at low saturation for the 29BC-GDL-A case (with the binder) that resembled the trend seen in the experimental data of Owejan et al. [603]. However, the GDL sample tested by Owejan et al. was a Toray GDL, which, as discussed before, did not contain a porous binder. Additionally, the previous implementation of the PSD model did not capture the effect of the binder pores on the relative liquid permeability (Figure 6.12b), although the permeability computed with that model was in a better agreement with the reconstruction data for SGL 39BA GDLs by Jung et al. [215]. Due to the lack of the experimental and reconstruction data that would show the effect of the small pores (the binder pores in the GDLs or the CL pores in general) on the gas and liquid permeability, it is difficult to say which of the two formulations of the PSD model is more realistic in that regard.

The last modification of the PSD model made in this thesis was in the calculation of the average Knudsen pore radius (Table 2.2). The dependency of $r_K$ on saturation predicted with the two formulations of the PSD model is shown in Figure 6.13 for the catalyst-layer PSD from Table 6.6. According to the earlier model, the average
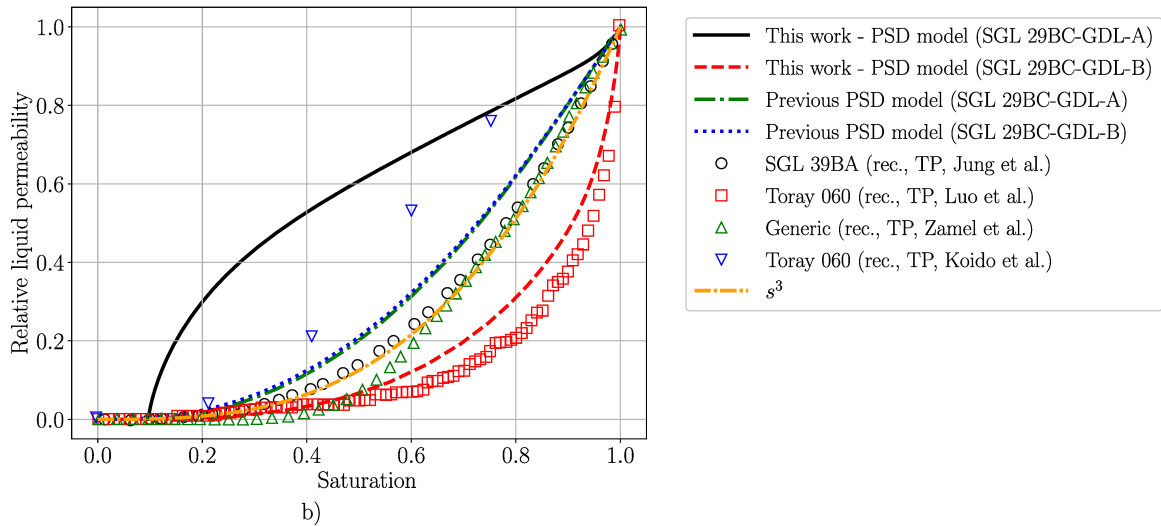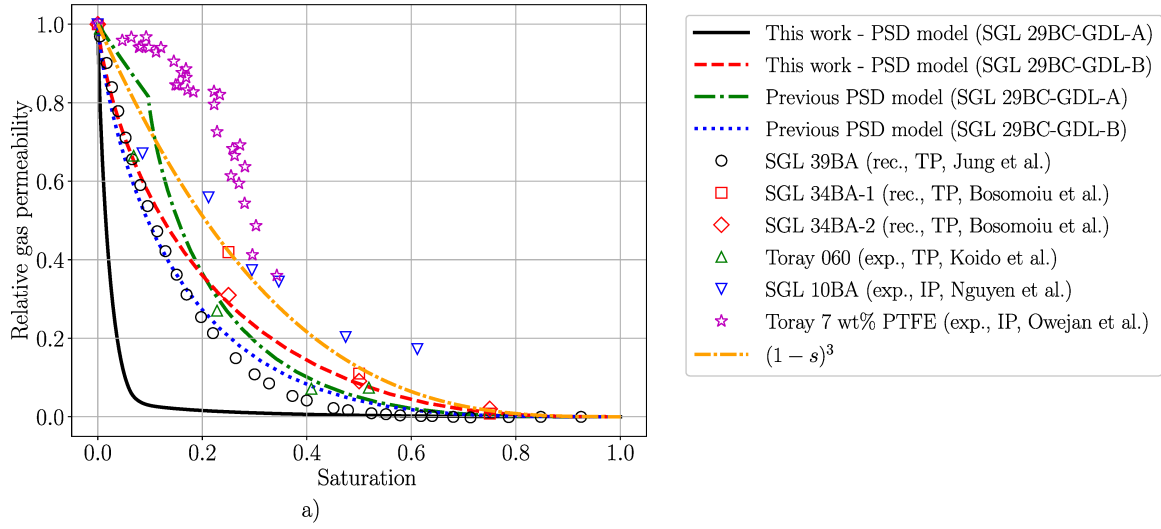
Figure 6.12: Comparison of the relative gas and liquid permeabilities of the GDL computed with the updated PSD model developed in this work and with the previous version of the model [34, 276, 342]. Experimental data ("exp.") from references [601–603] and reconstruction data ("rec.") from references [82, 205, 212, 217] are shown for comparison. Through-plane and in-plane directions are denoted "TP" and "IP", respectively. Error bars represent standard deviation.
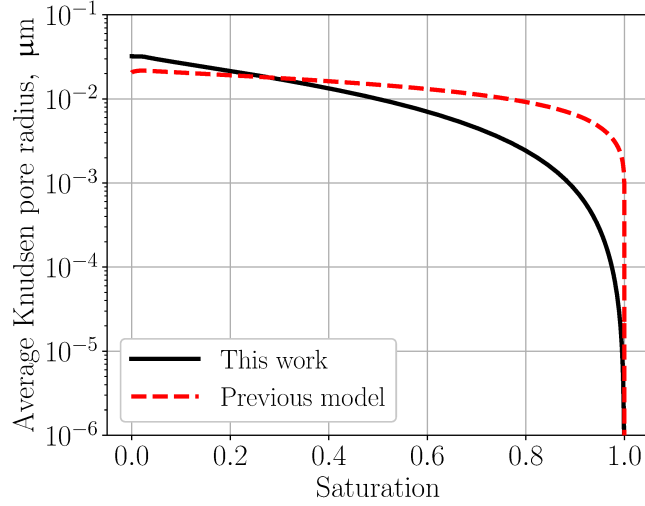
Figure 6.13: Comparison of the average Knudsen pore radius of the CL computed with the updated PSD model developed in this work and with the previous version of the model [34, 276, 342].

pore radius decreased in half only by the time the saturation reached the value of about 0.76, i.e., when the catalyst layer was three-quarters flooded. This appears to be less natural than the more gradual decrease in the Knudsen pore radius with an increase in the liquid saturation obtained with the updated PSD model. Further, an initial increase in $r_{\mathrm{K}}$ from 20.6 nm to 21.7 nm was predicted with the earlier model as saturation changed from $s = 0$ to $s = F_{\mathrm{HI}} = 0.0249$, while the average radius of the liquid-free pores should always decrease with an increase in saturation. The average Knudsen pore radius computed with the updated PSD model is, therefore, more in line with the physical expectations.

## 6.3.2 Comparison of the Transient Two-Phase PEMFC Simulations with Experimental Data

After the PSD model was validated, transient two-phase PEMFC simulations were performed, and their results were compared to in-house experimental data. The comparison was performed to verify whether the simulation results were physically sound and followed the general trends observed in experiments. The model inputs

that controlled liquid-water accumulation were adjusted as discussed in Section 6.1.2.

### 6.3.2.1 Voltage Sweeps at 0.44 mV/s with 1% Oxygen

First, two voltage sweeps were performed between the measured OCV and about 0.2 V at 0.44 mV/s for a cell operated with 1% oxygen content in the cathode channel prior to humidification. The polarization and HFR curves and the respective current-density and resistance transients are shown in Figure 6.14. Two experimental data sets, measured with two different cells, are labeled "cell 1" and "cell 2". The rate of oxygen dissolution in the ionomer film of the catalyst layers, $k_{O_2}$, was calibrated with the presented experimental data. Thus, good agreement was achieved in the polarization curve. A current density of 2 mA/cm$^2$ was predicted at the voltage that corresponded to the experimentally measured OCV (0.84 V). This was because the OCV in the simulations was higher, 1.20 V, as reactant crossover was not considered in the model. Hydrogen crossover has been recently implemented in OpenFCST by Moore et al. [312], and its inclusion in the model may improve the simulation results at low current density. Further, accounting for the transient platinum-oxide formation [154, 155] in the future may induce the polarization-curve hysteresis seen in the experimental data.

The simulated HFR plotted in Figures 6.14b and 6.14d revealed that the state of the polymer-electrolyte hydration in the simulations differed from that in the physical cell. Unlike the measured resistance, the computed HFR exhibited hysteresis: the resistance computed at the end of the first sweep was lower than at the start. This HFR behavior was discussed in Chapter 4 and was shown to be related to membrane hydration. For example, the average water content at the start of the simulation was 4.4 mol$_{H_2O}$/mol$_{SO_3^-}$ (with the corresponding protonic conductivity of 30 mS/cm), and it was 6.7 mol$_{H_2O}$/mol$_{SO_3^-}$ (conductivity 57 mS/cm) at the end of the first sweep. Because the physical cell was conditioned by holding it at 0.6 V for 15 minutes before each test, it is possible that the membrane was already well hydrated with liquid
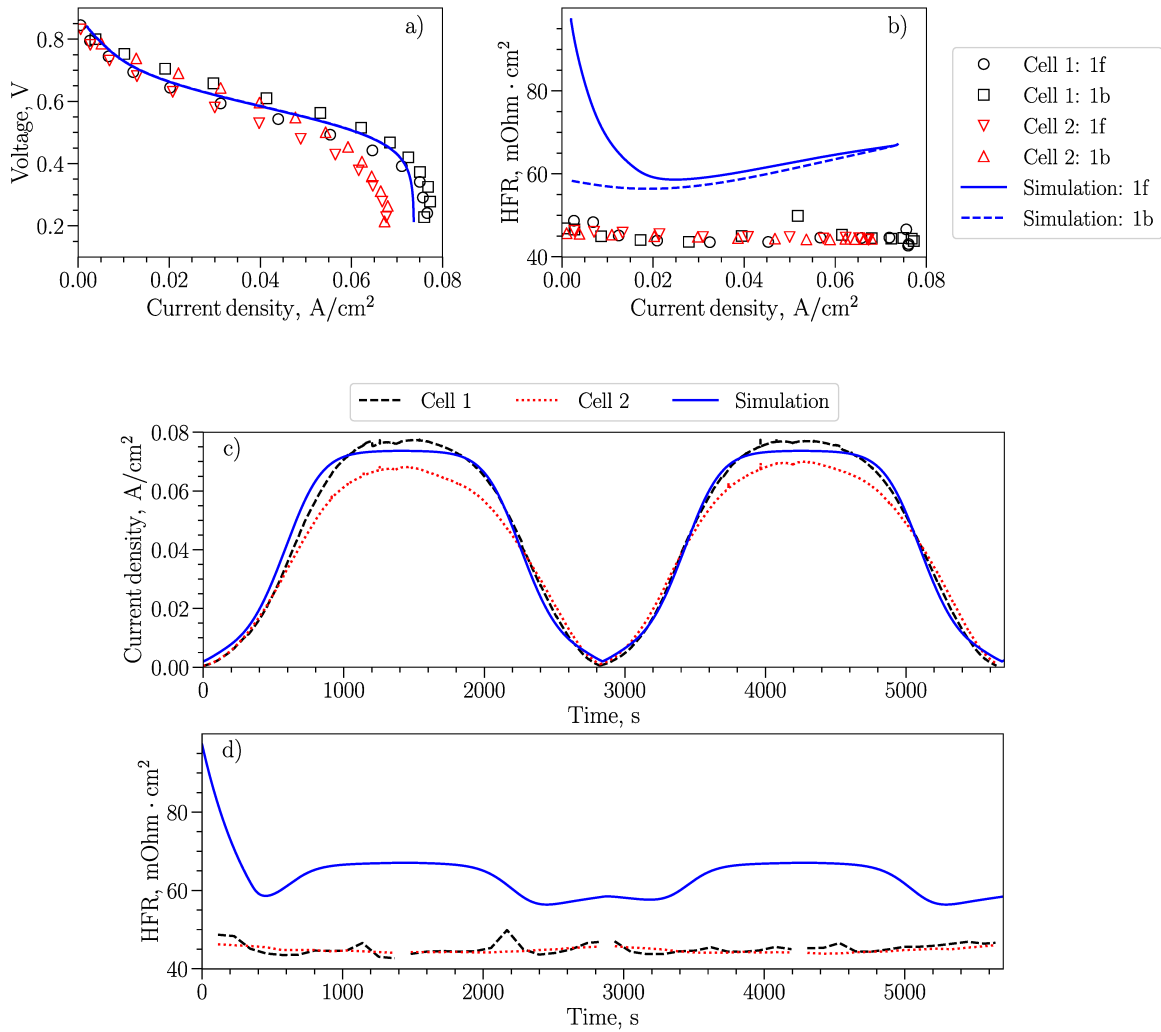
Figure 6.14: Comparison of the simulated and experimental current density and HFR. The forward and backward scans are labeled with letters "f" and "b" (for instance, "1f" denotes the first forward scan). Voltage sweeps were performed at 0.44 mV/s, and only the first sweep is shown in a) and b). The operating pressure was 140 kPa in the anode and 145 kPa in the cathode. The cathodic stream contained 1% of oxygen.

water when the polarization-curve measurements started. Including the conditioning step in the transient simulations might improve the predicted HFR dynamics. This hypothesis is supported by the fact that the measured HFR remained nearly constant during the sweeps.

Interestingly, the simulated HFR increased as the current density approached its limiting value by the end of the forward sweep. A similar curvature in the HFR was attributed to the membrane dry-out in Chapter 4. However, in this case, the water content in the membrane was higher (7.9 $mol_{H_2O}/mol_{SO_3^-}$, 71 mS/cm) at the limiting current than at the start of the simulation (4.4 $mol_{H_2O}/mol_{SO_3^-}$, 30 mS/cm). According to equation (2.156), the ohmic resistance of the membrane depends not only on its conductivity but also on the potential distribution within the layer. The distributions of the protonic potential in the CCM at the start of the simulation (0 s, 2 mA/cm$^2$) and at the limiting current density (1420.5 s, 74 mA/cm$^2$) are shown in Figure 6.15. These results indicate that, as the current density increased, the potential gradient shifted from across the thickness of the membrane to the diagonal direction, forcing protons to travel a longer distance within the membrane. This, in turn, led to an increase in the HFR. The nonuniform distribution of the protonic potential in the CCL seen in Figure 6.15 was due to the oxygen starvation under the land and the concentration of the ORR in the catalyst-layer area under the channel (and order-of-magnitude difference was observed in both oxygen content and the ORR current density between the channel and land areas).

### 6.3.2.2 Voltage Sweeps at 0.44 mV/s with Air

Voltage-sweep simulations were repeated with air in the cathode, and the results are compared in Figure 6.16 with the experimental data. As seen in the figure, the simulated performance was overpredicted. Because the single-phase version of the model was validated in Chapter 4 under dry operating conditions, it is likely that the difference between the simulated and experimental polarization curves observed
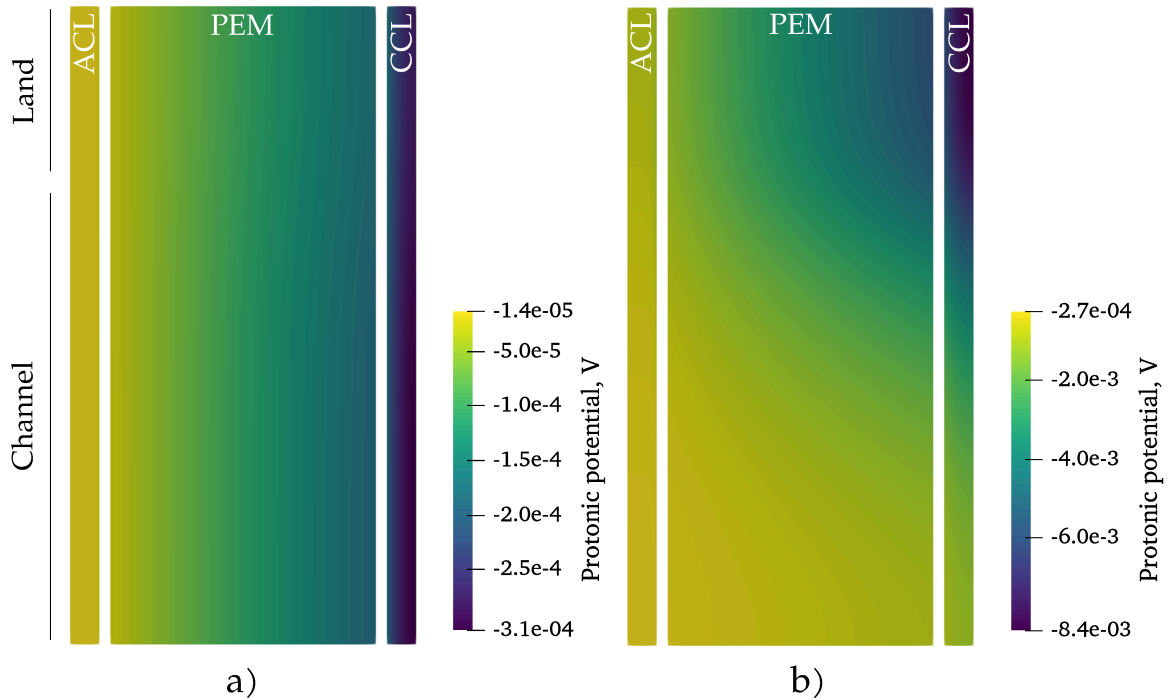
Figure 6.15: Simulated distribution of the protonic potential in the CCM: a) $t = 0$ s (0.83 V, 2 mA/cm$^2$) and b) $t = 1420.5$ s (0.215 V, 74 mA/cm$^2$). The domains were upscaled along the horizontal axis by a factor of 25 and gaps between the layers were added for clarity. The approximate locations of the land and the channel along the vertical axis are indicated.

in Figure 6.16 was due to the presence of liquid water in the physical cell. The larger under-the-land area of the cell used in this Chapter may have also made the model more sensitive to the in-plane transport properties compared with the model in Chapter 4, where a cell with a larger active area, multiple gas channels, and a channel-to-land ratio close to 1 was used.

The simulation results obtained with the single-phase model from Chapter 4 using the cell properties from this Chapter are also shown in Figure 6.16. The single-phase model could not capture the performance reduction due to the partial flooding of the electrode, and a higher performance was predicted at the voltage below 0.6 V. The HFR simulated with the two models was similar, except for the lower initial resistance obtained with the single-phase model. That was because the portion of water produced in the pore space of the CCL was assumed in the single-phase model
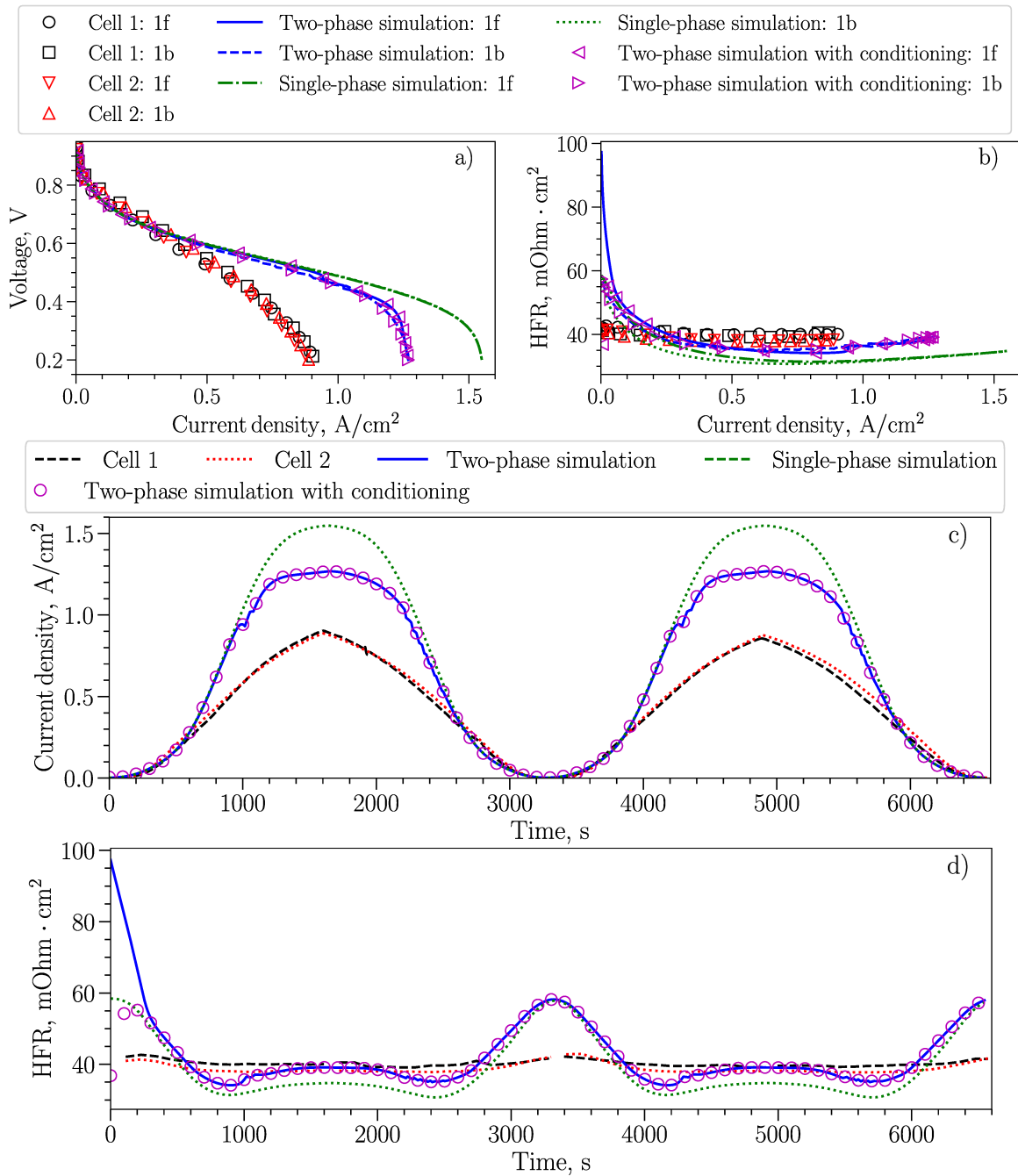
Figure 6.16: Comparison of the simulated and experimental current density and HFR. The forward and backward scans are labeled with letters "f" and "b" (for instance, "1f" denotes the first forward scan). Voltage sweeps were performed at 0.44 mV/s, and only the first sweep is shown in a) and b). The operating pressure was 140 kPa in the anode and 145 kPa in the cathode. Air was used in the cathode.

to be generated in the vapor form, which increased RH and the water uptake by the polymer electrolyte.

Although the decrease in the performance simulated with the two-phase model was significant, it was not sufficient compared with the experimental data. However, the degree of confidence in the measured data was limited, and more tests are required to verify the correct cell assembly and data repeatability. The experimental data were collected from two cells with single-channel bipolar plates that were designed in-house to minimize the effect of the channel blockage with liquid water, a shortcoming of the parallel-channel configuration used in Chapter 4. Flow rates of 0.5 slpm and 3 slpm for hydrogen and oxygen were used to minimize along-the-channel effects. The obtained experimental data did not follow the trends expected from the literature. Particularly, the flooding-induced polarization-curve hysteresis, where the performance during the backward scan (from low voltage to high voltage) is lower than during the forward scan [46, 49–52, 54], was not observed. However, significantly lower flow rates were used in the literature [46, 49–52, 54] (typically up to 0.5 slpm in the cathode compared with 3 slpm in this work), and thus more experiments are required to find out whether the absence of the two-phase hysteresis in the presented measurements was due to the large gas flow rates. Because of the new hardware and the manual assembly of the fuel cells with small (less than 1 cm$^2$) MEAs, significant performance variation was observed with some physical cells as a result of the misalignment of the cell components (not shown). Due to the global pandemic, limited repeatability validation was performed, and the measurements from only two cells are presented later in this Chapter. In the future, more repeatability tests will be conducted. In order to obtain more information on water transport within the fuel cell, the in-house water-balance setup developed by Kracher [604] will be used. The setup enables the measurement of the transient vapor flux across the cell and of the amount of liquid water ejected from it. This will allow for the more direct validation of the water-management description in the developed model compared with the transients of current density and the HFR

alone. Further, a larger MEA area can be used to reduce the edge effects, such as the misalignment of the MEA and the channel. Additionally, more operating conditions will be considered to validate the two-phase model during both dry and wet operation.

Matching both polarization-curve and HFR data at two oxygen contents and in transient is a challenging task complicated by the large number of the unknown parameters (such as the phase-change rates of water, the rate of liquid-water removal from the GDL-channel boundaries, and wettability of the porous MEA components, to name but a few). Parametric studies presented later in this Chapter show that it is possible to achieve a more significant electrode flooding and a lower cell performance in the simulations by modifying some of the unknown parameters.

A small polarization-curve hysteresis was observed in Figure 6.16a, where the cell performance during the backward scan was lower than during the forward scan. As discussed in Chapter 1 and as it will be demonstrated later, this orientation of the hysteresis is indicative of liquid-water accumulation.

The simulated HFR was in better agreement with the experimental data in Figure 6.16 than when the cell was operated with 1% oxygen (Figure 6.14). As current density increased during the first forward sweep, the simulated HFR decreased from 98 m$\Omega \cdot$ cm$^2$ to 39 m$\Omega \cdot$ cm$^2$ due to the better hydration of the membrane with the product water. A less significant resistance reduction, from about 42 m$\Omega \cdot$ cm$^2$ to 39 m$\Omega \cdot$ cm$^2$, was observed in the experiments. As discussed before, this might have been due to the presence of liquid water in the cell at the start of the polarization-curve measurements.

A hypothesis was formulated earlier that including the conditioning step in the transient simulation would improve the agreement with the experimental HFR at the start of the voltage sweeps. In order to check the hypothesis, an additional two-phase simulation was performed, this time holding the cell at 0.6 V for 15 minutes prior to the voltage sweeps in accordance with the testing protocol. As shown in Figures 6.16b and 6.16d, simulating the experimental conditioning step reduced the initial HFR

value from 98 m$\Omega \cdot$ cm$^2$ to about 37 m$\Omega \cdot$ cm$^2$, which was closer to the experimental resistance of 42 m$\Omega \cdot$ cm$^2$. Therefore, accounting for the cell conditioning in the transient simulations may be necessary for the correct prediction of the initial HFR. However, the simulated HFR rapidly increased and, by about 300 s (59 mA/cm$^2$), became indistinguishable from the resistance computed in the simulation without the conditioning step. The fact that such an increase was not observed experimentally may indicate the presence of liquid water in the physical cell at the start of the voltage sweep, as hypothesized earlier. Because the conditioning step had no effect on the simulated current density, as seen in Figures 6.16a and 6.16c, and because that step took approximately 6.5 hours to compute, the rest of the simulations shown in this Chapter were performed without the cell conditioning.

To analyze the dynamic liquid-water accumulation in the cell, the transients of the average saturation in the CCL, CMPL, CGDL and the average capillary pressure in the CGDL are shown in Figure 6.17 (saturation in the anode was negligible in all cases). The maximum catalyst-layer saturation matched the fraction of the hydrophilic pores in the CCL, approximately 2.5%. Similarly, the hydrophilic pores of the CMPL (1%) were flooded for extended periods of time during both sweeps (Figure 6.17b). To understand the reason why the CCL and CMPL saturation remained low during the simulation, Figure 6.5 needs to be analyzed. It is clear from that figure that, for liquid water to intrude the hydrophobic pores of the CMPL and the CCL, capillary pressure must exceed 1 kPa and 20 kPa, respectively. Those values are higher than the breakthrough pressure at the CGDL-channel boundary used in this Chapter, 0.77 kPa. Moreover, the CGDL will be completely flooded at 20 kPa. Even at 3 kPa, which is significantly higher than the breakthrough capillary pressure measured for SGL GDLs [112, 461], the MPL saturation computed with the PSD model is about 0.07, and only the hydrophilic pores of the CL are filled ($s = 0.0249$). Therefore, liquid water escapes through the cathode channel before enough capillary pressure could build up in the cathode for any significant portion of the CCL and

the CMPL to be flooded. A parametric study on the catalyst-layer wettability will be presented later in this Chapter.

The average CGDL saturation and capillary pressure exhibited oscillations in Figures 6.17c and 6.17d due to the liquid-water accumulation and drainage cycles. Those oscillations occurred between the breakthrough and minimum pressures in the boundary condition (6.1), 0.77 kPa and 0.65 kPa, except for the times when the current density was the highest and liquid water was continuously leaving the cell through the CGDL-channel interface (the breakthrough pressure was exceeded in those time intervals, 1,300–2,100 s and 4,600–5,400 s). The cyclic CGDL flooding induced the local fluctuations in the simulated current density and HFR seen in Figures 6.16a and 6.16c. However, such oscillations were not observed in the experimental data. Therefore, liquid water might have been leaving the physical cell continuously.

More information on the dynamic two-phase water management can be obtained with the developed model using the computed fluxes of water transport and phase change. For example, the cathodic fluxes of evaporation, condensation, and water leaving the MEA as liquid and vapor are plotted in Figure 6.18. They are presented in the dimensionless form

$$\beta = N_{H_2O} \frac{2F}{i_{ORR}},$$

where $N_{H_2O}$ is the water flux in mol/(cm$^2$ · s) and $i_{ORR}$ is the ORR current density in A/cm$^2$. For the phase change, flux $N_{H_2O}$ was computed by integrating the source term (2.23) over each porous layer and dividing the result by the sum of the channel and land widths in the computational domain. The sign of the resulting quantity was negative for evaporation ($\beta^c_{evap}$) and positive for condensation ($\beta^c_{cond}$). In that case, $N_{H_2O}$ bore the meaning of the total rate of evaporation or condensation per MEA area rather than a flux. The fluxes of liquid water and vapor, $\beta^c_{liq, ch}$ and $\beta^c_{vap, ch}$, were positive when water was leaving the cell and negative otherwise.

During each sweep (about 3273 s), a significant amount of water was evaporated and condensed in the cathode, as evident from the large peaks in $\beta^c_{evap}$ and $\beta^c_{cond}$.
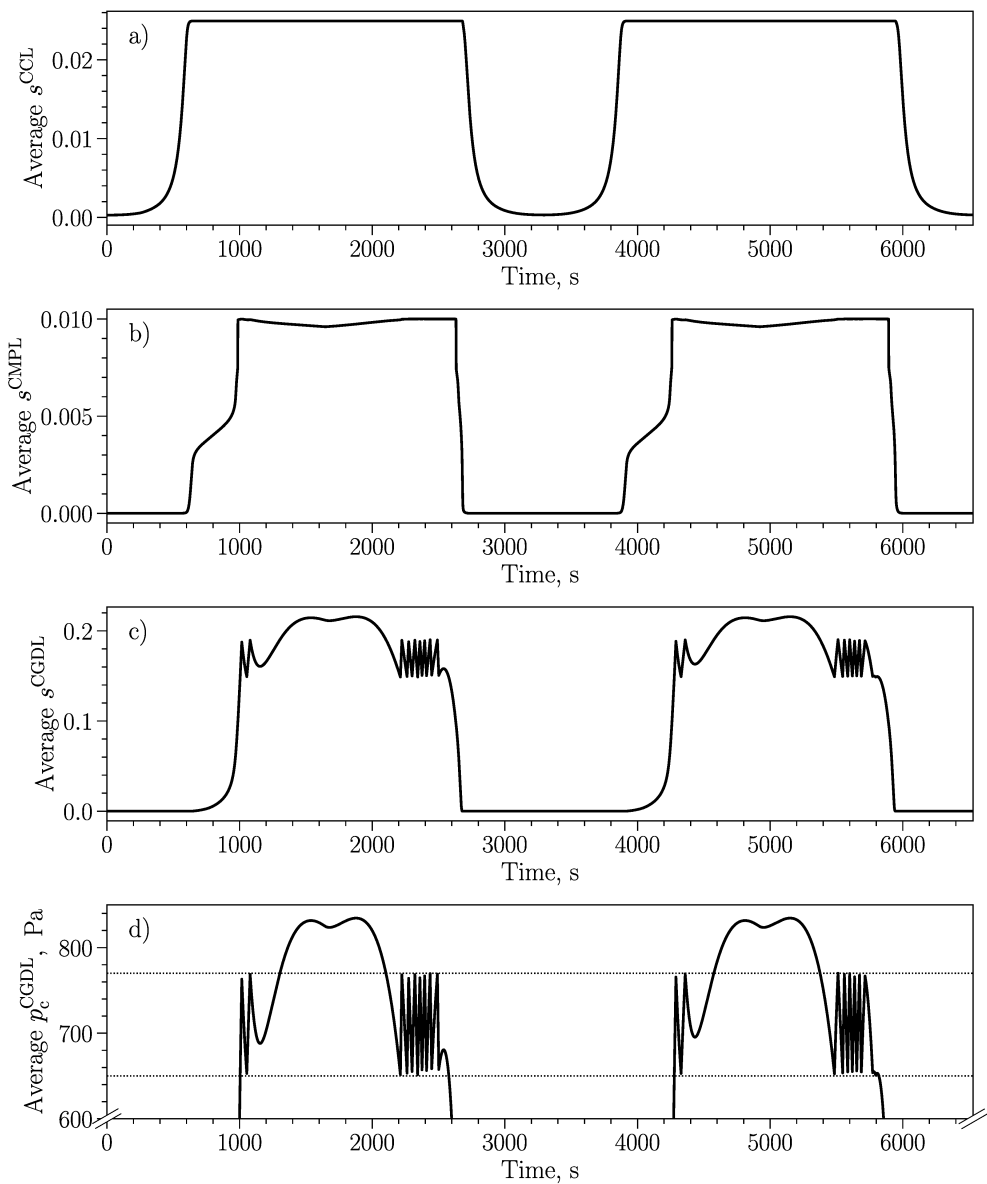
Figure 6.17: The simulated transients of the average saturation in the CCL (a), CMPL (b), and CGDL (c) and of the average capillary pressure in the CGDL (d). The vertical axis of the latter graph is limited to [600, 850] Pa for clarity. The horizontal dotted lines in graph d) denote the breakthrough and minimum pressures in the boundary condition (6.1), 0.77 kPa and 0.65 kPa. Two polarization-curve sweeps at 0.44 mV/s are shown. The operating pressure was 140 kPa in the anode and 145 kPa in the cathode. Air was used in the cathode.
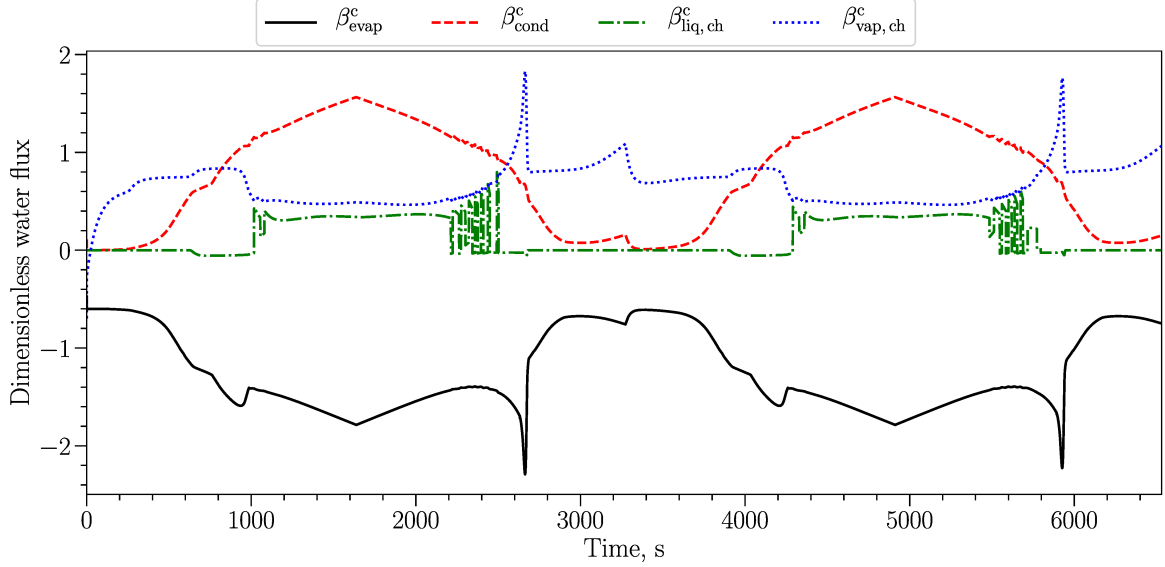
Figure 6.18: The simulated transients of the dimensionless cathodic fluxes of water evaporation ($\beta_{\text{evap}}^{\text{c}}$), condensation ($\beta_{\text{cond}}^{\text{c}}$), and of water leaving the MEA in the liquid form ($\beta_{\text{liq, ch}}^{\text{c}}$) and vapor form ($\beta_{\text{vap, ch}}^{\text{c}}$). Two polarization-curve sweeps at 0.44 mV/s are shown. The operating pressure was 140 kPa in the anode and 145 kPa in the cathode. Air was used in the cathode.

Throughout the simulation, liquid water evaporated mostly in the CCL and condensed at the CMPL-CGDL interface due to the 5 °C lower temperature in that area than in the catalyst layer. A similar observation was made by Zhou et al. [35]. This effect, termed the phase-change-induced flow of water (the heat-pipe effect), was reported in other publications as well [64, 211, 274, 605]. At the start of each sweep, water left the cathode in vapor form ($\beta_{\text{vap, ch}}^{\text{c}}$ was positive and $\beta_{\text{liq, ch}}^{\text{c}}$ was about zero). Once the CGDL capillary pressure reached the breakthrough value at about 1,000 s (Figure 6.17d), $\beta_{\text{liq, ch}}^{\text{c}}$ increased and began to oscillate as the drainage/accumulation cycles started. At the same time, $\beta_{\text{vap, ch}}^{\text{c}}$ dropped, and water left the cell in both vapor and liquid forms in comparable amounts for the next 1,500 s. The time intervals in Figure 6.17d where the breakthrough pressure was exceeded coincide with the intervals in Figure 6.18 where liquid water was leaving the cell continuously, without fluctuations. As current density decreased in the second half of each sweep, oscillations in $\beta_{\text{liq, ch}}^{\text{c}}$ stopped, and rapid release of vapor took place at about 2,664 s and

313

5,297 s. Just before the breakthrough took place, however, $\beta_{\text{liq, ch}}^{\text{c}}$ assumed a negative value of about -0.057, which indicated an artificial flux of liquid water entering the cathode from the channel. This flux was not physical and was a result of the numerical instability associated with the boundary condition (6.1) that could open and close the CGDL-channel interface for the liquid-water transport between the Newton iterations. Using a smaller time-step size may reduce this artificial flux.

### 6.3.2.3 Voltage Sweeps at 4.8 mV/s with Air

Voltage sweeps were performed next at a faster scan rate of 4.8 mV/s, and the results are shown in Figure 6.19. The magnitude of the polarization-curve hysteresis in Figure 6.19a increased in the simulations compared with the previous results obtained at a slower scan rate of 0.44 mV/s. A threshold point was observed in the simulated polarization curve at 0.648 A/cm$^2$ but not in the experiments (Figure 6.19a). The experimental data still did not exhibit hysteresis, in contrast to both the literature [46, 49–52, 54] and the simulation results in this work. The type of hysteresis seen in the simulated polarization curve in Figure 6.19a was discussed in detail in Chapter 1: the counterclockwise hysteresis to the left of the threshold point is indicative of the polymer-electrolyte hydration, and the clockwise hysteresis to the right of the threshold point represents flooding. The HFR hysteresis in Figure 6.19b was also larger than in Figure 6.16b due to the dynamic polymer-electrolyte hydration.

Further analysis of the observed two-phase hysteresis was performed at the three points marked in the polarization curve in Figure 6.19a: point A, where the performance started to rapidly decrease; point B, where the maximum current density was achieved; and point C, to which the current density decreased by the end of the first forward scan. It can be seen in Figure 6.19d that the HFR increased from points A and B to point C. This created a small counterclockwise hysteresis at high current density seen in Figure 6.19b and a threshold point in the HFR curve at 1.15 A/cm$^2$. It was concluded earlier that, in the simulations presented so far in this Chapter, an
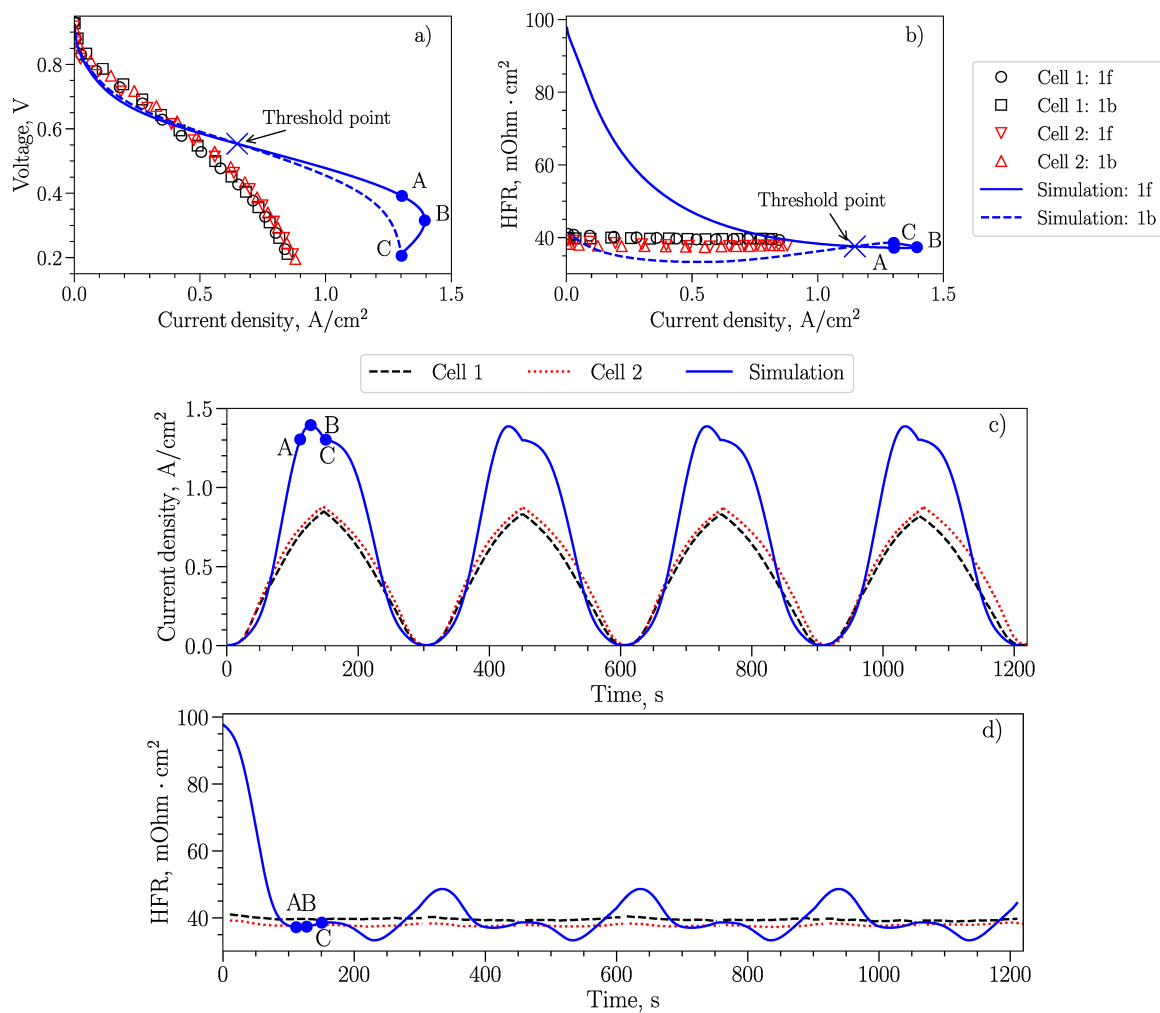
Figure 6.19: Comparison of the simulated and experimental current density and HFR. The forward and backward scans are labeled with letters "f" and "b" (for instance, "1f" denotes the first forward scan). Voltage sweeps were performed at 4.8 mV/s, and only the first sweep is shown in a) and b). The operating pressure was 140 kPa in the anode and 145 kPa in the cathode. Air was used in the cathode.
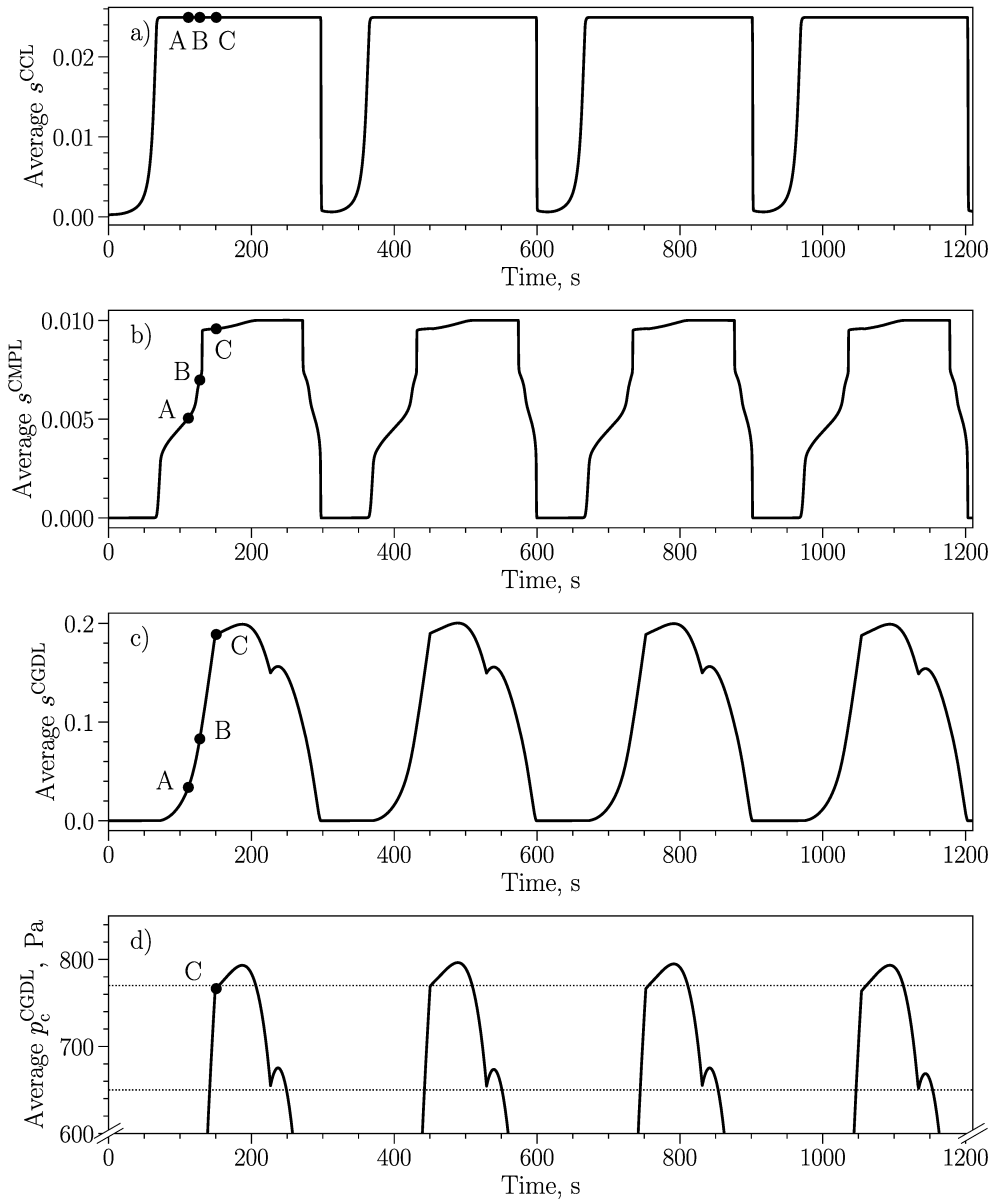
Figure 6.20: The simulated transients of the average saturation in the CCL (a), CMPL (b), and CGDL (c) and of the average capillary pressure in the CGDL (d). The vertical axis of the latter graph is limited to [600, 850] Pa for clarity. The horizontal dotted lines in graph d) denote the breakthrough and minimum pressures in the boundary condition (6.1), 0.77 kPa and 0.65 kPa. Four polarization-curve sweeps at 4.8 mV/s are shown. The operating pressure was 140 kPa in the anode and 145 kPa in the cathode. Air was used in the cathode.

316

increase in the HFR with current density was related to the oxygen starvation in the cathode. The analysis of points A–C in Figure 6.20 reveals that it was the case for the voltage sweep in Figure 6.19 as well. While the average CCL saturation was the same at those three points (Figure 6.20a) and the CMPL saturation was not significant (Figure 6.20b), rapid flooding took place in the CGDL, as seen in Figure 6.20c. Since liquid water occupied about 20% of the CGDL pore volume, oxygen-transport resistance increased, leading to a lower oxygen content under the land, redistribution of the ORR, and an increase in the HFR. Coincidentally, the breakthrough pressure was reached approximately at the same time as the forward scan ended at point C. As shown in Figure 6.20c, the capillary pressure in the CGDL continued to increase for about 53 s after that as more liquid water accumulated in the layer, even though the current density started to decrease in the backward scan. After that, the pressure dropped to the minimum value prescribed in the boundary condition (6.1) as liquid water escaped to the channel. Once the CGDL-channel boundary closed again, liquid water continued accumulating for a short duration of time, but then the CGDL quickly dried through evaporation.

### 6.3.3  Analysis of the Transient Two-Phase PEMFC Behavior

In order to understand how the model inputs affect the simulated cell performance under the two-phase operating conditions, a number of parametric studies were performed.

#### 6.3.3.1  Effect of the Breakthrough and Minimum Capillary Pressures at the CGDL-Channel Interface

First, the influence of the boundary condition (6.1) was analyzed. Voltage sweeps were simulated with the scan rate of 0.44 mV/s using two different sets of the breakthrough capillary pressure, $p_{c,\,bt}$, and the minimum capillary pressure, $p_{c,\,min}$. In the first set, $p_{c,\,min}$ was kept at 0.65 kPa but the breakthrough pressure was increased from 0.77 kPa to 1.6 kPa, the value measured by Ziegler [461]. The higher breakthrough pressure lets

more liquid water accumulate in the cell before it escapes through the channels. In the second set, $p_{c,\,bt}$ remained high but the minimum capillary pressure was raised to 1.1 kPa. The higher minimum pressure lets less liquid water escape before the GDL-channel boundaries close until the next breakthrough. The boundary condition was modified for both electrodes; however, as mentioned before, no significant saturation was predicted with the model in the anode, and thus all the observations made were related to the liquid-water accumulation in the cathode.

The results of these simulations are presented in Figures 6.21, 6.22, and 6.23, where the reference case is the same as in Figure 6.16. The current density and the HFR were less stable when the breakthrough pressure was increased. The two polarization curves with the higher breakthrough pressure followed the reference forward scan up to 0.94 A/cm$^2$ (Figure 6.21a), but then the current density rapidly decreased to 0.44 A/cm$^2$. The limiting current density was fully recovered by the end of the forward scan when the low minimum capillary pressure of 0.65 kPa at the CGDL-channel interface was used. In that case, the cell performance in the backward scan was higher at first than in the forward scan, then lower in the unstable region, and was recovered in a rapid change after reaching 0.36 A/cm$^2$. On the other hand, more current-density fluctuations were observed in the case of the higher $p_{c,\,min}$, with an overall decrease in the predicted cell performance compared with the other two cases. Such a performance instability due to liquid-water transport has been reported experimentally by Ziegler and Gerteisen [475]. The HFR exhibited the complex behavior shown in Figure 6.21b.

Figure 6.23 helps shed light on the cause of the cell-performance instability. While the CCL saturation remained nearly the same in all three cases, the amount of liquid water in the CMPL and, more notably, in the CGDL was changing rapidly during the voltage sweeps. It is clear from Figure 6.23c that the first decline in the current density and the first increase in the HFR during the forward scan were due to the rapid accumulation of liquid water in the CGDL, with 61% of the layer flooded by $t \approx 1133$ s
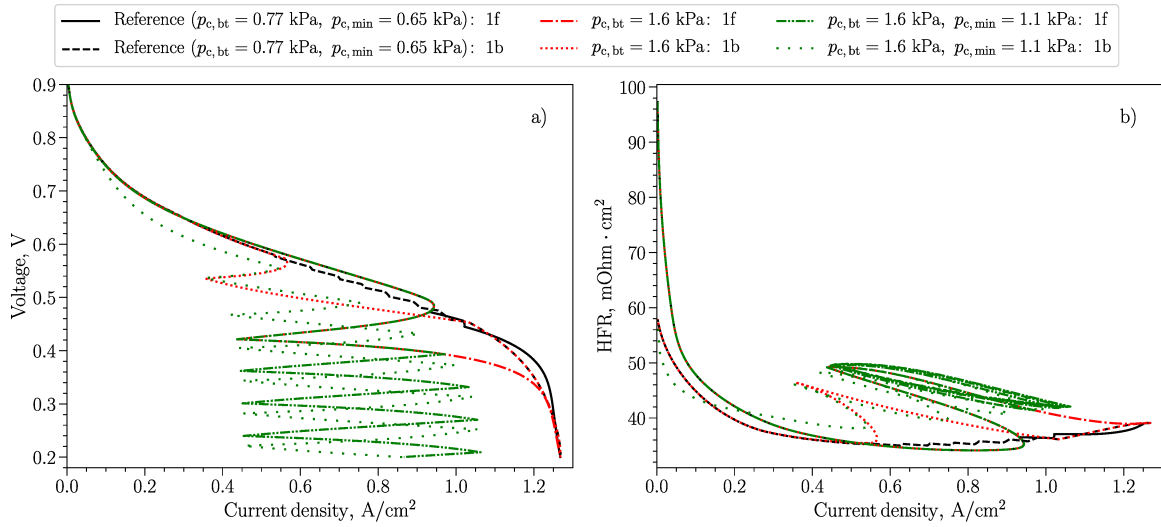
Figure 6.21: The effect of the breakthrough and minimum capillary pressures in the boundary condition (6.1) on the current density (a) and the HFR (b) during a voltage sweep simulated at 0.44 mV/s, 60 °C, 90% RH. The forward and backward scans are labeled with letters "f" and "b".
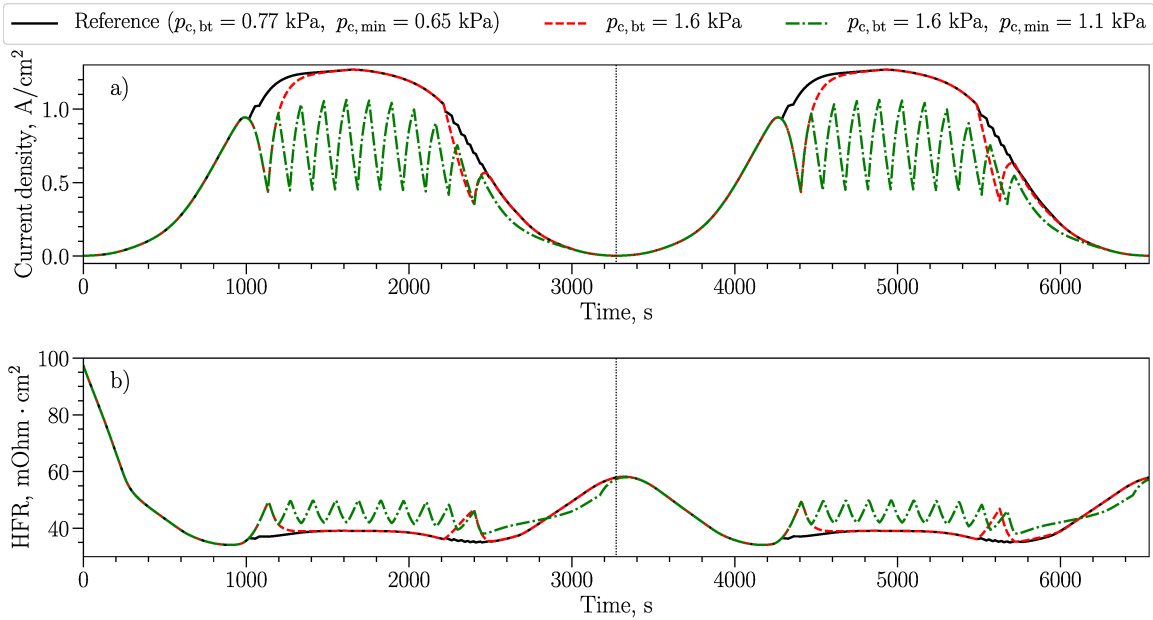


Figure 6.22: The effect of the breakthrough and minimum capillary pressures in the boundary condition (6.1) on the current-density (a) and HFR (b) transients during two voltage sweeps simulated at 0.44 mV/s, 60 °C, 90% RH, the first of which corresponds to Figure 6.21. The vertical dotted line separates the two sweeps.
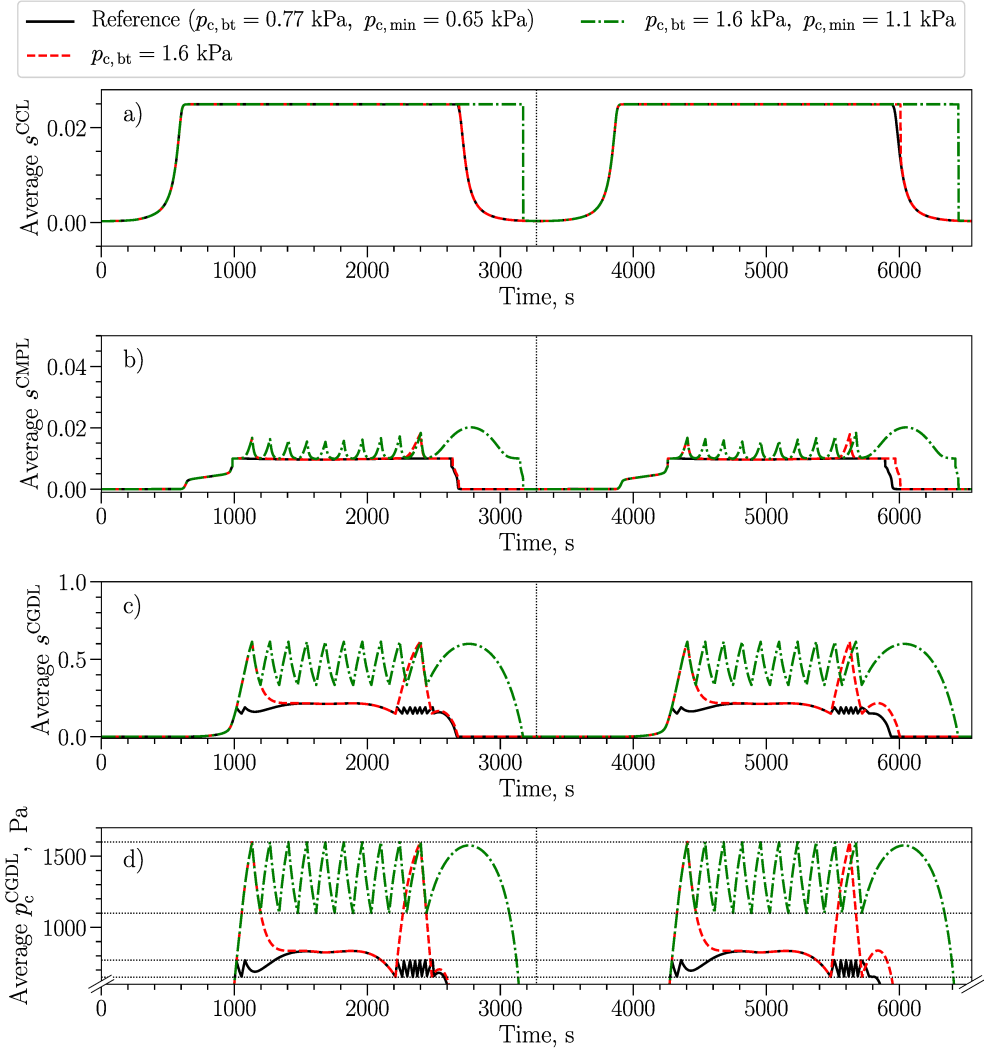
Figure 6.23: The effect of the breakthrough and minimum capillary pressures in the boundary condition (6.1) on the simulated transients of the average saturation in the CCL (a), CMPL (b), and CGDL (c) and of the average capillary pressure in the CGDL (d). The horizontal dotted lines in graph d) denote the breakthrough and minimum pressures (varied in this study). Two polarization-curve sweeps at 0.44 mV/s are shown, the first of which corresponds to Figure 6.21. The vertical dotted line separates the two sweeps.

320

when the breakthrough pressure was increased. After the liquid breakthrough took place (Figure 6.23d), liquid water started to escape the cell from the cathode channel. The amount of it that left the cell depended on $p_{c,\,min}$ and affected the severity of the current-density and HFR oscillations. Similarly, the spikes in the current density and HFR during the backward sweep were also related to the state of the CGDL flooding. The two limiting current densities observed in Figures 6.21a and 6.22a when both the breakthrough and minimum capillary pressures were increased corresponded to the bounds of the CGDL saturation in Figure 6.23c. The developed transient model, therefore, captures the dynamic transition between two different flooding states that, when modeled at steady state, may result in sharp changes and discontinuities in the polarization curve [342, 343].

As seen in Figures 6.21–6.23 and as discussed in Section 6.3.2.2, cell performance is more stable when liquid water leaves the MEA in a continuous manner, i.e., when the capillary pressure at the CGDL-channel interface is maintained in the open interval $(p_{c,\,min},\, p_{c,\,bt})$. The key to the stable performance reduction is, therefore, not allowing the capillary pressure to decrease to $p_{c,\,min}$ after the breakthrough until the current density becomes sufficiently low in the backward scan so that liquid water does not continue to accumulate. Such a water-removal regime can be achieved, in addition to modifying $p_{c,\,min}$ and $p_{c,\,bt}$, by reducing the rate at which liquid water erupts from the CGDL-channel interface. This is analyzed in the next parametric study.

### 6.3.3.2 Effect of the Liquid-Water Eruption Rate

When the breakthrough is reached in the boundary condition (6.1), liquid water erupts from the GDL-channel boundaries with the rate $k_{l,\,out}$. The slower this rate, the more difficult it is to remove liquid water from the cell. Therefore, $k_{l,\,out}$ is expected to have a significant impact on the results of the transient simulations.

Indeed, when the eruption rate was lowered by a factor of 100, the performance was severely reduced but stable (without oscillations), as seen in Figures 6.24a and 6.25a.
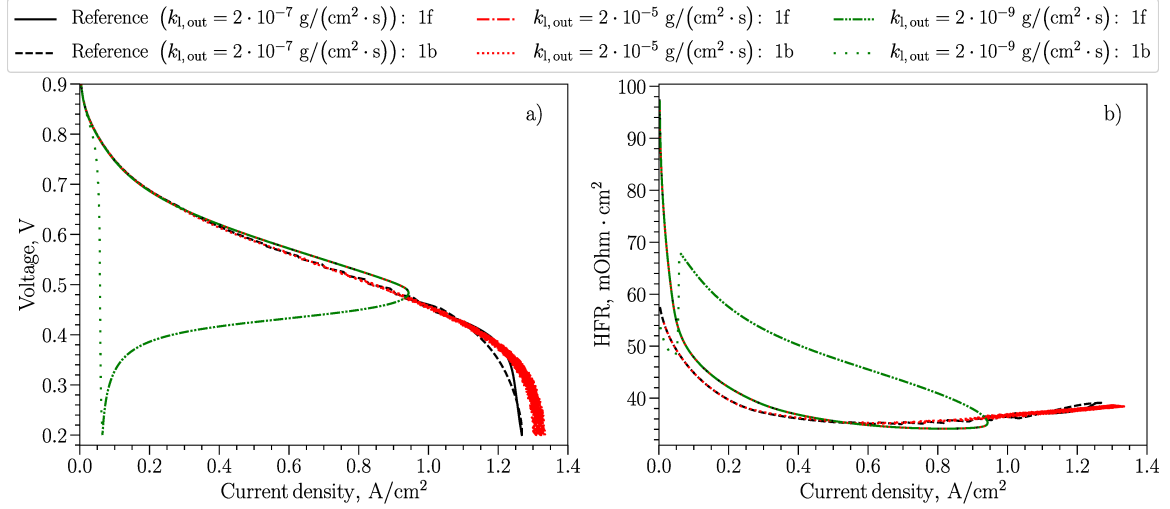
Figure 6.24: The effect of the liquid-water eruption rate in the boundary condition (6.1) on the current density (a) and the HFR (b) during a voltage sweep simulated at 0.44 mV/s, 60 °C, 90% RH. The forward and backward scans are labeled with letters "f" and "b".

This happened because of the severe CGDL flooding, illustrated in the saturation and capillary-pressure graphs in Figure 6.26, where up to 85% of the CGDL was filled with liquid water. Due to the pressure buildup, liquid-water saturation in the CMPL exceeded 1%, indicating the partial intrusion of its hydrophobic pores. Depletion of oxygen due to flooding led to the increase in the HFR during the forward scan (Figures 6.24b and 6.25b).

Because the cell performance during the forward scans coincided in all simulations up to 0.94 A/cm$^2$ in Figures 6.21a and 6.24a, it is clear that the rapid CGDL flooding during the voltage sweep is not the primary cause of the low current density measured in the experiments (Figure 6.16e). This supports the hypothesis that liquid water might have already been present in the physical cell at the start of the measurements. Hence, the fraction of the hydrophilic pores in the CCL, where liquid water resides at the start of the forward scan, might have been significantly higher than the assumed 2.49%. The effect of the catalyst-layer wettability on the simulation results is analyzed later in this Chapter.

With a fast eruption rate of $2 \cdot 10^{-5}$ g/(cm$^2 \cdot$ s), a higher limiting current was
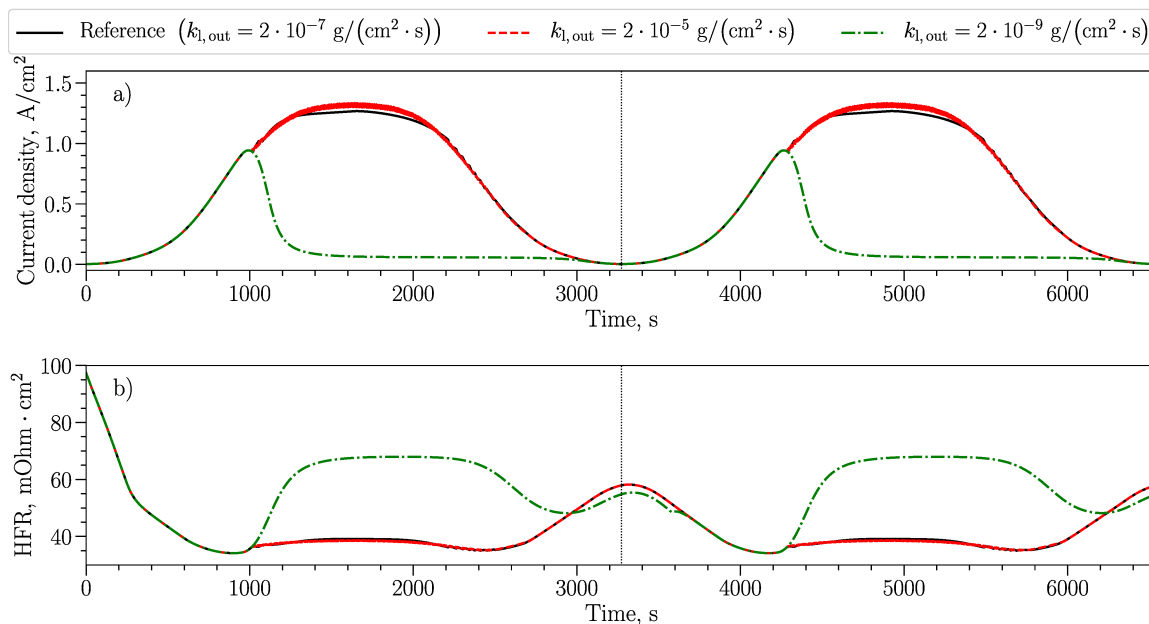
Figure 6.25: The effect of the liquid-water eruption rate in the boundary condition (6.1) on the current-density (a) and HFR (b) transients during two voltage sweeps simulated at 0.44 mV/s, 60 °C, 90% RH, the first of which corresponds to Figure 6.24. The vertical dotted line separates the two sweeps.

achieved, as seen in Figures 6.24a and 6.25a. The current density experienced frequent small-amplitude oscillations due to the liquid-water accumulation and drainage in the CGDL (Figures 6.26c and 6.26d).

### 6.3.3.3 Effect of the Liquid-Water Evaporation Rate

The rates at which water evaporates and condenses in the porous layers of the MEA have a direct effect on the two-phase operation of fuel cells. With the model inputs considered in this Chapter, it was found that increasing or decreasing the condensation rate of water by a factor of 10 had a negligible effect on the simulated current density, HFR, and cathode saturation. Therefore, only the results of the evaporation-rate study are presented.

As illustrated in Figures 6.27–6.29, the evaporation rate had a direct impact on the predicted current density. The faster was the evaporation, the less water was accumulated in the cathode and the higher was the cell performance. The increased evap-
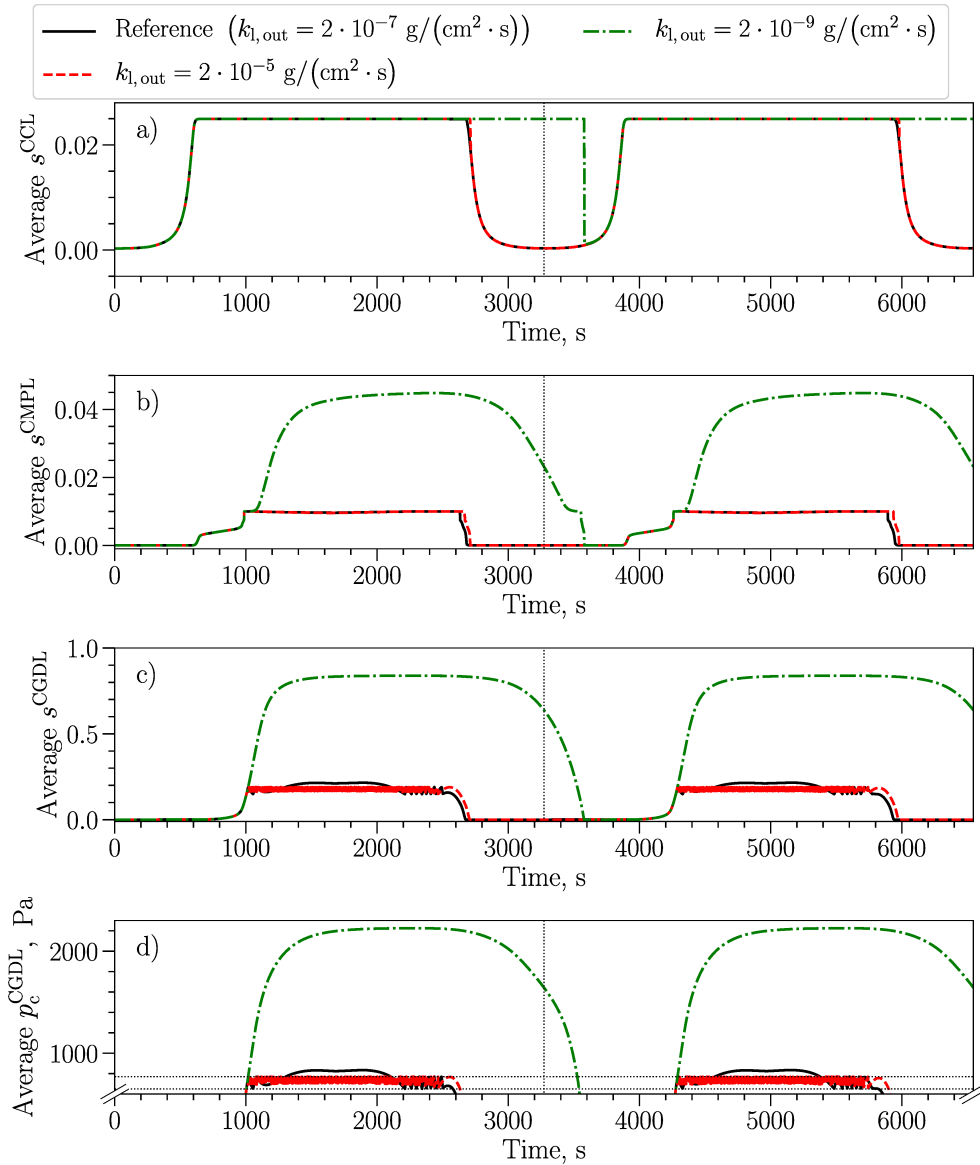
Figure 6.26: The effect of the liquid-water eruption rate in the boundary condition (6.1) on the simulated transients of the average saturation in the CCL (a), CMPL (b), and CGDL (c) and of the average capillary pressure in the CGDL (d). The horizontal dotted lines in graph d) denote the breakthrough and minimum capillary pressures, 0.77 kPa and 0.65 kPa. Two polarization-curve sweeps at 0.44 mV/s are shown, the first of which corresponds to Figure 6.24. The vertical dotted line separates the two sweeps.

oration rate also led to a decrease in the simulated HFR (Figures 6.27b and 6.28b). Since the liquid-water uptake was approximated by setting a fraction of the ORR water to be produced in the ionomer phase of the CCL and because that fraction was not modified in this study, the lower amount of liquid water in the pores did not increase the HFR. On the contrary, the conductivity of the membrane improved due to the increased amount of water vapor that could be absorbed by the polymer electrolyte.
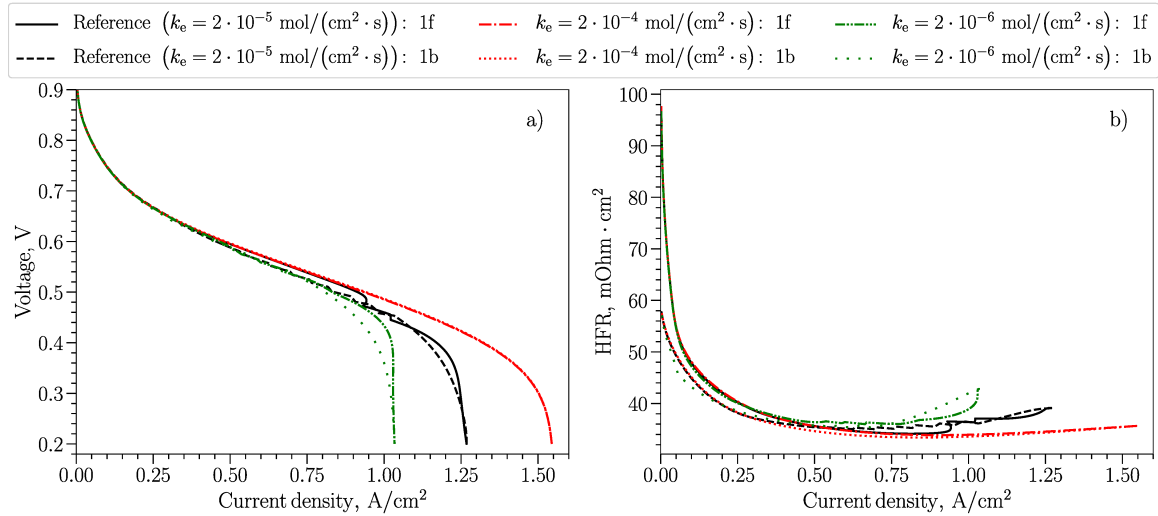


Figure 6.27: The effect of the liquid-water evaporation rate on the current density (a) and the HFR (b) during a voltage sweep simulated at 0.44 mV/s, 60 °C, 90% RH. The forward and backward scans are labeled with letters "f" and "b".

The results of this study indicate that using a lower evaporation rate of water would have resulted in better agreement between the fuel-cell model and the experimental polarization curves in Figures 6.16 and 6.19. Therefore, one of the future avenues toward improving that agreement is the reduction of the evaporation rate of water.

### 6.3.3.4 Effect of the Amount of Product Water Directly Absorbed by the CCL Ionomer

As discussed in Chapter 2, the amount of water produced at the catalyst surface under the ionomer film in the CCL was assumed to be directly absorbed into the polymer electrolyte and was controlled in the model with parameter $\xi \in [0, 1]$. The
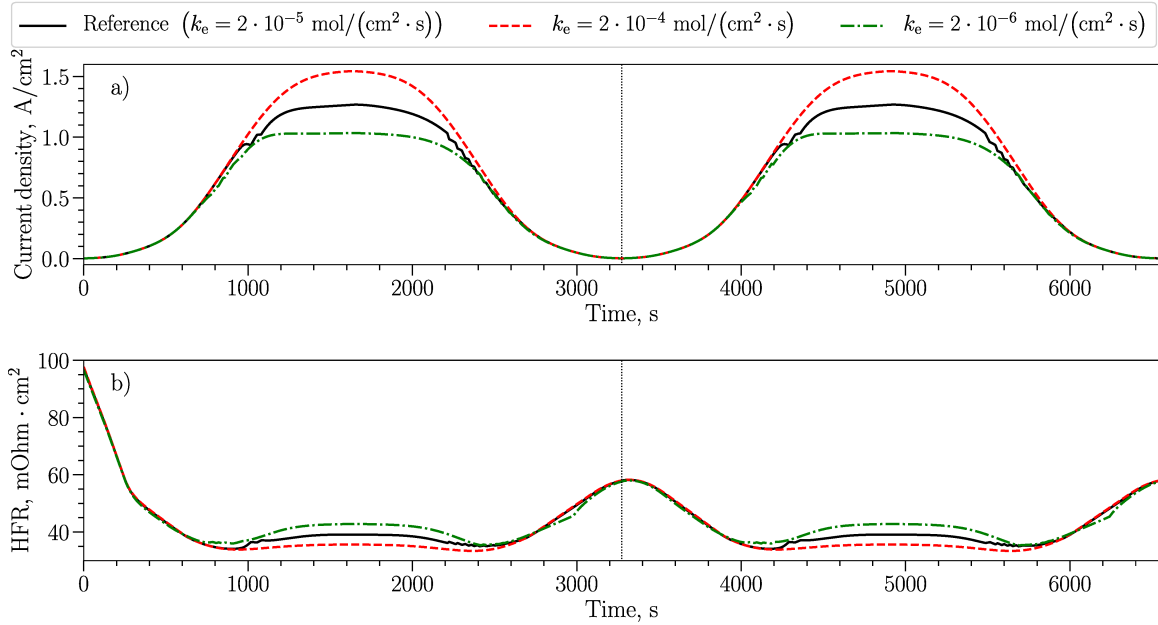
Figure 6.28: The effect of the liquid-water evaporation rate on the current-density (a) and HFR (b) transients during two voltage sweeps simulated at 0.44 mV/s, 60 °C, 90% RH, the first of which corresponds to Figure 6.27. The vertical dotted line separates the two sweeps.

closer $\xi$ was to 1, the more water was produced in the liquid form in the CCL pores and the less of it was directly absorbed by the ionomer. Therefore, parameter $\xi$ had a direct impact on both liquid-water accumulation and ohmic resistance. This impact was analyzed in a study where $\xi$ (0.4 in the reference case) was changed to 0 and to 1.

The simulation results in Figures 6.30–6.32 match the expectations: with all water produced in the ionomer of the CCL ($\xi = 1$), the performance was the highest, the HFR was the lowest, and the cathode was relatively dry. It can be seen in Figure 6.32 that, even though water was assumed in the model to be desorbed from the ionomer into the pores as vapor, some accumulation of liquid water still took place due to condensation. When water was set to be produced as liquid in the pore space of the CCL ($\xi = 0$), the simulated performance was the lowest (with the flooding-induced clockwise hysteresis) and the HFR was the highest, as depicted in Figures 6.30 and 6.31.

326
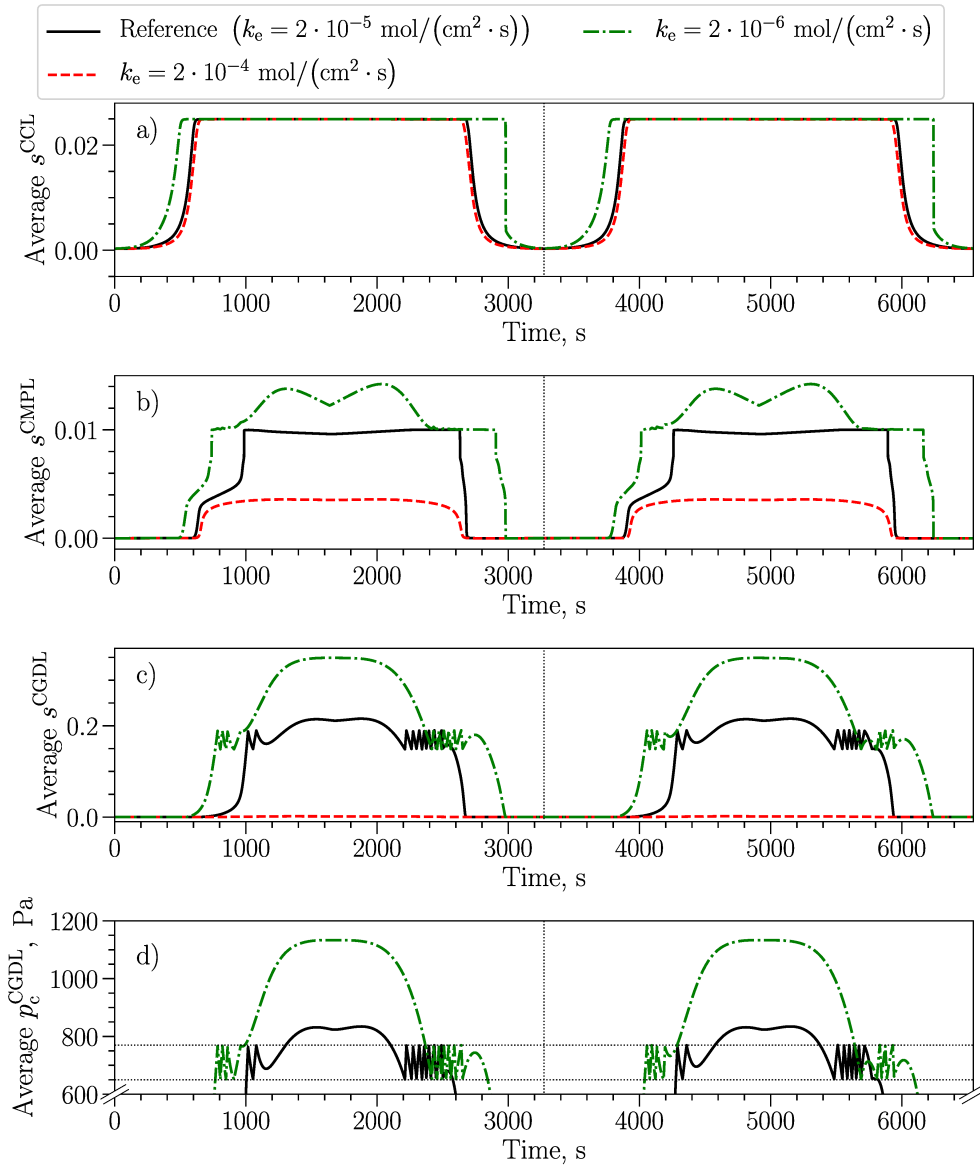
Figure 6.29: The effect of the liquid-water evaporation rate on the simulated transients of the average saturation in the CCL (a), CMPL (b), and CGDL (c) and of the average capillary pressure in the CGDL (d). The horizontal dotted lines in graph d) denote the breakthrough and minimum capillary pressures, 0.77 kPa and 0.65 kPa. Two polarization-curve sweeps at 0.44 mV/s are shown, the first of which corresponds to Figure 6.27. The vertical dotted line separates the two sweeps.
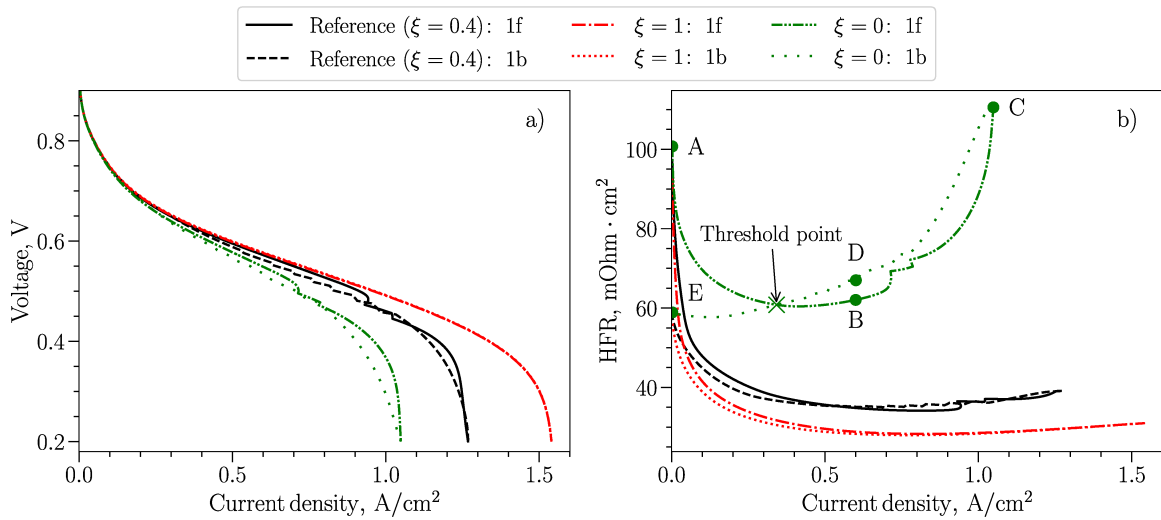
Figure 6.30: The effect of the amount of water produced directly in the CCL ionomer on the current density (a) and the HFR (b) during a voltage sweep simulated at 0.44 mV/s, 60 °C, 90% RH. The forward and backward scans are labeled with letters "f" and "b".
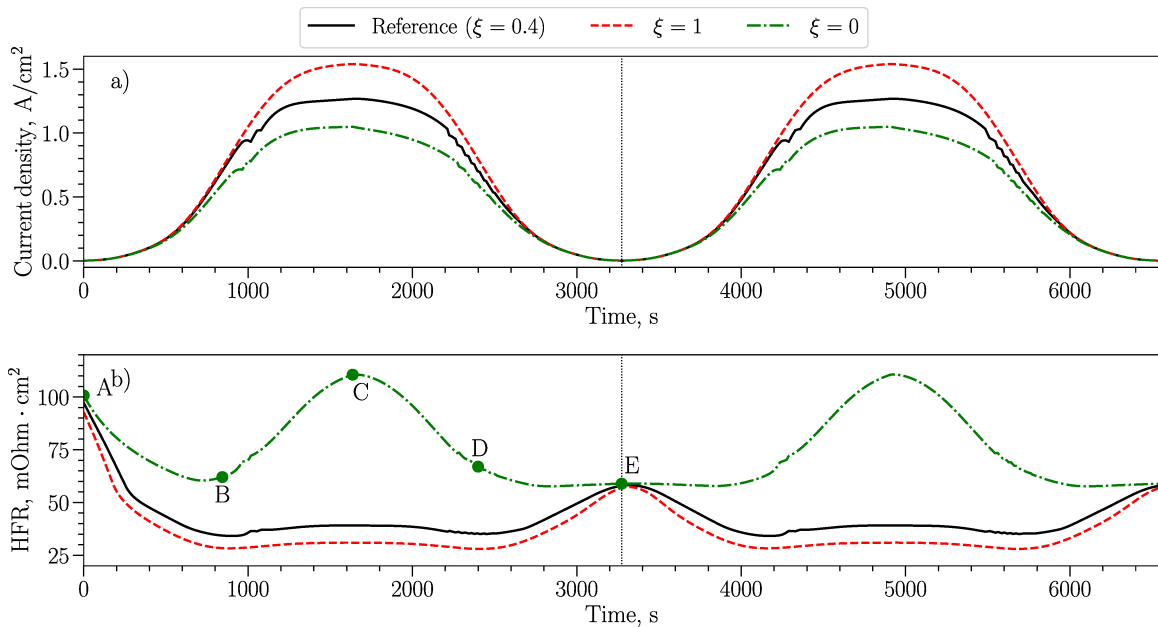


Figure 6.31: The effect of the amount of water produced directly in the CCL ionomer on the current-density (a) and HFR (b) transients during two voltage sweeps simulated at 0.44 mV/s, 60 °C, 90% RH, the first of which corresponds to Figure 6.30. The vertical dotted line separates the two sweeps.
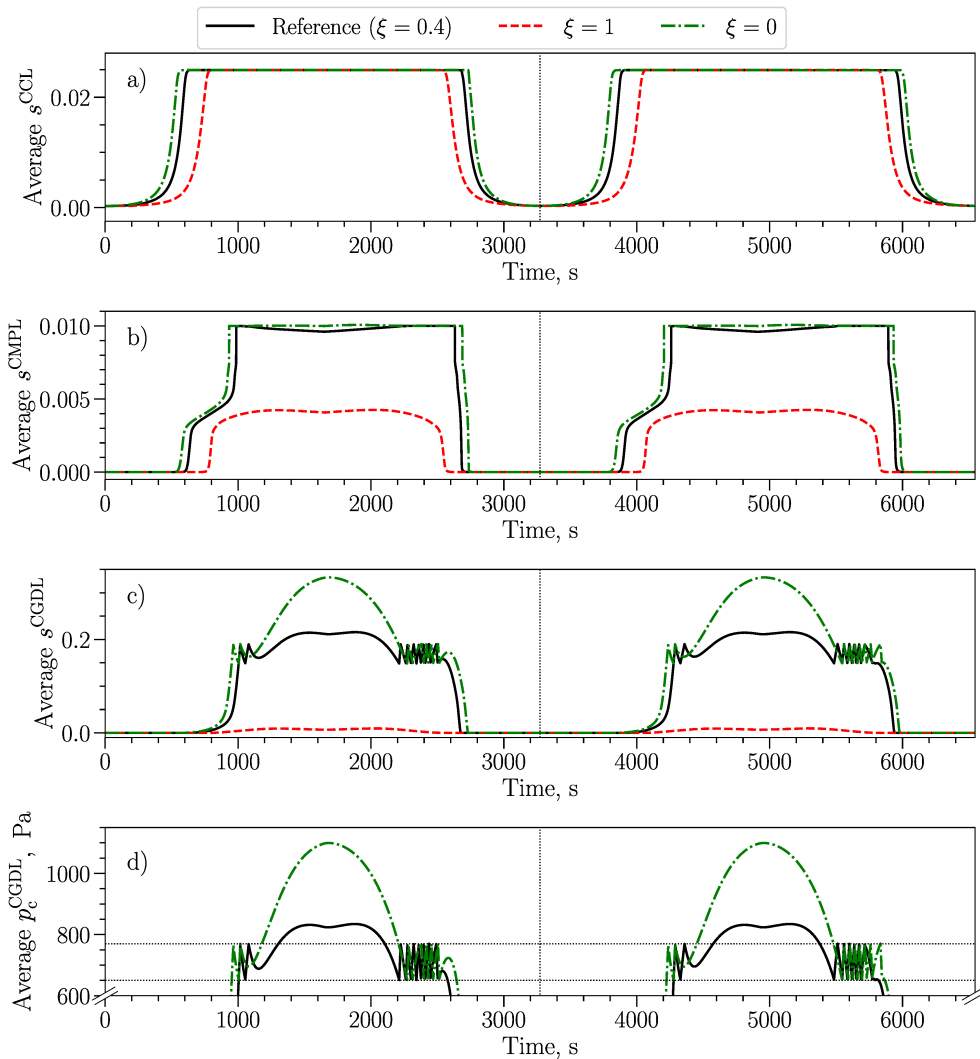
Figure 6.32: The effect of the amount of water produced directly in the CCL ionomer on the simulated transients of the average saturation in the CCL (a), CMPL (b), and CGDL (c) and of the average capillary pressure in the CGDL (d). The horizontal dotted lines in graph d) denote the breakthrough and minimum capillary pressures, 0.77 kPa and 0.65 kPa. Two polarization-curve sweeps at 0.44 mV/s are shown, the first of which corresponds to Figure 6.30. The vertical dotted line separates the two sweeps.
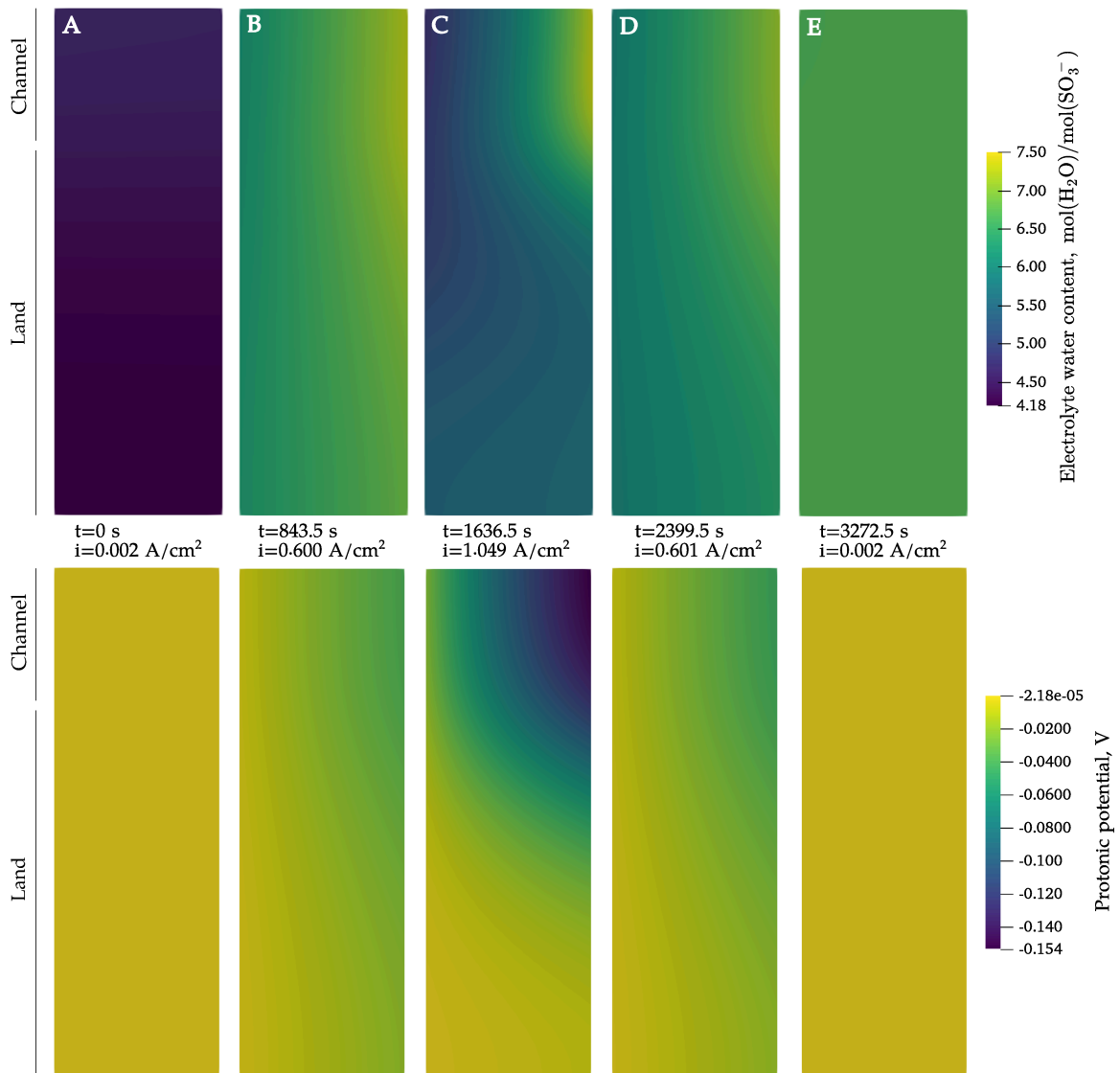
Figure 6.33: Simulated distributions of the water content and the protonic potential in the membrane at points A–E marked in Figures 6.30b and 6.31b. The domain was upscaled along the horizontal axis by a factor of 20 for clarity. The approximate locations of the land and the channel along the vertical axis are indicated.

To analyze the HFR dynamics, distributions of the water content and of the protonic potential in the membrane were plotted in Figure 6.33 at points A–E marked in Figures 6.30b and 6.31b. The distributions in Figure 6.33 indicate that, in this case, the significant increase in the HFR was due to both membrane dry-out and the change in the protonic-potential distribution from point A to point C. During the backward scan, the water content was lower at point D than at point B (both at about 0.6 A/cm$^2$) but higher at point E than at point A (both at 2 mA/cm$^2$). This created the threshold HFR point in Figure 6.30b. For comparison, the average water content in the membrane in the reference case was higher: for instance, it increased from 4.4 mol$_{H_2O}$/mol$_{SO_3^-}$ to 16.6 mol$_{H_2O}$/mol$_{SO_3^-}$ during the first forward scan. As a result, the corresponding HFR in Figures 6.30b and 6.31b was lower than in the case $\xi = 0$.

### 6.3.3.5 Effect of the GDL Binder and Its Wettability

The effect of the GDL binder and its wettability was analyzed next. The four GDLs from Table 6.4 were considered, with SGL 29BC-GDL-A being the reference case used so far. Cases 29BC-GDL-A/C/D differed in the assumption of the GDL wettability. The binder pores were assumed fully hydrophilic in case A, 90% hydrophobic in case C, and 50% hydrophobic in case D, and they were completely removed from the PSD in case B.

The simulation results in Figure 6.34 show that the GDL binder and its wettability did not have a strong effect on the HFR but impacted the cell performance at the current density above 1 A/cm$^2$. The lowest performance was achieved with the 29BC-GDL-B GDLs that did not contain the porous binder. In that case, the CGDL saturation was the highest, about 0.28, as shown in Figure 6.35c. Without the small binder pores, the liquid-gas interfacial area was lower for the 29BC-GDL-B GDLs (Figure 6.6a), which reduced their ability to evaporate liquid water. This is illustrated in Figure 6.36a, where the rate of water evaporation in the cathode is shown to be

331
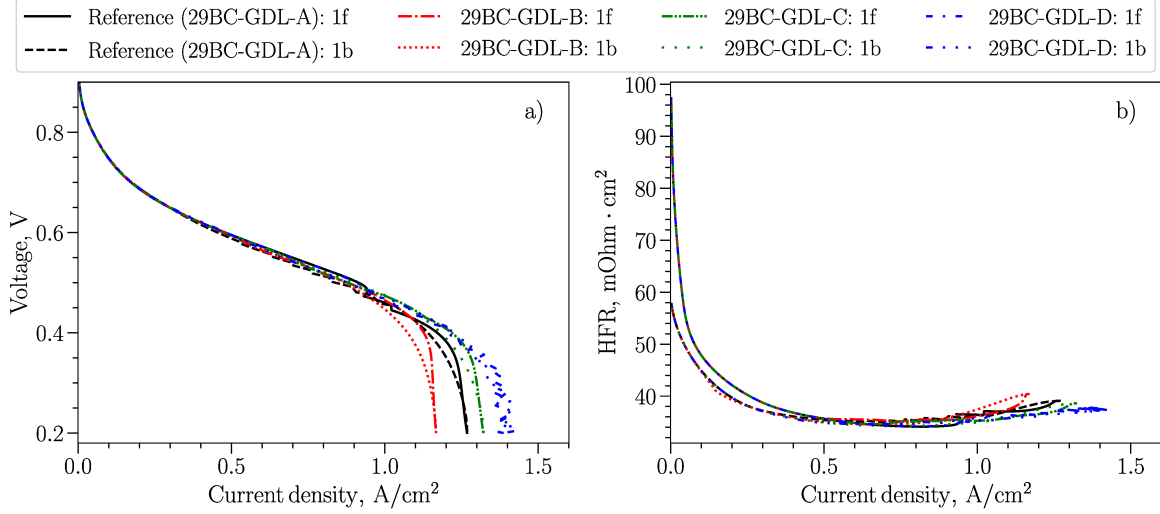
Figure 6.34: The effect of the GDL PSD and wettability on the current density (a) and the HFR (b) during a voltage sweep simulated at 0.44 mV/s, 60 °C, 90% RH. The forward and backward scans are labeled with letters "f" and "b".

the lowest for the cathode with the 29BC-GDL-B GDL.

The highest (although less stable) performance in Figure 6.34a was achieved with 29BC-GDL-D, which means there is an optimal binder wettability that results in the lowest saturation (Figure 6.35c). The existence of the optimal GDL wettability has also been reported experimentally by Lin and Nguyen [110] and numerically, with steady-state PSD-based models, by Weber et al. [26, 27] and Zhou et al. [298], however, the binder effect was not studied. Although it can be seen from Figure 6.36c that less liquid water was removed from the channel in case D, having the small binder pores only partially saturated helped retain more of the liquid-gas interface and thus aided evaporation. As illustrated in Figure 6.36a, the rate of water evaporation was the highest with 29BC-GDL-D, followed by cases 29BC-GDL-A, 29BC-GDL-C, and 29BC-GDL-B.

With 29BC-GDL-D, the transients of saturation and capillary pressure and of the flux of liquid water leaving the cathode differed between the first and second sweeps (Figures 6.35c, 6.35d, and 6.36c). It was found in other parametric studies that using a smaller time-step size helped achieve more consistent results between the two

Figure 6.35: The effect of the GDL PSD and wettability on the simulated transients of the average saturation in the CCL (a), CMPL (b), and CGDL (c) and of the average capillary pressure in the CGDL (d). The horizontal dotted lines in graph d) denote the breakthrough and minimum capillary pressures, 0.77 kPa and 0.65 kPa. Two polarization-curve sweeps at 0.44 mV/s are shown, the first of which corresponds to Figure 6.34. The vertical dotted line separates the two sweeps.

333
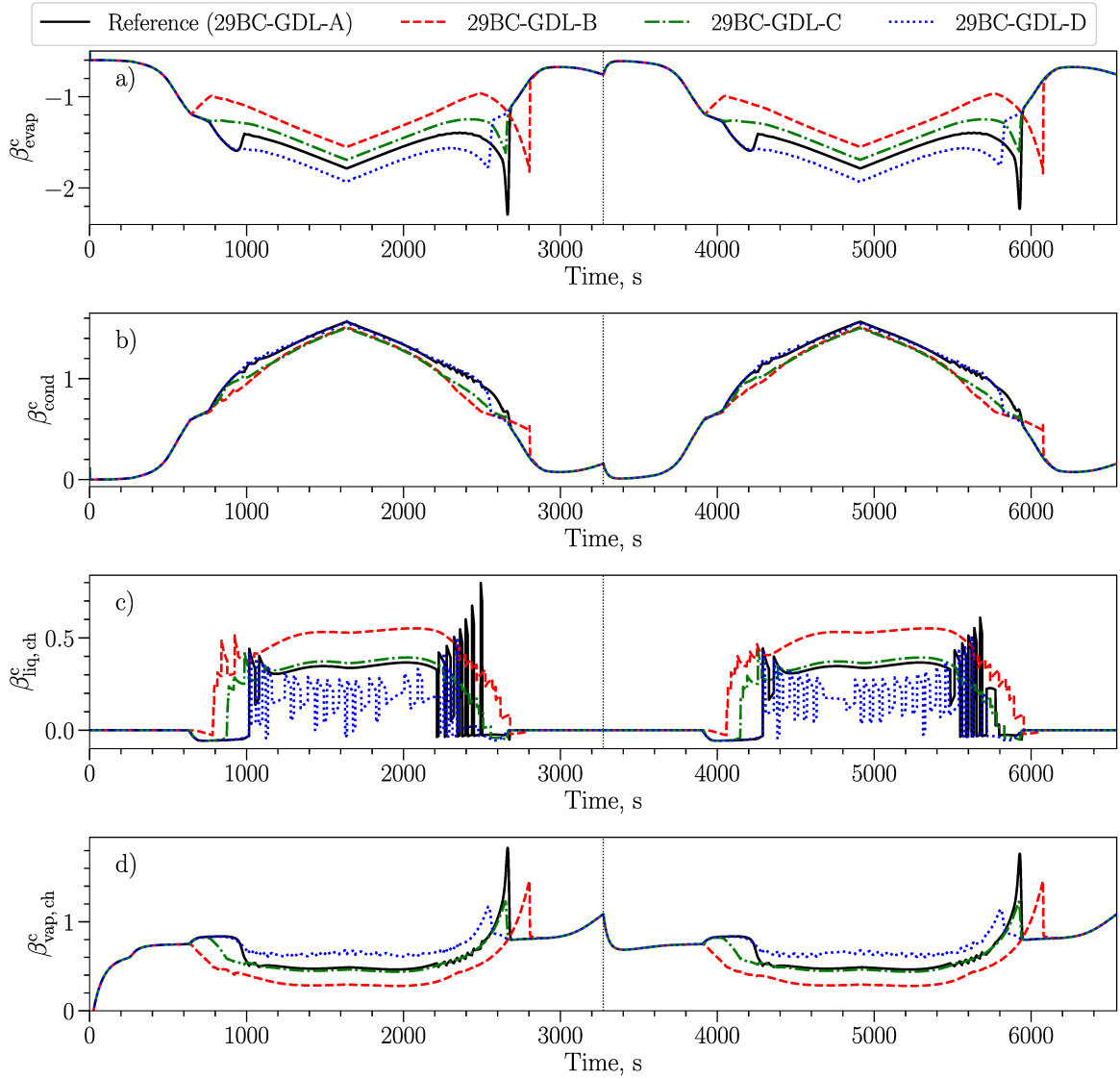
Figure 6.36: The effect of the GDL PSD and wettability on the simulated transients of the dimensionless cathodic fluxes of water evaporation ($\beta^{c}_{evap}$), condensation ($\beta^{c}_{cond}$), and of water leaving the MEA in the liquid form ($\beta^{c}_{liq,ch}$) and vapor form ($\beta^{c}_{vap,ch}$). Two polarization-curve sweeps at 0.44 mV/s are shown, the first of which corresponds to Figure 6.34. The vertical dotted line separates the two sweeps.

sweeps, but the range of the oscillations did not change. Using half the time-step size (0.5 s) did not significantly improve the results in this case, and an even smaller step size or adaptive time-stepping is needed to correctly resolve the rapid fluctuations in the liquid-water content.

### 6.3.3.6 Effect of the CCL Wettability

So far, saturation of only 2.5% was observed in the CCL due to the assumed volume fraction of the hydrophilic pores of 0.0249. In order to understand how the CCL wettability affects the liquid-water accumulation in PEMFCs, two voltage-sweep simulations were performed, where the fraction of the hydrophilic pores of the catalyst layers, $F_{HI}$, was increased to 0.27 and to 0.73.

The results of this study are presented in Figures 6.37–6.39. No significant change in the predicted current density and HFR was observed with $F_{HI} = 0.27$. The resistance did not change when $F_{HI} = 0.73$ was used either, but a lower limiting current density was obtained (Figure 6.37a) due to the significant flooding of the cathode catalyst layer (the CCL saturation, shown in Figure 6.39a, reached $F_{HI}$) that increased the oxygen-transport resistance. Interestingly, the CGDL saturation was lower for the more hydrophilic CCLs, as the latter could hold more liquid water during the voltage sweeps. With the most hydrophilic CCL of the three, the CGDL saturation oscillated more, and the continuous liquid-water removal, seen in the other two cases, was not observed. This oscillation can be minimized by modifying the breakthrough and minimum capillary pressure and the liquid-water eruption rate in the boundary condition (6.1). As it was the case in the study of the GDL-binder wettability, the time-step size needed to be reduced in order for the fluctuations in the CGDL saturation and capillary pressure in the case $F_{HI} = 0.73$ (Figure 6.39c and 6.39d) to be consistent between the two voltage sweeps. Using a twice lower time-step size (0.5 s), however, did not significantly improve the results, and an even lower time-step size is required in this case.
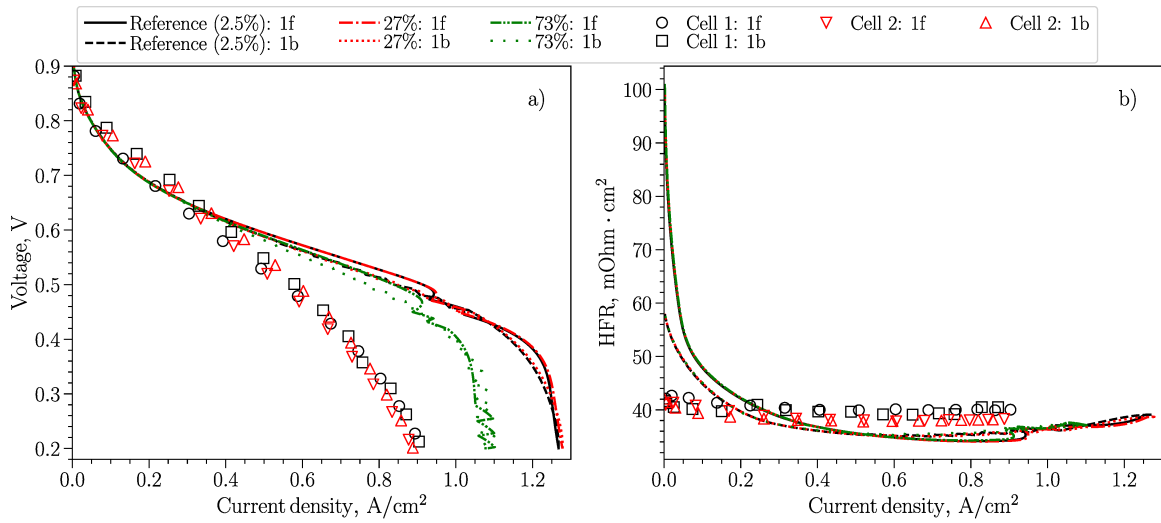
Figure 6.37: The effect of the fraction of the hydrophilic pore volume in the CCL on the current density (a) and the HFR (b) during a voltage sweep simulated at 0.44 mV/s, 60 °C, 90% RH. The forward and backward scans are labeled with letters "f" and "b".
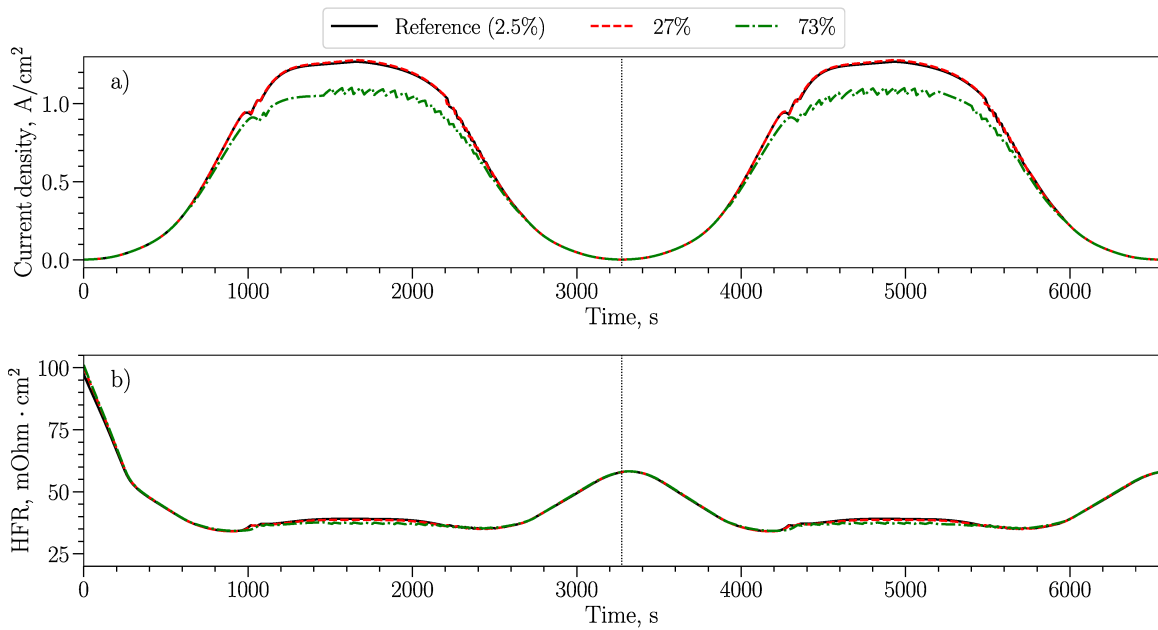


Figure 6.38: The effect of the fraction of the hydrophilic pore volume in the CCL on the current-density (a) and HFR (b) transients during two voltage sweeps simulated at 0.44 mV/s, 60 °C, 90% RH, the first of which corresponds to Figure 6.37. The vertical dotted line separates the two sweeps.
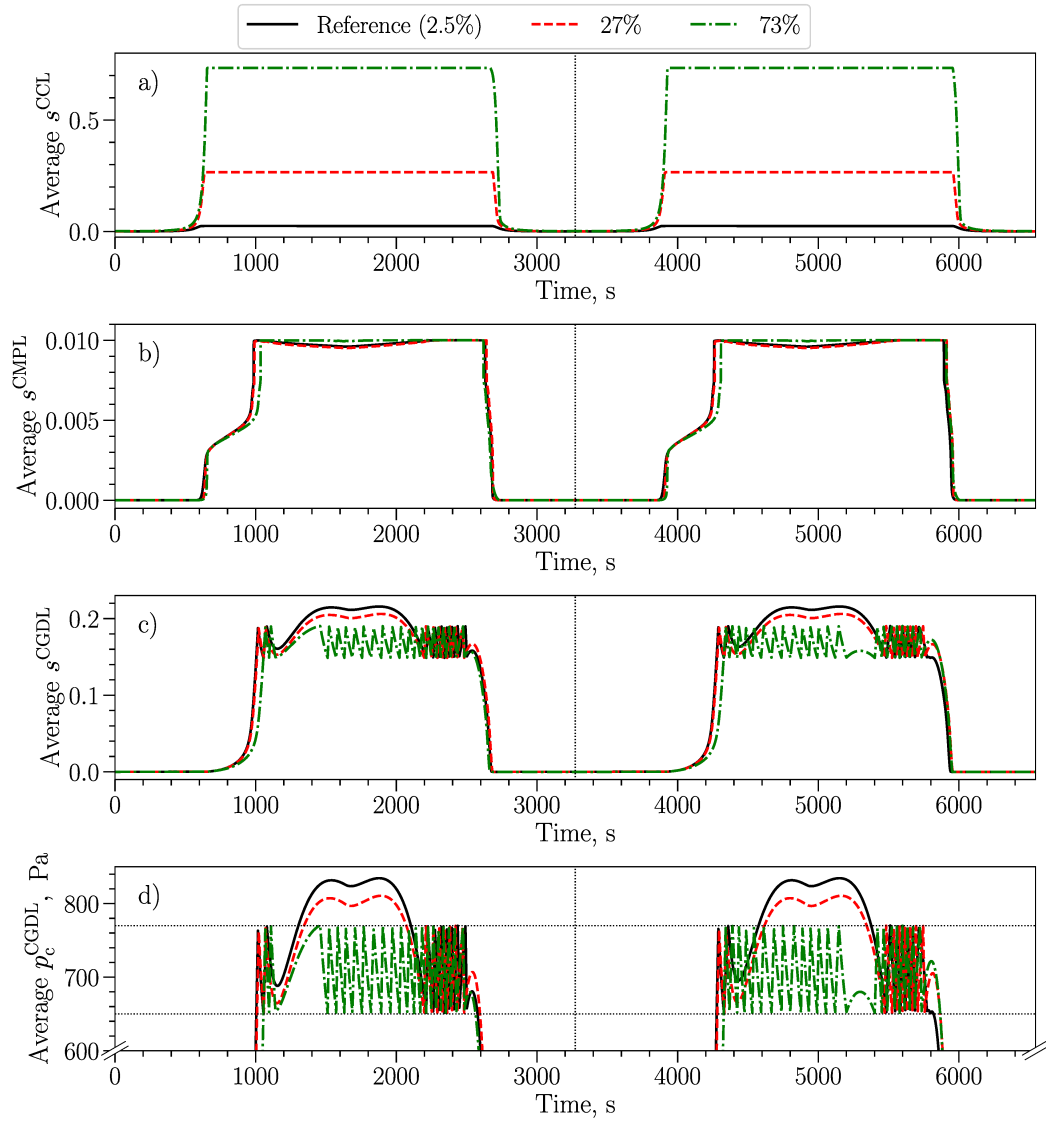
Figure 6.39: The effect of the fraction of the hydrophilic pore volume in the CCL on the simulated transients of the average saturation in the CCL (a), CMPL (b), and CGDL (c) and of the average capillary pressure in the CGDL (d). The horizontal dotted lines in graph d) denote the breakthrough and minimum capillary pressures, 0.77 kPa and 0.65 kPa. Two polarization-curve sweeps at 0.44 mV/s are shown, the first of which corresponds to Figure 6.37. The vertical dotted line separates the two sweeps.

The experimental data from Section 6.3.2.2 are shown in Figure 6.37 for comparison. Since the simulated polarization curve obtained with a 73% hydrophilic CCL was closer to the experimental measurements, it is possible that the CCL in the physical cell was saturated to a larger extent than predicted by the model with the baseline set of inputs. Because, as discussed in Section 6.3.2.2, the capillary pressure required to fill the baseline CCL with liquid water is significantly higher than the GDL breakthrough pressure, the catalyst layers fabricated in-house might have had a large portion of hydrophilic pores where liquid water would have been stored.

### 6.3.3.7 Effect of the Areal Platinum Loading in the CCL

Since decreasing the platinum loading is essential for the reduction of the PEMFC cost [16], it is important to understand how it affects the liquid-water accumulation in the cell. The numerical simulations by Kongkanand and Sinha [289] demonstrated that thin catalyst layers (with low areal catalyst loading) are prone to flooding. However, their computational domain only included the CCM (membrane and catalyst layers) and not GDLs and MPLs. Similar observations were made by Zenyuk et al. [274], who also showed that thicker catalyst layers can accommodate more liquid water, thereby reducing GDL flooding. In contrast, the simulations by Goshtasbi et al. [157] demonstrated that thinner CCLs are beneficial for water vaporization, as they result in an increased volumetric heat production in the ORR.

In the parametric study shown in Figures 6.40–6.42, four platinum loadings of the CCL were considered, where the catalyst-layer thickness was assumed to scale linearly with the catalyst loading [157, 274]. The platinum loading was $0.1\ \mathrm{mg_{Pt}/cm^2_{CL}}$ (layer thickness 2.8 μm) in the reference case and $0.046\ \mathrm{mg_{Pt}/cm^2_{CL}}$ (1.3 μm), $0.2\ \mathrm{mg_{Pt}/cm^2_{CL}}$ (5.6 μm), and $0.36\ \mathrm{mg_{Pt}/cm^2_{CL}}$ (10 μm) in the parametric cases. The rest of the properties, including the volumetric catalyst loading and active area, were the same as before.

As seen in Figure 6.40, the lowest performance and limiting current were achieved
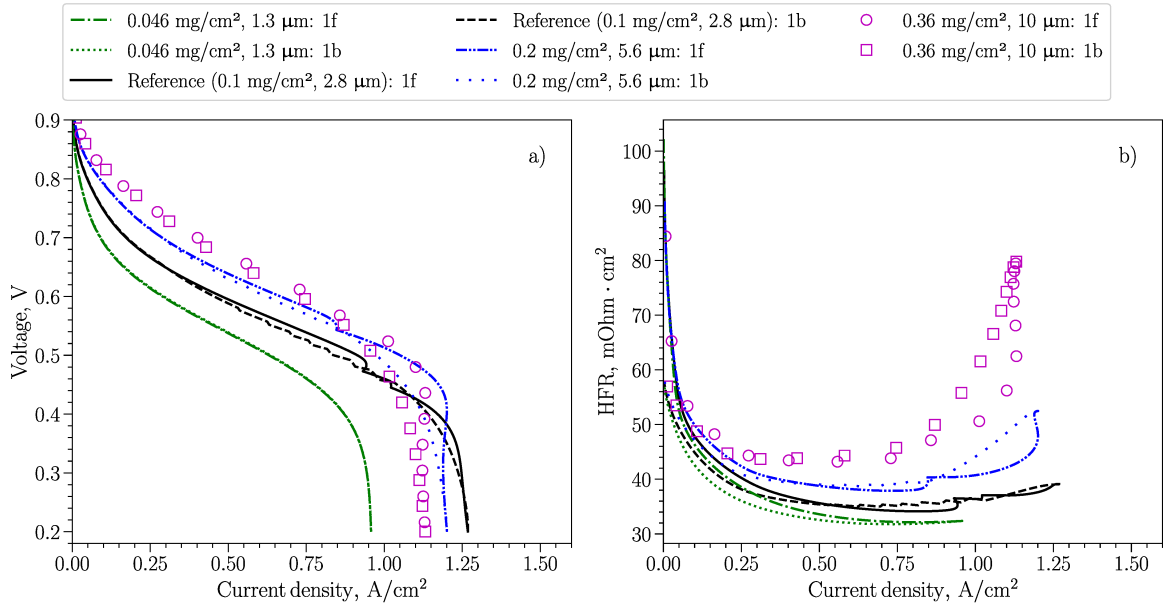
Figure 6.40: The effect of the areal platinum loading in the CCL on the current density (a) and the HFR (b) during a voltage sweep simulated at 0.44 mV/s, 60 °C, 90% RH. The forward and backward scans are labeled with letters "f" and "b".
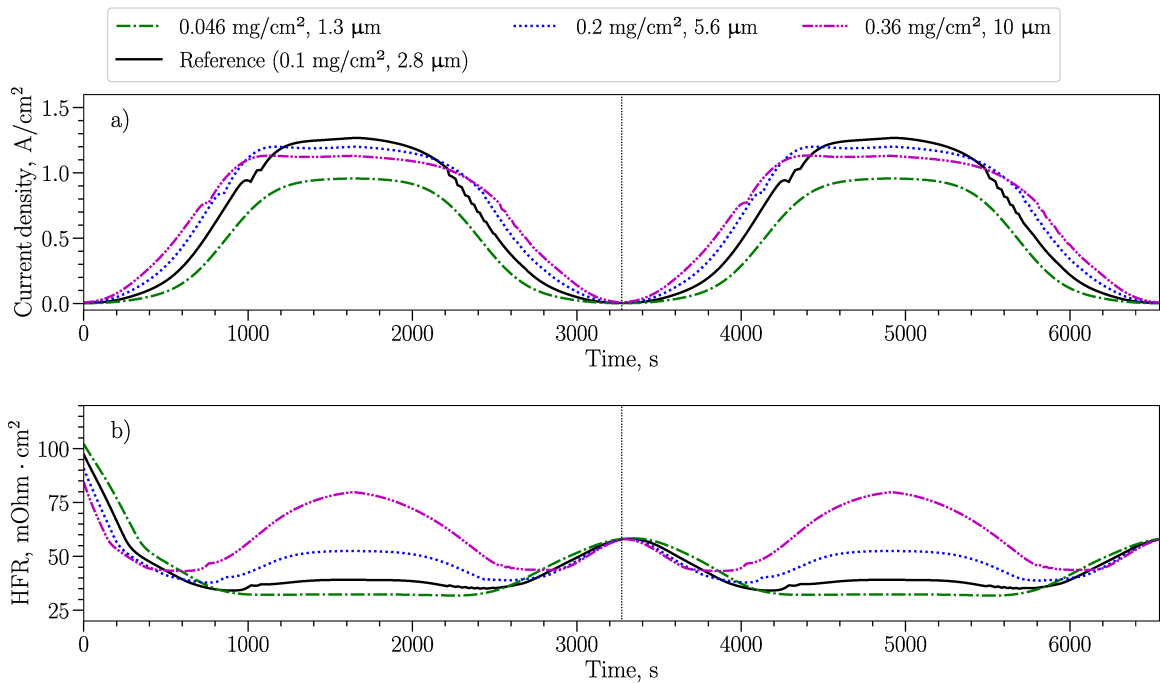


Figure 6.41: The effect of the areal platinum loading in the CCL on the current-density (a) and HFR (b) transients during two voltage sweeps simulated at 0.44 mV/s, 60 °C, 90% RH, the first of which corresponds to Figure 6.40. The vertical dotted line separates the two sweeps.
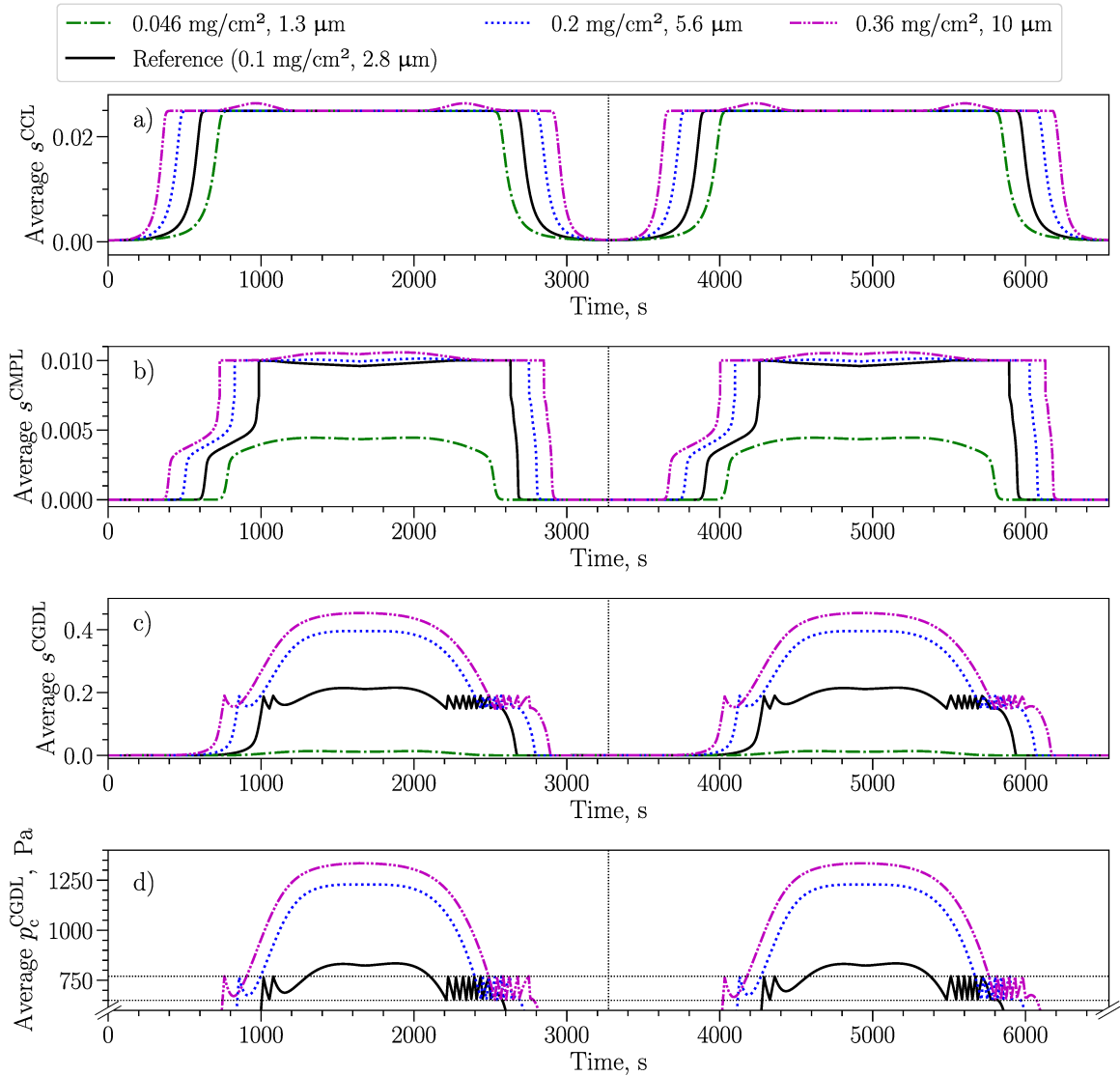
Figure 6.42: The effect of the areal platinum loading in the CCL on the simulated transients of the average saturation in the CCL (a), CMPL (b), and CGDL (c) and of the average capillary pressure in the CGDL (d). The horizontal dotted lines in graph d) denote the breakthrough and minimum capillary pressures, 0.77 kPa and 0.65 kPa. Two polarization-curve sweeps at 0.44 mV/s are shown, the first of which corresponds to Figure 6.40. The vertical dotted line separates the two sweeps.

with the lowest catalyst loading. Because saturation was relatively low in that case (Figure 6.42) and because the oxygen content in the pore space of the CCL at the limiting current was nearly twice as high as in the reference case (the average molar fraction of 0.095 compared with 0.058), the observed performance reduction was due to the lower overall amount of platinum in the thinner catalyst layer and thus more significant local oxygen-transport limitations in the CCL. This conclusion is supported by the reduced cell performance in the kinetic region of the polarization curve (0.7–0.9 V) at 0.046 $mg_{Pt}/cm^2_{CL}$. The HFR, on the other hand, was the lowest in that case due to the higher water content in the membrane, 16.6 $mol_{H_2O}/mol_{SO_3^-}$ at about 0.95 A/cm$^2$ compared with 15.7 $mol_{H_2O}/mol_{SO_3^-}$ in the reference case.

When the platinum loading was increased, the kinetic performance became better than in the reference case, but the limiting current was lower. This was because of the more severe CGDL flooding (Figure 6.42c). Because the CGDL saturation reached and exceeded 40% in those cases, the HFR in Figures 6.40b and 6.42b increased during the voltage sweeps due to the oxygen depletion. Therefore, an optimum areal platinum loading of the CCL exists that results in a sufficiently high kinetic performance and low electrode flooding.

### 6.3.3.8  Effect of the MPL Wettability

A parametric study on the MPL wettability was performed, where MPLs with 15% and 30% fraction of the hydrophilic pores were considered. Negligible changes in the simulation results were observed: the current density variations were within 20 mA/cm$^2$, there was no change in the HFR, and the CGDL saturation varied by less than 0.03. The CMPL saturation reached the expected maximum of 0.15 and 0.30 in the two parametric cases.

## 6.4　Conclusion

This Chapter was focused on the validation of the statistically consistent PSD sub-model derived in this thesis and on the analysis of the dynamic two-phase PEMFC behavior. The PSD model was compared with its previous implementation at ESDL [34, 276, 342]. It was demonstrated that the saturation-based approach to the statistical representation of the pore interconnectivity [26, 27, 34, 157, 276, 305, 342] cannot be applied to the computation of the liquid-gas interfacial area, as the microstructure of the material does not appear to be captured in that case. The liquid-water permeability of SGL GDLs was shown to be more sensitive in the new formulation to the appearance of the binder pores. Finally, a more gradual reduction in the average Knudsen radius was obtained with the new PSD model compared with the previous implementation.

The liquid- and gas-transport properties of the porous MEA components computed with the updated PSD model were compared with the experimental measurements and the results of numerical reconstructions taken from the available literature and with the in-house data. Good agreement was achieved in the mercury-intrusion curves, liquid-gas interfacial areas, and liquid and gas permeabilities computed with the PSDs that best reflected the experimental and reconstructed samples. The binder pores in the SGL GDLs and the large pores in the MPLs (cracks or the intermediate GDL-MPL pores) were shown to have a strong effect on the transport properties calculated from the PSD, and more data is needed to verify the model predictions when those pores are included in the pore-size distributions.

The developed PSD model, calibrated with the experimental and reconstruction data, was incorporated into the transient two-phase PEMFC model. A large number of the input parameters of the PEMFC model were unknown and had to be estimated. Those parameters include wettability of the porous MEA components, the rates of water evaporation and condensation, the amount of product water directly absorbed

by the CCL ionomer, the rate of water eruption at the GDL-channel interfaces, and the rate of oxygen dissolution into the catalyst-layer ionomer. With the model inputs used in this Chapter, the limiting current was overpredicted compared with the in-house experimental data measured with air in the cathode. As discussed before, the model inputs might require further adjustment so that more liquid-water accumulation and thus a lower performance are predicted in the simulations. On the other hand, more experimental measurements are needed to verify the data repeatability and consistency with the model, especially in the light of the lack of polarization-curve hysteresis in the experimental results. A larger MEA needs to be used to reduce the edge effects, and the water balance in the cell needs to be measured with the in-house setup [604] to obtain experimental data for the more direct validation of water management in the model.

Nevertheless, the developed transient fuel-cell model was capable of predicting the performance reduction and the formation of the two-phase polarization-curve hysteresis, discussed in Chapter 1, under the operating conditions that favored liquid-water accumulation. Oscillations in the GDL saturation and capillary pressure [112, 459–461] and the resulting fluctuations in the current density reported in the literature [462] were observed in the simulations. A number of parametric studies were performed with the transient PEMFC model in order to demonstrate its two-phase capabilities and to verify that the simulation results match the physical expectations.

The simulated cell performance and HFR were highly sensitive to the model inputs that control the liquid-water eruption at the CGDL-channel interface. With the higher liquid-water breakthrough pressure, the computed polarization curves were unstable and exhibited oscillations due to the dynamic flooding and draining cycles in the CGDL. Such a cyclic, unsteady behavior cannot be captured with steady-state models, which highlights the importance of transient PEMFC simulations. A significant performance reduction was observed when the minimum capillary-pressure at the CGDL-channel interface was increased or when the rate of liquid-water removal

was decreased due to the severe flooding of up to 85% of the CGDL pore volume. The resulting increase in the oxygen-transport resistance led to the concentration of the ORR in the under-the-channel area of the CCL and, in turn, a higher HFR due to the increased travel distance of protons in the membrane. The level of the cathode flooding and the HFR were shown to be dependent on a number of other model inputs as well, such as the liquid-water evaporation rate, the amount of product water directly absorbed by ionomer phase of the CCL, the presence and wettability of the CGDL binder, as well as the catalyst loading and wettability of the CCL. The presented parametric studies demonstrate that the developed model is capable of capturing the expected physical phenomena.

# Chapter 7

# Conclusions and Future Work

An open-source transient framework for the numerical modeling of proton-exchange-membrane fuel cells was developed in this thesis. The flexible architecture of the framework presented in Chapter 2 offers a variety of models for simulating dynamic physical processes taking place in hydrogen fuel cells, including the single-species transport model in Chapter 3, the single-electrode (catalyst-layer) model in Chapter 5, and the full-MEA models in Chapters 4–6. The models allow for the simulation of the transient fuel-cell behavior under both dry and wet operating conditions, with the main focus made on addressing water management, a strategy designed for preventing electrolyte dry-out and liquid-water flooding. To address liquid-water accumulation, a pore-size-distribution-based sub-model is developed that relates the microstructure of the porous cell components to their liquid- and gas-transport properties. The transient two-phase fuel-cell model presented in this thesis can be used as the means for designing MEAs that can achieve and sustain high-current-density operation without significant performance loss due to flooding. This, in turn, will reduce the required amount of platinum in the catalyst layers and, ultimately, the cost of hydrogen fuel cells, a major commercialization barrier.

For the first time in the literature, this thesis provides experimental researches with a comprehensive open-source software solution capable of simulating multiple transient characterization techniques: polarization curves, ohmic-resistance measure-

ments, and electrochemical impedance spectroscopy. This expands the possibilities for the model validation and enables the analysis of different types of experimental data to achieve a deeper, more complete understanding of a given physical process or a particular cell behavior.

The developed fuel-cell modeling framework was applied in this thesis to perform four physical studies:

1. assessment of the impact of the finite sample thickness on the chronoamperometric measurements of the oxygen-transport properties of polymer-electrolyte membranes [1];

2. investigation of the single-phase water-management signatures in the fuel-cell impedance spectra [2];

3. analysis of the relationships between the effective conductivity, ohmic resistance, and impedance of uniform and nonuniform catalyst layers [3];

4. study of the effect of the liquid-water accumulation on the dynamic performance of fuel cells [4].

Reliable measurement of gas-transport properties of polymer-electrolyte materials helps to synthesize membranes that prevent gas crossover between the electrodes and to design thin electrolyte films for the improved reactant delivery to the catalyst sites in the CLs. Both strategies are essential for enhancing fuel-cell performance. In Chapter 3, oxygen transport in polymer-electrolyte membranes was characterized at varying relative humidity by performing numerical simulations of the solid-state-cell chronoamperometry. In agreement with the experimental literature, an increase in diffusivity and a decrease in solubility of oxygen with an increase in RH were observed. However, as the diffusivity increased, the diffusion front reached the membrane surface opposite to the working electrode, and an inward oxygen flux took place. This rendered the common analytical chronoamperometry models [394–400], derived under

the assumption of semi-infinite diffusion, inapplicable. As a result, the discrepancy between the numerical and analytical estimates of the oxygen-transport properties was as high as 29% at 98% RH. This highlights the importance of using numerical models for analyzing the chronoamperometric measurements of the modern thin membranes and polymer-electrolyte films.

Electrochemical impedance spectroscopy is an experimental technique that separates the transient phenomena taking place at different time scales in the frequency domain and allows for the analysis of their relative importance in the dynamic behavior of fuel cells. The low-frequency inductive loops in the fuel-cell impedance spectra have been known in the literature to be related to the polymer-electrolyte hydration [159, 164, 191–197], but a deeper understanding of how this impedance feature is related to water management was not available. This was addressed in Chapter 3, where a single-phase version of the transient two-dimensional PEMFC model developed in Chapter 2 was first validated with the experimental polarization, ohmic-resistance, and impedance data and then applied to investigate the electrolyte-hydration nature of the fuel-cell inductance. A computationally efficient approach to computing impedance spectra from simulations of a rapid voltage step was employed and validated with the more conventional sine-wave method. It was shown in this thesis that, when the water exchange between the ionomer and the pore phase is slow and when both the exchange and the vapor transport are fast, fuel cells do not exhibit the low-frequency inductive behavior. Therefore, the finite-rate interfacial transport of water in the ionomer, a process commonly considered instantaneous in the modeling literature [49, 159, 227, 228, 238–240, 243, 253, 255, 257, 258, 261, 280, 289, 345], is directly related to the formation, frequency, and the size of the inductive loops in the fuel-cell impedance spectra. The performed parametric studies indicated that the strong inductance at 0.1–200 mHz depends on the polymer-electrolyte hydration in the membrane and in the catalyst layers; it becomes weaker when the ratio of the back-diffusion of water in the polymer electrolyte to the electroosmotic drag is

reduced. Diffusion and electroosmosis of water have an opposite effect on the minor inductance at 0.2–5 Hz that is attributed to the hydration dynamics of the ionomer in the catalyst layers. These observations can help experimentalists study single-phase water management of fuel cells by monitoring changes in the fuel-cell impedance at frequencies below 10 Hz.

The EIS capabilities of the developed model were used in Chapter 3 to validate the approach proposed by Secanell et al. [328] and Zhou et al. [35, 276] for calculating the ohmic resistance of the fuel-cell components from the ohmic heat generated by the passing current. An ohmic-resistance breakdown was performed with the model, and the HFR extracted from the simulated impedance spectra was shown to be in good agreement with the computed resistance of the membrane and of the electronically conductive components of the cell. This indicated that the high-frequency resistance of fuel cells does not contain the protonic resistance of the carbon-based catalyst layers and is, therefore, not equivalent to the total ohmic resistance.

The developed impedance-spectroscopy framework was utilized in Chapter 5 to assess the common experimental approach to measuring the catalyst-layer charge-transport properties via EIS. In this method, the impedance spectrum of a fuel cell is first corrected for the ohmic resistance of all components but the CLs, and then the linear 45° branch of the Nyquist plot is fitted with one of the analytical expressions for the impedance of uniform catalyst layers derived in the literature. An overview of those models from references [177, 182, 183] was provided, and a threefold discrepancy in the ohmic resistance predicted with the analytical equations from references [177, 183] and from reference [182] was highlighted. A transient one-dimensional catalyst-layer model was developed and used to generate impedance spectra for catalyst layers with various effective conductivities that were then fitted with the analytical models. The effective conductivity obtained with all of the analytical models under both $H_2/O_2$ and $H_2/N_2$ conditions was relatively accurate and matched the input of the numerical model relatively well. Using the ohmic-heating approach, the conductivity-

resistance relationship from reference [182] was proven accurate for the low-current $H_2/O_2$ EIS and for the $H_2/N_2$ EIS. Catalyst layers, however, are often nonuniform due to either their structural properties, such as the ionomer-loading and active-area distributions, or nonuniform ionomer hydration and layer degradation. With help of the numerical model, such layers were demonstrated to have a distorted high-frequency spectrum with no 45° branch. The previously developed transient PEMFC model was used to show that the linear branch in the fuel-cell impedance spectra can also be deformed when the contribution of the reference electrode (anode) is strong. No general analytical model exists for those cases, and numerical models should be employed instead to analyze the impedance spectra with such distortions. The outcomes of Chapter 5 were summarized as a set of practical recommendations for experimentalists so as to assist them in the charge-transport characterization of catalyst layers when designing future high-performance fuel cells.

The pore-size-distribution-based transient two-phase PEMFC model developed in Chapter 2 was used in Chapter 6 to analyze the impact of liquid-water accumulation on the dynamic fuel-cell performance. The PSD sub-model was validated with the mercury-intrusion curves, liquid-gas interfacial areas, and liquid and gas permeabilities obtained in-house and from the literature. Partial agreement was achieved between the transient two-phase PEMFC simulations and the experimental data, with the model predicting a higher limiting current density and HFR. Nevertheless, the impact of the liquid-water accumulation on the simulated cell performance matched the general physical expectations. The two-phase polarization-curve hysteresis was predicted in the model, and the fluctuations in the current density and the HFR due to the oscillating CGDL capillary pressure and saturation were captured. The parametric studies performed in Chapter 6 demonstrated that the cell performance is reduced and becomes less stable when, for instance, the breakthrough and the minimum capillary pressure in the CGDL are increased and the rates of liquid-water evaporation in the electrode and removal at the channel interface are reduced. The

amount of product water directly absorbed by the CCL ionomer, the wettability of the porous MEA components, and the CCL platinum loading were also shown to affect the degree of electrode flooding during the transient voltage sweeps.

## 7.1   Contributions

All numerical models presented in this work were implemented in the open-source fuel-cell simulation software OpenFCST [374, 375]. The code developed in the scope of this thesis, parameter files for reproducing the simulation results, working examples, and tutorials will be a part of the next public release of the software.

The contributions made in this work to the field of fuel-cell modeling include the development of:

1. a novel open-source framework for the transient simulation of fuel cells (MEAs, electrodes, single transport phenomena) capable of replicating the common experimental characterization techniques;

2. a framework for simulating and post-processing EIS with a computationally efficient single voltage-step simulation and with a series of sine-wave simulations;

3. an open-source Python script for the analytical estimation of the catalyst-layer charge-transport properties based on the results and conclusions of Chapter 5;

4. a pore-size-distribution-based sub-model for relating the microstructure of the MEA components to their transport properties and to the fuel-cell performance.

The contributions of this dissertation to the advancement of the scientific knowledge in the area of PEMFCs are:

1. highlighting the necessity of using numerical models for estimating gas-transport properties of thin polymer-electrolyte membranes and films via chronoamperometric experiments due to the shortcomings of the existing analytical models (Chapter 3);

2. demonstrating the strong influence of the bulk and finite-rate interfacial transport of water in the polymer electrolyte on the low-frequency inductance in fuel-cell impedance spectra, thus enabling experimental water-management characterization of PEMFCs via EIS (Chapter 4);

3. numerically validating the relationship between the effective catalyst-layer conductivity and ohmic resistance proposed by Kulikovsky [182] and providing practical recommendations for the experimental charge-transport characterization of uniform and nonuniform catalyst layers via EIS (Chapter 5);

4. illustrating the impact of the dynamic liquid-water accumulation and drainage cycles in the cathode GDL on the fuel-cell performance stability and demonstrating the role of the porous GDL binder in the two-phase water transport (Chapter 6).

Three journal papers [1–3] and a book chapter [6] were published during this Ph.D. Research findings were presented at a number of domestic and international conferences [606–616]. Another journal paper [4] and a book chapter [5] are currently in preparation.

## 7.2 Future Work

Development of the framework for solving time-dependent problems in OpenFCST has opened up the prospects for numerous physical studies that would not have been possible with a steady-state code. Transient material characterization, studies of hysteretic polarization curves and ohmic resistance, impedance spectroscopy, simulations of the dynamic single-phase and two-phase water management – these are only a handful of applications demonstrated in this thesis. The variety of the prospective studies can be extended in the future by building upon the implemented models and the transient framework.

The computational cost of the solid-state-cell model developed in Chapter 3 needs to be reduced to make the process of fitting chronoamperometric data quicker and more acceptable for the experimental characterization of the polymer-electrolyte materials. The works of Britz et al. [560, 561] might be a good starting point for this, although the suggested approaches for the semi-infinite-domain simulations might need modification for the finite-domain applications. Additionally, the finite-rate oxygen dissolution into the membrane at the open surface of the sample needs to be accounted for. This can be done with a Robin boundary condition similar to the one used in the ICCP sub-model discussed in Chapter 2.

Based on the experimental validation of the EIS framework in Chapters 4 and 5, the possible pathways for the improvement of the impedance-spectroscopy capabilities of the developed models could be implementation of transient electrochemical kinetics [571] and inclusion of a hydrogen-crossover sub-model [312]. Transient reaction kinetics will affect the simulated high-frequency $H_2/O_2$ spectrum and will enable cyclic-voltammetry studies [571]. Accounting for hydrogen crossover will improve the agreement between the simulated and experimental $H_2/N_2$ spectra at low frequencies [173, 174, 586, 588].

As demonstrated in Chapter 6, the transient two-phase PEMFC model developed in this thesis is capable of simulating the effect of liquid-water accumulation on the dynamic performance of fuel cells. Parameter calibration was performed with the in-house experimental data, and the model was shown to produce reasonable results and to be sensitive to the changes in the model inputs that controlled the two-phase water management, such as the wettability of the CGDL binder and of the CCL, the properties of the liquid-water breakthrough and removal through the GDL-channel interface, and the evaporation rate of water. However, the measured cell performance was overpredicted with the model in some cases. More experiments are required to understand whether the low performance measured with the physical cells was due to the misalignment of the cell components or the model inputs need to be adjusted to

induce a more significant electrode flooding. Additional water-balance measurements will also give the means for the direct validation of the simulated water transport in the MEA. The future physical studies will focus on multiple aspects that affect liquid-water accumulation in fuel cells that were discussed in Chapter 1, including: a) the role of the MPL; b) the effect of the MPL cracks and of the intermediate MPL-GDL layer; c) the influence of the CL PSD (including the structural changes with varying volumetric catalyst and ionomer loading).

The two-phase capabilities of the developed transient PEMFC model can be improved. The current model does not account for the liquid-water uptake by the polymer electrolyte; this effect is approximated in this thesis by setting a portion of water to be produced in the ionomer phase of the catalyst layers. In the future, the liquid-water uptake should be incorporated in the model, for instance, by implementing a dedicated sorption isotherm [29, 42, 157, 236, 242, 247, 274, 288, 293, 334, 339]. In addition to the uptake, the transport of liquid water through the polymer-electrolyte membrane should also be accounted for [26, 27, 43, 44, 49, 273, 274, 489, 562].

The framework for solving time-dependent problems in OpenFCST developed in this thesis will enable a variety of transient fuel-cell studies in the future, such as simulations of fuel-cell start-up and shutdown, studies of fuel-cell degradation, simulations of cyclic voltammetry, and analysis of the transient electrochemical kinetics with EIS. The developed framework is not limited to modeling fuel cells and can be adopted in the future to simulate other technical systems, such as water electrolyzers and lithium-ion batteries.

# Bibliography

[1] D. Novitski, A. Kosakian, T. Weissbach, M. Secanell, and S. Holdcroft, "Electrochemical reduction of dissolved oxygen in alkaline, solid polymer electrolyte films," *Journal of the American Chemical Society*, vol. 138, no. 47, pp. 15 465–15 472, 2016.

[2] A. Kosakian, L. Padilla Urbina, A. Heaman, and M. Secanell, "Understanding single-phase water-management signatures in fuel-cell impedance spectra: A numerical study," *Electrochimica Acta*, vol. 350, p. 136 204, 2020.

[3] A. Kosakian and M. Secanell, "Estimating charge-transport properties of fuel-cell and electrolyzer catalyst layers via electrochemical impedance spectroscopy," *Electrochimica Acta*, vol. 367, p. 137 521, 2021.

[4] A. Kosakian, F. Wei, S. Jung, J. Zhou, A. Punia, J. Liu, and M. Secanell, "A transient, pore-size-distribution-based model for the analysis of the two-phase water transport in fuel cells," (in preparation).

[5] M. Secanell and A. Kosakian, "Membrane-electrode-assembly modeling using OpenFCST," in *PEMFC characterization and modelling – Current trends and challenges*, J. Stumper and J. Jankovic, Eds. de Gruyter, (in preparation).

[6] M. Secanell, A. Jarauta, A. Kosakian, M. Sabharwal, and J. Zhou, "PEM fuel cells, modeling," in *Encyclopedia of Sustainability Science and Technology*, R. A. Meyers, Ed. Springer New York, 2017, pp. 1–61, ISBN: 978-1-4939-2493-6.

[7] *Fueling the future of mobility - Hydrogen and fuel cell solutions for transportation - Volume 1*, https://www2.deloitte.com/content/dam/Deloitte/cn/Documents/finance/deloitte-cn-fueling-the-future-of-mobility-en-200101.pdf, Accessed September 10, 2020.

[8] S. E. Hosseini and M. A. Wahid, "Hydrogen production from renewable and sustainable energy resources: Promising green energy carrier for clean development," *Renewable and Sustainable Energy Reviews*, vol. 57, pp. 850–866, 2016.

[9] *Canadian environmental sustainability indicators. Greenhouse gas emissions*, https://www.canada.ca/content/dam/eccc/documents/pdf/cesindicators/ghg-emissions/2020/greenhouse-gas-emissions-en.pdf, Accessed September 10, 2020.

[10]   *Sources of greenhouse gas emissions. Transportation sector emissions*, https://www.epa.gov/ghgemissions/sources-greenhouse-gas-emissions, Accessed September 10, 2020.

[11]   *Hydrogen fuel cell technology*, https://www.toyota.ca/toyota/en/safety-innovation/hydrogen-fuel-cell-mirai, Accessed September 10, 2020.

[12]   *Honda Clarity series*, https://automobiles.honda.com/clarity, Accessed September 10, 2020.

[13]   *Hyundai nexo*, https://www.hyundaicanada.com/en/vehicles/2019-nexo, Accessed September 10, 2020.

[14]   D. A. Cullen, K. C. Neyerlin, R. K. Ahluwalia, R. Mukundan, K. L. More, R. L. Borup, A. Z. Weber, D. J. Myers, and A. Kusoglu, "New roads and challenges for fuel cells in heavy-duty transportation," *Nature energy*, pp. 1–13, 2021.

[15]   U.S. Department of Energy, *Fuel cell technologies office multi-year research, development, and demonstration plan: Fuel cells*, https://energy.gov/sites/prod/files/2017/05/f34/fcto_myrdd_fuel_cells.pdf, 2017, Accessed November 10, 2019.

[16]   D. Papageorgopoulos, *Fuel cell R&D overview*, https://www.hydrogen.energy.gov/pdfs/review19/plenary_fuel_cell_papageorgopoulos_2019.pdf, 2019, Accessed September 10, 2020.

[17]   R Borup and A Weber, *Fuel cell R&D overview: Fuel cell performance and durability consortium*, https://www.hydrogen.energy.gov/pdfs/review20/fc135_borup_weber_2020_o.pdf, 2019, Accessed September 10, 2020.

[18]   D. Banham, J. Zou, S. Mukerjee, Z. Liu, D. Yang, Y. Zhang, Y. Peng, and A. Dong, "Ultralow platinum loading proton exchange membrane fuel cells: Performance losses and solutions," *Journal of Power Sources*, vol. 490, p. 229 515, 2021.

[19]   A. Kongkanand and M. F. Mathias, "The priority and challenge of high-power performance of low-platinum proton-exchange membrane fuel cells," *The journal of physical chemistry letters*, vol. 7, no. 7, pp. 1127–1137, 2016.

[20]   L. Osmieri, J. Park, D. A. Cullen, P. Zelenay, D. J. Myers, and K. C. Neyerlin, "Status and challenges for the application of platinum group metal-free catalysts in proton exchange membrane fuel cells," *Current Opinion in Electrochemistry*, 2020.

[21]   A. Z. Weber, R. L. Borup, R. M. Darling, P. K. Das, T. J. Dursch, W. Gu, D. Harvey, A. Kusoglu, S. Litster, M. M. Mench, R. Mukundan, J. P. Owejan, J. G. Pharoah, M. Secanell, and I. V. Zenyuk, "A critical review of modeling transport phenomena in polymer-electrolyte fuel cells," *Journal of The Electrochemical Society*, vol. 161, no. 12, F1254, 2014.

[22] T. Springer, T. Zawodzinski, and S. Gottesfeld, "Polymer electrolyte fuel cell model," *Journal of the Electrochemical Society*, vol. 138, no. 8, pp. 2334–2342, 1991.

[23] D. M. Bernardi and M. W. Verbrugge, "Mathematical model of a gas diffusion electrode bonded to a polymer electrolyte," *AIChE journal*, vol. 37, no. 8, pp. 1151–1163, 1991.

[24] D. M. Bernardi and M. W. Verbrugge, "A mathematical model of the solid-polymer-electrolyte fuel cell," *Journal of the Electrochemical Society*, vol. 139, no. 9, p. 2477, 1992.

[25] J. H. Nam and M. Kaviany, "Effective diffusivity and water-saturation distribution in single-and two-layer PEMFC diffusion medium," *International Journal of Heat and Mass Transfer*, vol. 46, no. 24, pp. 4595–4611, 2003.

[26] A. Z. Weber, "Modeling water management in polymer-electrolyte fuel cells," PhD thesis, University of California, Berkeley, 2004.

[27] A. Z. Weber, R. M. Darling, and J. Newman, "Modeling two-phase behavior in PEFCs," *Journal of the Electrochemical Society*, vol. 151, no. 10, A1715, 2004.

[28] A. Z. Weber and J. Newman, "Effects of microporous layers in polymer electrolyte fuel cells," *Journal of the Electrochemical Society*, vol. 152, no. 4, A677, 2005.

[29] H. Meng and C.-Y. Wang, "Model of two-phase flow and flooding dynamics in polymer electrolyte fuel cells," *Journal of the Electrochemical Society*, vol. 152, no. 9, A1733, 2005.

[30] H. Meng, "A two-phase non-isothermal mixed-domain PEM fuel cell model and its application to two-dimensional simulations," *Journal of Power Sources*, vol. 168, no. 1, pp. 218–228, 2007.

[31] M. Secanell, B Carnes, A Suleman, and N Djilali, "Numerical optimization of proton exchange membrane fuel cell cathodes," *Electrochimica Acta*, vol. 52, no. 7, pp. 2668–2682, 2007.

[32] M Secanell, K Karan, A Suleman, and N Djilali, "Optimal design of ultralow-platinum PEMFC anode electrodes," *Journal of the Electrochemical Society*, vol. 155, no. 2, B125–B134, 2008.

[33] M Bhaiya, A Putz, and M Secanell, "Analysis of non-isothermal effects on polymer electrolyte fuel cell electrode assemblies," *Electrochimica Acta*, vol. 147, pp. 294–309, 2014.

[34] J Zhou, A Putz, and M Secanell, "A mixed wettability pore size distribution based mathematical model for analyzing two-phase flow in porous electrodes I. Mathematical model," *Journal of The Electrochemical Society*, vol. 164, no. 6, F530–F539, 2017.

[35] J Zhou, S Shukla, A Putz, and M Secanell, "Analysis of the role of the microporous layer in improving polymer electrolyte fuel cell performance," *Electrochimica Acta*, vol. 268, pp. 366–382, 2018.

[36] M Moore, P Wardlaw, P Dobson, J. Boisvert, A Putz, R. Spiteri, and M Secanell, "Understanding the effect of kinetic and mass transport processes in cathode agglomerates," *Journal of the Electrochemical Society*, vol. 161, no. 8, E3125–E3137, 2014.

[37] C. Qin, D. Rensink, S. Fell, and S. M. Hassanizadeh, "Two-phase flow modeling for the cathode side of a polymer electrolyte fuel cell," *Journal of power sources*, vol. 197, pp. 136–144, 2012.

[38] A. Kalidindi, R Taspinar, S Litster, and E. Kumbur, "A two-phase model for studying the role of microporous layer and catalyst layer interface on polymer electrolyte fuel cell performance," *international journal of hydrogen energy*, vol. 38, no. 22, pp. 9297–9309, 2013.

[39] V. Mulone and K. Karan, "Analysis of capillary flow driven model for water transport in PEFC cathode catalyst layer: Consideration of mixed wettability and pore size distribution," *International journal of hydrogen energy*, vol. 38, no. 1, pp. 558–569, 2013.

[40] I. Zenyuk, R Taspinar, A. Kalidindi, E. Kumbur, and S Litster, "Computational and experimental analysis of water transport at component interfaces in polymer electrolyte fuel cells," *Journal of The Electrochemical Society*, vol. 161, no. 11, F3091, 2014.

[41] P. García-Salaberri, D. Sánchez, P. Boillat, M. Vera, and K. A. Friedrich, "Hydration and dehydration cycles in polymer electrolyte fuel cells operated with wet anode and dry cathode feed: A neutron imaging and modeling study," *Journal of power sources*, vol. 359, pp. 634–655, 2017.

[42] S. Li, J. Yuan, G. Xie, and B. Sundén, "Effects of agglomerate model parameters on transport characterization and performance of PEM fuel cells," *International Journal of Hydrogen Energy*, vol. 43, no. 17, pp. 8451–8463, 2018.

[43] L. M. Pant, M. R. Gerhardt, N. Macauley, R. Mukundan, R. L. Borup, and A. Z. Weber, "Along-the-channel modeling and analysis of PEFCs at low stoichiometry: Development of a 1+2D model," *Electrochimica Acta*, vol. 326, p. 134 963, 2019.

[44] M. R. Gerhardt, L. M. Pant, and A. Z. Weber, "Along-the-channel impacts of water management and carbon-dioxide contamination in hydroxide-exchange-membrane fuel cells: A modeling study," *Journal of The Electrochemical Society*, vol. 166, no. 7, F3180, 2019.

[45] K. Cooper, V. Ramani, J. M. Fenton, and H. Kunz, *Experimental methods and data analyses for polymer electrolyte fuel cells*. Scribner Associates, Inc., Illinois, 2009.

[46] H. Yu and C. Ziegler, "Transient behavior of a proton exchange membrane fuel cell under dry operation," *Journal of The Electrochemical Society*, vol. 153, no. 3, A570–A575, 2006.

[47] N Rajalakshmi, T. Jayanth, R Thangamuthu, G Sasikumar, P Sridhar, and K. Dhathathreyan, "Water transport characteristics of polymer electrolyte membrane fuel cell," *International Journal of Hydrogen Energy*, vol. 29, no. 10, pp. 1009–1014, 2004.

[48] J. Hamelin, K. Agbossou, A. Laperriere, F. Laurencelle, and T. K. Bose, "Dynamic behavior of a PEM fuel cell stack for stationary applications," *International Journal of Hydrogen Energy*, vol. 26, no. 6, pp. 625–629, 2001.

[49] C. Ziegler, H. M. Yu, and J. O. Schumacher, "Two-phase dynamic modeling of PEMFCs and simulation of cyclo-voltammograms," *Journal of The Electrochemical Society*, vol. 152, no. 8, A1555–A1567, 2005.

[50] L. Hao, H. Yu, J. Hou, W. Song, Z. Shao, and B. Yi, "Transient behavior of water generation in a proton exchange membrane fuel cell," *Journal of Power Sources*, vol. 177, no. 2, pp. 404–411, 2008.

[51] J. Hou, "A study on polarization hysteresis in PEM fuel cells by galvanostatic step sweep," *International Journal of Hydrogen Energy*, vol. 36, no. 12, pp. 7199–7206, 2011.

[52] D. Gerteisen, T. Heilmann, and C. Ziegler, "Modeling the phenomena of dehydration and flooding of a polymer electrolyte membrane fuel cell," *Journal of Power Sources*, vol. 187, no. 1, pp. 165–181, 2009.

[53] F. Laurencelle, R. Chahine, J. Hamelin, K. Agbossou, M. Fournier, T. K. Bose, and A. Laperriere, "Characterization of a Ballard MK5-E proton exchange membrane fuel cell stack," *Fuel cells*, vol. 1, no. 1, pp. 66–71, 2001.

[54] W. He, G. Lin, and T. Van Nguyen, "Diagnostic tool to detect electrode flooding in proton-exchange-membrane fuel cells," *AIChE Journal*, vol. 49, no. 12, pp. 3221–3228, 2003.

[55] X.-Z. Yuan, C. Song, H. Wang, and J. Zhang, *Electrochemical impedance spectroscopy in PEM fuel cells: Fundamentals and applications*. Springer Science & Business Media, 2009.

[56] M. E. Orazem and B. Tribollet, *Electrochemical impedance spectroscopy*, second edition. John Wiley & Sons, 2017.

[57] H. Lohse-Busch, K. Stutenberg, M. Duoba, X. Liu, A. Elgowainy, M. Wang, T. Wallner, B. Richard, and M. Christenson, "Automotive fuel cell stack and system efficiency and fuel consumption based on vehicle testing on a chassis dynamometer at minus 18 °C to positive 35 °C temperatures," *International Journal of Hydrogen Energy*, vol. 45, no. 1, pp. 861–872, 2020.

[58] G Correa, P. Muñoz, and C. Rodriguez, "A comparative energy and environmental analysis of a diesel, hybrid, hydrogen and electric urban bus," *Energy*, vol. 187, p. 115 906, 2019.

[59] R Lin, F Xiong, W. Tang, L Técher, J. Zhang, and J. Ma, "Investigation of dynamic driving cycle effect on the degradation of proton exchange membrane fuel cell by segmented cell technology," *Journal of Power Sources*, vol. 260, pp. 150–158, 2014.

[60] J. C. Kurnia, A. P. Sasmito, and T. Shamim, "Performance evaluation of a PEM fuel cell stack with variable inlet flows under simulated driving cycle conditions," *Applied Energy*, vol. 206, pp. 751–764, 2017.

[61] A. A. Kulikovsky, *Analytical modelling of fuel cells*. Elsevier, 2019.

[62] M. Eikerling and A. Kulikovsky, *Polymer electrolyte fuel cells: Physical principles of materials and operation*. CRC Press, 2014.

[63] R. O'Hayre, S.-W. Cha, W. Colella, and F. B. Prinz, *Fuel cell fundamentals*. John Wiley & Sons, 2016.

[64] A. Z. Weber and J. Newman, "Coupled thermal and water management in polymer electrolyte fuel cells," *Journal of The Electrochemical Society*, vol. 153, no. 12, A2205, 2006.

[65] M. Bhaiya, "An open-source two-phase non-isothermal mathematical model of a polymer electrolyte membrane fuel cell," Master's thesis, University of Alberta, 2014.

[66] R. A. Antunes, M. C. De Oliveira, G. Ett, and V. Ett, "Carbon materials in composite bipolar plates for polymer electrolyte membrane fuel cells: A review of the main challenges to improve electrical performance," *Journal of Power Sources*, vol. 196, no. 6, pp. 2945–2961, 2011.

[67] B. Cunningham, J Huang, and D. Baird, "Review of materials and processing methods used in the production of bipolar plates for fuel cells," *International materials reviews*, vol. 52, no. 1, pp. 1–13, 2007.

[68] S. Karimi, N. Fraser, B. Roberts, and F. R. Foulkes, "A review of metallic bipolar plates for proton exchange membrane fuel cells: Materials and fabrication methods," *Advances in Materials Science and Engineering*, vol. 2012, 2012.

[69] A. Hermann, T. Chaudhuri, and P. Spagnol, "Bipolar plates for PEM fuel cells: A review," *International journal of hydrogen Energy*, vol. 30, no. 12, pp. 1297–1302, 2005.

[70] H. Tawfik, Y. Hung, and D. Mahajan, "Metal bipolar plates for PEM fuel cell – A review," *Journal of Power Sources*, vol. 163, no. 2, pp. 755–767, 2007.

[71] Y. Song, C. Zhang, C.-Y. Ling, M. Han, R.-Y. Yong, D. Sun, and J. Chen, "Review on current research of materials, fabrication and application for bipolar plate in proton exchange membrane fuel cell," *International Journal of Hydrogen Energy*, 2019.

[72] X. Li and I. Sabir, "Review of bipolar plates in PEM fuel cells: Flow-field designs," *International journal of hydrogen energy*, vol. 30, no. 4, pp. 359–371, 2005.

[73] Z Lu, S. Kandlikar, C Rath, M Grimm, W Domigan, A. White, M Hardbarger, J. Owejan, and T. Trabold, "Water management studies in PEM fuel cells, Part II: Ex situ investigation of flow maldistribution, pressure drop and two-phase flow pattern in gas channels," *International Journal of Hydrogen Energy*, vol. 34, no. 8, pp. 3445–3456, 2009.

[74] Y. Kerkoub, A. Benzaoui, F. Haddad, and Y. K. Ziari, "Channel to rib width ratio influence with various flow field designs on performance of PEM fuel cell," *Energy Conversion and Management*, vol. 174, pp. 260–275, 2018.

[75] A. Ozden, S. Shahgaldi, X. Li, and F. Hamdullahpur, "A review of gas diffusion layers for proton exchange membrane fuel cells - With a focus on characteristics, characterization techniques, materials and designs," *Progress in Energy and Combustion Science*, vol. 74, pp. 50–102, 2019.

[76] I. V. Zenyuk, D. Y. Parkinson, L. G. Connolly, and A. Z. Weber, "Gas-diffusion-layer structural properties under compression via X-ray tomography," *Journal of Power Sources*, vol. 328, pp. 364–376, 2016.

[77] J. Becker, C. Wieser, S. Fell, and K. Steiner, "A multi-scale approach to material modeling of fuel cell diffusion media," *International Journal of Heat and Mass Transfer*, vol. 54, no. 7-8, pp. 1360–1368, 2011.

[78] N. B. Carrigy, L. M. Pant, S. Mitra, and M. Secanell, "Knudsen diffusivity and permeability of PEMFC microporous coated gas diffusion layers for different polytetrafluoroethylene loadings," *Journal of The Electrochemical Society*, vol. 160, no. 2, F81, 2012.

[79] H. Xu, "Experimental measurement of mass transport parameters of gas diffusion layer and catalyst layer in PEM fuel cell," Master's thesis, University of Alberta, 2019.

[80] J Hinebaugh and A Bazylak, "Stochastic modeling of polymer electrolyte membrane fuel cell gas diffusion layers - Part 1: Physical characterization," *International Journal of Hydrogen Energy*, vol. 42, no. 24, pp. 15 861–15 871, 2017.

[81] D. Froning, M. Drakselová, A. Tocháčková, R. Kodỳm, U. Reimer, W. Lehnert, and K. Bouzek, "Anisotropic properties of gas transport in non-woven gas diffusion layers of polymer electrolyte fuel cells," *Journal of Power Sources*, vol. 452, p. 227 828, 2020.

[82] M. Bosomoiu, G. Tsotridis, and T. Bednarek, "Study of effective transport properties of fresh and aged gas diffusion layers," *Journal of Power Sources*, vol. 285, pp. 568–579, 2015.

[83] N. Zamel, X. Li, and J. Shen, "Numerical estimation of the effective electrical conductivity in carbon paper diffusion media," *Applied energy*, vol. 93, pp. 39–44, 2012.

[84] N. Zamel, E. Litovsky, X. Li, and J. Kleiman, "Measurement of the through-plane thermal conductivity of carbon paper diffusion media for the temperature range from -50 to +120 °C," *international journal of hydrogen energy*, vol. 36, no. 19, pp. 12 618–12 625, 2011.

[85] N. Zamel, E. Litovsky, S. Shakhshir, X. Li, and J. Kleiman, "Measurement of in-plane thermal conductivity of carbon paper diffusion media in the temperature range of -20 °C to +120 °C," *Applied energy*, vol. 88, no. 9, pp. 3042–3050, 2011.

[86] H. K. Atiyeh, K. Karan, B. Peppley, A. Phoenix, E. Halliop, and J. Pharoah, "Experimental investigation of the role of a microporous layer on the water transport and performance of a PEM fuel cell," *Journal of Power Sources*, vol. 170, no. 1, pp. 111–121, 2007.

[87] R. Schweiss, C. Meiser, T. Damjanovic, I. Galbiati, and N. Haak, "SIGRACET gas diffusion layers for PEM fuel cells, electrolyzers and batteries," *White paper SGL Group*, 2016.

[88] E. Wargo, V. Schulz, A Çeçen, S. Kalidindi, and E. Kumbur, "Resolving macro-and micro-porous layer interaction in polymer electrolyte fuel cells using focused ion beam and X-ray computed tomography," *Electrochimica Acta*, vol. 87, pp. 201–212, 2013.

[89] A. El-Kharouf, T. J. Mason, D. J. Brett, and B. G. Pollet, "Ex-situ characterisation of gas diffusion layers for proton exchange membrane fuel cells," *Journal of Power Sources*, vol. 218, pp. 393–404, 2012.

[90] R. R. Rashapov and J. T. Gostick, "In-plane effective diffusivity in PEMFC gas diffusion layers," *Transport in Porous Media*, vol. 115, no. 3, pp. 411–433, 2016.

[91] P. A. García-Salaberri, I. V. Zenyuk, A. D. Shum, G. Hwang, M. Vera, A. Z. Weber, and J. T. Gostick, "Analysis of representative elementary volume and through-plane regional characteristics of carbon-fiber papers: Diffusivity, permeability and electrical/thermal conductivity," *International Journal of Heat and Mass Transfer*, vol. 127, pp. 687–703, 2018.

[92] O. S. Burheim, G. A. Crymble, R. Bock, N. Hussain, S. Pasupathi, A. du Plessis, S. le Roux, F. Seland, H. Su, and B. G. Pollet, "Thermal conductivity in the three layered regions of micro porous layer coated porous transport layers for the PEM fuel cell," *international journal of hydrogen energy*, vol. 40, no. 46, pp. 16 775–16 785, 2015.

[93] J. T. Gostick, M. A. Ioannidis, M. W. Fowler, and M. D. Pritzker, "On the role of the microporous layer in PEMFC operation," *Electrochemistry Communications*, vol. 11, no. 3, pp. 576–579, 2009.

[94] K. T. Cho and M. M. Mench, "Effect of material properties on evaporative water removal from polymer electrolyte fuel cell diffusion media," *Journal of Power Sources*, vol. 195, no. 19, pp. 6748–6757, 2010.

[95] M. G. George, J. Wang, R. Banerjee, and A. Bazylak, "Composition analysis of a polymer electrolyte membrane fuel cell microporous layer using scanning transmission X-ray microscopy and near edge X-ray absorption fine structure analysis," *Journal of Power Sources*, vol. 309, pp. 254–259, 2016.

[96] E. Wargo, A. Hanna, A Cecen, S. Kalidindi, and E. Kumbur, "Selection of representative volume elements for pore-scale analysis of transport in fuel cell materials," *Journal of power sources*, vol. 197, pp. 168–179, 2012.

[97] M. Andisheh-Tadbir, F. P. Orfino, and E. Kjeang, "Three-dimensional phase segregation of micro-porous layers for fuel cells by nano-scale X-ray computed tomography," *Journal of Power Sources*, vol. 310, pp. 61–69, 2016.

[98] M. J. Martínez-Rodríguez, T. Cui, S. Shimpalee, S. Seraphin, B. Duong, and J. W. Van Zee, "Effect of microporous layer on MacMullin number of carbon paper gas diffusion layer," *Journal of Power Sources*, vol. 207, pp. 91–100, 2012.

[99] A. Thomas, G. Maranzana, S. Didierjean, J. Dillet, and O. Lottin, "Thermal and water transfer in PEMFCs: Investigating the role of the microporous layer," *International Journal of Hydrogen Energy*, vol. 39, no. 6, pp. 2649–2658, 2014.

[100] M. Blanco and D. P. Wilkinson, "Investigation of the effect of microporous layers on water management in a proton exchange membrane fuel cell using novel diagnostic methods," *International journal of hydrogen energy*, vol. 39, no. 29, pp. 16 390–16 404, 2014.

[101] J. H. Chun, K. T. Park, D. H. Jo, J. Y. Lee, S. G. Kim, E. S. Lee, J.-Y. Jyoung, and S. H. Kim, "Determination of the pore size distribution of micro porous layer in PEMFC using pore forming agents under various drying conditions," *International Journal of Hydrogen Energy*, vol. 35, no. 20, pp. 11 148–11 153, 2010.

[102] S. Botelho and A Bazylak, "Impact of polymer electrolyte membrane fuel cell microporous layer nano-scale features on thermal conductance," *Journal of Power Sources*, vol. 280, pp. 173–181, 2015.

[103] W. Yoshimune, M. Harada, and Y. Akimoto, "Small-angle neutron scattering studies on the distribution of polytetrafluoroethylene within microporous layers for polymer electrolyte fuel cells," *Composites Part C: Open Access*, vol. 2, p. 100 015, 2020.

[104] M. El Hannach, R. Singh, N. Djilali, and E. Kjeang, "Micro-porous layer stochastic reconstruction and transport parameter determination," *Journal of Power Sources*, vol. 282, pp. 58–64, 2015.

[105] S.-Y. Lin and M.-H. Chang, "Effect of microporous layer composed of carbon nanotube and acetylene black on polymer electrolyte membrane fuel cell performance," *International Journal of Hydrogen Energy*, vol. 40, no. 24, pp. 7879–7885, 2015.

362

[106] C.-C. Fan and M.-H. Chang, "Improving proton exchange membrane fuel cell performance with carbon nanotubes as the material of cathode microporous layer," *International Journal of Energy Research*, vol. 40, no. 2, pp. 181–188, 2016.

[107] J Lee, R Banerjee, M. George, D Muirhead, P Shrestha, H Liu, N Ge, S Chevalier, and A Bazylak, "Multiwall carbon nanotube-based microporous layers for polymer electrolyte membrane fuel cells," *Journal of the electrochemical society*, vol. 164, no. 12, F1149, 2017.

[108] K. Karan, H. Atiyeh, A. Phoenix, E. Halliop, J. Pharoah, and B. Peppley, "An experimental investigation of water transport in PEMFCs: The role of microporous layers," *Electrochemical and Solid State Letters*, vol. 10, no. 2, B34, 2007.

[109] J. P. Owejan, J. E. Owejan, W. Gu, T. A. Trabold, T. W. Tighe, and M. F. Mathias, "Water transport mechanisms in PEMFC gas diffusion layers," *Journal of The Electrochemical Society*, vol. 157, no. 10, B1456, 2010.

[110] G. Lin and T. Van Nguyen, "Effect of thickness and hydrophobic polymer content of the gas diffusion layer on electrode flooding level in a PEMFC," *Journal of the Electrochemical Society*, vol. 152, no. 10, A1942, 2005.

[111] J. H. Kang, K.-J. Lee, S. H. Yu, J. H. Nam, and C.-J. Kim, "Demonstration of water management role of microporous layer by similarity model experiments," *international journal of hydrogen energy*, vol. 35, no. 9, pp. 4264–4269, 2010.

[112] Z. Lu, M. M. Daino, C. Rath, and S. G. Kandlikar, "Water management studies in PEM fuel cells, part III: Dynamic breakthrough and intermittent drainage characteristics from GDLs with and without MPLs," *International Journal of Hydrogen Energy*, vol. 35, no. 9, pp. 4222–4233, 2010.

[113] T. Sasabe, P. Deevanhxay, S. Tsushima, and S. Hirai, "Investigation on the effect of microstructure of proton exchange membrane fuel cell porous layers on liquid water behavior by soft X-ray radiography," *Journal of Power Sources*, vol. 196, no. 20, pp. 8197–8206, 2011.

[114] C.-Z. Qin, S. M. Hassanizadeh, and L. M. Van Oosterhout, "Pore-network modeling of water and vapor transport in the micro porous layer and gas diffusion layer of a polymer electrolyte fuel cell," *Computation*, vol. 4, no. 2, p. 21, 2016.

[115] M. N. Islam, U. Shrivastava, M. Atwa, X. Li, V. Birss, and K. Karan, "Highly ordered nanoporous carbon scaffold with controllable wettability as the microporous layer for fuel cells," *ACS Applied Materials & Interfaces*, vol. 12, no. 35, pp. 39 215–39 226, 2020.

[116] A. Kusoglu and A. Z. Weber, "New insights into perfluorinated sulfonic-acid ionomers," *Chemical reviews*, vol. 117, no. 3, pp. 987–1104, 2017.

[117] K. Karan, "Interesting facets of surface, interfacial, and bulk characteristics of perfluorinated ionomer films," *Langmuir*, vol. 35, no. 42, pp. 13 489–13 520, 2019.

[118] K. A. Mauritz and R. B. Moore, "State of understanding of Nafion," *Chemical reviews*, vol. 104, no. 10, pp. 4535–4586, 2004.

[119] G Sasikumar, J. Ihm, and H Ryu, "Optimum nafion content in PEM fuel cell electrodes," *Electrochimica Acta*, vol. 50, no. 2-3, pp. 601–605, 2004.

[120] T. Suzuki, H. Murata, T. Hatanaka, and Y. Morimoto, "Analysis of the catalyst layer of polymer electrolyte fuel cells," *R&D Review of Toyota CRDL*, vol. 39, no. 3, 2003.

[121] H. Iden, K. Sato, A. Ohma, and K. Shinohara, "Relationship among microstructure, ionomer property and proton transport in pseudo catalyst layers," *Journal of The Electrochemical Society*, vol. 158, no. 8, B987–B994, 2011.

[122] T. Soboleva, K. Malek, Z. Xie, T. Navessin, and S. Holdcroft, "PEMFC catalyst layers: The role of micropores and mesopores on water sorption and fuel cell activity," *ACS Applied Materials & Interfaces*, vol. 3, no. 6, pp. 1827–1837, 2011.

[123] O. S. Burheim, H. Su, H. H. Hauge, S. Pasupathi, and B. G. Pollet, "Study of thermal conductivity of pem fuel cell catalyst layers," *international journal of hydrogen energy*, vol. 39, no. 17, pp. 9397–9408, 2014.

[124] S. Shukla, K. Domican, K. Karan, S. Bhattacharjee, and M. Secanell, "Analysis of low platinum loading thin polymer electrolyte fuel cell electrodes prepared by inkjet printing," *Electrochimica Acta*, vol. 156, pp. 289–300, 2015.

[125] S. Shukla, D. Stanier, M. S. Saha, J. Stumper, and M. Secanell, "Analysis of inkjet printed PEFC electrodes with varying platinum loading," *Journal of The Electrochemical Society*, vol. 163, no. 7, F677–F687, 2016.

[126] S. Shukla, "Experimental analysis of inkjet printed polymer electrolyte fuel cell electrodes," PhD thesis, University of Alberta, 2016.

[127] S. Shukla, D. Stanier, M. S. Saha, B. Zahiri, M. Tam, J. Stumper, and M. Secanell, "Characterization of inkjet printed electrodes with improved porosity," *ECS Transactions*, vol. 77, no. 11, p. 1453, 2017.

[128] A. M. V. Putz, D. Susac, V. Berejnov, J. Wu, A. P. Hitchcock, and J. Stumper, "(plenary) doing more with less: Challenges for catalyst layer design," *ECS Transactions*, vol. 75, no. 14, p. 3, 2016.

[129] M Sabharwal, L. Pant, A Putz, D Susac, J Jankovic, and M Secanell, "Analysis of catalyst layer microstructures: From imaging to performance," *Fuel Cells*, vol. 16, no. 6, pp. 734–753, 2016.

[130] M. Sabharwal, L. M. Pant, N. Patel, and M. Secanell, "Computational analysis of gas transport in fuel cell catalyst layer under dry and partially saturated conditions," *Journal of The Electrochemical Society*, vol. 166, no. 7, F3065, 2019.

[131] M. Sabharwal, "Microstructural and performance analysis of fuel cell electrodes," PhD thesis, University of Alberta, 2019.

[132] J. Jankovic, S. Zhang, A. Putz, M. S. Saha, and D. Susac, "Multi-scale imaging and transport modeling for fuel cell electrode," *J Mater Res, 2017 MRS Fall Focus Issue*, vol. 34, 2019.

[133] S. J. Normile and I. V. Zenyuk, "Imaging ionomer in fuel cell catalyst layers with synchrotron nano transmission x-ray microscopy," *Solid State Ionics*, vol. 335, pp. 38–46, 2019.

[134] M. B. Sassin, Y. Garsany, R. W. Atkinson III, R. M. E. Hjelm, and K. E. Swider-Lyons, "Understanding the interplay between cathode catalyst layer porosity and thickness on transport limitations en route to high-performance PEMFCs," *International Journal of Hydrogen Energy*, vol. 44, no. 31, pp. 16 944–16 955, 2019.

[135] T. Mashio, K. Sato, and A. Ohma, "Analysis of water adsorption and condensation in catalyst layers for polymer electrolyte fuel cells," *Electrochimica Acta*, vol. 140, pp. 238–249, 2014.

[136] Z Yu, R. Carter, and J Zhang, "Measurements of pore size distribution, porosity, effective oxygen diffusivity, and tortuosity of PEM fuel cell electrodes," *Fuel Cells*, vol. 12, no. 4, pp. 557–565, 2012.

[137] D. Banham and S. Ye, "Current status and future development of catalyst materials and catalyst layers for proton exchange membrane fuel cells: An industrial perspective," *ACS Energy Letters*, vol. 2, no. 3, pp. 629–638, 2017.

[138] P. Satjaritanun and I. V. Zenyuk, "Water management strategies for PGM-free catalyst layers for polymer electrolyte fuel cells," *Current Opinion in Electrochemistry*, 2020.

[139] H. A. Gasteiger, S. S. Kocha, B. Sompalli, and F. T. Wagner, "Activity benchmarks and requirements for Pt, Pt-alloy, and non-Pt oxygen reduction catalysts for PEMFCs," *Applied Catalysis B: Environmental*, vol. 56, no. 1-2, pp. 9–35, 2005.

[140] N. Nonoyama, S. Okazaki, A. Z. Weber, Y. Ikogi, and T. Yoshida, "Analysis of oxygen-transport diffusion resistance in proton-exchange-membrane fuel cells," *Journal of The Electrochemical Society*, vol. 158, no. 4, B416–B423, 2011.

[141] T. Muzaffar, T. Kadyk, and M. Eikerling, "Tipping water balance and the Pt loading effect in polymer electrolyte fuel cells: A model-based analysis," *Sustainable Energy & Fuels*, vol. 2, no. 6, pp. 1189–1196, 2018.

[142] T. Muzaffar, "Physical modeling of local reaction conditions inside of cathode catalyst layer of polymer electrolyte fuel cells," PhD thesis, Simon Fraser University, 2018.

[143] J. Wu, L. G. Melo, X. Zhu, M. M. West, V. Berejnov, D. Susac, J. Stumper, and A. P. Hitchcock, "4D imaging of polymer electrolyte membrane fuel cell catalyst layers by soft X-ray spectro-tomography," *Journal of Power Sources*, vol. 381, pp. 72–83, 2018.

[144] S Kundu, M. Fowler, L. Simon, and S Grot, "Morphological features (defects) in fuel cell membrane electrode assemblies," *Journal of Power Sources*, vol. 157, no. 2, pp. 650–656, 2006.

[145] T. G. Tranter, M. Tam, and J. T. Gostick, "The effect of cracks on the in-plane electrical conductivity of PEFC catalyst layers," *Electroanalysis*, vol. 31, no. 4, pp. 619–623, 2019.

[146] N. Kumano, K. Kudo, A. Suda, Y. Akimoto, M. Ishii, and H. Nakamura, "Controlling cracking formation in fuel cell catalyst layers," *Journal of Power Sources*, vol. 419, pp. 219–228, 2019.

[147] S. M. Kim, C.-Y. Ahn, Y.-H. Cho, S. Kim, W. Hwang, S. Jang, S. Shin, G. Lee, Y.-E. Sung, and M. Choi, "High-performance fuel cell with stretched catalyst-coated membrane: One-step formation of cracked electrode," *Scientific reports*, vol. 6, no. 1, pp. 1–7, 2016.

[148] C.-Y. Ahn, S. Jang, Y.-H. Cho, J. Choi, S. Kim, S. M. Kim, Y.-E. Sung, and M. Choi, "Guided cracking of electrodes by stretching prism-patterned membrane electrode assemblies for high-performance fuel cells," *Scientific reports*, vol. 8, no. 1, pp. 1–9, 2018.

[149] M. Mandal, A. Valls, N. Gangnus, and M. Secanell, "Analysis of inkjet printed catalyst coated membranes for polymer electrolyte electrolyzers," *Journal of The Electrochemical Society*, vol. 165, no. 7, F543–F552, 2018.

[150] A. J. Bard and L. R. Faulkner, *Electrochemical methods: Fundamentals and applications.* New York: Wiley, 2001.

[151] K.-S. Choi, H.-M. Kim, and S.-M. Moon, "An experimental study on the enhancement of the water balance, electrochemical reaction and power density of the polymer electrolyte fuel cell by under-rib convection," *Electrochemistry Communications*, vol. 13, no. 12, pp. 1387–1390, 2011.

[152] A. Shah, G.-S. Kim, P. Sui, and D. Harvey, "Transient non-isothermal model of a polymer electrolyte fuel cell," *Journal of Power Sources*, vol. 163, no. 2, pp. 793–806, 2007. DOI: 10.1016/j.jpowsour.2006.09.022.

[153] J.-M. Le Canut, R. Latham, W. Mérida, and D. A. Harrington, "Impedance study of membrane dehydration and compression in proton exchange membrane fuel cells," *Journal of Power Sources*, vol. 192, no. 2, pp. 457–466, 2009.

[154] S. Sugawara, Y. Suzuki, S. S. Kocha, and K. Shinohara, "Electrocatalytic activity analysis of PEFC cathode by 1-D macrohomogeneous model of catalyst layer," *Electrochemistry*, vol. 79, no. 5, pp. 404–413, 2011.

[155] N. Subramanian, T. Greszler, J Zhang, W Gu, and R Makharia, "Pt-oxide coverage-dependent oxygen reduction reaction (ORR) kinetics," *Journal of The Electrochemical Society*, vol. 159, no. 5, B531, 2012.

[156] I. A. Pasti, N. M. Gavrilov, and S. V. Mentus, "Potentiodynamic investigation of oxygen reduction reaction on polycrystalline platinum surface in acidic solutions: The effect of the polarization rate on the kinetic parameters," *Int. J. Electrochem. Sci*, vol. 7, pp. 11 076–11 090, 2012.

[157] A. Goshtasbi, P. García-Salaberri, J. Chen, K. Talukdar, D. G. Sanchez, and T. Ersal, "Through-the-membrane transient phenomena in PEM fuel cells: A modeling study," *Journal of The Electrochemical Society*, vol. 166, no. 7, F3154–F3179, 2019.

[158] S. J. Andreasen, J. L. Jespersen, E. Schaltz, and S. K. Kær, "Characterisation and modelling of a high temperature PEM fuel cell stack using electrochemical impedance spectroscopy," *Fuel Cells*, vol. 9, no. 4, pp. 463–473, 2009.

[159] G. A. Futter, P. Gazdzicki, K. A. Friedrich, A. Latz, and T. Jahnke, "Physical modeling of polymer-electrolyte membrane fuel cells: Understanding water management and impedance spectra," *Journal of Power Sources*, vol. 391, pp. 148–161, 2018.

[160] D. Malevich, E. Halliop, B. A. Peppley, J. G. Pharoah, and K. Karan, "Investigation of charge-transfer and mass-transport resistances in PEMFCs with microporous layer using electrochemical impedance spectroscopy," *Journal of The Electrochemical Society*, vol. 156, no. 2, B216–B224, 2009.

[161] M. Heinzmann, A. Weber, and E. Ivers-Tiffée, "Impedance modelling of porous electrode structures in polymer electrolyte membrane fuel cells," *Journal of Power Sources*, vol. 444, p. 227 279, 2019.

[162] H. Wu, X. Li, and P. Berg, "Numerical analysis of dynamic processes in fully humidified PEM fuel cells," *International Journal of Hydrogen Energy*, vol. 32, no. 12, pp. 2022–2031, 2007.

[163] C. Brunetto, A. Moschetto, and G. Tina, "PEM fuel cell testing by electrochemical impedance spectroscopy," *Electric Power Systems Research*, vol. 79, no. 1, pp. 17–26, 2009.

[164] C. Bao and W. Bessler, "Two-dimensional modeling of a polymer electrolyte membrane fuel cell with long flow channel. Part II. Physics-based electrochemical impedance analysis," *Journal of Power Sources*, vol. 278, pp. 675–682, 2015.

[165] H. Wu, "Mathematical modeling of transient transport phenomena in PEM fuel cells," PhD thesis, 2009.

[166] R. Banerjee and S. G. Kandlikar, "Two-phase flow and thermal transients in proton exchange membrane fuel cells – A critical review," *International journal of hydrogen energy*, vol. 40, no. 10, pp. 3990–4010, 2015.

[167]   D. Svozil, "Electric resistance in a nafion® membrane exposed to air after a step change in the relative humidity," *Journal of Electroanalytical Chemistry*, vol. 385, pp. 269–271, 1995.

[168]   A. Kusoglu, A. Kwong, K. T. Clark, H. P. Gunterman, and A. Z. Weber, "Water uptake of fuel-cell catalyst layers," *Journal of The Electrochemical Society*, vol. 159, no. 9, F530–F535, 2012.

[169]   R. Borup, J. Meyers, B. Pivovar, Y. Kim, R. Mukundan, N. Garland, D. Myers, M. Wilson, F. Garzon, D. Wood, *et al.*, "Scientific aspects of polymer electrolyte fuel cell durability and degradation," *Chemical reviews*, vol. 107, no. 10, pp. 3904–3951, 2007.

[170]   L. Dubau, L. Castanheira, F. Maillard, M. Chatenet, O. Lottin, G. Maranzana, J. Dillet, A. Lamibrac, J.-C. Perrin, E. Moukheiber, A. ElKaddouri, G. De Moor, C. Bas, L. Flandin, and N. Caqué, "A review of PEM fuel cell durability: Materials degradation, local heterogeneities of aging and possible mitigation strategies," *Wiley Interdisciplinary Reviews: Energy and Environment*, vol. 3, no. 6, pp. 540–560, 2014.

[171]   I. Raistrick, "Impedance studies of porous electrodes," *Electrochimica Acta*, vol. 35, no. 10, pp. 1579–1586, 1990.

[172]   T. Springer, T. Zawodzinski, M. Wilson, and S. Gottesfeld, "Characterization of polymer electrolyte fuel cells using AC impedance spectroscopy," *Journal of the Electrochemical Society*, vol. 143, no. 2, pp. 587–599, 1996.

[173]   D. Malevich, B. R. Jayasankar, E. Halliop, J. G. Pharoah, B. A. Peppley, and K. Karan, "On the determination of PEM fuel cell catalyst layer resistance from impedance measurement in H2/N2 cells," *Journal of the Electrochemical Society*, vol. 159, no. 12, F888–F895, 2012.

[174]   M. Cimenti, D. Bessarabov, M. Tam, and J. Stumper, "Investigation of proton transport in the catalyst layer of PEM fuel cells by electrochemical impedance spectroscopy," *ECS transactions*, vol. 28, no. 23, pp. 147–157, 2010.

[175]   T. Gaumont, G. Maranzana, O. Lottin, J. Dillet, S. Didierjean, J. Pauchet, and L. Guétaz, "Measurement of protonic resistance of catalyst layers as a tool for degradation monitoring," *International Journal of Hydrogen Energy*, vol. 42, no. 3, pp. 1800–1812, 2017.

[176]   J. Hou, W. Song, H. Yu, Y. Fu, L. Hao, Z. Shao, and B. Yi, "Ionic resistance of the catalyst layer after the PEM fuel cell suffered freeze," *Journal of Power Sources*, vol. 176, no. 1, pp. 118–121, 2008.

[177]   R. Makharia, M. Mathias, and D. Baker, "Measurement of catalyst layer electrolyte resistance in PEFCs using electrochemical impedance spectroscopy," *Journal of The Electrochemical Society*, vol. 152, no. 5, A970–A977, 2005.

[178] F. Jaouen, G. Lindbergh, and K. Wiezell, "Transient techniques for investigating mass-transport limitations in gas diffusion electrodes II. Experimental characterization of the PEFC cathode," *Journal of The Electrochemical Society*, vol. 150, no. 12, A1711–A1717, 2003.

[179] N. Zamel, A. Bhattarai, and D. Gerteisen, "Measurement of spatially resolved impedance spectroscopy with local perturbation," *Fuel Cells*, vol. 13, no. 5, pp. 910–916, 2013.

[180] S Tant, S Rosini, P.-X. Thivel, F Druart, A Rakotondrainibe, T Geneston, and Y Bultel, "An algorithm for diagnosis of proton exchange membrane fuel cells by electrochemical impedance spectroscopy," *Electrochimica Acta*, vol. 135, pp. 368–379, 2014.

[181] S. M. R. Niya and M. Hoorfar, "Study of proton exchange membrane fuel cells using electrochemical impedance spectroscopy technique–A review," *Journal of Power Sources*, vol. 240, pp. 281–293, 2013.

[182] A. Kulikovsky, "A model for impedance of a PEM fuel cell cathode with poor electron conductivity," *Journal of Electroanalytical Chemistry*, vol. 801, pp. 122–128, 2017.

[183] M. Eikerling and A. Kornyshev, "Electrochemical impedance of the cathode catalyst layer in polymer electrolyte fuel cells," *Journal of Electroanalytical Chemistry*, vol. 475, no. 2, pp. 107–123, 1999.

[184] M.-J. Choo, K.-H. Oh, H.-T. Kim, and J.-K. Park, "Modulated ionomer distribution in the catalyst layer of polymer electrolyte membrane fuel cells for high temperature operation," *ChemSusChem*, vol. 7, no. 8, pp. 2335–2341, 2014.

[185] Y. Garsany, R. W. Atkinson, M. B. Sassin, R. M. Hjelm, B. D. Gould, and K. E. Swider-Lyons, "Improving pemfc performance using short-side-chain low-equivalent-weight PFSA ionomer in the cathode catalyst layer," *Journal of The Electrochemical Society*, vol. 165, no. 5, F381–F391, 2018.

[186] D. Malko, T. Lopes, E. A. Ticianelli, and A. Kucernak, "A catalyst layer optimisation approach using electrochemical impedance spectroscopy for PEM fuel cells operated with pyrolysed transition metal-NC catalysts," *Journal of Power Sources*, vol. 323, pp. 189–200, 2016.

[187] A Schiefer, M Heinzmann, and A Weber, "Inductive low-frequency processes in pemfc-impedance spectra," *Fuel Cells*, vol. 20, no. 4, pp. 499–506, 2020.

[188] K. Talukdar, S. Helmly, M. Schulze, D. G. Sanchez, M. Handl, R. Hiesgen, J. Kraut, and K. A. Friedrich, "Enveloping of catalyst powder by ionomer for dry spray coating in polymer electrolyte membrane fuel cells," *Journal of Power Sources*, vol. 424, pp. 82–90, 2019.

[189] Z. Xie, X. Zhao, M. Adachi, Z. Shi, T. Mashio, A. Ohma, K. Shinohara, S. Holdcroft, and T. Navessin, "Fuel cell cathode catalyst layers from "green" catalyst inks," *Energy & Environmental Science*, vol. 1, no. 1, pp. 184–193, 2008.

[190] A. Young, J Stumper, and E Gyenge, "Characterizing the structural degradation in a PEMFC cathode catalyst layer: carbon corrosion," *Journal of The Electrochemical Society*, vol. 156, no. 8, B913–B922, 2009.

[191] N. Holmström, K. Wiezell, and G. Lindbergh, "Studying low-humidity effects in PEFCs using EIS: I. Experimental," *Journal of The Electrochemical Society*, vol. 159, no. 8, F369, 2012.

[192] I. Pivac and F. Barbir, "Inductive phenomena at low frequencies in impedance spectra of proton exchange membrane fuel cells–A review," *Journal of Power Sources*, vol. 326, pp. 112–119, 2016.

[193] I. A. Schneider, M. H. Bayer, P. Boillat, A. Wokaun, and G. G. Scherer, "Formation of low frequency inductive loops in polymer electrolyte fuel cell (PEFC) impedance spectra under sub-saturated conditions," *ECS Transactions*, vol. 11, no. 1, p. 461, 2007.

[194] I. Schneider, M. Bayer, A. Wokaun, and G. Scherer, "Impedance response of the proton exchange membrane in polymer electrolyte fuel cells," *Journal of the electrochemical society*, vol. 155, no. 8, B783, 2008.

[195] K. Wiezell, N. Holmström, and G. Lindbergh, "Studying low-humidity effects in PEFCs using EIS II. Modeling," *Journal of the Electrochemical Society*, vol. 159, no. 8, F379, 2012.

[196] B. P. Setzler and T. F. Fuller, "A physics-based impedance model of proton exchange membrane fuel cells exhibiting low-frequency inductive loops," *Journal of The Electrochemical Society*, vol. 162, no. 6, F519–F530, 2015.

[197] P Moçotéguy, B Ludwig, D Beretta, and T Pedersen, "Study of the impact of water management on the performance of pemfc commercial stacks by impedance spectroscopy," *International Journal of Hydrogen Energy*, 2020, (in press).

[198] H. Nara, T. Momma, and T. Osaka, "Impedance analysis of the effect of flooding in the cathode catalyst layer of the polymer electrolyte fuel cell," *Electrochimica Acta*, vol. 113, pp. 720–729, 2013.

[199] S. Cruz-Manzo, R. Chen, and P. Greenwood, "An impedance model for analysis of EIS of polymer electrolyte fuel cells under hydrogen peroxide formation in the cathode," *Journal of Electroanalytical Chemistry*, vol. 745, pp. 28–36, 2015.

[200] S. Cruz-Manzo, C. Perezmitre-Cruz, P. Greenwood, and R. Chen, "An impedance model for analysis of EIS of polymer electrolyte fuel cells under platinum oxidation and hydrogen peroxide formation in the cathode," *Journal of Electroanalytical Chemistry*, vol. 771, pp. 94–105, 2016.

[201] S. Cruz-Manzo, U. Cano-Castillo, and P. Greenwood, "Impedance study on estimating electrochemical mechanisms in a polymer electrolyte fuel cell during gradual water accumulation," *Fuel Cells*, vol. 19, no. 1, pp. 71–83, 2019.

[202]   S. K. Roy, M. E. Orazem, and B. Tribollet, "Interpretation of low-frequency inductive loops in PEM fuel cells," *Journal of The Electrochemical Society*, vol. 154, no. 12, B1378, 2007.

[203]   A. Schiefer, M. Heinzmann, A. Weber, and E. Ivers-Tiffée, "Inductive low-frequency processes in PEMFC impedance spectra," in *EFCF 2019: Low-Temperature Fuel Cells, Electrolisers, & H₂ Processing, Chapter 03*, H. Gasteiger and A. Bandarenka, Eds., 2019, pp. 179–189.

[204]   N. Zamel, "Transport properties of the gas diffusion layer of pem fuel cells," 2011.

[205]   N. Zamel, X. Li, J. Becker, and A. Wiegmann, "Effect of liquid water on transport properties of the gas diffusion layer of polymer electrolyte membrane fuel cells," *International Journal of Hydrogen Energy*, vol. 36, no. 9, pp. 5466–5478, 2011.

[206]   N. Zamel, J. Becker, and A. Wiegmann, "Estimating the thermal conductivity and diffusion coefficient of the microporous layer of polymer electrolyte membrane fuel cells," *Journal of Power Sources*, vol. 207, pp. 70–80, 2012.

[207]   R Singh, A. Akhgar, P. Sui, K. Lange, and N Djilali, "Dual-beam FIB/SEM characterization, statistical reconstruction, and pore scale modeling of a PEMFC catalyst layer," *Journal of The Electrochemical Society*, vol. 161, no. 4, F415, 2014.

[208]   J Hinebaugh, J Gostick, and A Bazylak, "Stochastic modeling of polymer electrolyte membrane fuel cell gas diffusion layers–part 2: A comprehensive substrate model with pore size distribution and heterogeneity effects," *International Journal of Hydrogen Energy*, vol. 42, no. 24, pp. 15 872–15 886, 2017.

[209]   I. V. Zenyuk, A. Lamibrac, J. Eller, D. Y. Parkinson, F. Marone, F. N. Büchi, and A. Z. Weber, "Investigating evaporation in gas diffusion layers for fuel cells with X-ray computed tomography," *The Journal of Physical Chemistry C*, vol. 120, no. 50, pp. 28 701–28 711, 2016.

[210]   M. Sabharwal, J. T. Gostick, and M. Secanell, "Virtual liquid water intrusion in fuel cell gas diffusion media," *Journal of the Electrochemical Society*, vol. 165, no. 7, F553, 2018.

[211]   A. D. Shum, D. Y. Parkinson, X. Xiao, A. Z. Weber, O. S. Burheim, and I. V. Zenyuk, "Investigating phase-change-induced flow in gas diffusion layers in fuel cells with X-ray computed tomography," *Electrochimica Acta*, vol. 256, pp. 279–290, 2017.

[212]   S. Jung, "Estimation of relative transport properties of fuel cell and electrolyzer transport layers by pore network and continuum based direct simulations," Master's thesis, University of Alberta, 2020.

[213] M Sepe, P Satjaritanun, S Hirano, I. Zenyuk, N Tippayawong, and S Shimpalee, "Investigating liquid water transport in different pore structure of gas diffusion layers for PEMFC using lattice Boltzmann method," *Journal of The Electrochemical Society*, vol. 167, no. 10, p. 104 516, 2020.

[214] J. B. Grunewald, N. Goswami, P. P. Mukherjee, and T. F. Fuller, "Two-phase dynamics and hysteresis in the PEM fuel cell catalyst layer with the lattice-Boltzmann method," *Journal of The Electrochemical Society*, vol. 168, no. 2, p. 024 521, 2021.

[215] S. Jung, M. Sabharwal, A. Jarauta, F Wei, J. Gostick, M. Gingras, and M. Secanell, "Estimation of relative transport properties in porous transport layers using pore-scale and pore-network simulations," *Journal of The Electrochemical Society*, 2021.

[216] J. T. Gostick, M. A. Ioannidis, M. W. Fowler, and M. D. Pritzker, "Pore network modeling of fibrous gas diffusion layers for polymer electrolyte membrane fuel cells," *Journal of Power Sources*, vol. 173, no. 1, pp. 277–290, 2007.

[217] G. Luo, Y. Ji, C.-Y. Wang, and P. K. Sinha, "Modeling liquid water transport in gas diffusion layers by topologically equivalent pore network," *Electrochimica Acta*, vol. 55, no. 19, pp. 5332–5341, 2010.

[218] J. T. Gostick, "Random pore network modeling of fibrous PEMFC gas diffusion media using Voronoi and Delaunay tessellations," *Journal of the Electrochemical Society*, vol. 160, no. 8, F731, 2013.

[219] M. Fazeli, "Pore network modeling of multiphase transport in polymer electrolyte membrane fuel cell gas diffusion layers," Master's thesis, 2015.

[220] M Fazeli, J Hinebaugh, and A Bazylak, "Investigating inlet condition effects on pemfc gdl liquid water transport through pore network modeling," *Journal of The Electrochemical Society*, vol. 162, no. 7, F661, 2015.

[221] C. Qin, "Water transport in the gas diffusion layer of a polymer electrolyte fuel cell: Dynamic pore-network modeling," *Journal of the Electrochemical Society*, vol. 162, no. 9, F1036, 2015.

[222] M. Aghighi, M. A. Hoeh, W. Lehnert, G. Merle, and J. Gostick, "Simulation of a full fuel cell membrane electrode assembly using pore network modeling," *Journal of The Electrochemical Society*, vol. 163, no. 5, F384, 2016.

[223] M. Aghighi and J. Gostick, "Pore network modeling of phase change in PEM fuel cell fibrous cathode," *Journal of Applied Electrochemistry*, vol. 47, no. 12, pp. 1323–1338, 2017.

[224] P. Carrere and M. Prat, "Liquid water in cathode gas diffusion layers of PEM fuel cells: Identification of various pore filling regimes from pore network simulations," *International Journal of Heat and Mass Transfer*, vol. 129, pp. 1043–1056, 2019.

[225] P. A. García-Salaberri, I. V. Zenyuk, J. T. Gostick, and A. Z. Weber, "Modeling gas diffusion layers in polymer electrolyte fuel cells using a continuum-based pore-network formulation," *ECS Transactions*, vol. 97, no. 7, p. 615, 2020.

[226] T. Berning and N. Djilali, "A 3D, multiphase, multicomponent model of the cathode and anode of a PEM fuel cell," *Journal of the Electrochemical Society*, vol. 150, no. 12, A1589, 2003.

[227] Y. Wang and C.-Y. Wang, "Transient analysis of polymer electrolyte fuel cells," *Electrochimica Acta*, vol. 50, no. 6, pp. 1307–1315, 2005.

[228] Y. Wang and C.-Y. Wang, "Dynamics of polymer electrolyte fuel cells undergoing load changes," *Electrochimica Acta*, vol. 51, no. 19, pp. 3924–3933, 2006.

[229] S Shimpalee, W.-K. Lee, J. Van Zee, and H Naseri-Neshat, "Predicting the transient response of a serpentine flow-field PEMFC: I. Excess to normal fuel and air," *Journal of Power Sources*, vol. 156, no. 2, pp. 355–368, 2006.

[230] J. Peng, J. Shin, and T. Song, "Transient response of high temperature PEM fuel cell," *Journal of Power Sources*, vol. 179, no. 1, pp. 220–231, 2008.

[231] A. D. Le and B. Zhou, "A general model of proton exchange membrane fuel cell," *Journal of power sources*, vol. 182, no. 1, pp. 197–222, 2008.

[232] A. Roy, M. F. Serincan, U. Pasaogullari, M. W. Renfro, and B. M. Cetegen, "Transient computational analysis of proton exchange membrane fuel cells during load change and non-isothermal start-up," in *ASME 2009 7th International Conference on Fuel Cell Science, Engineering and Technology*, American Society of Mechanical Engineers, 2009, pp. 429–438.

[233] N Khajeh-Hosseini-Dalasm, K. Fushinobu, and K. Okazaki, "Three-dimensional transient two-phase study of the cathode side of a PEM fuel cell," *International journal of hydrogen energy*, vol. 35, no. 9, pp. 4234–4246, 2010.

[234] H. Wu, P. Berg, and X. Li, "Modeling of PEMFC transients with finite-rate phase-transfer processes," *Journal of The Electrochemical Society*, vol. 157, no. 1, B1–B12, 2010.

[235] H.-Y. Li, W.-C. Weng, W.-M. Yan, and X.-D. Wang, "Transient characteristics of proton exchange membrane fuel cells with different flow field designs," *Journal of Power Sources*, vol. 196, no. 1, pp. 235–245, 2011.

[236] X.-D. Wang, J.-L. Xu, W.-M. Yan, D.-J. Lee, and A. Su, "Transient response of PEM fuel cells with parallel and interdigitated flow field designs," *International Journal of Heat and Mass Transfer*, vol. 54, no. 11, pp. 2375–2386, 2011.

[237] Z. Zhang, L. Jia, X. Wang, and L. Ba, "Effects of inlet humidification on PEM fuel cell dynamic behaviors," *International Journal of Energy Research*, vol. 35, no. 5, pp. 376–388, 2011.

[238]  J. Ko and H. Ju, "Comparison of numerical simulation results and experimental data during cold-start of polymer electrolyte fuel cells," *Applied energy*, vol. 94, pp. 364–374, 2012.

[239]  J. Ko and H. Ju, "Effects of cathode catalyst layer design parameters on cold start behavior of polymer electrolyte fuel cells (PEFCs)," *international journal of hydrogen energy*, vol. 38, no. 1, pp. 682–691, 2013.

[240]  J. Ko and H. Ju, "Numerical evaluation of a dual-function microporous layer under subzero and normal operating temperatures for use in automotive fuel cells," *International journal of hydrogen energy*, vol. 39, no. 6, pp. 2854–2862, 2014.

[241]  X. Chen, B. Jia, Y. Yin, and Q. Du, "Numerical simulation of transient response of inlet relative humidity for high temperature PEM fuel cells with material properties," in *Advanced Materials Research*, Trans Tech Publ, vol. 625, 2013, pp. 226–229.

[242]  P. Choopanya and Z. Yang, "Transient performance investigation of different flow-field designs of automotive polymer electrolyte membrane fuel cell (PEMFC) using computational fluid dynamics (CFD)," in *Proceedings of the 10th International Conference on Heat Transfer, Fluid Mechanics and Thermodynamics*, International Conference on Heat Transfer, Fluid Mechanics and Thermodynamics, 2014.

[243]  A. Jo, S. Lee, W. Kim, J. Ko, and H. Ju, "Large-scale cold-start simulations for automotive fuel cells," *International Journal of Hydrogen Energy*, vol. 40, no. 2, pp. 1305–1315, 2015.

[244]  R. Kamal and S. H. Chan, "Sensitivity analysis of anode overpotential during start-up process of a high temperature proton exchange membrane fuel cell," *Electrochimica Acta*, vol. 176, pp. 965–975, 2015.

[245]  R. K. A. Rasheed and S. H. Chan, "Transient carbon monoxide poisoning kinetics during warm-up period of a high-temperature PEMFC – Physical model and parametric study," *Applied Energy*, vol. 140, pp. 44–51, 2015.

[246]  H. Kim, S. Jeon, D. Cha, and Y. Kim, "Numerical analysis of a high-temperature proton exchange membrane fuel cell under humidified operation with stepwise reactant supply," *International Journal of Hydrogen Energy*, vol. 41, no. 31, pp. 13 657–13 665, 2016.

[247]  G. Zhang, L. Fan, J. Sun, and K. Jiao, "A 3D model of PEMFC considering detailed multiphase flow and anisotropic transport properties," *International Journal of Heat and Mass Transfer*, vol. 115, pp. 714–724, 2017.

[248]  R. B. Ferreira, D. S. Falcão, V. B. Oliveira, and A. M. Pinto, "1D+3D two-phase flow numerical model of a proton exchange membrane fuel cell," *Applied Energy*, vol. 203, pp. 474–495, 2017.

[249] W. G. Bessler, "Rapid impedance modeling via potential step and current relaxation simulations," *Journal of The Electrochemical Society*, vol. 154, no. 11, B1186–B1191, 2007.

[250] M. K. Baboli and M. Kermani, "A two-dimensional, transient, compressible isothermal and two-phase model for the air-side electrode of PEM fuel cells," *Electrochimica Acta*, vol. 53, no. 26, pp. 7644–7654, 2008.

[251] A. P. Sasmito and A. S. Mujumdar, "Performance evaluation of a polymer electrolyte fuel cell with a dead-end anode: A computational fluid dynamic study," *International Journal of Hydrogen Energy*, vol. 36, no. 17, pp. 10 917–10 933, 2011.

[252] A. Gomez, A. Raj, A. Sasmito, and T. Shamim, "Effect of operating parameters on the transient performance of a polymer electrolyte membrane fuel cell stack with a dead-end anode," *Applied Energy*, vol. 130, pp. 692–701, 2014.

[253] A. Baricci, M. Zago, and A. Casalegno, "A quasi 2D model of a high temperature polymer fuel cell for the interpretation of impedance spectra," *Fuel Cells*, vol. 14, no. 6, pp. 926–937, 2014.

[254] O Shamardina, M. Kondratenko, A. Chertovich, and A. Kulikovsky, "A simple transient model for a high temperature PEM fuel cell impedance," *international journal of hydrogen energy*, vol. 39, no. 5, pp. 2224–2235, 2014.

[255] A Verma and R Pitchumani, "Influence of membrane properties on the transient behavior of polymer electrolyte fuel cells," *Journal of Power Sources*, vol. 268, pp. 733–743, 2014.

[256] A. Verma and R. Pitchumani, "Analysis and optimization of transient response of polymer electrolyte fuel cells," *Journal of Fuel Cell Science and Technology*, vol. 12, no. 1, p. 011 005, 2015.

[257] C. Bao and W. Bessler, "Two-dimensional modeling of a polymer electrolyte membrane fuel cell with long flow channel. Part I. Model development," *Journal of Power Sources*, vol. 275, pp. 922–934, 2015.

[258] J. Vang, F. Zhou, S. Andreasen, and S. Kær, "Estimating important electrode parameters of high temperature PEM fuel cells by fitting a model to polarisation curves and impedance spectra," *Ecs Transactions*, vol. 68, no. 3, pp. 13–34, 2015.

[259] A. Kulikovsky, J Divisek, and A. Kornyshev, "Modeling the cathode compartment of polymer electrolyte fuel cells: Dead and active reaction zones," *Journal of the Electrochemical Society*, vol. 146, no. 11, pp. 3981–3991, 1999.

[260] D. Natarajan and T. Van Nguyen, "A two-dimensional, two-phase, multicomponent, transient model for the cathode of a proton exchange membrane fuel cell using conventional gas distributors," *Journal of the Electrochemical Society*, vol. 148, no. 12, A1324, 2001.

[261] H. Wu, P. Berg, and X. Li, "Non-isothermal transient modeling of water transport in PEM fuel cells," *Journal of Power Sources*, vol. 165, no. 1, pp. 232–243, 2007.

[262] M. Secanell, "Computational modeling and optimization of proton exchange membrane fuel cells," PhD thesis, University of Victoria, 2007.

[263] M Secanell, R Songprakorp, A Suleman, and N Djilali, "Multi-objective optimization of a polymer electrolyte fuel cell membrane electrode assembly," *Energy & Environmental Science*, vol. 1, no. 3, pp. 378–388, 2008.

[264] R. Songprakorp, "Investigation of transient phenomena of proton exchange membrane fuel cells," PhD thesis, University of Victoria, 2008.

[265] M. Secanell, R. Songprakorp, N. Djilali, and A. Suleman, "Optimization of a proton exchange membrane fuel cell membrane electrode assembly," *Structural and Multidisciplinary Optimization*, vol. 40, no. 1-6, p. 563, 2010.

[266] R. Balliet, "Modeling cold start in a polymer-electrolyte fuel cell," PhD thesis, University of California, Berkeley, 2010.

[267] R. Balliet and J. Newman, "Two-dimensional model for cold start in a polymer-electrolyte-membrane fuel cell," *ECS Transactions*, vol. 33, no. 1, pp. 1545–1559, 2010.

[268] R. J. Balliet and J. Newman, "Cold start of a polymer-electrolyte fuel cell I. Development of a two-dimensional model," *Journal of the Electrochemical Society*, vol. 158, no. 8, B927–B938, 2011.

[269] P. Dobson, "Investigation of the polymer electrolyte membrane fuel cell catalyst layer microstructure," Master's thesis, University of Alberta, 2011.

[270] M. Moore, "Investigation of the double-trap intrinsic kinetic equation for oxygen reduction reaction and its implementation into a membrane electrode assembly model," Master's thesis, University of Alberta, 2012.

[271] M. Moore, A. Putz, and M. Secanell, "Development of a cathode electrode model using the ORR dual-trap intrinsic kinetic model," in *International Conference on Fuel Cell Science, Engineering and Technology*, American Society of Mechanical Engineers, vol. 44823, 2012, pp. 367–376.

[272] P. Wardlaw, "Modelling of PEMFC Catalyst Layer Mass Transport and Electro-Chemical Reactions Using Multi-scale Simulations," Master's thesis, University of Alberta, 2014.

[273] I. V. Zenyuk, E. Medici, J. Allen, and A. Z. Weber, "Coupling continuum and pore-network models for polymer-electrolyte fuel cells," *International Journal of Hydrogen Energy*, vol. 40, no. 46, pp. 16 831–16 845, 2015.

[274] I. Zenyuk, P. Das, and A. Weber, "Understanding impacts of catalyst-layer thickness on fuel-cell performance via mathematical modeling," *Journal of The Electrochemical Society*, vol. 163, no. 7, F691–F703, 2016.

[275] Z. Zhan, H. Zhao, P. C. Sui, P. Jiang, M. Pan, and N. Djilali, "Numerical analysis of ice-induced stresses in the membrane electrode assembly of a PEM fuel cell under sub-freezing operating conditions," *International Journal of Hydrogen Energy*, vol. 43, no. 9, pp. 4563–4582, 2018.

[276] J. Zhou, "Analyzing multiphase flow in membrane electrode assembly using a mixed wettability mathematical model," PhD thesis, University of Alberta, 2018.

[277] K. Adzakpa, K. Agbossou, Y. Dube, M. Dostie, M. Fournier, and A. Poulin, "PEM fuel cells modeling and analysis through current and voltage transient behaviors," *IEEE Transactions on Energy Conversion*, vol. 23, no. 2, pp. 581–591, 2008.

[278] S. Culubret, M. A. Rubio, D. G. Sanchez, and A. Urquia, "Dynamic modeling of the effect of water management on polymer electrolyte fuel cells performance," *International Journal of Hydrogen Energy*, vol. 45, no. 9, pp. 5710–5722, 2020.

[279] M. Eikerling and A. A. Kornyshev, "Modelling the performance of the cathode catalyst layer of polymer electrolyte fuel cells," *Journal of Electroanalytical Chemistry*, vol. 453, no. 1-2, pp. 89–106, 1998.

[280] D. Genevey, M. von Spakovsky, M. Ellis, D. Nelson, B. Olsommer, F. Topin, and N. Siegel, "Transient model of heat, mass, and charge transfer as well as electrochemistry in the cathode catalyst layer of a PEMFC," in *ASME 2002 International Mechanical Engineering Congress and Exposition*, American Society of Mechanical Engineers, 2002, pp. 393–406.

[281] D. Song, Q. Wang, Z. Liu, T. Navessin, M. Eikerling, and S. Holdcroft, "Numerical optimization study of the catalyst layer of PEM fuel cell cathode," *Journal of Power Sources*, vol. 126, no. 1-2, pp. 104–111, 2004.

[282] M. Eikerling, "Water management in cathode catalyst layers of PEM fuel cells: A structure-based model," *Journal of The Electrochemical Society*, vol. 153, no. 3, E58, 2006.

[283] A. A. Franco and M. Tembely, "Transient multiscale modeling of aging mechanisms in a PEFC cathode," *Journal of the Electrochemical Society*, vol. 154, no. 7, B712–B723, 2007.

[284] A. Franco and M. Gerard, "Multiscale model of carbon corrosion in a PEFC: Coupling with electrocatalysis and impact on performance degradation," *Journal of The Electrochemical Society*, vol. 155, no. 4, B367–B384, 2008.

[285] N. Zamel and X. Li, "Transient analysis of carbon monoxide poisoning and oxygen bleeding in a PEM fuel cell anode catalyst layer," *International Journal of Hydrogen Energy*, vol. 33, no. 4, pp. 1335–1344, 2008.

[286] A. Franco, M. Guinard, B. Barthe, and O. Lemaire, "Impact of carbon monoxide on PEFC catalyst carbon support degradation under current-cycled operating conditions," *Electrochimica Acta*, vol. 54, no. 22, pp. 5267–5279, 2009.

[287] R. Coulon, W. Bessler, and A. Franco, "Modeling chemical degradation of a polymer electrolyte membrane and its impact on fuel cell performance," *ECS Transactions*, vol. 25, no. 35, pp. 259–273, 2010.

[288] P. Olapade, J. Meyers, R. Mukundan, J. Davey, and R. Borup, "Modeling the dynamic behavior of proton-exchange membrane fuel cells," *Journal of the Electrochemical Society*, vol. 158, no. 5, B536–B549, 2011.

[289] A. Kongkanand and P. K. Sinha, "Load transients of nanostructured thin film electrodes in polymer electrolyte fuel cells," *Journal of The Electrochemical Society*, vol. 158, no. 6, B703–B711, 2011.

[290] A. Kulikovsky, "A physical model for catalyst layer impedance," *Journal of Electroanalytical Chemistry*, vol. 669, pp. 28–34, 2012.

[291] A. Kulikovsky and M Eikerling, "Analytical solutions for impedance of the cathode catalyst layer in PEM fuel cell: Layer parameters from impedance spectrum without fitting," *Journal of Electroanalytical Chemistry*, vol. 691, pp. 13–17, 2013.

[292] A. Kulikovsky, "Analytical physics–based impedance of the cathode catalyst layer in a PEM fuel cell at typical working currents," *Electrochimica Acta*, vol. 225, pp. 559–565, 2017.

[293] S. Huo, K. Jiao, and J. W. Park, "On the water transport behavior and phase transition mechanisms in cold start operation of PEM fuel cell," *Applied Energy*, vol. 233, pp. 776–788, 2019.

[294] A. Kulikovsky, "Analysis of proton and electron transport impedance of a pem fuel cell in $H_2/N_2$ regime," *Electrochemical Science Advances*, 2020.

[295] M. Rebai and M. Prat, "Scale effect and two-phase flow in a thin hydrophobic porous layer. Application to water transport in gas diffusion layers of proton exchange membrane fuel cells," *Journal of Power Sources*, vol. 192, no. 2, pp. 534–543, 2009.

[296] P. A. García-Salaberri, J. T. Gostick, G. Hwang, A. Z. Weber, and M. Vera, "Effective diffusivity in partially-saturated carbon-fiber gas diffusion layers: Effect of local saturation and application to macroscopic continuum models," *Journal of Power Sources*, vol. 296, pp. 440–453, 2015.

[297] P. A. García-Salaberri, I. V. Zenyuk, G. Hwang, M. Vera, A. Z. Weber, and J. T. Gostick, "Implications of inherent inhomogeneities in thin carbon fiber-based gas diffusion layers: A comparative modeling study," *Electrochimica Acta*, vol. 295, pp. 861–874, 2019.

[298] J Zhou, D Stanier, A Putz, and M Secanell, "A mixed wettability pore size distribution based mathematical model for analyzing two-phase flow in porous electrodes II. Model validation and analysis of micro-structural parameters," *Journal of The Electrochemical Society*, vol. 164, no. 6, F540–F556, 2017.

[299] A Vorobev, O Zikanov, and T Shamim, "A computational model of a PEM fuel cell with finite vapor absorption rate," *Journal of Power Sources*, vol. 166, no. 1, pp. 92–103, 2007.

[300] C. A. Balen, "A multi-component mass transport model for polymer electrolyte fuel cells," Master's thesis, University of Alberta, 2016.

[301] A. Jarauta, V. Zingan, P. Minev, and M. Secanell, "A compressible fluid flow model coupling channel and porous media flows and its application to fuel cell materials," *Transport in Porous Media*, vol. 134, no. 2, pp. 351–386, 2020.

[302] À. Jarauta Arabí, "Modeling of droplet dynamics in a proton exchange fuel cell electrode channel," PhD thesis, Universitat Politècnica de Catalunya, 2016.

[303] A. Jarauta and P. Ryzhakov, "Challenges in computational modeling of two-phase transport in polymer electrolyte fuel cells flow channels: A review," *Archives of Computational Methods in Engineering*, vol. 25, no. 4, pp. 1027–1057, 2018.

[304] Z. Wang, C. Wang, and K. Chen, "Two-phase flow and transport in the air cathode of proton exchange membrane fuel cells," *Journal of Power Sources*, vol. 94, no. 1, pp. 40–50, 2001.

[305] A. Z. Weber, "Improved modeling and understanding of diffusion-media wettability on polymer-electrolyte-fuel-cell performance," *journal of Power Sources*, vol. 195, no. 16, pp. 5292–5304, 2010.

[306] S. Ebrahimi, B. Ghorbani, and K. Vijayaraghavan, "Optimization of catalyst distribution along PEMFC channel through a numerical two-phase model and genetic algorithm," *Renewable Energy*, vol. 113, pp. 846–854, 2017.

[307] J. X. Wang, T. E. Springer, and R. R. Adzic, "Dual-pathway kinetic equation for the hydrogen oxidation reaction on Pt electrodes," *Journal of the Electrochemical Society*, vol. 153, no. 9, A1732–A1740, 2006.

[308] J. X. Wang, F. A. Uribe, T. E. Springer, J. Zhang, and R. R. Adzic, "Intrinsic kinetic equation for oxygen reduction reaction in acidic media: The double Tafel slope and fuel cell applications," *Faraday discussions*, vol. 140, pp. 347–362, 2009.

[309] A. Parthasarathy, S. Srinivasan, A. J. Appleby, and C. R. Martin, "Temperature dependence of the electrode kinetics of oxygen reduction at the platinum/-nafion® interface - A microelectrode investigation," *Journal of the Electrochemical Society*, vol. 139, no. 9, pp. 2530–2537, 1992.

[310] A. Parthasarathy, S. Srinivasan, A. J. Appleby, and C. R. Martin, "Pressure dependence of the oxygen reduction reaction at the platinum microelectrode/-Nafion interface: Electrode kinetics and mass transport," *Journal of the Electrochemical Society*, vol. 139, no. 10, pp. 2856–2862, 1992.

[311] M. Moore, A. Putz, and M. Secanell, "Investigation of the ORR using the double-trap intrinsic kinetic model," *Journal of the Electrochemical Society*, vol. 160, no. 6, F670–F681, 2013.

[312] M. Moore, S. Shukla, S. Voss, K. Karan, A. Z. Weber, I. Zenyuk, and M. Secanell, "A numerical study on the impact of cathode catalyst layer loading on the open circuit voltage in a proton exchange membrane fuel cell," *Journal of The Electrochemical Society*, vol. 168, no. 4, p. 044 519, 2021.

[313] H. Meng, "Numerical investigation of transient responses of a PEM fuel cell using a two-phase non-isothermal mixed-domain model," *Journal of Power Sources*, vol. 171, no. 2, pp. 738–746, 2007.

[314] S. Qu, X. Li, C. Ke, Z.-G. Shao, and B. Yi, "Experimental and modeling study on water dynamic transport of the proton exchange membrane fuel cell under transient air flow and load change," *Journal of Power Sources*, vol. 195, no. 19, pp. 6629–6636, 2010.

[315] H. Meng and B. Ruan, "Numerical studies of cold-start phenomena in PEM fuel cells: A review," *International Journal of Energy Research*, vol. 35, no. 1, pp. 2–14, 2011.

[316] G.-H. Song and H. Meng, "Numerical modeling and simulation of PEM fuel cells: Progress and perspective," *Acta Mechanica Sinica*, vol. 29, no. 3, pp. 318–334, 2013.

[317] X. Yang, Y. Yin, B. Jia, and Q. Du, "Analysis of voltage losses in high temperature proton exchange membrane fuel cells with properties of membrane materials and fluent software," in *Advanced Materials Research*, Trans Tech Publ, vol. 625, 2013, pp. 235–238.

[318] Y. Yin, J. Wang, X. Yang, Q. Du, J. Fang, and K. Jiao, "Modeling of high temperature proton exchange membrane fuel cells with novel sulfonated polybenzimidazole membranes," *international journal of hydrogen energy*, vol. 39, no. 25, pp. 13 671–13 680, 2014.

[319] X. Li, K. Han, and Y. Song, "Dynamic behaviors of PEM fuel cells under load changes," *International Journal of Hydrogen Energy*, vol. 45, no. 39, pp. 20 312–20 320, 2020.

[320] Q. Wang, F. Tang, B. Li, H. Dai, J. P. Zheng, C. Zhang, and P. Ming, "Numerical analysis of static and dynamic heat transfer behaviors inside proton exchange membrane fuel cell," *Journal of Power Sources*, vol. 488, p. 229 419, 2021.

[321] A. Z. Weber and A. Kusoglu, "Unexplained transport resistances for low-loaded fuel-cell catalyst layers," *Journal of Materials Chemistry A*, vol. 2, no. 41, pp. 17 207–17 211, 2014.

[322] T. Schuler, A. Chowdhury, A. T. Freiberg, B. Sneed, F. B. Spingler, M. C. Tucker, K. L. More, C. J. Radke, and A. Z. Weber, "Fuel-cell catalyst-layer resistance via hydrogen limiting-current measurements," *Journal of The Electrochemical Society*, vol. 166, no. 7, F3020, 2019.

[323] K. Kudo, T. Suzuki, and Y. Morimoto, "Analysis of oxygen dissolution rate from gas phase into Nafion surface and development of an agglomerate model," *ECS Transactions*, vol. 33, no. 1, p. 1495, 2010.

[324] K. Kudo and Y. Morimoto, "Analysis of oxygen transport resistance of Nafion thin film on Pt electrode," *ECS Transactions*, vol. 50, no. 2, p. 1487, 2013.

[325] K. Kudo, R. Jinnouchi, and Y. Morimoto, "Humidity and temperature dependences of oxygen transport resistance of Nafion thin film on platinum electrode," *Electrochimica Acta*, vol. 209, pp. 682–690, 2016.

[326] R. Jinnouchi, K. Kudo, N. Kitano, and Y. Morimoto, "Molecular dynamics simulations on o2 permeation through nafion ionomer on platinum surface," *Electrochimica Acta*, vol. 188, pp. 767–776, 2016.

[327] A. Kulikovsky, "The effect of Nafion film on the cathode catalyst layer performance in a low–Pt PEM fuel cell," *Electrochemistry communications*, vol. 103, pp. 61–65, 2019.

[328] M. Secanell, A. Putz, S. Shukla, P. Wardlaw, M. Bhaiya, L. M. Pant, and M. Sabharwal, "Mathematical Modelling and Experimental Analysis of Thin, Low-Loading Fuel Cell Electrodes," *ECS Transactions*, vol. 69, no. 17, pp. 157–187, 2015.

[329] J. Hwang and P. Chen, "Heat/mass transfer in porous electrodes of fuel cells," *International Journal of Heat and Mass Transfer*, vol. 49, no. 13, pp. 2315–2327, 2006.

[330] J. Hwang, C. Chao, and W. Wu, "Thermal-fluid transports in a five-layer membrane-electrode assembly of a PEM fuel cell," *Journal of Power Sources*, vol. 163, no. 1, pp. 450–459, 2006.

[331] J. Hwang, C. Chao, C. Chang, W. Ho, and D. Wang, "Modeling of two-phase temperatures in a two-layer porous cathode of polymer electrolyte fuel cells," *International Journal of Hydrogen Energy*, vol. 32, no. 3, pp. 405–414, 2007.

[332] M. Sabharwal, F. N. Büchi, S. Nagashima, F. Marone, and J. Eller, "Investigation of the transient freeze start behavior of polymer electrolyte fuel cells," *Journal of Power Sources*, vol. 489, p. 229 447, 2021.

[333] Z. Zhang, L. Jia, H. He, X. Wang, and L. Yang, "Modeling dynamic behaviors of a single cell proton exchange membrane fuel cell under different operating conditions," *Journal of the Taiwan Institute of Chemical Engineers*, vol. 41, no. 6, pp. 689–698, 2010.

[334] S. Chaudhary, V. K. Sachan, and P. K. Bhattacharya, "Two dimensional modelling of water uptake in proton exchange membrane fuel cell," *international journal of hydrogen energy*, vol. 39, no. 31, pp. 17 802–17 818, 2014.

[335] E. J. Dickinson, "Review of methods for modelling two-phase phenomena in a polymer electrolyte membrane fuel cell (PEMFC)," National Physics Laboratory, 2020, Accessed April 30, 2021.

[336]  S. Litster and N. Djilali, "Two-phase transport in porous gas diffusion electrodes," in *Transport Phenomena in Fuel Cells*, B. Sundén and F. M., Eds., ser. Developments in Heat Transfer. WIT Press, 2005, vol. 19, pp. 175–213.

[337]  E. C. Kumbur, K. V. Sharp, and M. M. Mench, "Validated Leverett approach for multiphase flow in PEFC diffusion media: I. Hydrophobicity effect," *Journal of the Electrochemical Society*, vol. 154, no. 12, B1295, 2007.

[338]  E. C. Kumbur, "Fundamental characterization of multi-phase transport in thin-film fuel cell diffusion media," PhD thesis, Pennsylvania State University, 2007.

[339]  T. Berning, M. Odgaard, and S. K. Kær, "Water balance simulations of a polymer-electrolyte membrane fuel cell using a two-fluid model," *Journal of Power Sources*, vol. 196, no. 15, pp. 6305–6317, 2011.

[340]  S. Li, J. Yuan, M. Andersson, G. Xie, and B. Sundén, "Wavy surface cathode gas flow channel effects on transport processes in a proton exchange membrane fuel cell," *Journal of Electrochemical Energy Conversion and Storage*, vol. 14, no. 3, 2017.

[341]  R. Vetter and J. O. Schumacher, "Free open reference implementation of a two-phase PEM fuel cell model," *Computer Physics Communications*, vol. 234, pp. 223–234, 2019.

[342]  P. A. Mateo Villanueva, "A mixed wettability pore size distribution model for the analysis of water transport in PEMFC materials," Master's thesis, University of Alberta, 2013.

[343]  J. Liu and M. Eikerling, "Model of cathode catalyst layers for polymer electrolyte fuel cells: The role of porous structure and water accumulation," *Electrochimica Acta*, vol. 53, no. 13, pp. 4435–4446, 2008.

[344]  A. Kongkanand, "Interfacial water transport measurements in Nafion thin films using a quartz-crystal microbalance," *The Journal of Physical Chemistry C*, vol. 115, no. 22, pp. 11 318–11 325, 2011.

[345]  E. J. Dickinson and G. Smith, "Modelling the proton-conductive membrane in practical polymer electrolyte membrane fuel cell (PEMFC) simulation: A review," *Membranes*, vol. 10, no. 11, p. 310, 2020.

[346]  K. P. Domican, "Mathematical modeling and experimental validation of thin low platinum content and functionally graded cathode catalyst layers," Master's thesis, University of Alberta, 2014.

[347]  C.-Y. Jung and S.-C. Yi, "Influence of the water uptake in the catalyst layer for the proton exchange membrane fuel cells," *Electrochemistry Communications*, vol. 35, pp. 34–37, 2013.

[348]  G. C. Abuin, M. C. Fuertes, and H. R. Corti, "Substrate effect on the swelling and water sorption of Nafion nanomembranes," *Journal of membrane science*, vol. 428, pp. 507–515, 2013.

[349] A. Kusoglu, D. Kushner, D. K. Paul, K. Karan, M. A. Hickner, and A. Z. Weber, "Impact of substrate and processing on confinement of Nafion thin films," *Advanced Functional Materials*, vol. 24, no. 30, pp. 4763–4774, 2014.

[350] H. K. Shim, D. K. Paul, and K. Karan, "Resolving the contradiction between anomalously high water uptake and low conductivity of nanothin Nafion films on SiO2 substrate," *Macromolecules*, vol. 48, no. 22, pp. 8394–8397, 2015.

[351] H. K. Shim, "Water sorption properties of sub-micron thin ionomer films," Master's thesis, Queen's University, 2016.

[352] U. N. Shrivastava, H. Fritzsche, and K. Karan, "Interfacial and bulk water in ultrathin films of Nafion, 3M PFSA, and 3M PFIA ionomers on a polycrystalline platinum surface," *Macromolecules*, vol. 51, no. 23, pp. 9839–9849, 2018.

[353] T. A. Zawodzinski Jr, M. Neeman, L. O. Sillerud, and S. Gottesfeld, "Determination of water diffusion coefficients in perfluorosulfonate ionomeric membranes," *The Journal of Physical Chemistry*, vol. 95, no. 15, pp. 6040–6044, 1991.

[354] J. T. Hinatsu, M. Mizuhata, and H. Takenaka, "Water uptake of perfluorosulfonic acid membranes from liquid water and water vapor," *Journal of the Electrochemical Society*, vol. 141, no. 6, pp. 1493–1498, 1994.

[355] C. K. Mittelsteadt and H. Liu, "Conductivity, permeability, and ohmic shorting of ionomeric membranes," in *Handbook of fuel cells: Fundamentals technology and applications: Advances in electrocatalysis, materials, diagnostics and durability*, W. Vielstich, H. A. Gasteiger, and H. Yokokawa, Eds. John Wiley & Sons: Springer New York, 2009, pp. 345–358.

[356] C. Robin, M. Gérard, M. Quinaud, J. d'Arbigny, and Y. Bultel, "Proton exchange membrane fuel cell model for aging predictions: Simulated equivalent active surface area loss and comparisons with durability tests," *Journal of Power Sources*, vol. 326, pp. 417–427, 2016.

[357] T. Jahnke, G. A. Futter, A. Baricci, C. Rabissi, and A. Casalegno, "Physical modeling of catalyst degradation in low temperature fuel cells: Platinum oxidation, dissolution, particle growth and platinum band formation," *Journal of The Electrochemical Society*, vol. 167, no. 1, p. 013 523, 2019.

[358] J. Meyers and R. Darling, "Model of carbon corrosion in PEM fuel cells," *Journal of the Electrochemical Society*, vol. 153, no. 8, A1432–A1442, 2006.

[359] K. Jiao, Y. Zhou, Q. Du, Y. Yin, S. Yu, and X. Li, "Numerical simulations of carbon monoxide poisoning in high temperature proton exchange membrane fuel cells with various flow channel designs," *Applied energy*, vol. 104, pp. 21–41, 2013.

[360] N. Khattra, A. Karlsson, M. Santare, P. Walsh, and F. Busby, "Effect of time-dependent material properties on the mechanical behavior of PFSA membranes subjected to humidity cycling," *Journal of Power Sources*, vol. 214, pp. 365–376, 2012.

[361] T. Yu, Y. Sha, W.-G. Liu, B. Merinov, P. Shirvanian, and W. Goddard III, "Mechanism for degradation of Nafion in PEM fuel cells from quantum mechanics calculations," *Journal of the American Chemical Society*, vol. 133, no. 49, pp. 19 857–19 863, 2011.

[362] R. Feynman, *The character of physical law*. MIT press, 2017.

[363] J. I. Gazzarri, "Impedance model of a solid oxide fuel cell for degradation diagnosis," PhD thesis, University of British Columbia, 2007.

[364] T. Sousa, M. Mamlouk, and K. Scott, "A dynamic non-isothermal model of a laboratory intermediate temperature fuel cell using PBI doped phosphoric acid membranes," *international journal of hydrogen energy*, vol. 35, no. 21, pp. 12 065–12 080, 2010.

[365] Y. Shao, L. Xu, J. Li, and M. Ouyang, "Numerical modeling and performance prediction of water transport for PEM fuel cell," *Energy Procedia*, vol. 158, pp. 2256–2265, 2019.

[366] S. Dutta, S. Shimpalee, and J. Van Zee, "Numerical prediction of mass-exchange between cathode and anode channels in a PEM fuel cell," *International Journal of Heat and Mass Transfer*, vol. 44, no. 11, pp. 2029–2042, 2001.

[367] J. Carton and A.-G. Olabi, "Three-dimensional proton exchange membrane fuel cell model: Comparison of double channel and open pore cellular foam flow plates," *Energy*, vol. 136, pp. 185–195, 2017.

[368] C. Wang, M. Nehrir, and S. Shaw, "Dynamic models and model validation for PEM fuel cells using electrical circuits," *IEEE transactions on energy conversion*, vol. 20, no. 2, pp. 442–451, 2005.

[369] J. Vang, S. Andreasen, and S. Kær, "A transient fuel cell model to simulate HTPEM fuel cell impedance spectra," *Journal of Fuel Cell Science and Technology*, vol. 9, no. 2, p. 021 005, 2012.

[370] *Fast-FC (official website)*, https://www.fastsimulations.com, Accessed April 30, 2021.

[371] *OpenFuelCell GitHub page*, https://github.com/OpenFuelCell, Accessed May 26, 2021.

[372] J. Gostick, M. Aghighi, J. Hinebaugh, T. Tranter, M. A. Hoeh, H. Day, B. Spellacy, M. H. Sharqawy, A. Bazylak, A. Burns, *et al.*, "OpenPNM: A pore network modeling package," *Computing in Science & Engineering*, vol. 18, no. 4, pp. 60–74, 2016.

[373] *OpenPNM (official website)*, http://openpnm.org/, Accessed April 30, 2021.

[374]  M. Secanell, A. Putz, P. Wardlaw, V. Zingan, M. Bhaiya, M. Moore, J. Zhou, C. Balen, and K. Domican, "OpenFCST: An open-source mathematical modelling software for polymer electrolyte fuel cells," *ECS Transactions*, vol. 64, no. 3, p. 655, 2014.

[375]  *OpenFCST: Open-Source Fuel Cell Simulation Toolbox (official website)*, http://www.openfcst.org, Accessed April 30, 2021.

[376]  *Fast-FC GitHub page*, https://github.com/fastsimulations, Accessed April 30, 2021.

[377]  S. B. Beale, H.-W. Choi, J. G. Pharoah, H. K. Roth, H. Jasak, and D. H. Jeon, "Open-source computational model of a solid oxide fuel cell," *Computer physics communications*, vol. 200, pp. 15–26, 2016.

[378]  *OpenPNM GitHub page*, https://github.com/PMEAL/OpenPNM, Accessed April 30, 2021.

[379]  *OpenFCST GitHub page*, https://github.com/OpenFCST, Accessed April 30, 2021.

[380]  W. Bangerth, R. Hartmann, and G. Kanschat, "Deal.II – A general-purpose object-oriented finite element library," *ACM Transactions on Mathematical Software (TOMS)*, vol. 33, no. 4, p. 24, 2007.

[381]  W. Bangerth, D. Davydov, T. Heister, L. Heltai, G. Kanschat, M. Kronbichler, M. Maier, B. Turcksin, and D. Wells, "The deal.II library, version 8.4," *Journal of Numerical Mathematics*, vol. 24, no. 3, pp. 135–141, 2016.

[382]  D. Arndt, W. Bangerth, B. Blais, T. C. Clevenger, M. Fehling, A. V. Grayver, T. Heister, L. Heltai, M. Kronbichler, M. Maier, P. Munch, J.-P. Pelteret, R. Rastak, I. Thomas, B. Turcksin, Z. Wang, and D. Wells, "The `deal.II` library, version 9.2," *Journal of Numerical Mathematics*, vol. 28, no. 3, pp. 131–146, 2020.

[383]  S. Kundu, M. Fowler, L. C. Simon, and R. Abouatallah, "Reversible and irreversible degradation in fuel cells during open circuit voltage durability testing," *Journal of Power Sources*, vol. 182, no. 1, pp. 254–258, 2008.

[384]  C. Winlove, K. Parker, and R. Oxenham, "The measurement of oxygen diffusivity and concentration by chronoamperometry using microelectrodes," *Journal of electroanalytical chemistry and interfacial electrochemistry*, vol. 170, no. 1, pp. 293–304, 1984.

[385]  A. Parthasarathy, C. R. Martin, and S. Srinivasan, "Investigations of the O2 reduction reaction at the platinum/Nafion® interface using a solid-state electrochemical cell," *Journal of the Electrochemical Society*, vol. 138, no. 4, p. 916, 1991.

[386]  F. N. Büchi, M. Wakizoe, and S. Srinivasan, "Microelectrode investigation of oxygen permeation in perfluorinated proton exchange membranes with different equivalent weights," *Journal of The Electrochemical Society*, vol. 143, no. 3, pp. 927–932, 1996.

[387] S. Mitsushima, N. Araki, N. Kamiya, and K.-i. Ota, "Analysis of oxygen reduction on Pt microelectrode with polymer electrolytes of various exchange capacities," *Journal of the Electrochemical Society*, vol. 149, no. 10, A1370, 2002.

[388] Y. Takamura, E. Nakashima, H. Yamada, A. Tasaka, and M. Inaba, "Effects of temperature and relative humidity on oxygen permeation in nafion® and sulfonated poly (Arylene Ether Sulfone)," *ECS Transactions*, vol. 16, no. 2, pp. 881–889, 2008.

[389] I. Gunasekara, M. Lee, D. Abbott, and S. Mukerjee, "Mass transport and oxygen reduction kinetics at an anion exchange membrane interface: Microelectrode studies on effect of carbonate exchange," *ECS Electrochemistry Letters*, vol. 1, no. 2, F16–F19, 2012.

[390] D. Novitski, Z. Xie, and S. Holdcroft, "Oxygen transport parameters in nafion® 117 under controlled relative humidity," *ECS Transactions*, vol. 58, no. 1, pp. 1097–1103, 2013.

[391] D. Novitski and S. Holdcroft, "Determination of $O_2$ mass transport at the pt |pfsa ionomer interface under reduced relative humidity," *ACS Applied Materials & Interfaces*, vol. 7, no. 49, pp. 27 314–27 323, 2015.

[392] D. Novitski, "Oxygen mass transport parameters in ionomer films under controlled relative humidity," PhD thesis, Simon Fraser University, 2017.

[393] H. Liu, W. K. Epting, and S. Litster, "Gas transport resistance in polymer electrolyte thin films on oxygen reduction reaction catalysts," *Langmuir*, vol. 31, no. 36, pp. 9853–9858, 2015.

[394] F. Cottrell, "Residual current in galvanic polarization regarded as a diffusion problem," *Z Phys Chem*, vol. 42, pp. 385–431, 1903.

[395] Z. G. Soos and P. J. Lingane, "Derivation of the chronoamperometric constant for unshielded, circular, planar electrodes," *The Journal of Physical Chemistry*, vol. 68, no. 12, pp. 3821–3828, 1964.

[396] K. Aoki and J. Osteryoung, "Diffusion-controlled current at the stationary finite disk electrode: Theory," *Journal of Electroanalytical Chemistry and Interfacial Electrochemistry*, vol. 122, pp. 19–35, 1981.

[397] D. Shoup and A. Szabo, "Chronoamperometric current at finite disk electrodes," *Journal of Electroanalytical Chemistry and Interfacial Electrochemistry*, vol. 140, no. 2, pp. 237–245, 1982.

[398] K. Aoki and J. Osteryoung, "Formulation of the diffusion-controlled current at very small stationary disk electrodes," *Journal of electroanalytical chemistry and interfacial electrochemistry*, vol. 160, no. 1, pp. 335–339, 1984.

[399] L Rajendran and M. Sangaranarayanan, "Diffusion at ultramicro disk electrodes: Chronoamperometric current for steady-state Ec' reaction using scattering analogue techniques," *The Journal of Physical Chemistry B*, vol. 103, no. 9, pp. 1518–1524, 1999.

[400]  P. J. Mahon and K. B. Oldham, "The transient current at the disk electrode under diffusion control: A new determination by the Cope–Tallman method," *Electrochimica acta*, vol. 49, no. 28, pp. 5041–5048, 2004.

[401]  M. Ciureanu and R. Roberge, "Electrochemical impedance study of PEM fuel cells. experimental diagnostics and modeling of air cathodes," *The Journal of Physical Chemistry B*, vol. 105, no. 17, pp. 3531–3539, 2001.

[402]  M. Heinzmann, A. Weber, and E. Ivers-Tiffée, "Advanced modelling of PEMFC impedance spectra," in *EFCF 2019: Low-Temperature Fuel Cells, Electrolisers, & H₂ Processing, Chapter 03*, H. Gasteiger and A. Bandarenka, Eds., 2019, pp. 232–243.

[403]  S. Cruz-Manzo and R. Chen, "A generic electrical circuit for performance analysis of the fuel cell cathode catalyst layer through electrochemical impedance spectroscopy," *Journal of Electroanalytical Chemistry*, vol. 694, pp. 45–55, 2013.

[404]  D. Gerteisen, "Impact of inhomogeneous catalyst layer properties on impedance spectra of polymer electrolyte membrane fuel cells," *Journal of The Electrochemical Society*, vol. 162, no. 14, F1431–F1438, 2015.

[405]  A. Kulikovsky, "Impedance of a PEM fuel cell cathode with nonuniform ionomer loading: Analytical and numerical study," *Journal of Electroanalytical Chemistry*, vol. 789, pp. 174–180, 2017.

[406]  A. Kulikovsky and O. Shamardina, "A model for PEM fuel cell impedance: Oxygen flow in the channel triggers spatial and frequency oscillations of the local impedance," *Journal of The Electrochemical Society*, vol. 162, no. 9, F1068–F1077, 2015.

[407]  T. Reshetenko and A. Kulikovsky, "Comparison of two physical models for fitting PEM fuel cell impedance spectra measured at a low air flow stoichiometry," *Journal of The Electrochemical Society*, vol. 163, no. 3, F238–F246, 2016.

[408]  T. Schuler, J. M. Ciccone, B. Krentscher, F. Marone, C. Peter, T. J. Schmidt, and F. N. Büchi, "Hierarchically structured porous transport layers for polymer electrolyte water electrolysis," *Advanced Energy Materials*, vol. 10, no. 2, p. 1 903 216, 2020.

[409]  M. Bernt, A. Siebel, and H. A. Gasteiger, "Analysis of voltage losses in PEM water electrolyzers with low platinum group metal loadings," *Journal of the Electrochemical Society*, vol. 165, no. 5, F305, 2018.

[410]  C. Rozain, E. Mayousse, N. Guillet, and P. Millet, "Influence of iridium oxide loadings on the performance of PEM water electrolysis cells: Part I–Pure IrO2-based anodes," *Applied Catalysis B: Environmental*, vol. 182, pp. 153–160, 2016.

[411] C. Rozain, E. Mayousse, N. Guillet, and P. Millet, "Influence of iridium oxide loadings on the performance of PEM water electrolysis cells: Part II–Advanced oxygen electrodes," *Applied Catalysis B: Environmental*, vol. 182, pp. 123–131, 2016.

[412] D. R. Morris, S. P. Liu, D. Villegas Gonzalez, and J. T. Gostick, "Effect of water sorption on the electronic conductivity of porous polymer electrolyte membrane fuel cell catalyst layers," *ACS Applied Materials & Interfaces*, vol. 6, no. 21, pp. 18 609–18 618, 2014.

[413] A. Krasnova, N. Glebova, A. Nechitailov, A. Tomasov, and N. Zelenina, "Charge transfer in hydrogen fuel cell electrode containing carbon nanofibers," *International Scientific Journal for Alternative Energy and Ecology*, no. 19-21, pp. 40–51, 2018, (in Russian).

[414] U. Babic, E. Nilsson, A. Pătru, T. J. Schmidt, and L. Gubler, "Proton transport in catalyst layers of a polymer electrolyte water electrolyzer: Effect of the anode catalyst loading," *Journal of The Electrochemical Society*, vol. 166, no. 4, F214, 2019.

[415] M. Mandal, M. Moore, and M. Secanell, "Measurement of the protonic and electronic conductivities of pem water electrolyzer electrodes," *ACS Applied Materials & Interfaces*, vol. 12, no. 44, pp. 49 549–49 562, 2020.

[416] J. W. Lim, Y.-H. Cho, M. Ahn, D. Y. Chung, Y.-H. Cho, N. Jung, Y. S. Kang, O.-H. Kim, M. J. Lee, M. Kim, *et al.*, "Ionic resistance of a cathode catalyst layer with various thicknesses by electrochemical impedance spectroscopy for PEMFC," *Journal of The Electrochemical Society*, vol. 159, no. 4, B378–B384, 2012.

[417] Z. Xie, T. Navessin, K. Shi, R. Chow, Q. Wang, D. Song, B. Andreaus, M. Eikerling, Z. Liu, and S. Holdcroft, "Functionally graded cathode catalyst layers for polymer electrolyte fuel cells II. Experimental study of the effect of nafion distribution," *Journal of the Electrochemical Society*, vol. 152, no. 6, A1171–A1179, 2005.

[418] Q. Xue, D. jun Yang, B. Li, P. wen Ming, and C. man Zhang, "Quantitative analysis effect of the cathode catalyst layer with various ionomer ratio on PEMFC by protonic resistance," *ECS Transactions*, vol. 89, no. 7, p. 23, 2019.

[419] S. Vierrath, M. Breitwieser, M. Klingele, B. Britton, S. Holdcroft, R. Zengerle, and S. Thiele, "The reasons for the high power density of fuel cells fabricated with directly deposited membranes," *Journal of Power Sources*, vol. 326, pp. 170–175, 2016.

[420] A. D. Modestov, A. V. Kapustin, V. B. Avakov, I. K. Landgraf, and M. R. Tarasevich, "Cathode catalyst layers with ionomer to carbon mass ratios in the range 0–2 studied by electrochemical impedance spectroscopy, cyclic voltammetry, and performance measurements," *Journal of Power Sources*, vol. 272, pp. 735–742, 2014.

[421] M. Darab, A. O. Barnett, G. Lindbergh, M. S. Thomassen, and S. Sunde, "The influence of catalyst layer thickness on the performance and degradation of PEM fuel cell cathodes with constant catalyst loading," *Electrochimica Acta*, vol. 232, pp. 505–516, 2017.

[422] J. Gazzarri, M. Eikerling, Q. Wang, and Z.-S. Liu, "Estimation of local relative humidity in cathode catalyst layers of PEFC," *Electrochemical and Solid-State Letters*, vol. 13, no. 6, B58–B62, 2010.

[423] J. Peron, D. Edwards, M. Haldane, X. Luo, Y. Zhang, S. Holdcroft, and Z. Shi, "Fuel cell catalyst layers containing short-side-chain perfluorosulfonic acid ionomers," *Journal of Power Sources*, vol. 196, no. 1, pp. 179–181, 2011.

[424] M. S. Kondratenko, M. O. Gallyamov, and A. R. Khokhlov, "Performance of high temperature fuel cells with different types of PBI membranes as analysed by impedance spectroscopy," *International Journal of Hydrogen Energy*, vol. 37, no. 3, pp. 2596–2602, 2012.

[425] X. Zhao, X. Fan, S. Wang, S. Yang, B. Yi, Q. Xin, and G. Sun, "Determination of ionic resistance and optimal composition in the anodic catalyst layers of DMFC using AC impedance," *International journal of hydrogen energy*, vol. 30, no. 9, pp. 1003–1010, 2005.

[426] A Havranek and K Wippermann, "Determination of proton conductivity in anode catalyst layers of the direct methanol fuel cell (DMFC)," *Journal of Electroanalytical Chemistry*, vol. 567, no. 2, pp. 305–315, 2004.

[427] S. Tominaka, K. Goto, T. Momma, and T. Osaka, "Ionic conductivity improvement in primary pores of fuel cell catalyst layers: Electropolymerization of m-aminobenzenesulfonic acid and its effect on the performance," *Journal of Power Sources*, vol. 192, no. 2, pp. 316–323, 2009.

[428] Y. Qi, J. Liu, D. C. Sabarirajan, Y. Huang, A. Perego, A. Haug, and I. Zenyuk, "Interpreting ionic conductivity for polymer electrolyte fuel cell catalyst layers with electrochemical impedance spectroscopy and transmission line modeling," *Journal of The Electrochemical Society*, 2021.

[429] U. Babic, T. J. Schmidt, and L. Gubler, "Communication—Contribution of catalyst layer proton transport resistance to voltage loss in polymer electrolyte water electrolyzers," *Journal of The Electrochemical Society*, vol. 165, no. 15, J3016–J3018, 2018.

[430] C Boyer, S Gamburzev, O Velev, S Srinivasan, and A. Appleby, "Measurements of proton conductivity in the active layer of PEM fuel cell gas diffusion electrodes," *Electrochimica Acta*, vol. 43, no. 24, pp. 3703–3709, 1998.

[431] H. Iden, A. Ohma, and K. Shinohara, "Analysis of proton transport in pseudo catalyst layers," *ECS Transactions*, vol. 16, no. 2, p. 1751, 2008.

[432] H. Iden, A. Ohma, and K. Shinohara, "Analysis of proton transport in pseudo catalyst layers," *Journal of The Electrochemical Society*, vol. 156, no. 9, B1078–B1084, 2009.

[433]  M. Mandal, M. Moore, and M. Secanell, "Measurement of ionic conductivity of PEM water electrolyzer electrodes," *ECS Transactions*, vol. 92, no. 8, p. 757, 2019.

[434]  D. C. Sabarirajan, J. Liu, Y. Qi, A. Perego, A. Haug, and I. Zenyuk, "Determining proton transport in pseudo catalyst layers using hydrogen pump DC and AC techniques," *Journal of the Electrochemical Society*, 2020.

[435]  L. Xing, W. Shi, H. Su, Q. Xu, P. K. Das, B. Mao, and K. Scott, "Membrane electrode assemblies for PEM fuel cells: A review of functional graded design and optimization," *Energy*, vol. 177, pp. 445–464, 2019.

[436]  T. Reshetenko and A. Kulikovsky, "On the origin of high frequency impedance feature in a PEM fuel cell," *Journal of The Electrochemical Society*, vol. 166, no. 15, F1253–F1257, 2019.

[437]  T Romero-Castanon, L. Arriaga, and U Cano-Castillo, "Impedance spectroscopy as a tool in the evaluation of MEA's," *Journal of power sources*, vol. 118, no. 1-2, pp. 179–182, 2003.

[438]  M. C. Lefebvre, R. B. Martin, and P. G. Pickup, "Characterization of ionic conductivity profiles within proton exchange membrane fuel cell gas diffusion electrodes by impedance spectroscopy," *Electrochemical and Solid State Letters*, vol. 2, no. 6, p. 259, 1999.

[439]  V. Paganin, C. Oliveira, E. Ticianelli, T. Springer, and E. Gonzalez, "Modelistic interpretation of the impedance response of a polymer electrolyte fuel cell," *Electrochimica Acta*, vol. 43, no. 24, pp. 3761–3766, 1998.

[440]  F. J. Pinar, N. Pilinski, M. Rastedt, and P. Wagner, "Performance of a high-temperature PEM fuel cell operated with oxygen enriched cathode air and hydrogen from synthetic reformate," *International Journal of Hydrogen Energy*, vol. 40, no. 15, pp. 5432–5438, 2015.

[441]  T. Reshetenko and A. Kulikovsky, "PEM fuel cell characterization by means of the physical model for impedance spectra," *Journal of The Electrochemical Society*, vol. 162, no. 7, F627, 2015.

[442]  G. Inoue, K. Yokoyama, J. Ooyama, T. Terao, T. Tokunaga, N. Kubo, and M. Kawase, "Theoretical examination of effective oxygen diffusion coefficient and electrical conductivity of polymer electrolyte fuel cell porous components," *Journal of Power Sources*, vol. 327, pp. 610–621, 2016.

[443]  S. Shukla, F. Wei, M. Mandal, J. Zhou, M. S. Saha, J. Stumper, and M. Secanell, "Determination of PEFC gas diffusion layer and catalyst layer porosity utilizing Archimedes principle," *Journal of The Electrochemical Society*, vol. 166, no. 15, F1142–F1147, 2019.

[444]  G. Inoue and M. Kawase, "Effect of porous structure of catalyst layer on effective oxygen diffusion coefficient in polymer electrolyte fuel cell," *Journal of Power Sources*, vol. 327, pp. 1–10, 2016.

[445]  G. S. Harzer, A. Orfanidi, H. El-Sayed, P. Madkikar, and H. A. Gasteiger, "Tailoring catalyst morphology towards high performance for low Pt loaded PEMFC cathodes," *Journal of The Electrochemical Society*, vol. 165, no. 10, F770, 2018.

[446]  A. D. Taylor, E. Y. Kim, V. P. Humes, J. Kizuka, and L. T. Thompson, "Inkjet printing of carbon supported platinum 3-D catalyst layers for use in fuel cells," *Journal of Power Sources*, vol. 171, no. 1, pp. 101–106, 2007.

[447]  V. Berejnov, M. Saha, D. Susac, J. Stumper, M. West, and A. P. Hitchcock, "Advances in structural characterization using soft x-ray scanning transmission microscopy (STXM): Mapping and measuring porosity in PEM-FC catalyst layers," *ECS Transactions*, vol. 80, no. 8, p. 241, 2017.

[448]  H. Arai, M. Irita, and N. Katayama, "Investigation of multilayered catalyst layers for polymer electrolyte fuel cells by electrospray deposition," *ECS Transactions*, vol. 98, no. 9, p. 333, 2020.

[449]  A Fischer, J Jindra, and H Wendt, "Porosity and catalyst utilization of thin layer cathodes in air operated PEM-fuel cells," *Journal of Applied Electrochemistry*, vol. 28, no. 3, pp. 277–282, 1998.

[450]  S. Gamburzev and A. J. Appleby, "Recent progress in performance improvement of the proton exchange membrane fuel cell (PEMFC)," *Journal of power sources*, vol. 107, no. 1, pp. 5–12, 2002.

[451]  M. K. Debe, A. K. Schmoeckel, G. D. Vernstrom, and R. Atanasoski, "High voltage stability of nanostructured thin film catalysts for PEM fuel cells," *Journal of Power Sources*, vol. 161, no. 2, pp. 1002–1011, 2006.

[452]  M. K. Debe, R. T. Atanasoski, and A. J. Steinbach, "Nanostructured thin film electrocatalysts-current status and future potential," *ECS transactions*, vol. 41, no. 1, p. 937, 2011.

[453]  M. K. Debe, "Electrocatalyst approaches and challenges for automotive fuel cells," *Nature*, vol. 486, no. 7401, pp. 43–51, 2012.

[454]  M. K. Debe, "Tutorial on the fundamental characteristics and practical properties of nanostructured thin film (NSTF) catalysts," *Journal of the Electrochemical Society*, vol. 160, no. 6, F522, 2013.

[455]  L. Dunsmore and S. Litster, "Parametric modeling study of PEM fuel cell with platinum group metal-free cathode catalyst layer," in *ECS Meeting Abstracts*, IOP Publishing, 2020, p. 2099.

[456]  C.-J. Tseng and S.-K. Lo, "Effects of microstructure characteristics of gas diffusion layer and microporous layer on the performance of PEMFC," *Energy conversion and management*, vol. 51, no. 4, pp. 677–684, 2010.

[457]  G.-G. Park, Y.-J. Sohn, T.-H. Yang, Y.-G. Yoon, W.-Y. Lee, and C.-S. Kim, "Effect of PTFE contents in the gas diffusion media on the performance of PEMFC," *Journal of Power Sources*, vol. 131, no. 1-2, pp. 182–187, 2004.

[458] D Gerteisen, T Heilmann, and C Ziegler, "Enhancing liquid water transport by laser perforation of a GDL in a PEM fuel cell," *Journal of Power Sources*, vol. 177, no. 2, pp. 348–354, 2008.

[459] C. Hartnig, I. Manke, R. Kuhn, S. Kleinau, J. Goebbels, and J. Banhart, "High-resolution in-plane investigation of the water evolution and transport in PEM fuel cells," *Journal of Power Sources*, vol. 188, no. 2, pp. 468–474, 2009.

[460] J. T. Gostick, M. A. Ioannidis, M. D. Pritzker, and M. W. Fowler, "Impact of liquid water on reactant mass transfer in PEM fuel cell electrodes," *Journal of the Electrochemical Society*, vol. 157, no. 4, B563, 2010.

[461] D. Ziegler, "Liquid water management in gas diffusion layers (GDL) for proton exchange membrane fuel cells (PEMFC)," Bachelor's thesis, Hochschule Mannheim / University of Alberta, 2020.

[462] F.-B. Weng, C.-Y. Hsu, and M.-C. Su, "Experimental study of micro-porous layers for PEMFC with gradient hydrophobicity under various humidity conditions," *International journal of hydrogen energy*, vol. 36, no. 21, pp. 13 708–13 714, 2011.

[463] Y. Nagai, J. Eller, T. Hatanaka, S. Yamaguchi, S. Kato, A. Kato, F. Marone, H. Xu, and F. N. Büchi, "Improving water management in fuel cells through microporous layer modifications: Fast operando tomographic imaging of liquid water," *Journal of Power Sources*, vol. 435, p. 226 809, 2019.

[464] H. Tang, S. Wang, M. Pan, and R. Yuan, "Porosity-graded micro-porous layers for polymer electrolyte membrane fuel cells," *Journal of power sources*, vol. 166, no. 1, pp. 41–46, 2007.

[465] J. H. Chun, D. H. Jo, S. G. Kim, S. H. Park, C. H. Lee, E. S. Lee, J.-Y. Jyoung, and S. H. Kim, "Development of a porosity-graded micro porous layer using thermal expandable graphite for proton exchange membrane fuel cells," *Renewable energy*, vol. 58, pp. 28–33, 2013.

[466] T. Kitahara, H. Nakajima, and K. Mori, "Hydrophilic and hydrophobic double microporous layer coated gas diffusion layer for enhancing performance of polymer electrolyte fuel cells under no-humidification at the cathode," *Journal of Power Sources*, vol. 199, pp. 29–36, 2012.

[467] T. Kitahara, H. Nakajima, M. Inamoto, and M. Morishita, "Novel hydrophilic and hydrophobic double microporous layer coated gas diffusion layer to enhance performance of polymer electrolyte fuel cells under both low and high humidity," *Journal of power sources*, vol. 234, pp. 129–138, 2013.

[468] T. Kitahara, H. Nakajima, M. Inamoto, and K. Shinto, "Triple microporous layer coated gas diffusion layer for performance enhancement of polymer electrolyte fuel cells under both low and high humidity conditions," *Journal of Power Sources*, vol. 248, pp. 1256–1263, 2014.

[469]  T. Kitahara, H. Nakajima, and K. Okamura, "Gas diffusion layers coated with a microporous layer containing hydrophilic carbon nanotubes for performance enhancement of polymer electrolyte fuel cells under both low and high humidity conditions," *Journal of Power Sources*, vol. 283, pp. 115–124, 2015.

[470]  T. Kitahara, H. Nakajima, and K. Ishikawa, "Microporous layer-coated gas diffusion layer for performance enhancement of polymer electrolyte fuel cells without humidification using anode gas recirculation," *Journal of The Electrochemical Society*, vol. 163, no. 13, F1366, 2016.

[471]  M. Secanell, A. Jarauta, A. Kosakian, M. Sabharwal, and J. Zhou, "PEM fuel cells, modeling," in *Encyclopedia of Sustainability Science and Technology*, R. A. Meyers, Ed. New York, NY: Springer New York, 2017, pp. 1–61, ISBN: 978-1-4939-2493-6. DOI: 10.1007/978-1-4939-2493-6_1019-1.

[472]  R. B. Bird, W. E. Stewart, and E. N. Lightfoot, *Transport Phenomena*, second edition. Wiley international, 2002.

[473]  A. Z. Weber and J. Newman, "Modeling transport in polymer-electrolyte fuel cells," *Chemical reviews*, vol. 104, no. 10, pp. 4679–4726, 2004.

[474]  M Secanell, K Karan, A Suleman, and N Djilali, "Multi-variable optimization of PEMFC cathodes using an agglomerate model," *Electrochimica Acta*, vol. 52, no. 22, pp. 6318–6337, 2007.

[475]  C. Ziegler and D. Gerteisen, "Validity of two-phase polymer electrolyte membrane fuel cell models with respect to the gas diffusion layer," *Journal of Power Sources*, vol. 188, no. 1, pp. 184–191, 2009.

[476]  S. Kim and M. M. Mench, "Investigation of temperature-driven water transport in polymer electrolyte fuel cell: Thermo-osmosis in membranes," *Journal of Membrane Science*, vol. 328, no. 1-2, pp. 113–120, 2009.

[477]  F. A. Dullien, *Porous media: Fluid transport and pore structure*. Academic press, 2012.

[478]  G. A. Martynov and R. R. Salem, *Electrical double layer at a metal-dilute electrolyte solution interface*. Springer Science & Business Media, 1983.

[479]  D. Pletcher, R. Greff, R. Peat, L. M. Peter, and J. Robinson, *Instrumental methods in electrochemistry*. Elsevier, 2001.

[480]  D. Caballero Flores, "Analysis of proton exchange membrane fuel cell (PEMFC) design parameters by simulation using OpenFCST," Master's thesis, Universitat Politècnica de Catalunya / University of Alberta, 2018.

[481]  M. M. Tomadakis and S. V Sotirchos, "Ordinary and transition regime diffusion in random fiber structures," *AIChE Journal*, vol. 39, no. 3, pp. 397–412, 1993.

[482]  G. L. Vignoles, "Modelling binary, Knudsen and transition regime diffusion inside complex porous media," *Le Journal de Physique IV*, vol. 5, no. C5, pp. C5–159, 1995.

[483]  C. K. Ho and S. W. Webb, *Gas transport in porous media.* Springer, 2006, vol. 20.

[484]  M Eikerling, A. S. Ioselevich, and A. A. Kornyshev, "How good are the electrodes we use in PEFC? (Understanding structure vs. performance of membrane-electrode assemblies)," *Fuel Cells*, vol. 4, no. 3, pp. 131–140, 2004.

[485]  P. Krtil, A. Trojánek, and Z. Samec, "Kinetics of water sorption in Nafion thin films: Quartz crystal microbalance study," *The Journal of Physical Chemistry B*, vol. 105, no. 33, pp. 7979–7983, 2001.

[486]  P. Virtanen, R. Gommers, T. E. Oliphant, M. Haberland, T. Reddy, D. Cournapeau, E. Burovski, P. Peterson, W. Weckesser, J. Bright, *et al.*, "SciPy 1.0: Fundamental algorithms for scientific computing in Python," *Nature methods*, vol. 17, no. 3, pp. 261–272, 2020.

[487]  K.-D. Kreuer, "The role of internal pressure for the hydration and transport properties of ionomers and polyelectrolytes," *Solid State Ionics*, vol. 252, pp. 93–101, 2013.

[488]  L. Xing, P. K. Das, X. Song, M. Mamlouk, and K. Scott, "Numerical analysis of the optimum membrane/ionomer water content of PEMFCs: The interaction of nafion® ionomer content and cathode relative humidity," *Applied Energy*, vol. 138, pp. 242–257, 2015.

[489]  A. Z. Weber and J. Newman, "Transport in polymer-electrolyte membranes II. Mathematical model," *Journal of The Electrochemical Society*, vol. 151, no. 2, A311–A325, 2004.

[490]  S. Ge, X. Li, B. Yi, and I.-M. Hsing, "Absorption, desorption, and transport of water in polymer electrolyte membranes for fuel cells," *Journal of the Electrochemical Society*, vol. 152, no. 6, A1149–A1157, 2005.

[491]  S. Motupally, A. J. Becker, and J. W. Weidner, "Diffusion of water in Nafion 115 membranes," *Journal of The Electrochemical Society*, vol. 147, no. 9, pp. 3171–3177, 2000.

[492]  X. Ye and C.-Y. Wang, "Measurement of water transport properties through membrane-electrode assemblies: I. Membranes," *Journal of the Electrochemical Society*, vol. 154, no. 7, B676, 2007.

[493]  S. Ge, B. Yi, and P. Ming, "Experimental determination of electro-osmotic drag coefficient in nafion membrane for fuel cells," *Journal of The Electrochemical Society*, vol. 153, no. 8, A1443–A1450, 2006.

[494]  W. Braff and C. K. Mittelsteadt, "Electroosmotic drag coefficient of proton exchange membrane as a function of relative humidity," *ECS Transactions*, vol. 16, no. 2, p. 309, 2008.

[495]  F. Xu, S. Leclerc, D. Stemmelen, J.-C. Perrin, A. Retournard, and D. Canet, "Study of electro-osmotic drag coefficients in Nafion membrane in acid, sodium and potassium forms by electrophoresis NMR," *Journal of membrane science*, vol. 536, pp. 116–122, 2017.

[496] R. Bock, A. Shum, T. Khoza, F. Seland, N. Hussain, I. V. Zenyuk, and O. S. Burheim, "Experimental study of thermal conductivity and compression measurements of the gdl-mpl interfacial composite region," *ECS Transactions*, vol. 75, no. 14, pp. 189–199, 2016.

[497] P. Dobson, C. Lei, T. Navessin, and M. Secanell, "Characterization of the PEM fuel cell catalyst layer microstructure by nonlinear least-squares parameter estimation," *Journal of the Electrochemical Society*, vol. 159, no. 5, B514–B523, 2012.

[498] M. Khandelwal and M. Mench, "Direct measurement of through-plane thermal conductivity and contact resistance in fuel cell materials," *Journal of Power Sources*, vol. 161, no. 2, pp. 1106–1115, 2006.

[499] O. Burheim, P. J. S. Vie, J. G. Pharoah, and S. Kjelstrup, "Ex situ measurements of through-plane thermal conductivities in a polymer electrolyte fuel cell," *Journal of Power Sources*, vol. 195, no. 1, pp. 249–256, 2010.

[500] O. S. Burheim, H. Su, S. Pasupathi, J. G. Pharoah, and B. G. Pollet, "Thermal conductivity and temperature profiles of the micro porous layers used for the polymer electrolyte membrane fuel cell," *International Journal of Hydrogen Energy*, vol. 38, no. 20, pp. 8437–8447, 2013.

[501] J. Bear, *Dynamics of fluids in porous media*. Courier Corporation, 2013.

[502] S. Whitaker, *The method of volume averaging*, ser. Theory and applications of transport in porous media: v. 13. Dordrecht; Boston: Kluwer Academic, 1999.

[503] K. Atkinson, W. Han, and D. E. Stewart, *Numerical solution of ordinary differential equations*. John Wiley & Sons, 2009.

[504] E. Haier and G. Wanner, *Solving Ordinary Differential Equations II: Stiff and Differential-Algebraic Problems*. Springer-Verlag Berlin Heidelberg, 1996, ISBN: 978-3-642-05220-0.

[505] U. M. Ascher and L. R. Petzold, *Computer methods for ordinary differential equations and differential-algebraic equations*. SIAM, 1998, vol. 61.

[506] E. Haier, S. Nørsett, and G. Wanner, *Solving Ordinary Differential Equations I: Nonstiff Problems*. Springer-Verlag Berlin Heidelberg, 1993, ISBN: 978-3-540-78862-1.

[507] M. Sofroniou and R. Knapp, *Advanced numerical differential equation solving in Mathematica*, http://www.johnboccio.com/MathematicaTutorials/05_AdvancedNumericalDifferentialEquationSolvingInMathematica.pdf, 2008, Accessed November 21, 2016.

[508] R. Ashino, M. Nagase, and R. Vaillancourt, "Behind and beyond the MATLAB ODE suite," *Computers & Mathematics with Applications*, vol. 40, no. 4, pp. 491–512, 2000.

[509] E. Hairer and G. Wanner, "Stiff differential equations solved by Radau methods," *Journal of Computational and Applied Mathematics*, vol. 111, no. 1, pp. 93–111, 1999.

[510]  L. Petzold, "A description of DASSL: A differential/algebraic system solver," in *Proc. IMACS World Congress*, 1982, pp. 430–432.

[511]  L. Petzold, "Automatic selection of methods for solving stiff and nonstiff systems of ordinary differential equations," *SIAM journal on scientific and statistical computing*, vol. 4, no. 1, pp. 136–148, 1983.

[512]  K. Radhakrishnan and A. Hindmarsh, "Description and use of LSODE, the Livermore solver for ordinary differential equations," Lawrence Livermore National Lab., CA (United States), Tech. Rep., 1993.

[513]  A. Hindmarsh, "ODEPACK. A collection of ODE system solvers," Lawrence Livermore National Lab., CA (United States), Tech. Rep., 1992.

[514]  P. Brown, G. Byrne, and A. Hindmarsh, "VODE: A variable-coefficient ODE solver," *SIAM journal on scientific and statistical computing*, vol. 10, no. 5, pp. 1038–1051, 1989.

[515]  A. C. Hindmarsh, P. N. Brown, K. E. Grant, S. L. Lee, R. Serban, D. E. Shumaker, and C. S. Woodward, "SUNDIALS: Suite of nonlinear and differential/algebraic equation solvers," *ACM Transactions on Mathematical Software (TOMS)*, vol. 31, no. 3, pp. 363–396, 2005.

[516]  L. Shampine and M. Reichelt, "The MATLAB ODE suite," *SIAM journal on scientific computing*, vol. 18, no. 1, pp. 1–22, 1997.

[517]  H. Langtangen and L. Wang, *A tutorial for the odespy interface to ODE solvers*, http://hplgit.github.io/odespy/doc/pub/tutorial/odespy.pdf, 2015, Accessed March 31, 2021.

[518]  R. Grigorieff, "Stability of multistep-methods on variable grids," *Numerische Mathematik*, vol. 42, no. 3, pp. 359–377, 1983.

[519]  M. Calvo, T. Grande, and R. Grigorieff, "On the zero stability of the variable order variable stepsize BDF-formulas," *Numerische Mathematik*, vol. 57, no. 1, pp. 39–50, 1990.

[520]  N. Guglielmi and M. Zennaro, "On the zero-stability of variable stepsize multistep methods: The spectral radius approach," *Numerische Mathematik*, vol. 88, no. 3, pp. 445–458, 2001.

[521]  S. Eckert, H. Baaser, D. Gross, and O. Scherf, "A BDF2 integration method with step size control for elasto-plasticity," *Computational Mechanics*, vol. 34, no. 5, pp. 377–386, 2004.

[522]  D. Wang and S. Ruuth, "Variable step-size implicit-explicit linear multistep methods for time-dependent partial differential equations," *Journal of Computational Mathematics*, pp. 838–855, 2008.

[523]  L. Liu, F. Felgner, and G. Frey, "Comparison of 4 numerical solvers for stiff and hybrid systems simulation," in *Emerging Technologies and Factory Automation (ETFA), 2010 IEEE Conference on*, IEEE, 2010, pp. 1–8.

[524] J. Kanney, C. Miller, and D. Barry, "Comparison of fully coupled approaches for approximating nonlinear transport and reaction problems," *Advances in Water Resources*, vol. 26, no. 4, pp. 353–372, 2003.

[525] A. Sandu, J. Verwer, M. Van Loon, G. Carmichael, F. Potra, D. Dabdub, and J. Seinfeld, "Benchmarking stiff ODE solvers for atmospheric chemistry problems I: Implicit versus explicit," *CWI Report NM-R9603 and Report in Computational Mathematics*, no. 85, 1996.

[526] A. Hay, S. Etienne, D. Pelletier, and A. Garon, "Hp-Adaptive time integration based on the BDF for viscous flows," *Journal of Computational Physics*, vol. 291, pp. 151–176, 2015.

[527] L. F. Shampine, "Local error estimation by doubling," *Computing*, vol. 34, no. 2, pp. 179–190, 1985.

[528] B. Belfort, J. Carrayrou, and F. Lehmann, "Implementation of richardson extrapolation in an efficient adaptive time stepping method: Applications to reactive transport and unsaturated flow in porous media," *Transport in porous media*, vol. 69, no. 1, pp. 123–138, 2007.

[529] I. Faragó, Á. Havasi, and Z. Zlatev, "Efficient implementation of stable richardson extrapolation algorithms," *Computers & Mathematics with Applications*, vol. 60, no. 8, pp. 2309–2325, 2010.

[530] P. R. Turner, *Numerical analysis*. Macmillan, 1994.

[531] H. P. Langtangen and S. Linge, *Finite difference computing with PDEs: A modern software approach*. Springer Nature, 2017.

[532] M. B. Allen III and E. L. Isaacson, *Numerical analysis for applied science, second edition*. John Wiley & Sons, 2019.

[533] G. E. Forsythe, M. A. Malcolm, and C. B. Moler, *Computer Methods for Mathematical Computationss*. Prentice Hall New Jersey, 1977.

[534] W. H. Press, S. A. Teukolsky, W. T. Vetterling, and B. P. Flannery, *Numerical recipes: The art of scientific computing*, third edition. Cambridge University Press, 2007.

[535] T. Durbin and D. Delemos, "Adaptive underrelaxation of Picard iterations in ground water models," *Groundwater*, vol. 45, no. 5, pp. 648–651, 2007.

[536] D. G. Luenberger, *Optimization by vector space methods*. John Wiley & Sons, 1997.

[537] G. Strang, *Calculus*. Wellesley-Cambridge Press, 1991.

[538] C. T. Kelley, *Iterative methods for linear and nonlinear equations*. SIAM, 1995.

[539] C. T. Kelley, *Solving nonlinear equations with Newton's method*. SIAM, 2003.

[540] J. N. Reddy, *Introduction to the finite element method*. McGraw-Hill Education, 2019.

[541]  D. Kelly, D. S. Gago, O. Zienkiewicz, I Babuska, *et al.*, "A posteriori error analysis and adaptive processes in the finite element method: Part I — Error analysis," *International journal for numerical methods in engineering*, vol. 19, no. 11, pp. 1593–1619, 1983.

[542]  T. A. Davis, "Algorithm 832: UMFPACK V4. 3 — An unsymmetric-pattern multifrontal method," *ACM Transactions on Mathematical Software (TOMS)*, vol. 30, no. 2, pp. 196–199, 2004.

[543]  T. A. Davis, "A column pre-ordering strategy for the unsymmetric-pattern multifrontal method," *ACM Transactions on Mathematical Software (TOMS)*, vol. 30, no. 2, pp. 165–195, 2004.

[544]  T. A. Davis, *Direct methods for sparse linear systems*. SIAM, 2006.

[545]  P. R. Amestoy, I. S. Duff, J.-Y. L'Excellent, and J. Koster, "MUMPS: A general purpose distributed memory sparse solver," in *International Workshop on Applied Parallel Computing*, Springer, 2000, pp. 121–130.

[546]  *SuiteSparse: A suite of sparse matrix software (official website)*, https://people.engr.tamu.edu/davis/suitesparse.html, Accessed May 31, 2021.

[547]  *PETSc/TAO: Portable, Extensible Toolkit for Scientific Computation, Toolkit for Advanced Optimization*, https://www.mcs.anl.gov/petsc/, Accessed May 31, 2021.

[548]  E. Bueler, *PETSc for Partial Differential Equations: Numerical Solutions in C and Python*. SIAM, 2020.

[549]  H. Wiese and K. G. Weil, "An efficient fourier transform algorithm for frequency domains of several decades using logarithmically spaced time samples," *IEEE Transactions on Acoustics, Speech, and Signal Processing*, vol. 36, no. 7, pp. 1096–1099, 1988.

[550]  B. Bullecks, R. Suresh, and R. Rengaswamy, "Rapid impedance measurement using chirp signals for electrochemical system analysis," *Computers & Chemical Engineering*, vol. 106, pp. 421–436, 2017.

[551]  R. Suresh, S. Swaminathan, and R. Rengaswamy, "Rapid impedance spectroscopy using dual phase shifted chirp signals for electrochemical applications," *International Journal of Hydrogen Energy*, vol. 45, no. 17, pp. 10 536–10 548, 2020.

[552]  J. Keiner, S. Kunis, and D. Potts, "Using NFFT 3 — a software library for various nonequispaced fast Fourier transforms," *ACM Transactions on Mathematical Software (TOMS)*, vol. 36, no. 4, p. 19, 2009.

[553]  A. J. Wheeler and A. R. Ganji, *Introduction to engineering experimentation*, third edition. Prentice Hall New Jersey, 2010.

[554]  A. Ribes and C. Caremoli, "Salome platform component model for numerical simulation," in *31st annual international computer software and applications conference (COMPSAC 2007)*, IEEE, vol. 2, 2007, pp. 553–564.

[555]  *SALOME: The Open Source Integration Platform for Numerical Simulation)*, https://www.salome-platform.org/, Accessed May 1, 2021.

[556]  L. Xiong, L. Aldous, M. C. Henstridge, and R. G. Compton, "Investigation of the optimal transient times for chronoamperometric analysis of diffusion coefficients and concentrations in non-aqueous solvents and ionic liquids," *Analytical Methods*, vol. 4, no. 2, pp. 371–376, 2012.

[557]  A. D. Polyanin and V. E. Nazaikinskii, "Handbook of linear partial differential equations for engineers and scientists," 2016.

[558]  O. Østerby, "Five ways of reducing the crank–nicolson oscillations," *BIT Numerical Mathematics*, vol. 43, no. 4, pp. 811–822, 2003.

[559]  D. Pooley, "Numerical methods for nonlinear equations in option pricing," PhD thesis, University of Waterloo, 2003.

[560]  D. Britz, O. Østerby, and J. Strutwolf, "Minimum grid digital simulation of chronoamperometry at a disk electrode," *Electrochimica acta*, vol. 78, pp. 365–376, 2012.

[561]  D. Britz, K. Poulsen, and J. Strutwolf, "Reference values of the diffusion-limited current at a microdisk electrode," *Electrochimica acta*, vol. 50, no. 1, pp. 107–113, 2004.

[562]  T. F. Fuller, "Solid-polymer-electrolyte fuel cells," PhD thesis, University of California, Berkeley, 1992.

[563]  Lion Specialty Chemicals Co., Ltd., *KETJENBLACK Highly Electro-Conductive Carbon Black (Product Information)*, https://www.lion-specialty-chem.co.jp/en/product/carbon/carbon01.htm, Accessed on November 10, 2019.

[564]  *Properties and characteristics of graphite*, https://www.entegris.com/content/dam/web/resources/manuals-and-guides/manual-properties-and-characteristics-of-graphite-109441.pdf, Accessed May 14, 2021.

[565]  *Specific heats for metals*, https://www.engineeringtoolbox.com/specific-heat-metals-d_152.html, Accessed May 14, 2021.

[566]  *(PTFE) Polytetrafluoroethylene*, https://www.bearingworks.com/uploaded-assets/pdfs/retainers/ptfe-datasheet.pdf, Accessed May 14, 2021.

[567]  P. Mangal, "Experimental study of mass transport parameters of PEMFC porous media," Master's thesis, University of Alberta, 2014.

[568]  K. Cooper, "In situ PEM fuel cell electrochemical surface area & catalyst utilization measurement," *Fuel cell*, 2009.

[569]  M. Schönleber, D. Klotz, and E Ivers-Tiffée, "A method for improving the robustness of linear Kramers-Kronig validity tests," *Electrochimica Acta*, vol. 131, pp. 20–27, 2014.

[570]  K. Cooper and M. Smith, "Electrical test methods for on-line fuel cell ohmic resistance measurement," *Journal of Power Sources*, vol. 160, no. 2, pp. 1088–1095, 2006.

[571]  B. Jayasankar and K. Karan, "O2 electrochemistry on Pt: A unified multi-step model for oxygen reduction and oxide growth," *Electrochimica Acta*, vol. 273, pp. 367–378, 2018.

[572]  G. Maranzana, J. Mainka, O. Lottin, J. Dillet, A. Lamibrac, A. Thomas, and S. Didierjean, "A proton exchange membrane fuel cell impedance model taking into account convection along the air channel: On the bias between the low frequency limit of the impedance and the slope of the polarization curve," *Electrochimica Acta*, vol. 83, pp. 13–27, 2012.

[573]  A. Kulikovsky, "A model for local impedance of the cathode side of pem fuel cell with segmented electrodes," *Journal of the Electrochemical Society*, vol. 159, no. 7, F294–F300, 2012.

[574]  A. Lasia, "Modeling of impedance of porous electrodes," in *Modern Aspects of Electrochemistry, vol. 43*. Springer, 2008, pp. 67–137.

[575]  W. Sun, B. A. Peppley, and K. Karan, "An improved two-dimensional agglomerate cathode model to study the influence of catalyst layer structural parameters," *Electrochimica acta*, vol. 50, no. 16-17, pp. 3359–3374, 2005.

[576]  T. Reshetenko and A. Kulikovsky, "Impedance spectroscopy study of the PEM fuel cell cathode with nonuniform Nafion loading," *Journal of The Electrochemical Society*, vol. 164, no. 11, E3016–E3021, 2017.

[577]  G. Li and P. G. Pickup, "Ionic conductivity of PEMFC electrodes effect of Nafion loading," *Journal of The Electrochemical Society*, vol. 150, no. 11, pp. C745–C752, 2003.

[578]  I. Nitta, T. Hottinen, O. Himanen, and M. Mikkola, "Inhomogeneous compression of PEMFC gas diffusion layer: Part I. Experimental," *Journal of Power Sources*, vol. 171, no. 1, pp. 26–36, 2007.

[579]  H. Sadeghifar, "In-plane and through-plane electrical conductivities and contact resistances of a Mercedes-Benz catalyst-coated membrane, gas diffusion and micro-porous layers and a ballard graphite bipolar plate: Impact of humidity, compressive load and polytetrafluoroethylene," *Energy Conversion and Management*, vol. 154, pp. 191–202, 2017.

[580]  J Kleemann, F Finsterwalder, and W Tillmetz, "Characterisation of mechanical behaviour and coupled electrical properties of polymer electrolyte membrane fuel cell gas diffusion layers," *Journal of Power Sources*, vol. 190, no. 1, pp. 92–102, 2009.

[581]  M. Ismail, T Damjanovic, D. Ingham, M Pourkashanian, and A Westwood, "Effect of polytetrafluoroethylene-treatment and microporous layer-coating on the electrical conductivity of gas diffusion layers used in proton exchange membrane fuel cells," *Journal of Power Sources*, vol. 195, no. 9, pp. 2700–2708, 2010.

[582] D. R. Morris and J. T. Gostick, "Determination of the in-plane components of the electrical conductivity tensor in PEM fuel cell gas diffusion layers," *Electrochimica acta*, vol. 85, pp. 665–673, 2012.

[583] R De Levie, "On porous electrodes in electrolyte solutions—IV," *Electrochimica Acta*, vol. 9, no. 9, pp. 1231–1245, 1964.

[584] M. Lefebvre, Z. Qi, D. Rana, and P. G. Pickup, "Chemical synthesis, characterization, and electrochemical studies of poly (3, 4-ethylenedioxythiophene)/poly (styrene-4-sulfonate) composites," *Chemistry of materials*, vol. 11, no. 2, pp. 262–268, 1999.

[585] T. Reshetenko, A. Serov, M. Odgaard, G. Randolf, L. Osmieri, and A. Kulikovsky, "Electron and proton conductivity of Fe-NC cathodes for PEM fuel cells: A model-based electrochemical impedance spectroscopy measurement," *Electrochemistry Communications*, p. 106 795, 2020.

[586] M. Obermaier, A. S. Bandarenka, and C. Lohri-Tymozhynsky, "A comprehensive physical impedance model of polymer electrolyte fuel cell cathodes in oxygen-free atmosphere," *Scientific reports*, vol. 8, no. 1, pp. 1–9, 2018.

[587] T. Soboleva, Z. Xie, Z. Shi, E. Tsang, T. Navessin, and S. Holdcroft, "Investigation of the through-plane impedance technique for evaluation of anisotropy of proton conducting polymer membranes," *Journal of Electroanalytical Chemistry*, vol. 622, no. 2, pp. 145–152, 2008.

[588] A. Kulikovsky, "Hydrogen crossover impedance of a PEM fuel cell at open circuit," *Electrochimica Acta*, vol. 247, pp. 730–735, 2017.

[589] *Water - specific heat*, https://www.engineeringtoolbox.com/specific-heat-capacity-water-d_660.html, Accessed May 22, 2021.

[590] P. Mangal, M. Dumontier, N. Carrigy, and M. Secanell, "Measurements of permeability and effective in-plane gas diffusivity of gas diffusion media under compression," *ECS Transactions*, vol. 64, no. 3, p. 487, 2014.

[591] P. Mangal, L. M. Pant, N. Carrigy, M. Dumontier, V. Zingan, S. Mitra, and M. Secanell, "Experimental study of mass transport in PEMFCs: Through plane permeability and molecular diffusivity in GDLs," *Electrochimica Acta*, vol. 167, pp. 160–171, 2015.

[592] L. M. Pant, S. K. Mitra, and M. Secanell, "Absolute permeability and knudsen diffusivity measurements in pemfc gas diffusion layers and micro porous layers," *Journal of Power Sources*, vol. 206, pp. 153–160, 2012.

[593] A. Savitzky and M. J. E. Golay, "Smoothing and differentiation of data by simplified least squares procedures.," *Analytical chemistry*, vol. 36, no. 8, pp. 1627–1639, 1964.

[594] A. K. Singh and B. S. Bhadauria, "Finite difference formulae for unequal subintervals using Lagrange's interpolation formula," *Int. J. Math. Anal*, vol. 3, no. 17, p. 815, 2009.

[595] K. Dalbey, M. S. Eldred, G. Geraci, J. D. Jakeman, K. A. Maupin, J. A. Monschke, D. T. Seidl, L. P. Swiler, A. Tran, F. Menhorn, *et al.*, "Dakota, a multilevel parallel object-oriented framework for design optimization parameter estimation uncertainty quantification and sensitivity analysis: Version 6.12 theory manual.," Sandia National Lab.(SNL-NM), Albuquerque, NM (United States), Tech. Rep., 2020.

[596] J. T. Gostick, M. A. Ioannidis, M. W. Fowler, and M. D. Pritzker, "Wettability and capillary behavior of fibrous gas diffusion media for polymer electrolyte membrane fuel cells," *Journal of Power Sources*, vol. 194, no. 1, pp. 433–444, 2009.

[597] J. T. Gostick, M. A. Ioannidis, M. W. Fowler, and M. D. Pritzker, "Direct measurement of the capillary pressure characteristics of water–air–gas diffusion layer systems for PEM fuel cells," *Electrochemistry Communications*, vol. 10, no. 10, pp. 1520–1523, 2008.

[598] I. R. Harkness, N. Hussain, L. Smith, and J. D. B. Sharman, "The use of a novel water porosimeter to predict the water handling behaviour of gas diffusion media used in polymer electrolyte fuel cells," *Journal of Power Sources*, vol. 193, no. 1, pp. 122–129, 2009.

[599] T. G. Tranter, J. T. Gostick, A. D. Burns, and W. F. Gale, "Capillary hysteresis in neutrally wettable fibrous media: A pore network study of a fuel cell electrode," *Transport in porous media*, vol. 121, no. 3, pp. 597–620, 2018.

[600] A. A. Wong, M. J. Aziz, and S. Rubinstein, "Direct visualization of electrochemical reactions and comparison of commercial carbon papers in operando by fluorescence microscopy using a quinone-based flow cell," *ECS Transactions*, vol. 77, no. 11, p. 153, 2017.

[601] T. Koido, T. Furusawa, and K. Moriyama, "An approach to modeling two-phase transport in the gas diffusion layer of a proton exchange membrane fuel cell," *Journal of Power Sources*, vol. 175, no. 1, pp. 127–136, 2008.

[602] T. Nguyen, G. Lin, H. Ohn, D. Hussey, D. Jacobson, and M. Arif, "Measurements of two-phase flow properties of the porous media used in PEM fuel cells," *ECS transactions*, vol. 3, no. 1, p. 415, 2006.

[603] J. P. Owejan, T. Trabold, D. L. Jacobson, D. Baker, D. S. Hussey, and M. Arif, "In situ investigation of water transport in an operating PEM fuel cell using neutron radiography: Part 2 – Transient water accumulation in an interdigitated cathode flow field," *International Journal of Heat and Mass Transfer*, vol. 49, no. 25-26, pp. 4721–4731, 2006.

[604] J. R. Kracher, "Experimental analysis of transient water fluxes in PEM fuel cells," Master's thesis, University of Alberta, 2018.

[605] S. Kim and M. M. Mench, "Investigation of temperature-driven water transport in polymer electrolyte fuel cell: Phase-change-induced flow," *Journal of The Electrochemical Society*, vol. 156, no. 3, B353, 2009.

[606] A. Kosakian, M. Secanell, D. Novitski, and S. Holdcroft, "A numerical algorithm for estimation of oxygen transport properties in thin polymer membranes," 5th Annual CaRPE-FC Technical Review Meeting, Vancouver, BC, Canada, 2016.

[607] A. Kosakian, M. Secanell, D. Novitski, and S. Holdcroft, "Numerical estimation of oxygen transport properties in thin polymer membranes," in *Proceedings of the Canadian Society of Mechanical Engineering International Congress*, 2016.

[608] A. Kosakian, L. Padilla Urbina, A. Heaman, and M. Secanell, "A mathematical model for predicting the polarization curve hysteresis in proton exchange membrane fuel cells," in *Meeting Abstracts, Canadian Section of The Electrochemical Society*, 2018.

[609] A. Kosakian, L. Padilla Urbina, A. Heaman, and M. Secanell, "An open-source multiscale transient model for numerical characterization of proton exchange membrane fuel cells," Gordon Research Seminar, Smithfield, RI, USA, 2018.

[610] A. Kosakian, L. Padilla Urbina, A. Heaman, and M. Secanell, "An open-source multiscale transient model for numerical characterization of proton exchange membrane fuel cells," Gordon Research Conference, Smithfield, RI, USA, 2018.

[611] A. Kosakian, L. Padilla Urbina, A. Heaman, and M. Secanell, "An open-source multiscale transient model for numerical characterization of proton exchange membrane fuel cells," in *ECS Meeting Abstracts*, IOP Publishing, 2018, p. 1353.

[612] A. Kosakian, L. Padilla Urbina, A. Heaman, and M. Secanell, "An open-source multiscale transient model for numerical characterization of proton exchange membrane fuel cells," CREATE ME2 Annual Meeting - Energy Conversion and Storage Technologies, Calgary, AB, Canada, 2018.

[613] A. Kosakian, L. Padilla Urbina, A. Heaman, and M. Secanell, "An open-source transient model for numerical characterization of water management in proton exchange membrane fuel cells," CREATE ME2 Annual Meeting - Energy Conversion and Storage Technologies, Calgary, AB, Canada, 2019.

[614] A. Kosakian, L. Padilla Urbina, A. Heaman, and M. Secanell, "Analysis of single-phase water-management signatures in fuel-cell impedance spectra," 71st Annual Meeting of the International Society of Electrochemistry, Belgrade, Serbia, 2020.

[615] A. Kosakian, L. Padilla Urbina, A. Heaman, and M. Secanell, "Understanding fuel-cell impedance spectra via numerical modeling: A single-phase water-management study," in *ECS Meeting Abstracts*, IOP Publishing, 2020, p. 1607.

[616] A. Kosakian and M. Secanell, "A transient model for impedance analysis of proton-exchange-membrane fuel cells," Meeting Abstracts, Canadian Section of The Electrochemical Society, 2020.

# Appendix A: Relationship Between Pore-Size Distribution and Volume Averaging

The superficial and intrinsic averages [502] for the liquid phase are given by

$$\langle \phi \rangle = \frac{1}{V_{\mathrm{REV}}} \int\limits_{V_{\mathrm{lw}}} \phi \, dV$$

and

$$\langle \phi \rangle^{\mathrm{lw}} = \frac{1}{V_{\mathrm{lw}}} \int\limits_{V_{\mathrm{lw}}} \phi \, dV,$$

respectively, where $V_{\mathrm{REV}}$ is a representative elementary volume of the medium and $\phi$ is the averaged quantity. In this case, $\langle 1 \rangle = V_{\mathrm{lw}}/V_{\mathrm{REV}} = \varepsilon_{\mathrm{p}} s$ and $\langle \phi \rangle = \varepsilon_{\mathrm{p}} s \langle \phi \rangle^{\mathrm{lw}}$. Relation between volume averaging and pore-size distribution is straightforward:

$$\langle \phi \rangle = \frac{1}{V_{\mathrm{REV}}} \int\limits_{V_{\mathrm{lw}}} \phi \, dV = \underbrace{\frac{V_{\mathrm{p}}}{V_{\mathrm{REV}}}}_{\varepsilon_{\mathrm{p}}} \int\limits_{V_{\mathrm{lw}}} \phi \underbrace{\frac{dV}{V_{\mathrm{p}}}}_{dX} = \varepsilon_{\mathrm{p}} \int\limits_{r} \phi \frac{dX}{dr} dr, \tag{A.1}$$

$$\langle \phi \rangle^{\mathrm{lw}} = \frac{1}{V_{\mathrm{lw}}} \int\limits_{V_{\mathrm{lw}}} \phi \, dV = \underbrace{\frac{V_{\mathrm{p}}}{V_{\mathrm{lw}}}}_{1/s} \int\limits_{V_{\mathrm{lw}}} \phi \underbrace{\frac{dV}{V_{\mathrm{p}}}}_{dX} = \frac{1}{s} \int\limits_{r} \phi \frac{dX}{dr} dr. \tag{A.2}$$

Similarly, for the gas phase,

$$\langle \phi \rangle = -\frac{1}{V_{\mathrm{REV}}} \int\limits_{V_{\mathrm{g}}} \phi \, dV = -\underbrace{\frac{V_{\mathrm{p}}}{V_{\mathrm{REV}}}}_{\varepsilon_{\mathrm{p}}} \int\limits_{V_{\mathrm{g}}} \phi \underbrace{\frac{dV}{V_{\mathrm{p}}}}_{dX_{\mathrm{g}}} = \varepsilon_{\mathrm{p}} \int\limits_{r_{\mathrm{g}}} \phi \frac{dX}{dr} dr, \tag{A.3}$$

$$\langle \phi \rangle^{\mathrm{g}} = -\frac{1}{V_{\mathrm{g}}} \int\limits_{V_{\mathrm{g}}} \phi \, dV = -\underbrace{\frac{V_{\mathrm{p}}}{V_{\mathrm{g}}}}_{1/(1-s)} \int\limits_{V_{\mathrm{g}}} \phi \underbrace{\frac{dV}{V_{\mathrm{p}}}}_{dX_{\mathrm{g}}} = \frac{1}{1-s} \int\limits_{r_{\mathrm{g}}} \phi \frac{dX}{dr} dr. \tag{A.4}$$

Negative sign in the first two integrals in equations (A.3) and (A.4) is due to $dV < 0$ for the gas phase during liquid intrusion. The final results in equations (A.3) and (A.4) are obtained through the transition to the liquid-phase $dX$ from the gas-phase $dX_{\mathrm{g}} =$

$-dX$. Integration there is performed over $r_{\mathrm{g}}$, which denotes radii of gas-filled (liquid-free) pores.

Since the PSD model often involves integration of certain powers of $r$ with some constant weights, the following integration result is useful:

$$\int_r r^n \frac{dX}{dr} dr = \int_r r^n \sum_{i=\mathrm{HI,\,HO}} \sum_k \frac{F_i f_{i,k}}{r s_{i,k} \sqrt{2\pi}} \exp\left(-\left[\frac{\ln(r) - \ln(r_{i,k})}{s_{i,k}\sqrt{2}}\right]^2\right) dr$$

$$= \sum_{i=\mathrm{HI,\,HO}} \sum_k \frac{F_i f_{i,k}}{2} r_{i,k}^n \exp\left(\frac{n^2}{2}s_{i,k}^2\right) \mathrm{erf}\left(\frac{\ln(r) - \ln(r_{i,k})}{s_{i,k}\sqrt{2}} - \frac{n\sqrt{2}}{2}s_{i,k}\right) + C. \quad (\mathrm{A.5})$$

Additionally, some derivations shown in this work involve averaging of a product of two variables, $\langle \phi\psi \rangle$. In order to transform the average of the product into the product of the averages, one needs to use spatial decomposition [502]: $\phi = \langle\phi\rangle^{\mathrm{lw}} + \tilde{\phi}$, where $\tilde{\phi}$ is a spatial deviation. Then, the following is true:

$$\langle\phi\psi\rangle = \langle(\langle\phi\rangle^{\mathrm{lw}} + \tilde{\phi})(\langle\psi\rangle^{\mathrm{lw}} + \tilde{\psi})\rangle = \langle\langle\phi\rangle^{\mathrm{lw}}\langle\psi\rangle^{\mathrm{lw}} + O(\tilde{\phi}, \tilde{\psi})\rangle$$

$$\approx \langle\phi\rangle^{\mathrm{lw}}\langle\psi\rangle^{\mathrm{lw}} \underbrace{\langle 1\rangle}_{\varepsilon_{\mathrm{p}}s} = \langle\phi\rangle^{\mathrm{lw}}\langle\psi\rangle = \langle\phi\rangle\langle\psi\rangle^{\mathrm{lw}} = \frac{1}{\varepsilon_{\mathrm{p}}s}\langle\phi\rangle\langle\psi\rangle. \quad (\mathrm{A.6})$$

# Appendix B: Coupling Newton's Linearization and BDF Temporal Discretization

An example of coupling Newton's linearization and BDF temporal discretization is shown here for the fuel-cell-cathode model in OpenFCST that is governed by the following equations:

$$\varepsilon_p c_{tot} \frac{\partial x_{O_2}}{\partial t} - \nabla \cdot \left( c_{tot} D^{eff}_{O_2} \nabla x_{O_2} \right) = -\frac{j \left( x_{O_2}, \phi_{H^+}, \phi_{e^-} \right)}{4F}, \quad \text{(B.1)}$$

$$-C_{dl} \frac{\partial \phi_{e^-}}{\partial t} + C_{dl} \frac{\partial \phi_{H^+}}{\partial t} - \nabla \cdot \left( \sigma^{eff}_{H^+} \nabla \phi_{H^+} \right) = -j \left( x_{O_2}, \phi_{H^+}, \phi_{e^-} \right), \quad \text{(B.2)}$$

$$C_{dl} \frac{\partial \phi_{e^-}}{\partial t} - C_{dl} \frac{\partial \phi_{H^+}}{\partial t} - \nabla \cdot \left( \sigma^{eff}_{e^-} \nabla \phi_{e^-} \right) = j \left( x_{O_2}, \phi_{H^+}, \phi_{e^-} \right), \quad \text{(B.3)}$$

where $\varepsilon_p$ is porosity; $c_{tot}$ is total gas concentration; $x_{O_2}$ is molar fraction of oxygen; $D^{eff}_{O_2}$ is effective oxygen diffusivity; $j$ is volumetric faradaic current density; $C_{dl}$ is volumetric double-layer capacitance; $\phi_{e^-}$ and $\phi_{H^+}$ are potentials of the electronically and protonically conductive phases, respectively; $\sigma^{eff}_{e^-}$ and $\sigma^{eff}_{H^+}$ are effective conductivities of the said phases. Solver coupling is performed in a similar fashion in all other models. Spatial discretization is not considered here.

Applying the general BDF method (2.113) to (B.1)-(B.3), one obtains

$$\varepsilon_p \frac{c_{tot}}{\tau} \sum_{i=n-k+1}^{i=n+1} \left[ \alpha_i x_{O_2}^{(i)} \right] - \nabla \cdot \left( c_{tot} D^{eff}_{O_2} \nabla x_{O_2}^{(n+1)} \right) = -\frac{j^{(n+1)}}{4F},$$

$$\frac{C_{dl}}{\tau} \sum_{i=n-k+1}^{i=n+1} \left[ \alpha_i \left( \phi_{H^+}^{(i)} - \phi_{e^-}^{(i)} \right) \right] - \nabla \cdot \left( \sigma^{eff}_{H^+} \nabla \phi_{H^+}^{(n+1)} \right) = -j^{(n+1)},$$

$$\frac{C_{dl}}{\tau} \sum_{i=n-k+1}^{i=n+1} \left[ \alpha_i \left( \phi_{e^-}^{(i)} - \phi_{H^+}^{(i)} \right) \right] - \nabla \cdot \left( \sigma^{eff}_{e^-} \nabla \phi_{e^-}^{(n+1)} \right) = j^{(n+1)}.$$

where $j^{(n+1)} = j \left( x_{O_2}^{(n+1)}, \phi_{H^+}^{(n+1)}, \phi_{e^-}^{(n+1)} \right)$. These equations are nonlinear with respect to the solution vector

$$\boldsymbol{u}^{(n+1)} = \left( x_{O_2}^{(n+1)}, \phi_{H^+}^{(n+1)}, \phi_{e^-}^{(n+1)} \right)^{T}$$

from the new time layer with index $n + 1$. In Newton's method, it is approximated as $\boldsymbol{u}^{(n+1,m+1)} = \boldsymbol{u}^{(n+1,m)} + \delta\boldsymbol{u}$, $\boldsymbol{u}^{(n+1,0)} = \boldsymbol{u}^{(n)}$, where $\delta\boldsymbol{u}$ is the solution update. As a result, the diffusive terms are decomposed into two parts,

$$\nabla \cdot \left( A_\alpha \nabla u_\alpha^{(n+1,m+1)} \right) = \nabla \cdot \left( A_\alpha \nabla u_\alpha^{(n+1,m)} \right) + \nabla \cdot \left( A_\alpha \nabla \delta u_\alpha \right), \qquad \text{(B.4)}$$

where subscript $\alpha$ indicates the solution-variable index and $A_\alpha$ is the effective diffusion coefficient or the effective conductivity. The nonlinear expression for the volumetric current density is linearized using the Taylor series as

$$f_\alpha \left( \boldsymbol{u}^{(n+1,m+1)} \right) = f_\alpha(\boldsymbol{u}^{(n+1,m)} + \delta\boldsymbol{u}) \approx f_\alpha \left( \boldsymbol{u}^{(n+1,m)} \right) + \sum_\beta \left. \frac{\partial f_\alpha(\boldsymbol{u})}{\partial u_\beta} \right|_{\boldsymbol{u}=\boldsymbol{u}^{(n+1,m)}} \delta u_\beta. \quad \text{(B.5)}$$

Rewriting now the system of equations with respect to the new solution variable $\delta\boldsymbol{u}$, one arrives at

$$\left( \varepsilon_{\mathrm{p}} \frac{c_{\mathrm{tot}}}{\tau} \alpha_{n+1} - \nabla \cdot \left( c_{\mathrm{tot}} D_{\mathrm{O_2}}^{\mathrm{eff}} \nabla \right) + \frac{1}{4F} \frac{\partial j^{(n+1,m)}}{\partial x_{\mathrm{O_2}}} \right) \delta x_{\mathrm{O_2}}$$

$$+ \frac{1}{4F} \frac{\partial j^{(n+1,m)}}{\partial \phi_{\mathrm{H^+}}} \delta\phi_{\mathrm{H^+}} + \frac{1}{4F} \frac{\partial j^{(n+1,m)}}{\partial \phi_{\mathrm{e^-}}} \delta\phi_{\mathrm{e^-}}$$

$$= -\varepsilon_{\mathrm{p}} \frac{c_{\mathrm{tot}}}{\tau} \left[ \alpha_{n+1} x_{\mathrm{O_2}}^{(n+1,m)} + \sum_{i=n-k+1}^{i=n} \alpha_i x_{\mathrm{O_2}}^{(i)} \right] + \nabla \cdot \left( c_{\mathrm{tot}} D_{\mathrm{O_2}}^{\mathrm{eff}} \nabla x_{\mathrm{O_2}}^{(n+1,m)} \right) - \frac{j^{(n+1,m)}}{4F},$$

$$\frac{\partial j^{(n+1,m)}}{\partial x_{\mathrm{O_2}}} \delta x_{\mathrm{O_2}} + \left( \frac{C_{\mathrm{dl}}}{\tau} \alpha_{n+1} - \nabla \cdot \left( \sigma_{\mathrm{H^+}}^{\mathrm{eff}} \nabla \right) + \frac{\partial j^{(n+1,m)}}{\partial \phi_{\mathrm{H^+}}} \right) \delta\phi_{\mathrm{H^+}}$$

$$+ \left( \frac{\partial j^{(n+1,m)}}{\partial \phi_{\mathrm{e^-}}} - \frac{C_{\mathrm{dl}}}{\tau} \alpha_{n+1} \right) \delta\phi_{\mathrm{e^-}}$$

$$= \frac{C_{\mathrm{dl}}}{\tau} \left[ \alpha_{n+1} \left( \phi_{\mathrm{e^-}}^{(n+1,m)} - \phi_{\mathrm{H^+}}^{(n+1,m)} \right) + \sum_{i=n-k+1}^{i=n} \left[ \alpha_i \left( \phi_{\mathrm{e^-}}^{(i)} - \phi_{\mathrm{H^+}}^{(i)} \right) \right] \right]$$

$$+ \nabla \cdot \left( \sigma_{\mathrm{m}} \nabla \phi_{\mathrm{H^+}}^{(n+1,m)} \right) - j^{(n+1,m)},$$

$$- \frac{\partial j^{(n+1,m)}}{\partial x_{\mathrm{O_2}}} \delta x_{\mathrm{O_2}} - \left( \frac{C_{\mathrm{dl}}}{\tau} \alpha_{n+1} + \frac{\partial j^{(n+1,m)}}{\partial \phi_{\mathrm{H^+}}} \right) \delta\phi_{\mathrm{H^+}}$$

$$+ \left( \frac{C_{\mathrm{dl}}}{\tau} \alpha_{n+1} - \nabla \cdot \left( \sigma_{\mathrm{e^-}}^{\mathrm{eff}} \nabla \right) - \frac{\partial j^{(n+1,m)}}{\partial \phi_{\mathrm{e^-}}} \right) \delta\phi_{\mathrm{e^-}}$$

$$= \frac{C_{\mathrm{dl}}}{\tau} \left[ \alpha_{n+1} \left( \phi_{\mathrm{H^+}}^{(n+1,m)} - \phi_{\mathrm{e^-}}^{(n+1,m)} \right) + \sum_{i=n-k+1}^{i=n} \left[ \alpha_i \left( \phi_{\mathrm{H^+}}^{(i)} - \phi_{\mathrm{e^-}}^{(i)} \right) \right] \right]$$

$$+ \nabla \cdot \left( \sigma_{\mathrm{s}} \nabla \phi_{\mathrm{e^-}}^{(n+1,m)} \right) + j^{(n+1,m)}.$$

These equations represent two iterative processes: outer time-layer iterations with index $n$ and inner Newton iterations with index $m$.

# Appendix C: Derivation of equation (5.7) from equation (5.2)

Consider a problem of one-dimensional proton transport in a cathode catalyst layer with fast oxygen and electron transport. Under the assumption of Tafel kinetics (equation (2.52)) and constant and uniform protonic conductivity and temperature, equation (5.2) is transformed into

$$-C_{dl}\frac{\partial \eta}{\partial t} - \sigma_{H^+}^{eff}\frac{\partial^2 \phi_{H^+}}{\partial x^2} = -\xi \exp\left(-\frac{\eta}{b}\right), \tag{C.1}$$

where we denote $\xi = i_0 A_v \left(c_{O_2}^{cat|i}/c_{O_2}^{ref}\right)^\gamma$ for convenience. Based on the definition of the overpotential ($\eta = \phi_{e^-} - \phi_{H^+} - E_{th}$) and the assumption that the layer is highly electronically conductive, $\phi_{H^+}$ can be replaced with $-\eta$ under the spatial derivative in equation (C.1) (the theoretical half-cell potential $E_{th}$ is independent of $t$ and $x$ in the considered case). When overpotential $\eta$ is small, the exponent in equation (C.1) can be linearized to give

$$-C_{dl}\frac{\partial \eta}{\partial t} + \sigma_{H^+}^{eff}\frac{\partial^2 \eta}{\partial x^2} = -\xi \left(1 - \frac{\eta}{b}\right), \tag{C.2}$$

where $\xi = i_0 A_v$ due to negligible mass-transport limitations.

Let us represent the applied harmonic perturbation in the overpotential as

$$\eta(t, x, \omega) = \bar{\eta}(x) + \tilde{\eta}(x, \omega)\exp(i\omega t). \tag{C.3}$$

Substituting equation (C.3) into equation (C.2) and noting that $\bar{\eta}(x)$ is the steady-state solution of the latter, one gets

$$\frac{\partial^2 \tilde{\eta}}{\partial x^2}\exp(i\omega t) = \frac{\tilde{\eta}}{\sigma_{H^+}^{eff}}\left(\frac{\xi}{b} + i\omega C_{dl}\right)\exp(i\omega t). \tag{C.4}$$

Equation (C.4) must hold for all $t$ and $\omega$, and thus the following ordinary differential equation for the perturbation $\tilde{\eta}(x, \omega)$ is obtained:

$$\frac{\partial^2 \tilde{\eta}}{\partial x^2} = \frac{\tilde{\eta}}{\sigma_{H^+}^{eff}}\left(\frac{\xi}{b} + i\omega C_{dl}\right). \tag{C.5}$$

Because only protonic transport is considered, perturbation $\tilde{\eta}(x, \omega)$ is driven through the proton-exchange membrane of the cell. Thus, a boundary condition

$$\tilde{\eta}(0, \omega) = \tilde{\eta}^0(\omega) \tag{C.6}$$

is imposed at the CL-PEM interface ($x = 0$). Since the gas-diffusion layer is not protonically conductive, $-\sigma_{\mathrm{H^+}}^{\mathrm{eff}} \partial \phi_{\mathrm{H^+}}/\partial x = 0$ must be satisfied at the CL-PTL interface ($x = L$). This is equivalent to setting

$$\frac{\partial \bar{\eta}}{\partial x}(L) + \frac{\partial \tilde{\eta}}{\partial x}(L, \omega) \exp(\mathrm{i}\omega t) = 0. \tag{C.7}$$

Protonic flux through the CL-PTL boundary must be zero at steady state as well, and thus $\partial \bar{\eta}/\partial x = 0$ at $x = L$. Therefore, the second term of equation (C.7) must be zero for all $t$ and $\omega$, from where it follows that

$$\frac{\partial \tilde{\eta}}{\partial x}(L, \omega) = 0. \tag{C.8}$$

We will search for the solution to equation (C.5) in the form [56]

$$\tilde{\eta}(x, \omega) = A(\omega) \exp\left((L - x)\tilde{Z}(\omega)\right) + B(\omega) \exp\left(-(L - x)\tilde{Z}(\omega)\right), \tag{C.9}$$

where

$$\tilde{Z}(\omega) = \sqrt{\frac{1}{\sigma_{\mathrm{H^+}}^{\mathrm{eff}}} \left(\frac{\xi}{b} + \mathrm{i}\omega C_{\mathrm{dl}}\right)}. \tag{C.10}$$

Substitution of equation (C.9) into the boundary conditions (C.6) and (C.8) gives

$$A(\omega) = B(\omega) = \frac{\tilde{\eta}^0(\omega)}{\exp\left(L\tilde{Z}\right) + \exp\left(-L\tilde{Z}\right)}, \tag{C.11}$$

although having $A(\omega) = B(\omega)$ is sufficient to derive the impedance.

The volumetric protonic current density (A/cm$^3$) is defined as

$$j_{\mathrm{H^+}} = -\sigma_{\mathrm{H^+}}^{\mathrm{eff}} \frac{\partial^2 \phi_{\mathrm{H^+}}}{\partial x^2} = \sigma_{\mathrm{H^+}}^{\mathrm{eff}} \frac{\partial^2 \eta}{\partial x^2},$$

and thus

$$\tilde{j}_{\mathrm{H^+}}(x, \omega) = \sigma_{\mathrm{H^+}}^{\mathrm{eff}} \frac{\partial^2 \tilde{\eta}}{\partial x^2}(x, \omega) = \sigma_{\mathrm{H^+}}^{\mathrm{eff}} \tilde{Z}^2(\omega)\tilde{\eta}(x, \omega). \tag{C.12}$$

Integration of equation (C.12) from $x = 0$ to $x = L$ results in the current-density perturbation (A/cm$^2$)

$$\tilde{i}_{\mathrm{H^+}}(\omega) = \sigma_{\mathrm{H^+}}^{\mathrm{eff}} \tilde{Z}(\omega) A(\omega) \left(\exp\left(L\tilde{Z}\right) - \exp\left(-L\tilde{Z}\right)\right).$$

Impedance ($\Omega \cdot$ cm$^2$) is computed as

$$Z(\omega) = \frac{\tilde{\eta}(0, \omega)}{\tilde{i}_{\mathrm{H^+}}(\omega)} = \frac{\tilde{\eta}^0(\omega)}{\tilde{i}_{\mathrm{H^+}}(\omega)} = \frac{1}{\sigma_{\mathrm{H^+}}^{\mathrm{eff}} \tilde{Z}(\omega)} \coth\left(L\tilde{Z}(\omega)\right). \tag{C.13}$$

Rearranging equation (C.13), we obtain

$$Z(\omega) = \sqrt{R_{\mathrm{H^+}} Z_{\mathrm{int}}(\omega)} \coth\left(\sqrt{\frac{R_{\mathrm{H^+}}}{Z_{\mathrm{int}}(\omega)}}\right),$$

where $Z_{\text{int}}(\omega)$ and $R_{\text{H}^+}$ are defined in equations (5.8) and (5.10), respectively, and

$$R_{\text{ct}} = \frac{b}{\xi L}, \quad C_{\text{dl}}^* = C_{\text{dl}}L. \tag{C.14}$$

As discussed in the main text, equation (5.10) cannot be used to obtain the effective protonic resistance; it is used here to illustrate the similarity of equations (C.13) and (5.7) only. Note that the charge-transfer resistance defined in equation (C.14) was obtained with the assumption of small overpotential (small operating current). It is equivalent to the charge-transfer resistance computed directly from the Tafel kinetics (2.52),

$$R_{\text{ct}}^{\text{Tafel}} = \frac{\partial \eta}{\partial i} = -\frac{b}{i},$$

when $\eta = 0$. The negative sign in the equation above is due to $i$ being the protonic current density in this derivation.